Imperial College
London

The Spectrum and Term Analysis of Doubly-Ionised Iron

Florence Concepcion Mairey
2022

Department of Physics
Imperial College London

A thesis submitted in part fulfilment of the requirements
for the degree of Doctor of Philosophy in Physics

I declare that the work presented in this thesis is my own research. Where the work is not my own, I have clearly referenced and acknowledged it.

Florence Concepcion Mairey
16 March 2022

The copyright of this thesis and related documents rests with the author and is made available under a Creative Commons Attribution Non-Commercial No Derivatives licence. Researchers are free to copy, distribute or transmit the thesis on the condition that they attribute it, that they do not use it for commercial purposes and that they do not alter, transform or build upon it. For any reuse or redistribution, researchers must make clear to others the licence terms of this work.

Abstract

The study of astrophysical spectra is reliant on accurate atomic data, and there is a need for the atomic data of iron as its spectral lines are present and numerous in many astrophysical sources, due to its high relative abundance and complex spectrum.

This PhD thesis reports the results of the term analysis of doubly-ionised iron (Fe III). A Penning discharge lamp is used to generate the spectrum of Fe III, which is recorded using the Fourier transform spectrometer (FTS) at Imperial College London, UK. The FTS recorded high-resolution Fe III lines in the UV range of $33,826$ cm^{-1} to $65,508$ cm^{-1}. This was supplemented with grating spectral data at high wavenumbers ($55,090$ cm^{-1} to $111,121$ cm^{-1}) from the normal incidence vacuum spectrograph at the National Institute of Standards and Technology in Maryland, USA. The linelists created from the FTS and grating data were wavenumber calibrated using the accurate Fe II Ritz wavelengths produced by Nave & Johansson (2013) [1]. FTS line wavenumbers were calibrated to an accuracy of $5-8.5$ parts per 10^8, depending on the spectrum, with uncertainties of strong lines typically between 0.0024 cm^{-1} and 0.0074 cm^{-1}. The uncertainties of the grating lines are between 0.091 cm^{-1} and 0.86 cm^{-1}.

The classified spectral lines are used in the term analysis to revise 305 Fe III energy level values in configurations $3d^6$, $3d^54s$, $3d^54p$, $3d^54d$, $3d^55s$, and $3d^55d$. The Ritz wavenumbers of 1599 classified Fe III lines were calculated, providing wavenumbers at least an order of magnitude more accurate than previously published linelists. The Ritz wavenumbers for 432 parity-forbidden lines were also calculated. The results of this thesis will be used by astronomers for the identification and analysis of Fe III spectral lines in astrophysical spectra.

Contents

1 Introduction **19**

1.1 The Importance of Spectroscopy in Astrophysics 19

1.1.1 Advancements in Astronomical Instrumentation 19

1.1.2 Atomic Data in Astronomy 21

1.1.3 Experimentally Measured Atomic Data for Astronomy 22

1.1.4 Atomic Databases 23

1.1.5 The Importance of Iron 23

1.1.6 The Importance of Doubly-Ionised Iron 25

1.2 Experimental Measurements of Fe III 27

1.2.1 Previous Studies in Fe III 27

1.2.2 New Fe III Measurements 30

1.3 Thesis Structure 31

2 Laboratory Measurements **33**

2.1 The Imperial College VUV Fourier Transform Spectrometer 33

2.1.1 Finite Aperture Size 36

2.1.2 Digital Sampling of the Interferogram 36

2.1.3 FTS Experimental Arrangement 37

2.2 NIST Normal Incidence Vacuum Spectrograph (NIVS) 38

2.2.1 Detector Plates 41

2.3 The Penning Discharge Lamp 41

2.3.1 PDL Design 42

2.4 Standard Deuterium Lamps for Intensity Calibration 47

2.5 Spectrometer Comparison 49

2.6 IC VUV FTS Experimental Details 51

2.6.1 Preparing the FTS 51

2.6.1.1 Filters and Detectors 52

2.6.2 Preparing the PDL 55

2.6.2.1 Optimal Current and Buffer Gas Pressure 57

2.6.2.2 Neon Spectral Lines 60

2.6.2.3 Buffer Gas Type 60

2.6.2.4 Reusing Cathodes and Cleaning the PDL 60

2.7 Final Measurements 64

2.7.1 FTS Measurements . . . 64
2.7.2 Grating Measurements . . . 64
2.8 Summary . . . 66

3 Linelist Preparation **67**
3.1 The FTS Linelist . . . 67
3.1.1 Spectrum Extraction . . . 67
3.1.1.1 Co-adding Interferograms . . . 67
3.1.1.2 Phase Correction . . . 68
3.1.1.3 Signal-to-Noise Ratio . . . 68
3.1.1.4 Line Shape . . . 71
3.1.1.5 Line fitting . . . 74
3.1.2 Intensity Calibration . . . 75
3.1.2.1 PDL MgF_2 window . . . 76
3.1.2.2 Instrument Response Functions . . . 77
3.1.2.3 Common intensity scale . . . 79
3.1.3 Wavenumber Calibration . . . 79
3.1.4 Wavenumber Uncertainties . . . 84
3.1.4.1 Calibration Uncertainty . . . 84
3.1.4.2 Statistical Uncertainty . . . 87
3.1.4.3 Total Wavenumber Uncertainty . . . 87
3.1.5 Merging FTS Linelists . . . 87
3.2 The Grating Linelist . . . 88
3.2.1 Spectrum Selection . . . 88
3.2.2 Linelist Extraction . . . 91
3.2.3 Intensity Scale . . . 94
3.2.4 Wavelength Calibration of Grating Spectrum . . . 95
3.2.5 Wavelength Uncertainties . . . 97
3.2.6 Merging Grating Linelist . . . 98
3.3 Comparison of the FTS and Grating Linelists . . . 98
3.4 Comparison to Ekberg wavenumbers . . . 100
3.4.1 Comparison of Ekberg to FTS line wavenumbers . . . 100
3.4.2 Comparison of Ekberg to grating line wavenumbers . . . 101
3.5 Summary . . . 103

4 Term Analysis of Fe III **105**
4.1 Atomic Theory . . . 105
4.1.1 The Energy Level Structure of the Singly Excited Fe III system . . . 105
4.1.2 ***LS*** coupling . . . 107
4.1.3 Selection Rules . . . 108
4.1.3.1 Electric Dipole Radiation Selection Rules . . . 108
4.1.3.2 LS coupling Selection Rules . . . 108
4.2 Term Analysis Method . . . 109

4.2.1 Classification of Observed Spectral Lines . . . 110
4.2.2 Energy Level Optimisation . . . 112
4.2.3 The *STRANS-LOPT* Iterative Process . . . 113
4.2.4 Search for New Energy Levels . . . 113
4.3 Term Analysis Results . . . 114
4.3.1 Revised Energy Levels for Fe III . . . 115
4.3.2 The Classified Fe III Linelists . . . 121
4.3.3 Ritz Wavenumbers of Parity-Forbidden Fe III Lines . . . 126
4.3.4 Reassignment of the Energy Level Labels . . . 127
4.3.5 Summary . . . 127

5 Conclusions and Future Work **129**
5.1 New Classified Linelists for Fe III . . . 129
5.2 Revised Energy Levels for Fe III . . . 130
5.3 Future Work . . . 131
5.3.1 Continuation of the Term Analysis of Fe III . . . 131
5.3.1.1 Extension of the FTS linelist . . . 131
5.3.1.2 Extension of the grating linelist . . . 131
5.3.1.3 Revision of the Remaining Levels and New Level Search . 133
5.3.2 Transition Probabilities of Parity-forbidden Fe III lines . . . 133
5.3.3 Further Investigation of Fe II Lines and Energy Levels . . . 133
5.4 Conclusion . . . 134

References **135**

Appendices **144**
A Energy Levels of Fe III . . . 145
B Fe III Classified FTS Linelist . . . 159
C Fe III Classified Grating Linelist . . . 194
D Parity-forbidden Fe III Transitions . . . 262
E FTS Spectral Plots . . . 279
E.1 Fe327 . . . 280
E.2 Fe116 . . . 285
E.3 Fe831 . . . 291
E.4 Fe832 . . . 297
E.5 Fe903 . . . 302
E.6 Fe103 . . . 307
E.7 Fe121 . . . 313
E.8 Fe203 . . . 316
F Grating Plates and Spectral Plots . . . 321
F.1 Image x1015_plate2a, Track 5.1, 5-minute exposure . . . 322
F.2 Image x1015_plate2a, Track 5.1, 45-minute exposure . . . 330
F.3 Image x1015_plate2b, Track 5.1, 5-minute exposure . . . 338

F.4 Image x1015_plate2b, Track 5.1, 45-minute exposure 346
F.5 Image x1015_plate1b, Track 5.3, 5-minute exposure 354
F.6 Image x1015_plate1b, Track 5.3, 45-minute exposure 363
F.7 Image x1015_plate2a, Track 5.3, 5-minute exposure 372
F.8 Image x1015_plate2a, Track 5.3, 45-minute exposure 380
F.9 Image x1015_plate2b, Track 5.3, 5-minute exposure 388
F.10 Image x1015_plate2b, Track 5.3, 45-minute exposure 396

List of Figures

1.1 Improved spectra of χ Lupi, from Leckrone *et al.* [14] 20
1.2 Binding energies per nucleus for atoms of astrophysical interest. 24
1.3 Relative elemental Solar System abundances. 24
1.4 The ion fraction of some iron-group elements with respect to temperature. 26
1.5 A section of the spectrum of Gamma Pegasi from Pickering *et al.* [61]. . . . 26
1.6 Fe III energy level term diagram 29

2.1 Michelson interferometer diagram. 34
2.2 Interferogram and spectrum of the PDL with iron cathodes and the standard deuterium lamp. 35
2.3 Sampling of the interferogram at regular intervals. 37
2.4 Diagram of the FTS arrangement. 39
2.5 Image of the nosepiece of the FTS. 39
2.6 Image of the NIST NIVS 39
2.7 Segment of scan of detector plate from NIST NIVS 40
2.8 Schematic Diagram of the Penning Discharge Lamp. 42
2.9 Plan and side photographs of the PDL 43
2.10 Photographs of the PDL iron cathodes. 45
2.11 Photograph of the top view of the PDL without the top cathode in place. . 45
2.12 A comparison of the spectra observed from the 'working' deuterium lamp and the 'calibrated' deuterium lamp. 48
2.13 The filtered deuterium lamp spectra of repeated measurements. 48
2.14 Comparison of the iron spectrum in the FTS spectrum and the grating spectrum at $56,000$ cm^{-1} 50
2.15 Wavenumbers of Strong Fe II and Fe III Spectral Lines. 53
2.16 PMT quantum efficiencies and filters' transmittance. 53
2.17 The filtered spectra of the deuterium lamp with various filters, and the calculated response functions using the spectra observed. 54
2.18 Intensity-normalised spectra of deuterium lamp through 185 nm filters. . 56
2.19 Iron cathodes after failed experiments. 57
2.20 The SNR of the iron lines in the PDL varying with current and pressure. . 59
2.21 Photographs of the PDL plasma 61
2.22 The cathodes and anode after reusing cathodes in the PDL. 63

3.1 The polynomial fits used for the phase correction of the IC VUV FTS spectra Fe327, Fe116 and Fe831 . . . 69
3.2 The polynomial fits used for the phase correction of the IC VUV FTS spectra Fe832, Fe903 and Fe103 . . . 70
3.3 The polynomial fit used for the phase correction of the IC VUV FTS spectrum Fe121. . . . 71
3.4 The isotopic structure in the Fe II line at 9999.7 cm^{-1}. . . . 72
3.5 A photograph of the MgF_2 window located between the PDL and nose piece. 76
3.6 The deuterium spectra observed using the PDL MgF_2 window, new MgF_2 window and no MgF_2 window . . . 77
3.7 The observed deuterium lamp, filtered spectrum and deuterium lamp calibration data. . . . 78
3.8 The instrument response functions for the IC VUV FTS data. . . . 78
3.9 The ratio of the equivalent widths for lines in the Fe103 to the Fe327 spectra. 80
3.10 Wavenumber calibration fits for FTS spectra calibrated with Fe II . . . 83
3.11 The upper energy levels of the Fe II lines used for calibration compared to their wavenumber. . . . 85
3.12 The fits for the wavenumber calibration of Fe831 using Fe II lines with the upper energy levels $> 55,000$ cm^{-1} and $< 55,000$ cm^{-1}. . . . 86
3.13 The fits for the wavenumber calibration of Fe116 using Fe II lines with the upper energy levels $> 55,000$ cm^{-1} and $< 55,000$ cm^{-1}. . . . 86
3.14 Plot of wavelength ranges of the scanned images for the Tracks 5.1 and 5.3 on plates x1015. . . . 89
3.15 The 5-minute and 45-minute exposures of a segment of the x1015 plate1b image for Track 5.3 . . . 90
3.16 An image of the computer display screen of the ASPAS software I edited for this project. . . . 92
3.17 Images of problematic lines in grating spectra. . . . 93
3.18 Track 5.1 in the images x1015_plate2a and x1015_plate2b . . . 95
3.19 Calibration polynomial and residuals for grating spectra . . . 96
3.20 Wavenumber comparison of the FTS and grating linelists. . . . 99
3.21 Comparison of the Iron Spectrum in the FTS Spectrum and the Grating Spectrum at $57,000$ cm^{-1} . . . 99
3.22 Comparison of the FTS wavenumbers with Ekberg wavenumbers. . . . 100
3.23 The comparison of the Ekberg and grating wavenumbers in the $55,700$ $cm^{-1} < \sigma < 71,800$ cm^{-1} region. . . . 102
3.24 The comparison of the Ekberg and grating wavenumbers in the $82,200$ $cm^{-1} < \sigma < 111,100$ cm^{-1} region. . . . 102

4.1 The term diagram displaying the levels that have been revised in this thesis. 106
4.2 Flow chart of the Term Analysis procedure . . . 111
4.3 The groups of energy levels connected by FTS lines. . . . 115

4.4 The number of lines used for each level in the energy level optimisation process. 116
4.5 The difference between the revised and previously published energy levels. 118
4.6 The difference between the revised and previously published energy levels with the revised energy level uncertainties with respect to the ground level. 119
4.7 The difference between the revised and previously published energy levels with the revised energy level uncertainties with respect to the energy level system. 120
4.8 The difference between the observed and Ritz wavenumbers of the lines in the classified FTS linelist. 123
4.9 The difference between the observed and Ritz wavenumbers of the lines in the classified grating lines. 124
4.10 Comparison of the classified Fe III line wavenumbers from this work with the linelist wavenumbers published by Ekberg 125
4.11 Comparison of the classified Fe III line wavenumbers from this work with the linelist wavenumbers published by Corliss & Sugar (1982) [87] 126

List of Tables

1.1 Fe III transitions and their spectral regions 30

2.1 The angles of the grating and detector plates and the corresponding wavelength ranges for NIST NIVS 40
2.2 Comparison of image detector plates 41
2.3 Comparison of Spectrometers' capabilities 49
2.4 The detector and filter combinations tested to optimise the SNR of Fe III lines 54
2.5 Data recorded without cleaning the PDL or replacing used cathodes. . . . 62
2.6 The selected iron spectra for use in the final FTS linelist. 65
2.7 Selected grating data recorded at NIST NIVS 66

3.1 Details of the polynomial fit for phase correction of the IC VUV FTS spectra 68
3.2 Summary of the FTS linelists used in the master linelist 75
3.3 Deuterium data recorded for intensity calibration of FTS data 78
3.4 Details of the wavenumber calibration of FTS spectra. 82
3.5 The correction factors calculated for Fe116 and Fe831 using a selection of Fe II lines 85
3.6 Table of wavelength ranges of the scanned images for the Tracks 5.1 and 5.3 on plates x1015 89
3.7 Description of labels used in the grating linelist 93
3.8 Details of the polynomial fits for the grating linelists. 97

4.1 Selection rules for magnetic dipole (M1) and electric quadrupole (E2) transitions. 127
4.2 New level labels for Fe III energy levels 128

Abbreviations and Units

EW	equivalent width
FTS	Fourier Transform Spectrometer
FWHM	full width at half maximum
HCL	Hollow Cathode lamp
IC	Imperial College
IR	infrared
NIST	National Institute of Standards and Technology, USA
NIST NIVS	NIST Normal Incidence Vacuum Spectrograph
PDL	Penning Discharge lamp
PMT	Photomultiplier tube
SNR	signal-to-noise ratio
VUV	vacuum ultraviolet ($\lambda < 2000$ Å, $\sigma > 50,000$ cm^{-1})

Units:
1 nm = 10 Å.
The wavenumber, σ (cm^{-1}), and wavelength, λ (Å), relationship in vacuum is

$$\sigma\ [\text{cm}^{-1}] = \frac{10^8}{\lambda\ [\text{Å}]}\ .$$

Chapter 1

Introduction

1.1 The Importance of Spectroscopy in Astrophysics

Spectroscopy is essential in astrophysics with ground and space-based telescopes recording high-resolution spectra throughout the electromagnetic spectrum. All fields of astrophysics rely on spectroscopy, from the detection of molecules essential to life on exo-planets, to the study of galactic evolution [2, 3]. Astrophysical spectra are used to decipher the composition and evolution of astrophysical objects, mechanisms and processes, including nebulae, exo-planets, stars, supernovae, galaxies, and Active Galactic Nuclei (AGN). Every element and molecule, and their ionisation states, has a unique spectrum which allows for the determination of properties of astronomical objects, including chemical compositions, temperatures and velocities.

1.1.1 Advancements in Astronomical Instrumentation

Huge advancements have been made in the capabilities of astronomical telescopes and their spectrographs in the last few decades [4]. An example of the dramatic advancements in space-based instrumentation can be seen in Figure 1.1, which displays the spectrum of χ Lupi as observed by the International Ultraviolet Explorer (IUE) and by the newer Goddard High Resolution Spectrograph (GHRS) on the Hubble Space Telescope (HST). The HST provided a much higher resolution spectrum, enabling the observation and identification of spectral lines.

Current telescopes record high-resolution spectral data from the vacuum ultraviolet (VUV, $\lambda < 2000$ Å, $\sigma > 50,000$ cm^{-1}) into the infrared (IR) regions, including the Space Telescope Imaging Spectrograph (STIS) on the HST, (1150 Å to 3100 Å with resolving power, R $\sim 30,000 - 114,000$ [5]), the High Resolution Echelle Spectrometer (HIRES) at the ground-based Keck Observatory (0.3 to 1.0 μm with R $\sim 25,000 - 85,000$ [6]) and the CRyogenic high-resolution InfraRed Echelle Spectrograph (CRIRES) installed on the ground-based Very Large Telescope array (VLT) (0.95 to 5.3 μm with R $\sim 100,000$ [7]). Many large telescopes also now have a multi-object spectrograph (MOS) which allows for the spectra of multiple astronomical sources to be recorded within a single exposure, including WEAVE [8], 4MOST [9], and the Near-Infrared Spectrograph (NIRSpec) on the

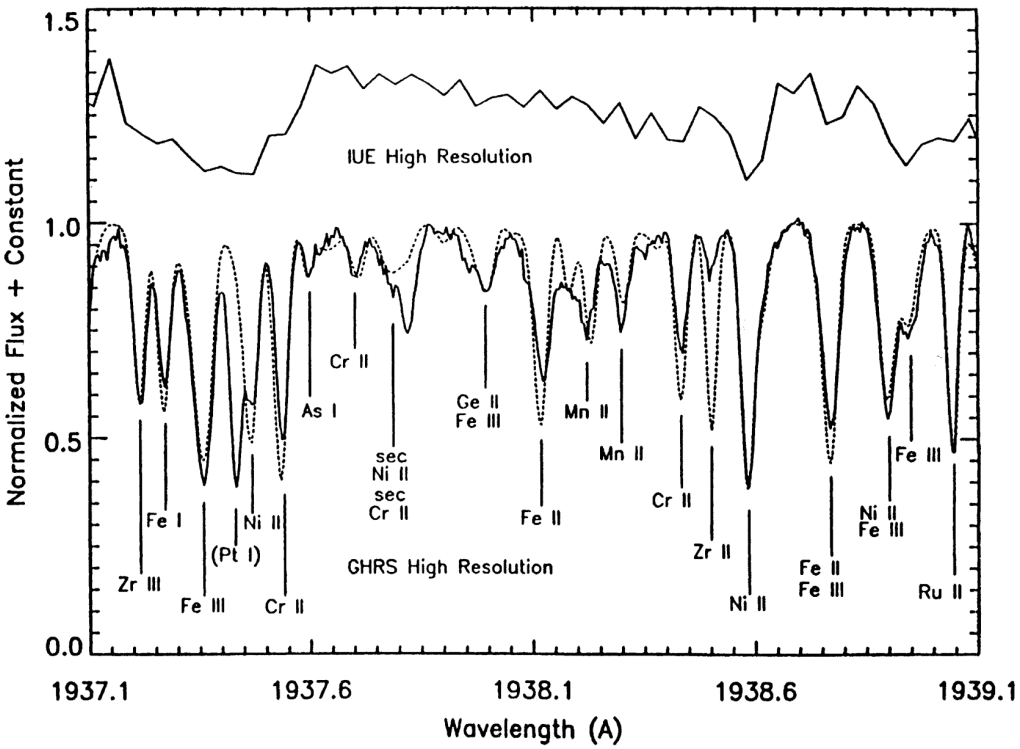


Figure 1.1: This image from Leckrone *et al.* [14] displays the high dispersion spectra of χ Lupi, showing a comparison between the International Ultraviolet Explorer (IUE) satellite data (top) and the improved data from the Goddard High Resolution Spectrograph (GHRS) on the HST (bottom, solid line). The dashed line displayed the theoretical synthetic spectrum.

James Webb Space Telescope (JWST) [10].

Advancements in high-resolution instruments and in multi-object spectrographs enable current and future spectroscopic surveys, including APOGEE [11], Gaia-ESO [12] and GALAH [13], to collect a vast amount of high resolution data with the aim to measure high precision stellar and galactic chemical abundances.

The Advanced Spectral Library (ASTRAL) [15] project is devoted to the collection of the high quality UV spectra from STIS for a varied sample of stars with the aim to build a library for astrophysical study. This collection of high resolution data in the ultraviolet spectrum is used to test current spectral models of stars, improving current synthetic stellar spectra, and providing updated chemical abundances, an example of which can be seen at Nielsen *et al.* [16]. UV spectroscopy is particularly important for the study of stars, as it can reveal processes unseen in the visible region [17]. Future missions in the UV include the Habitable Exoplanet Observatory (HabEx) [18] and the Large UV/Optical/Infrared Surveyor (LUVOIR) [19], which have science goals in a broad range of astrophysics including the observation of Solar System bodies; the discovery and characterisation of exoplanets (and determining habitability); the study of galaxy formation and evolution; and the study of star and planet formation.

1.1.2 Atomic Data in Astronomy

The applications of spectroscopy are numerous and the study of our universe is reliant on the successful analysis of astrophysical spectra. Properties of astronomical objects that can be defined from spectra include, composition, chemical abundances, temperatures, velocity of motion, orbital velocity and magnetic field strength. However, the high quality astrophysical spectral data collected cannot be fully analysed without accurate atomic data and, in chemical abundance analyses, realistic models [20].

The accuracies of astrophysical models also directly rely on the quality of the input atomic data [21]. For example, to better understand stellar spectra, models are created and tailored to observed spectral features using available theoretical and experimental atomic data, producing synthetic spectra [21]. An example of a calculated synthetic spectrum compared to the observed spectrum can be seen in Figure 1.1 for χ Lupi. Many of the spectral features of the synthetic spectrum align with the observed spectrum. Therefore, several spectral lines can be identified and properties of the astronomical object such as chemical abundances, temperature, and rotational velocity may also be determined. However, there are features of the calculated synthetic spectrum that do not align with the observed spectrum. This could be due to incorrect or missing atomic data input into the model that created the synthetic spectrum or due to the use of an incorrect stellar model.

Missing or inaccurate atomic data lead to the misidentification of spectral lines and contribute large uncertainties in chemical abundances. Missing data may be obvious when comparing spectra line by line, but when a spectrum produced using millions of lines does not fit the observed, it is difficult to determine where the inaccuracies lie:

> " ... limited atomic data and simplistic modelling means that we cannot derive reliable elemental masses from the analysis carried out so far. "
>
> (Smartt *et al.* [22], a study on the electromagnetic counterpart to a binary neutron star merger.)

To get the full scientific benefit, astronomical spectra must be analysed using accurate and precise atomic data. The atomic data used to analyse astronomical spectra is still often incomplete or with large uncertainties. An example of this is the Gaia-ESO Survey pipeline. Due to the lack of atomic data, in some cases, a singular atomic line is used in the identification and abundance calculation of elements in stellar spectra [23].

Our understanding of stellar evolution and solar system formation rely on the successful analysis of the composition of our closest star, the Sun [24]. With the release of new and more accurate atomic data, previously determined chemical abundances in the Sun and other stars have been recalculated [25–27]), but there continues to be unidentified spectral lines in the solar spectrum [2, 28, 29].

In Kasen *et al.* [30], the lack of accurate atomic data hinders the study of the optical counterpart of the first binary neutron star merger, AT2017gfo, detected via gravitational waves. It is theorised that neutron star mergers account for the production of lanthanides, and a calculated neutron star merger rate could solve the discrepancy between the ex-

pected and observed r-process abundances [31]. However, the absence of accurate atomic data has led to conflicting conclusions on the chemical abundances [22, 32]:

> " Uncertainties in the current atomic line data sources limit... spectral analysis, but with improved atomic inputs a more detailed compositional breakdown is within reach. "
>
> (Kasen *et al.* [30], a study on the origin of heavy elements.)

1.1.3 Experimentally Measured Atomic Data for Astronomy

The improvements in astronomical spectroscopy have resulted in a tremendous need for high-accuracy atomic data [33]. The atomic data required to fully analyse astronomical spectra includes atomic energy level values, wavelengths of transitions, transition probabilities and isotope structure [33] which can be experimentally measured within a laboratory.

The spectral line wavelengths can be experimentally measured and used to determine the energy level structure. The accurate energy levels are then used to calculate the transition Ritz wavelengths (calculated as the energy difference between two energy levels), which have uncertainties lower than the spectral lines measured directly in the laboratory. Wavelengths of high accuracy can then be used as wavelength standards to calibrate observed astronomical or laboratory spectra. Using the energy level values, the Ritz wavelengths of parity forbidden lines can also be calculated. This is particularly important as these lines arise from transitions that violate the selection rules for electric dipole radiation and, therefore, cannot be observed in a laboratory environment (discussed further in Section 4.1.3). The wavelengths of forbidden lines are essential to the study of low-density astrophysical plasmas.

Previously published energy levels can be missing, inaccurate or imprecise, resulting in a lack of accurate wavelengths or incomplete linelists. The accuracy of wavelengths should be of better quality than the astronomical spectra obtained in order to ensure its successful analysis. An improvement of an order-of-magnitude in accuracy is needed for wavelengths and energy levels [34].

The transition probabilities or oscillator strengths ($\log(gf)$ values) are used to determine the abundance of an element from the intensity of a spectral line. These are essential to stellar chemical abundance calculations. Transition probabilities are calculated using branching fractions (BFs) and mean lifetimes. BFs are calculated by determining relative line intensities, and the mean lifetime of an upper energy level is the time in which the electron population of the level decays to $\frac{1}{e}$ of its initial value [20]. Both BFs and mean lifetimes can be experimentally measured. Transition probabilities with an uncertainty of < 10 % are needed for stellar chemical abundance calculations [35] and, ideally, are experimentally measured with uncertainties of a few percent [34].

In general, the more complete accurate atomic data becomes, the better chance for the successful analysis of astronomical spectra, including spectral line identification and the determination of spectral features such as blends. This is key around important spectral lines which are used to determine other properties of astronomical objects. For example,

a forbidden oxygen line widely used for abundance calculations was determined to be blended with a nickel line which resulted in inaccurate oxygen abundances in metal-rich stars, as the intensity contribution due to the previously neglected nickel line had not been taken into account (see Allende Prieto *et al.* (2001) [36]). The nickel line structure also had some isotopic shift (discussed in Section 3.1.1.4) present which must also be experimentally measured [37] to successfully decipher each line intensity and therefore the correct elemental abundance.

This PhD project focusses on experimentally measuring the transition wavelengths to a high accuracy and using them to determine the energy level structure of Fe III (discussed further in Section 1.2.2).

1.1.4 Atomic Databases

It is becoming increasingly important to communicate new data from the atomic experimentalists and theorists to the astrophysicists that need it [20, 38]. Atomic data are usually accessed by astronomers via atomic databases, such as BRASS [39], CHIANTI [40], NIST ASD [41], Kurucz [42], VALD [43], and VAMDC [44]. Software directly makes use of these databases to analyse and model astronomical spectra. An example of this is the TARDIS [45] code which generates synthetic spectra using CHIANTI, NIST ASD and Kurucz databases for the analysis of supernovae and, more recently, kilonovae [22, 46].

It is important that these atomic databases contain the most up-to-date information for accurate modelling. However, astronomers are not always aware that atomic databases may not be quality checked for accuracy and precision, or may not contain the latest release of experimentally measured atomic data.

1.1.5 The Importance of Iron

High mass stars will undergo "Silicon burning" in the final stages of stellar nucleosynthesis. This exothermic process involves silicon nuclei (^{28}Si) fusing with helium, creating heavier elements until nickel (^{56}Ni) is produced. The next predicted step of ^{56}Ni to ^{60}Zn is endothermic, and so it is not favourable for nickel or heavier nuclei to undergo fusion within a star. This is due to the binding energies of heavier nuclei providing an energy deficit. These binding energies are shown in Figure 1.2. However, ^{56}Ni is not stable and undergoes radioactive (beta) decay until the formation of stable iron, ^{56}Fe [50]. As seen in Figure 1.2, ^{56}Fe has the third highest mean binding energy, and so it is favourable to stop fusion here [47]. Stellar nucleosynthesis provides an explanation for the high abundance of iron and other iron-group elements (chromium, manganese, cobalt, and nickel) in comparison to heavier elements. The relative elemental abundances are shown in Figure 1.3 where the iron peak has been highlighted.

Although lower mass elements such as hydrogen and helium are far more abundant than the iron-group elements, stellar spectra are dominated by iron-group elements. These elements have an atomic structure described as complex (see Section 4.1), which results in the production of many more spectral lines than lighter atoms [51].

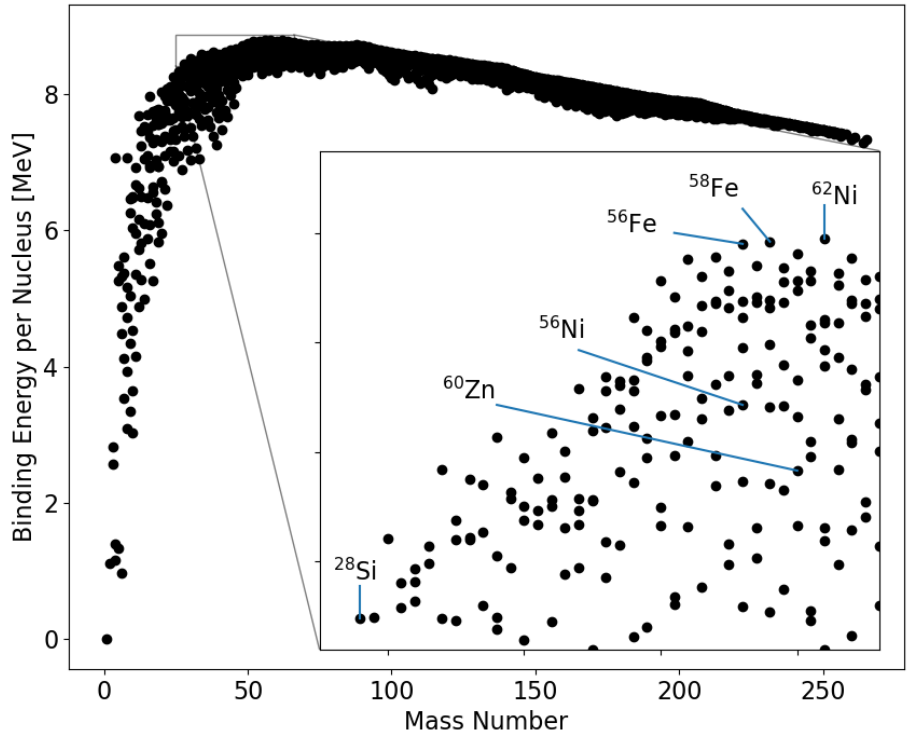


Figure 1.2: Binding energy per nucleus vs mass number. Note that ^{56}Fe is close to the peak of the curve, with only ^{62}Ni and ^{58}Fe nuclei being slightly more stable [47]. Data from [48].

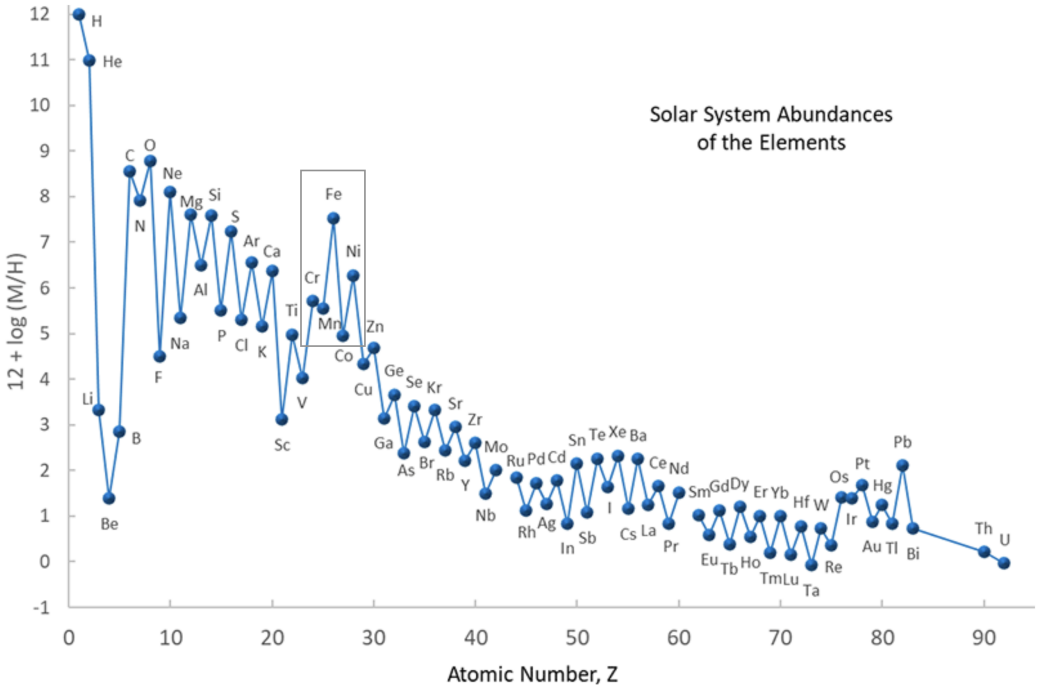


Figure 1.3: Relative elemental Solar System abundances with iron-group elements highlighted (Figure 4 from Lodders [49]).

The atomic data of iron is needed for the successful analysis of stellar spectra (see examples in Grevesse & Sauval (1999) [52] and Nave *et al.* (2013) [53]). Iron spectroscopic features are used to measure stellar metallicity and iron abundance from which overall metal content and other elemental abundances can be calculated [24, 54]. The absorption and emission features of iron are seen in every stellar spectral type, with Fe I and Fe II spectral lines dominating the spectra of F-type and cooler stars. For example, about 30% of the identified lines in the spectrum of our Sun belong to iron (higher than any other element) [55]. Likewise, in the red giant Arcturus (K star) 86% of the features in the 2250 Å to 2930 Å region of the spectrum are due to Fe II [56].

1.1.6 The Importance of Doubly-Ionised Iron

Hotter stars, (type O and B), have temperatures ranging from 10,000 K (10^4 K) to over 30,000 K ($10^{4.48}$ K). This temperature range has the highest ion fraction of singly, doubly and even triply ionised iron-group elements. Figure 1.4 shows these ion fractions for Cr, Mn, Fe and Co. As expected, the copious spectral lines of Fe III are seen in hot stars and are the cause of the most prominent features present in early B stars, excluding hydrogen and helium [57, 58]. An example of the singly and doubly-ionised iron-group elements dominating the spectrum of a B-type star can be seen in Figure 1.5. It displays the observed and synthetic spectra of the star Gamma Pegasi with over 80 identified spectral lines.

The *ASTRAL-II: Hot Stars* library project [17] focuses on the UV spectra of stars with stellar classification between type early-O and early-A, where in particular there are highly-ionised iron-group element lines present [55]. The project is in need of new accurate, experimentally measured atomic data for doubly ionized iron-group elements, including Fe III.

The need for accurate Fe III atomic data is not limited to the study of stellar spectra, as Fe III lines are observed in many astronomical objects including AGN, quasars and nebula [62–64]. As iron is key in the final stages of stellar nucleosynthesis, its atomic data are also vital in supernova formation calculations and in the study of supernovae remnants [65–67].

In the absence of experimentally measured atomic data, theorists have produced atomic data for astrophysicists using previously measured experimental data [64, 68, 69]. These, however, are inaccurate for Fe III as stated by Laha *et al.* [64]:

> " We conclude that the existing discrepancies between theory and observation for Fe III line ratios in nebular plasmas cannot be fully resolved using currently available atomic data. "

For the study of Fe III, the atomic structure cannot be precisely determined by current theoretical models, due to its complex structure. Therefore, the spectrum of Fe III must be measured via experimental laboratory measurements to obtain accurate wavelengths and energy levels. This experimentally measured atomic data can then be used to improve atomic models and future theoretical atomic data [70–72].

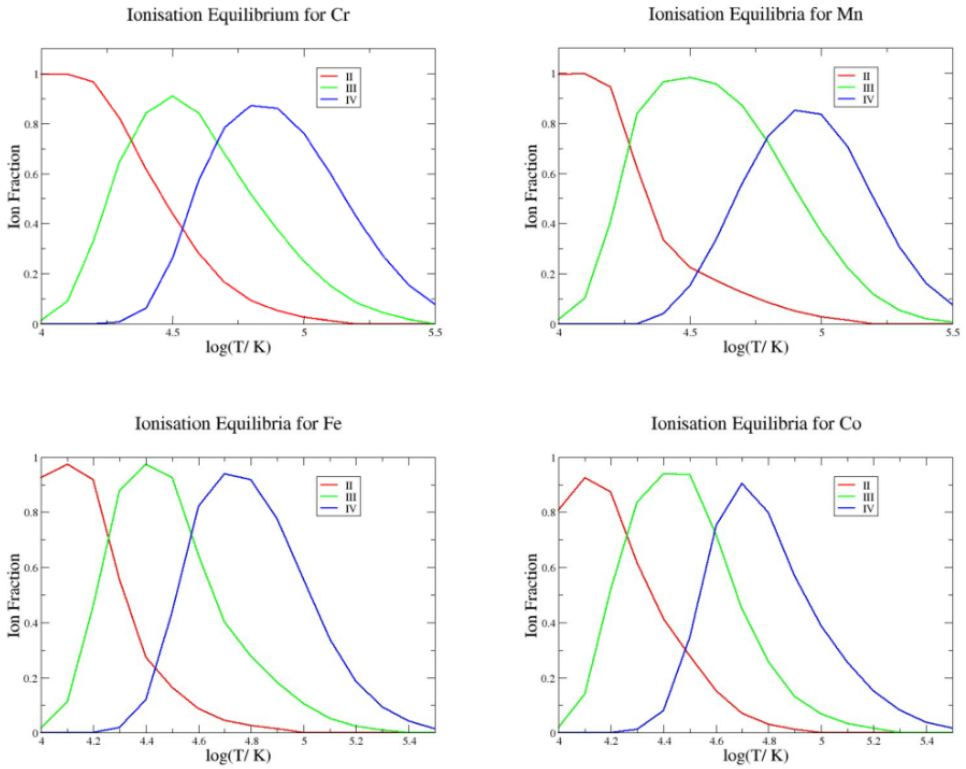


Figure 1.4: The ion fraction of the iron-group elements chromium, manganese, iron and cobalt with respect to temperature. Image from Liggins [59] using data from Mazzotta, P. *et al.* [60].

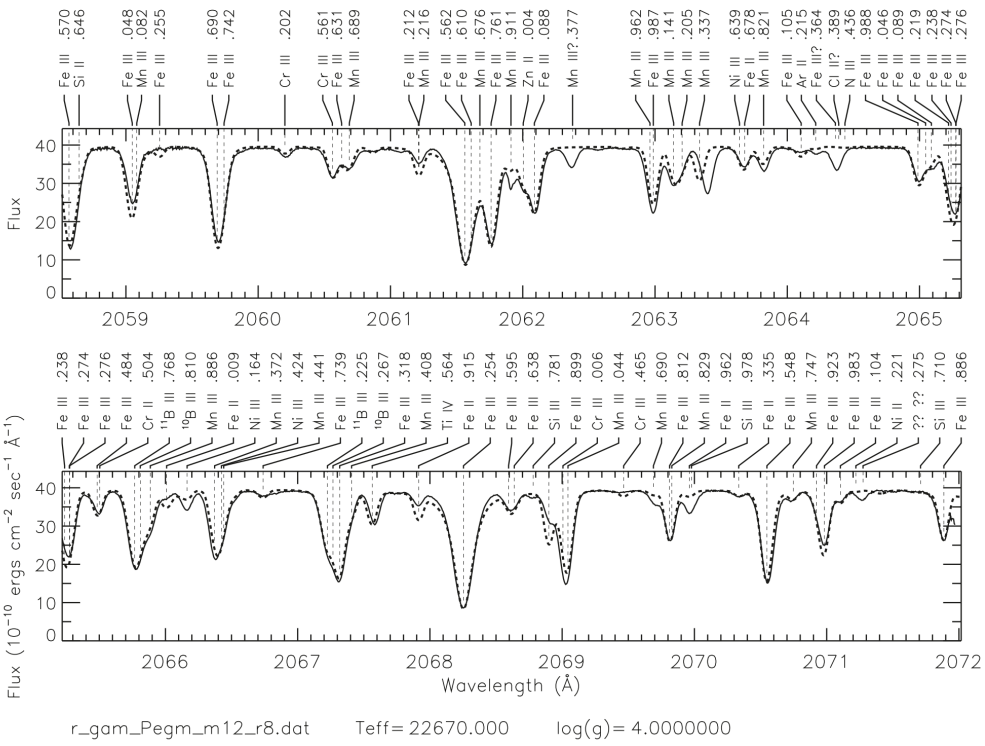


Figure 1.5: A section of the spectrum of Gamma Pegasi (B-type) from Pickering *et al.* [61], with identified transitions. It was observed using the STIS (solid black curve), and compared to synthetic spectra (dashed curve).

1.2 Experimental Measurements of Fe III

As the collection of spectra from space has become higher quality than that experimentally measured within laboratories, astrophysicists are limited by the lack of research in atomic data within a laboratory setting [2, 30, 38]. There is a need for laboratory measured atomic data from IR to UV [4, 34, 73–75].

The Spectroscopy group at IC, in collaboration with NIST, has been publishing new atomic data and improving the accuracy of previously published wavelengths and energy levels by an order of magnitude. The neutral and singly ionised iron-group elements have been studied, with new accurate wavelengths and energy levels published [76–82], and the study of doubly-ionised iron-group elements has begun [83–85]. A summary of the progress on the iron-group elements can be found in Pickering *et al.* (2020) [4]

My PhD project will record the emission spectrum of Fe III. The previous studies in Fe III and the atomic data needed for the term analysis of Fe III are discussed in Section 1.2.1 and 1.2.2, respectively.

1.2.1 Previous Studies in Fe III

There have been previous studies into the spectral emission lines and atomic structure of Fe III. In 1942, Edlén & Swings [57] studied the spectrum of Fe III in the range 500 Å to 6500 Å ($\sim$15,000 cm^{-1} to 200,000 cm^{-1}), recorded with a grazing-incidence spectrograph, a normal-incidence spectrograph and a quartz-prism spectrograph, using a spark between pure iron rods in vacuum or in nitrogen at a pressure of $1/2$ atm. Edlén & Swings classified approximately 1500 spectral lines, corresponding to 320 energy levels. Spectral lines were observed connecting the majority of the theoretically predicted lowest lying energy levels with the configurations $3d^6$, $3d^5 4s$ and $3d^5 4p$ (see Section 4.1 for details on atomic structure). However, many of the transitions between the $3d^6$ and $3d^5$ $4p$ levels were observed as parts of unresolved blends. Lines to the 4d and 5s energy levels were unobserved, except for those in the (^{6}S) parent term system. No uncertainties were published for the spectral lines or the calculated energy level values.

In 1955, Glad [86] experimentally measured lines in the 2600 Å to 8600 Å range ($\sim$12,000 cm^{-1} to $\sim$38,000 cm^{-1}) with a large glass-prism spectrograph using a hollow cathode discharge. The measured spectral lines have an error estimated to be < 0.02 Å for the well-measured lines, and in the range of 0.02 Å to 0.05 Å for the remaining lines. Glad built on the work of Edlén & Swings, classifying over 2000 Fe III lines, of which approximately 800 were newly-classified, and determining the energy levels of $3d^5 4d$, $3d^5 5s$, $3d^5 5d$, $3d^5 5p$ and $3d^5 6s$. Further to this, Glad determined the configuration terms $3d^5 5f$, $3d^5 6p$, $3d^5 6d$, $3d^5 6g$, $3d^5 6h$ and $3d^5 7s$ for the (^{6}S) parent term system and the ionisation potential of Fe III at 247221 cm^{-1}.

Corliss & Sugar (1982) [87] compiled an Fe III energy level list by combining the energy level lists from Edlén & Swings (1942) [57] and Glad (1955) [86].

Ekberg (1993)

Ekberg (1993) [88] analysed the spectrum of Fe III, recorded using a low voltage sliding spark discharge on the Normal Incidence Vacuum Spectrograph at the National Institute of Standards and Technology, USA (NIST NIVS, Section 2.2). Ekberg observed over 2700 lines in the wavelength range 500 Å to 2105 Å (∼48,000 cm^{-1} to 200,000 cm^{-1}), of which 1500 were previously unobserved, and assigned them a wavelength uncertainty of 0.005 Å. Line intensities were judged by estimating the blackening on the photographic plates the spectra were recorded on and were not corrected for any instrument efficiencies. Outside of this range, >2105 Å (< 48,000 cm^{-1}), Ekberg supplemented his linelist with over 500 lines from Edlén & Swings [57] and Glad [86], assigning the line uncertainties between 0.020 Å and 0.050 Å.

Ekberg determined 29 new levels, with all but 7 of the theorised energy levels in the $3d^6$, $3d^54s$, $3d^54p$ configurations published. The uncertainty for 75% of energy levels determined by Ekberg is < 0.15 cm^{-1} and for the remaining levels < 0.45 cm^{-1}. Ekberg planned to determine the energy level values of the $3d^54d$ and $3d^55s$ configurations, but could not as the lines were saturated on the detector plates.

Pickering (1997)

J. C. Pickering used the Imperial College Vacuum Ultraviolet Fourier Transform Spectrometer (IC VUV FTS, Section 2.1) with the Penning Discharge Lamp (PDL, Section 2.3) to measure the Fe III spectrum in the $\sim 35,000$ cm^{-1} to $\sim 56,000$ cm^{-1} (~ 1800 Å to ~ 2800 Å) region. This region contains the transitions between the $3d^54s$ and $3d^54p$ levels, with wavelength uncertainties of ~ 0.0005 Å, an order of magnitude improvement over the work of Ekberg [88]. However, no intensity data was recorded to take into account the instrument efficiency. Pickering also measured the Fe III spectrum in the IR and visible regions (σ <28,000 cm^{-1}, $\lambda > 3571$ Å) using the FTS at NIST, including intensity calibration data. This spectral region contains the lines due to transitions between the higher-lying energy levels of Fe III, such as $3d^54d$, $3d^55s$, $3d^55p$, $3d^55d$ and $3d^56s$. No linelists were made from these spectra at the time.

Although new accurate spectra have been recorded for transitions between the $3d^54s$ and $3d^54p$ levels, and for transitions between higher-lying levels, there is still a need for the data to connect these groups, namely the $3d^54p$ to $3d^54d$ or $3d^55s$ transitions lying in the $\sim 55,000$ cm^{-1} to $\sim 73,000$ cm^{-1} (~ 1400 Å to ~ 1800 Å) region.

Smillie (2007)

Smillie (2007) [85] observed the Fe III spectrum on the NIST NIVS using the PDL, with the aim to observe the needed $3d^54p$ to $3d^54d$ or $3d^55s$ transitions. He classified 787 Fe III lines between 1100 Å and 2000 Å (50,000 cm^{-1} and 90,000 cm^{-1}) with line uncertainties of $\sim 0.005 - 0.01$ Å. Only 53% of lines were unblended or singly-identified, with 112 classified as the needed $3d^54p$ to $3d^54d$ or $3d^55s$ transitions [85].

Smillie used Phosphor image plate detectors to measure the Fe III spectrum on the

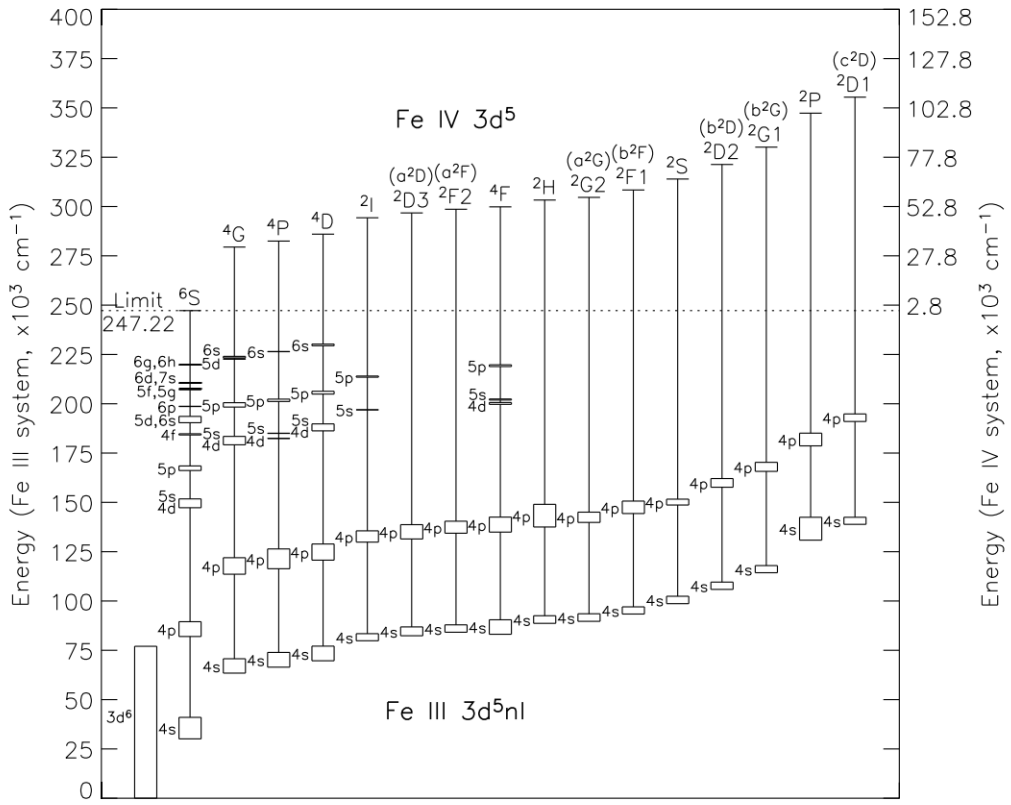


Figure 1.6: The energy level term diagram for Fe III [85] using the energy levels values published by Ekberg (1993) [88] and Corliss & Sugar (1982) [87]. The ionisation energy of Fe III is drawn as a dotted line and the boxes represent the energy level values for each subconfiguration belonging to each parent term. This term diagram is explained in detail in Section 4.1.

NIST NIVS. These plates have been tested to have a linear intensity response and can be scanned multiple times to remove saturation, avoiding the issue Ekberg [88] experienced. However, it has since been determined that these phosphor image plate detectors in fact create a spectrum with a lower resolution than the alternative photographic plates [89].

Smillie used the energy levels from Ekberg for the $3d^6$, $3d^5 4s$ and $3d^5 4p$ configurations as they are most accurate to date, and Corliss & Sugar [87] for the remaining configurations to classify the recorded Fe III lines. Figure 1.6 displays the Fe III energy level term diagram created by Smillie which displays the energy level values for the configurations in each parent term. This is discussed in more detail in Section 4.1.1.

Belmonte (2019)

In April 2019, M. T. Belmonte collaborated with G. Nave at NIST NIVS to improve on Smillie's data and obtain the essential $3d^5 4p$ to $3d^5 4d$ or $3d^5 5s$ transitions. The iron spectrum was recorded using the PDL from 525 Å to 3520 Å (~28,000 cm^{-1} to 190,000 cm^{-1}) on photographic plates which provide a resolution five times better than the Phosphor image plate detectors. These spectra are used to create a grating linelist, as explained in Section 3.2.

Transitions	Approx. Wavenumber Region	Approx. Wavelength Region
$3d^6$ to $3d^54p$	$85,000$ cm^{-1} to $130,000$ cm^{-1} (weaker lines up to $170,000$ cm^{-1})	770 Å to 1180 Å (weaker lines from 590 Å)
$3d^54s$ to $3d^54p$	$40,000$ cm^{-1} to $60,000$ cm^{-1}	1670 Å to 2500 Å
$3d^5$ 4p to $3d^54d$ or $3d^5$ 4p to $3d^55s$	$55,000$ cm^{-1} to $73,000$ cm^{-1}	1370 Å to 1820 Å

Table 1.1: The Fe III transitions and their spectral regions determined in this project.

1.2.2 New Fe III Measurements

In order to determine the energy level structure of Fe III, transitions between the Fe III energy levels must be observed and classified. The classified transitions are then used to revise previously published energy level values. This process is called term analysis and the methodology is explained in Section 4.2.

The focus of this PhD project are the transitions and energy level values of the levels with configurations $3d^6$, $3d^5$ 4s, $3d^5$ 4p, $3d^5$ 4d and $3d^5$ 5s. The spectral regions in which the transitions between these energy levels are expected to be found are listed in Table 1.1. Overall, the desired transitions lie approximately in the spectral regions $40,000$ cm^{-1} to $73,000$ cm^{-1} (1370 Å to 2500 Å) and $85,000$ cm^{-1} to $170,000$ cm^{-1} (590 Å to 1180 Å). The higher-lying energy levels are not the focus of this PhD project but will be included if the necessary transitions are observed. The spectral region containing the majority of the transitions to higher-lying energy levels have been recorded by Pickering on a FTS (σ <28,000 cm^{-1}, $\lambda > 3571$ Å), but no linelist for these transitions is available at this time.

The instruments providing data used in this project are the Imperial College vacuum ultraviolet Fourier Transform Spectrometer (IC VUV FTS, Section 2.1) and the normal incidence vacuum spectrograph at the National Institute of Standards and Technology (NIST NIVS, Section 2.2). The IC VUV FTS provides higher resolution data over grating spectroscopy, but has a wavenumber limit of approximately $\sigma < 71,000$ cm^{-1} ($\lambda >\sim 1400$ Å), with the efficiency of the instrument diminishing towards this limit (see Section 2.1). The grating spectrometer can reach higher wavenumbers of ~685,000 cm^{-1} (146 Å) and detect lower intensity lines in comparison to the FTS capabilities (see Section 2.5). The most recently published data for the lowest lying energy levels ($3d^6$, $3d^54s$, and $3d^54p$) were determined by Ekberg (1993) [88] using grating measurements. Corliss & Sugar (1982) [87] listed the most recently published data available for the higher-lying Fe III energy levels. With the FTS instrument, the accuracy of previously published wavelengths and therefore energy levels can be improved by at least an order of magnitude.

Ideally, the entire desired spectral region ($40,000$ cm^{-1} to $170,000$ cm^{-1}) would be measured with the IC VUV FTS but the instrument is limited to $\sigma < 71,000$ cm^{-1}. Therefore, the Fe III spectrum is measured on the FTS from $40,000$ cm^{-1} to $71,000$ cm^{-1}

(1400 Å to 2500 Å), with the aim to observe the transitions $3d^5 4s$ to $3d^5 4p$, $3d^5 4p$ to $3d^5 4d$ and $3d^5 4p$ to $3d^5 5s$. Pickering began the improvement of the wavelengths for the $3d^5 4s$ to $3d^5 4p$ transitions using the FTS in the $\sim 35,000$ cm^{-1} to $\sim 56,000$ cm^{-1} (~ 1800 Å to ~ 2800 Å) region. However, no linelist was made at the time and no intensity data was recorded. In this PhD project, the final FTS linelist contains 4623 spectral lines from $33,826$ cm^{-1} to $65,508$ cm^{-1} (1527 Å to 2956 Å) , with uncertainties of strong lines typically between 0.0024 cm^{-1} and 0.0074 cm^{-1}. These lines are at least an order of magnitude more accurate in comparison to the linelist previously published by Ekberg (1993) [88] which are between 0.05 Å and 0.005 Å (between 1.25 cm^{-1} to 0.13 cm^{-1} at 50000 cm^{-1}).

The FTS-measured linelist will be supplemented with grating spectra at higher wavenumbers and, where needed, with low intensity lines. The Fe III spectrum recorded by Belmonte in 2019 on the NIST NIVS is used to create an improved grating linelist over the lines published by Ekberg (1993) [88]. Belmonte recorded the Fe III spectrum with multiple exposure times (which Ekberg did not) allowing for the detection of weaker lines and better determination of the wavelengths of stronger, saturated lines. This linelist will provide the wavelengths for the transition $3d^6$ to $3d^5 4p$, and the needed $3d^5 4p$ to $3d^5 4d$ or $3d^5 5s$ transitions which Ekberg did not record. The final grating linelist contains 6626 lines from $55,090$ cm^{-1} to $111,121$ cm^{-1} (900 Å to 1815 Å) , with uncertainties between 0.0912 cm^{-1} and 0.864 cm^{-1} (0.003 Å to 0.007 Å). These lines were of comparable accuracy to the linelist previously published by Ekberg (1993) [88].

The linelists created in this PhD project will be used in the term analysis to revise the previously published Fe III energy levels, producing higher accuracy energy levels and Ritz wavenumbers for the observed transitions. The Ritz wavenumbers for parity-forbidden spectral lines were also calculated for use by astronomers.

1.3 Thesis Structure

This PhD project measured the emission spectrum of Fe III with the Imperial College VUV Fourier transform spectrometer, to create a list of accurate wavenumbers. It is supplemented with grating measurements from the normal incidence vacuum spectrograph (NIVS) at the National Institute of Standards and Technology (NIST) in Gaithersburg, Maryland, USA. The term analysis of Fe III using these data will revise previously published energy levels and produce accurate Ritz wavenumbers for Fe III spectral lines.

The accurate Fe III data will be used in many astronomical fields including as wavelength standards, for line identification, to determine chemical abundances, and to improve astrophysical spectral models [20].

The first section of this thesis described the use of spectroscopy in astrophysics, the need for accurate Fe III atomic data and the relevant previous studies of Fe III. The structure of the remainder of this thesis is as follows:

Chapter 2 The methodology used to record the Fe III spectrum using the Fourier transform spectrometer at Imperial College London and the NIST Normal Incidence

Vacuum Spectrograph is described. This includes information on the Penning discharge lamp used in this experiment and its optimal running conditions.

Chapter 3 The process of creating, calibrating and integrating spectral linelists from the recorded FTS and grating data is discussed here.

Chapter 4 The necessary atomic theory and terminology used in the term analysis, the term analysis process, and the results of the term analysis are stated here. The results revised energy level values and level, Ritz wavenumber of FTS and grating classified linelists, and the Ritz wavenumbers for parity-forbidden transitions.

Chapter 5 This last chapter contains the concluding remarks of this PhD project and planned future work for further improvement of the Fe III data.

Appendices The Appendices contain the full list of revised energy levels; the Ritz wavenumbers and classifications of the FTS-measure and grating-measured Fe III spectral lines; the Ritz wavenumbers for parity-forbidden Fe III transitions; the FTS spectral plots ; and the grating plates and spectral plots.

Chapter 2

Laboratory Measurements

In this chapter the experimental methodology used to generate and record the emission spectrum of Fe III is discussed. In this PhD thesis, spectra were observed using two different instruments: the Fourier transform spectrometer at Imperial College London (IC VUV FTS, Section 2.1) and the NIST Normal Incidence Vacuum Spectrograph (NIVS, Section 2.2). The advantages of each instrument are discussed in Section 2.5. Descriptions of the light sources used in this experiment are in Section 2.3 and 2.4. The experimental details of the final measurements recorded in this PhD research are listed in Section 2.7.

2.1 The Imperial College VUV Fourier Transform Spectrometer

The vacuum ultraviolet (VUV, $\lambda < 2000$ Å, $\sigma > 50,000$ cm^{-1}) Fourier Transform Spectrometer (FTS) at Imperial College (IC) London provides high resolution spectra. It is a Michelson interferometer which relies on the interference of light [90]. Figure 2.1 displays a schematic diagram of the Michelson interferometer. The source light beam with amplitude, A, is split by the beam splitter, to be reflected (path r_1, r_4, r_3, r_2) and transmitted (path t_1, r_5, r_6, r_7). The split beams are reflected off the retroreflectors (named 'fixed mirror' and 'movable mirror' in Figure 2.1), to the beam recombiner. Here each beam is again reflected and transmitted, resulting in two recombined output beams. The unbalanced beam, O_{unb}, will be the combination of light beams that have either been reflected twice at the beam splitter or recombiner (path r_1, r_4, r_3, r_2, r_9) or transmitted twice at the beam splitter or recombiner (path t_1, r_5, r_6, r_7, t_1). The balanced beam, O_{bal}, will be the recombination of beams that have been transmitted and reflected once at either the beam splitter or recombiner (paths r_1, r_4, r_3, r_2, t_2 and t_1, r_5, r_6, r_7, r_8). The intensity of the recombined balanced beam, O_{bal}, is recorded at intervals while moving the movable mirror over some distance, δx [90]. The intensity of the constructive and destructive interference of the balanced beam is recorded as a function of δx and is known as an interferogram.

In the ideal case, the interferogram intensity at optical path difference, x, and wavenumber, σ is given as

$$dI(x) = B(\sigma)d\sigma \cos(2\pi\sigma x) \tag{2.1}$$

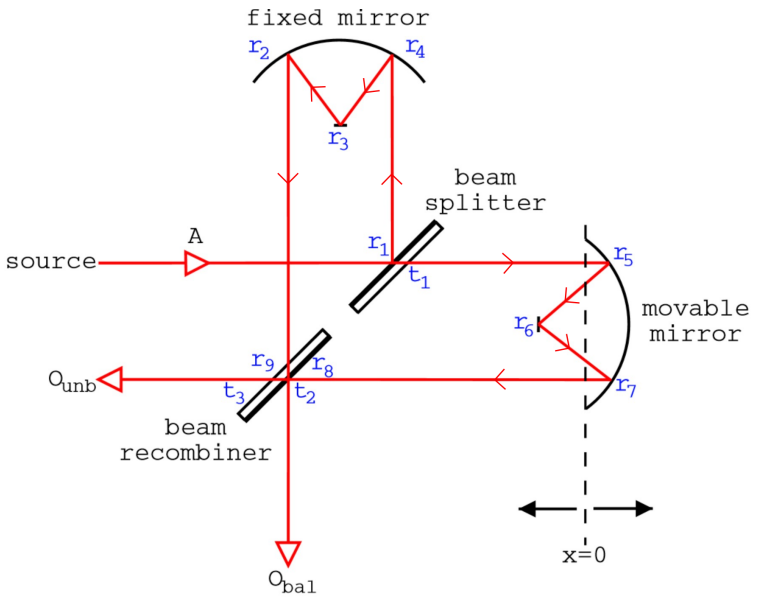


Figure 2.1: A Michelson interferometer with catseye retroflectors, adapted from Smillie [85]. In the IC VUV FTS, the beam splitter and beam recombiner are part of a single unit.

for a source function $B(\sigma)$ which describes the flux variation with respect to σ [90]. The total intensity at the optical path difference, x, is

$$I(x) = \int_{-\infty}^{\infty} B(\sigma)\cos(2\pi\sigma x)d\sigma \ . \tag{2.2}$$

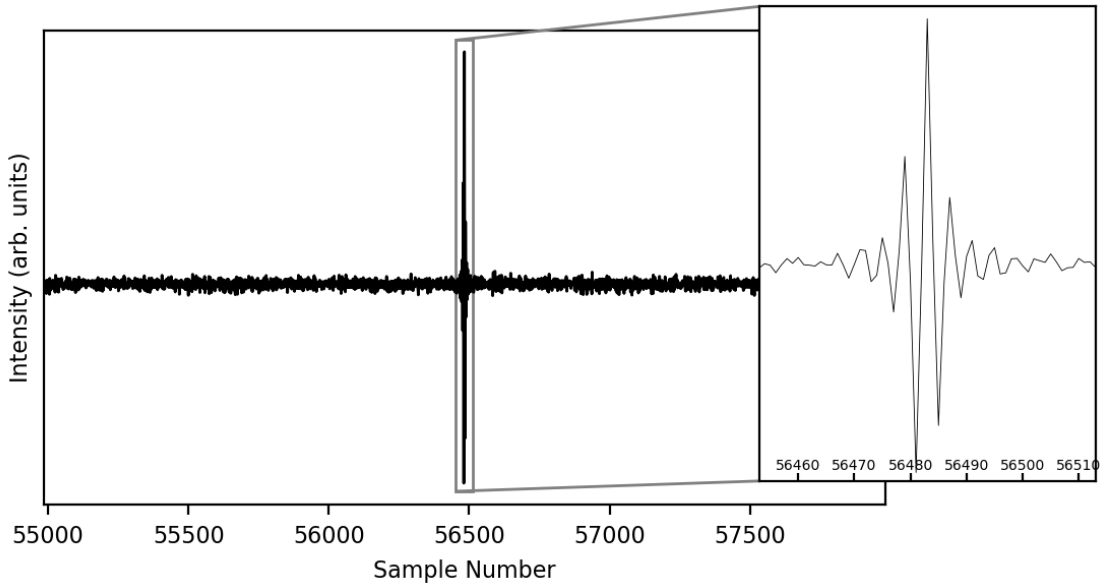
This interferogram is then inverse cosine Fourier transformed to obtain the spectral distribution, $B(\sigma)$ [51]:

$$B(\sigma) = \int_{-\infty}^{\infty} I(x)\cos(2\pi\sigma x)dx \ . \tag{2.3}$$

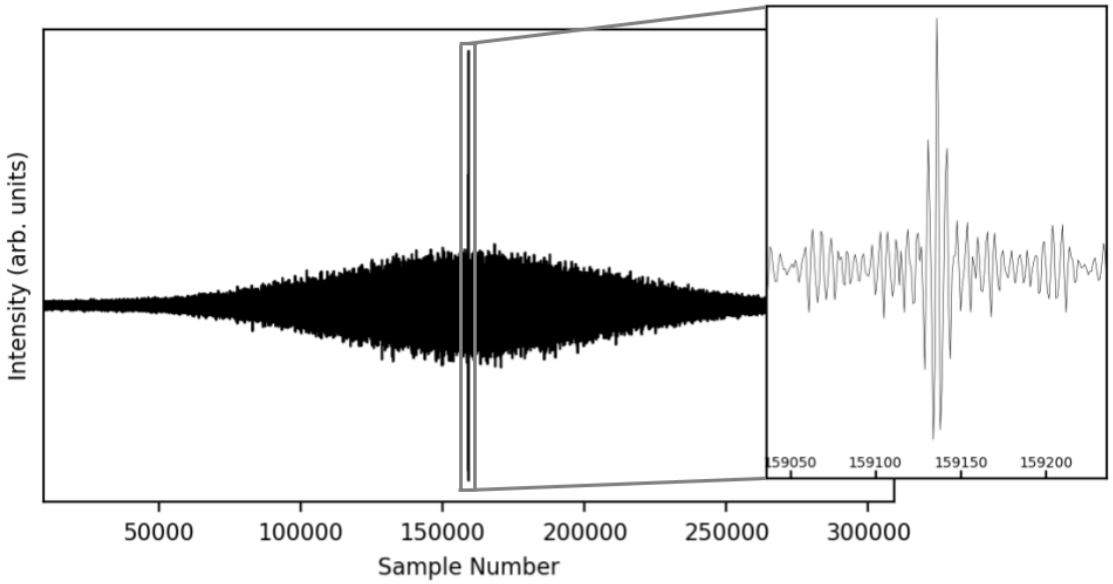
The equations for the interferogram, $I(x)$, and spectrum, $B(\sigma)$, are physically exact. Mathematically, the result is not a single spectrum of $B(\sigma)$ at positive wavenumbers, but also its physically unreal mirror image, $B(-\sigma)$ [90].

The cosine Fourier transform requires symmetry in these functions. Ideally, the interferogram and spectrum are symmetrical about $x = 0$, however, in reality the interferogram is asymmetrical. The interferogram function $I(x)$ can be split into its even and odd components which, when inverse cosine transformed, produces a complex spectrum, $B(\sigma)$, with real (even) and imaginary (odd) components. It is the real component of the complex spectrum that is used for spectral analysis. However, there is valuable spectral information (such as line shape, height and position) in the complex component of the spectrum that could be lost. To minimise the loss of this information, a process called phase correction is applied to the complex spectrum to minimise the information in the imaginary component and maximise the real spectrum. Further information on the Fourier transformation of interferograms can be found in Davis *et al.* (2001) [90] and Thorne *et al.* (1999) [51].

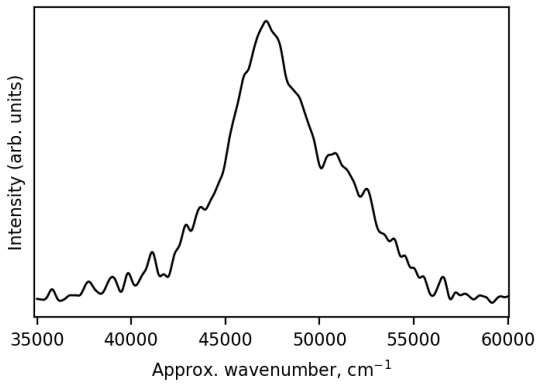
Figure 2.2 displays the interferograms and corresponding transformed spectra of the



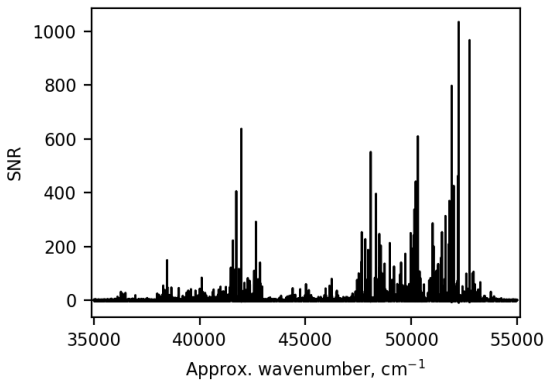
(a) An interferogram recorded of a standard deuterium lamp, with an inset of the central burst region.



(b) An interferogram recorded of the PDL with iron cathodes with an inset of the central burst region.



(c) The transformed spectrum of the standard deuterium lamp.



(d) The transformed spectrum of the PDL with iron cathodes.

Figure 2.2: Interferograms recorded on the IC VUV FTS and Fourier transformed using Xgremlin software[91].

two light sources used in this project: a standard deuterium lamp (Section 2.4) and a Penning discharge lamp (PDL, Section 2.3). The interferogram shapes differ depending on the spectrum of the light source. The deuterium lamp produces a flat interferogram (Figure 2.2a) as it is a continuum light source in the observed spectral region (Figure 2.2c), while the interferogram of the PDL (Figure 2.2b) displays some structure as the spectrum is dense with spectral lines (Figure 2.2d). Interferograms of any light source will peak at the zero path difference, $x = 0$, which is the point at which light of all wavelengths constructively interfere. This central burst is highlighted in Figures 2.2a and 2.2b. The analyses of interferograms and spectra are discussed further in Section 3.1.

2.1.1 Finite Aperture Size

In the ideal spectrometer, the interferogram is created by radiation travelling in the x direction, along the axis of the moving mirror. However, this is only possible when the aperture is treated as a point source and, in practice, a large aperture size (a few mm) is required for a measurable amount of radiation to enter the instrument. The collimated light travels from the aperture at an off-axis angle in the spectrometer, creating multiple path difference values where there would other be a single path difference value for on-axis radiation. This change in path difference of the interferogram results in a scaled change in the wavenumbers of the spectrum.

Another impact of a large aperture size is the reduction in resolving power, R [90]. Therefore, the aperture size must be carefully chosen to ensure sufficient radiation is entering the spectrometer, while maintaining sufficient resolving power.

2.1.2 Digital Sampling of the Interferogram

The ideal interferogram is continuous, with its Fourier transform producing a spectrum in the positive wavenumber space and its mirror image in the negative wavenumber space, as seen in the first row of Figure 2.3. However, in practice, the FTS is digitally sampled at regular time intervals as the movable mirror scans, and software converts these to fixed path difference intervals, δx [93]. Each sample recorded can be modelled as a delta function at δx, known as a Dirac comb, $III(x)$ [90], which can be seen in the middle row of Figure 2.3. The results of the Fourier transformation of the Dirac comb is another Dirac comb with the spacing of $\delta\sigma = \frac{1}{\delta x}$. The Fourier transformation of the multiplication of the continuous interferogram with the Dirac comb of δx, is the same as the convolution of the spectrum with the Dirac comb of $\delta\sigma$. The result is the spectrum of the interferogram replicated at the $\delta\sigma$ intervals. These copies are known as aliases which can be seen in the bottom row of Figure 2.3.

To prevent the overlapping of the aliases, the minimum sampling interval (known as the Nyquist sampling interval) must be [51]

$$\delta x \leq \frac{1}{2\sigma_{\max}} \,. \tag{2.4}$$

This would require a huge number of samples and be time consuming. By band-limiting

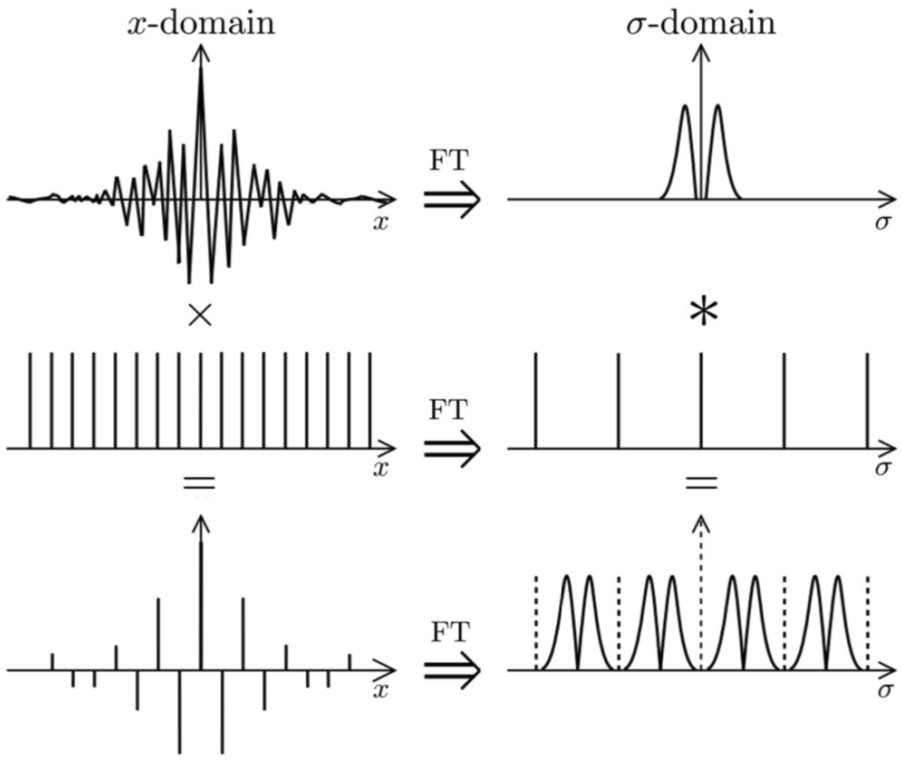


Figure 2.3: The sampling of the interferogram at regular intervals is modelled as a Dirac comb which results in the replication of the Fourier transformed spectrum (aliases) at intervals. Image taken from Clear (2018) [92]

the spectrum with strategically chosen filters and detectors between σ_1 and σ_2, it is possible to under sample the interferogram while still recovering the Fourier transformed spectrum with no issue in the free spectral range of $\Delta\sigma \leq \sigma_2 - \sigma_1$. More information on this can be found at Brault (1996) [93], Thorne *et al.* (1999) [51] and Davis *et al.* (2001) [90].

2.1.3 FTS Experimental Arrangement

The IC VUV FTS is used to provide high resolution spectra from the VUV at 1400 Å ($\sim$71,000 cm^{-1}) to the IR at 1.15 μm ($\sim$8,700 cm^{-1}). The magnesium fluoride (MgF_2) beam splitter and windows allows light transmission to > 1200 Å. However, the signal-to-noise ratio (SNR) of spectral lines will worsen when approaching this wavelength limit, and so in practice the limit of the IC VUV FTS is 1400 Å [94].

The resolving power, $R = \sigma/\delta\sigma$, of an FTS is determined by the maximum path difference, L [90]. For the IC VUV FTS, $L = 20$ cm which equates to a minimum resolution ($\delta\sigma = 1/(2L)$) of 0.025 cm^{-1}. At 2000 Å ($\sim$50,000 cm^{-1}), the maximum resolving power is $R = 2,000,000$.

The experimental arrangement of the IC VUV FTS is shown in Figure 2.4. The optics of the FTS are housed in a sealed tank, with MgF_2 windows connecting to the nosepiece and detectors. This allows for the FTS to be evacuated of air, minimising the absorption of radiation by oxygen and reducing acoustic vibrations. The detectors used are photo-multiplier tube (PMT) detectors and are located in casings A and B. The balanced beam (O_{bal} from Figure 2.1) is projected onto PMT A, and is the detector used throughout these

measurements. The filters are secured in a wheel around the PMT so that the filter located between the FTS and detector can be easily changed during an experiment.

A stable light source is required throughout the FTS measurements as fluctuations in intensity will result in additional noise to the source noise in the recorded spectra [51]. In this experiment, the PDL (Section 2.3) will produce Fe III emission with constant intensity. For the intensity calibration of spectra, a standard calibration lamp must be measured under the same conditions as the PDL. The standard deuterium lamp (Section 2.4) will be used for intensity calibration. Both light sources are connected to the nosepiece, as seen in Figures 2.4 and 2.5, which has a selector mirror enabling the light source entering the FTS to be easily switched between the two lamps.

2.2 NIST Normal Incidence Vacuum Spectrograph (NIVS)

The normal incidence vacuum spectrograph (NIVS) is a grating spectrometer located at the National Institute of Standards and Technology (NIST) in Gaithersburg, Maryland, USA. It is shown in Figure 2.6. It was built in 1964 and was at the time the largest commercial spectrograph in the world, with a focal length of 10.7 m [96]. The NIST NIVS has a spectral range of 146 Å (∼685,000 cm^{-1}) to 4380 Å (∼22,800 cm^{-1}) and a resolving power of $R \sim 150,000$. The entire apparatus can be placed under vacuum to record in the VUV and although windows and filters can be used, they are not required, and so the wavelength range is not limited by MgF_2 windows like the IC VUV FTS.

The light source is placed behind the slit of the grating spectrometer which is in a fixed position. The radiation reflects off a concave grating which is made of reflective grooves, focusing the radiation from the slit onto the detectors, which are two photographic plates. This reflected radiation interferes, with intensity maxima at angles of constructive interference, producing spectral lines on the detectors. These spectral lines are recorded as dark lines on the photographic plates. The blackening of the line on the plate is correlated to the strength of the line and the exposure time. While the light source and slit of the grating spectrometer are in a fixed position, the grating and detector plates can be rotated and translated so that the slit, the grating and the plates are placed on a virtual Rowland circle (where the diameter equals the radius of the concave grating), with the angle of rotation determining the spectral region exposed to the detector plates. Table 2.1 shows the angles of rotation and the corresponding wavelength ranges displayed across the two detector plates. This is essential information when creating and calibrating a linelist from the plates, as discussed in Section 3.2.1.

For two detector plates placed side by side, the range recorded in a single exposure is ~ 700 Å. An adjustable width mask is placed over the plates which limits the part of the plates exposed to a single thin horizontal strip. By adjusting the width of the mask during the experiment, multiple exposure times can be recorded for the same lamp conditions and spectral range without moving the detector plate. This prevents any blurry images and allows for the same wavelength calibration to be applied across all exposure times, as discussed in Section 3.2.4. A section of the recorded detector plate can be seen in

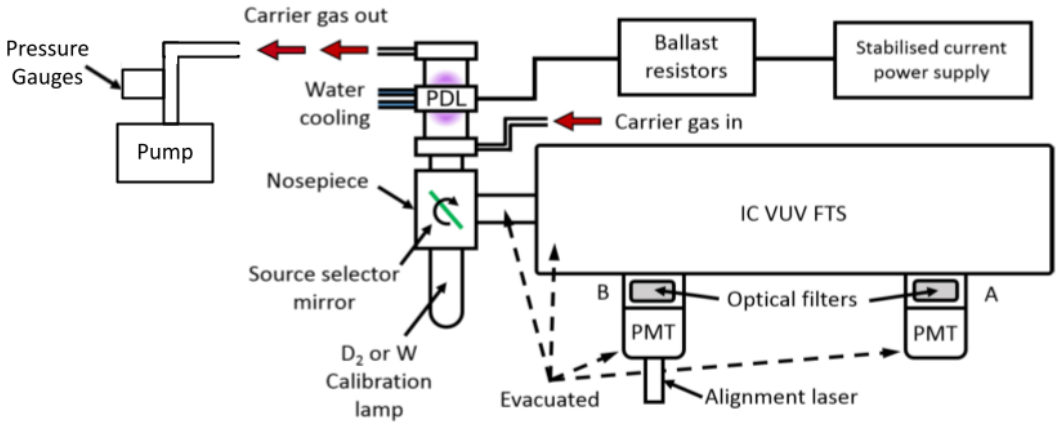


Figure 2.4: Diagram of the FTS instrument arrangement, adapted from Clear [92].

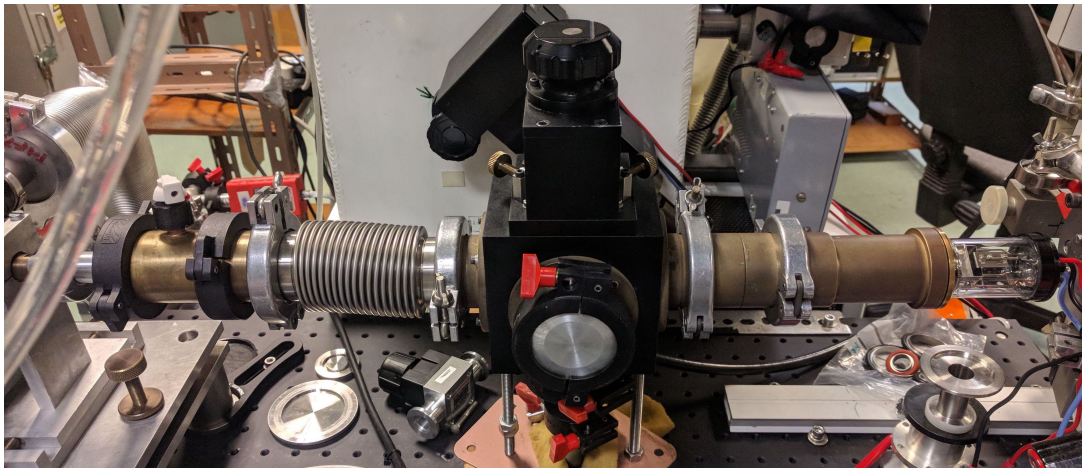


Figure 2.5: Image of the nosepiece of the FTS. The Penning discharge lamp (out of image) is connected on the left and the deuterium lamp is connected on the right. The wheel on the top of the nosepiece is used to rotate the mirror reflecting the source into the FTS input aperture.

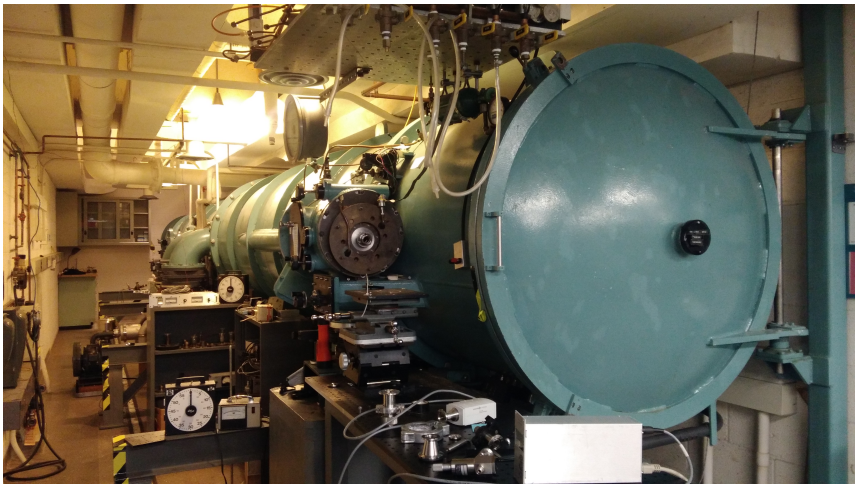


Figure 2.6: Image of the NIST NIVS [95]

Grating Angle (°)	Approx. Wavelength Range (Å)
3.7	146 - 862
4	234 - 950
5	525 - 1238
6	820 - 1520
7	1100 - 1800
8	1400 - 2100
9	1685 - 2390
10	1950 - 2650
11	2230 - 2920
12	2520 - 3220
13	2820 - 3520
14	3100 - 3800
15	3405 - 4100
16	3680 - 4380

Table 2.1: The angles of rotation of the grating plate and detector plates and their corresponding wavelength ranges on the detector plates at NIST NIVS.

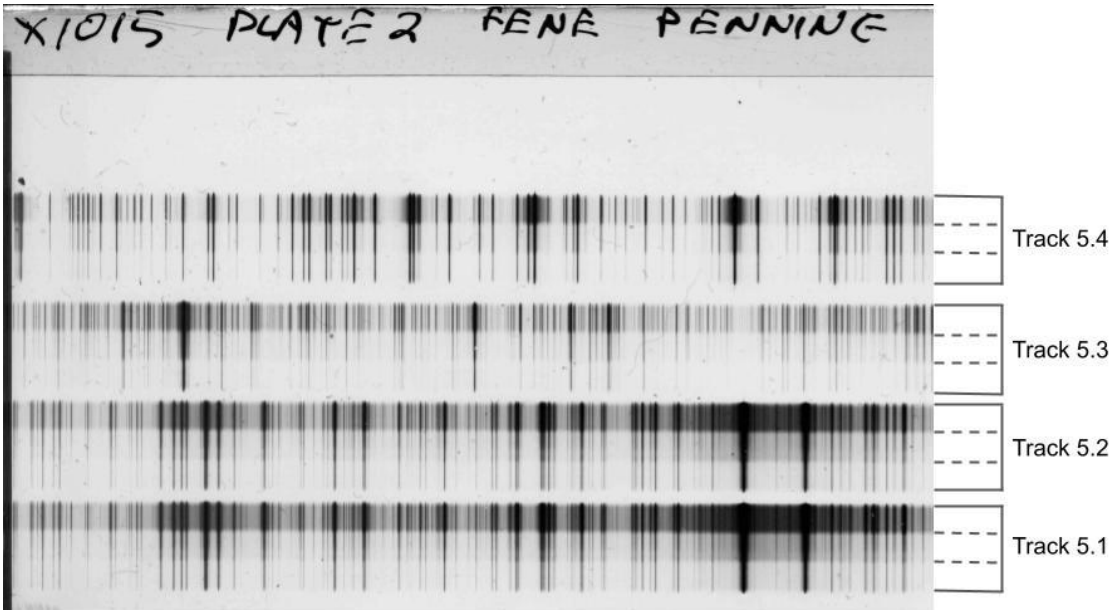


Figure 2.7: Part of the scanned image of the second detector plate for x1015 (image x1015_plate2a, discussed in Section 3.2.1). To the right of the image, the boundaries of each track is marked with a solid line and has been labelled. The dashed lines mark the boundaries of the different exposure times recorded.

Photographic plates	Phosphor image plates
Non-linear intensity scale	Linear intensity scale
No longer manufactured	Commercially available
Single use	Reusable
Resolution of a few μm (scanner dependant [99])	Resolution of 42 μm (scanner dependant [98])

Table 2.2: Comparison of photographic detector plates and phosphor image detector plates [59]

Figure 2.7. On this plate, four segments of the iron spectrum were recorded, each with 3 exposure times (5, 10 and 45 minutes). By observing each section of the spectrum with different exposure times, the wavelengths of spectral lines will be more accurately determined: stronger lines will be better defined and less saturated in the spectrum with lowest exposure time, and weaker lines will appear in the spectrum with the highest exposure time.

2.2.1 Detector Plates

As stated in Section 1.2.1, in 2019 Belmonte recorded the iron spectrum on photographic detector plates at NIST NIVS. These plates were chosen over the phosphor image plates used by Smillie (2007) [85]. There are advantages to using the phosphor image plate detectors over the photographic plates, such as a linear intensity response which would provide valuable atomic data [97]. The phosphor image plate detectors are also commercially available while the photographic plates are no longer produced and so there is a finite supply [97]. A comparison of the detector plates is shown in Table 2.2

A key advantage of the photographic plates is that their resolution is over 5 times better than the resolution of the phosphor image plates. The resolution of the phosphor image plates is limited by the scanner used to read them [98]. The resolution of the photographic plates are also limited by the detector pixel size in the flatbed scanner which created the images used to make the grating linelist. More information on the scanner used can be found in Wyatt & Nave (2017) [99]. By using the photographic detector plates, the result will be a more accurate wavelength linelist, which is essential to the term analysis process.

The measurements recorded by Belmonte using the NIST NIVS are listed in Section 2.7.2.

2.3 The Penning Discharge Lamp

The light source in this PhD research is the Penning discharge lamp, which is able to remain stable for hours while creating and exciting doubly-ionised iron. Previous studies have proven that the PDL can successfully produce the Fe III spectrum (Section 1.2.1).

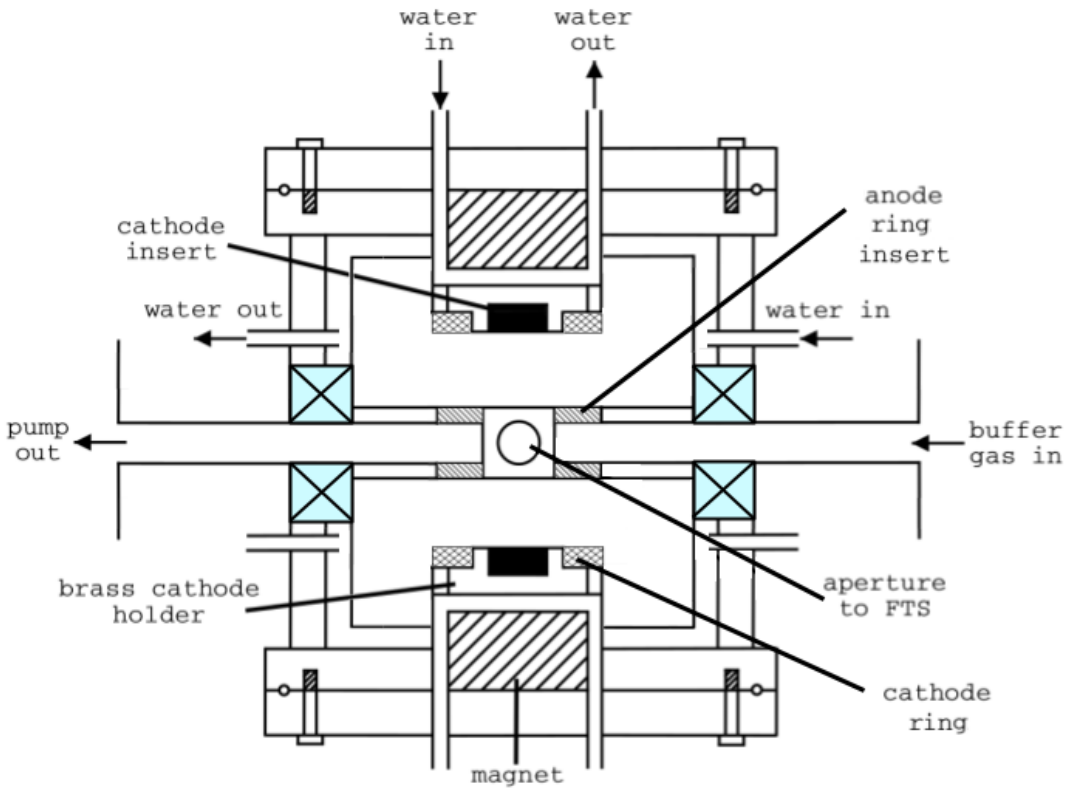
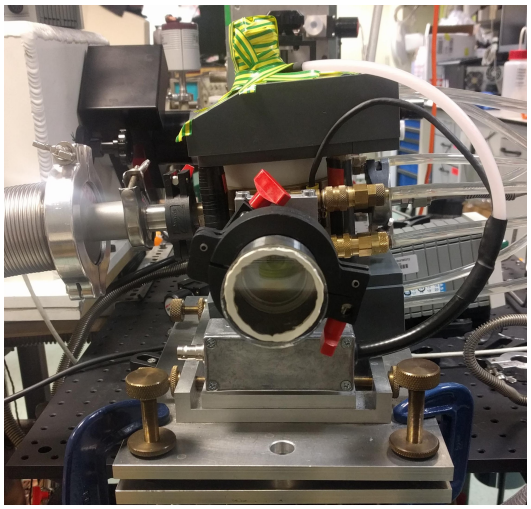


Figure 2.8: Schematic diagram of the Penning discharge lamp, adapted from Smillie [85]. The insulating Delrin rings are represented by shaded light blue and a single cross.

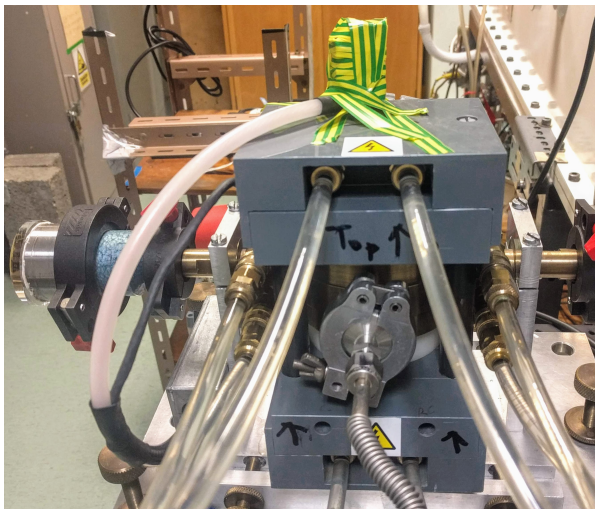
2.3.1 PDL Design

Heise *et al.* [100] designed the PDL to emit lines of multiple ionisations of metals for VUV observation, based on a design by Finley *et al.* [101]. Figure 2.8 shows an approximate cross-section of the PDL, and Figure 2.9 shows photographs of the PDL as used with the IC VUV FTS in this thesis work.

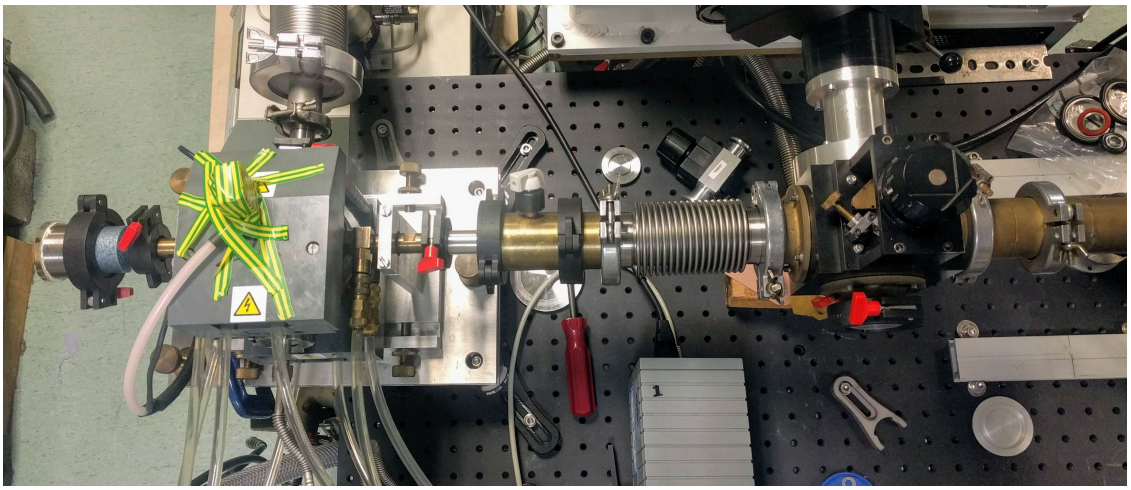
A large potential is applied to the cathodes on either side of the grounded central anode ring. A buffer gas sputters the metal cathodes, emitting electrons which are confined to oscillate between the cathodes through the anode ring. This is due to the magnetic field created by the strong magnets behind each cathode. The operation of the PDL relies on the parallel electric and magnetic fields to create a Penning trap for the electrons between the two cathodes facing each other [100]. The high energy electrons will ionise a buffer gas, which in turn will encourage the bombardment and excitation of the metal from the cathodes. The oscillating electrons, with the ions from the buffer gas and the sputtered ions from the metal cathodes, form a plasma. A higher buffer gas pressure will increase the collision rate in the plasma, reducing the kinetic energy of the ions and, in turn, reducing the sputtering rate of the metal from the cathodes. For this reason, a low buffer gas pressure is required. As the cathode material is sputtered, a crater is formed in the cathode, and the metal is deposited onto the anode. The lamp will stop running when the cathodes are completely worn away. Photographs of the new and cratered iron cathodes are in Figures 2.10a and 2.10b. Before every experiment, new cathodes are placed in



(a) Port gas pumping (left); visual observation port (centre); port for gas inlet (right); high voltage connection (white cable, top).



(b) Visual observation port (left); port for gas inlet (centre); port for FTS input (right); high voltage connection (white cable, top).



(c) Visual observation port (left); high voltage connection (white cable, centre); port for gas inlet (via silver flexible pipe, bottom); port for FTS input (right); port for gas pumping (top).

Figure 2.9: Photographs of the plan and side views of the Penning discharge lamp.

the lamp and the PDL is cleaned of any previously deposited metal and wiped of any impurities with ethanol.

In order to measure the iron spectrum, high purity iron cathodes ($99.8+\%$) were made to be used in the PDL using iron rods manufactured by Goodfellow. By reducing impurities, the number of spectral lines observed of other elements is reduced.

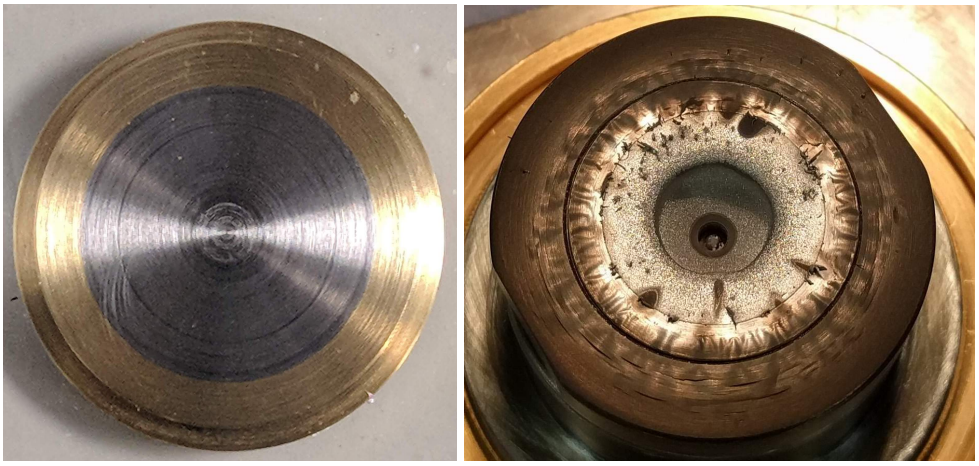
For every experiment, two new solid cathode discs of thickness ~ 8 mm and diameter ~ 23 mm set in brass are required (Figure 2.10a). These cathodes are placed in the brass frame of the PDL, and held in place by removable brass rings, above and below the anode ring insert located at the centre of the PDL. The cathode inserts, the brass cathode holders, and the removable brass rings sit flush with each other.

The PDL has four perpendicularly aligned ports, meeting in the centre of the anode ring. A picture of the anode ring can be seen at the centre of the PDL in Figure 2.11. One port is for the inlet of the buffer gas, with the opposite port connected to a vacuum pump, allowing for control over the gas flow. The other two ports are used for the FTS instrument input and visual observation. These ports can be seen in the photographs in Figure 2.9.

The buffer gas the PDL requires to operate must be a noble gas [100]. It is known that the PDL has successfully operated with iron cathodes and neon gas (Pickering, Smillie (2007) [85]). However, in this PhD work, a mixture of gases was tested with the iron cathodes in the PDL. To accommodate this, Swagelock stainless steel $1/4$ inch gas pipes were used to connect the compressed gas cylinders' regulators to two fine control needle valves (Edwards LV10K). These fine needle valves vary the gas flow from completely open to completely closed in small increments. These two valves provide control over the ratio of gases input to the PDL. The gases were combined and connected to another fine control needle valve (Edwards FCV10K) before connecting to the PDL with flexible tubing of length ~ 10 cm.

At the start of the measurements, a cold trap was placed between the final gas mixture and the fine needle valve to test for impurities in the gases. As no impurities were found in early experiments and the gas source did not change, the cold trap was not activated for later experiments.

To ensure the low pressures needed in the PDL ($\sim 10^{-5}$ mbar) are achieved, a turbomolecular pump is used. The turbomolecular pump can create pressures as low as $\sim 10^{-6}$ mbar in the PDL, whereas a rotary oil vacuum pump can only produce pressures as low as $\sim 10^{-2}$ mbar. Two pressure gauges were used to record the pressure inside the PDL: Edwards APG-M-NW16 Al Active Pirani, D02171000; and Edwards AIM-S-NW25, D14545000. The APG gauge measures over the pressure range $1\cdot 10^{-4}$ mbar to $1\cdot 10^{3}$ mbar and the AIM gauge measures from $1\cdot 10^{-9}$ mbar to $1\cdot 10^{-2}$ mbar. Before measurements, the readings of these gauges were compared to newly-calibrated gauges under equal conditions to ensure correct calibration for each gauge. However, the pressure calibration plots provided by Edwards showed some deviation of the measured pressure from the test pressure for each instrument. Therefore, to prevent any inconsistencies, the pressures at $> 2\cdot 10^{-3}$ mbar were recorded using the APG gauge, and the pressures below this value



(a) Photograph of the face of a new iron cathode used in the PDL.

(b) Photograph of the iron cathode completely worn away by use in the PDL.

Figure 2.10: Photographs of the new and completely sputtered PDL iron cathodes. The iron cathode inset has a diameter of ~ 23 mm, and the crater depth is the same thickness as the iron cathode, ~ 8 mm.

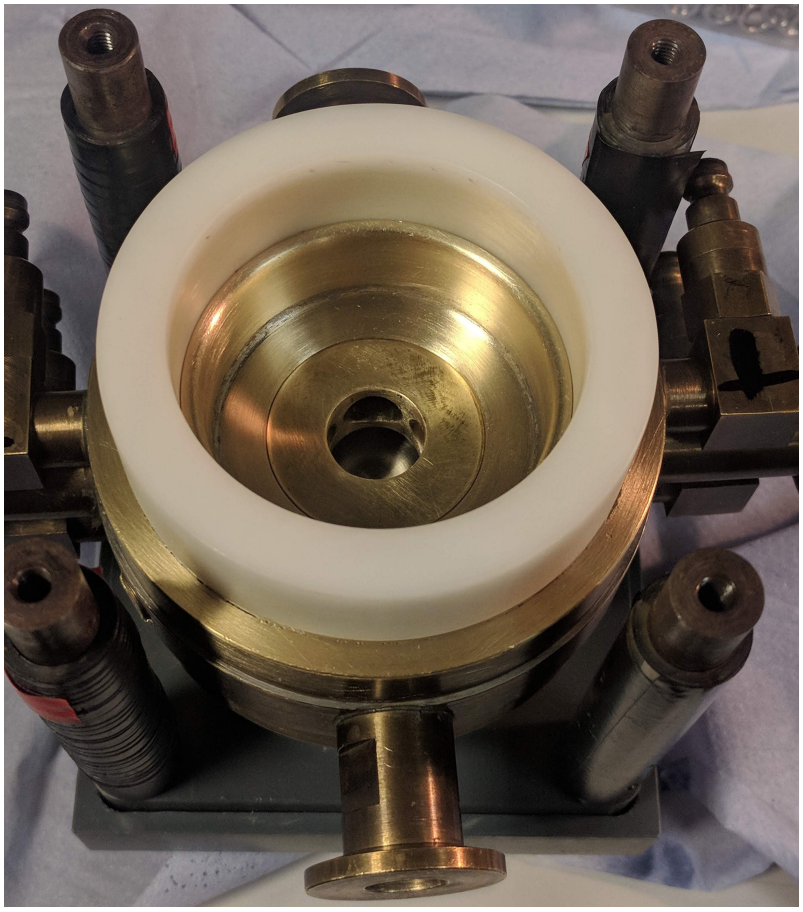


Figure 2.11: Photograph of the top view of the PDL without the top cathode in place. The removable anode ring can be seen in the centre of the PDL and the white ring placed on top is the Delrin ring used to insulate the cathode from the anode.

were recorded using the AIM gauge.

The two pressure gauges were joined onto a cross shaped vacuum fitting mounted onto the turbomolecular pump input. This fitting was then connected to the PDL via flexible tubing of diameter 5 cm and a compressed length of 50 cm. These values are important when comparing PDL pressures between experiments at different locations as the gauge readings will depend on their location relative to the lamp.

When using the PDL with the FTS, a MgF_2 window is placed between the lamp and the FTS nosepiece. This allows the transmission of radiation for wavelengths > 120 nm, the lamp pressure to be controlled independently of the nosepiece and prevents material from sputtering onto the FTS optics. The window is housed in a brass casing between the lamp and the FTS nosepiece, which can be seen next to a silver-coloured flexible bellow in Figure 2.9c.

When observing the PDL with the FTS, the observation port is useful for determining plasma stability and for optimal instrument alignment. An alignment laser is used to ensure optimum alignment is consistently used between the PDL and the detectors. The alignment laser, located in detector housing B (Figure 2.4), is switched on and the FTS aperture size is set to the smallest opening, 0.8 mm. The laser light should be seen going through the centre of the lamp aperture and onto the wall on the far side of the lamp beyond the viewing point. To ensure the internal laser alignment has not shifted, the laser point should mark the same place on the wall at every experiment. The alignment of the PDL with the FTS optics was checked before every experiment, to ensure that the maximum intensity from the PDL is fully aligned with the FTS optics and detectors. The PDL was secured on an adjustable mount which allowed the lamp to be removed for cleaning and cathode replacement, whilst keeping the optical alignment intact. This is essential in saving time and to achieving reproducible results, as the cathodes are changed and the lamp is cleaned before every experiment. This grey mount can be seen in Figures 2.9a and 2.9c.

During the experiment, the anode remains grounded while a large potential is applied to the cathodes. The power supply is connected to a ballast resistance of 250 Ω, and can apply a current up to 2 A at 2.5 kV. The voltage typically was not observed above 1.1 kV. Two white Delrin rings separate the cathodes and anode, acting as insulators. An image of a Delrin ring is seen in Figure 2.11.

Four strong permanent neodymium magnets (NdFeB) are stacked behind each cathode, creating a magnetic field parallel to the electric field. The magnetic field strength was measured to be ~ 0.10 T at the centre of the PDL using a Hall probe at the start of experiments. The magnets are magnetically clamped to ferromagnetic steel cathode plates which are connected with the four columns (which can be seen in Figure 2.11).

In order to prevent the degradation of the magnets due to the high temperatures of the PDL, and to reduce the width of the spectral lines (Doppler width, Section 3.1.1.4), the magnets and the PDL body are water-cooled, as shown in Figure 2.8. The water-cooling system included input and output pressure gauges, an adjustable water pressure valve, and each connection to the lamp had a water flow indicator. These were used to ensure

that the system was working as expected, and that there was sufficient flow to the lamp to prevent overheating. The clear tubes used for water cooling can be seen in Figure 2.9b.

2.4 Standard Deuterium Lamps for Intensity Calibration

By observing the spectrum of a lamp of known spectral intensity and comparing it to the calibration data of this lamp, the instrument response function of the FTS can be calculated and the recorded PDL spectra can be intensity calibrated. Intensity calibration is not required to determine line wavenumbers but is useful in providing a guide to the relative strength of spectral lines, which is useful in the term analysis (as discussed in Section 4.2). Intensity calibration of the FTS data is described in Section 3.1.2.

With the IC VUV FTS, a standard deuterium lamp was used to intensity calibrate in the region 1160 Å to 4100 Å ($\sim$ 24400 cm^{-1} to $\sim$ 86200 cm^{-1}) . The deuterium lamp was observed in equal conditions to the iron experimental data, including the same detector, filters and FTS tank pressures. To ensure this, the deuterium lamp was recorded just after the desired PDL data was collected. The standard lamp was mounted on the opposite side of the nosepiece, and the light source input to the FTS is switched using a mirror in the nosepiece.

To ensure alignment with the FTS optics was optimal the lamp was aligned with the alignment laser. However, during measurements with the nosepiece under vacuum, the lamp could not be moved and the mirror in the nosepiece was adjusted until the maximum intensity of the lamp was observed on the detector. This arrangement is shown in Figures 2.4 and 2.5.

The 'working' calibration lamp, (HCL Deuterium, V03, AJ026, 12/12/90) was used after every successful PDL observation. This meant the lamp was used at least once a week over 6 months including a 30-minute warm-up time before every observation. As this lamp was used very often there is a chance its spectrum may have drifted from the calibration data. To ensure the intensity calibration data recorded is valid, the spectrum of the 'working' V03 AJ026 lamp was compared to another HCL Deuterium V03 lamp (Heraeus Noblelight GmbH, V03, V0394) which has been rarely used since its calibration by the Physikalisch-Technische Bundesanstalt, Germany, on 20/01/2011. For each lamp, 25 co-adds were recorded twice with the measurements alternating between the 'working' and 'calibrated' deuterium lamps. These measurements were taken successively, within a single day of experiments. Figure 2.12 displays a comparison over the entire spectral region of FTS observations of the spectra observed from the 'working' deuterium lamp and the 'calibrated' deuterium lamp. The differences between the two lamps were found to be within the calibration uncertainties, which are 7% for region $24,390$ cm^{-1} to $58,824$ cm^{-1} (1700 Å to 4100 Å) and 14% for the region $58,824$ cm^{-1} to $81,433$ cm^{-1} (1230 Å to 1700 Å). Therefore, no corrections were made to the calculated instrument response function due to using the 'working' lamp.

As seen in Figure 2.12, repeated measurements of the same deuterium lamp have some variation in the observed spectra. To investigate the discrepancies in the repeated

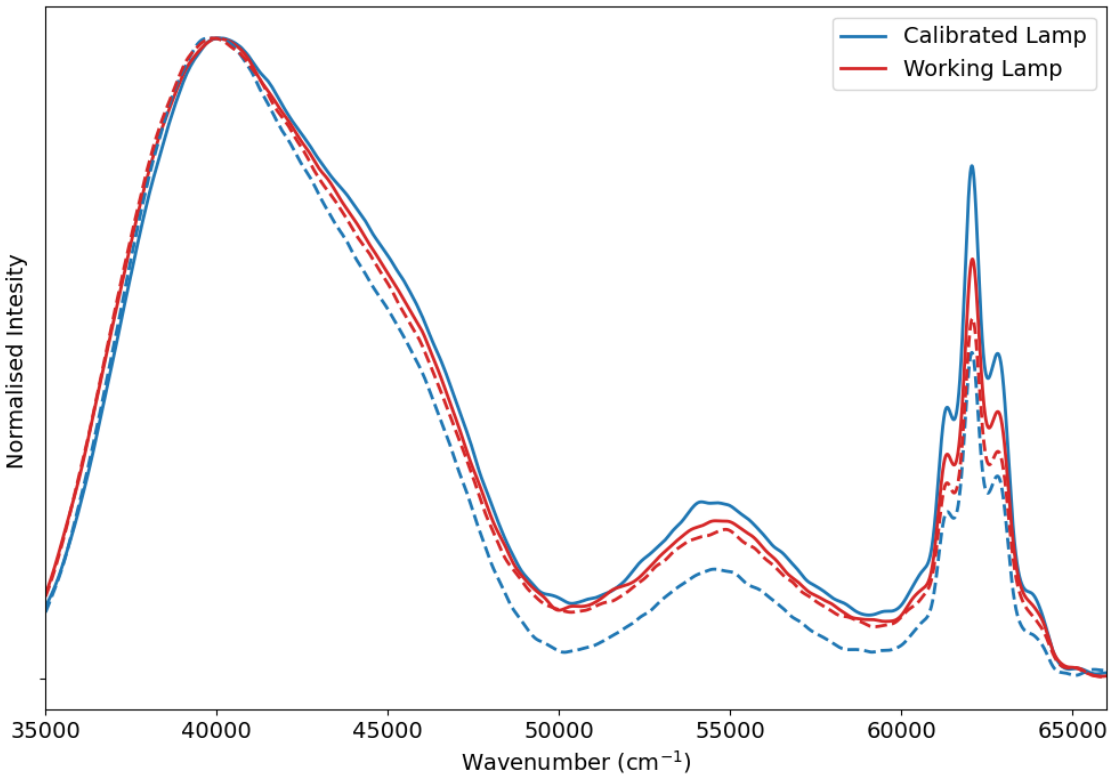


Figure 2.12: A comparison of the spectra observed from the 'working' deuterium lamp (red) and the 'calibrated' deuterium lamp (blue). Each observation consists of 25 co-adds. The first observation of each lamp is shown with a solid line, and the subsequent measurement is shown with a dashed line.

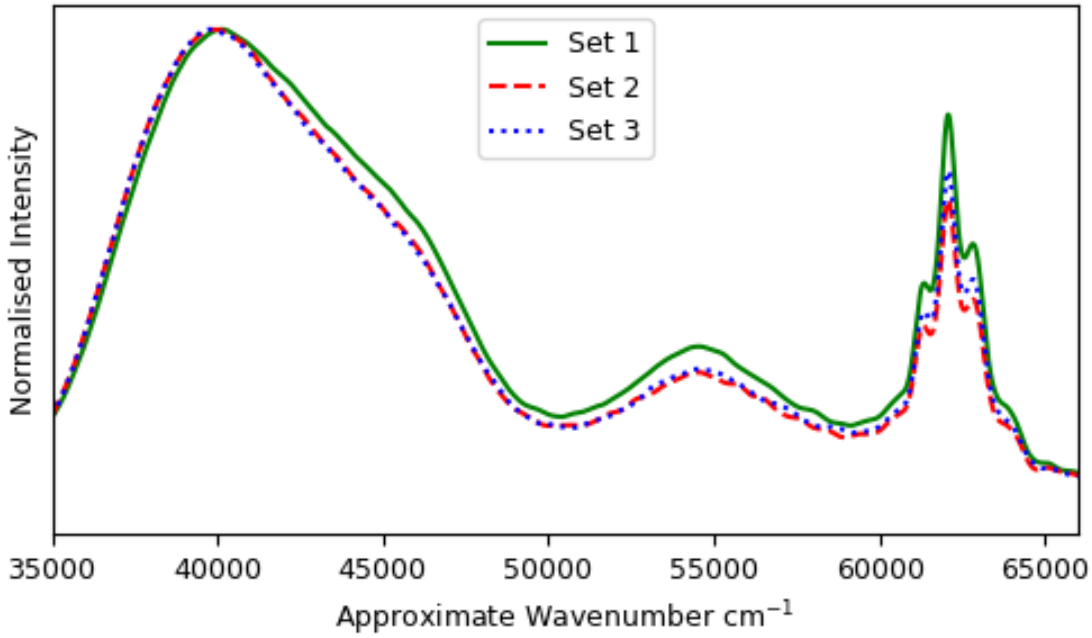


Figure 2.13: The filtered deuterium lamp spectra of repeated measurements using the PMT R1220 with no filter on the IC VUV FTS. Between each measurement the lamp was removed from the nosepiece and replaced, and the nosepiece was moved and returned to the optimal position

	IC VUV FTS	NIST NIVS
Resolving Power	2,000,000 at 2000Å	$\sim 150,000$
Approx. Wavelength Range	1400 Å to 1.15 μm (71,000 cm^{-1} to 11,000 cm^{-1})	146 Å to 4380 Å (685,000 cm^{-1} to 22,800 cm^{-1})
Light source	Requires stability for several hours	Does not have to be stable

Table 2.3: Comparison of the IC VUV FTS and the NIST NIVS capabilities.

measurements, the repeatability of the experiments on the IC VUV FTS was tested. The deuterium lamp was recorded for 3 sets of 25 co-adds on the FTS using the detector PMT R1220 with no filter, in the range $33,000$ cm^{-1} to $67,000$ cm^{-1} (1490 Å to 3030 Å) . These measurements were taken successively in a single day. Between each set of measurements, the deuterium lamp was removed from the nosepiece and replaced, and the mirror in the nosepiece was moved and returned back to the optimal position as determined by the peak intensity on the detector. The intensity-normalised filtered spectrum of each data set is compared and shown in Figure 2.13. The small variations in the spectra seen here could be due to small changes in the position of the mirror or a change in another condition such as the FTS tank pressure.

The uncertainty in the relative line intensity of FTS lines within a particular recorded spectrum is a combination of deuterium lamp calibration uncertainty, uncertainty from the SNR of the observed deuterium spectrum ($\frac{1}{SNR}$), and the uncertainty in the fitted line equivalent width ($\frac{1}{SNR}$). The uncertainty in the repeatability is smaller than these factors. For this research, lines from different spectra are selected for the final linelist, meaning that line intensities (equivalent width) will be useful as a guide to relative line strengths but not statistically accurate. This means that the linelist created in this project is suitable only for the term analysis process and not for the determination of branching fractions.

2.5 Spectrometer Comparison

The capabilities of the IC VUV FTS and the NIST NIVS have been discussed in Sections 2.1 and 2.2, respectively. In this section, the resolving powers and wavelength ranges are compared and used to determine the spectral regions that will be measured by each instrument.

Table 2.3 compares the capabilities of the instruments and a comparison of a section of the iron spectrum as observed on the IC VUV FTS and a photographic plate from NIST NIVS is shown in Figure 2.14. In this comparison, it is easy to see the difference made by an order of magnitude improvement in resolving power. The FTS measures resolved lines where the grating spectrometer records wider and blended lines, as seen at $\sim 55,927$ cm^{-1} in Figure 2.14. Therefore, the line uncertainties of grating lines are much greater than the FTS lines, and for this reason, the high-resolution FTS lines are used

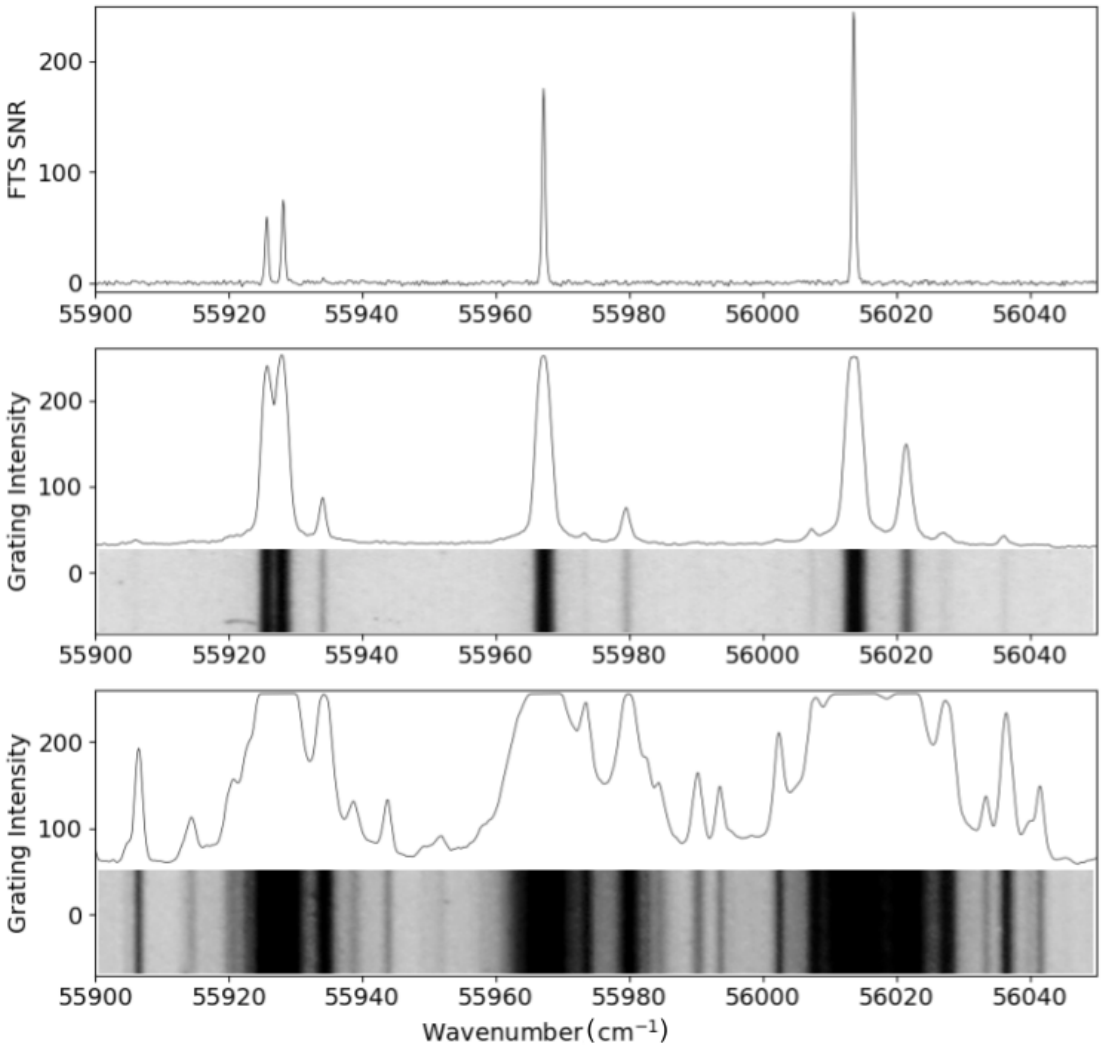


Figure 2.14: A section of the iron spectrum at $56,000$ cm^{-1} in the FTS spectrum [top] (Fe121, discussed in Section 2.7.1) and the photographic plate spectrum of the 5-minute [middle] and 45-minute exposures [bottom] (x1015_plate2b Track 5.3, discussed in Section 3.2.1).

where possible in spectrum analysis.

As mentioned in Table 1.1, the estimated wavenumber regions that need to be observed are $40,000$ cm^{-1} to $73,000$ cm^{-1} ($\sim$ 1370 Å to $\sim$ 2500 Å) and $85,000$ cm^{-1} to $130,000$ cm^{-1} ($\sim$ 770 Å to $\sim$ 1180 Å). As the IC VUV FTS is limited to $\sigma < 71,000$ cm^{-1} ($\lambda > 1400$ Å) , the FTS data will be supplemented with the NIST NIVS (Belmonte, 2019) data. Another advantage of the NIVS is that it records weaker lines which are unseen in the FTS spectra, as seen in Figure 2.14.

The PDL is suitable as a light source for both spectrometers, as it can create and excite Fe III at a stable intensity for hours as required by the FTS. The NIVS, however, has no restriction on the stability of the light source intensity. In this research, the PDL was successfully used with the IC VUV FTS to record the spectrum between $33,826$ cm^{-1} and $65,508$ cm^{-1} (1527 Å and 2956 Å) . Belmonte used the PDL to record the iron spectrum on NIST NIVS between $28,400$ cm^{-1} and $190,476$ cm^{-1} (525 Å to 3520 Å).

2.6 IC VUV FTS Experimental Details

2.6.1 Preparing the FTS

As light is absorbed by air in the spectral region $\sigma > 50,000$ cm^{-1} ($\lambda < 2000$ Å) [51], in order to observe at these wavelengths with the IC VUV FTS, the entire apparatus including the FTS tank, nosepiece and detector casings must be vacuum pumped to low pressures. The lower pressures also reduced any acoustic vibrations which could alter the measured interferograms.

To start the experiment, the main tank housing the FTS optics must be evacuated. This requires two pumps: a rotary oil vacuum pump and a diffusion pump. The rotary pump is used to bring the tank pressure to $10^{-1} - 10^{-2}$ mbar. When the tank has reached this pressure, it can be brought to lower pressures using the diffusion pump. However, the diffusion pump requires its backing pressure to be $< 10^{-1}$ mbar, and so the rotary pump is now used to pump the backing of the diffusion pump instead of the FTS tank.

The advantage of the diffusion pump is that it has no moving parts, and so produces no noise or vibrations. This is essential when measuring with the FTS as any vibration will contribute noise to the recorded data and could cause a change in alignment of the optics, preventing the FTS from measuring interferograms successfully. The rotary pump, which is located under the FTS tank, does cause vibrations, and so is switched off during measurements, provided that the pressure of the diffusion pump backing remains sufficiently low. A liquid nitrogen cold trap placed at the input to the rotary pump helps to maintain the vacuum and prevents any oil from the rotary pump backstreaming into the FTS tank. The diffusion pump also relies on water cooling and liquid nitrogen.

Next, the detector housing and nosepiece must be evacuated together, as these both rely on the same sorption pump. The sorption pump is a passive pumping method. It relies on the rotary pump first evacuating the detector housing and nosepiece, but subsequently will hold the pressure to $\sim 10^{-2}$ mbar with no vibration or noise. The sorption pump also requires liquid nitrogen with frequent replenishing throughout a

day of measurements. The filters are placed in a filter wheel located in the detector housing, which can be rotated externally. Therefore, filters can be changed easily during an experiment and without breaking the vacuum seal on the housing. The nosepiece can only be pumped once the chosen lamps have been secured and attached. A flexible bellows connects the PDL to the nosepiece, allowing for changes in alignment to be made while the nosepiece is under vacuum.

2.6.1.1 Filters and Detectors

As stated in Section 2.1.2, the spectrum must be band limited to the spectral range measured. This means that the intensity at the edges of the spectrum recorded must be reduced to zero so that the interferogram can be successfully converted to a spectrum [51]. This is achieved by selectively choosing the detector and filter for each spectrum.

In the Fe-Ne PDL spectrum, lines will primarily be due to the excitation of Fe II or Fe III. Spectral lines from other iron ionisation states and the carrier gas will also be seen. Figure 2.15 displays the relative line strengths and wavenumbers of Fe II and Fe III lines as calculated by Kurucz [42]. As mentioned in Table 1.1, the $3d^5 4s$ to $3d^5 4p$ transitions lie between $40,000$ cm^{-1} to $60,000$ cm^{-1} and the $3d^5 4p$ to $3d^5 4d/5s$ transitions lie between $55,000$ cm^{-1} to $73,000$ cm^{-1}. Using Figure 2.15 as a guide, it would be favourable to avoid the many strong Fe II lines at $\sigma < 45,000$ cm^{-1} and some Fe II lines at $55,000$ cm$^{-1} < \sigma < 60,000$ cm^{-1} as these will contribute noise to the final spectrum. The Fe III regions of focus are $45,000$ cm^{-1} to $55,000$ cm^{-1} and $60,000$ cm^{-1} to $70,000$ cm^{-1}. These will be referred to as Region 1 and Region 2, respectively, and their limits have been drawn on Figure 2.15.

Detector and filter combinations were chosen to ensure maximum transmission in Regions 1 and 2, whilst minimising contributions from Fe II lines outside of these regions. The best detectors for the desired spectral range are the Hamamatsu photomultiplier tubes (PMTs) R1220, R1259 and R7154. These each have a different spectral response between $\sim 31,250$ cm^{-1} and $\sim 86,900$ cm^{-1}. The filters in the desired spectral range are named after their peak transmittance: 185 nm, 172 nm, 156 nm and 135 nm. The PMT spectral responses and the filter transmittance curves can be seen in Figure 2.16. Note the 135 nm transmittance curve is an estimate only as the datasheet for the 135 nm filter is missing and recall that the FTS is limited to $\sigma < 71,000$ cm^{-1} ($\lambda > 1400$ Å).

To test the transmittance of the 135 nm filter, the spectrum of the deuterium lamp was observed using the PMT R1259 detector with no filter, a 135 nm filter and a 156 nm filter. The filtered spectra are compared in Figure 2.17a. Using these spectra and the deuterium lamp calibration data, estimated instrument response functions were calculated (using methodology stated in Section 3.1.2) for each of these filters and the R1259 detector, and are shown in Figure 2.17b. As seen in Figure 2.16, the 135 nm and 156 nm filters have a low filter transmittance which results in the large intensity difference seen in Figure 2.17b between the response functions with and without filters.

Multiple combinations of filters and detectors were tested to optimise the SNR of the Fe III spectral lines while minimising the number of Fe II lines included and their SNR.

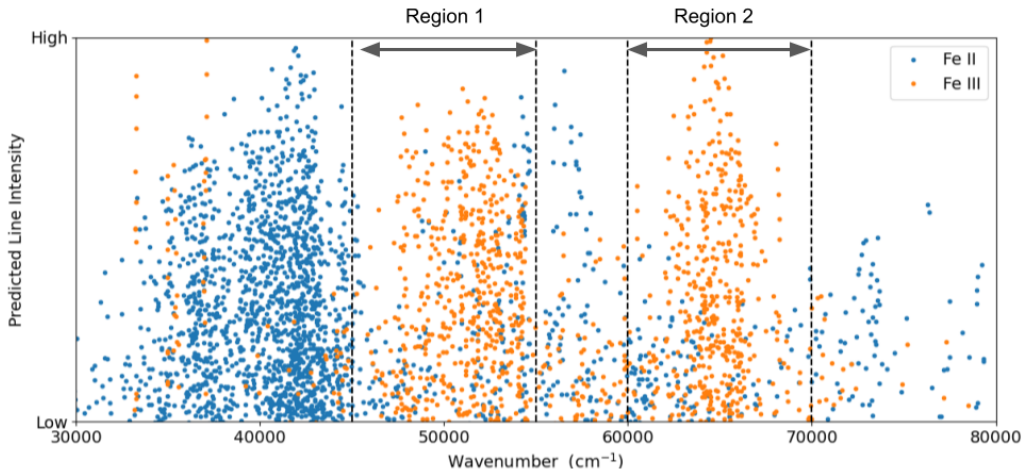


Figure 2.15: The wavenumbers of the strong Fe II (blue) and Fe III (orange) lines in the region $\sim 30,000\,\mathrm{cm}^{-1}$ to $\sim 80,000\,\mathrm{cm}^{-1}$. The predicted line instensity shown is calculated by Kurucz [42] with 2.0 [High] $> \log(gf) > -1.0$ [Low]. The limits of Regions 1 and 2 are indicated by vertical dashed lines.

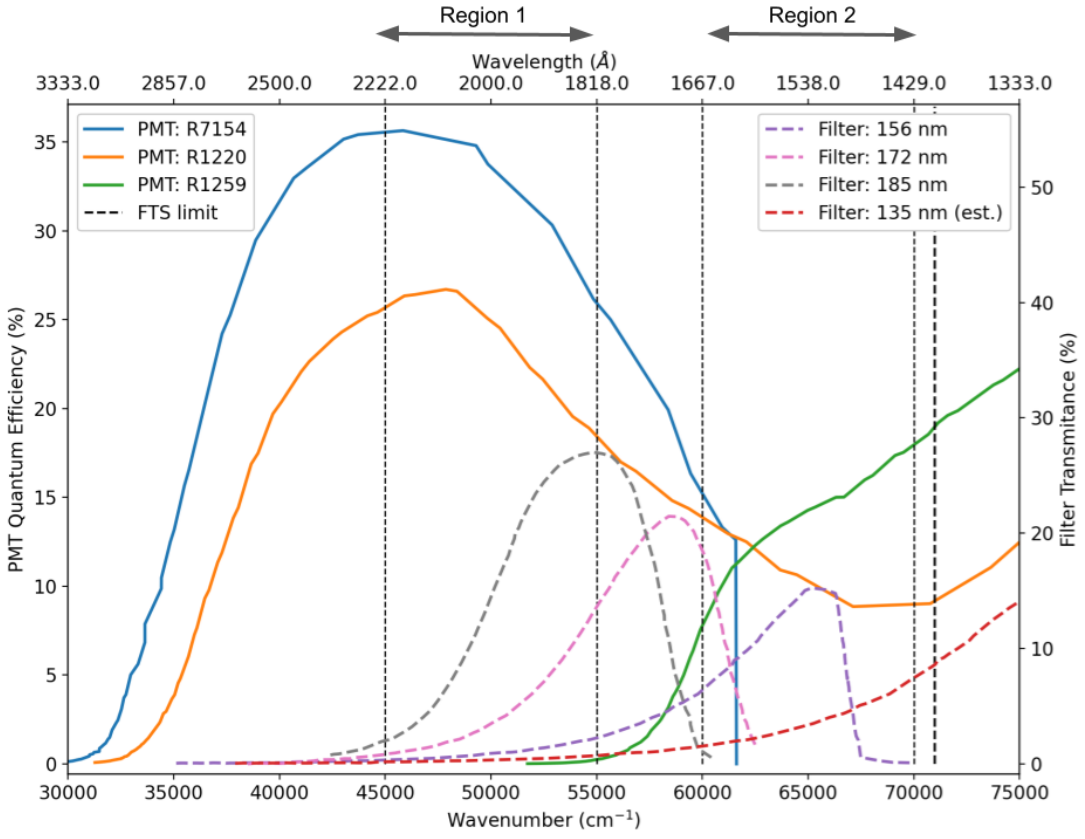
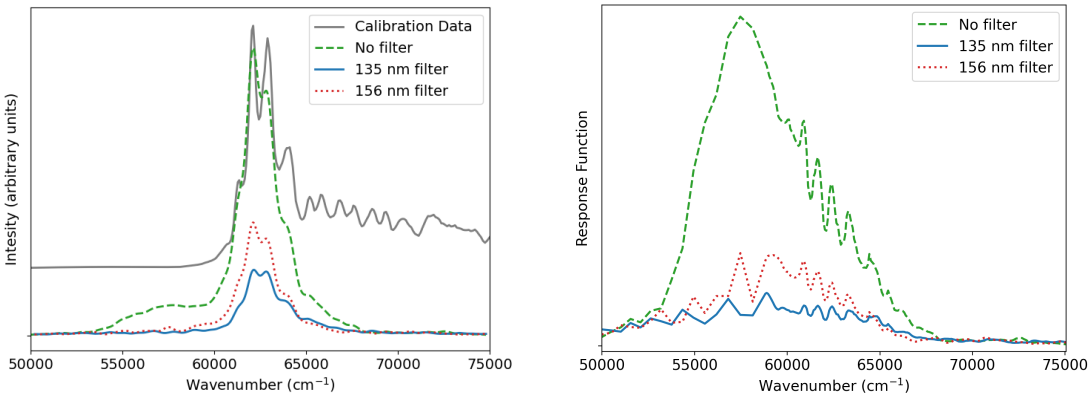


Figure 2.16: PMT quantum efficiencies for the detectors used in this project (R1220, R1259 and R7154 [102]) and the transmittance for the filters used in this project (185 nm, 172 nm, 156 nm and 135 nm [103]) in the spectral region of interest. The datasheets containing this information are provided with the purchase of the detectors and filters. However, the datasheet for the 135 nm filter is missing, and so the transmittance plotted for this filter is an estimate only. The vertical lines are the limits of Regions 1 and 2 and the FTS limit of 71,000 cm^{-1}.



(a) The filtered deuterium lamp spectra and deuterium lamp calibration data

(b) The estimated instrument response function

Figure 2.17: (2.17a) The filtered spectra of the deuterium lamp observed using the R1259 detector with no filter, the 135 nm filter and the 156 nm filter. The deuterium lamp calibration data (Section 2.4) is also shown at a scale to match the intensities of the filtered spectra of the R1259 detector with no filter. (2.17b) The estimated instrument response functions calculated using the observed spectra and the deuterium lamp calibration data.

Region of Interest	Detector PMT	Filter
Region 1	R7154	None
	R7154	185 nm
	R7154	172 nm
	R1220	185 nm
	R1220	172 nm
Region 2	R1220	156 nm
	R1220	135 nm
	R1259	None
	R1259	156 nm
	R1259	135 nm

Table 2.4: The detector and filter combinations tested to optimise the SNR of the Fe III lines in the Regions 1 and 2.

The complete list of the combinations tested for each region is in Table 2.4.

The combination providing the highest SNR for Fe III lines in Region 1 ($45,000\,\mathrm{cm}^{-1} < \sigma < 55,000\,\mathrm{cm}^{-1}$) was the PMT R7154 with the 185 nm filter, and for Region 2 ($60,000\,\mathrm{cm}^{-1}$ to $70,000\ \mathrm{cm}^{-1}$), the PMT R1259 with no filter was optimal.

During these measurements, the impact of the orientation of the filters was also examined. The filters are orientated perpendicularly to the output beam in the filter wheel but are free to tilt within the casing. To test the effect of the angle of the filter within the limits of the casing, the deuterium lamp was observed through a newly-purchased 185 nm filter (named 185 nm19A, discussed further below) with the filter held perpendicular to the beam and with the filter held at the largest angle possible within the wheel. For this filter, no differences were found in the intensity-normalised spectra recorded between $30,000\ \mathrm{cm}^{-1}$ and $60,000\ \mathrm{cm}^{-1}$ (between 1700 Å and 3300 Å) using the detector PMT R7154.

The 185 nm filters

In early experiments of this PhD research, the spectra recorded with the 185 nm filter (later named 185nmOLD) displayed an unexpected spectral response. To test if this was due to degradation of an old filter, the other 185 nm filters available were compared using the deuterium standard lamp. The filters are named after their purchase date: 185nmOLD (unknown year of purchase), 185nm04 (2004), and 185nm19A (2019, newly purchased for this project). There was a notably higher overall intensity on the R7154 detector with measurements using the 185nm04 and 185nm19A filters. Figure 2.18 shows the comparison of the intensity-normalised deuterium standard spectra observed with the PMT R7154 and the 185 nm filters. The intensity of the deuterium lamp varies linearly and gradually over this part of the spectral region, so these spectra are a good representation of the relative instrument response function with these filters. There is a clear shift from the expected peak wavelength in the spectrum of the aged filters in comparison to the newest filter.

Although the regions of focus do not include $55,000\ \mathrm{cm}^{-1}$ to $60,000\ \mathrm{cm}^{-1}$, there are expected Fe III lines in this region which have never before been observed on the FTS. Therefore, the spectra recorded with the highest SNRs in this region were also included in the creation of the final linelist (Section 2.7.1). Spectra using all three of the 185 nm filters (185nmOLD, 185nm04 and 185nm19A) contributed to the final linelist (details of the spectra used are in Section 2.7.1).

2.6.2 Preparing the PDL

To run the PDL, it must be cleaned of any previously sputtered material, and cleaned of any impurities using ethanol. New iron cathodes are fitted into the PDL frame and it is re-constructed. The lamp is first secured to its mount which is attached to the optical table. Then the lamp is attached at the four ports to the gas input, the turbo pump, the FTS nosepiece and the vacuum fitting with a sealed window (for visual observation).

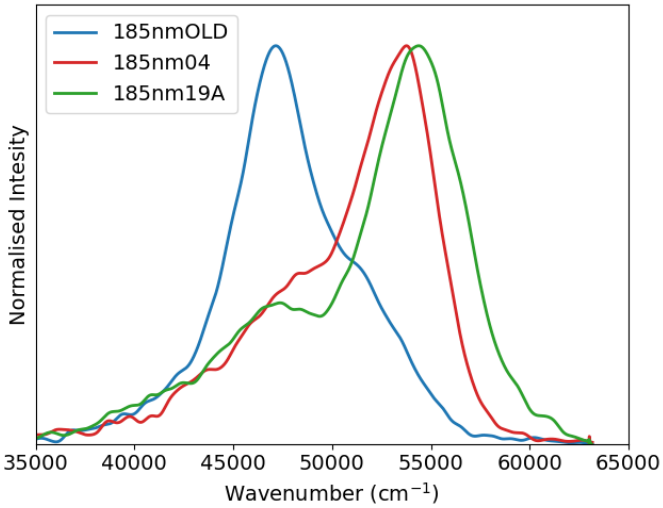


Figure 2.18: The intensity-normalised spectra of the deuterium lamp through three 185 nm filters named 185nmOLD, 185nm04 and 185nm19A, using the detector PMT R7154.

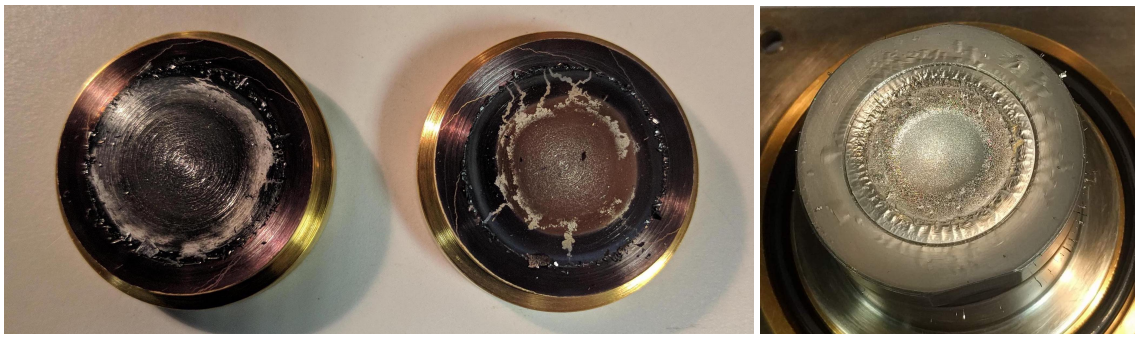
The PDL is now air-tight and the turbo pump is started. The lamp is pumped for an hour before the start of the experiment, evacuating air from the lamp and ensuring there are no leaks in the joins of the pumping tubing and the PDL. The pump evacuated the lamp to a minimum pressure of $\sim 10^{-6}$ mbar before every experiment. Before every measurement, each gas tubing line was also evacuated and leak tested. The lamp and gas lines were then flushed with the chosen buffer gas to ensure any remaining impurities are removed prior to ignition.

Once the nose piece of the FTS pumped, the PDL can be aligned with the FTS optics and, finally, the lamp is securely connected to the stabilised-current power supply via a ground and live wire and a resistor bank.

Creating a Plasma

In order to run the PDL, an acclimatisation period of one hour is required [85, 100] as the PDL will remain stable only when changes in conditions are made slowly. To start, a voltage is applied to the PDL. Then, during the acclimatisation period, the current in the PDL is slowly increased from 0 A to the desired value (1.0 A to 1.7 A) in steps of 0.1 A to 0.2 A and the buffer gas pressure is slowly decreased from $\sim 10^{-3}$ mbar to the desired value ($\sim 10^{-4}$ to $\sim 10^{-5}$ mbar). During this process the voltage across the PDL increases. If the conditions of the PDL are not changed gradually, or the duration of the acclimatising period is not at least one hour, the PDL does not consistently run stably at high currents (> 1.1 A) or low pressures ($< 5 \cdot 10^{-5}$ mbar).

During the acclimatising period, the anode and inside chamber of the PDL becomes coated with deposited iron. This process should be gradual to prevent the deposited material becoming flaky, which results in a short circuit between the anode and cathode. Figure 2.19 displays cathodes after failed experiments, likely due to a short circuits. Figure 2.19a is a picture of cathodes after the lamp failed to ignite. The cathode shown in Figure 2.19b is from an experiment which began as expected but became unstable. This



(a) Cathodes after the PDL failed to strike.

(b) Cathode after discharge became unstable.

Figure 2.19: Iron cathodes from the PDL after failed experiments. Notice the iron flakes in both images, on either the cathodes or cathode holder.

happened when the acclimatisation process was too short. Notice the shallow crater in the cathode and flakes of iron on the side of the cathode holder. If the PDL does not remain stable during the acclimatisation process, or does not work at all due to a short circuit, the experiment has to be restarted. This includes cleaning the lamp of deposited iron, evacuating the lamp for an hour, and replacing the cathodes.

During the operation of the PDL, the cathodes become eroded due to sputtering of material from their surfaces and the iron is deposited on the anode, coating the inside of the PDL. This is the factor limiting the duration of the experiment. Once the plasma was stable, the lamp typically ran for $5 - 8$ hours before the cathodes were completely eroded, depending on the sputtering rate which varied with the operating conditions of the lamp. Once the cathodes are completely eroded, the plasma becomes unstable which is unsuitable for measurement with the FTS (see Section 2.1.3).

There are many variables in the operation of the PDL, including the gas type, gas pressure, current applied, magnetic field strength and variation in the methodology of running the lamp.

2.6.2.1 Optimal Current and Buffer Gas Pressure

The spectral lines from the PDL will be primarily due to Fe II, Fe III or Ne II. The neon lines are not numerous or strong in this spectrum, and are discussed in Section 2.6.2.2. In these measurements, the optimal PDL conditions will produce the ideal spectrum of strong Fe III lines with comparatively weaker Fe II lines.

The current across the lamp and the pressure of the buffer gas can be varied to determine the optimal conditions, but should remain constant throughout the measurement to ensure stable emission intensity [100]. Heise *et al.* (1994) [100] found that a constant gas pressure and current in the PDL results in constant line intensity, when tested with a neon buffer gas and aluminium cathodes. To test this with iron, the PDL was observed for over 3 hours on the FTS using iron cathodes, neon buffer gas at a pressure of $6 \cdot 10^{-5}$ mbar and a current of 1.6 A. In this time, 65 measurements were recorded successively and throughout these measurements the SNR of the strong Fe III line at $52,757.3$ cm^{-1} generally

remained constant, falling by at most 7%. It is clear the PDL meets the FTS requirement of a stable light source with a reasonably constant intensity over several hours.

To determine the optimal gas pressure and current for Fe III, the PDL was run using the conditions Pickering and Smillie used, as a starting point. Smillie used neon gas pressures of $8.5 - 10.0 \cdot 10^{-4}$ mbar with a current of 1.6 A and Pickering used a neon gas pressure of $7.0 \cdot 10^{-5}$ mbar with a current of 1.2 A.

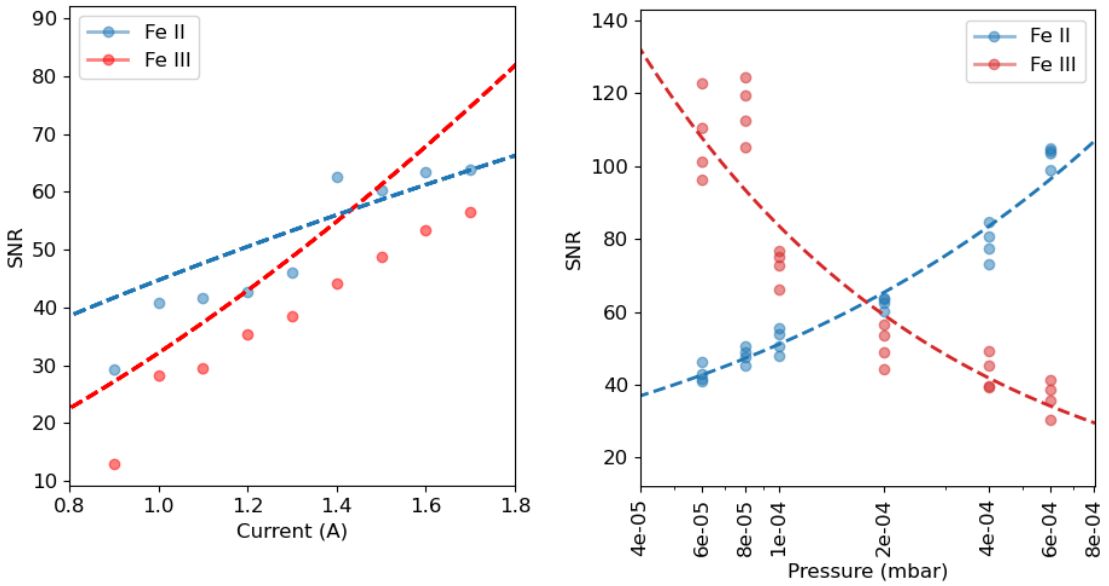
Once the lamp was running successfully with iron cathodes and neon gas, various pressure and current combinations were tested. In these tests, a stable combination was defined as a set of conditions that ran for at least 10 minutes with no change in intensity or voltage. It was usual for the voltage across the lamp to decrease by $100 - 200$ V during the duration of the experiment with a constant current and buffer gas pressure, but this change was observed over several hours. The unstable conditions usually did not run for more than a few minutes. The current was tested at every 0.1 A interval between 0.9 A and 1.7 A. For every current value, every pressure in the following list was tested for stability: $4 \cdot 10^{-5}$ mbar, $6 \cdot 10^{-5}$ mbar, $8 \cdot 10^{-5}$ mbar, $1 \cdot 10^{-4}$ mbar, $2 \cdot 10^{-4}$ mbar, $4 \cdot 10^{-4}$ mbar, and $6 \cdot 10^{-4}$ mbar. At pressures $< 4 \cdot 10^{-5}$ mbar the discharge in the PDL did not remain stable, likely due to insufficient gas pressure leading to insufficient sputtered material to populate the plasma. With a pressure of $4 \cdot 10^{-5}$ mbar, the lamp would not run for more than 10 minutes at currents higher than 1.1 A. During these tests, it became apparent that conditions with a current $>$ 1.3 A or a pressure $< 8 \cdot 10^{-5}$ mbar require a longer acclimatisation period to run stably.

Figures 2.20a and 2.20b display the variation in the approximate SNR of an Fe II and Fe III line with current and pressure. These Fe II and Fe III lines, at $41,472.2$ cm^{-1} and $52,757.3$ cm^{-1} respectively, were chosen as they were visible in every spectrum, and their SNRs are a good representation of the SNRs of the majority of Fe II and Fe III lines present in the spectrum. The lines of best fit in Figures 2.20a and 2.20b are discussed below with a comparison to Heise *et al.* [100].

As seen in Figure 2.20a, there is a positive correlation between the SNR of both Fe II and Fe III lines with the current applied. By using the highest current possible the SNR of Fe III lines will be maximised. Figure 2.20b shows opposing correlations for the SNRs of the Fe II and Fe III lines with increasing gas pressure. To maximise Fe III lines, it is clear that a lower pressure is optimal ($6 - 8 \cdot 10^{-5}$ mbar). This is due to the fact that higher buffer gas pressures will contribute more to the de-excitation of Fe III ions via collisions in the plasma. To minimise the SNR of the Fe II lines, it is also favourable to use the lowest buffer gas pressures. In conclusion, to maximise Fe III in the PDL with iron cathodes and neon buffer gas, the highest current and lowest pressure ($< 1 \cdot 10^{-4}$ mbar) that will run stably will provide the desired results.

Comparison to the PDL studies of Heise *et al.* [100]

Heise *et al.* (1994) [100] studied the PDL with aluminium cathodes and neon buffer gas. Heise *et al.* [100] found that the intensity of an emission line, L, roughly increases with the current, I, by $\mathrm{L} \propto \mathrm{I}^r$, where r is equal to the ionisation stage for the metal lines.



(a) Signal-to-noise Ratio of Spectral Lines at Various Currents.

(b) Signal-to-noise Ratio of Spectral Lines at Various Pressures.

Figure 2.20: The SNR of the Fe II ($41,472.2$ cm^{-1}) and Fe III ($52,757.3$ cm^{-1}) lines in the PDL varying with current and pressure. The data in Figure 2.20a displays the data for the pressure $2 \cdot 10^{-4}$ mbar only, but the line of best fit was calculated using all pressures. Figure 2.20b displays only data with current > 1.3 A, with which the line of best fit was calculated.

For Fe II lines ($r = 1$), it would be expected that L $\propto$ I, and for Fe III ($r = 2$), it is expected to be L $\propto$ I^2.

While determining the optimal currents and buffer gas pressures, the spectra recorded were not intensity calibrated (a process described in Section 3.1.2) and so no line intensities were calculated. However, every observation was measured on the IC VUV FTS under the same filter and detector conditions within a relatively short time frame. This should result in very similar instrument response functions (used for intensity calibration), and so it can be assumed that any variation in SNR is due to changes in the plasma. Therefore, the SNR can be used as a similar measure of line strength.

Using the model, SNR $\propto$ I^t, for Fe II t was calculated to be 0.7 and for Fe III, $t = 1.6$. These lines are shown on Figure 2.20a. These values are not the same as the r values calculated by Heise *et al.* [100], but the same trend is present in the t values. It confirms that higher ionisation ions have a larger increase in intensity with current in comparison to lower ionisation ions.

Heise *et al.* [100] also stated that for the ionised metal atoms tested, line intensities fall with increasing gas pressure and that the rate of decrease is greater for higher ionisations. The observation of the SNR of the Fe III line in Figure 2.20b concurs with this. Applying the model of SNR $\propto$ P^t on the Fe III line data (for currents > 1.3 A) results in $t = -0.50$. However, the Fe II trend opposes the conclusion by Heise *et al.* [100], with a calculated t value of 0.35. These lines are plotted on Figure 2.20b. This difference in trends observed could be due to the fact that Heise *et al.* [100] did not study iron-group elements, but aluminium.

2.6.2.2 Neon Spectral Lines

The NIST Atomic Spectra Database (ASD) [41] states that the strongest Ne II line expected (by far) in the FTS spectral region observed is at $52,189.84$ cm^{-1}. This line was investigated with varying currents and gas pressures. The line appeared weak and there was no significant correlation between the SNR and the pressures or currents tested. Therefore, the optimal conditions for the PDL were varied regardless of the effect these have on the neon spectral line strengths.

Smillie (2007) [85] also did not find any significant trends in the intensity of the neon gas lines over the current and pressures used in the PDL with iron cathodes. Heise *et al.* [100] found that for the ionised buffer neon gas, the line intensity dropped with an increase in gas pressure. The results presented here could not confirm this, although it may be due to the limited range of gas pressures tested in this research. However, Heise *et al.* [100] also stated that the intensity difference is greater for metal ions than for the buffer gas ions, and so a correlation for the neon data would be more difficult to observe in comparison to the iron data.

2.6.2.3 Buffer Gas Type

Previous studies by Smillie (2007) [85] and Pickering used neon as a buffer gas to successfully create and excite Fe III, but any noble gas could theoretically be used. By varying the buffer gas used in the PDL with iron cathodes, different Fe III levels may be excited in the plasma. Smillie (2007) [85] tested the metals Fe, Cr and Co in the PDL with neon, argon and neon-helium gas mixtures, but found success with neon only. Pickering tested neon and argon with iron cathodes and also found no success with argon.

In this project, neon, argon and helium buffer gases were tested with iron cathodes in the PDL for stability. The plasma was unstable with the argon and helium gases but successful with neon, and so neon-helium and neon-argon gas mixtures were also tested. Figure 2.21 displays photographs of the plasma in the PDL using different buffer gases. The gas type determined the dominant light emitted and therefore the colour of the plasma and as the gas pressure was decreased, the colour would become more white.

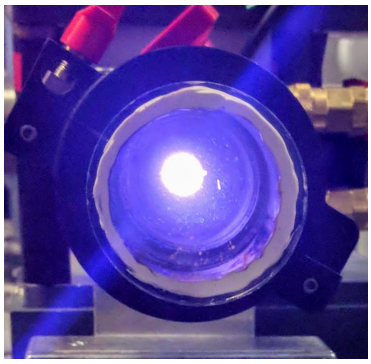
The neon-helium gas mixtures with ratios 1:1 and 1:2 were successful in creating a stable plasma with iron cathodes in the PDL. The combined pressures throughout the successful observations were between $6 \cdot 10^{-5}$ mbar and $4 \cdot 10^{-5}$ mbar, which is lower than the minimum operating gas pressure for neon alone in the PDL ($6 \cdot 10^{-5}$ mbar). However with the addition of helium, the duration of the lamp stability was reduced with no increase in SNR of the Fe III lines relative to Fe II lines. Therefore, the spectra used in the final linelist were measured using neon as the buffer gas.

2.6.2.4 Reusing Cathodes and Cleaning the PDL

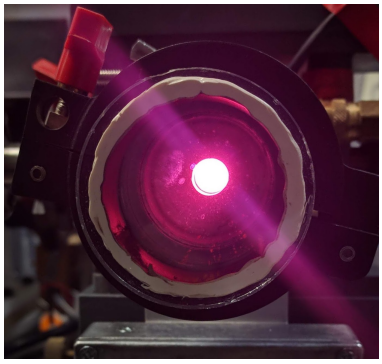
At the start of every experiment, the used iron cathodes are replaced and the lamp cleaned of any iron deposits. However, if partially used cathodes could be used at the start of the experiment, and the PDL did not have to be cleaned of iron deposit between



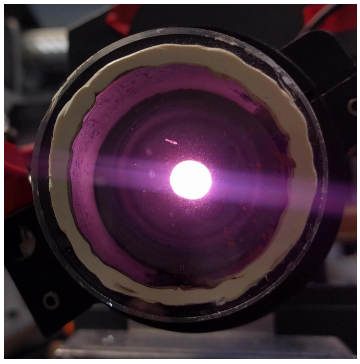
(a) Photograph of the PDL plasma. The cathodes are located above and below the image.



(b) PDL plasma with argon gas.



(c) PDL plasma with neon gas.



(d) PDL plasma with neon-helium gas mixture.

Figure 2.21: Photographs of the PDL plasma with iron cathodes under different running conditions as seen through the optical port.

Dataset Label	Day Observed	Pressure (mbar)	Current	Voltage	Observations Recorded
-	Day 1 (29-08-2019)	-	-	-	0
A	Day 2 (30-08-2019)	$1 \cdot 10^{-4}$	1.0 A	750 V	60
B	Day 2 (30-08-2019)	$9 \cdot 10^{-5}$	1.4 A	840 V	37
C	Day 2 (30-08-2019)	$6 \cdot 10^{-5}$	1.5 A	900 V	2
D	Day 3 (03-09-2019)	$6 \cdot 10^{-5}$	1.6 A	940 V	65

Table 2.5: Summary of the data recorded using the PDL on subsequent days without cleaning the PDL of iron deposit or replacing used cathodes. The number of observations in each set will be co-added (as discussed in Section 3.1.1.1).

experiments, iron cathode material waste could be minimised and time spent cleaning the lamps between experiments could be saved.

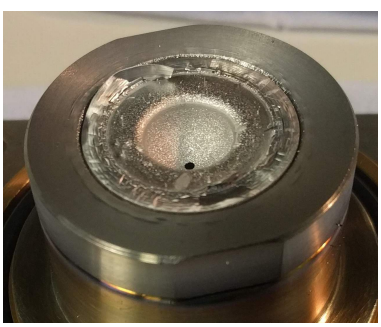
To test if the spectra observed using partly-used cathodes and a PDL coated with a thin iron deposit would provide data of quality comparable to a clean PDL with new cathodes, the PDL was run daily with the same pair of iron cathodes without cleaning the PDL between experiments, until the PDL would no longer run. The same 185nm04 filter, R7154 PMT detector and neon gas source was used for all observations, summarised in Table 2.5.

After an unsuccessful attempt to operate the PDL (on Day 1), the lamp was opened and any loose flakes were removed to prevent a short circuit when restarting on Day 2. The cathodes appeared similar to the image in Figure 2.19b, with no crater formed but some signs of use on the cathode surface. A very thin layer of iron had deposited on the anode and the inside chamber of the PDL which was left untouched. During Days 2 and 3, the lamp ran very smoothly with similar acclimatisation times. Each data set was recorded at the lowest pressure and highest current possible whilst maintaining plasma stability. As seen in Table 2.5, with a longer running time, the achievable pressure is lowered and the achievable current is greater.

The PDL failed to restart after a short-circuit on Day 3. The reason was obvious once the lamp was opened; the cathodes had completely eroded. The image of the cathodes and anode after Day 3 can be seen in Figure 2.22. Notice the thickness of the iron deposit on the anode.

The SNRs of the Fe II lines were consistent in all the Datasets B, C and D. As Dataset D was recorded at the highest current and lowest pressure achieved in this test, it was expected to provide the highest SNR of Fe III lines relative to Fe II lines. However, after comparing a single observation from each data set it was unexpectedly found that the spectrum with the lowest current, Dataset B, had the better relative SNR for Fe III lines. The build up of deposited iron increased with each measurement and may have impacted the conditions in the plasma, reducing the presence of Fe III.

In conclusion, although the PDL will run stably without changing any cathodes and without cleaning deposited iron, the quality of data is not a match to the spectra created



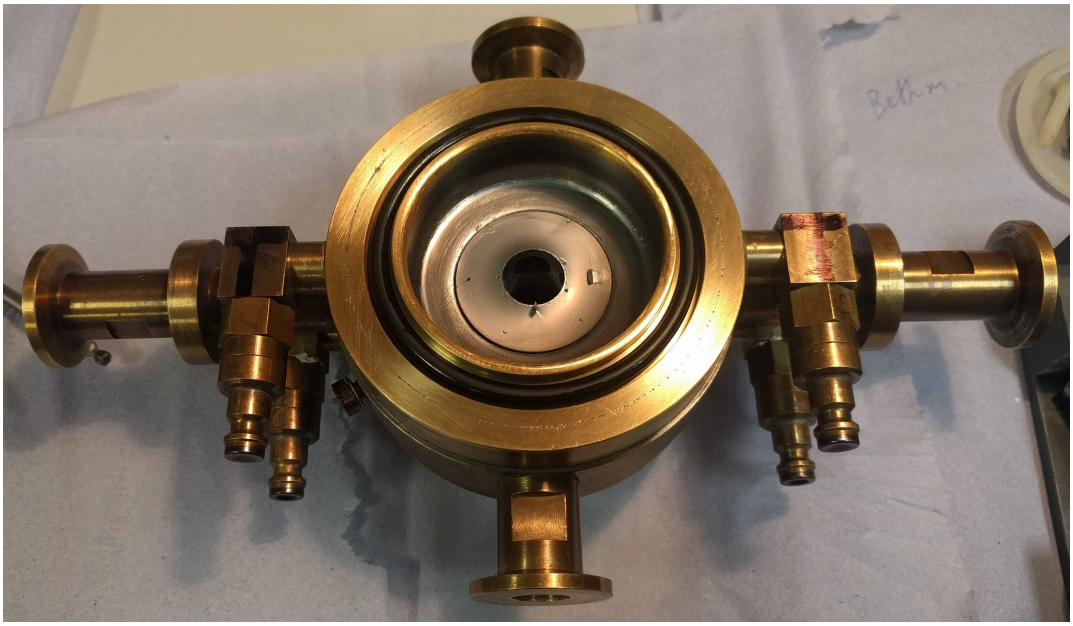
(a) Upper cathode



(b) Lower cathode



(c) Bottom side of anode



(d) Top view of the centre part of the PDL, including the upper side of anode

Figure 2.22: The cathodes and anode after reusing cathodes in the PDL. Generally, the images of the PDL are taken at a distance to prevent damage to the camera from the strong magnets behind the cathodes.

using a clean lamp with new cathodes. Therefore, it is still optimal to clean the PDL and replace the cathodes before every experiment.

2.7 Final Measurements

2.7.1 FTS Measurements

During this project, 21 high quality iron spectra were recorded using the PDL on the IC VUV FTS, in the region $33,493$ cm^{-1} to $65,508$ cm^{-1} ($\sim$ 1500 Å to $\sim$ 3000 Å). The spectra with the highest SNR lines, in any part of the spectral region where Fe III lines are present, were selected for use in the final linelist. These spectra are listed in Table 2.6 alongside the conditions of the PDL at the time of observation, the detectors and filters used, and the aperture size. The spectral ranges and resolutions of the resultant spectra are also included. For each of these data sets the deuterium lamp was also recorded for intensity calibration (discussed further in Section 3.1.2).

The spectrum recorded by Pickering (Section 1.2.1) has some Fe III lines with SNR higher than any of the data sets recorded on the IC VUV FTS. Therefore, this spectrum (Fe203) will be also used to create the final linelist as detailed in Section 3.1.

2.7.2 Grating Measurements

As stated in Table 1.1, the iron spectrum is needed between $40,000$ cm^{-1} and $130,000$ cm^{-1} (770 Å to 2500 Å) to record the spectral lines due to the transitions between the lower-lying levels of Fe III. As mentioned in Section 2.5, FTS data will be used where possible due to its much greater resolution and supplemented with grating data beyond the FTS lower wavelength limit. As seen in Section 2.7.1, the highest wavenumber line recorded on the FTS is $65,508$ cm^{-1} (1527 Å) and a preliminary check found that the Fe III lines observed using the FTS at $\sigma > 60,000$ cm^{-1} ($\lambda < 1667$ Å) region were weak. Therefore, the grating linelist should have substantial wavenumber overlap with the FTS linelist to ensure Fe III spectral lines are recorded in the desired regions. As previously mentioned (Sections 1.2.1 and 2.2.1), Belmonte recorded the iron spectrum of an Fe-Ne PDL using the NIST NIVS on photographic detector plates between 525 Å and 3520 Å (~28,000 cm^{-1} and 190,000 cm^{-1}), with a grating slit width of 21μm. The tracks and plates which contain data in the desired spectral region ($\sigma > 60,000$ cm^{-1}, $\lambda < 1667$ Å) are listed in Table 2.7.

The spectral region observed on the detector plates used at NIST NIVS is determined by the grating angle of rotation. The data in Table 2.1 is used to determine the wavelength region exposed across the two plates.

As seen in Table 2.7, Tracks 5.1 and 5.2 measured the same spectral region with different PDL conditions. Part of the Tracks 5.1 and 5.2 can be seen as the fourth and third tracks in Figure 2.7, respectively. Although the observation with the lowest PDL pressure, Track 5.2, is expected to provide the better Fe III data (Section 2.6.2.1), both tracks appeared very similar by eye in terms of the presence and strength of spectral lines. Track 5.1 was chosen for the final linelist, as the image of the track appeared to have less dirt on the scanner, which would provide the most accurate wavelengths. Tracks 3.1 and 5.3

Data set	PDL conditions: Current, Pressure and Voltage	PMT Detector (10 stage)	Filter	Res. (cm^{-1})	Apt. (mm)	Spectral range (cm^{-1})
Fe327 (29)	1.3 A ; $9.0 \cdot 10^{-5}$ mbar; 850 V	R7154	185nmOLD	0.1	1.5	35306 to 58753
Fe116 (94)	1.5 A ; $6.0 \cdot 10^{-5}$ mbar; 910 V	R7154	185nm04	0.13	2.0	33493 to 60260
Fe831 (96)	1.0 A ; $1.0 \cdot 10^{-4}$ mbar; 750 V	R7154	185nm04	0.13	2.0	33826 to 61147
Fe832 (35)	1.4 A ; $9.0 \cdot 10^{-5}$ mbar; 840 V	R7154	185nm04	0.13	2.0	35913 to 58753
Fe903 (63)	1.6 A ; $6.0 \cdot 10^{-5}$ mbar; 940 V	R7154	185nm04	0.13	2.0	35913 to 58753
Fe103 (95)	1.4 A ; $7.0 \cdot 10^{-5}$ mbar; 860 V	R7154	185nm19A	0.13	2.0	33493 to 61664
Fe121 (26)	1.5 A ; $7.2 \cdot 10^{-5}$ mbar; 890 V	R1259	None	0.22	2.5	51912 to 65508
Recorded by Pickering:						
Fe203 (16)	1.2 A ; $7.0 \cdot 10^{-5}$ mbar; 800 V	R166 (earlier version of R7154)	185 nm	0.2	2.5	33889 to 55591

Table 2.6: The selected data sets for use in the final FTS linelist. All the data sets were recorded during this PhD project, except Fe203 which was recorded by Pickering in 1997. The data were recorded on the IC VUV FTS using the PDL with iron cathodes and neon gas. The voltage stated in the PDL conditions is the voltage recorded at the start of measurements. The number of observations in each set is in parentheses after the data set name, which are co-added to create the spectrum as discussed in Section 3.1.1.1. The Res. column lists the resolution of the spectra and the column named Apt. lists the aperture size of the FTS used during the measurements.

Track ID	Plates name	Exposure times (mins)	Tank Pressure (mbar)	PDL conditions: Current, Pressure and Voltage	Grating Angle	Grating Window
3.1	x1013	5, 10, 43	$2.0 \cdot 10^{-5}$	1.5 A ; $1.2 \cdot 10^{-3}$ mbar; 1.01 kV	7 °	MgF_2 window
5.1	x1015	5, 10, 45	$1.6 \cdot 10^{-5}$	1.5 A ; $1.2 \cdot 10^{-3}$ mbar; 1.01 kV	5 °	None
5.2	x1015	5, 10, 45	$1.6 \cdot 10^{-5}$	1.2 A ; $6.0 \cdot 10^{-4}$ mbar; 1.01 kV	5 °	None
5.3	x1015	5, 10, 45	$1.6 \cdot 10^{-5}$	1.2 A ; $5.8 \cdot 10^{-4}$ mbar; 1.0 kV	7 °	None

Table 2.7: Selected grating data recorded at NIST NIVS by Belmonte in 2019. Each track recorded on a plate has been given a Track ID in order of exposure.

are both measured at 7°, but the recording of the Track 3.1 used a MgF_2 window which limits the transmission of radiation in the wavelength region < 1200 Å ($\sigma > 83,300\,\text{cm}^{-1}$). Therefore, Tracks 5.3 and 5.1 on the plates named x1015 will be used to create a grating linelist, providing grating data from $55,556\,\text{cm}^{-1}$ to $190,476\,\text{cm}^{-1}$ (525 Å to 1800 Å) . The creation of the grating linelist is explained in Section 3.2.

2.8 Summary

This chapter detailed the spectrometers and light sources used to obtain the Fe III spectrum. The experiments using the PDL and IC VUV FTS are detailed, including the process of determining the PDL optimal running conditions. The capabilities of the IC VUV FTS and NIST NIVS are compared and used to determine the spectral regions that will be studied by each instrument. The best results for the Fe III spectra recorded on the FTS have been summarised and supplemented with selected data recorded by Belmonte on the NIST NIVS. In the next chapter, the linelists are acquired from the experimentally measured FTS and grating data, for use in the term analysis process.

Chapter 3

Linelist Preparation

In this chapter, the creation of spectral linelists from the FTS data and the grating image plates is described. In Section 3.1, the individual FTS observations are used to create wavenumber and intensity calibrated linelists. All the FTS data were then placed on the same relative intensity scale and merged into a single master FTS linelist for the region $33,826$ cm^{-1} to $65,508$ cm^{-1} (1527 Å to 2956 Å) . Section 3.2 details the process of creating wavenumber calibrated linelists from the grating photographic detector plate images. These linelists were then combined to create a single master grating linelist in the spectral region $55,090$ cm^{-1} to $111,121$ cm^{-1} (900 Å to 1815 Å). Finally, these linelists are compared to each other and the results of previous Fe III publications in Section 3.3.

3.1 The FTS Linelist

This section describes the process of creating a linelist for each FTS data set listed in Table 2.6 and the merging of these linelists to create a master FTS linelist (Section 3.1.5). The program *Xgremlin* [91] is used for the analysis of FTS spectra. In this project, it was used for the spectrum extraction, creation of the linelist and the intensity calibration.

3.1.1 Spectrum Extraction

3.1.1.1 Co-adding Interferograms

For each data set recorded on the FTS, multiple interferograms were measured consecutively under the same PDL conditions. These interferograms were then "co-added" together, resulting in the signal constructively interfering, increasing the signal by the number of interferograms, N. The random white noise, however, increases by a factor of $\sqrt{N}$. The final co-added spectrum has an improved signal-to-noise ratio (SNR) equal to $\frac{N}{\sqrt{N}} = \sqrt{N}$. By improving the SNR of spectral lines, their statistical uncertainty is reduced resulting in more accurate wavenumbers (Section 3.1.4.2). The number of interferograms co-added in each data set is listed in parentheses after the data set name in Table 2.6. For each data set, the largest possible number of co-adds were recorded. However, this number varied for each measurement as it relied on the stability of the PDL.

Data set	Number of points in interferogram	Point number of centre of interferogram	Number of terms	Intensity discriminator
Fe327	631920	309271	4	0.024
Fe116	486092	245111	8	0.020
Fe831	486092	249467	3	0.020
Fe832	486092	249463	4	0.020
Fe903	486092	248055	6	0.019
Fe103	486092	249651	6	0.018
Fe121	155363	79596	8	0.027

Table 3.1: Details of the polynomial fit for phase correction of the IC VUV FTS spectra. The intensity discriminator is measured relative to the peak intensity.

3.1.1.2 Phase Correction

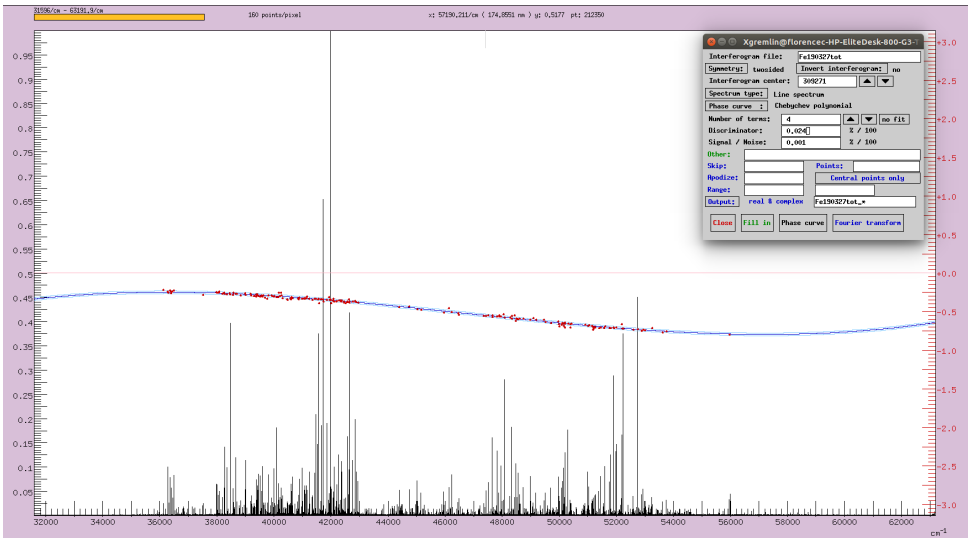
The co-added interferogram is then Fourier transformed, producing a complex spectrum with a real and imaginary component of the light source observed. Ideally, the interferogram is completely symmetrical, resulting in a zero imaginary component of the spectrum [104]. Realistically, measured interferograms are asymmetric so some information on line shape, position and height is lost in the imaginary component of the spectrum [90]. The phase correction is the process of minimising the imaginary component in the Fourier transformation, and therefore reducing the information loss [90].

In *Xgremlin*, the phase correction is determined by fitting a Chebyshev polynomial to suitable spectral lines. In this case, the lines with the highest intensities were deemed suitable and selected using an intensity discriminator relative to the peak intensity of the spectrum. The intensity discriminator, the number of terms used in the polynomial and the point in the interferogram identifying the central fringe are all varied to determine the optimal polynomial fit to the phase shift across the spectrum. The details of the polynomials for the phase corrections of the FTS spectra are listed in Table 3.1. The Chebyshev polynomial fitted to the phase shifts for the FTS data can be seen in Figures 3.1, 3.2 and 3.3. The red dots are the phase shifts for individual lines and the dark blue line is the polynomial fit. The light blue lines indicate the 66% confidence level of the fit. The Fe203 spectrum was phase corrected by Pickering and the details of the polynomial used for correction are not available.

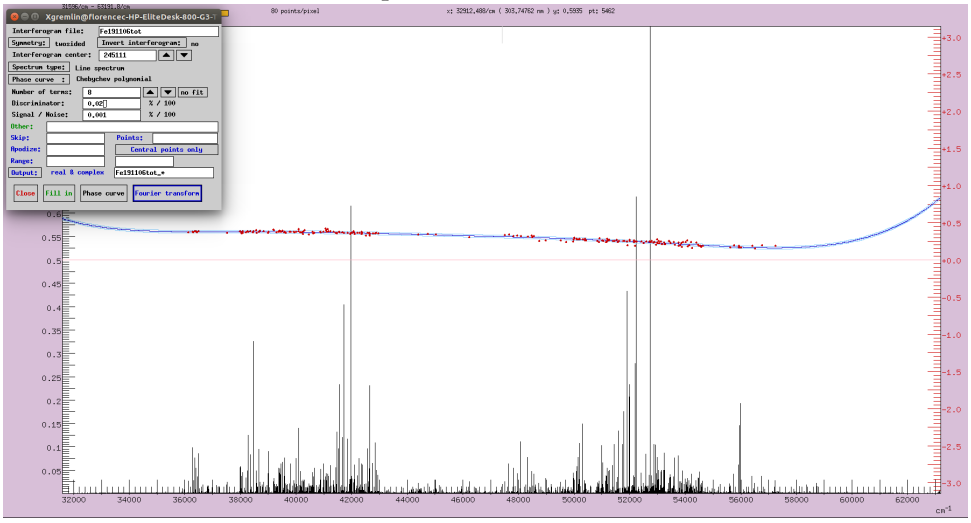
The interferogram is then transformed using the chosen polynomial and the real component of the complex spectrum is saved for subsequent spectral analysis.

3.1.1.3 Signal-to-Noise Ratio

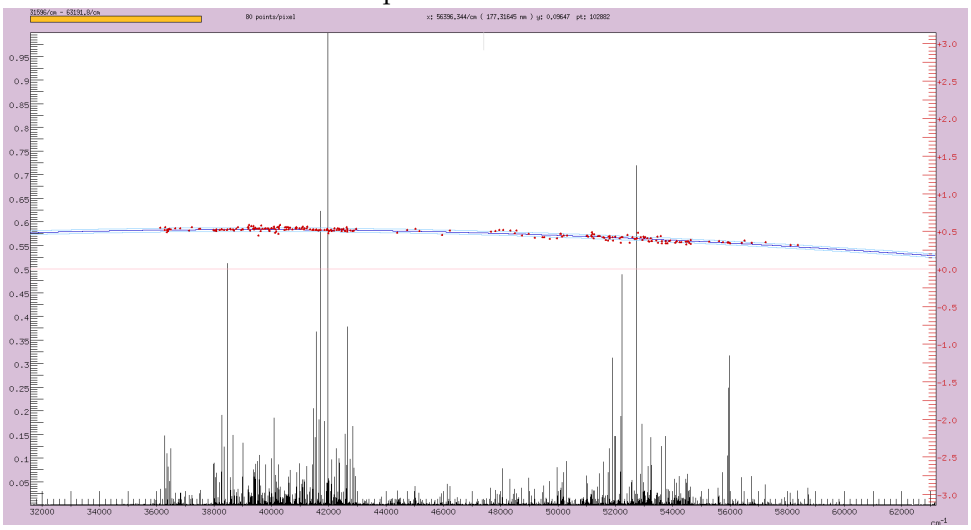
The intensity scale of the spectrum is arbitrary. It is beneficial to place the peak values of the spectral lines on a scale relative to the noise present throughout the spectrum. To determine the noise level, *Xgremlin* is used to calculate the root-mean-square (RMS) deviation in a region of the spectrum with no spectral lines. To ensure no spectral lines



(a) The phase correction of Fe327

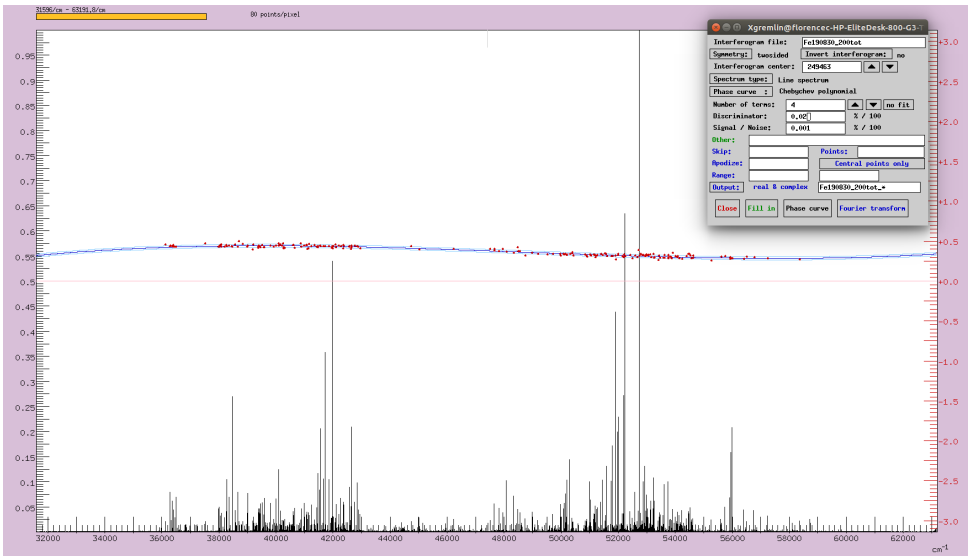


(b) The phase correction of Fe116

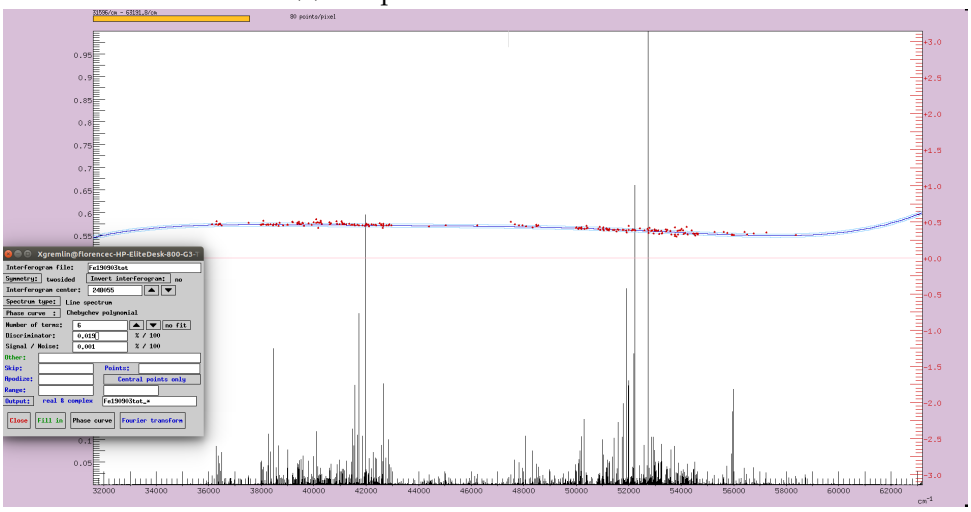


(c) The phase correction of Fe831

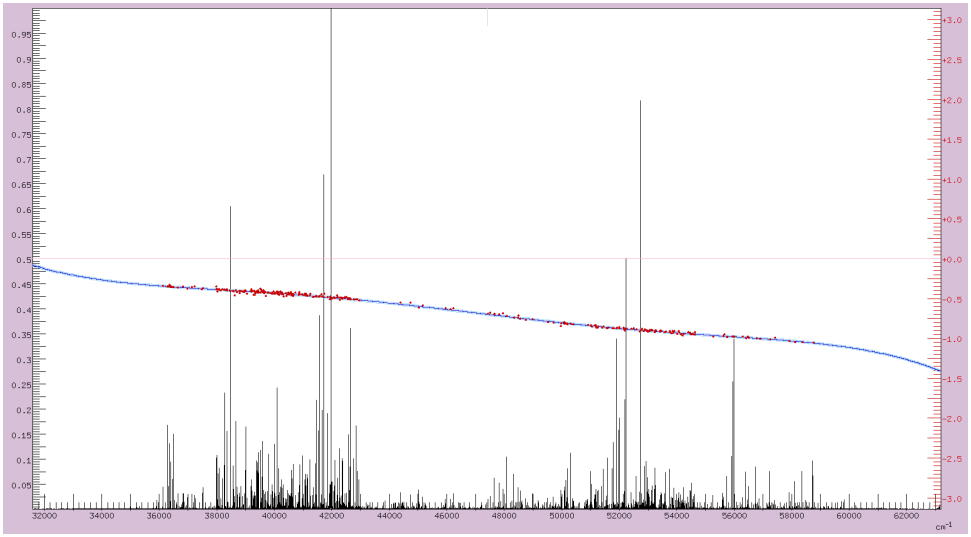
Figure 3.1: The polynomial fits used for the phase correction of the IC VUV FTS spectra Fe327, Fe116 and Fe831. The x axes are the wavenumbers in cm^{-1} and the y axes are the intensities relative to the strongest spectral lines. The red dots indicate the phase shift of individual lines and the dark blue line is the polynomial fit.



(a) The phase correction of Fe832

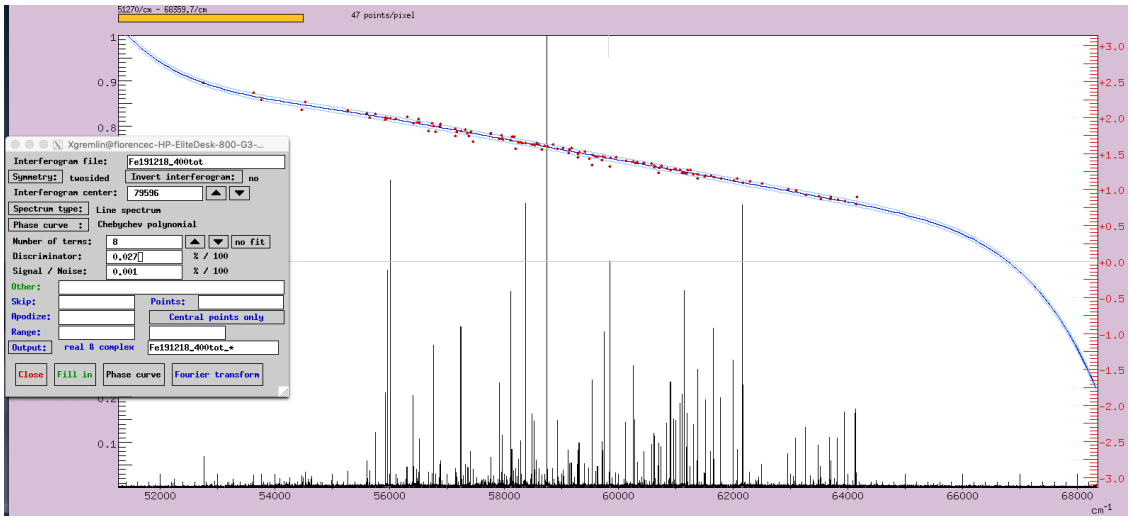


(b) The phase correction of Fe903



(c) The phase correction of Fe103

Figure 3.2: As in Figure 3.1, the polynomial fits used for the phase correction but for the IC VUV FTS spectra Fe832, Fe903 and Fe103.



(a) The phase correction of Fe121

Figure 3.3: As in Figure 3.1, the polynomial fit used for the phase correction but for the IC VUV FTS spectrum Fe121.

are included in the calculation, the region is selected using the noise level and shape at the boundaries of the spectrum (where no signal is present due to filter, detector or instrument limitations) as a guide. By scaling the intensity of the entire spectrum by the inverse of the RMS, the noise level is set to 1 and the peaks of the spectral lines are signal-to-noise ratios (SNRs). These SNRs are more meaningful than arbitrary intensities and are used in wavenumber uncertainty calculations (Section 3.1.4.2). This process was applied to the FTS data sets listed in Table 2.6.

3.1.1.4 Line Shape

To make a linelist of wavenumbers, relative intensities, FWHMs and SNRs, the observed spectral lines need to be fitted and to fit the spectral lines accurately, it is important to consider their line shape. The shape of the spectral lines emitted from the PDL is influenced by many processes. Here the effects of the iron isotope structure, the presence of an external electric field and the presence of an external magnetic field are investigated. The spectral lines are also broadened by three main processes which will be discussed in this section: natural broadening, pressure broadening and Doppler broadening. These result in spectral lines with a Voigt profile. Further details on line shapes and line broadening can be found at Thorne *et al.* (1999) [51], Svanberg (2004) [105] and Bransden & Joachain (2010) [106].

Isotope structure

The presence of isotopes can result in isotope shifts of the spectral lines due to differences in the nuclei. Iron has many naturally occurring isotopes with the most abundant isotope being ^{56}Fe ($\sim 92\%$), followed by ^{54}Fe ($\sim 6\%$) [108]. It is clear that the ^{56}Fe isotope will be the major contributor to the spectral lines due to its high relative abundance. The iron isotope structure was investigated by Rosberg *et al.* (1993) [107] and one of the lines

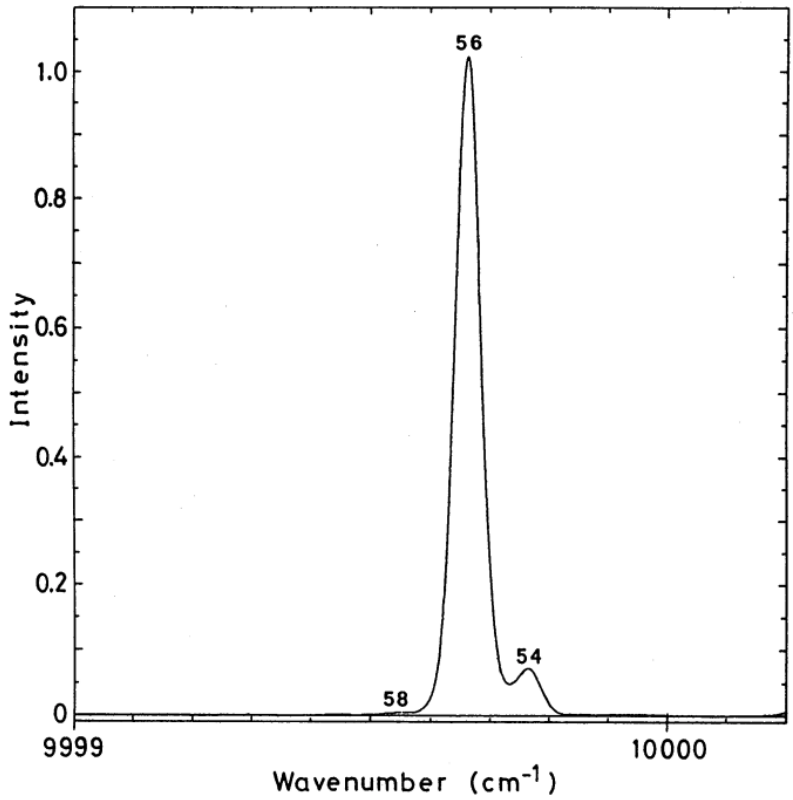


Figure 3.4: This image from Rosberg *et al.* (1993) [107] displays the isotopic structure in the Fe II line at 9999.7 cm^{-1}.

studied can be seen in Figure 3.4. The isotopic shift between the isotopes ^{56}Fe and ^{54}Fe was calculated to be ~ 0.10 cm^{-1}. However, the spectral lines in this project are observed with a full width at half maximum (FWHM) of ~ 0.40 cm^{-1} and so it is unlikely that any isotopic shift will be seen. Isotope structure was not considered in this project, and it was found that the majority of the unblended lines in the FTS spectra were symmetric.

Stark effect

The Stark effect is the splitting of energy levels, and therefore the observed spectral lines, due to the presence of an external electric field. To observe Stark splitting the electric field strength must be greater than $10^6 - 10^7$ Vm^{-1} [51]. The discharge voltage on the PDL remained lower than 1 kV in this project, and for the discharge region of ~ 24 mm in the PDL, the electric field is estimated to be less than 10^5 Vm^{-1}. Therefore, Stark splitting will not be observed in spectral lines from the PDL.

Zeeman effect

The Zeeman effect is the splitting of a spectral line due to an external magnetic field. The shift in the energy level, ΔE, due to a magnetic field of strength, B, is

$$\Delta E = g_J \mu_B m_J B \,, \tag{3.1}$$

where g_J is the Landé g factor, μ_B is the Bohr magneton constant and m_J is the projection of the total angular momentum, J, (defined in Section 4.1) in the axis of the magnetic field, with $m_J = -J, -J+1, ..., J-1, J$ [51].

For the PDL with a magnetic field strength of ~ 0.1 T and by approximating g_J as 1 [51], for $m_J = 1$ the magnitude of the energy splitting is 0.047 cm^{-1}. As the splitting is symmetric the result is an overall energy spread of 0.093 cm^{-1}. However, the width of the spectral lines in the PDL are typically about 0.4 cm^{-1}, and so this splitting would be unseen in the this work.

Natural broadening

Natural broadening is the limiting factor of the width of the observed spectral lines and is the consequence of the finite natural lifetime of an excited energy level, after which spontaneous emission occurs. The Heisenberg uncertainty principle states $\Delta E \cdot \Delta t \sim \hbar$, relating the uncertainty of the lifetime of the level, Δt, with the uncertainty of the transition energy, ΔE. For a finite level lifetime, there is an uncertainty in the energy of the emitted photon, which over several emissions will cause the observed frequency to spread about a central wavenumber, broadening the line. The population of the excited level is modelled as exponentially decaying over time and the Fourier transformation of the exponential decay produces a Lorentzian shape in the frequency domain [51].

Pressure broadening

There is also line broadening due to the collisions of particles called pressure broadening which is dependent on the density and temperature of the plasma [51]. Collisions transfer kinetic energy which can result in the emission of a photon, effectively reducing the natural lifetime of an excited state due to spontaneous emission only. The number of undisturbed atoms is modelled by an exponential decay which, similarly to the Natural broadening, results in an increase in the energy uncertainty and produces a Lorentzian profile in the frequency space.

Doppler broadening

Spectral lines are also broadened by Doppler broadening. The Doppler shift refers to the small wavelength shift of photons emitted due to the motion of a particles within the plasma relative to the line of sight. This motion is due to thermal energy and therefore correlates with temperature. The velocities are modelled using a Maxwell distribution, which results in an observed Gaussian distribution about the central wavenumber in the frequency domain [51, 106]. This is the dominant broadening process in the spectral lines of the PDL. As Doppler broadening correlates with temperature, the widths of the spectral lines can be reduced by water-cooling the PDL, which in turn improves the wavenumber accuracy.

Voigt profile

For types of line broadening that are independent, the resultant line profile is the convolution of the independent line profiles. In this case, combining the profiles of the broadening processes listed above results in the convolution of the Gaussian and Lorentzian profiles, producing a Voigt profile.

The Voigt profile is used to fit the spectral lines observed by the FTS from the PDL, determining wavenumbers, peak line intensities (SNRs), line widths and equivalent widths for each line (discussed further in Section 3.1.1.5). The ratio of Gaussian to Lorentzian contribution used in the fitting of the Voigt profile is varied for each individual line. As the spectral lines in this work are dominated by Doppler broadening, the majority of lines were fit using a Voigt profile that was mostly Gaussian, with about 50% of the lines fit to a pure Gaussian profile.

3.1.1.5 Line fitting

As stated in Section 3.1.1.4, the Voigt profile is a good fit for resolved spectral lines measured on the FTS from the PDL.

Least-Square Fit

Xgremlin was used to execute least-squares (LSQ) fits on spectral lines to a Voigt profile, providing many line parameters including the line:

- wavenumber (cm^{-1}),
- peak height (SNR),
- full width at half maximum, FWHM (cm^{-1}),
- and integrated intensity, as the equivalent width (cm^{-1}).

The intensity is defined as the area under the spectral line, and is measured using the equivalent width (cm^{-1}) of the Voigt profile and the peak height (SNR).

Centre-of-Gravity fit

If a spectral line is heavily blended, asymmetrical or noisy, it cannot be fitted well to the Voigt profile and a Centre-of-Gravity (CoG) fit is used. *Xgremlin* calculates a weighted central wavenumber of the line between manually selected limits. This means the area under the spectral line will be equal on either side of the weighted central wavenumber. These lines have larger uncertainties than LSQ fit lines.

Linelist creation

Xgremlin automatically finds spectral lines with a SNR above a given value and executes LSQ fits. However, the residuals of the fits are visually inspected and some lines are added if missed, refitted or removed as needed. These linelists with LSQ and CoG fitted

File name	Linelist range (cm^{-1})	Total number of lines	Complete linelist?	Number of lines used in final linelist
Fe327	35306 to 58753	1946	Yes	993
Fe116	33493 to 60260	1327	Yes	276
Fe831	33826 to 61147	1754	Yes	618
Fe832	35913 to 58753	577	Partial	53
Fe903	35913 to 58753	591	Partial	36
Fe103	33493 to 61664	1761	Yes	983
Fe121	51912 to 65508	1427	Yes	1249
Fe203	33889 to 55591	1093	Yes	415

Table 3.2: A summary of the FTS linelists used in the combined master FTS linelist

lines were made for each FTS spectrum. For the Fe832 and Fe903 spectra, only partial linelists were made, meaning that not every line in the spectrum was included in the linelist. These spectra contained some Fe III lines which were not observed in the other spectra, and so those lines along with Fe II calibration lines were the only lines included in the linelists. The number of lines in each linelist and their spectral ranges are listed in Table 3.2. The number of lines used in the final FTS linelist from each spectrum is also stated (discussed further in Section 3.1.5).

These linelists are now ready to be intensity and wavenumber calibrated.

3.1.2 Intensity Calibration

In the FTS spectra, the SNR and equivalent width of a spectral line does not provide a true intensity of the line as the efficiencies of the FTS optics, filters and detectors have not been taken into account.

As mentioned in Section 2.4, by comparing the observed spectrum of a calibration lamp, L_{obs} with the expected calibrated spectrum, L_{standard}, the response function of the spectrometer, R, can be calculated by

$$R = \frac{L_{\text{obs}}}{L_{\text{standard}}} \, . \tag{3.2}$$

This response function includes the efficiency of the entire instrument and is used to compute the true relative intensity of the observed spectral lines.

The intensity of a line is defined as the area under the spectral line profile, and is recorded in the linelist in the form of the equivalent width (cm^{-1}). During intensity calibration, the equivalent width is divided by the calculated response function to reflect the true relative intensity of the lines. Therefore once intensity calibrated, it is possible for two lines observed in different wavenumber regions of a spectrum to have the same SNR, but different equivalent widths and, by definition, different relative intensities.

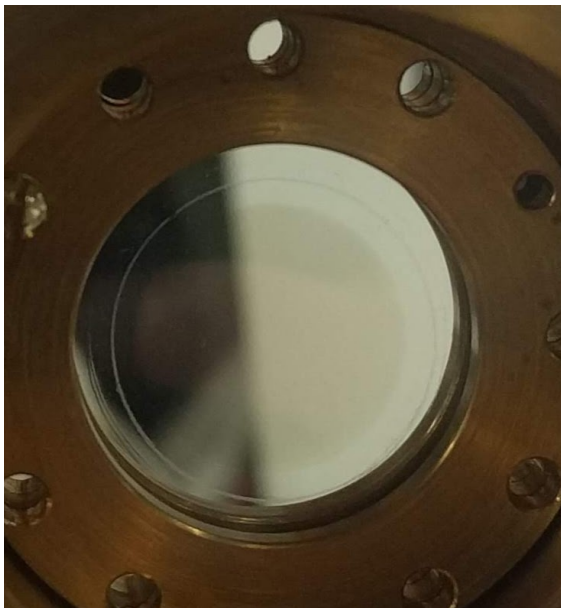


Figure 3.5: A photograph of the MgF_2 window placed between the PDL and nose piece.

3.1.2.1 PDL MgF_2 window

The deuterium calibration lamp is used to intensity calibrate spectra in the VUV. The deuterium spectrum must be obtained under the same instrument conditions (i.e. filter, detector, FTS tank pressure, etc.) as the light source and several other factors must also be considered, as described below.

As seen in Figures 2.4 and 2.5, both the deuterium lamp and PDL are connected to the FTS nosepiece. However, as mentioned in Section 2.3, a MgF_2 window is placed between the PDL and the FTS nosepiece which will not be included in the calculated instrument response function as it is not also in the light path to the deuterium lamp.

This MgF_2 window was new at the start of the experiment, but had very small amounts of iron deposited on it throughout the measurements. A photograph of the window at the end of this project is shown in Figure 3.5. The faint ring due to contact with an O-ring can be seen, and inside it, the very slightly darkened circle seen is due to material sputtered from the PDL onto the window. A variation in transmissivity with respect to wavenumber due to this window would result in an incorrect instrument response function. In order to test if the addition of this darkened window changed the spectrum of the PDL entering the FTS, the transmission of the following windows were compared using the standard deuterium lamp and the PMT R1220: the used PDL MgF_2 window, a new MgF_2 window, and no MgF_2 window.

The deuterium spectra recorded without a MgF_2 window present had the highest intensity relative to the spectra with a MgF_2 window. A reduction in intensity is expected beyond $\sim 47,600\ \text{cm}^{-1}$ (1200 Å) as the transmission of the MgF_2 window decreases from $\sim 94\%$ to a maximum of $\sim 60\%$ between approximately 2100 Å and 1200 Å ($\sim 47,600\ \text{cm}^{-1}$ to $\sim 83,300\ \text{cm}^{-1}$) [109].

Figure 3.6 displays the deuterium spectra, as observed with PMT R1220, for the spectral region measured in this project through the used PDL MgF_2 window, a new

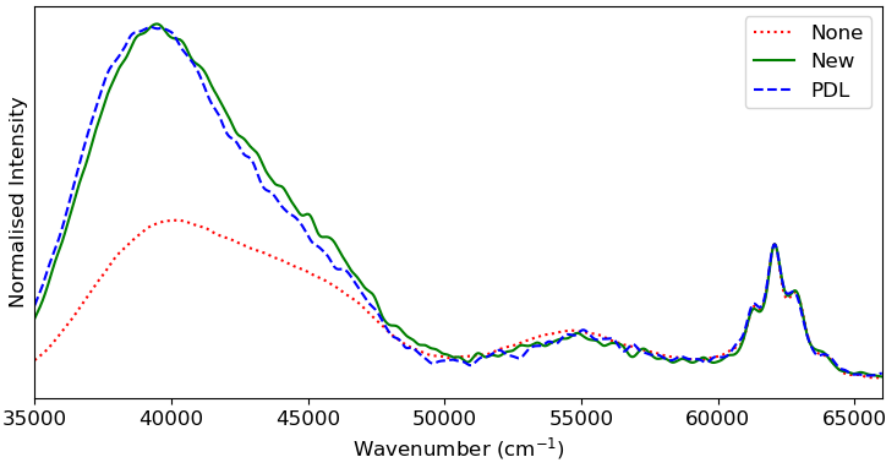


Figure 3.6: The deuterium spectra as observed with PMT R1220, for the spectral region measured in this project through the used PDL MgF_2 window, a new MgF_2 window, and no MgF_2 window. The deuterium spectra is intensity-normalised to the peak intensity at $63,000$ cm^{-1}.

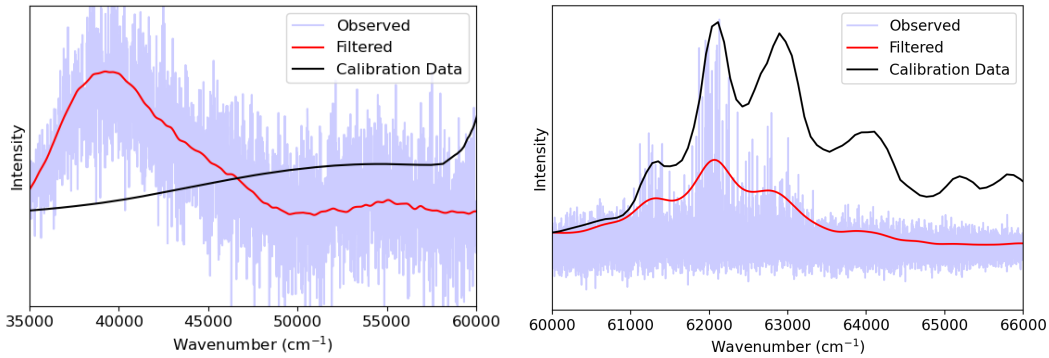
MgF_2 window, and no MgF_2 window. The spectra are normalised to the intensity at $63,000$ cm^{-1} to better compare the spectral response in the region where Fe III lines are observed in the FTS measured spectra, $\sigma > 45,000\,\text{cm}^{-1}$. In this region, the spectra appear very similar, and so no corrections will be made to the calculated instrument response functions.

3.1.2.2 Instrument Response Functions

As mentioned in Section 2.4, the deuterium lamp data for each spectrum is recorded after the PDL measurements under the same spectrometer conditions, except for a variation in aperture size. For the deuterium lamp, the spectra was recorded at a resolution of 0.5 cm^{-1} with an aperture size of 4 mm. Using *Xgremlin*, the deuterium interferograms are co-added, phase corrected and Fourier transformed. The resultant spectrum is used to determine the instrument response function. First, the deuterium spectrum is filtered to the same resolution as the calibration certificate data provided with the lamp. For the region 1228 Å to 1700 Å ($58,823$ cm^{-1} to $81,433$ cm^{-1}) the calibration certificate data was recorded at 2 Å intervals and for the region 1700 Å to 4100 Å ($24,390$ cm^{-1} to $58,823$ cm^{-1}) the intervals were 10 Å apart.

Figure 3.7 displays the observed deuterium lamp spectrum, the filtered lamp spectrum and the deuterium lamp calibration data in the spectral region $35,000$ cm^{-1} to $66,000$ cm^{-1} ($\sim$1520 Å to $\sim$2900 Å) . The spectrum of the deuterium lamp varies gradually between $35,000$ cm^{-1} and $60,000$ cm^{-1} ($\sim$1670 Å and $\sim$2900 Å) as seen in Figure 3.7a, but there are line features at higher wavenumbers. Figure 3.7b displays the need for filtering the observed spectrum to match the calibration data which is at a much lower resolution than the observed spectrum.

Once the spectrum is filtered, it is compared to the calibration data to obtain the instrument response function, R, with respect to wavenumber. The deuterium lamp data



(a) The region $35,000$ cm^{-1} to $60,000$ cm^{-1}.

(b) The region $60,000$ cm^{-1} to $66,000$ cm^{-1}.

Figure 3.7: The observed deuterium lamp, the filtered spectrum and the deuterium lamp calibration data for the spectral region $35,000$ cm^{-1} to $66,000$ cm^{-1}. The calibration data has been scaled to match the intensities in the filtered spectrum.

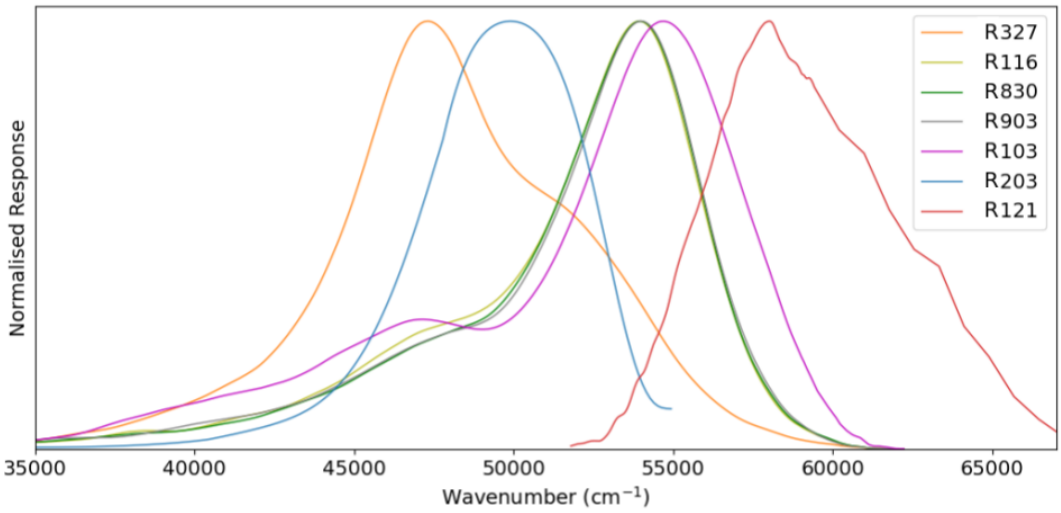


Figure 3.8: The instrument response functions for the IC VUV FTS data. Note that the response function named Fe830 is used for Fe831 and Fe832.

Response function	Deuterium data set	Number of co-adds	Spectrum
R327	D190327.001 - 016	16	Fe327
R116	D191106.010 - 034	25	Fe116
R830	D190830.001 - 025	25	Fe831, Fe832
R903	D190903.001 - 025	25	Fe903
R103	D191030.001 - 025	25	Fe103
R121	D191218.001 - 128	128	Fe121

Table 3.3: Deuterium data recorded for intensity calibration of the IC VUV FTS spectra. All spectra were recorded with a resolution of 0.5 cm^{-1}. The details of the spectral region, filters and detectors for each spectrum are listed in Table 2.6.

and the created response functions for each spectrum are listed in Table 3.3. Note, the response function named R830 is used for both the Fe831 and Fe832 spectra as these spectra were recorded under the same filter, detector, and FTS conditions. The calculated instrument response functions can be seen in Figure 3.8. As stated in Section 2.7.1, each spectrum used to create the final FTS linelist had the highest SNR lines in a spectral region where Fe III lines are present. In Figure 3.8 it can be seen in which region each spectrum is likely to have the superior SNR lines.

For the Fe203 spectrum, the intensity calibration data was not recorded at the time of measurement and so an instrument response function could not be calculated using deuterium data. However, by assuming that the PDL excited the strongest lines equally in the observation of Fe203 and the other FTS spectra, an instrument response function for Fe203 can be estimated. By calculating the ratio of the uncalibrated Fe203 equivalent widths with the calibrated equivalent widths of other spectra, an approximate response function is determined. The smoothed plot of the ratio of the Fe203 equivalent widths with the calibrated Fe832 equivalent widths provided a reasonable response function, as seen in Figure 3.8. This response function may not be accurate due to variations in excitation in the PDL. To check the response function is a reasonable estimate, the calculation was repeated for all spectra with overlapping lines producing similar results. As a final check, the FTS spectra were also overplotted and the relative SNRs were as expected from their response functions.

The linelist of each data set was then intensity corrected using the corresponding response function, and exported from *Xgremlin*. This was done for all IC VUV FTS data sets using the deuterium data listed in Table 3.3.

3.1.2.3 Common intensity scale

Once all linelists were intensity calibrated, all FTS spectra were placed on the same intensity scale. Using the overlapping lines between spectra, an average ratio of the equivalent widths between each spectrum and the Fe327 spectrum was calculated and used to bring all lines to the same intensity scale. As an example, the ratio for lines between the Fe103 and Fe327 spectra can be seen in Figure 3.9. Some scatter is expected, as the varying PDL plasma conditions will result in different ratios of line intensities.

The uncertainties on the calibration lamp data, as stated in Section 2.4, are between 7% and 14%. No further uncertainties were calculated for the intensities listed in the linelist. The intensity calibration executed here is an estimate and to be used only as a guide. The intensity calibration data are useful in the term analysis process, but not essential.

3.1.3 Wavenumber Calibration

The FTS uses the interference fringes of a frequency-stabilised He-Ne laser that takes the same optical path through the FTS tank as the light source to determine the sampling intervals of the interferogram [110]. Therefore, the observed FT spectrum is already on a scale linearly proportional to the true wavenumbers. To calibrate the wavenumbers in

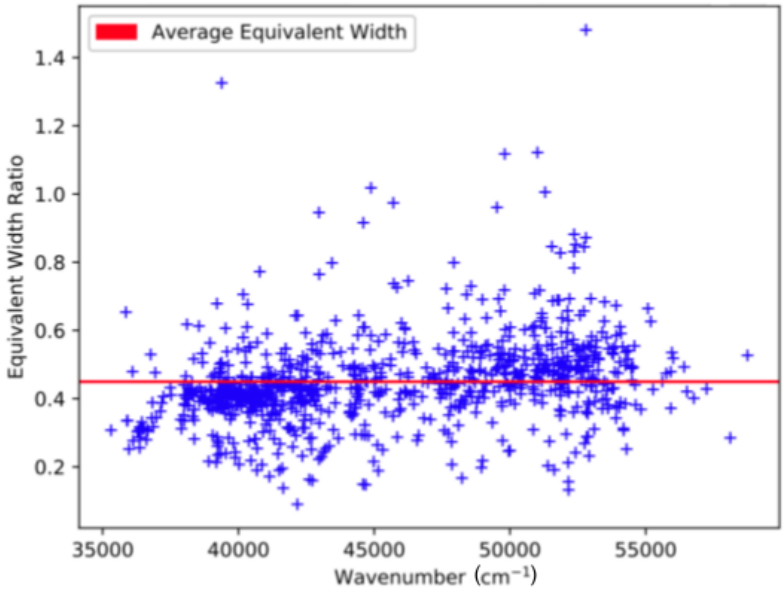


Figure 3.9: The ratio of the equivalent widths for lines in the Fe103 to the Fe327 spectra.

the spectrum, only a small wavenumber dependent shift is required using the equation

$$\sigma_{\text{calib}} = (1 + k_{\text{eff}}) \cdot \sigma_{\text{obs}} \,, \tag{3.3}$$

where σ_{obs} and σ_{calib} are the observed and calibrated wavenumbers and k_{eff} is the correction factor. The correction factor is calculated by comparing the wavenumbers of the calibrated reference lines to their observed wavenumbers. Although theoretically, the correction factor could be calculated using a single reference line, by using several reference lines, the error is greatly reduced [79]. A single line correction factor, k_i, is defined as

$$k_i = \frac{\sigma_{\text{ref}}}{\sigma_{\text{obs}}} - 1 \,, \tag{3.4}$$

where σ_{ref} is the wavenumber of the reference line. The uncertainty of this single line correction factor, δk_i, is the addition in quadrature of the relative uncertainty of the reference line and the relative uncertainty of the observed line:

$$\delta k_i = \sqrt{\left(\frac{\delta\sigma_{\text{ref}}}{\sigma_{\text{ref}}}\right)^2 + \left(\frac{\delta\sigma_{\text{obs}}}{\sigma_{\text{obs}}}\right)^2} \,. \tag{3.5}$$

where $\delta\sigma_{\text{ref}}$ is the uncertainty of the reference line and $\delta\sigma_{\text{obs}}$ is the uncertainty of the observed line. The uncertainty of the observed line, in this case, is equal to the statistical uncertainty of the line (Chapter 3.1.4). The single line correction factors, k_i, are weighted by their uncertainty and combined into a single correction factor for a spectrum, k_{eff}, by

$$k_{\text{eff}} = \frac{\sum_i k_i \cdot \omega_i}{\sum_i \omega_i} \quad \text{where} \quad \omega_i = \frac{1}{\delta {k_i}^2} \,. \tag{3.6}$$

The accurately measured wavenumbers and term analysis of the Fe II spectrum was

published by Nave & Johansson (2013) [1]. Their data was recorded using hollow cathode discharge lamps on various FT spectrometers and the NIST NIVS. Their Ritz wavenumbers were calculated using the energy level values determined during the term analysis. These lines have lower wavenumber uncertainties than the observed spectral lines and therefore can be used as standards to wavenumber calibrate the observed Fe III spectra. The lines published by Nave & Johansson lie in the range 900 Å to $49,777$ Å with Ritz uncertainties ranging from 0.00004 Å to 0.4 Å. These wavelengths and their uncertainties are converted to wavenumbers using methodology stated in Section 3.2.5. The wavenumbers of the spectral lines range from $2,009$ cm^{-1} to $111,122$ cm^{-1} with uncertainties ranging from 0.00032 cm^{-1} to 0.093 cm^{-1}. These Fe II Ritz wavenumbers were used to wavenumber calibrate the recorded FTS spectra in this thesis.

For each FTS spectrum, Fe II lines are selected for calibration and ideally are spread evenly throughout the spectrum. Lines were selected based on their properties as observed by Nave & Johansson to ensure they are likely to be strong and unblended, and their calculated Ritz wavenumber uncertainty to minimise the uncertainty in the calculated correction factor. The Fe II lines were selected from the Nave & Johansson linelist using the following criteria:

- The line must be observed with no known issue (i.e. blended),
- the line must be observed with an uncertainty < 0.01 cm^{-1},
- the line can be observed via any method of observation (i.e. grating, FTS), and
- the Ritz wavenumber uncertainty of the line must be below a given limit (which varied for each spectrum).

The selected Fe II lines from the Nave & Johansson linelist were matched to lines in the observed FTS spectra within a wavenumber tolerance, which varied for each spectrum. The observed lines were only suitable for calibration if the spectral line:

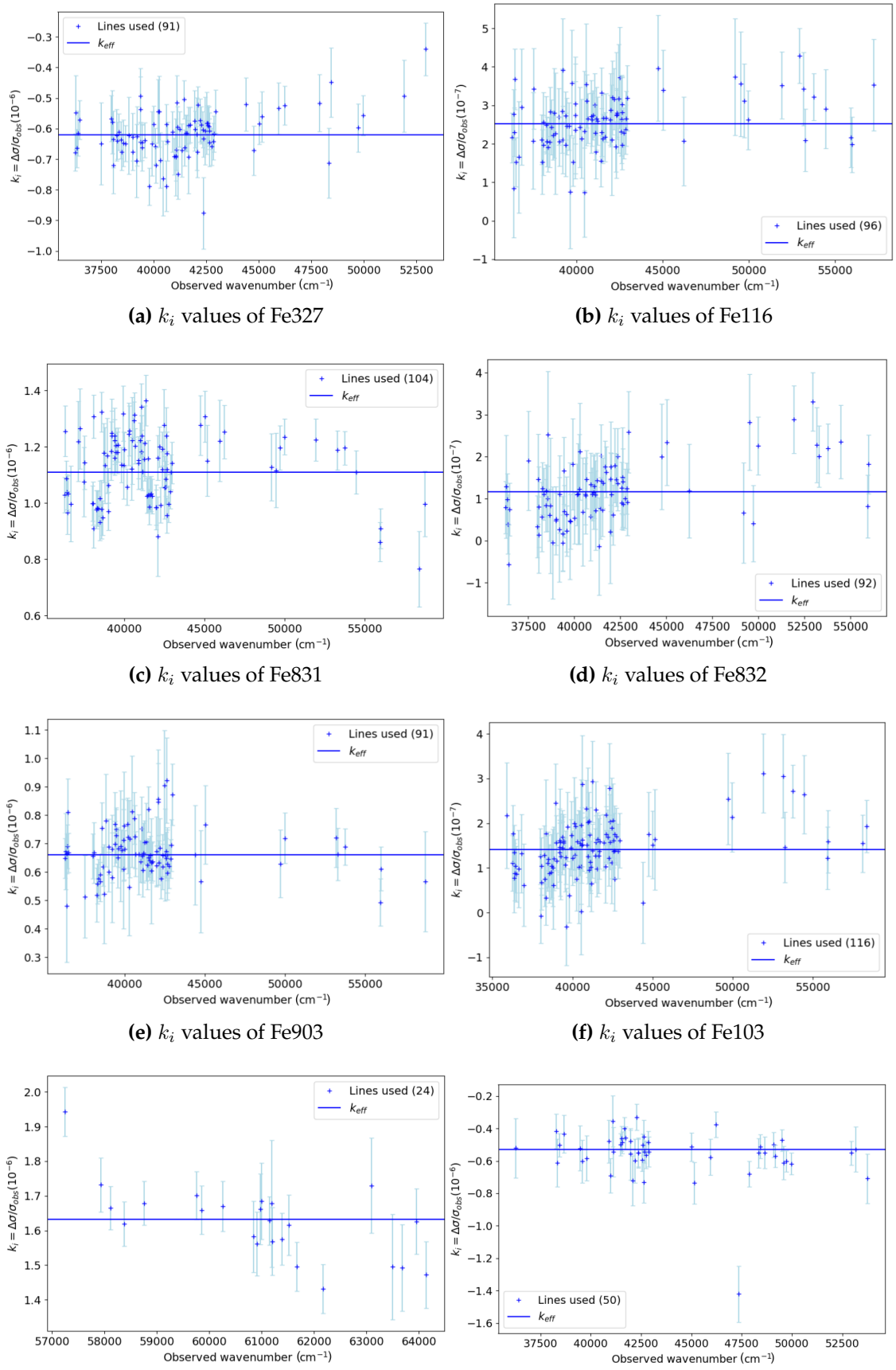
- had no known issue (i.e. blended),
- was fitted with a *lsqfit*, and
- had a SNR greater than a lower limit (which varied for each spectrum)

These selection criteria ensured no questionable lines were used for calibration.

The details of the selection criteria for the lines used for calibration are listed in Table 3.4. For each spectrum, the table lists the observed linelist spectral range; the spectral range of the Fe II lines used for calibration; the maximum allowed Ritz wavenumber uncertainty of the Fe II reference lines (as calculated by Nave & Johansson); the minimum allowed SNR of the observed FTS lines; the wavenumber tolerance used to identify the Fe II reference lines in the observed linelist; the total number of Fe II reference lines used for wavenumber calibration; the calculated calibration factor, k_{eff}; and calculated calibration factor uncertainty, δk_{eff}, (discussed in Section 3.1.4.1).

Spectrum Name	Linelist range (cm^{-1})	Wavenumber Calibration range (cm^{-1})	Maximum Ritz unc. of Fe II ref. lines (cm^{-1})	Minimum SNR of Obs. lines	Matching tolerance (cm^{-1})	Number of Lines Used	Correction factor, k_{eff}	Correction factor unc., δk_{eff}
Fe327	35306 to 58753	36277 to 52946	0.0035	30	0.04	91	$-6.196 \cdot 10^{-7}$	$1.01 \cdot 10^{-8}$
Fe116	33493 to 60260	36277 to 57247	0.0060	30	0.03	96	$2.513 \cdot 10^{-7}$	$2.14 \cdot 10^{-8}$
Fe831	33826 to 61147	36277 to 58753	0.0060	30	0.07	104	$1.107 \cdot 10^{-6}$	$8.50 \cdot 10^{-8}$ *
Fe832	35913 to 58753	36277 to 55967	0.0080	30	0.02	92	$1.172 \cdot 10^{-7}$	$1.83 \cdot 10^{-8}$
Fe903	35913 to 58753	36277 to 58753	0.0060	25	0.04	91	$6.605 \cdot 10^{-7}$	$3.43 \cdot 10^{-8}$ *
Fe103	33493 to 61664	35913 to 58377	0.0060	35	0.02	116	$1.423 \cdot 10^{-7}$	$1.55 \cdot 10^{-8}$ *
Fe121	51912 to 65508	57247 to 64140	0.0080	15	0.13	25	$1.633 \cdot 10^{-6}$	$3.01 \cdot 10^{-8}$
Fe203	33889 to 55591	36277 to 53762	0.0050	30	0.08	50	$-5.295 \cdot 10^{-7}$	$5.05 \cdot 10^{-8}$ *

Table 3.4: Details of the selection criteria for the Fe II reference lines and for the observed FTS lines used for wavenumber calibration, and the calculated correction factors and uncertainties. These are discussed in detail in Sections 3.1.3 and 3.1.4.1. The calibration factor uncertainties, δk_{eff}, with an asterisk (*) have an increased uncertainty and have been calculated differently, as explained in Section 3.1.4.1.



(a) k_i values of Fe327

(b) k_i values of Fe116

(c) k_i values of Fe831

(d) k_i values of Fe832

(e) k_i values of Fe903

(f) k_i values of Fe103

(g) k_i values of Fe121

(h) k_i values of Fe203

Figure 3.10: The fits for the wavenumber calibration of the FTS spectra calibrated with the Fe II Ritz lines. Each data point is a k_i value, and the solid blue horizontal line is the calculated k_{eff}. The error bars (light blue) include the Fe II Ritz wavenumber uncertainties and the statistical wavenumber uncertainties of the observed lines.

To visually check that the wavenumber differences between the reference and the observed Fe II lines are consistent across the spectrum, the single line correction factors, k_i, have been plotted for each calibration line used in each spectrum as shown in Figure 3.10. Ideally, the k_i values would be constant and small, and the Fe II calibration lines will be evenly spread throughout the spectrum. For the spectra with the range $\sim 35,000$ cm^{-1} to $\sim 60,000$ cm^{-1}, it is clear the majority of the Fe II lines used for calibration are $\sigma < 44,000$ cm^{-1}. There may also be a shift or trend in the k_i values at $\sigma > 44,000$ cm^{-1}, best seen in Figure 3.10f. This will be discussed further in the next section, Section 3.1.4.

Once all the FTS spectra had been wavenumber calibrated, the newly calibrated Fe II lines were compared to the wavenumber standards to confirm the data was correctly calibrated.

3.1.4 Wavenumber Uncertainties

To calculate the total wavenumber uncertainty for each spectral line, both the calibration uncertainty and statistical uncertainty must be taken into account. The calculation of each uncertainty and the total wavenumber uncertainty is discussed here.

3.1.4.1 Calibration Uncertainty

The calibration uncertainty, $\delta\sigma_{\text{calib}}$, is calculated for each spectrum as it depends on the correction factor uncertainty, δk_{eff}, for each data set. The weighted uncertainty of the correction factor is calculated by

$$\delta k_{\text{eff}} = \frac{\sqrt{\sum_i \left[\omega_i + \omega_i^2 \cdot (k_{\text{eff}} - k_i)^2\right]}}{\sum_i \omega_i}\,, \tag{3.7}$$

where $\omega_i = \frac{1}{\delta k_i^2}$ [111].

However, as previously mentioned, the Figures 3.10c and 3.10f show an unexpected trend in k_i values for $\sigma > 44,000$ cm^{-1}. It is possible the differences in the plasma conditions between the Penning discharge and the hollow cathode discharge (HCL) may result in a shift in observed energy levels, and therefore a relative shift in some wavenumbers. The data used in Nave & Johansson (2013) [1] in the HCL were obtained with pressures 3.3 mbar to 8.0 mbar and currents < 1.4 A, whereas the pressures used in the PDL are of the order 10^{-5} mbar with currents 1.0 A to 1.6 A.

To investigate this, the values of the upper energy levels of the Fe II lines used for calibration in the Fe831 data set were compared to their wavenumber, as seen in Figure 3.11. It is clear that lines $\sigma > 44,000$ cm^{-1} originate from upper energy levels $> 55,000$ cm^{-1}. A shift in lines with the upper energy level $> 55,000$ cm^{-1} would explain the shift in k_i values seen at $\sigma > 44,000$ cm^{-1} in Figures 3.10c and 3.10f.

For all the FTS spectra (except Fe121), the calculation of the correction factor was repeated using lines only from an upper energy level above $55,000$ cm^{-1} and again for below $55,000$ cm^{-1}. Fe121 was not included as all lines used for calibration in this data set originate from an upper energy level above $55,000$ cm^{-1}. The results for the Fe831

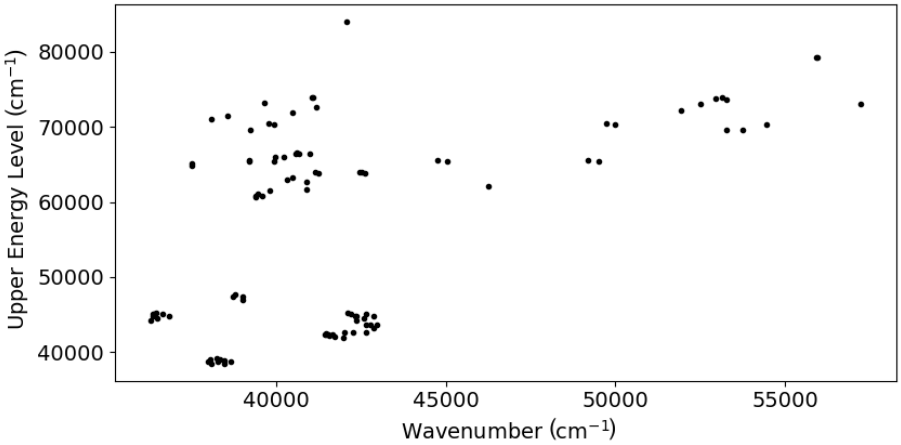


Figure 3.11: The upper energy levels of the Fe II lines used for calibration in the Fe831 data set, compared to their wavenumber.

Data Set	Upper Energy Levels included.	Lines Used	Correction factor, k_{eff}	Correction factor unc., δk_{eff}
Fe116	all	96	$2.51 \cdot 10^{-7}$	$1.01 \cdot 10^{-8}$
Fe116	$> 55,000$ cm^{-1}	52	$2.64 \cdot 10^{-7}$	$1.55 \cdot 10^{-8}$
Fe116	$< 55,000$ cm^{-1}	44	$2.41 \cdot 10^{-7}$	$1.31 \cdot 10^{-8}$
Fe831	all	104	$1.11 \cdot 10^{-6}$	$1.14 \cdot 10^{-8}$
Fe831	$> 55,000$ cm^{-1}	60	$1.19 \cdot 10^{-6}$	$1.77 \cdot 10^{-8}$
Fe831	$< 55,000$ cm^{-1}	44	$1.04 \cdot 10^{-6}$	$1.49 \cdot 10^{-8}$

Table 3.5: The correction factors calculated for Fe116 and Fe831 using Fe II lines with the upper energy levels $> 55,000$ cm^{-1} and $< 55,000$ cm^{-1}, compared to the correction factors calculated when using all lines. The correction factors for each data set is plotted in Figures 3.12 and 3.13. The number of lines included in each data set is in the column "Lines Used".

and Fe116 data sets are shown in Figures 3.12 and 3.13 and listed in Table 3.5. These data sets are displayed here as they show the extremes of differences in calculated correction factors. For Fe116 in Figure 3.13, the differences in correction factors are of similar value to the correction factor uncertainty calculated for all lines, as seen in Table 3.5. However, for Fe831 in Figure 3.12, the differences between the correction factors calculated separately are much larger than the correction factor uncertainty calculated when using all lines (Table 3.5). Therefore, the correction factor uncertainty for the data set Fe831 is raised by half the difference in the correction factors calculated separately. This process was repeated for all spectra, and large differences were found for the data sets Fe831, Fe903, Fe103, and Fe203. These all had their correction factor uncertainties, k_{eff}, raised in the same way and are listed with an asterisk (*) in Table 3.4.

The correction factor calculated using upper energy levels $> 55,000$ cm^{-1} has been greater than the correction factor calculated using upper energy levels $< 55,000$ cm^{-1} for all the data sets with an increased correction factor uncertainty except Fe203. The data

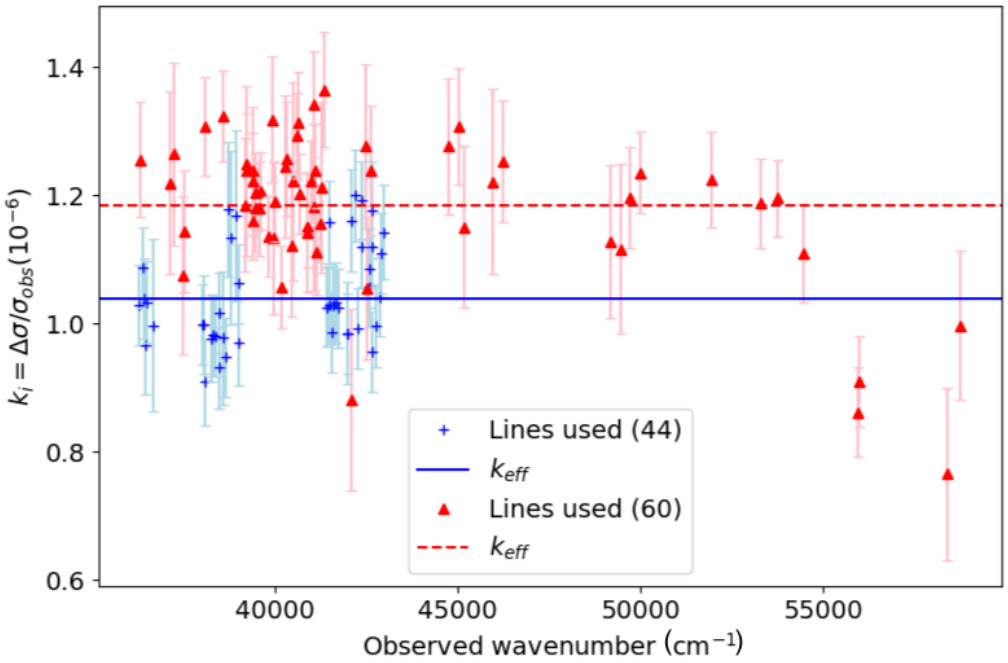


Figure 3.12: The fits for the wavenumber calibration of Fe831 using Fe II lines with the upper energy levels $> 55,000$ cm^{-1} (red triangles) and $< 55,000$ cm^{-1} (blue crosses). The details of the calibration factors calculated with each set are listed in Table 3.5.

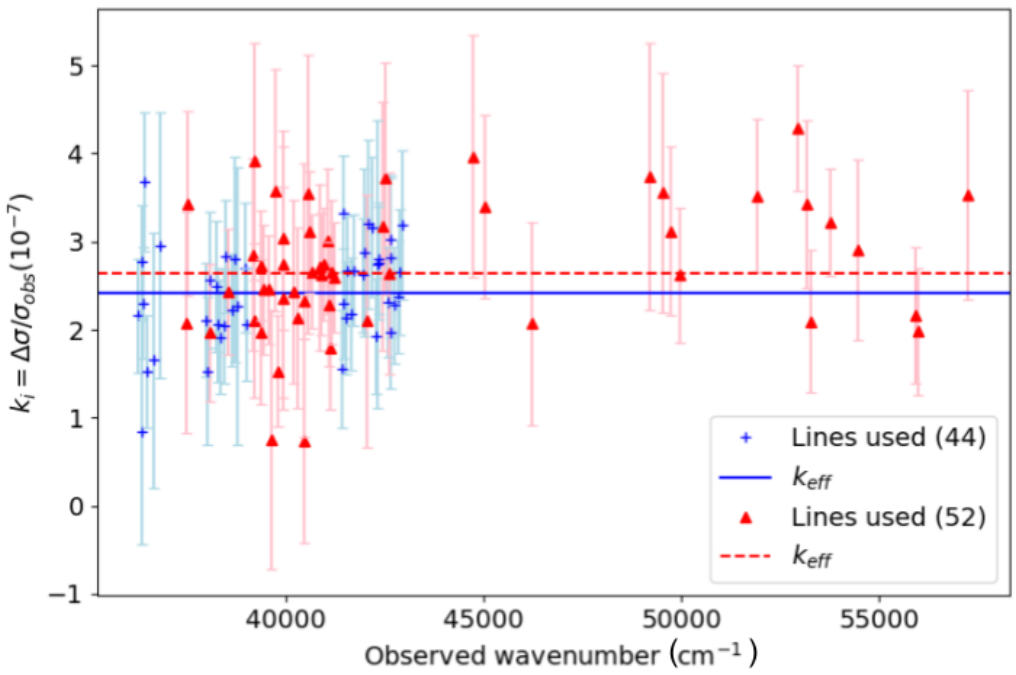


Figure 3.13: The fits for the wavenumber calibration of Fe116 using Fe II lines with the upper energy levels $> 55,000$ cm^{-1} (red triangles) and $< 55,000$ cm^{-1} (blue crosses). The details of the calibration factors calculated with each set are listed in Table 3.5.

sets with the largest increases in correction factor uncertainties, Fe831, Fe203 and Fe903, also had the lowest and highest currents and voltages in the PDL. Fe831 and Fe203 were recorded at 1.0 A and 1.2 A with voltages of 750 V and 800 V, and Fe903 was recorded at 1.6 A with 940 V. This may be an indication that the conditions in the Penning lamp were different for these data sets.

The calibration uncertainty must also include the uncertainty of the Fe II reference lines used to calculate the correction factor. The entire Fe II linelist has a global calibration uncertainty of four parts in 10^8 [1], which includes the propagation of the uncertainties of the standard Ar II lines from Whaling *et al.* (1995) [112] that Nave & Johansson (2013) [1] used for calibration. For this project, the total calibration uncertainty, $\delta\sigma_{\text{calib}}$, is calculated by

$$\delta\sigma_{\text{calib}} = \sigma_{\text{calib}}(\delta k_{\text{eff}} + \delta\kappa_{\text{global}}) \,, \tag{3.8}$$

where $\delta\kappa_{\text{global}}$ is the global calibration uncertainty of the Fe II linelist of four parts in 10^8 [1].

3.1.4.2 Statistical Uncertainty

The statistical uncertainty, $\delta\sigma_{\text{stat}}$, for an LSQ fitted line is approximated to

$$\delta\sigma_{\text{stat}} = \frac{\text{FWHM}}{2 \cdot \text{SNR}} \,, \tag{3.9}$$

where FWHM and SNR is its full width at half maximum and signal-to-noise ratio, respectively [90]. A line with low statistical uncertainty will be well-defined with a low FWHM and a high SNR. To prevent unreasonably low uncertainties, the SNR is capped at 100 for the statistical uncertainty calculation. For CoG fitted lines, the uncertainty is calculated in the same way and then doubled [113], as these lines do not use a fitted profile but rather rely on the manual selection of the spectral line boundaries and, typically, are blended or have another issue.

3.1.4.3 Total Wavenumber Uncertainty

The total uncertainty, $\delta\sigma_{\text{tot}}$, for each line will be the addition in quadrature of the statistical uncertainty, $\delta\sigma_{\text{stat}}$, and the calibration uncertainty, $\delta\sigma_{\text{calib}}$:

$$\delta\sigma_{\text{tot}} = \sqrt{(\delta\sigma_{\text{stat}})^2 + (\delta\sigma_{\text{calib}})^2} \,. \tag{3.10}$$

In a given spectrum, both high and low SNR lines will have the same calibration uncertainty. However, for weak lines, the dominant source of uncertainty will be the statistical uncertainty due to the low SNR.

3.1.5 Merging FTS Linelists

For the term analysis, a single combined master FTS linelist is required. As all the linelists are on the same absolute wavenumber scale and relative intensity scale, the

linelists can be merged. However, only one observation per spectral line is needed, and so for every spectral line, the observation with the minimum uncertainty was selected for the master FTS linelist. Table 3.2 displays the number of lines used from each linelist to create the final master FTS linelist, which contained a total of 4623 spectral lines from $33,826$ cm^{-1} to $65,508$ cm^{-1} (1527 Å to 2956 Å).

The plots of the 8 FTS spectra used in this project are displayed in Appendix E. The spectra are displayed in $1,000$ cm^{-1} segments, with the SNR shown on a linear and log scale to best display the weakest lines.

3.2 The Grating Linelist

As stated in Section 1.2.1, M. T. Belmonte recorded new neon-iron spectra on photographic plates at NIST NIVS (Section 2.2). In this section, the process of creating spectral linelists from the images of the detector plates is detailed. The linelists are then wavelength calibrated using wavelength standards and converted to wavenumbers. The spectra are not intensity calibrated as no intensity data was recorded and the detector plates do not have a linear response. A final master grating linelist is made by merging the linelists created from each image.

3.2.1 Spectrum Selection

As stated in Section 2.7.2, the grating measurements selected to make a linelist are the Tracks 5.1 and 5.3 on the plates named x1015, providing grating data from $55,556$ cm^{-1} to $190,476$ cm^{-1} (525 Å to 1800 Å). The plates were scanned by Belmonte, creating images in a TIFF format. It is these images that were used in this thesis work to create spectral linelists.

The scanner used to create the images of the plates is approximately two-thirds the length of a single plate. Therefore, the two plates used in the x1015 observation are recorded as four images. The approximate wavelength ranges in each image for the Tracks 5.1 and 5.3 in each image are listed in Table 3.6 and displayed in Figure 3.14.

Each track has the spectrum recorded for three exposure times: 5, 10 and 45 minutes. Figure 2.7 displays part of the x1015_plate2a image, in which the three exposure times for each track can be seen. Appendix F displays the grating plates and line profiles used in this work in 10 Å segments. The wavelengths provided in the images in Appendix F are not wavelength calibrated.

In the 5-minute exposures the strongest lines appeared unsaturated or less saturated than in the 45-minutes exposures, and the weak lines only appeared in the 45-minute exposures of the tracks. An example of this can be seen in Figure 3.15 which displays a 10 Å segment of the 5-minute and 45-minute exposures of the Track 5.3 in image x1015 plate1b, and the line profiles of each plate. The strongest lines in the 5-minute exposure at $\sim$ 1381.7 Å, $\sim$ 1382.0 Å and $\sim$ 1387.1 Å are saturated or close to saturation in the 45-minute exposure, as seen by the flat top in the line profiles. Therefore, to determine an accurate wavelength for these lines, a 5-minute exposure is needed to create the linelist.

Plates name	Plate number	Scan ID	Belmonte TIFF Image name	Track ID	Wavelength Limits (Å)	Exposure times (mins)
x1015	1	a	x1015_plate1a	5.1	525 to 763	5, 10, 45
				5.3	1100 to 1333	5, 10, 45
		b	x1015_plate1b	5.1	644 to 882	5, 10, 45
				5.3	1217 to 1450	5, 10, 45
	2	a	x1015_plate2a	5.1	882 to 1119	5, 10, 45
				5.3	1450 to 1683	5, 10, 45
		b	x1015_plate2b	5.1	1000 to 1238	5, 10, 45
				5.3	1567 to 1800	5, 10, 45

Table 3.6: Table of the approximate wavelength ranges of the scanned images for the Tracks 5.1 and 5.3 on plates x1015. The wavelength limits were estimated using Table 2.1.

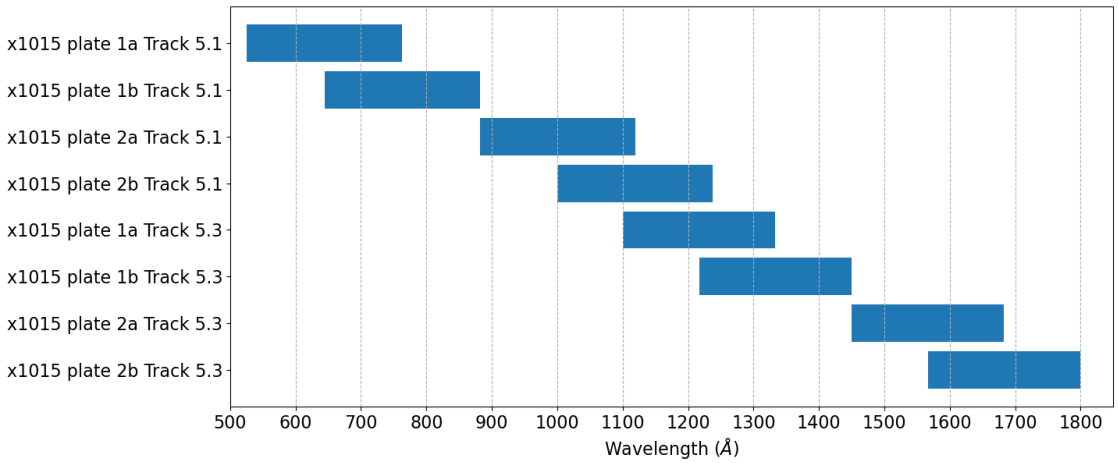


Figure 3.14: Plot of the approximate wavelength ranges of the scanned images for the Tracks 5.1 and 5.3 on plates x1015. The wavelength limits were estimated using Table 2.1.

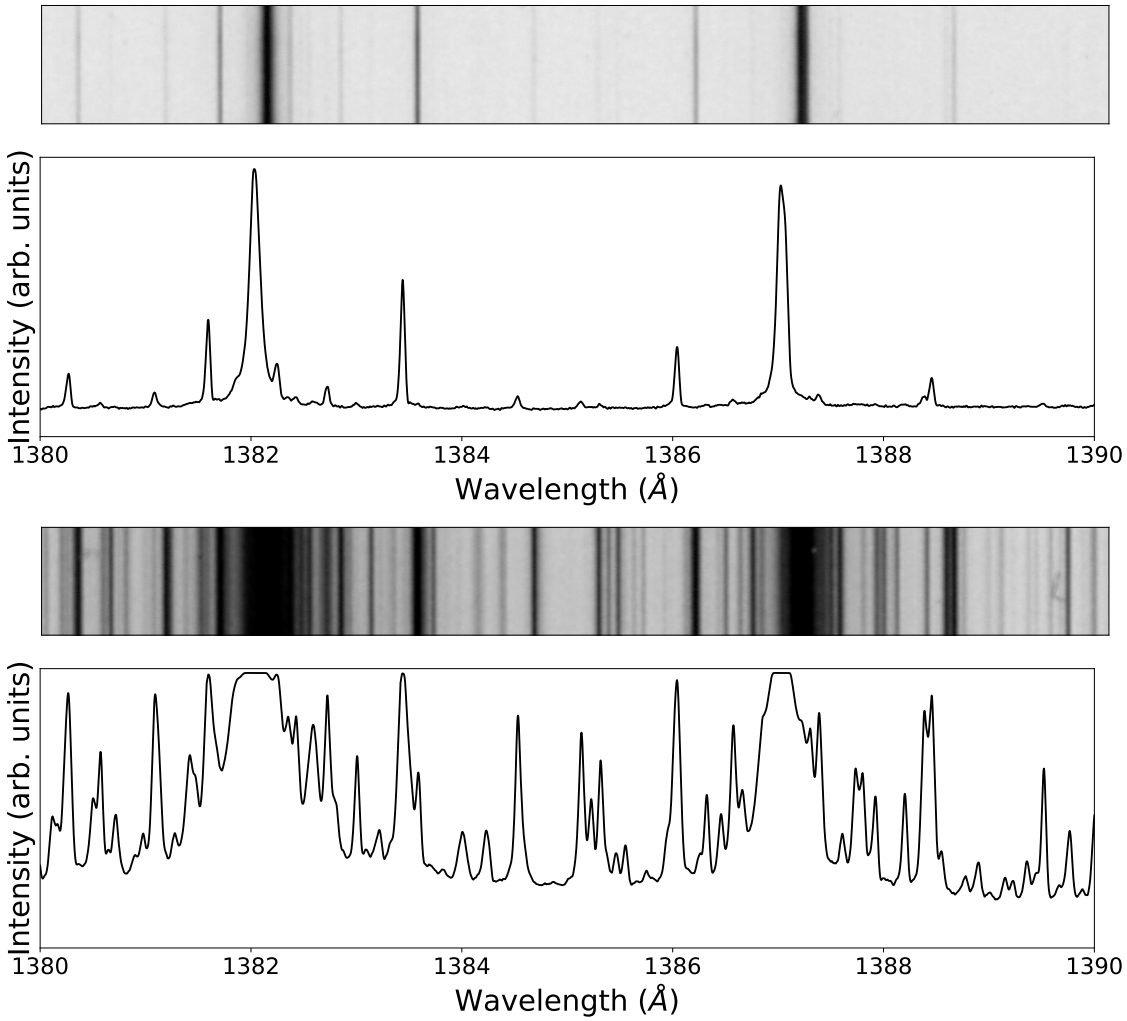


Figure 3.15: The 5-minute (above) and 45-minute (below) exposures of a segment of the x1015 plate1b image for Track 5.3 and the line profiles of each image. These are copied from Appendices F.5 and F.6.

In the 5-minute exposure, between 1384.0 Å and 1386.0 Å there are $2-3$ faint lines which appear strong and well-defined in the 45-minute exposure. In this region there are also numerous lines in the 45-minute exposure which were unseen in the 5-minute exposure. For this reason, a linelist should also be created from the 45-minute exposure images. The recorded intensity for the lines in the 45-minute exposures are typically between 3-7 times larger than the same lines observed in the 5-minute exposures. However, this does not take into account the "background" intensity (Section 3.2.3) which varied greatly. The 10-minute exposures did not provide any new advantage and so linelists were made from the 5-minute and 45-minute exposures only.

A limiting factor in the creation of the grating linelist is the availability of the wavelength standards used for calibration. In this thesis, the Fe II lines used for calibration are limited to $\lambda > 899.9$ Å ($\sigma < 111,123.5$ cm^{-1}, discussed further in Section 3.2.4). Therefore, the data from the images x1015_plate1a and x1015_plate1b for Track 5.1 cannot be wavelength calibrated at this time. Figure 3.14 displays sufficient wavelength overlap between images x1015_plate2b Track 5.1 and x1015_plate1b Track 5.3, so the x1015_plate1a

Track 5.3 image is not needed. In summary, grating linelists were made for the 5-minute and 45-minute exposure times of the images x1015_plate2a, Track 5.1; x1015_plate2b, Track 5.1; x1015_plate1b, Track 5.3; x1015_plate2a, Track 5.3; and x1015_plate2b, Track 5.3.

3.2.2 Linelist Extraction

The program Atomic Spectrum Photoplate Analysis Software (ASPAS, [114]) was created to study scanned copies of spectra photoplates from NIST's archive. In this project, ASPAS is used to create a linelist from a digitised grating spectrum in a bitmap image file format. For this reason, each TIFF image is cropped to the desired track and exposure time, and converted into a bitmap file. A full guide on how to use ASPAS can be found at [114]. During this project, I edited the program slightly to automate some of the linelist creation process, but the main operation of the program remained the same. An image of the computer display screen of the ASPAS program used in this project is shown in Figure 3.16.

ASPAS displays the line profiles of a segment of the selected plate image. The profiles are calculated by averaging the intensity of each column of the bitmap and performing a cubic interpolation perpendicular to the length of the track. The average intensity is then linearly scaled to arbitrary units between 0 and 256.

As seen in Figure 3.16, the photoplate image appears at the top of the window and the average intensity interpolation of the line profiles underneath it. The red line indicates the part of the plate that will be shown magnified (black) with its reflection (grey) in the mirror window in the bottom left corner. Here the red line can be finely adjusted to the central line position by comparing the spectrum with its reflection. Once the central line position is chosen, the line can then be added to (or removed from) a linelist with or without a comment. This program does not fit the spectral lines to a distribution, but only records the position on the track and the average intensity at that position. The position is recorded in millimetres from the start of the track, using the resolution of 2400 DPI.

During this project, I edited a copy of the ASPAS program to automate the identification of the peak position of spectral lines and save them to the linelist. In Figure 3.16, the auto-identified peak of the spectral lines are labelled by red crosses, and previously saved lines are labelled by blue lines. This automation proved reliable when compared to a manually created linelist, and provides repeatability to the linelist process for a given image. Regardless, every automatically identified line was visually inspected to confirm a good peak value has been selected and any missed lines were manually added to the linelist.

For symmetrical, resolved lines, the central line position can be determined accurately. However, for many lines the peak position of a line is uncertain and the line is labelled with the issue as a comment. These lines will have their wavelength uncertainties raised. The exception to this being the label "A" which identifies the lines automatically identified. The labels used in the grating linelist are listed in Table 3.7.

Examples of the spectral line profiles can be seen in Figure 3.17. It displays 3 segments of the grating plate images with their interpolated line profiles. Figure 3.17a displays three

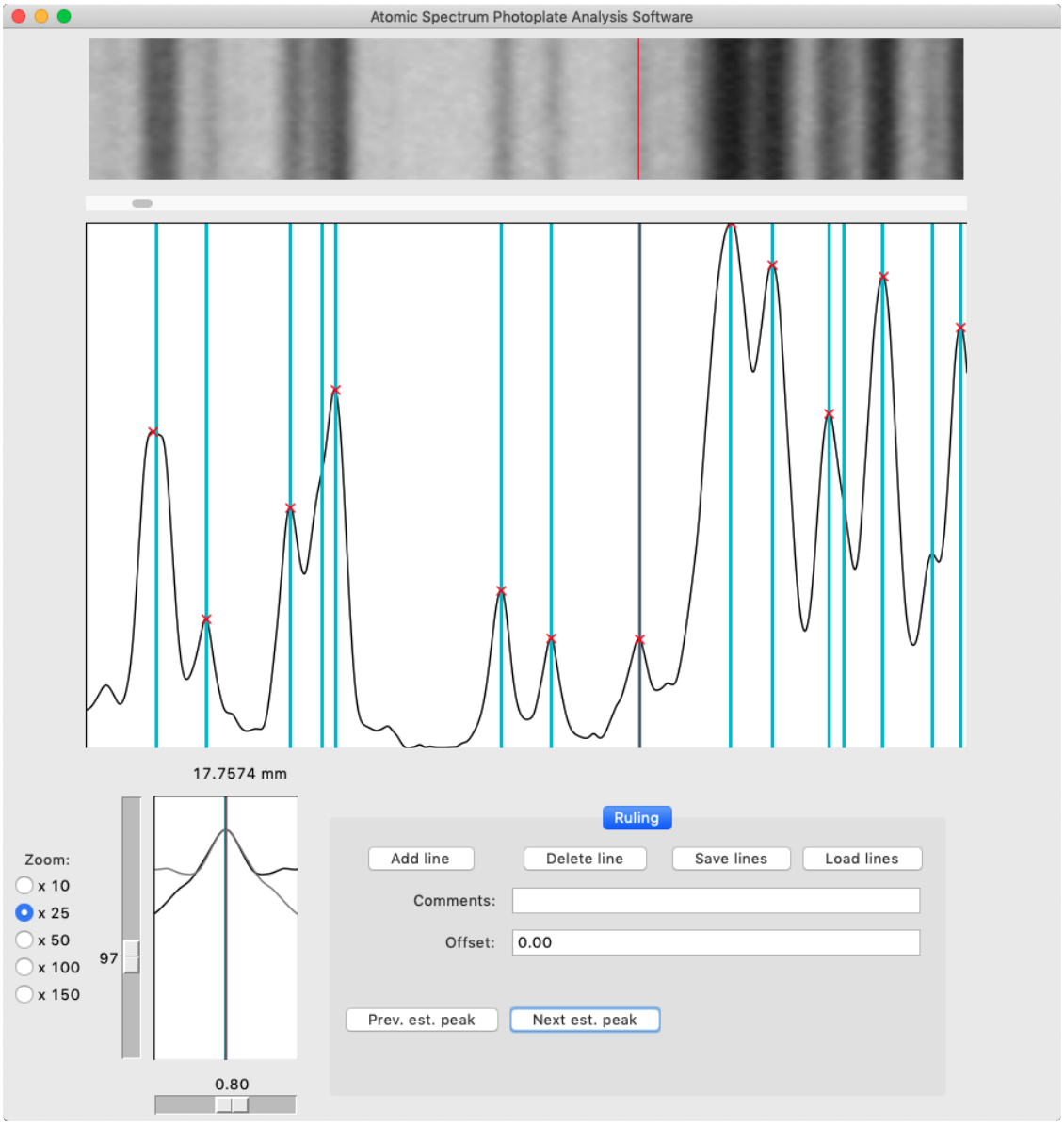
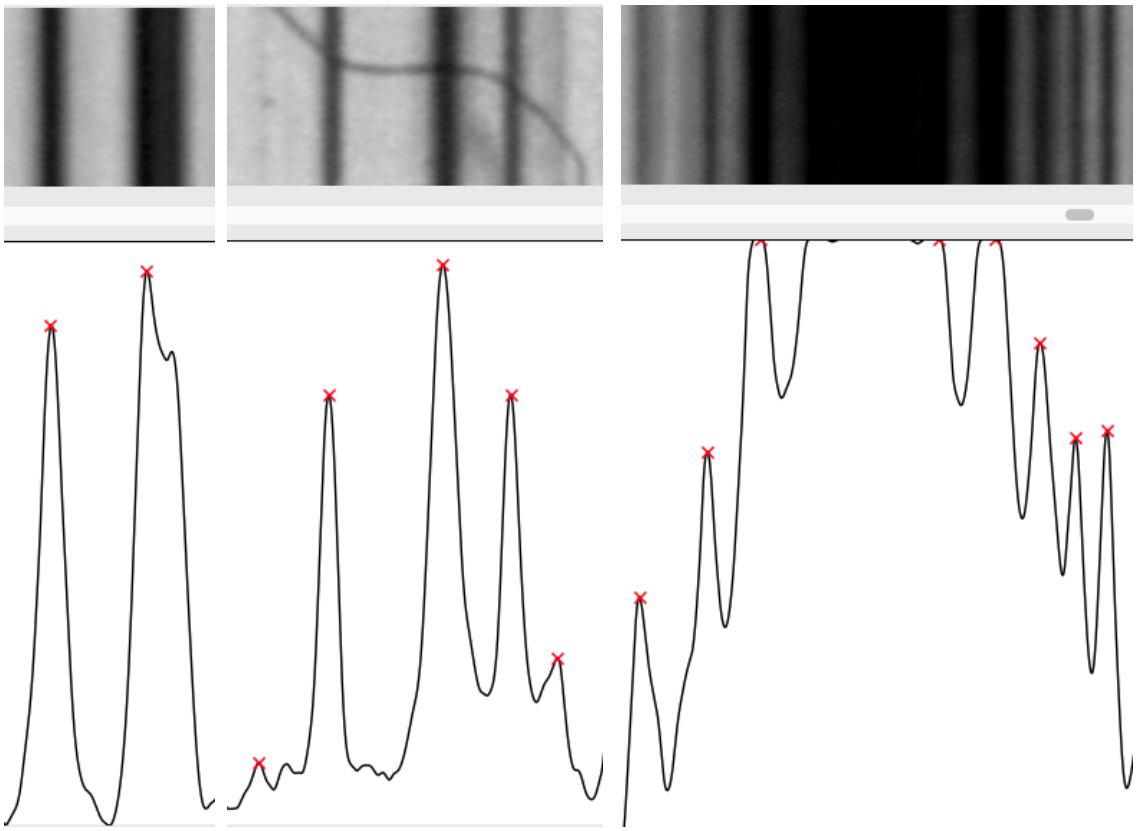


Figure 3.16: An image of the computer display screen of the ASPAS software I edited for this project. The red crosses are positions of the auto-identified peaks of spectral lines and the blue lines are the positions of lines saved in a linelist.

Label	Description
A	Peak position auto-identified by program
B	Line blended (i.e. in the wing of a stronger line)
D	Dirt on image from plate/scanner
F	Badly fit lines, typically asymmetrical or 'bumpy'
H	High intensity, possibly saturated
L	Low intensity
S	Saturated (usually flat topped line profile)
X	Very broad line
V	Very blended line
Z	Line outside of wavelength calibrated range

Table 3.7: Description of labels used in the grating linelist to label problematic lines and lines auto-identified by the edited ASPAS program.



(a) Blended spectral lines.

(b) Dirt on the scanner.

(c) Broad, saturated spectral line

Figure 3.17: Images of lines with labels in the grating spectra.

spectral lines. The first line is symmetrical with no issues, and so has no problematic label. The following two lines are heavily blended and will be labelled "B" or "V" depending on how the fit appears in the magnified mirror window. The apparent peak position of these blended lines will be altered from their true position. The "V" label was created late in the linelist creation process, and so it is found most frequently in the linelist created using the 45-minutes exposure of plate 2a, Track 5.1. Figure 3.17b displays part of the image with dirt on the scanner. All the spectral lines in this image will have the label "D" for dirt, as their peak line position may be altered by the presence of the dirt. Figure 3.17c shows a very broad and saturated line with weaker lines either side. This strong line is labelled "S" as it is clearly saturated as seen by the flat top of the line profile, and labelled "X" as the line is broad and interfering with its neighbouring lines. The neighbouring lines will also have their true position altered by the underlying line and will be labelled with "B" or "S", as needed. Throughout the entire spectrum, lines with intensities > 245 are labelled with "H" to increase the uncertainty of lines that are saturated or close to saturation but have not be identified as problematic by eye.

Once the linelists had been created using ASPAS for every track and exposure time, the linelists were wavelength calibrated. The linelists are not intensity calibrated which will be discussed in the next section.

3.2.3 Intensity Scale

It would be useful to scale the spectral lines relative to the intensity of the "background" level, the area of the spectrum with no spectral lines. The background intensity varied per image and throughout the spectrum. An example of the varying background intensity can be seen in Figure 3.18 which displays segments of the 5-minute exposures for Track 5.1 in the images x1015_plate2a and x1015_plate2b. These are images of the same plate (x1015, plate 2) scanned at different positions to include different parts of the spectrum. Notice the differences in line intensities throughout the plot and the different line profiles at approximately 1110.5 Å and 1112.1 Å.

Relative intensity shifts were not made between plates as not all plates overlapped, therefore no scaling was made with respect to a global background intensity. However, the line intensities relative to the background are considered, with lines close to the local background level given the "L" label. This ensures that weak lines are given a higher wavelength uncertainty.

As the intensity value is given only as the peak of the spectral line, the intensity of the line is not a reliable way of determining line strength. The intensity of a line can appear high due to a tail of another strong, broad line (as seen in Figure 3.17c), or a line may have an incorrect intensity due to the presence of dirt on the scanner (Figure 3.17b).

The efficiencies of the scanner and detector plates were not taken into account. There was no absolute intensity calibration applied to the grating linelist. As mentioned in Section 2.2.1, the plates do not have a linear intensity response and this grating data contains no line width parameters. However, the focus of this thesis work relies on the accurate wavelengths of the spectral lines and so an intensity calibration is not required,

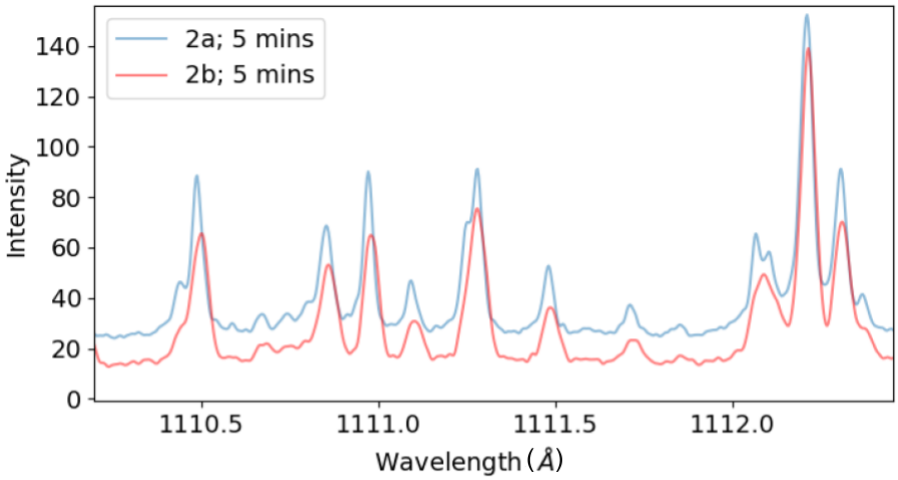


Figure 3.18: The 5-minute exposure for Track 5.1 in the images x1015_plate2a and x1015_plate2b.

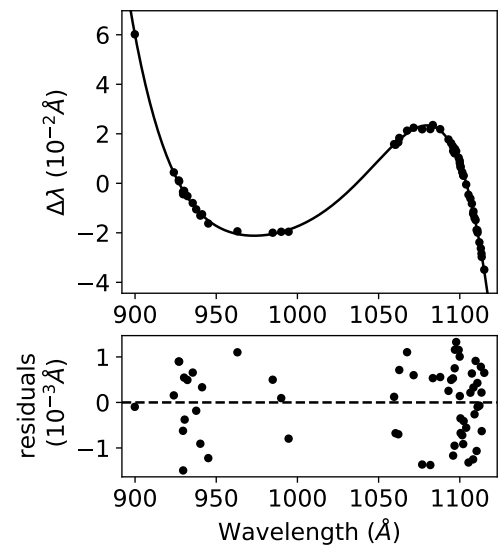
and an approximate guide to the strength of the spectral lines is sufficient.

3.2.4 Wavelength Calibration of Grating Spectrum

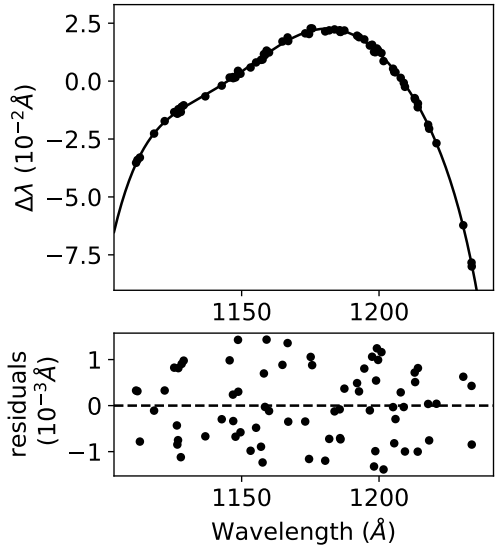
Unlike the FTS, the grating data are not on a linear wavenumber scale. To calibrate a linelist from millimetre positions to wavelengths in angstrom (Å), the wavelength standards are identified in the linelist and used to place the entire linelists on the wavelength scale. As with the FTS data (Section 3.1.3), the Ritz wavelengths of Fe II lines calculated by Nave are used as the wavelength standards. The lower limit of the Fe II data and therefore the calibrated grating linelist is ~ 899 Å ($\sim 111,121$ cm^{-1}). The Ritz wavenumber uncertainties of the Fe II calibration lines range from 0.000024 Å to 0.0013 Å (which correspond to the uncertainties 0.0008 cm^{-1} to 0.09 cm^{-1} when converted).

The Fe II lines used for calibration must appear in the spectrum well-defined, and without issue. Ideally, the Fe II lines are evenly spread throughout the spectrum too. To identify the Fe II lines, each spectrum was linearly scaled so that the edges of the plates are set to the values stated in Table 3.6 and shifted as needed. Once the known Fe II lines had been identified, they were used to place the millimetre positions onto the wavelength scale via a polynomial. The Chebychev polynomial fit is calculated using a program called *polyfit* created by U. Griesmann. The best fit would have the residuals to the fit evenly spread about zero. The fitted polynomials and residuals for each 5-minute exposure linelist are shown in Figure 3.19, and the details of the fits are listed in Table 3.8. Figure 3.19 shows that the polynomial fits can vary substantially across the spectrum, emphasising the importance of having calibration lines evenly spread throughout the spectrum.

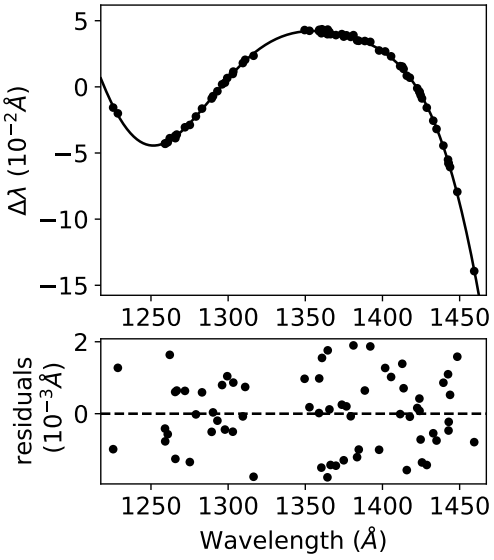
Lines close to the plate edges are usually just outside the range of calibrated data and were given the label "Z". This happened at plate boundaries where there was no overlap in data, 1459 Å $< \lambda < 1463$ Å (~ 68350 cm^{-1} $< \sigma <\sim 68540$ cm^{-1}) and $\lambda > 1809$Å ($\sigma <\sim 55280$ cm^{-1}). There may also be spectral lines in this region which are unseen due to the plate boundaries.



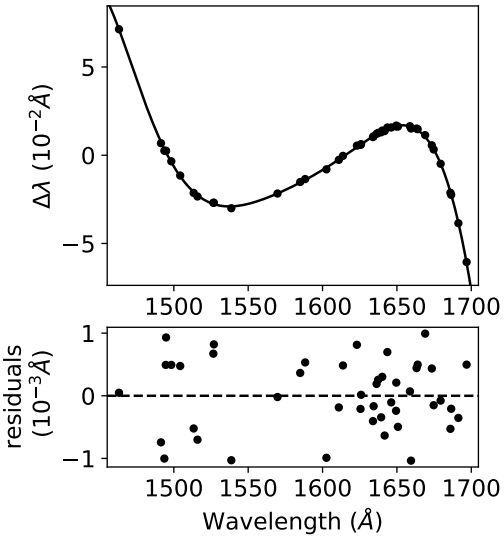
(a) Fit for x1015_plate2a, Track 5.1



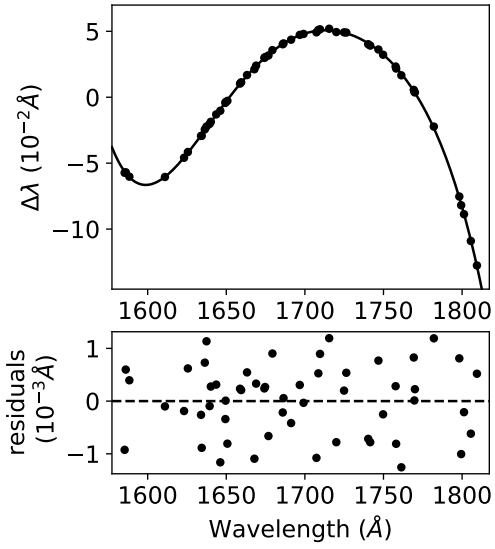
(b) Fit for x1015_plate2b, Track 5.1



(c) Fit for x1015_plate1b, Track 5.3



(d) Fit for x1015_plate2a, Track 5.3



(e) Fit for x1015_plate2b, Track 5.3

Figure 3.19: The calibration polynomials and residuals for wavelength calibration of the 5-minute exposure linelists using the Fe II Ritz wavenumbers. The Ritz wavenumber uncertainties for these lines are between 0.000024 Å and 0.0013 Å.

Plate image	Track	Total lines	Calibration lines	Fit	Std. dev. (Å)	Wavelength calibration limits (Å)	Offset for 45 mins (mm)
x1015_plate2a	5.1	490	62	6	$7.83 \cdot 10^{-4}$	923 to 1115	0.0
x1015_plate2b	5.1	294	72	7	$7.85 \cdot 10^{-4}$	1112 to 1234	0.0245
x1015_plate1b	5.3	207	68	7	$1.00 \cdot 10^{-3}$	1225 to 1459	-0.0046
x1015_plate2a	5.3	456	45	7	$5.56 \cdot 10^{-4}$	1463 to 1697	0.0033
x1015_plate2b	5.3	496	54	5	$6.64 \cdot 10^{-4}$	1585 to 1809	0.0137

Table 3.8: The details of the polynomial fits used to calibrate the 5-minute exposure grating linelists. The fit number corresponds to the polynomial order of the fit.

As the detector plate is not moved during the observation, the tracks are parallel on the plate. Therefore, the polynomial calculated for the 5-minute exposure can also be used for the 45-minute exposure. To ensure this is correct, the offset between the positions of the lines observed in both the 5-minute and 45-minute exposures were checked. The offsets needed to adjust the line positions of the 45-minute exposures to match the line positions of 5-minute exposures are listed in Table 3.8. If there was a shift needed, it was small and due to the fact that the plate was at a very small angle in the scanned image. The line positions in the 45-minute linelist were adjusted by the small offset before applying the polynomial for wavelength calibration.

To check for consistency in the calibration, the wavelengths of the newly calibrated lines in both the 5-minute and 45-minute exposures were compared to the Fe II calibration lines, confirming the data had been correctly calibrated within uncertainties.

3.2.5 Wavelength Uncertainties

The wavelength uncertainty of each spectral line was estimated according to the quality of the line. For spectral lines with no label (except "A") the lower uncertainty of 0.003 Å was used. This was calculated by comparing lines that were present in the overlapping regions of the images for each plate. These lines were calibrated independently to each other and by measuring the standard deviation of the differences between the wavelength values for each line, an estimate for the uncertainty is made. This was repeated for lines labelled with an issue and produced the estimated uncertainty of 0.007 Å.

As the term analysis process (described in Section 4.2) will use wavenumbers, the vacuum wavelengths are converted by

$$\sigma\ [\mathrm{cm}^{-1}] = \frac{10^8}{\lambda\ [\text{Å}]}\ , \tag{3.11}$$

and the wavelength uncertainties are converted to wavenumber uncertainties by [59]

$$\delta\sigma\ [\mathrm{cm}^{-1}] = \frac{\delta\lambda\ [\text{Å}]\ \cdot\ 10^8}{\lambda\ [\text{Å}]^2}\ . \tag{3.12}$$

For a wavelength of 1000 Å with an uncertainty of 0.003 Å the wavenumber and uncertainty will be $100,000$ cm^{-1} and 0.30 cm^{-1}. For an uncertainty of 0.007 Å the wavenumber uncertainty will be 0.70 cm^{-1}.

3.2.6 Merging Grating Linelist

For the term analysis process, a single grating linelist is needed. In the regions of multiple observations for a given exposure, a cut is made at a wavelength in the overlapping regions, producing a linelist of single observations for the 5-minute and 45-minute exposures. For lines observed in both exposure times, the line with the minimal uncertainty is chosen. If the uncertainties were equal, the lines that were not saturated, very broad or very blended were prioritised for selection for the main linelist. Otherwise, the line with the highest intensity was selected.

The master grating linelist has 6626 lines, ranging from $55,090$ cm^{-1} to $111,121$ cm^{-1} (899.916 Å to 1815.204 Å), with uncertainties ranging from 0.091 cm^{-1} to 0.864 cm^{-1}.

The spectral plots for each image of the grating spectra used in this work are presented in Appendix F. Each image spans approximately 240 Å and has been divided into 10 Å segments. The line profiles are calculated by performing a cubic interpolation of the average intensity of each column. The wavelengths in these images are an approximation only and the intensity is in arbitrary units.

3.3 Comparison of the FTS and Grating Linelists

In this Chapter, two linelists have been created. The final master FTS linelist contains 4623 lines from $33,826$ cm^{-1} to $65,508$ cm^{-1} and the final master grating linelist contains 6626 lines from $55,090$ cm^{-1} to $111,121$ cm^{-1}. These linelists overlap between $55,090$ cm^{-1} and $65,508$ cm^{-1}.

As the FTS wavenumber calibration is linear and significantly more accurate, it can be reliably used to test the grating calibration. Figure 3.20 displays a wavenumber comparison of the FTS and grating linelists in the overlapping region. The uncertainties plotted include the FTS uncertainty, but are largely due to the grating wavenumber uncertainties. Only FTS and grating lines without identified issues were included in a closest match algorithm. FTS lines that were included had SNR > 5, FWHM > 0.350 cm^{-1} and were LSQ fitted. Typically, lines with FWHM < 0.350 cm^{-1} and SNR < 5 were badly-fit. There are no dominating trends or systematic offsets in Figure 3.20, confirming a good grating calibration in this spectral region.

As stated in Section 2.5, there is an order of magnitude difference in the resolving powers of the instruments, which is reflected in the line wavenumber uncertainties. The uncertainties of the lines in the FTS linelist range from 0.0024 cm^{-1} to 0.460 cm^{-1}, with uncertainties of strong lines (SNR > 50) typically between 0.0024 cm^{-1} to 0.0074 cm^{-1}. Overall, 92% of lines have an uncertainty of 0.091 cm^{-1} or less. The uncertainties of lines in the grating linelist range from 0.0912 cm^{-1} and 0.864 cm^{-1} (0.003 Å to 0.007 Å), with 80% of lines having an uncertainty of 0.45 cm^{-1} or less. As the FTS data are more accurate,

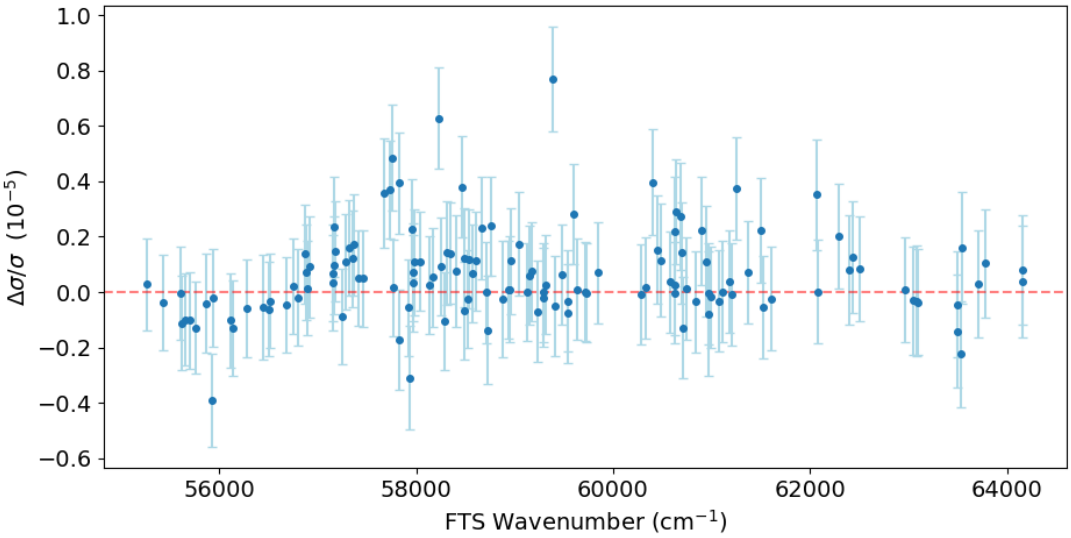


Figure 3.20: Wavenumber comparison of the FTS and grating linelists in the region the linelists overlap, $55,090$ cm^{-1} to $65,508$ cm^{-1}. The uncertainties plotted are the addition in quadrature of the grating and FTS line wavenumber uncertainties. However, the FTS uncertainty is negligible in comparison to the grating uncertainty. FTS lines that were included had SNR > 5, FWHM > 0.350 cm^{-1} and were LSQ fitted. Only grating lines with no known issues were used.

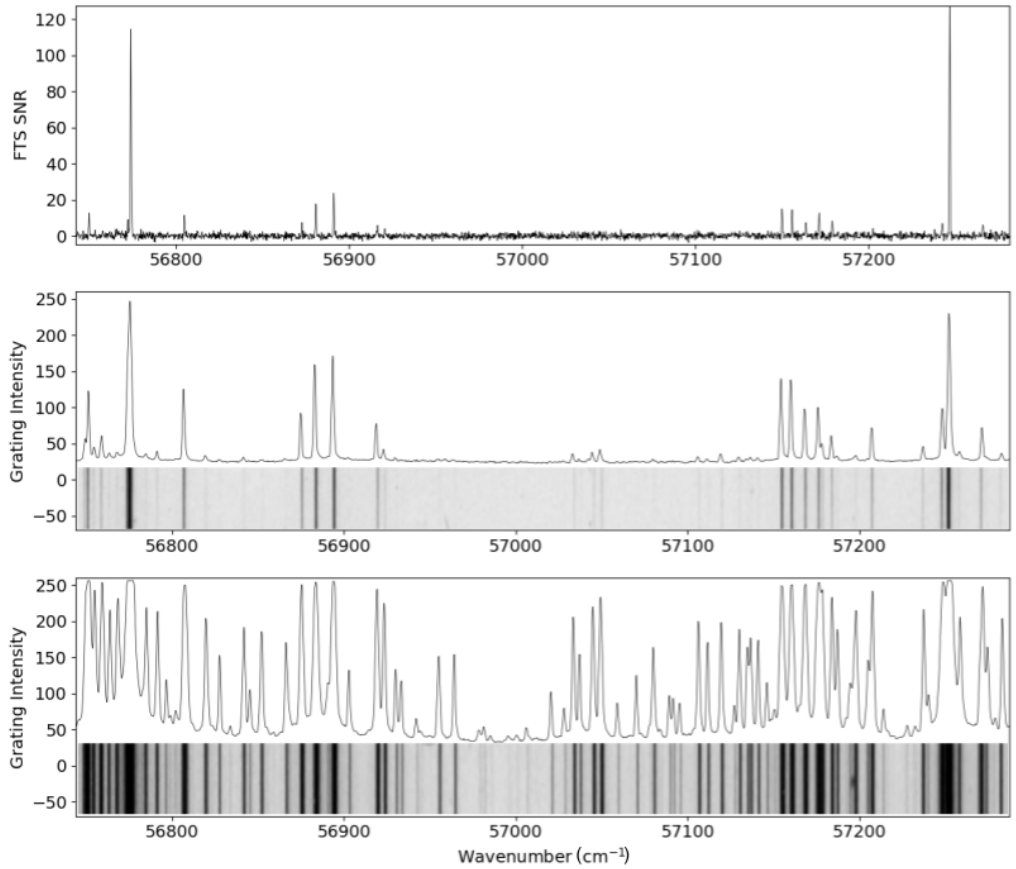


Figure 3.21: A section of the Iron Spectrum at $57,000$ cm^{-1} in the FTS Spectrum (Fe121) and the Photographic Plate Spectrum (x1015_plate2b Track 5.3, 5-minute and 45-minute exposure).

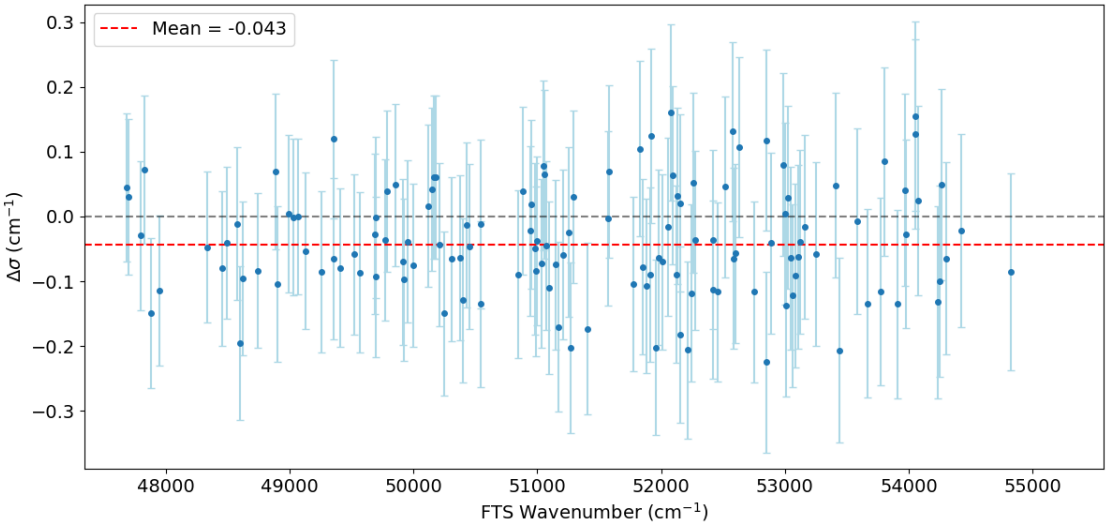


Figure 3.22: A comparison of the wavenumbers of FTS and Ekberg lines. The uncertainties shown are the addition in quadrature of the FTS and Ekberg uncertainties. FTS lines that were included had SNR > 5, FWHM > 0.350 cm^{-1} and were LSQ fit.

it appears it would be advantageous to use the FTS data up to $65,508$ cm^{-1}. However, the grating spectra contains weaker lines that are unseen in the FTS data. Although the intensity values of the FTS and grating linelists cannot be directly compared, Figures 2.14 and 3.21 display comparisons of the observed lines in the Fe121 FTS Spectrum with the 5-minute and 45-minute exposures of Track 5.3 from image x1015_plate2b. It is clear that there are numerous lines in the grating spectra which are unseen in the FTS. It is for these reasons that both linelists will be used in this overlapping region for the term analysis process (Section 4.2).

3.4 Comparison to Ekberg wavenumbers

The Ekberg (1993) [88] energy levels are used as the starting point for the term analysis (discussed in Section 4.2). Therefore, it is useful to check for any large inconsistencies in the Ekberg line wavenumbers. In this section, the Ekberg wavenumbers will be compared to their closest wavenumber match in the FTS and grating linelists.

3.4.1 Comparison of Ekberg to FTS line wavenumbers

Figure 3.22 displays the wavenumber comparison of the FTS lines with the Ekberg lines. As Ekberg's data were measured on a grating spectrometer, some spread in the difference between the Ekberg wavenumbers and the FTS wavenumbers, $\Delta\sigma$, is expected. The lines were selected for reliability and matched by a closest wavenumber algorithm I created. The uncertainties plotted are the addition in quadrature of the FTS and Ekberg uncertainties, but are dominated by far by the Ekberg wavenumber uncertainties. As previously stated, the uncertainties of the FTS lines are between 0.0024 cm^{-1} and 0.460 cm^{-1}. 80% of the FTS measured lines have an uncertainty of 0.053 cm^{-1} or less, whereas the line uncertainties of Ekberg's spectral lines are an order of magnitude higher, between 0.05 Å

and 0.005 Å (between 0.13 cm^{-1} and 1.25 cm^{-1} at 50000 cm^{-1}). There is an even spread in $\Delta\sigma$, with a mean shift of $\Delta\sigma = -0.043$ cm^{-1} which is likely due to and well within Ekberg's wavenumber uncertainties. The lack of structure in the plot signifies that the Ekberg lines were calibrated correctly in this spectral region.

3.4.2 Comparison of Ekberg to grating line wavenumbers

The Ekberg's grating line wavenumbers were also compared to this thesis grating wavenumbers. However, as these linelists have much higher uncertainties and the iron spectrum is so dense, the line matching algorithm had many false matches. Recall that the uncertainties of Ekberg's data were between 0.05 Å and 0.005 Å (between 1.25 cm^{-1} to 0.13 cm^{-1} at 50000 cm^{-1}) and the uncertainties in the grating linelist are between 0.003 Å to 0.007 Å (0.0912 cm^{-1} and 0.864 cm^{-1}). Therefore, this comparison was made after the Fe III lines were identified in the grating spectrum (Section 4.2), to ensure a correct match. The matches of reliable lines were found in the regions $55,700$ cm$^{-1} < \sigma < 71,800$ cm^{-1} (1393 Å to 1795 Å) and $82,200$ cm$^{-1} < \sigma < 111,100$ cm^{-1} (900 Å to 1217 Å). The wavenumber comparisons for these regions are displayed in Figures 3.23 and 3.24. The uncertainties displayed are a combination of the grating linelist wavenumber uncertainties and the Ekberg grating wavenumber uncertainties which are comparable.

In Figure 3.23, the spread in $\Delta\sigma$ is about zero within the uncertainties. In Figure 3.24, there is a mean shift of $\Delta\sigma = -0.36$ cm^{-1} from zero for the lines between $82,200$ cm$^{-1} < \sigma < 111,100$ cm^{-1}. However, there is a larger discrepancy ($\Delta\sigma = -0.6$ cm^{-1}) between Ekberg's wavenumbers and the grating wavenumbers of this thesis in the region $97,200$ cm$^{-1} < \sigma < 108,100$ cm^{-1}. This shift is unlikely to be due a calibration issue on one of the plates in this work. In this project, the x1015_plate2a image for Track 5.1 extends to $89,686$ cm$^{-1} < \sigma < 108,342$ cm^{-1}, and so the shift would have been seen throughout the entire plot in Figure 3.24 if it was due to a calibration issue in my work. It is most likely this is due to an incorrectly calibrated detector plate in the previously published work. Ekberg did not state the spectral ranges of the detectors used in their work so this cannot be confirmed.

In Figure 3.24, in the regions $87,000$ cm$^{-1} < \sigma < 95,000$ cm^{-1} (1053 Å to 1149 Å) and $109,000$ cm$^{-1} < \sigma < 112,000$ cm^{-1} (900 Å to 917 Å) there appears to be some structure. The polynomial shapes seen in these regions are similar to those seen in this research when the incorrect polynomial was used to calibrate the grating data (during the wavelength calibration process). Again, it is most likely these features are due to an incorrect calibration in Ekberg's work as Ekberg calibrated his linelist using multiple sources, including references from carbon, oxygen, silicon and grating Fe II data.

In the term analysis of Co III, Smillie *et al.* (2016) [83] observed much larger differences (relative to the uncertainties stated) in the shape of a curve between his newly-observed FTS wavenumbers and the previously published results by Raassen & Ortin (1984) [115]. Smillie also stated this could be due to the fitting of an incorrect polynomial during the wavelength calibration of the previously published data [115].

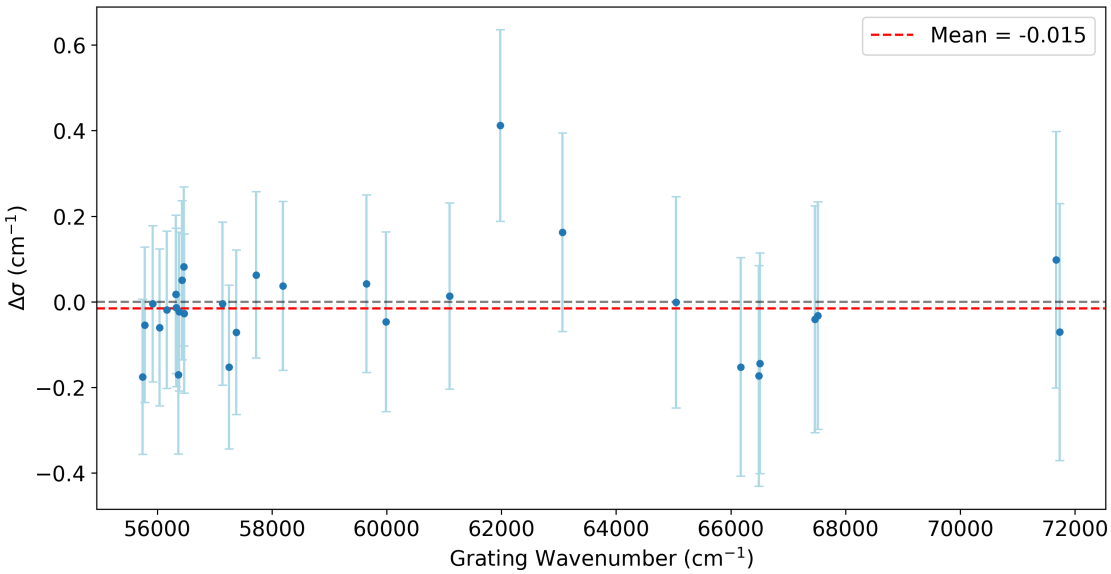


Figure 3.23: The comparison of the Ekberg grating and this work grating wavenumbers in the $55,700\ \mathrm{cm}^{-1} < \sigma < 71,800\ \mathrm{cm}^{-1}$ region. The uncertainties shown are the addition in quadrature of the grating and Ekberg uncertainties. Lines corresponding to any blends were removed as well as grating lines with any labelled issues.

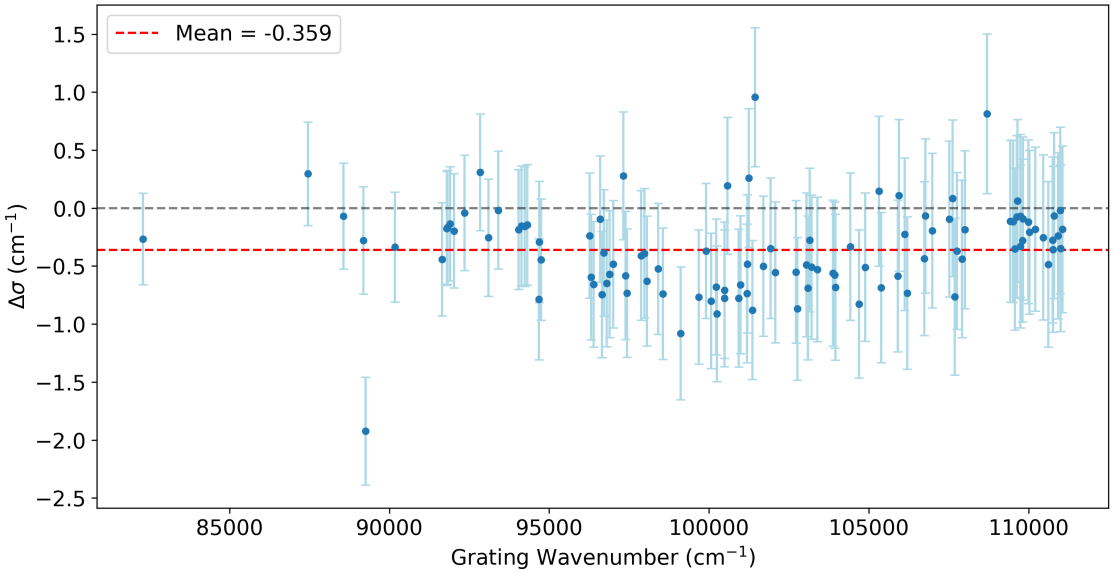


Figure 3.24: The comparison of the Ekberg grating wavenumbers and the grating wavenumbers of this thesis in the $82,200\ \mathrm{cm}^{-1} < \sigma < 111,100\ \mathrm{cm}^{-1}$ region. The uncertainties shown are the addition in quadrature of the grating (this work) and grating (Ekberg) wavenumber uncertainties. Lines corresponding to any blends were removed as well as grating lines with any labelled issues.

3.5 Summary

In this Chapter, the process of creating wavenumber calibrated linelists from FTS and grating data has been detailed. This includes the spectrum extraction, wavenumber calibration, and merging of data from 8 FTS spectra and 10 grating images. The spectral plots of the FTS and grating spectra can be seen in Appendices E and F, respectively.

Each newly calibrated data set was compared to the Fe II calibration lines, confirming a correct wavenumber calibration. Additionally, the final grating linelist was compared to the FTS data, as another check of the wavenumber calibration. Finally, the linelists created were compared to the previously published Fe III wavenumbers by Ekberg to check for any large inconsistencies before beginning the term analysis process. The term analysis using these linelists is explained in the next Chapter. In this process, the Fe III spectral lines are identified in the linelists and used to optimise the Fe III energy levels.

Chapter 4

Term Analysis of Fe III

The term analysis process is the derivation of the energy level structure using observed spectral lines. To complete the term analysis, the underlying atomic theory must be understood. Section 4.1 explains the necessary atomic theory and terminology used in the term analysis and Section 4.2 describes the process for the term analysis of Fe III. Finally, Section 4.3 shows the results of the term analysis, including the revised energy level values and labels, the classified FTS and grating linelists, and the Ritz wavenumbers for parity-forbidden transitions.

4.1 Atomic Theory

In this section the atomic structure of Fe III is examined. Fe III has a partially filled 3d shell, which results in the production of a "complex" spectrum that is rich in lines due to the large number of possible transitions [51, 116]. The analysis of complex spectra is not simple [116]. Further reading on the atomic theory discussed in this section can be found at Thorne *et al.* (1999) [51], Johansson (1996) [116] and Cowan (1981) [117].

4.1.1 The Energy Level Structure of the Singly Excited Fe III system

The binding energies of the 3d and 4s subshells are approximately equal in the iron group elements [51]. As the 3d subshell provides a shielding effect, the 4s subshells become more tightly bound to the nucleus. For this reason, there is competition in the order that these energy levels are filled. Due to the overlap in subshells, in Fe III there are 3 overlapping lower configurations, $3d^6$, $3d^5 4s$ and $3d^4 4s^2$, with the ground level term $3d^6\ ^5D_4$.

The parent terms represent the states of Fe III without the valence electron and are therefore the ground terms of Fe IV and are described by $3d^5\ ^M L$. When the parent term is coupled to the valence electron, nl, the singly-excited system is described using the configurations $3d^5(^M L)\ nl$. The doubly-excited spectrum of Fe III is not examined in this PhD thesis.

Figure 4.1 displays the term diagram of the singly-excited Fe III system. The diagram was created by Smillie (2007) [85] using energy levels published by Ekberg (1993) [88]

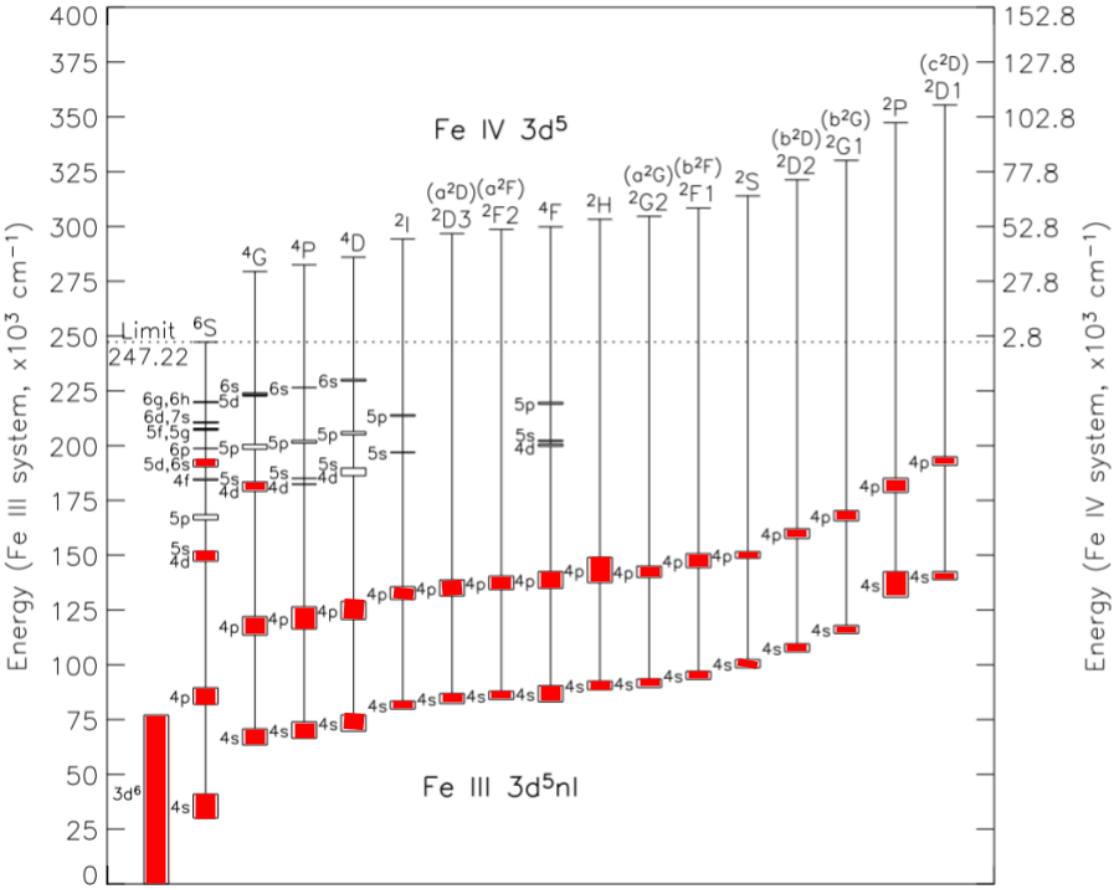


Figure 4.1: The term diagram of Fe III [85] using the energy levels published by Ekberg (1993) [88] and Corliss & Sugar (1982) [87]. The red shaded boxes indicate levels that have been revised in this thesis.

and Corliss & Sugar (1982) [87]. The ionisation level is the lowest energy of the ionisation of a parent term, and is indicated by a dashed line at $247,220\ \mathrm{cm}^{-1}$ at Figure 4.1.

Complex atoms, including iron, have several parent terms. As seen in Figure 4.1, Fe III has 16 parent terms: ^{6}S, ^{4}G, ^{4}P, ^{4}D, ^{2}I, a^{2}D, a^{2}F, ^{4}F, ^{2}H, a^{2}G, b^{2}F, ^{2}S, b^{2}D, b^{2}G, ^{2}P, and c^{2}D. The levels belonging to each of these parent terms are grouped vertically in the term diagram shown in Figure 4.1. Vertical lines connect the subconfigurations belonging to each parent term which are listed in order of the ground level value of Fe IV. The vertical height of the boxes in each parent term represent the ranges of known energy levels for each subconfiguration. Levels within the 3d^6 configuration cannot be split into parent terms as once the valence electron is added to the core, the electrons within the 3d shell are equivalent and indistinguishable. Therefore, 3d^6 levels are not assigned to a parent term.

In Figure 4.1, the levels shaded in red represent levels that have been revised in this thesis. The levels include the majority of the 3d^6, 3d^5 4s and 3d^5 4p levels for all parent terms, and some 3d^5 4p, 3d^5 5s and 3d^5 5d levels for the ^{6}S and ^{4}G parent terms.

4.1.2 *LS* coupling

The LS coupling scheme [118] is used to model the interactions between electrons in an atom or ion. It provides suitable labels for each energy level which represent the result of the interaction between the core electrons and a valence electron. This coupling scheme assumes that the non-central electron-electron interaction between electrons is much stronger than the spin-orbit interaction. This means that the individual spin angular momenta, s_i, for each electron, $s_i \pm \frac{1}{2}$, can be coupled together to create the total spin angular momentum, S, and the individual orbital angular momenta for each electron, l_i, can be coupled together to create the total orbital angular momentum, L:

$$\vec{L} = \sum_i \vec{l_i} \quad \text{and} \quad \vec{S} = \sum_i \vec{s_i} \, .$$

The total angular momentum quantum numbers, $L = 0, 1, 2, 3, ...$, are named S, P, D, F, and continue alphabetically with the exception of the letter J. Filled shells will have a total $L = 0$ and $S = 0$ and so only the valence electron and electrons in the unfilled 3d shell are considered.

Due to spin–orbit coupling, a final smaller energy split is created and is referred to as the fine structure. These energy shifts are due to the interaction of the magnetic moment of the electron spin (proportional to S) and the magnetic field created by the orbiting electron (proportional to L). The result is the coupling of L and S to create a total electron angular momentum, J, defined as

$$\vec{J} = \vec{L} + \vec{S} \, . \tag{4.1}$$

Each possible state can only be occupied by a single electron and so each level has a unique combination of the n, L, S and J quantum numbers and is described by

$$^{M}L_{J}$$

where M is the multiplicity, defined as $2S + 1$.

Parity

The parity of an atomic state is described as either even or odd and is defined by the parity of the sum of the angular momenta. To distinguish states otherwise described by identical terms, for states with even parity, the letters 'a', 'b', 'c', and so on are used as a prefix, starting with the term of the lowest energy. For terms with odd parity, the letters used are 'z', 'y', 'x', and so on are used with the lowest energy term using a 'z'. This is how the multiple parent terms of Fe III described with $M = 2$ and $L = 2$ are differentiated as a^2D, b^2D and c^2D.

4.1.3 Selection Rules

There are restrictions to the transitions allowed between energy levels. These are known as selection rules and transitions that violate these rules are known as "forbidden" transitions. However, forbidden transitions can be observed under certain circumstances and are generally weaker than transitions that follow the selection rules. These are discussed below.

4.1.3.1 Electric Dipole Radiation Selection Rules

For electric dipole transitions, the dominant form of radiation for an excited atom or ion, there are strict rules that must be satisfied [51]:

- $\Delta J = 0, \pm 1$ (but not $J = 0$ to $J = 0$)
- Upper and lower energy levels must have opposite parity, i.e $\Delta l = \pm 1$

These selection rules hold true for all transitions in the spectra observed in this PhD work in the laboratory.

Parity-Forbidden Transitions

Transitions that violate the parity change rule are observed due to "metastable" levels. These are energy levels that only have lower levels of the same parity, and therefore electrons in these metastable levels cannot transition via electric dipole radiation, but instead via collisions or via magnetic dipole or electric quadrupole radiation as these have different selection rules. It is for this reason, parity-forbidden transitions are only observed in dilute astrophysical plasmas. Parity-forbidden transitions are observed with intensities several orders of magnitudes weaker than electric dipole transitions and their wavenumbers must be calculated as Ritz wavenumbers from energy levels determined via the term analysis of laboratory spectra.

4.1.3.2 LS coupling Selection Rules

The LS coupling scheme also has three further rules for allowed transitions, which apply when describing the levels by L, S and J:

- $\Delta S = 0$
- $\Delta L = 0, \pm 1$ (but not $L = 0$ to $L = 0$)
- Upper and lower energy levels must have the same parent term

However, many levels are not 'pure' and there is a 'mixing' of the subconfigurations, resulting in transitions that appear to violate the LS coupling selection rules called forbidden lines. This happens when a transition is allowed to a term which is mixed with the apparent forbidden term. The degree of mixing is measured by percentage contributions of subconfigurations to each energy level value. In this project, the calculations by

Kurucz [119] are used as a guide to determine the correct quantum label designation for the energy levels of Fe III.

Forbidden lines that violate the LS coupling rules are commonly observed in the spectrum of Fe III and are useful in placing levels that are not otherwise 'connected' via fully allowed transitions in the LS coupling scheme. This places levels of different multiplicities and from different parents onto the same relative energy scale.

Inter-Combination Transitions

Forbidden lines that occur between levels whose multiplicities violate the LS coupling rule $\Delta S \neq 0$ are called inter-combination lines. These transitions are observed in the spectrum of Fe III. The transitions are due to level mixing and are invaluable in the energy level fitting process as these transitions link subconfigurations of different multiplicities $M = (2S + 1)$. These are common and their line strengths are typically equal or an order of magnitude smaller than transitions allowed by the LS coupling model [120].

Inter-Parent Transitions

Transitions between subconfigurations belonging to different parent terms, are called inter-parent transitions. These lines also occur from level mixing and are common in complex spectra [121]. Without these lines, the energy level structures of each parent term would not be placed onto a common scale relative to the ground state.

4.2 Term Analysis Method

The term analysis process is the determining of the energy level structure of an atom or ion using observed and classified spectral lines. Each spectral line is the result of the transition of an electron between two energy levels and the photon produced has equal energy to the difference of the energy levels. Therefore a spectral linelist can be used to determine the energy level structure of an atom or ion. The term analysis process relies on identifying Fe III spectral lines to determine the energy level structure of Fe III. In this work, the FTS and grating linelists were initially classified using the previously determined energy levels by Ekberg (1993) [88], and used to revise the values and labels of the Fe III energy levels.

The term analysis process can be complicated, especially for complex atomic structures, such as elements of the iron group. Every spectral line classification and energy level value must be manually inspected, to confirm they are genuine [116]. It is easy to obtain spurious line classifications resulting in incorrect energy level values. This process is made more difficult by the dense complex spectrum of Fe III which increases the likelihood of blended spectral lines and by the presence of additional lines due to other ionisation states and elements. In addition, data may also be missing due to instrumental constraints (i.e. detector plate boundaries) or the lack of energy level population in the observed plasma. Cowan (1981) [117] described the term analysis process like a puzzle:

> " The problem is rather like that of trying to put the pieces of a complicated jigsaw together, when the pieces never fit exactly, some pieces fit spuriously, some critical pieces are missing and there are pieces present that belong to one or more entirely different puzzles. "

To use the analogy by Cowan, the full puzzle may never be complete but by using the data produced in this work important parts of the picture can be determined.

A summary of the term analysis process is shown in Figure 4.2. The term analysis stages are as follows.

1. Classification of the Fe III lines in the linelists, and identification of lines due to other iron ionisation states and other elements.

2. Classified lines are used to optimise Fe III energy level values.

3. Optimised energy levels and remaining unclassified spectral lines can then be used to identify new Fe III energy levels.

4.2.1 Classification of Observed Spectral Lines

The final FTS and grating linelists contained 4623 and 6626 lines, respectively. It is important to classify the observed spectral lines in these linelists. By identifying to which ion spectrum the lines belong, lines which are not produced by Fe III are labelled and flagged as possibly unreliable in the case they are also identified as an Fe III line. Doubly-identified lines may have a compromised wavenumber and will not be used in the level optimisation process until the correct identification has been determined.

The linelists contain spectral lines due to other iron ionisation states, the neon buffer gas, and other impurities. The purity of the iron cathodes used in this PhD thesis was $99.8+\%$ which resulted in no known metal impurity lines being observed in the linelists.

The program *STRANS* was created by the Atomic Astrophysics Group at Lund University, Sweden to classify spectral lines in a linelist using a list of known energy levels. The program calculates the Ritz wavenumbers of every possible transition that abides by the electric dipole radiation selection rules ($\Delta J = 0$, parity must change) between the group of energy levels. The selection rules for LS coupling are not taken into account as lines that violate these rules are commonly observed due to level mixing (as mentioned in Section 4.1.3) and are essential in the term analysis process. *STRANS* then matches the observed spectral lines to the calculated Ritz wavenumbers within a given tolerance. The process relies on relatively accurate energy level values, as incorrect values produce false identifications and can exclude legitimate Fe III lines.

As there are large numbers of Fe III and Fe II lines in the linelists, these species were identified using *STRANS*. However, there were far fewer (and weaker SNR) spectral lines due to Fe I, Fe IV and neon. Therefore, a compilation of the strongest observed lines for these ions was created using NIST ASD [41] and used to identify lines from these atoms and ions.

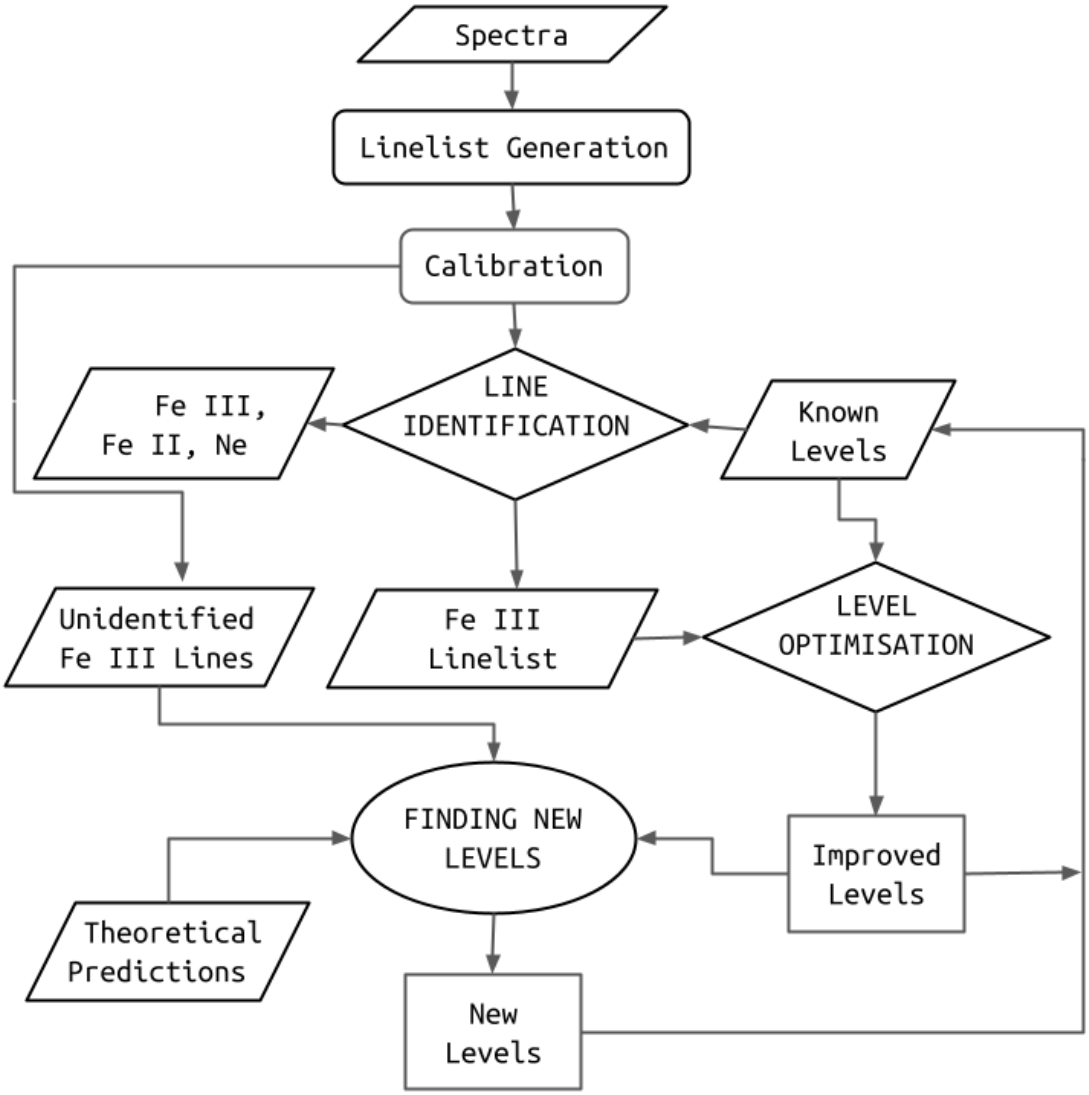


Figure 4.2: Flow chart of the term analysis procedure, adapted from Thorne *et al.* (1999) [51]. The rhomboids represent input data and the rectangles represent output data from the term analysis. The rounded rectangles indicate a process and the diamonds indicate the use of computer programs.

Fe II lines were identified using *STRANS* and energy levels published by Nave & Johansson (2013) [1]. In the FTS and grating linelists, 900 and 269 Fe II lines were identified using *STRANS*, respectively.

Fe III spectral lines were initially identified in the FTS and grating linelists using *STRANS* with the energy levels published by Ekberg (1993) [88] for the $3d^6$, $3d^5$ 4s and $3d^5$ 4p levels, and the levels published by Corliss & Sugar (1982) [87] for the higher-lying levels. For the high accuracy FTS lines, a line matching tolerance of 0.06 cm^{-1} was used in *STRANS*, which identified the majority of Fe III lines. The Ekberg levels had uncertainties larger than the tolerance in some cases (< 0.15 cm^{-1} to 0.45 cm^{-1}) and so the level values had to be adjusted in the *STRANS* input until all expected lines were found in the linelist. During this adjustment process, it was found that by shifting the Fe III energy levels by ~ 0.15 cm^{-1} the majority of the expected Fe III lines were identified, indicative of a

systematic offset in the levels published by Ekberg (1993) [88]. However, for the grating spectra even with the maximum tolerance allowed in *STRANS* of 0.29 cm^{-1}, many Fe III lines were not identified. This was due to the higher line uncertainties of the grating spectra (0.09 cm^{-1} to 0.86 cm^{-1}) exceeding the STRANS matching tolerance. Lines that were not identified by *STRANS* were manually identified using the Ritz wavenumbers, the lines published by Ekberg (1993) [88] and the calculations provided by Kurucz [119] as guides. For Fe III lines listed in both the FTS and grating linelists, the line with the lowest uncertainty was used in the final linelist.

In this project, of the 4623 observed spectral lines in the FTS linelist, 3186 remain unidentified and for the grating linelist, out of 6626 spectral lines, 5295 are remain unidentified. As Fe I and Fe II were not the focus of this study, it is likely spectral lines belonging to these species were not identified, especially if the line had a weak SNR. The identification and classification of these remaining spectral lines is planned for future work (Section 5.3.2).

4.2.2 Energy Level Optimisation

Following the identification of Fe III transitions in the linelist, their wavenumbers and uncertainties are then used to optimise the Fe III energy levels. By using multiple observed lines to calculate energy level values, the energy levels can be more accurate than the observed lines. For this process, the least-squares fitting program *LOPT* [122] developed by A. Kramida was used to calculate optimised energy level values using uncertainty-weighted transition lines. *LOPT* requires wavenumbers, uncertainties and classifications of the observed spectral lines. "Unreliable" lines, such as those that are doubly-identified or those very blended in the grating linelist (labelled "V", Section 3.2.2), are 'weighted-out' by significantly increasing their uncertainty in the input to the optimisation process. This means that these unreliable lines are not used in the revising of the energy level values, but are retained in the output files to aid in line identification.

LOPT outputs a list of optimised energy level values, their uncertainties and the number of lines used to calculate each energy level value. The energy of the ground level is set to zero by definition and all other levels are optimised relative to it. There are two different relevant uncertainty values provided by *LOPT* for each energy level [122]: the first is the dispersion relative to any other energy level, and the second is the uncertainty of the levels relative to the ground level. *LOPT* also returns the list of lines used in the optimisation process with newly-calculated Ritz wavenumbers and uncertainties, and the difference between the Ritz and the observed wavenumbers ($\Delta\sigma_{obs-Ritz}$). Lines with a large $\Delta\sigma_{obs-Ritz}$ suggest an issue in the level optimisation input and this is indicative of a poorly-fitted spectral line. A value of $\Delta\sigma_{obs-Ritz}$ larger than 1.5 times the observed line wavenumber uncertainty is flagged as "problematic" and the line is reviewed in the original spectrum in the case of an unlabelled issue. The identification of the line is also reviewed in case it is a misidentification and needs to be manually removed from the classified linelist. Other transitions to the relevant energy levels are also examined in case there are other spurious lines causing a shift in the optimised energy level.

4.2.3 The *STRANS-LOPT* Iterative Process

At the start of the term analysis process, the classification of spectral lines and the energy level optimisation process is carried out for a small subset of energy levels. The subset of energy levels will include levels of both even and odd parity, and the levels chosen, are expected to have strong transitions between them and therefore typically belong to the same parent term.

To ensure all expected transitions have been identified by *STRANS*, lines connecting each newly added level are inspected. They are compared to line strengths observed by Ekberg (1993) [88] and the log(gf) values calculated by Kurucz [119] for confirmation. The intensity and log(gf) values were used as a guide to the relative line strengths of the transitions involved, which is useful in determining if the identification of a line is valid. Typically lines with a listed intensity value greater than 13 as published by Ekberg (ranging up to 25) and log(gf) > -1.0 as calculated by Kurucz were observed in the FTS spectrum. For the grating spectrum, lines with any intensity value as published by Ekberg and log(gf) > -2.5 as calculated by Kurucz were typically observed.

Next, any lines flagged with $\Delta\sigma_{obs-Ritz} > 1.5$ times the observed uncertainty are examined and for every level the $\Delta\sigma_{obs-Ritz}$ offset of the transitions are examined as a whole for any large inconsistent shifts which could also indicate a problematic line. Identified problematic lines are either removed usually due to a misidentification or 'weighted-out' with a huge uncertainty in the *LOPT* input so that they have no influence in the level optimisation process.

Once a subset of energy levels has been successfully optimised, the new energy level values from *LOPT* can replace the original level values in *STRANS* and the process can be repeated. This allows for more accurate Ritz wavenumbers to be calculated in *STRANS* and therefore maximises the number of lines correctly identified and minimises any misidentifications.

Once the first subset of energy levels is confirmed to be well connected and correctly optimised, another small subset of energy levels is added to the system. Adding levels in small batches prevents a large number of spurious lines in the level optimisation program at a single time which ensures accurately set energy levels with confirmed valid transitions. This process is repeated with subsets of energy levels until all previously published levels are included. After this, new energy levels can be identified and added to the system.

4.2.4 Search for New Energy Levels

The spectral linelist of unclassified lines and optimised energy levels can be used to identify potential new energy levels. The wavenumber of every spectral line is added to or subtracted from a set of energy levels of the same parity, to obtain possible new energy level values. If more than 3 possible new energy level values coincide within a certain tolerance and are within the expected wavenumber range, the value is a candidate for a new energy level. Due to the large number of lines and energy levels, there are likely to be many spurious coincidences. To examine the possible new energy levels, the ΔJ

values and relative intensities of the proposed transitions to the new levels are examined. The calculations by Kurucz [119] are also used as a guide to predict and confirm the new energy level values.

If the new energy level value is confirmed, it is treated like the previously optimised energy levels and added into the system via *STRANS* and *LOPT*. The final output will include both improved and newly discovered energy levels. Term analysis ends when no further levels can be identified or optimised, typically due to the lack of observed spectral lines.

New levels were not searched for in this PhD project, but this is planned for future work and discussed in Section 5.3.1.3.

4.3 Term Analysis Results

In this PhD thesis, 305 previously published Fe III energy levels and labels are revised. As stated in Section 1.2.1, Ekberg (1993) [88] most recently published energy level values for all but 7 of the $3d^6$, $3d^5 4s$ and $3d^5 4p$ configurations and Corliss & Sugar (1982) [87] compiled an Fe III energy level list for some higher-lying levels (including 4d, 4f, 5s, 5p, 5d, etc.) from earlier publications. The aim of the term analysis is to increase the accuracy of these known energy levels by using the high accuracy FTS lines.

As FTS lines have higher wavenumber accuracy, it is preferable to first create systems of energy levels using FTS lines only. Levels were added to *LOPT* until the transitions needed to connect levels were no longer observed in the FTS spectra. The strongest lines were consistently found to be for transitions between subconfigurations with the same multiplicity and within the same parent term. As stated in Section 4.1.3, the transitions within a parent term system and with no change in multiplicity obey the LS coupling selection rules, and inter-combination and inter-parent transitions will generally be weaker. The levels successfully connected using FTS data are shown in Figure 4.3, in the colours red, orange, purple, blue and green. There is a particularly high degree of level mixing in levels belonging to the subconfigurations of ^{4}G, ^{4}P and ^{4}D parent terms, producing many strong lines between these levels and creating the well-connected system shown in orange. Many 4s and 4p levels could only be connected to other levels within the same parent term and these connections are shown in green in Figure 4.3. In some cases, the 4s and 4p energy levels within a parent could not be fully connected by FTS observed transitions and so multiple connected level systems were made in *LOPT* within a single parent set of levels. This is usually due to the different multiplicities. For example, the two green lines between the 4s and 4p levels in the b^{2}G parent term represent two systems, each connecting levels with a multiplicity of either $M = 1$ or $M = 3$. Figure 4.3 displays the need for forbidden lines that violate the LS coupling selection rules (inter-combination and inter-parent transitions). All 4s and 4p levels were connected to at least one other level via FTS lines, except the levels (a^{2}F)4p ^{3}D$_1$, (b^{2}G)4p ^{3}F$_3$, (b^{2}G)4p ^{3}G$_4$, (^{2}P)4s ^{3}P$_0$, (^{2}P)4p ^{3}P$_0$, (^{2}P)4p ^{3}P$_1$, (c^{2}D)4p ^{3}D$_2$ and (c^{2}D)4p ^{1}D$_2$. The lack of transitions involving these levels in the FTS linelist are an indicator of the reduced population in the

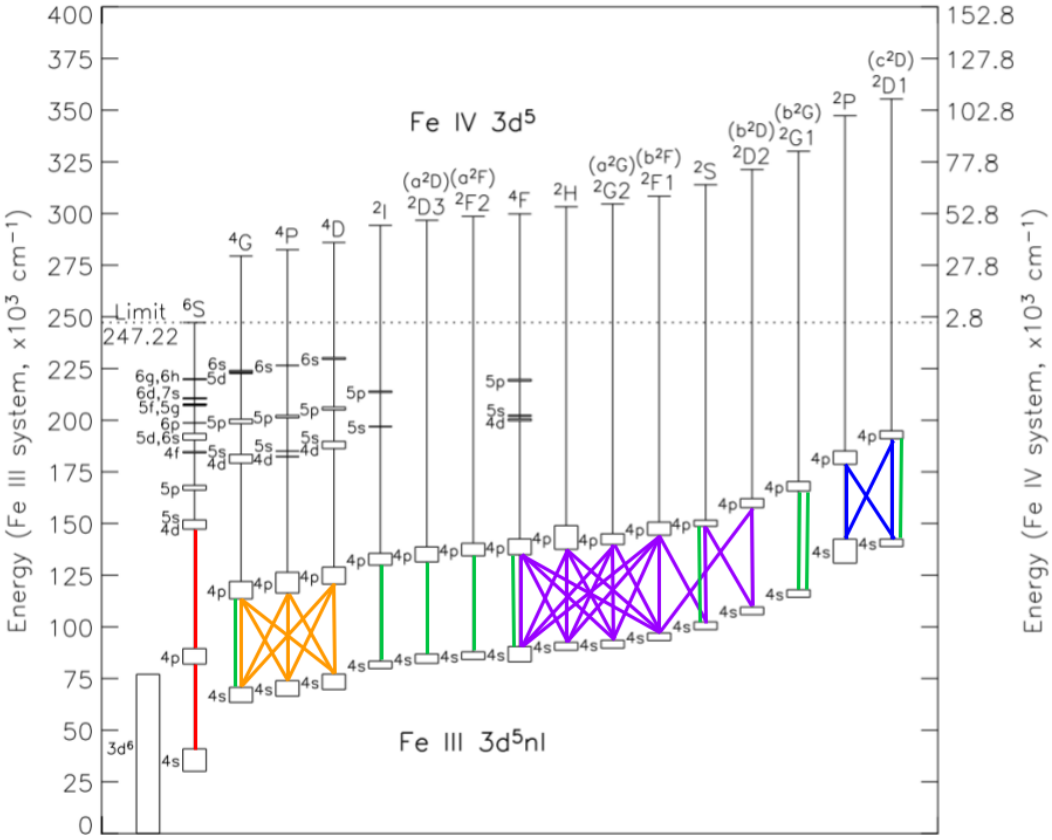


Figure 4.3: The groups of energy levels connected by FTS lines. The levels were connected using FTS lines until no further connections could be found. In some cases, only the transitions between 4s and 4p levels within the same parent term system were observed, resulting in the systems represented by the green lines. In other cases, transitions to energy levels outside the parent term system were also found, and these connected energy level systems have been displayed including the transitions between the 4s and 4p levels in each parent term in orange, purple and blue. The red system within the $3d^5$ (^{6}S) parent term displays transitions found between the 4s, 4p, 4d and 5s levels.

relatively high-lying levels in comparison to the lower-lying levels in the PDL plasma. In addition, the 4d and 5s levels for the $3d^5$ (^{6}S) parent term were also connected via FTS lines.

Once the energy levels in each independent FTS-line level connected system were optimised relative to each other, the systems were then connected to each other and anchored to the ground level using lines from the grating linelist. This places all levels onto the same energy scale relative to the ground level ($3d^6\ ^5D_4$) which was fixed to $0.0\ \mathrm{cm}^{-1}$.

The final results presented are the revised Fe III energy levels and labels, and the classified FTS and grating lines.

4.3.1 Revised Energy Levels for Fe III

Overall, 305 energy levels were revised in this work, including 286 levels of the $3d^6$, $3d^54s$ and $3d^54p$ configurations determined by Ekberg (1993) [88]. In addition, 19

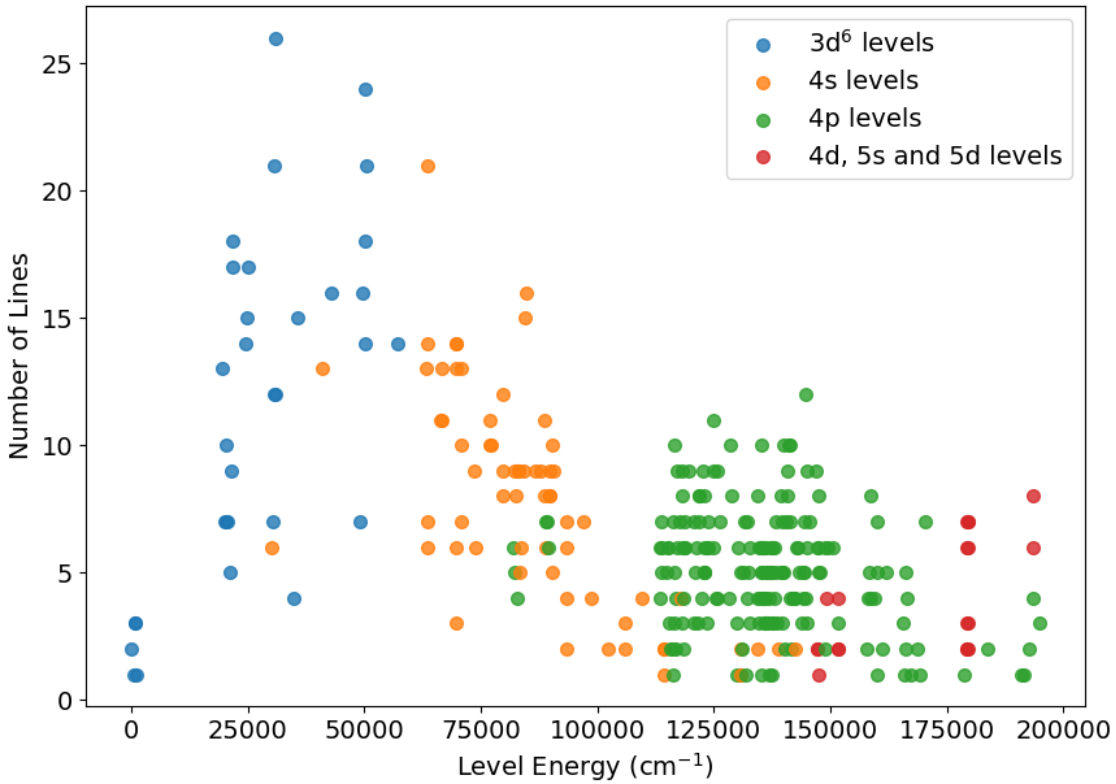


Figure 4.4: The number of lines used for each level in the energy level optimisation process.

selected levels previously published by Corliss & Sugar (1982) [87] in the 3d^5 (^{4}G) 4d and 3d^5 (^{6}S) 4d, 5s and 5d configurations were included. The revised energy level values and uncertainties are listed in Appendix A and are separated by configuration. The table columns for the tables in Appendix A include the level designations (labels); level energies and uncertainties; the difference between the level energy and the previously published level value; and the number of lines used to fit each level in *LOPT*.

Some of the levels published by Ekberg (1993) [88] and Corliss & Sugar (1982) [87] were not revised in this work due to insufficient observed transitions. These levels, when added to the system, had very few or no reliable transitions and so may be spurious and were not included in the final results. All but one of the 3d^6 levels that Ekberg determined were revised. The level 3d^6 b^{1}D$_2$ that Ekberg determined to be at 77044.53 cm^{-1} could not be confirmed. 65 out of the 74 3d^{5}4s levels and 192 out of the 208 3d^{5}4p levels determined by Ekberg were confirmed in this work. In some cases, very few transitions were expected to involve these levels such as those with very high or low J values which can make it difficult to find multiple transitions. In general, the number of transitions observed decreased with increasing energy level value, due to the reduced population of high-lying energy levels in the PDL plasma producing weakly-observed spectral lines. Figure 4.4 displays the number of lines used in the fitting of each energy level. To confirm the levels not included are not spurious, they must be reviewed with the addition of new transitions included in *LOPT*. This can be done by including more levels and extending the linelists, which is proposed as future work and is discussed in Section 5.3.

Figure 4.5 shows the comparison between the revised Fe III energy levels and the previously published values of Ekberg (1993) [88] shown in black ($3d^6$, $3d^5$ 4s and $3d^5$ 4p levels) and Corliss & Sugar (1982) [87] shown in green ($3d^5$ 4d, $3d^5$ 5s and $3d^5$ 5d levels). The blue and red error bars are the revised energy level uncertainties with respect to the ground level and to any other term in the energy level system, respectively. The shaded orange regions are representative of the Ekberg uncertainties at ± 0.15 cm^{-1} and ± 0.45 cm^{-1} and are drawn to provide a visual comparison of energy level uncertainties. Corliss & Sugar (1982) [87] did not provide any level uncertainties. Figures 4.6 and 4.7 display the same data, but with only the one set of uncertainties. These are discussed further below.

There is an average shift of 0.11 cm^{-1} and 0.18 cm^{-1} between the revised energy levels and the levels published by Ekberg and Corliss & Sugar, respectively. This shift is comparable to the level uncertainty Ekberg stated. However, the shift is consistent across all the energy levels which could be due to an incorrectly calibrated plate in Ekberg's data.

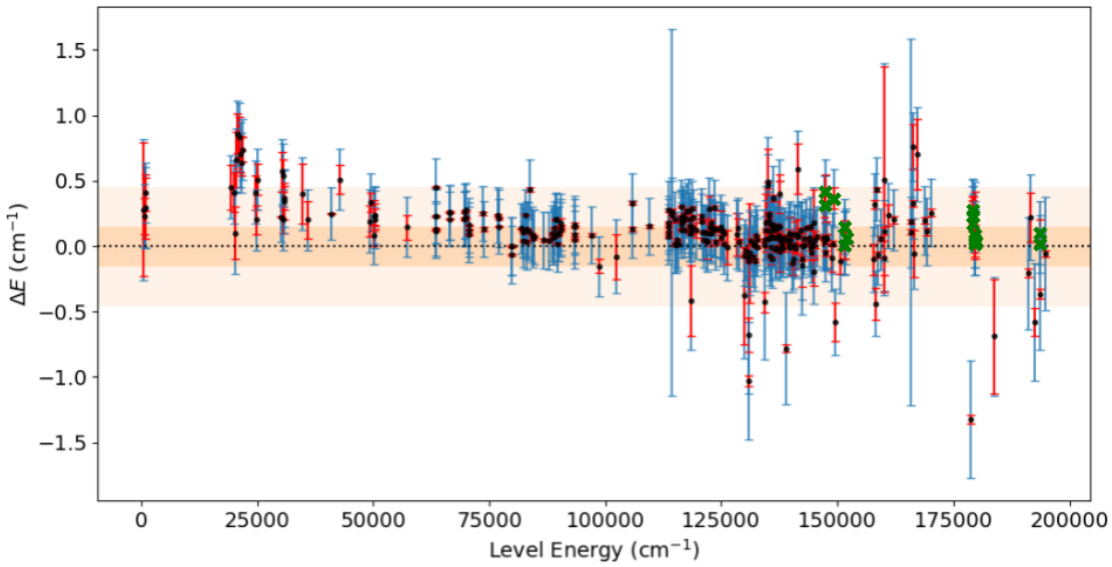
Energy Level Uncertainties

The uncertainties shown in Figure 4.5 are the energy level uncertainties with respect to the ground level (blue) and with respect to any other term in the energy level system (red). These are an output of *LOPT* and the equations used to calculate the uncertainties can be found in Kramida (2011) [122].

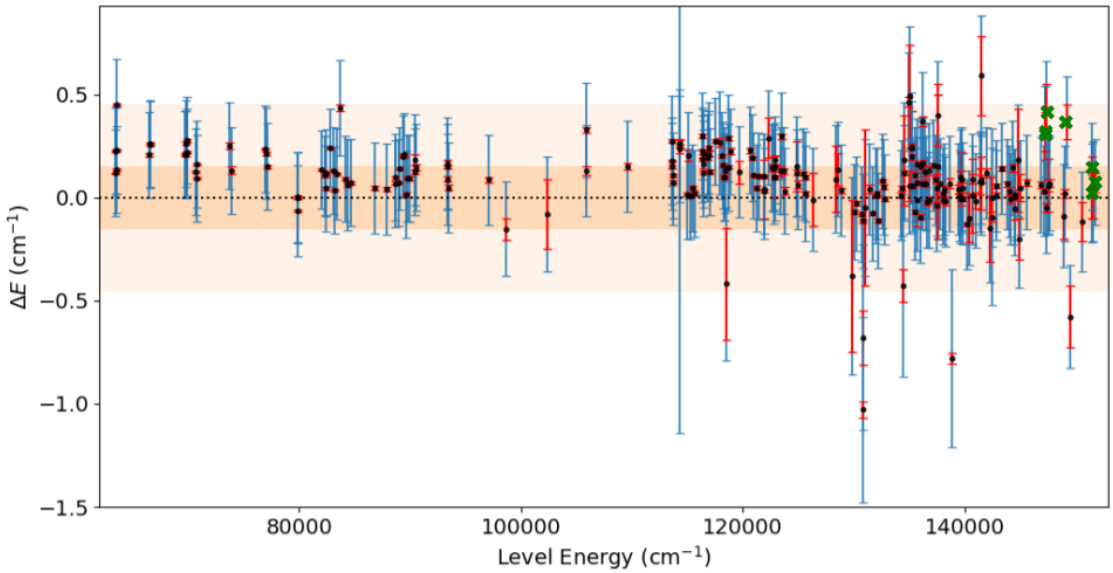
However, as all the lines used for optimisation were calibrated using Fe II Ritz wavelengths from Nave & Johansson (2013) [1], they all have an equal calibration component within the total line uncertainty which is essentially "weighted out" during the energy level optimisation process. The data by Nave & Johansson (2013) [1] have a global calibration uncertainty of 4 parts in 10^8 (Section 3.1.4.1), which must be reintroduced for accurate energy level data. The *LOPT* provided uncertainties were added linearly to the global calibration uncertainty of Fe II of 4 parts in 10^8 to calculate the total energy level uncertainties for each level. However, this additional uncertainty is small. For example, for a level at $80,000$ cm^{-1}, the uncertainty is increased by 0.003 cm^{-1}.

The uncertainties with respect to the ground are the true uncertainty of the level, as the levels are set relative to the ground level. These are the blue error bars in Figure 4.5 and (excluding the ground level uncertainty) range from 0.19 cm^{-1} to 1.4 cm^{-1}, with 93% of levels having an uncertainty equal to or less than 0.32 cm^{-1}. These are also plotted in Figure 4.6. These are comparable to the uncertainties of the previously published energy levels. Ekberg did not provide uncertainties for individual energy levels, but stated that 75% of levels had an uncertainty less than 0.15 cm^{-1}, and the remaining levels had an uncertainty of 0.45 cm^{-1} or less. These are shown in an orange shaded area to provide a visual comparison of the energy level uncertainties.

The uncertainties with respect to the ground rely on the accuracy of the transitions to the ground level $3d^6\ {}^5D_4$. These important transitions are called resonance lines and in Fe III are located in the spectral range of $82,334$ cm^{-1} to $141,001$ cm^{-1} (709 Å to 1215 Å). However, the calibration of the grating linelist relied on the Fe II spectral

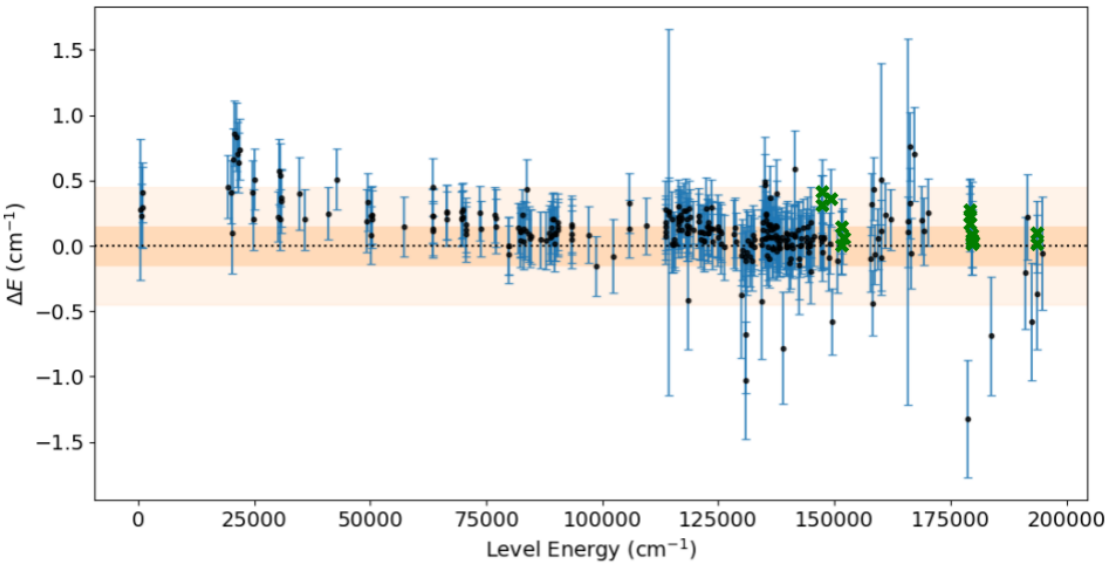


(a) The revised energy levels.

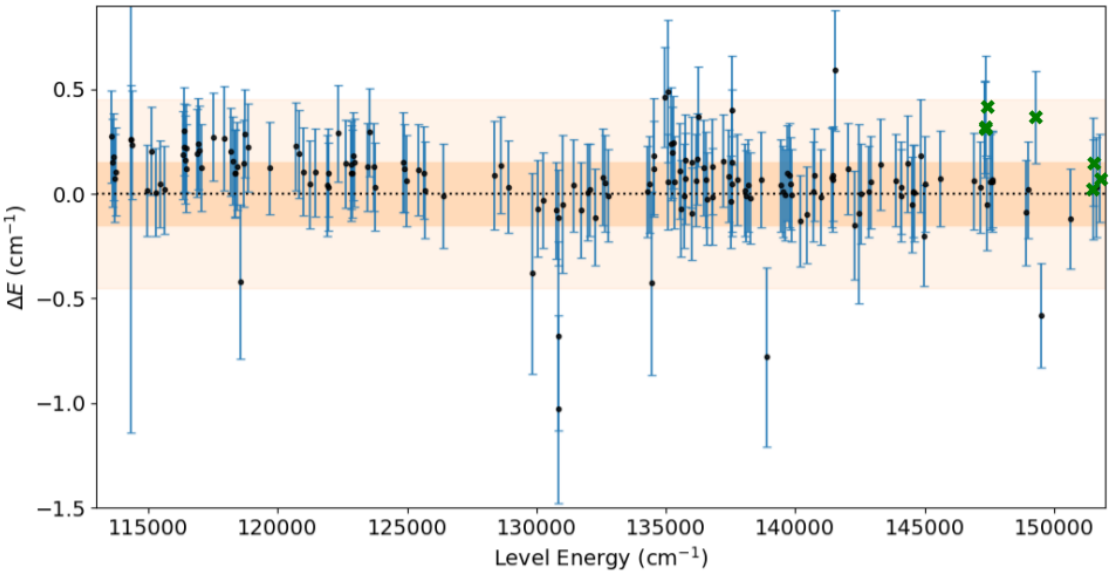


(b) The revised energy levels expanded to show detail between $62,000$ cm^{-1} and $153,000$ cm^{-1}.

Figure 4.5: The difference between the revised energy levels and the previously published levels by Ekberg (1993) [88] (in black circles, for the $3d^6$, 4s and 4p levels) and Corliss & Sugar (1982) [87] (in green crosses, for the remaining levels) are shown here. The error bars shown in blue and red are the revised energy level uncertainties with respect to the ground level and the energy level system as whole, respectively. Ekberg states that 75% of levels had an uncertainty less than 0.15 cm^{-1}, and the remaining, 0.45 cm^{-1} or less. The region ± 0.15 cm^{-1} and ± 0.45 cm^{-1} has been shaded in dark orange and light orange, respectively, to represent the uncertainties of the energy levels published by Ekberg (1993) [88]. No level uncertainties were provided in Corliss & Sugar (1982) [87].

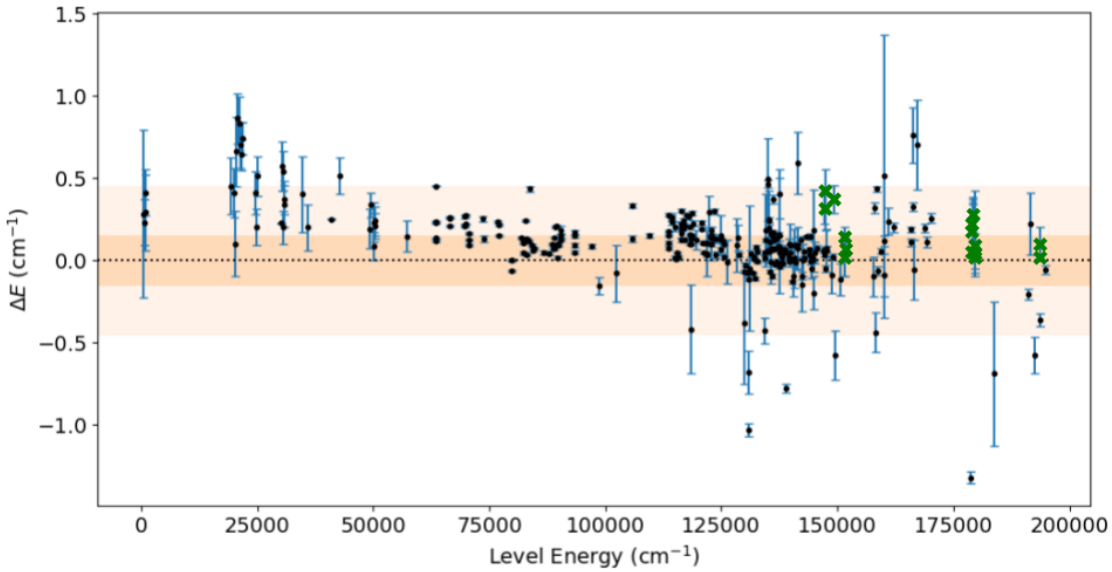


(a) The revised energy levels.

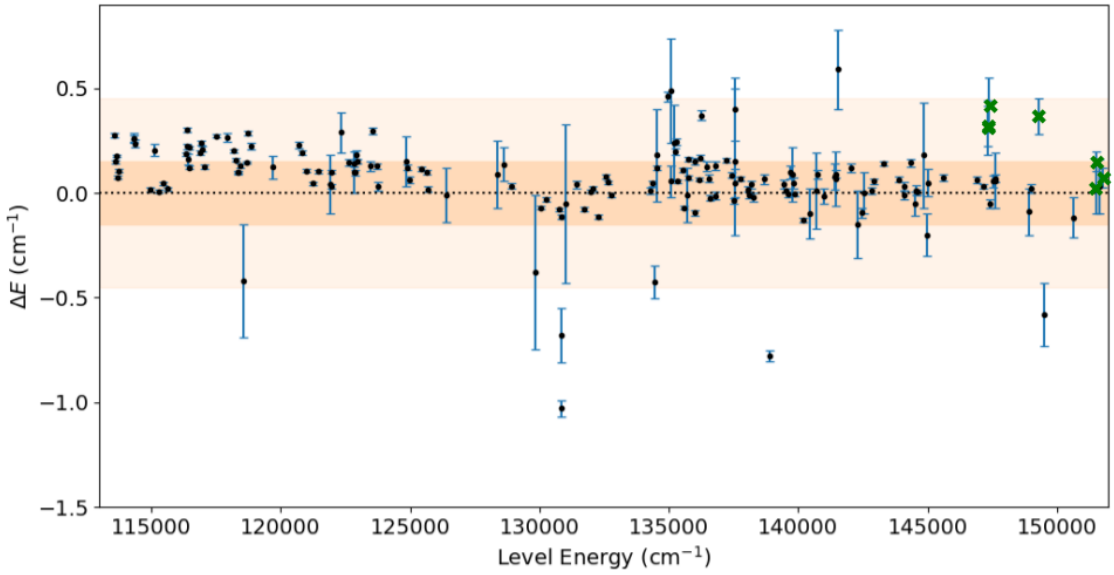


(b) The revised energy levels expanded to show detail between $62,000$ cm^{-1} and $153,000$ cm^{-1}.

Figure 4.6: As in Figure 4.5, but the error bars shown in blue are the revised energy level uncertainties with respect to the ground level.



(a) The revised energy levels.



(b) The revised energy levels expanded to show detail between $62,000$ cm^{-1} and $153,000$ cm^{-1}.

Figure 4.7: As in Figure 4.5, but the error bars shown in blue are the revised energy level uncertainties with respect to the energy level system as whole.

lines observed by Nave & Johansson (2013) [1] which was limited to the spectral range $\sigma < 111,121$ cm^{-1} ($\lambda > 900$ Å), resulting in the observation of only two resonance lines with the uncertainties 0.20 cm^{-1} and 0.56 cm^{-1}. Therefore, although the 4s and 4p level energies may be set using accurate FTS lines relative to each other (such as the orange system in Figure 4.3), there will always be a minimum "offset" of an additional uncertainty with respect to the ground level present. The uncertainties with respect to the ground will be improved by including more resonance lines with the expansion of the grating linelist at $\sigma > 111,121$ cm^{-1} ($\lambda < 900$ Å). This is planned as future work to improve the accuracy of the energy levels and is discussed in Section 5.3.1.2.

The uncertainties with respect to the energy level system are displayed in red in Figure 4.5 and in blue in Figure 4.7. It is clear from these figures that the uncertainties are much smaller than the uncertainties with respect to the ground, and the level uncertainties published by Ekberg. The uncertainties with respect to the energy level system range from 0.003 cm^{-1} and 0.86 cm^{-1}, with the uncertainty equal to or less than 0.15 cm^{-1} for 90 % of the revised energy levels. There is a large difference in the uncertainties with respect to the system to the uncertainties with respect to the ground. For 90% of the revised levels, the difference between the uncertainty with respect to the system and the uncertainty with respect to the ground is lower than 0.22 cm^{-1}. However, the uncertainties with respect to the ground can be high as 1.4 cm^{-1} greater than the uncertainties with respect to the system. These low uncertainties with respect to the energy level system are an improvement over previously published energy levels and provide high accuracy Ritz wavenumbers which are discussed later in this section.

4.3.2 The Classified Fe III Linelists

In total, 1599 observed spectral lines were identified as Fe III. Of these, 959 lines were used to optimise Fe III energy level values in this work, of which 239 were FTS-measured and 720 were grating-measured. The remaining 640 identified spectral lines were "problematic" (i.e. doubly-identified, heavily-blended, misshapen) and so not influential in the energy level optimisation process. They are included to aid in line identification and so that Ritz wavenumbers and uncertainties can be calculated for these classified lines.

The Ritz wavenumbers and uncertainties are calculated by *LOPT* for every classified line using the revised energy levels. As with the uncertainties of the revised energy levels, the global calibration uncertainty of the Fe II data used for calibration must be reintroduced. The Ritz wavenumber uncertainties provided by *LOPT* were added linearly to the global calibration uncertainty of Fe II of 4 parts in 10^8 to calculate the total Ritz wavenumber uncertainties.

The classified Fe III FTS linelist is presented in Appendix B. The columns in the table are as follows. Columns 1-5 state the observed spectral lines' properties: calibrated relative intensities (ln (EW)), SNRs, FWHMs, observed wavenumbers and observed wavenumber uncertainties. Columns 6-7 state the Ritz wavenumbers and Ritz wavenumber uncertainties. Column 8 lists the energy levels of the classified transition. The linelist of the classified grating linelist is shown in Appendix C. Columns 1-4 state the observed line

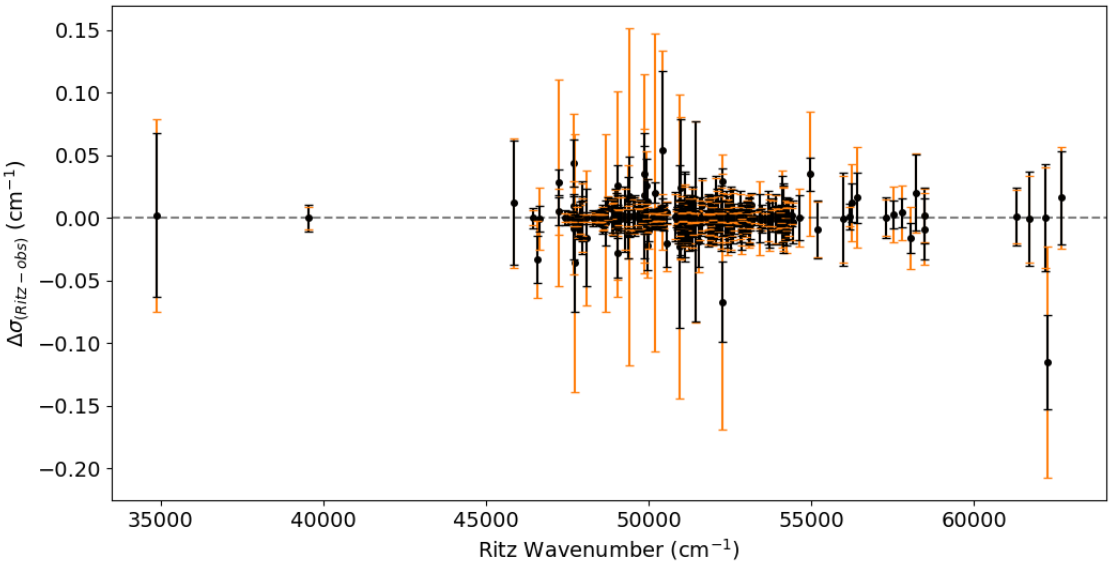
properties: the exposure time, the intensity, the observed wavenumber and the observed wavenumber uncertainty. Columns 5-6 state the Ritz wavenumbers and Ritz wavenumber uncertainties. Column 7 lists the energy levels of the identified transitions. In both classified linelists, lines with multiple Fe III identifications are listed for every identification found and lines weighted out of the energy level optimisation process are indicated by an asterisk (*) after the observed wavenumber uncertainty.

The difference between the observed and Ritz wavenumbers for the spectral lines used in the Fe III term analysis are shown in Figures 4.8 and 4.9 for the FTS and grating linelists, respectively. Both the observed (orange) and Ritz (black) wavenumber uncertainties are shown. It can be seen in Figure 4.8 that the Ritz wavenumber uncertainties are either much lower or comparable to the observed wavenumber uncertainties. The mean shift of the Ritz from the observed wavenumbers for the FTS data is -0.00004 cm^{-1} with a standard deviation of 0.013 cm^{-1}. This small shift is well within the line uncertainties. In Figure 4.9, the drastic difference in accuracy between the observed wavenumbers and the Ritz wavenumbers can be seen. For this grating data the mean shift of the Ritz wavenumbers from the observed is -0.0022 cm^{-1} with a standard deviation of 0.28 cm^{-1}. A greater spread in data is expected for the grating data in comparison to the FTS, due to the larger uncertainties. No large systematic shift appeared in either linelist, confirming the energy levels were successfully determined by *LOPT*.

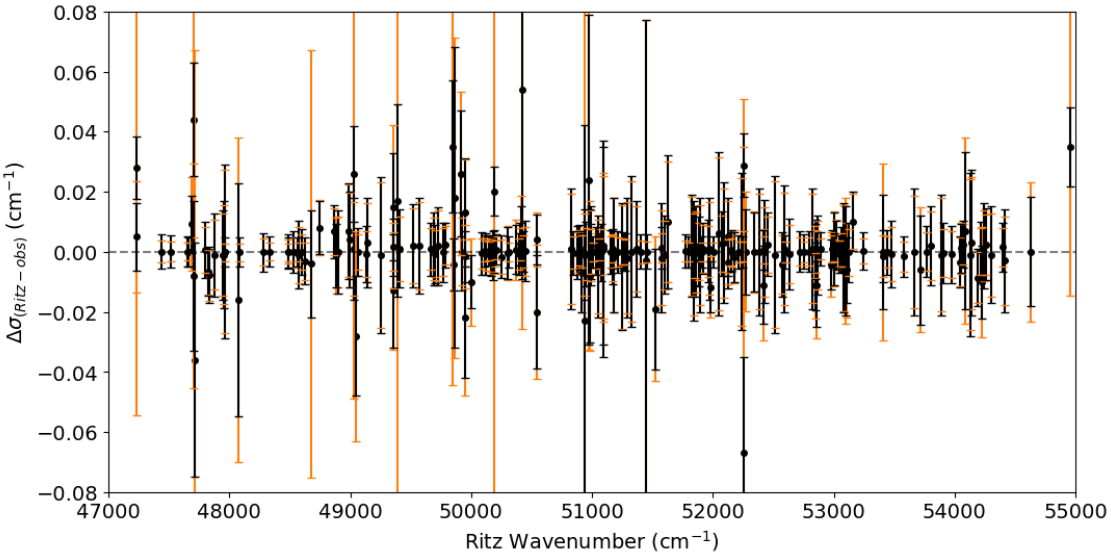
Figure 4.10 displays a comparison of the classified Fe III lines from this work with the linelist published by Ekberg (1993) [88]. These are the lines corresponding to transitions between the $3d^6$, $3d^5 4s$ and $3d^5 4p$ configurations. The lines in blue were used in the energy level optimisation process, but the Fe III classified lines that were labelled "problematic" (i.e. blend in the spectrum, or a double-identification) and not used in the optimisation process are shown in red. The wavenumber uncertainties published by Ekberg are displayed in grey and it is clear that for the majority of lines there is a large improvement in accuracy. There is a mean shift of -0.15 cm^{-1} between the Ritz wavenumbers calculated in this PhD project and the observed wavenumbers published by Ekberg (1993) [88]. In Section 3.4.2, the observed grating wavenumbers were compared to Ekberg's linelist and it was concluded that the Ekberg wavenumbers were likely shifted due to an incorrect wavelength calibration in his work.

For FTS-measured lines used in the energy level fitting process, the Ritz wavenumber uncertainties range from 0.0048 cm^{-1} to 0.08 cm^{-1}. When including the "problematic" FTS-measured classified Fe III lines, 85% of lines had a Ritz wavenumber uncertainty of 0.079 cm^{-1} or less. This is an improvement in accuracy of an order of magnitude when compared to the line uncertainties published by Ekberg, which range from 0.113 cm^{-1} to 0.617 cm^{-1}. Examples of the lines with dramatically decreased uncertainties can be seen in Figure 4.10b. For the grating-measured spectral lines, the Ritz wavenumber uncertainties range from 0.011 cm^{-1} to 0.85 cm^{-1}, with 93% of the lines having an uncertainty of 0.15 cm^{-1} or less. For some of these values, the uncertainties are comparable, but for others this is an order of magnitude improvement in uncertainty.

Figure 4.11 shows the comparison of the classified Fe III lines from this work with the

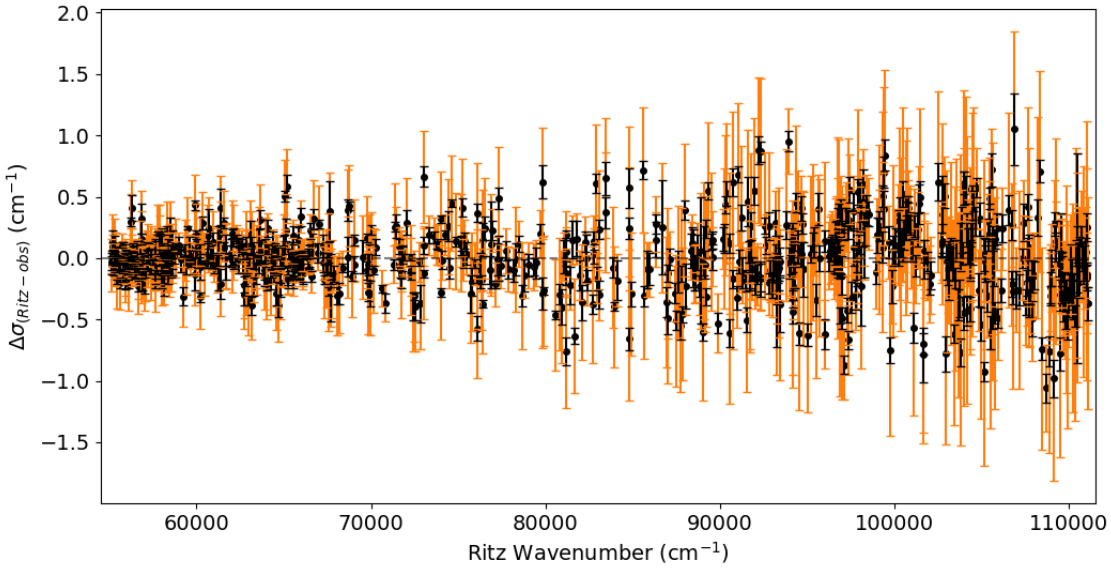


(a) The spectral region containing classified FTS lines

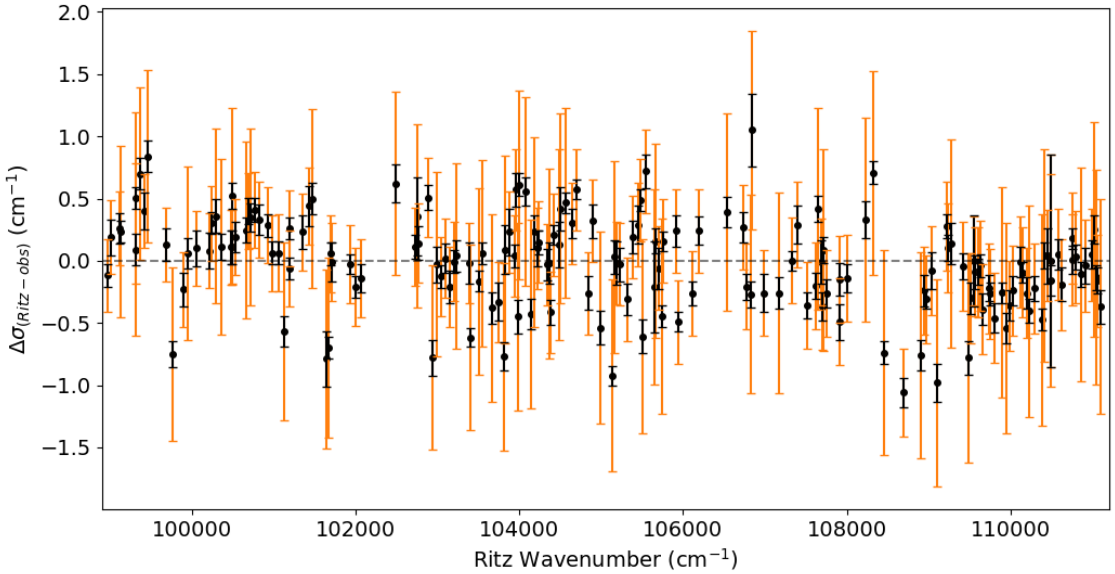


(b) The FTS spectral region expanded to show detail between $47,000$ cm^{-1} and $55,000$ cm^{-1}.

Figure 4.8: The difference between the observed and Ritz wavenumbers of the lines used in the level optimisation in the classified FTS linelist. The Ritz wavenumber uncertainties (black) and the observed spectral line uncertainties (orange) are overplotted.

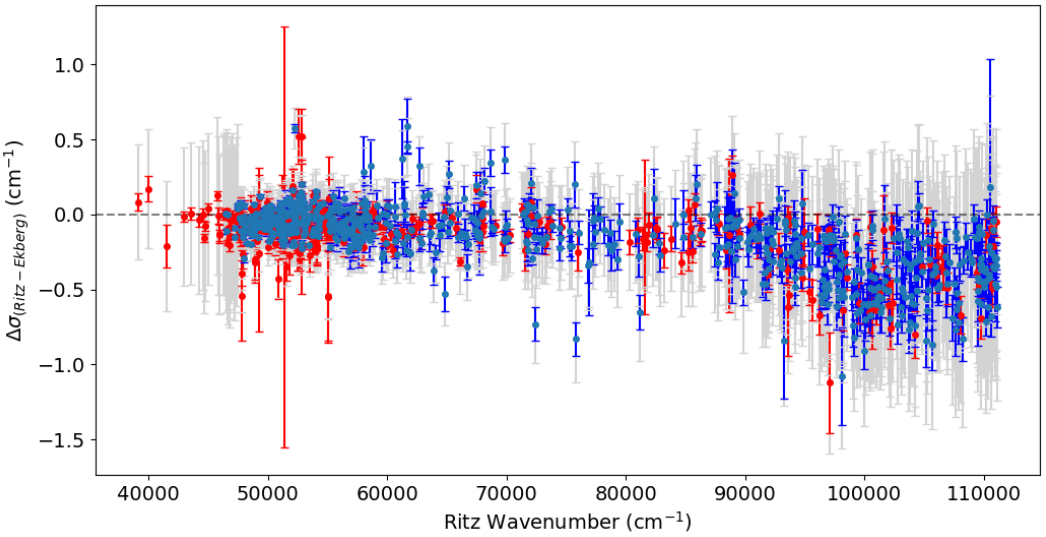


(a) The spectral region containing classified grating lines

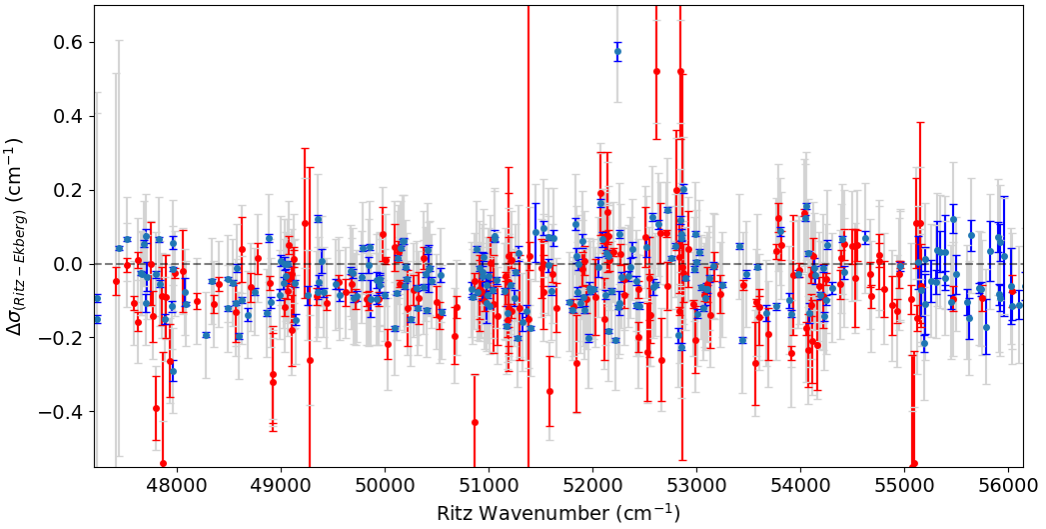


(b) The grating spectral region expanded to show detail between $98,900$ cm^{-1} and $111,200$ cm^{-1}.

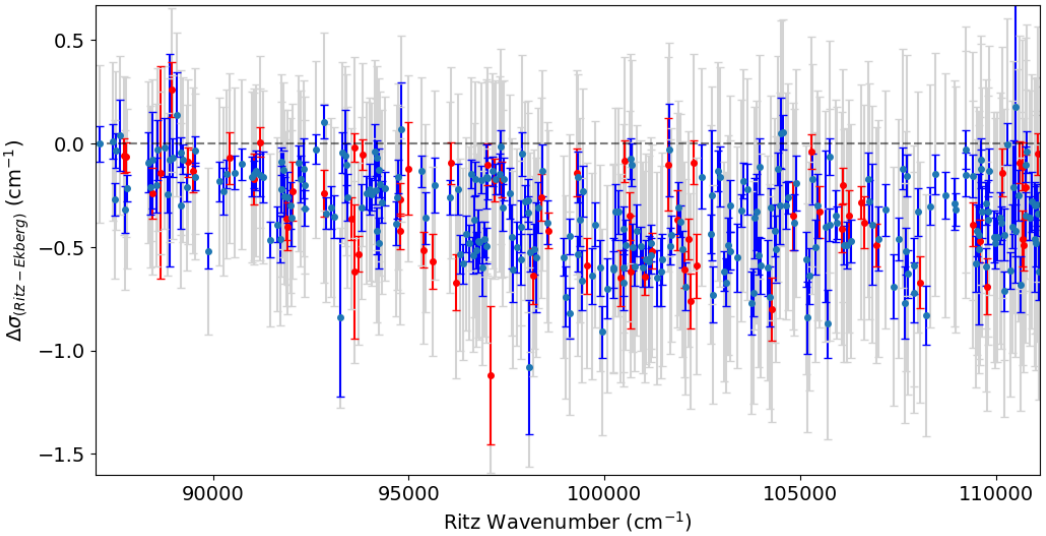
Figure 4.9: The difference between the observed and Ritz wavenumbers of the lines used in the level optimisation in the classified grating linelist. The Ritz wavenumber uncertainties (black) and the observed spectral line uncertainties (orange) are overplotted.



(a) The entire spectral region of the FTS and grating linelists.



(b) The spectral region expanded to show detail between $47,000$ cm^{-1} and $56,100$ cm^{-1}.



(c) The spectral region expanded to show detail between $87,000$ cm^{-1} and $111,000$ cm^{-1}.

Figure 4.10: The comparison of the classified Fe III line wavenumbers from this work with the wavenumbers from the linelist published by Ekberg (1993) [88]. The lines used in the energy level optimisation process are shown in blue, and the "problematic" lines that were classified as Fe III but did not contribute to the energy level optimisation process are shown in red. The Ekberg wavenumber uncertainties are displayed in grey. Lines with multiple Fe III identification for a single spectral line were not included.

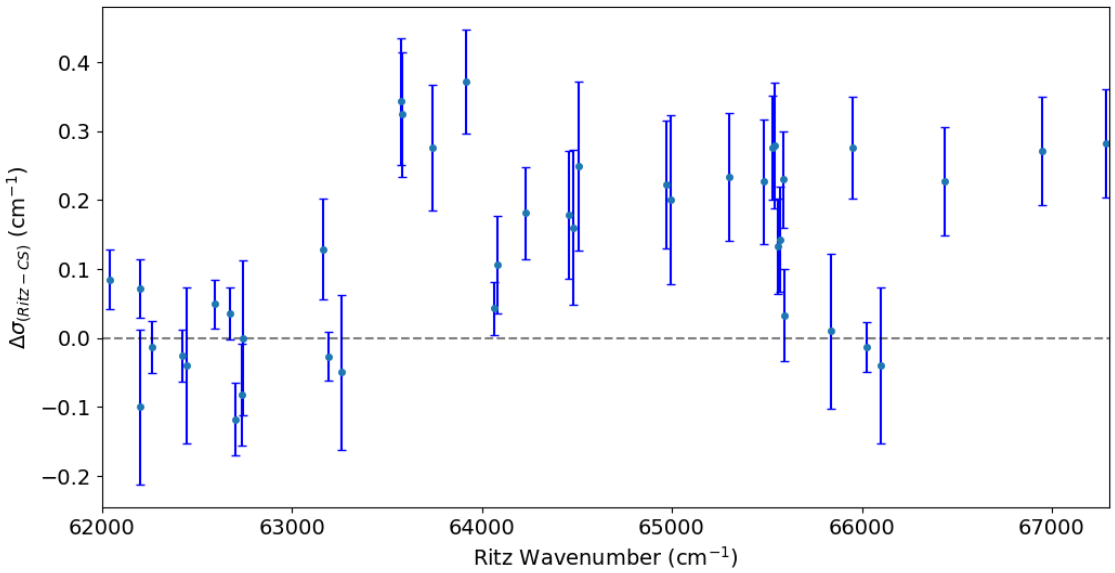


Figure 4.11: The comparison of the classified Fe III Ritz wavenumbers from this work with the wavenumbers from the linelist published by Corliss & Sugar (1982) [87]. The error bars displayed are the uncertainties of the Ritz wavenumbers from this work. Corliss & Sugar (1982) [87] did not provide any uncertainties, but these lines were first published by Glad (1955) [86] with uncertainties between 0.8 cm^{-1} and 2.3 cm^{-1}. These have not been plotted as they are so much larger than the Ritz wavenumber uncertainties.

linelist published by Corliss & Sugar (1982) [87]. These lines belong to transitions involving the 3d^5 4d, 3d^5 5s and 3d^5 5d configurations. The linelist provided by Corliss & Sugar is a compilation of the previously published linelists by Glad (1955) [86] and Edlén & Swings (1942) [57]. The lines in this region were obtained from Glad (1955) [86] which states uncertainties between 0.02 Å and 0.05 Å for the lines shown in Figure 4.11, which correspond to the uncertainties between 0.8 cm^{-1} and 2.3 cm^{-1}. These uncertainty values dwarf the uncertainties determined in this work, and so are not shown in Figure 4.11. The Ritz wavenumber uncertainties for the lines shown in Figure 4.11 range from 0.036 cm^{-1} to 0.12 cm^{-1}. The Ritz wavenumbers for the transitions involving the 3d^5 4d, 3d^5 5s and 3d^5 5d configurations have had at least an order of magnitude improvement in accuracies.

4.3.3 Ritz Wavenumbers of Parity-Forbidden Fe III Lines

The wavenumbers of parity-forbidden transitions are essential for the study of dilute astrophysical plasmas. As mentioned in Section 4.1.3, these can only be determined with the required accuracy by energy levels determined via term analysis. Using the revised energy level values, Ritz wavenumbers for parity-forbidden transitions between the 3d^6 and 3d^5 4s configurations in Fe III have been calculated.

The selection rules for magnetic dipole (M1) and electric quadrupole (E2) transitions are different to the electric dipole radiation rules stated in Section 4.1.3 and are listed in Table 4.1. Using the revised energy levels and the selection rules in Table 4.1, 432 Ritz wavenumbers and uncertainties for parity-forbidden transitions have been calculated. The program *LOPT* was used to calculate these values and so, as mentioned earlier, the

Radiation Type	Parity Change?	ΔJ Restrictions	
Electric dipole (E1)	Yes	$0, \pm 1$	$0 \not\leftrightarrow 0$
Magnetic dipole (M1)	No	$0, \pm 1$	$0 \not\leftrightarrow 0$
Electric quadrupole (E2)	No	$0, \pm 1, \pm 2$	$0 \not\leftrightarrow 0, 1$; $\frac{1}{2} \not\leftrightarrow \frac{1}{2}$

Table 4.1: Selection rules for magnetic dipole (M1) and electric quadrupole (E2) transitions.

global calibration uncertainty of the Fe II data used for Fe III linelist calibration must be reintroduced to these lines. The Ritz wavenumber uncertainties were increased by 4 parts in 10^8 to provide the accurate Ritz wavenumber uncertainty. This corresponds to a contribution of 0.002 cm^{-1} to the Ritz wavenumber uncertainty for a line at 50,000 cm^{-1}.

The calculated parity-forbidden transitions are listed in Appendix D. The columns in the table are the Ritz wavenumbers, Ritz wavenumber uncertainties, energy levels of the transitions and the type of radiation. The Ritz wavenumbers are between 302 cm^{-1} and 113,939 cm^{-1} (878 Å and 330,360 Å) and 92% of the calculated parity-forbidden lines have a Ritz wavenumber uncertainty less than 0.35 cm^{-1}. As these levels are between the 3d^6 and 3d^5 4s configurations, these uncertainties will be reduced with the addition of transitions to the 3d^6 energy levels by the extension of the linelist that is planned for future work (Section 5.3.1.2).

4.3.4 Reassignment of the Energy Level Labels

For some energy levels, the label assigned by Ekberg (1993) [88] was not consistent with the transitions observed. In these cases, the label assigned to this level was reviewed and re-assigned using the calculations of Kurucz [119] as a guide. For example, the level at $118,246.65$ cm^{-1} was assigned the label 3d^5 (^{4}P) 4p ^{5}P$_3$ by Ekberg. However, the strongest transitions to this level were from levels with the parent term ^{4}G and with the multiplicity $M = 3$. Kurucz' calculation stated that the eigenvector component with the highest percentage (75%) was (^{4}G) 4p ^{3}F$_3$ for this value, and so this level was reassigned to this label. Table 4.2 states the 12 levels with a change of label in this work.

4.3.5 Summary

The term analysis method and results for Fe III have been detailed in this section. This PhD thesis presents the first term analysis of Fe III using high resolution FTS data. 959 classified spectral lines, of which 239 were FTS-measured, were used to revise 305 energy levels. The levels are listed and compared to the previously published levels. As a result of this term analysis, 12 energy level labels have been re-assigned. The Ritz wavenumbers and uncertainties for 1599 classified spectral lines have been listed and compared where possible to the linelist published by Ekberg (1993) [88]. No uncertainty comparisons could be made with the linelist previously published by Corliss & Sugar (1982) [87] as they did not provide line uncertainties. This research presents wavenumbers with an

Energy (cm^{-1})	Previous Label	New Label
116898.3731	(^{4}G) 4p $^5F_2$	(^{4}P) 4p $^5S_2$
116975.200	(^{4}P) 4p $^5S_2$	(^{4}G) 4p $^5F_2$
118246.6473	(^{4}P) 4p $^5P_3$	(^{4}G) 4p $^3F_3$
118443.111	(^{4}G) 4p $^3F_3$	(^{4}P) 4p $^5P_3$
122628.395	(^{4}D) 4p $^5D_2$	(^{4}P) 4p $^3D_2$
122843.179	(^{4}D) 4p $^5D_1$	(^{4}P) 4p $^3D_1$
122898.717	(^{4}P) 4p $^3D_2$	(^{4}D) 4p $^5D_2$
122921.561	(^{4}P) 4p $^3D_1$	(^{4}D) 4p $^5D_1$
136236.080	(a^{2}F) 4p $^3D_1$	(^{4}F) 4p $^5F_1$
136464.706	(^{4}F) 4p $^5F_1$	(a^{2}F) 4p $^3D_1$
136532.189	(a^{2}F) 4p $^3D_2$	(a^{2}F) 4p $^3F_2$
136793.71	(a^{2}F) 4p $^3F_2$	(a^{2}F) 4p $^3D_2$

Table 4.2: New level labels for Fe III energy levels using the intensities of observed transitions and the transition probabilities calculated by Kurucz [119].

increase in accuracy of up to two magnitude over the Ekberg (1993) [88] linelist.

The Ritz wavenumbers of 432 parity-forbidden lines calculated using the newly-revised energy levels are also presented here.

Chapter 5

Conclusions and Future Work

In this PhD thesis, an extensive classified linelist of FTS-measured Fe III lines in the UV range of $33,826$ cm^{-1} to $65,508$ cm^{-1} (1526.5 Å to 2956.3 Å) is reported for the first time. These lines are at least an order-of magnitude improvement in accuracy over previous measurements. These, paired with grating-measured Fe III lines in the UV, are used to revise many of the Fe III energy level values and labels reported by Ekberg (1993) [88] and Corliss & Sugar (1982) [87]. The uncertainties of the energy levels with respect to the ground level are similar to the previously published levels, due to the lack of observed spectral lines to the ground term. However, the derived energy level uncertainties relative to any other level in the system (excluding the ground term) have been greatly reduced in comparison to previous results. This results in a substantial increase in accuracy of the Fe III Ritz wavenumbers in comparison to the previously published Fe III linelist. While this is a significant improvement over previous Fe III data, further improvement is planned which will be discussed in this chapter.

5.1 New Classified Linelists for Fe III

The Fe III spectrum was recorded on the IC VUV FTS with the Penning discharge lamp, producing the most accurate Fe III linelist to date. The spectrum was intensity calibrated using a standard deuterium lamp and wavenumber calibrated using the accurate Ritz wavenumbers for Fe II published by Nave & Johansson (2013) [1]. The final FTS linelist contains 4623 unique spectral lines from $33,826$ cm^{-1} to $65,508$ cm^{-1} (1526.5 Å to 2956.3 Å). In total 537 of the observed FTS spectral lines were identified as Fe III. Of these, 239 lines were suitable for the level optimisation process and used in the term analysis. The remaining 298 lines were deemed unreliable for use in the term analysis, due to being doubly-identified or misshapen due to line blending or poor signal-to-noise ratios. The remaining lines in the observed FTS linelist were identified as belonging to Fe I, Fe II or Ne II, or were unidentified.

The linelist was compared to the most recently published Fe III data created by Ekberg (1993) [88] using grating data. The linelist overlapped in the range $47,500$ cm^{-1} to $55,000$ cm^{-1}, where a consistent small shift was found in the wavenumbers between the new FTS data and the lines published by Ekberg. The mean shift was 0.043 cm^{-1} which

was well within the Ekberg's grating uncertainties.

The FTS data were supplemented with grating spectra recorded on the NIST NIVS with the Penning discharge lamp by Belmonte in 2019. The grating spectrum was wavelength calibrated using the accurate Ritz wavenumbers for Fe II published by Nave & Johansson (2013) [1] and was not intensity calibrated. The final grating linelist contains 6626 unique lines from $55,090$ cm^{-1} to $111,121$ cm^{-1} (899.9 Å to 1815.2 Å). In total, 1062 of the observed grating lines were classified as Fe III, of which 720 were found to be suitable for use in the level optimisation process. The remaining lines were problematic, typically due to multiple-identifications or heavy blends in the recorded spectra. The remaining lines in the observed grating linelist were identified as belonging to Fe I, Fe II, Fe IV, Fe V, Ne I, Ne II and Ne III, or were left unidentified.

The wavenumbers of this grating linelist were also compared to the Fe III wavenumbers published by Ekberg. The linelist overlapped in two regions, from $55,700$ cm^{-1} to $71,800$ cm^{-1} (1393 Å to 1795 Å) and from $82,200$ cm^{-1} to $111,100$ cm^{-1} (900 Å to 1217 Å). For the region $55,700$ cm^{-1} to $71,800$ cm^{-1}, there was a small shift of -0.015 cm^{-1} between the wavenumbers of the grating lines determined in this work and the wavenumbers published by Ekberg, which are well within the grating uncertainties. In the region $82,200$ cm^{-1} to $111,100$ cm^{-1}, a mean shift of $\Delta\sigma = -0.359$ cm^{-1} was found between the wavenumbers of this grating linelist and the wavenumbers published by Ekberg. A linear shift of $\Delta\sigma = -0.6$ cm^{-1} in the range $97,200$ cm^{-1} to $108,100$ cm^{-1} (925 Å to 1029 Å) and the presence of curves in $\Delta\sigma$ for the remainder of the region was likely due to incorrectly calibrated detector plates by Ekberg.

5.2 Revised Energy Levels for Fe III

In this PhD project, the term analysis of Fe III revised 305 known energy levels. The revised energy levels were compared to the energy level values determined in previous publications. A mean shift of 0.12 cm^{-1} and 0.18 cm^{-1} was found between the revised energy levels and the levels published by Ekberg (1993) [88] and Corliss & Sugar (1982) [87], respectively.

The system of energy levels is anchored to the ground level via only two resonance lines, of which one was saturated. For this reason, the revised energy levels have high uncertainties with respect to the ground level, comparable to the energy level uncertainties of the data published by Ekberg. However, using the new accurate FTS data, the uncertainties of the energy levels relative to the level system as a whole have been vastly improved. This results in the production of high accuracy Ritz wavenumbers for Fe III. The energy level labels assigned by Ekberg were also reviewed and 12 energy level label changes were made using Kurucz' [119] calculations as a guide.

Using the revised energy level values, new accurate Fe III Ritz wavenumbers for parity-forbidden transitions are also reported for 432 transitions between the $3d^6$ and $3d^5$ 4s configurations. These forbidden lines cannot be directly measured in a laboratory setting and are observed only in low density astrophysical spectra. The wavenumbers of

the forbidden lines reported in this PhD project can be used by astronomers to identify the presence of Fe III and its transitions.

5.3 Future Work

5.3.1 Continuation of the Term Analysis of Fe III

To improve and expand on the data produced in this PhD project, the spectral linelists should be extended. This will provide more lines to increase the accuracy of the levels in the system. Levels not included were usually omitted due to the lack of observed suitable spectral lines. Energy levels must have multiple, reliable transitions to be included in the level optimisation process to confirm they are not spurious levels.

By including more transitions, in general, the accuracy of the levels present in the system will be increased. In addition, by including more energy levels in the system there are more transitions observed for each level, which in turn increases the accuracy of the energy levels. For example, the levels with ^{2}P and c^{2}D parent terms that had no observed transitions could be included with the observation of additional lines. Kurucz predicts these levels will have observed transitions to levels 3d^5 (^{4}G) 5p, 3d^5 (^{4}D) 5p, 3d^5 (^{4}P) 5p and 3d^5 (^{4}F) 5p due to level mixing within the wavenumber region of the linelists made in this project. Therefore, these levels may be connected with the addition of 5p levels in future work.

The uncertainties of all the revised energy levels with respect to the ground are high due to the observation of only two resonance lines with high uncertainties connecting to the ground level. The energy level uncertainties of the whole system can be improved by including the remaining resonance lines of varying strengths that lie between $113,677$ cm^{-1} and $141,001$ cm^{-1}. Ekberg (1993) [88] observed 32 resonance lines in this spectral region. The extension of the grating linelist to include these transitions is discussed below.

5.3.1.1 Extension of the FTS linelist

As mentioned in Section 1.2.1, Pickering recorded the Fe III spectrum in the IR and visible regions (σ <28,000 cm^{-1}, $\lambda > 3571$ Å) using the FTS at NIST. A linelist created from these data can be used to extend the FTS linelist using the same methodology stated in Section 3.1. The transitions between the higher-lying levels lie in this spectral region, including the transitions 4d to 5p, 4f to 5g, 5s to 5p, and 5p to 5d or 6s. For the ^{6}S parent term in particular, the transitions 5d to 5f, 5f to 6g, 5g to 6h, and 6p to 6d will also be observed. The extension of the linelist will enable the revision of these higher-lying Fe III energy levels.

5.3.1.2 Extension of the grating linelist

Belmonte recorded the grating spectrum of Fe III from ∼28,000 cm^{-1} to 190,000 cm^{-1} (525 Å to 3520 Å). However, the wavenumber calibration of the grating linelist in this

work relied on the Fe II Ritz wavenumbers published by Nave & Johansson (2013) [1]. As observed Fe II wavenumbers were only available in the range $2,009$ cm^{-1} to $111,122$ cm^{-1} (900 Å to $49,777$ Å), the grating linelist in this work was limited to the upper wavenumber limit of $111,121$ cm^{-1} (899.916 Å).

The lower wavenumber limit of the grating linelist can be extended to $\sim 28,000$ cm^{-1} (~ 3571 Å) using the Fe II lines for calibration and the same methodology stated Section 3.2. This would provide additional grating data of the Fe III spectrum from $28,000$ cm^{-1} to $55,090$ cm^{-1} (1815 Å to 3571 Å) . Although these lines would not be of higher accuracy than the FTS data in that region, this linelist would provide data on the weaker spectral lines which may be key in the term analysis, such as the transitions between the higher-lying 4s levels and lower-lying 4p levels. This spectral range will also provide data for the 4d to 4f transitions in the ^{6}S parent term system.

As Nave & Johansson did not observe the Fe II spectrum for $\sigma > 111,122$ cm^{-1} ($\lambda < 899.9$ Å), the Ritz wavenumbers of the lines used for calibration can be calculated using the Fe II energy levels published by Nave & Johansson and the program *STRANS*. Kurucz [119] has also calculated transition wavenumbers and transition probabilities using the published Fe II energy levels (up to $132,149$ cm^{-1}) which can be used as a guide to confirm the validity of the Fe II Ritz wavenumbers calculated by *STRANS*. Once the legitimate Fe II lines have been identified, the lines can be used to calibrate the grating spectrum using the same methodology stated in Section 3.2.4. An alternative method of identifying calibration lines at $\sigma > 111,122$ cm^{-1} is to derive Fe III Ritz wavelengths from the Fe III energy levels revised in this work. These lines, paired with the Kurucz calculations of transition wavenumbers and transition probabilities, can be used to calibrate the remaining grating linelist at $\sigma > 111,122$ cm^{-1} with the methodology stated in Section 3.2.4.

Another method to obtain the Fe III spectrum in the spectral region $\sigma > 111,122$ cm^{-1} ($\lambda < 899.9$ Å) is to re-calibrate the classified linelist published by Ekberg (1993) [88] from $48,000$ cm^{-1} to $200,000$ cm^{-1} (500 Å to 2105 Å) using the accurate Ritz wavenumbers calculated from the energy levels revised in this PhD project. A disadvantage to this is that there are weak Fe III spectral lines that were observed in the grating linelist created in this PhD project but not classified by Ekberg. Ekberg also only classified transitions between the levels 3d^6, 4s and 4p, and so any lines in this spectral region corresponding to a transition to other levels will not be listed. Therefore, by using the linelist classified by Ekberg, there may be unlisted spectral lines, which is particularly important for identifying transitions to energy levels that Ekberg could not identify. Another factor to consider is the differences in the uncertainties: Ekberg estimated a minimum uncertainty of 0.005 Å for the spectral lines, while the grating linelist made in this PhD project had uncertainties of 0.003 Å or 0.007 Å. It is likely that by creating the linelist in the range $\sigma > 111,122$ cm^{-1} using the data recorded by Belmonte, the spectral lines will have a reduced uncertainty in comparison to the linelist made by Ekberg.

5.3.1.3 Revision of the Remaining Levels and New Level Search

In the FTS and grating linelists, 3186 and 5295 observed spectral lines remained unidentified, respectively. With identification and classification of these remaining spectral lines and the additional spectral lines from the extended FTS and grating linelists, the term analysis process can be continued. The levels currently included in the energy level system will be more accurately determined with the addition of spectral lines. This is especially important to confirm the validity of the energy levels with few or no reliable transitions. The addition of the resonance lines in particular will contribute to the anchoring the energy level system to the ground level and will therefore increase the accuracy of all the energy levels with respect to the ground level.

The remaining energy levels determined by Ekberg (1993) [88] (4s and 4p levels) and Corliss & Sugar (1982) [87] (higher-lying levels) can also be revised and there can be a search for new energy levels. Kurucz [119] has calculated values for previously published energy levels and theoretical energy levels which will be used as a guide in the search and identification of the new energy levels.

5.3.2 Transition Probabilities of Parity-forbidden Fe III lines

Once the term analysis has been completed, the Ritz wavelengths of the parity-forbidden Fe III transitions can be re-calculated with the new and revised accurate levels. These can be compared to previous publications of Fe III parity-forbidden lines that have been determined using astronomical spectra, including the works by Jordan *et al.* (1986) [123] (21 lines, 1452 Å to 1575 Å), McKenna *et al.* (1997) [124] (11 lines, 4658 Å to 4930 Å) and Johansson *et al.* (2000) [125] (5 lines, 2438 Å to 2501 Å).

In addition to this, the transition probabilities can be calculated for these parity-forbidden lines using data provided by Kurucz [119], as was done by Ruffoni & Pickering (2013) [126] for Co II and V II. These data will aid astronomers further in the analysis of spectra from dilute astrophysical plasmas.

5.3.3 Further Investigation of Fe II Lines and Energy Levels

A brief investigation of the Ritz wavenumbers produced by *STRANS* with the Fe II energy levels published by Nave & Johansson (2013) [1] concluded that there are Fe II lines observed in the FTS linelist created in this PhD work that Nave & Johansson did not observe in their study of the Fe II spectrum. This is likely due to the vastly different plasma conditions between the PDL used in this project and the HCL used by Nave & Johansson. For this reason, the linelists created in this work will be examined for Fe II lines that Nave & Johansson did not observe. The proposed newly-observed transitions can be confirmed using Kurucz's calculations of Fe II transition wavenumbers and transition probabilities, as was done by Castelli & Kurucz (2010) [127]. These newly-observed transitions would be a useful resource in the identification of Fe II lines in stellar spectra.

As stated in Section 3.1.4, a shift between the observed and expected Fe II wavenumbers was observed for transitions with an upper energy level $> 55,000$ cm^{-1}. This could be,

again, due to the differences in the plasma conditions. This correlation should be more closely investigated throughout the linelists created using the PDL.

5.4 Conclusion

This PhD presented the spectrum and term analysis of Fe III which provides astronomers with the most accurate UV-VUV linelist of Fe III Ritz wavenumbers to date. These Fe III line wavenumbers can be used for the calibration of VUV spectra of hot stars and for the identification and analysis of Fe III spectral lines in astrophysical objects.

References

[1] G. Nave and S. Johansson, "The Spectrum of Fe II," *ApJS*, vol. 204, p. 1, 2013.

[2] J. F. Atkins and P. V. Baranov, "Nailing fingerprints in the stars," *Nature*, vol. 503, iss. 7477, p. 437, 2013.

[3] T. S. Barman, Q. M. Konopacky, B. Macintosh, *et al.*, "Simultaneous Detection of Water, Methane, and Carbon Monoxide in the Atmosphere of Exoplanet HR8799b," *ApJ*, vol. 804, iss. 1, p. 61, 2015.

[4] J. C. Pickering, M. T. Belmonte, C. P. Clear, *et al.*, "Recent advances in experimental laboratory astrophysics for stellar astrophysics applications and future data needs," in *Laboratory Astrophysics: From Observations to Interpretation*, vol. 350, p. 220, 2020.

[5] D. Branton, A. Riley, and *et al.*, *STIS Instrument Handbook*. Version 20.0, (Baltimore: STScI), 2021.

[6] S. S. Vogt, S. L. Allen, B. C. Bigelow, *et al.*, "HIRES: the high-resolution echelle spectrometer on the Keck 10-m Telescope," in *Instrumentation in Astronomy VIII*, D. L. Crawford and E. R. Craine, Eds., ser. Society of Photo-Optical Instrumentation Engineers (SPIE) Conference Series, vol. 2198, p. 362, 1994.

[7] H.-U. Kaeufl, P. Ballester, P. Biereichel, *et al.*, "CRIRES: a high-resolution infrared spectrograph for ESO's VLT," in *Ground-based Instrumentation for Astronomy*, A. F. M. Moorwood and M. Iye, Eds., ser. Society of Photo-Optical Instrumentation Engineers (SPIE) Conference Series, vol. 5492, p. 1218, 2004.

[8] G. Dalton, S. Trager, D. C. Abrams, *et al.*, "Final design and progress of WEAVE: the next generation wide-field spectroscopy facility for the William Herschel Telescope," in *Ground-based and Airborne Instrumentation for Astronomy VI*, C. J. Evans, L. Simard, and H. Takami, Eds., ser. Society of Photo-Optical Instrumentation Engineers (SPIE) Conference Series, vol. 9908, 99081G, 2016.

[9] R. S. de Jong, 4MOST Consortium, and 4MOST Spectroscopy Consortium, "Complementing asteroseismology with 4MOST spectroscopy," *Astronomische Nachrichten*, vol. 337, iss. 8-9, p. 964, 2016.

[10] P. Ferruit, P. Jakobsen, G. Giardino, *et al.*, "The Near-Infrared Spectrograph (NIRSpec) on the James Webb Space Telescope. II. Multi-object spectroscopy (MOS)," *A&A*, vol. 661, A81, 2022.

[11] S. R. Majewski, R. P. Schiavon, P. M. Frinchaboy, *et al.*, "The Apache Point Observatory Galactic Evolution Experiment (APOGEE)," *AJ*, vol. 154, iss. 3, p. 94, 2017.

[12] G. Gilmore, S. Randich, M. Asplund, *et al.*, "The Gaia-ESO Public Spectroscopic Survey," *The Messenger*, vol. 147, p. 25, 2012.

[13] S. L. Martell, S. Sharma, S. Buder, *et al.*, "The GALAH survey: observational overview and Gaia DR1 companion," *MNRAS*, vol. 465, iss. 3, p. 3203, 2017.

[14] D. S. Leckrone, S. Johansson, G. M. Wahlgren, *et al.*, "High resolution UV stellar spectroscopy with the HST/GHRS, challenges and opportunities for atomic physics," *Physica Scripta*, vol. T47, p. 149, 1993.

[15] K. G. Carpenter and T. R. Ayres, "The HST Treasury "Advanced Spectral Library" (ASTRAL) Programs," G. T. van Belle and H. C. Harris, Eds., ser. Cambridge Workshop on Cool Stars, Stellar Systems, and the Sun, vol. 18, p. 1041, 2015.

[16] K. E. Nielsen, K. G. Carpenter, G. V. Kober, *et al.*, "The Advanced Spectral Library (ASTRAL): Abundance Analysis of the Chemically Peculiar Star HR 465," *ApJ*, vol. 899, iss. 2, p. 166, 2020.

[17] T. R. Ayres, "HST/STIS Advanced Spectral Library (ASTRAL)," in *Astronomical Society of India Conference Series*, vol. 11, 2014.

[18] B. S. Gaudi, S. Seager, B. Mennesson, *et al.*, "The Habitable Exoplanet Observatory (HabEx) Mission Concept Study Final Report," *arXiv e-prints*, arXiv:2001.06683, 2020.

[19] The LUVOIR Team, "The LUVOIR Mission Concept Study Final Report," *arXiv e-prints*, arXiv:1912.06219, 2019.

[20] M. T. Belmonte, J. C. Pickering, C. P. Clear, *et al.*, "The Laboratory Astrophysics Spectroscopy Programme at Imperial College London," *Galaxies*, vol. 6, iss. 4, 2018.

[21] M. Bergemann, "Role of input atomic data in spectroscopic analyses of the sun and metal-poor stars," *ArXiv:1104.1640*, Uncertainties in Atomic Data and How They Propagate in Chemical Abundances, 2011.

[22] S. J. Smartt, T. .-W. Chen, A. Jerkstrand, *et al.*, "A kilonova as the electromagnetic counterpart to a gravitational-wave source," *Nature*, vol. 551, iss. 7678, p. 75, 2017.

[23] U. Heiter, K. Lind, M. Bergemann, *et al.*, "Atomic data for the Gaia-ESO Survey," *A&A*, vol. 645, A106, 2021.

[24] M. Asplund, N. Grevesse, A. J. Sauval, *et al.*, "The Chemical Composition of the Sun," *ARA&A*, vol. 47, iss. 1, p. 481, 2009.

[25] N. Grevesse, M. Asplund, A. J. Sauval, *et al.*, "The chemical composition of the Sun," *Astrophysics and Space Science*, vol. 328, iss. 1, pp. 179–183, 2010.

[26] P. Scott, M. Asplund, N. Grevesse, *et al.*, "The elemental composition of the Sun. II. The iron group elements Sc to Ni," *A&A*, vol. 573, A26, 2015.

[27] M. P. Wood, C. Sneden, J. E. Lawler, *et al.*, "Vanadium Transitions in the Spectrum of Arcturus," *ApJS*, vol. 234, p. 25, 2018.

[28] P. Foukal, *Solar Astrophysics*, 2nd edition. Wiley, p. 69, 2004.

[29] J. R. Kitamura, L. P. Martins, and P. Coelho, "A study on missing lines in the synthetic solar spectrum near the Ca triplet," *A&A*, vol. 600, A58, 2017.

[30] D. Kasen, B. Metzger, J. Barnes, *et al.*, "Origin of the heavy elements in binary neutron-star mergers from a gravitational-wave event," *Nature*, vol. 551, iss. 7678, p. 80, 2017.

[31] S. Goriely and G. Martínez Pinedo, "The production of transuranium elements by the r-process nucleosynthesis," *Nuclear Physics A*, vol. 944, p. 158, 2015.

[32] D. Watson, C. J. Hansen, J. Selsing, *et al.*, "Identification of strontium in the merger of two neutron stars," *Nature*, vol. 574, iss. 7779, p. 497, 2019.

[33] S. Johansson, "Atomic Data for Astrophysics — Parameters Precision, Priorities," in *Precision Spectroscopy in Astrophysics*, N. C. Santos, L. Pasquini, A. C. M. Correia, *et al.*, Eds., p. 123, 2008.

[34] J. C. Pickering, "High resolution Fourier transform spectroscopy with the Imperial College (IC) UV-FT spectrometer, and its applications to astrophysics and atmospheric physics: A review," *Vibrational Spectroscopy*, vol. 29, iss. 1-2, p. 27, 2002.

[35] D. S. Leckrone, S. Johansson, G. M. Wahlgren, *et al.*, "Stellar chemical abundances with the GHRS.," *Physica Scripta Volume T*, vol. 65, p. 110, 1996.

[36] C. Allende Prieto, D. L. Lambert, and M. Asplund, "The Forbidden Abundance of Oxygen in the Sun," *ApJL*, vol. 556, iss. 1, p. L63, 2001.

[37] S. Johansson, U. Litzén, H. Lundberg, *et al.*, "Experimental f-Value and Isotopic Structure for the Ni I Line Blended with [O I] at 6300 Å," *ApJL*, vol. 584, iss. 2, p. L107, 2003.

[38] R. Smith, J.-M. Li, A. Müller, *et al.*, "Special issue on atomic and molecular data for astrophysics," *Journal of Physics B Atomic Molecular Physics*, vol. 50, iss. 6, p. 060 201, 2017.

[39] M. Laverick, A. Lobel, T. Merle, *et al.*, "The Belgian repository of fundamental atomic data and stellar spectra (BRASS). I. Cross-matching atomic databases of astrophysical interest," *A&A*, vol. 612, A60, 2018.

[40] G. Del Zanna, K. P. Dere, P. R. Young, *et al.*, "CHIANTI—An Atomic Database for Emission Lines. XVI. Version 10, Further Extensions," *ApJ*, vol. 909, iss. 1, p. 38, 2021.

[41] A. Kramida, Y. Ralchenko, J. Reader, *et al.*, *Nist atomic spectra database (version 5.8), [online]*, Available: https://physics.nist.gov/asd [2021]. National Institute of Standards and Technology, Gaithersburg, MD.

[42] R. Kurucz and B. Bell, "Atomic Line Data," *Atomic Line Data (R.L. Kurucz and B. Bell) Kurucz CD-ROM No. 23. Cambridge*, vol. 23, 1995.

[43] T. Ryabchikova, N. Piskunov, R. L. Kurucz, *et al.*, "A major upgrade of the VALD database," *Phys. Scr.*, vol. 90, iss. 5, p. 054 005, 2015.

[44] M. L. Dubernet, B. K. Antony, Y. A. Ba, *et al.*, "The virtual atomic and molecular data centre (VAMDC) consortium," *Journal of Physics B Atomic Molecular Physics*, vol. 49, iss. 7, p. 074 003, 2016.

[45] W. E. Kerzendorf and S. A. Sim, "A spectral synthesis code for rapid modelling of supernovae," *MNRAS*, vol. 440, iss. 1, p. 387, 2014.

[46] J. H. Gillanders, M. McCann, S. Sim, *et al.*, "Constraints on the presence of platinum and gold in the spectra of the kilonova at2017gfo," *MNRAS*, vol. 506, iss. 3, p. 3560, 2021.

[47] M. P. Fewell, "The atomic nuclide with the highest mean binding energy," *American Journal of Physics*, vol. 63, p. 653, 1995.

[48] Einstein Online, *Atomic data from the atomic mass data center, [online]*, Available: https://web.archive.org/web/20060309210852/http://www.einstein-online.info/en/spotlights/binding_energy/binding_energy/index.txt [2006].

[49] K. Lodders, "Solar elemental abundances," in *Oxford Research Encyclopedia of Planetary Science*, Oxford University Press, 2020.

[50] J. Wheeler, *Cosmic Catastrophes: Exploding Stars, Black Holes, and Mapping the Universe*. Cambridge University Press, 2007.

[51] A. Thorne, U. Litzén, and S. Johansson, *Spectrophysics: Principles and Applications*. Springer Berlin Heidelberg, 1999.

[52] N. Grevesse and A. J. Sauval, "The solar abundance of iron and the photospheric model," *A&A*, vol. 347, p. 348, 1999.

[53] G. Nave, C. J. Sansonetti, J. C. Pickering, *et al.*, "Atomic data for iron-group elements of astrophysical interest," in *AIP Conference Proceedings*, vol. 1545, p. 27, 2013.

[54] T. Spohn, D. Breuer, and T. Johnson, *Encyclopedia of the Solar System*. Elsevier Science, 2014.

[55] C. Jaschek and M. Jaschek, *The Behavior of Chemical Elements in Stars*. Cambridge University Press, 1995.

[56] K. G. Carpenter, R. F. Wing, and R. E. Stencel, "Line identifications, line strengths, and continuum flux measurements in the ultraviolet spectrum of Arcturus," *ApJS*, vol. 57, p. 405, 1985.

[57] B. Edlén and P. Swings, "Term Analysis of the Third Spectrum of Iron (Fe III).," *ApJ*, vol. 95, p. 532, 1942.

[58] D. S. Leckrone, C. R. Proffitt, G. M. Wahlgren, *et al.*, "Very High Resolution Ultraviolet Spectroscopy of a Chemically Peculiar Star: Results of the χ LUPI Pathfinder Project," *AJ*, vol. 117, iss. 3, p. 1454, 1999.

[59] F. Liggins, "The spectrum and term analysis of singly-ionised manganese," PhD Thesis, Imperial College London, 2017.

[60] Mazzotta, P., Mazzitelli, G., Colafrancesco, S., *et al.*, "Ionization balance for optically thin plasmas: Rate coefficients for all atoms and ions of the elements H to Ni," *A&AS*, vol. 133, iss. 3, p. 403, 1998.

[61] J. C. Pickering, R. Blackwell-Whitehead, A. P. Thorne, *et al.*, "Laboratory measurements of oscillator strengths and their astrophysical applications," *Canadian Journal of Physics*, vol. 89, iss. 4, p. 387, 2011.

[62] K. M. Leighly, J. P. Halpern, E. B. Jenkins, *et al.*, "The Intrinsically X-Ray-weak Quasar PHL 1811. II. Optical and UV Spectra and Analysis," *ApJS*, vol. 173, iss. 1, p. 1, 2007.

[63] C. Esteban, M. Peimbert, J. García-Rojas, *et al.*, "A reappraisal of the chemical composition of the Orion nebula based on Very Large Telescope echelle spectrophotometry," *MNRAS*, vol. 355, iss. 1, p. 229, 2004.

[64] S. Laha, N. B. Tyndall, F. P. Keenan, *et al.*, "Emission Line Ratios of Fe III as Astrophysical Plasma Diagnostics," *ApJ*, vol. 841, iss. 1, p. 3, 2017.

[65] K. D. Wilk, D. J. Hillier, and L. Dessart, "Ejecta mass diagnostics of Type Ia supernovae," *MNRAS*, vol. 474, p. 3187, 2018.

[66] S. Woosley and T. Janka, "The physics of core-collapse supernovae," *Nature Physics*, vol. 1, p. 147, 2005.

[67] D. L. Miller and P. Pinto, "Synthetic spectra and lightcurves of supernovae – the black hole of atomic physics needs," *Physica Scripta*, vol. 1999, iss. T83, p. 125, 1999.

[68] M. J. Temple, G. J. Ferland, A. L. Rankine, *et al.*, "Fe III emission in quasars: evidence for a dense turbulent medium," *MNRAS*, vol. 496, iss. 3, p. 2565, 2020.

[69] C. M. Cassidy, C. A. Ramsbottom, M. P. Scott, *et al.*, "Electron-impact excitation of Fe-peak ions for astrophysical applications," in *Journal of Physics Conference Series*, ser. Journal of Physics Conference Series, vol. 194, p. 012 019, 2009.

[70] P. Quinet, "Transition probabilities for forbidden lines of Fe III.," *A&AS*, vol. 116, p. 573, 1996.

[71] S. N. Nahar and A. K. Pradhan, "Atomic data from the Iron Project. XVII. Radiative transition probabilities for dipole allowed and forbidden transitions in Fe III.," *A&AS*, vol. 119, p. 509, 1996.

[72] T. Ryabchikova, Personal Communication, 2018.

[73] M. J. Seaton, "New Atomic Data for Astronomy: an Introductory Review," in *Astrophysical Applications of Powerful New Databases*, S. J. Adelman and W. L. Wiese, Eds., ser. Astronomical Society of the Pacific Conference Series, vol. 78, p. 1, 1995.

[74] R. L. Kurucz, "Atomic and Molecular Data Needs for Astrophysics," in *Atomic and Molecular Data and Their Applications*, D. R. Schultz, P. S. Krstic, and F. Ownby, Eds., ser. American Institute of Physics Conference Series, vol. 636, p. 134, 2002.

[75] G. M. Wahlgren, "Atomic data for stellar astrophysics: from the UV to the IR.," *Canadian Journal of Physics*, vol. 89, iss. 4, p. 345, 2011.

[76] R. J. Blackwell-Whitehead, A. Toner, A. Hibbert, *et al.*, "Hyperfine structure of the ground state in singly ionized manganese," *MNRAS*, vol. 364, p. 705, 2005.

[77] R. J. Blackwell-Whitehead, J. C. Pickering, O. Pearse, *et al.*, "Hyperfine Structure Measurements of Neutral Manganese with Fourier Transform Spectroscopy," *ApJS*, vol. 157, p. 402, 2005.

[78] M. Ding and J. C. Pickering, "Measurements of the Hyperfine Structure of Atomic Energy Levels in Co II," *ApJS*, vol. 251, iss. 2, p. 24, 2020.

[79] F. S. Liggins, J. C. Pickering, G. Nave, *et al.*, "The Spectrum and Term Analysis of Singly Ionized Manganese," *ApJS*, vol. 252, iss. 1, p. 10, 2021.

[80] F. S. Liggins, J. C. Pickering, G. Nave, *et al.*, "New Ritz Wavelengths and Transition Probabilities of Parity-forbidden [Mn II] Lines of Astrophysical Interest," *ApJ*, vol. 907, iss. 2, p. 69, 2021.

[81] A. P. Thorne, J. C. Pickering, and J. I. Semeniuk, "The Spectrum and Term Analysis of V II," *ApJS*, vol. 207, p. 13, 2013.

[82] A. P. Thorne, J. C. Pickering, and J. Semeniuk, "The Spectrum and Term Analysis of V I," *ApJS*, vol. 192, iss. 1, p. 11, 2011.

[83] D. G. Smillie, J. C. Pickering, G. Nave, *et al.*, "The Spectrum and Term Analysis of Co III Measured Using Fourier Transform and Grating Spectroscopy," *ApJS*, vol. 223, p. 12, 2016.

[84] D. G. Smillie, J. C. Pickering, and P. L. Smith, "Reference ultraviolet wavelengths of CrIII measured by Fourier transform spectrometry," *MNRAS*, vol. 390, iss. 2, p. 733, 2008.

[85] D. Smillie, "Fourier Transform and Grating Spectroscopy of Doubly Ionised Iron Group Elements and Astrophysical Applications," PhD Thesis, Imperial College London, 2007.

[86] S. Glad, "Extension of the analysis of the third spectrum of iron, FeIII," *Arkiv Fysik*, vol. 10, p. 291, 1955.

[87] C. Corliss and J. Sugar, "Energy Levels of Iron, Fe I Through Fe XXVI," *Journal of Physical and Chemical Reference Data*, vol. 11, iss. 1, p. 135, 1982.

[88] J. O. Ekberg, "Wavelengths and Transition Probabilities of the $3d^6 - 3d^5 4p$ and $3d^5 4s - 3d^5 4p$ Transition Arrays of Fe III," *A&AS*, vol. 101, p. 1, 1993.

[89] G. Nave, Personal Communication, 2018.

[90] S. P. Davis, M. C. Abrams, and J. W. Brault, *Fourier Transform Spectrometry*. Academic Press, 2001.

[91] G. Nave, U. Griesmann, J. W. Brault, *et al.*, *Xgremlin: Interferograms and spectra from Fourier transform spectrometers analysis*, Astrophysics Source Code Library, 2015.

[92] C. Clear, "The Spectrum and Term Analysis of Singly Ionised Nickel," PhD Thesis, Imperial College London, 2018.

[93] J. W. Brault, "New approach to high-precision Fourier transform spectrometer design," *AO*, vol. 35, iss. 16, p. 2891, 1996.

[94] A. Thorne, "Fourier transform spectrometry in the vacuum ultraviolet: Applications and progress," *Physica Scripta*, vol. T65, p. 31, 1996.

[95] M. Belmonte, Personal Communication, 2022.

[96] Jarrell-Ash Engineering, "10.7-Meter Vacuum Spectrograph," *Preliminary technical release EB-116, Jarrell-Ash Technical Bullitin*, 1964.

[97] G. Nave, C. J. Sansonetti, C. I. Szabo, *et al.*, "Use of phosphor image plates for measuring intensities in vacuum ultraviolet spectra," *Review of Scientific Instruments*, vol. 82, iss. 1, p. 013 107, 2011.

[98] J. Reader, C. J. Sansonetti, and R. D. Deslattes, "Image Plates for Registration of Far-Ultraviolet Spectra," *AO*, vol. 39, iss. 4, p. 637, 2000.

[99] M. Wyatt and G. Nave, "Evaluation of resolution and periodic errors of a flatbed scanner used for digitizing spectroscopic photographic plates," *Applied optics*, vol. 56, iss. 13, p. 3744, 2017.

[100] C. Heise, R. Kling, M. Kock, *et al.*, "Radiometric characterization of a Penning discharge in the vacuum ultraviolet," *Appl. Opt.*, vol. 33, p. 5111, 1994.

[101] D. S. Finley, P. Jelinsky, S. Bowyer, *et al.*, "A Penning discharge source for extreme ultraviolet calibration," in *X-ray calibration: Techniques, sources, and detectors*, ser. Society of Photo-Optical Instrumentation Engineers (SPIE) Conference Series, vol. 689, p. 6, 1986.

[102] Hamamatsu, *Hamamatsu head-on type photomultiplier tubes, [online]*, Available: https://www.hamamatsu.com/eu/en/product/optical-sensors/pmt/pmt_tube-alone/head-on-type.html [2022].

[103] Teledyne Acton Optics, *Teledyne Acton Optics Products: VUV/UV Narrowband Filters, [online]*, Available: https://www.actonoptics.com/products/filters-narrowband [2022].

[104] R. C. M. Learner, A. P. Thorne, I. Wynne-Jones, *et al.*, "Phase correction of emission line Fourier transform spectra," *Journal of the Optical Society of America A*, vol. 12, iss. 10, p. 2165, 1995.

[105] S. Svanberg, *Atomic and Molecular Spectroscopy: Basic Aspects and Practical Applications*, 4th, ser. Advanced Texts in Physics. Springer, 2004.

[106] B. Bransden and C. Joachain, *Physics of Atoms and Molecules*, 2nd edition. Pearson Education, 2010.

[107] M. Rosberg, U. Litzen, and S. Johansson, "Experimental isotopic shifts in Ni II and Fe II," *MNRAS*, vol. 262, iss. 1, pp. L1–L5, 1993.

[108] W. M. Haynes, *CRC Handbook of Chemistry and Physics, 96th Edition Part 0 - 10*, 96th ed., ser. CRC Handbook of Chemistry Physics. CRC Press, 2015.

[109] Crystran, *Magnesium fluoride (mgf2) data sheet, [online]*, Available: https://www.crystran.co.uk/optical-materials/magnesium-fluoride-mgf2 [2022].

[110] R. C. Learner, a. P. Thorne, and J. W. Brault, "Ghosts and artifacts in Fourier-transform spectrometry.," *Applied optics*, vol. 35, iss. 16, pp. 2947–2954, 1996.

[111] K. Haris and A. Kramida, "Critically Evaluated Spectral Data for Neutral Carbon (C I)," *ApJS*, vol. 233, iss. 1, p. 16, 2017.

[112] W. Whaling, W. H. C. Anderson, M. T. Carle, *et al.*, "Argon ion linelist and level energies in the hollow-cathode discharge.," *JQSRT*, vol. 53, iss. 1, pp. 1–22, 1995.

[113] J. C. Pickering and A. P. Thorne, "The Spectrum and Term Analysis of Co I," *ApJS*, vol. 107, p. 761, 1996.

[114] G. Nave, *ASPAS, [online]*, Available: https://github.com/gnave/ASPAS [2020].

[115] A. J. J. Raassen and S. O. Ortin, "Extension of the analysis of the three lowest configurations in the third spectrum of cobalt (Co III)," *Physica B+C*, vol. 123, iss. 3, p. 353, 1984.

[116] S. Johansson, "Term analysis of a complex spectrum," *Physica Scripta*, vol. 1996, iss. T65, p. 7, 1996.

[117] R. D. Cowan, *The theory of atomic structure and spectra*, ser. Los Alamos series in basic and applied sciences. Berkeley ; University of California Press, 1981.

[118] H. N. Russell and F. A. Saunders, "New Regularities in the Spectra of the Alkaline Earths," *ApJ*, vol. 61, p. 38, 1925.

[119] R. L. Kurucz, *Kurucz atomic linelists, [online]*, Available: http://kurucz.harvard.edu/linelists.html [2022].

[120] S. Johansson, "High Resolution Spectroscopy of Singly Ionized Transition Elements," in *Laboratory and Astronomical High Resolution Spectra*, ser. Astronomical Society of the Pacific Conference Series, vol. 81, p. 151, 1995.

[121] S. Johansson, "The laboratory spectrum and atomic structure of Fe II," in *IAU Colloq. 94: Physics of Formation of FE II Lines Outside LTE*, R. Viotti, A. Vittone, and M. Friedjung, Eds., ser. Astrophysics and Space Science Library, vol. 138, p. 13, 1988.

[122] A. E. Kramida, "The program LOPT for least-squares optimization of energy levels," *Computer Physics Communications*, vol. 182, iss. 2, p. 419, 2011.

[123] C. Jordan, J. .-D. F. Bartoe, G. E. Brueckner, *et al.*, "Identification of [Fe III] in the solar ultraviolet spectrum," *Nature*, vol. 324, iss. 6096, p. 444, 1986.

[124] F. C. McKenna, F. P. Keenan, N. C. Hambly, *et al.*, "The Optical Spectral Line List of RR Telescopii," *ApJS*, vol. 109, iss. 1, p. 225, 1997.

[125] S. Johansson, T. Zethson, H. Hartman, *et al.*, "New forbidden and fluorescent Fe III lines identified in HST spectra of eta Carinae," *A&A*, vol. 361, p. 977, 2000.

[126] M. P. Ruffoni and J. C. Pickering, "Accurate Ritz Wavelengths of Parity-forbidden Co II and V II Lines of Astrophysical Interest," *ApJS*, vol. 207, iss. 2, p. 20, 2013.

[127] F. Castelli and R. L. Kurucz, "New Fe II energy levels from stellar spectra," *A&A*, vol. 520, A57, 2010.

Appendices

A Energy Levels of Fe III

The revised energy levels for Fe III in this PhD project are presented in the tables below. The tables are separated by subshell: $3d^6$, 4s, 4p, and the remaining levels (4d, 5s and 5d). The table consists of seven columns:

Designation: The energy levels labels assigned using *LS* coupling.

J: The total angular momentum quantum number.

Energy: The energy level value in cm^{-1}.

E_{rev} - E_{prev} : The difference between the revised energy levels and the previously published levels in cm^{-1}. Previous values for the $3d^6$, 4s and 4p levels were taken from Ekberg (1993) [88] and for the other levels, Corliss & Sugar (1982) [87].

Level Unc. : The uncertainty of the energy level with respect to ground in cm^{-1}.

Rel. Unc.: The uncertainty of the energy level relative to the system in cm^{-1}.

Lines: The number of spectral lines used to fit the level in *LOPT*, with the number of reliable lines used in parenthesis.

Table of $3d^6$ levels

Designation	J	Energy (cm^{-1})	E_{rev} - E_{prev} (cm^{-1})	Level Unc. (cm^{-1})	Rel. Unc. (cm^{-1})	Lines
$3d^6\ ^5D_4$	4	0.00	0.00	0	0.19	2 (2)
$3d^6\ ^5D_3$	3	436.08	0.28	0.54	0.51	4 (1)
$3d^6\ ^5D_2$	2	738.78	0.23	0.24	0.14	3 (3)
$3d^6\ ^5D_1$	1	932.47	0.41	0.23	0.14	3 (3)
$3d^6\ ^5D_0$	0	1027.29	0.29	0.31	0.23	1 (1)
$3d^6\ a^3P_2$	2	19404.64	0.45	0.24	0.17	19 (13)
$3d^6\ ^3H_6$	6	20051.46	0.41	0.24	0.15	9 (7)
$3d^6\ ^3H_5$	5	20300.5	0.1	0.31	0.2	11 (7)
$3d^6\ ^3H_4$	4	20482.24	0.66	0.24	0.21	16 (10)
$3d^6\ a^3P_1$	1	20688.64	0.86	0.25	0.15	14 (7)
$3d^6\ a^3P_0$	0	21208.59	0.83	0.26	0.16	6 (5)
$3d^6\ a^3F_4$	4	21462.37	0.70	0.25	0.14	17 (9)
$3d^6\ a^3F_3$	3	21700.079	0.639	0.23	0.097	25 (18)
$3d^6\ a^3F_2$	2	21857.498	0.738	0.23	0.097	20 (17)
$3d^6\ ^3G_5$	5	24558.66	0.41	0.24	0.13	17 (14)
$3d^6\ ^3G_4$	4	24941.15	0.20	0.23	0.11	28 (15)
$3d^6\ ^3G_3$	3	25142.51	0.51	0.23	0.12	23 (17)
$3d^6\ ^1I_6$	6	30356.09	0.57	0.25	0.15	11 (7)
$3d^6\ ^3D_2$	2	30715.9	0.2	0.23	0.1	33 (21)
$3d^6\ ^3D_1$	1	30725.88	0.54	0.24	0.12	18 (12)
$3d^6\ ^3D_3$	3	30857.688	0.368	0.22	0.089	37 (26)
$3d^6\ a^1G_4$	4	30886.35	0.34	0.24	0.14	19 (12)
$3d^6\ a^1S_0$	0	34812.14	0.40	0.28	0.23	4 (4)
$3d^6\ a^1D_2$	2	35803.19	0.20	0.23	0.14	21 (15)
$3d^6\ ^1F_3$	3	42896.48	0.51	0.23	0.11	25 (16)
$3d^6\ b^3P_0$	0	49149.46	0.19	0.24	0.12	8 (7)
$3d^6\ b^3P_1$	1	49577.154	0.334	0.22	0.075	21 (16)

Table of $3d^6$ levels continued

Designation	J	Energy (cm^{-1})	E_{rev} - E_{prev} (cm^{-1})	Level Unc. (cm^{-1})	Rel. Unc. (cm^{-1})	Lines
$3d^6\ b^3F_2$	2	50184.88	0.23	0.22	0.12	29 (14)
$3d^6\ b^3F_4$	4	50275.923	0.083	0.22	0.083	40 (18)
$3d^6\ b^3F_3$	3	50295.097	0.207	0.22	0.077	33 (24)
$3d^6\ b^3P_2$	2	50411.928	0.238	0.22	0.087	29 (21)
$3d^6\ b^1G_4$	4	57221.155	0.145	0.23	0.095	26 (14)

Table of 4s levels

Designation	J	Energy (cm^{-1})	E_{rev} - E_{prev} (cm^{-1})	Level Unc. (cm^{-1})	Rel. Unc. (cm^{-1})	Lines
$3d^5$ (^{6}S) 4s $^7S_3$	3	30089.6443	0.2240	0.19	0.0031	7 (6)
$3d^5$ (^{6}S) 4s $^5S_2$	2	41000.3376	0.2480	0.2	0.0033	18 (13)
$3d^5$ (^{4}G) 4s $^5G_6$	6	63425.7155	0.2260	0.21	0.0044	16 (13)
$3d^5$ (^{4}G) 4s $^5G_5$	5	63466.7868	0.1170	0.21	0.0043	18 (14)
$3d^5$ (^{4}G) 4s $^5G_4$	4	63487.2143	0.1340	0.21	0.0043	27 (21)
$3d^5$ (^{4}G) 4s $^5G_3$	3	63494.6107	0.2310	0.21	0.0058	25 (7)
$3d^5$ (^{4}G) 4s $^5G_2$	2	63495.030	0.450	0.22	0.005	21 (6)
$3d^5$ (^{4}P) 4s $^5P_3$	3	66465.0062	0.2060	0.21	0.0057	20 (11)
$3d^5$ (^{4}P) 4s $^5P_2$	2	66523.2761	0.2560	0.21	0.0063	19 (13)
$3d^5$ (^{4}P) 4s $^5P_1$	1	66592.0390	0.2590	0.21	0.0065	14 (11)
$3d^5$ (^{4}D) 4s $^5D_4$	4	69696.0972	0.2070	0.21	0.0054	24 (14)
$3d^5$ (^{4}D) 4s $^5D_0$	0	69747.8992	0.2090	0.21	0.0095	6 (3)
$3d^5$ (^{4}D) 4s $^5D_1$	1	69788.4932	0.2630	0.21	0.0074	11 (6)
$3d^5$ (^{4}D) 4s $^5D_3$	3	69837.1082	0.2180	0.21	0.0056	20 (13)
$3d^5$ (^{4}D) 4s $^5D_2$	2	69838.1653	0.2750	0.21	0.0064	23 (14)
$3d^5$ (^{4}G) 4s $^3G_5$	5	70694.2944	0.1240	0.21	0.0047	18 (13)
$3d^5$ (^{4}G) 4s $^3G_3$	3	70725.3809	0.1610	0.21	0.0051	17 (7)
$3d^5$ (^{4}G) 4s $^3G_4$	4	70729.0206	0.0910	0.21	0.0056	30 (10)
$3d^5$ (^{4}P) 4s $^3P_2$	2	73728.040	0.250	0.21	0.014	22 (9)
$3d^5$ (^{4}P) 4s $^3P_1$	1	73849.261	0.131	0.21	0.018	14 (6)
$3d^5$ (^{4}D) 4s $^3D_3$	3	76956.9959	0.2360	0.21	0.0065	17 (11)
$3d^5$ (^{4}D) 4s $^3D_1$	1	77075.6027	0.2130	0.22	0.0083	15 (10)
$3d^5$ (^{4}D) 4s $^3D_2$	2	77102.5598	0.1500	0.21	0.0073	20 (10)
$3d^5$ (^{2}I) 4s $^3I_7$	7	79840.1909	0.0010	0.22	0.0076	13 (9)
$3d^5$ (^{2}I) 4s $^3I_6$	6	79844.764	-0.066	0.22	0.006	16 (8)
$3d^5$ (^{2}I) 4s $^3I_5$	5	79860.4983	-0.0020	0.22	0.0061	16 (12)
$3d^5$ (a^{2}D) 4s $^3D_3$	3	82382.9379	0.1180	0.21	0.0074	21 (9)

Table of 4s levels continued

Designation	J	Energy (cm^{-1})	E_{rev} - E_{prev} (cm^{-1})	Level Unc. (cm^{-1})	Rel. Unc. (cm^{-1})	Lines
$3d^5$ (a^2D) 4s $^3D_2$	2	82410.9733	0.0430	0.21	0.0088	16 (8)
$3d^5$ (^4F) 4s $^5F_5$	5	83138.5000	0.1300	0.21	0.0056	14 (9)
$3d^5$ (^4F) 4s $^5F_4$	4	83161.6337	0.0340	0.21	0.0064	14 (9)
$3d^5$ (^2I) 4s $^1I_6$	6	83429.6348	0.1150	0.22	0.0055	12 (5)
$3d^5$ (^4F) 4s $^5F_1$	1	83647.434	0.434	0.23	0.016	10 (6)
$3d^5$ (a^2F) 4s $^3F_4$	4	84159.5896	0.0900	0.21	0.0072	15 (9)
$3d^5$ (a^2F) 4s $^3F_2$	2	84369.9400	0.0600	0.22	0.0086	21 (15)
$3d^5$ (a^2F) 4s $^3F_3$	3	84671.9011	0.0710	0.21	0.0082	23 (16)
$3d^5$ (a^2D) 4s $^1D_2$	2	86847.035	0.045	0.22	0.011	15 (9)
$3d^5$ (a^2F) 4s $^1F_3$	3	87901.8999	0.0400	0.22	0.0096	20 (9)
$3d^5$ (^2H) 4s $^3H_4$	4	88663.9562	0.0960	0.21	0.0079	15 (8)
$3d^5$ (^2H) 4s $^3H_5$	5	88694.7585	0.0680	0.21	0.0067	16 (11)
$3d^5$ (^2H) 4s $^3H_6$	6	88923.1620	0.0720	0.21	0.0067	10 (6)
$3d^5$ (a^2G) 4s $^3G_3$	3	89697.486	0.016	0.21	0.011	18 (9)
$3d^5$ (a^2G) 4s $^3G_4$	4	89783.6446	0.0950	0.21	0.0095	22 (8)
$3d^5$ (a^2G) 4s $^3G_5$	5	89907.9316	0.0920	0.21	0.0087	18 (8)
$3d^5$ (^4F) 4s $^3F_2$	2	90423.723	0.183	0.22	0.026	12 (5)
$3d^5$ (^4F) 4s $^3F_4$	4	90472.495	0.125	0.21	0.011	21 (10)
$3d^5$ (^4F) 4s $^3F_3$	3	90484.077	0.147	0.21	0.015	18 (9)
$3d^5$ (b^2F) 4s $^3F_4$	4	93388.697	0.167	0.22	0.013	16 (7)
$3d^5$ (b^2F) 4s $^3F_3$	3	93392.4478	0.1480	0.21	0.0098	9 (2)
$3d^5$ (b^2F) 4s $^3F_2$	2	93412.919	0.089	0.22	0.012	13 (4)
$3d^5$ (a^2G) 4s $^1G_4$	4	93512.568	0.048	0.22	0.011	14 (6)
$3d^5$ (b^2F) 4s $^1F_3$	3	97041.385	0.085	0.22	0.012	11 (7)
$3d^5$ (^2S) 4s $^3S_1$	1	98662.367	-0.153	0.23	0.052	6 (4)
$3d^5$ (^2S) 4s $^1S_0$	0	102410.02	-0.08	0.28	0.17	4 (2)
$3d^5$ (b^2D) 4s $^3D_2$	2	105906.149	0.129	0.22	0.019	6 (2)

Table of 4s levels continued

Designation	J	Energy (cm^{-1})	E_{rev} - E_{prev} (cm^{-1})	Level Unc. (cm^{-1})	Rel. Unc. (cm^{-1})	Lines
$3d^5$ (b^2D) 4s $^3D_3$	3	105929.328	0.328	0.23	0.013	7 (3)
$3d^5$ (b^2D) 4s $^1D_2$	2	109570.951	0.151	0.22	0.014	6 (4)
$3d^5$ (b^2G) 4s $^3G_5$	5	114325.552	0.262	0.26	0.022	4 (2)
$3d^5$ (b^2G) 4s $^3G_4$	4	114340.279	0.259	1.4	0.016	2 (1)
$3d^5$ (b^2G) 4s $^3G_3$	3	114352.165	0.235	0.26	0.019	2 (2)
$3d^5$ (b^2G) 4s $^1G_4$	4	117950.186	0.266	0.25	0.019	5 (4)
$3d^5$ (^2P) 4s $^3P_2$	2	130856.06	-0.68	0.45	0.13	2 (1)
$3d^5$ (^2P) 4s $^3P_1$	1	130860.62	-1.03	0.45	0.04	2 (2)
$3d^5$ (^2P) 4s $^1P_1$	1	134443.262	-0.428	0.44	0.078	3 (2)
$3d^5$ (c^2D) 4s $^3D_2$	2	138880.159	-0.781	0.43	0.026	2 (2)
$3d^5$ (c^2D) 4s $^1D_2$	2	142460.245	-0.095	0.43	0.023	3 (2)

Table of 4p levels

Designation	J	Energy (cm^{-1})	E_{rev} - E_{prev} (cm^{-1})	Level Unc. (cm^{-1})	Rel. Unc. (cm^{-1})	Lines
$3d^5$ (^{6}S) 4p $^7P_2$	2	82002.0147	0.1350	0.19	0.0065	7 (6)
$3d^5$ (^{6}S) 4p $^7P_3$	3	82334.3359	0.1060	0.19	0.0065	7 (5)
$3d^5$ (^{6}S) 4p $^7P_4$	4	82846.9399	0.2400	0.19	0.0069	5 (4)
$3d^5$ (^{6}S) 4p $^5P_3$	3	89085.0894	0.1390	0.2	0.0066	12 (7)
$3d^5$ (^{6}S) 4p $^5P_2$	2	89334.8304	0.2000	0.2	0.0066	10 (7)
$3d^5$ (^{6}S) 4p $^5P_1$	1	89491.7070	0.2070	0.2	0.0066	7 (6)
$3d^5$ (^{4}G) 4p $^5G_2$	2	113584.3045	0.2740	0.22	0.0096	9 (6)
$3d^5$ (^{4}G) 4p $^5G_3$	3	113605.6000	0.1500	0.21	0.0074	6 (4)
$3d^5$ (^{4}G) 4p $^5G_4$	4	113635.5167	0.1770	0.21	0.0072	10 (6)
$3d^5$ (^{4}G) 4p $^5G_5$	5	113677.1144	0.0740	0.21	0.0073	8 (7)
$3d^5$ (^{4}G) 4p $^5G_6$	6	113739.8459	0.1060	0.21	0.0076	5 (5)
$3d^5$ (^{4}G) 4p $^5H_3$	3	114948.6762	0.0160	0.22	0.0081	10 (5)
$3d^5$ (^{4}G) 4p $^5H_4$	4	115111.354	0.204	0.21	0.028	10 (6)
$3d^5$ (^{4}G) 4p $^5H_5$	5	115290.0382	0.0080	0.21	0.0078	8 (6)
$3d^5$ (^{4}G) 4p $^5H_6$	6	115474.3467	0.0470	0.21	0.0078	5 (3)
$3d^5$ (^{4}G) 4p $^5H_7$	7	115642.4595	0.0190	0.21	0.0081	3 (2)
$3d^5$ (^{4}G) 4p $^5F_5$	5	116316.7656	0.1860	0.21	0.0083	11 (7)
$3d^5$ (^{4}P) 4p $^5D_0$	0	116365.013	0.223	0.21	0.013	2 (1)
$3d^5$ (^{4}P) 4p $^5D_1$	1	116380.24	0.30	0.21	0.01	7 (2)
$3d^5$ (^{4}P) 4p $^5D_2$	2	116419.623	0.163	0.21	0.025	7 (3)
$3d^5$ (^{4}G) 4p $^5F_4$	4	116467.5612	0.1210	0.21	0.0083	11 (5)
$3d^5$ (^{4}G) 4p $^5F_3$	3	116475.5055	0.2160	0.21	0.0087	16 (10)
$3d^5$ (^{4}P) 4p $^5S_2$	2	116898.3731	0.1931	0.21	0.0088	8 (4)
$3d^5$ (^{4}G) 4p $^5F_1$	1	116937.81	0.24	0.22	0.01	4 (2)
$3d^5$ (^{4}G) 4p $^5F_2$	2	116975.200	0.21	0.21	0.013	10 (6)
$3d^5$ (^{4}P) 4p $^5D_3$	3	117068.7153	0.1250	0.21	0.0093	14 (9)
$3d^5$ (^{4}P) 4p $^5D_4$	4	117521.952	0.272	0.21	0.008	10 (7)

Table of 4p levels continued

Designation	J	Energy (cm^{-1})	E_{rev} - E_{prev} (cm^{-1})	Level Unc. (cm^{-1})	Rel. Unc. (cm^{-1})	Lines
$3d^5$ (^4G) 4p $^3F_2$	2	118163.6420	0.2020	0.21	0.0085	10 (6)
$3d^5$ (^4G) 4p $^3F_3$	3	118246.6473	0.1573	0.21	0.0081	14 (8)
$3d^5$ (^4G) 4p $^3F_4$	4	118350.2991	0.0990	0.21	0.0077	12 (9)
$3d^5$ (^4G) 4p $^3H_6$	6	118355.0674	0.0970	0.21	0.0076	4 (3)
$3d^5$ (^4P) 4p $^5P_3$	3	118443.111	0.131	0.21	0.011	8 (4)
$3d^5$ (^4G) 4p $^3H_5$	5	118556.71	-0.42	0.37	0.27	9 (2)
$3d^5$ (^4G) 4p $^3H_4$	4	118686.3063	0.1460	0.21	0.0076	7 (6)
$3d^5$ (^4P) 4p $^5P_2$	2	118721.727	0.287	0.21	0.012	10 (7)
$3d^5$ (^4P) 4p $^5P_1$	1	118867.982	0.222	0.21	0.016	9 (6)
$3d^5$ (^4P) 4p $^3P_2$	2	119697.553	0.123	0.22	0.056	17 (9)
$3d^5$ (^4D) 4p $^5F_1$	1	120697.498	0.228	0.21	0.014	7 (3)
$3d^5$ (^4D) 4p $^5F_2$	2	120826.2208	0.1910	0.21	0.0094	9 (7)
$3d^5$ (^4D) 4p $^5F_3$	3	121008.8062	0.1060	0.21	0.0088	11 (5)
$3d^5$ (^4D) 4p $^5F_4$	4	121241.7348	0.0450	0.21	0.0085	12 (6)
$3d^5$ (^4D) 4p $^5F_5$	5	121468.9534	0.1030	0.21	0.0084	4 (3)
$3d^5$ (^4G) 4p $^3G_3$	3	121919.64	0.04	0.24	0.14	9 (7)
$3d^5$ (^4G) 4p $^3G_4$	4	121941.2617	0.0320	0.21	0.0097	12 (8)
$3d^5$ (^4G) 4p $^3G_5$	5	121949.6405	0.1010	0.21	0.0091	12 (8)
$3d^5$ (^4P) 4p $^3D_3$	3	122346.829	0.289	0.23	0.097	12 (4)
$3d^5$ (^4P) 4p $^3D_2$	2	122628.395	0.145	0.21	0.017	15 (9)
$3d^5$ (^4D) 4p $^5D_3$	3	122829.5	0.1	0.23	0.1	12 (5)
$3d^5$ (^4P) 4p $^3D_1$	1	122843.179	0.139	0.21	0.014	11 (8)
$3d^5$ (^4D) 4p $^5D_2$	2	122898.717	0.097	0.21	0.011	16 (5)
$3d^5$ (^4D) 4p $^5D_1$	1	122921.561	0.181	0.21	0.021	9 (6)
$3d^5$ (^4D) 4p $^5D_4$	4	122944.100	0.150	0.21	0.009	7 (5)
$3d^5$ (^4D) 4p $^5D_0$	0	123455.769	0.129	0.21	0.024	3 (3)
$3d^5$ (^4D) 4p $^5P_1$	1	123553.076	0.296	0.21	0.015	9 (6)

Table of 4p levels continued

Designation	J	Energy (cm^{-1})	E_{rev} - E_{prev} (cm^{-1})	Level Unc. (cm^{-1})	Rel. Unc. (cm^{-1})	Lines
$3d^5$ (^{4}D) 4p $^5P_2$	2	123697.078	0.128	0.21	0.013	12 (7)
$3d^5$ (^{4}D) 4p $^5P_3$	3	123750.452	0.032	0.21	0.019	15 (6)
$3d^5$ (^{4}D) 4p $^3D_3$	3	124854.01	0.15	0.24	0.12	16 (9)
$3d^5$ (^{4}D) 4p $^3D_2$	2	124903.931	0.121	0.21	0.012	15 (11)
$3d^5$ (^{4}D) 4p $^3D_1$	1	124954.973	0.063	0.22	0.017	8 (6)
$3d^5$ (^{4}D) 4p $^3F_4$	4	125443.5945	0.1150	0.22	0.0088	11 (4)
$3d^5$ (^{4}D) 4p $^3F_3$	3	125637.97	0.10	0.22	0.01	13 (9)
$3d^5$ (^{4}D) 4p $^3F_2$	2	125672.798	0.018	0.23	0.011	6 (4)
$3d^5$ (^{4}P) 4p $^3S_1$	1	126390.46	-0.01	0.25	0.13	10 (7)
$3d^5$ (^{4}D) 4p $^3P_0$	0	128371.83	0.09	0.26	0.16	6 (4)
$3d^5$ (^{4}D) 4p $^3P_1$	1	128605.617	0.137	0.23	0.079	15 (10)
$3d^5$ (^{4}D) 4p $^3P_2$	2	128917.484	0.034	0.22	0.013	11 (8)
$3d^5$ (^{2}I) 4p $^3K_6$	6	129854.43	-0.38	0.48	0.37	1 (1)
$3d^5$ (^{2}I) 4p $^3K_7$	7	130040.32	-0.07	0.23	0.01	5 (3)
$3d^5$ (^{2}I) 4p $^3I_5$	5	130256.16	-0.03	0.23	0.01	10 (6)
$3d^5$ (^{2}I) 4p $^3I_6$	6	130756.600	-0.080	0.23	0.009	8 (5)
$3d^5$ (^{2}I) 4p $^3K_8$	8	130852.0263	-0.1140	0.23	0.0084	1 (1)
$3d^5$ (^{2}I) 4p $^3I_7$	7	131034.87	-0.05	0.33	0.38	5 (2)
$3d^5$ (a^{2}D) 4p $^1D_2$	2	131444.96	0.04	0.22	0.02	10 (5)
$3d^5$ (^{2}I) 4p $^1H_5$	5	131710.4120	-0.0780	0.23	0.0095	9 (7)
$3d^5$ (^{2}I) 4p $^1K_7$	7	131991.3884	0.0080	0.23	0.0083	4 (1)
$3d^5$ (a^{2}D) 4p $^3F_3$	3	132079.81	0.02	0.22	0.01	14 (7)
$3d^5$ (^{2}I) 4p $^3H_6$	6	132262.3581	-0.1120	0.23	0.0098	4 (4)
$3d^5$ (^{2}I) 4p $^3H_5$	5	132564.6898	0.0800	0.23	0.0099	7 (5)
$3d^5$ (^{2}I) 4p $^3H_4$	4	132659.20	0.05	0.23	0.01	6 (3)
$3d^5$ (a^{2}D) 4p $^3F_4$	4	132785.2111	-0.0090	0.22	0.0098	9 (6)
$3d^5$ (a^{2}D) 4p $^3P_2$	2	134265.281	0.011	0.22	0.015	9 (4)

Table of 4p levels continued

Designation	J	Energy (cm^{-1})	E_{rev} - E_{prev} (cm^{-1})	Level Unc. (cm^{-1})	Rel. Unc. (cm^{-1})	Lines
$3d^5$ (a^2F) 4p $^1G_4$	4	134360.235	0.045	0.23	0.011	14 (8)
$3d^5$ (a^2F) 4p $^3G_3$	3	134548.840	0.120	0.23	0.012	14 (6)
$3d^5$ (a^2D) 4p $^3P_1$	1	134549.37	0.18	0.28	0.22	8 (3)
$3d^5$ (^4F) 4p $^5G_2$	2	134938.302	0.462	0.24	0.024	5 (4)
$3d^5$ (a^2D) 4p $^3P_0$	0	135088.72	0.49	0.34	0.25	1 (1)
$3d^5$ (^4F) 4p $^5G_3$	3	135096.867	0.057	0.23	0.075	16 (10)
$3d^5$ (a^2D) 4p $^3D_1$	1	135217.19	0.24	0.27	0.18	6 (5)
$3d^5$ (^4F) 4p $^5G_4$	4	135239.757	0.197	0.22	0.014	11 (6)
$3d^5$ (a^2D) 4p $^3D_2$	2	135278.906	0.246	0.22	0.016	7 (5)
$3d^5$ (a^2F) 4p $^3G_5$	5	135316.4551	0.0550	0.22	0.0098	8 (6)
$3d^5$ (a^2F) 4p $^3G_4$	4	135554.260	0.110	0.23	0.012	11 (4)
$3d^5$ (^2I) 4p $^1I_6$	6	135581.78	-0.07	0.23	0.01	7 (6)
$3d^5$ (a^2F) 4p $^3D_3$	3	135705.30	-0.01	0.25	0.13	9 (3)
$3d^5$ (^4F) 4p $^5G_5$	5	135735.28	0.16	0.22	0.01	7 (6)
$3d^5$ (^4F) 4p $^5G_6$	6	135739.4632	0.0730	0.22	0.0089	6 (4)
$3d^5$ (^4F) 4p $^5F_4$	4	135990.605	-0.095	0.22	0.013	9 (4)
$3d^5$ (^4F) 4p $^5F_3$	3	136008.801	0.151	0.22	0.014	10 (3)
$3d^5$ (^4F) 4p $^5F_5$	5	136184.9152	0.0650	0.22	0.0093	9 (5)
$3d^5$ (a^2D) 4p $^1F_3$	3	136199.907	0.167	0.22	0.013	14 (6)
$3d^5$ (^4F) 4p $^5F_1$	1	136236.080	0.37	0.24	0.024	4 (3)
$3d^5$ (a^2F) 4p $^3D_1$	1	136464.706	0.126	0.23	0.023	6 (5)
$3d^5$ (a^2F) 4p $^3F_2$	2	136532.189	0.069	0.23	0.018	11 (3)
$3d^5$ (a^2F) 4p $^3F_4$	4	136612.596	-0.024	0.22	0.014	11 (5)
$3d^5$ (a^2F) 4p $^3D_2$	2	136793.71	0.13	0.23	0.02	4 (1)
$3d^5$ (a^2F) 4p $^3F_3$	3	136796.697	-0.013	0.23	0.017	11 (4)
$3d^5$ (^4F) 4p $^5D_4$	4	137209.727	0.157	0.22	0.011	8 (5)
$3d^5$ (^4F) 4p $^5D_3$	3	137422.725	0.085	0.22	0.012	7 (6)

Table of 4p levels continued

Designation	J	Energy (cm^{-1})	E_{rev} - E_{prev} (cm^{-1})	Level Unc. (cm^{-1})	Rel. Unc. (cm^{-1})	Lines
$3d^5$ (^{2}H) 4p $^3H_4$	4	137527.822	-0.038	0.22	0.013	12 (6)
$3d^5$ (^{4}F) 4p $^5D_2$	2	137544.426	0.046	0.23	0.069	7 (5)
$3d^5$ (^{4}F) 4p $^5D_1$	1	137560.99	0.15	0.35	0.35	6 (3)
$3d^5$ (^{4}F) 4p $^5D_0$	0	137573.34	0.40	0.26	0.15	2 (1)
$3d^5$ (^{2}H) 4p $^3H_5$	5	137763.448	0.068	0.22	0.011	8 (3)
$3d^5$ (^{2}H) 4p $^3G_5$	5	138054.418	0.018	0.22	0.013	9 (6)
$3d^5$ (^{2}H) 4p $^3G_4$	4	138103.000	-0.010	0.22	0.017	8 (4)
$3d^5$ (^{2}H) 4p $^3G_3$	3	138187.800	0.040	0.22	0.018	11 (7)
$3d^5$ (^{2}H) 4p $^3H_6$	6	138264.33	-0.02	0.22	0.02	9 (5)
$3d^5$ (a^{2}D) 4p $^1P_1$	1	138691.637	0.067	0.23	0.024	5 (3)
$3d^5$ (^{4}F) 4p $^3G_5$	5	139463.131	0.041	0.22	0.021	11 (8)
$3d^5$ (^{2}H) 4p $^3I_5$	5	139509.22	0.01	0.22	0.01	7 (5)
$3d^5$ (^{4}F) 4p $^3G_4$	4	139625.065	-0.005	0.22	0.013	14 (7)
$3d^5$ (^{4}F) 4p $^3G_3$	3	139680.24	0.10	0.23	0.03	9 (3)
$3d^5$ (a^{2}F) 4p $^1D_2$	2	139764.35	0.09	0.25	0.13	9 (5)
$3d^5$ (a^{2}G) 4p $^1G_4$	4	139826.998	0.048	0.22	0.026	17 (10)
$3d^5$ (^{2}H) 4p $^3I_6$	6	139846.024	-0.006	0.22	0.011	6 (5)
$3d^5$ (^{2}H) 4p $^3I_7$	7	140196.1200	-0.1300	0.22	0.0097	3 (2)
$3d^5$ (a^{2}F) 4p $^1F_3$	3	140452.85	-0.10	0.23	0.12	15 (7)
$3d^5$ (a^{2}G) 4p $^3F_3$	3	140693.15	0.01	0.24	0.18	16 (9)
$3d^5$ (a^{2}G) 4p $^3F_2$	2	140750.680	0.090	0.22	0.022	11 (8)
$3d^5$ (a^{2}G) 4p $^3F_4$	4	141002.734	-0.016	0.23	0.038	19 (10)
$3d^5$ (^{4}F) 4p $^3D_2$	2	141399.117	0.077	0.24	0.063	10 (7)
$3d^5$ (^{4}F) 4p $^3D_3$	3	141466.480	0.090	0.22	0.017	12 (10)
$3d^5$ (^{4}F) 4p $^3D_1$	1	141469.28	0.07	0.25	0.13	7 (4)
$3d^5$ (^{2}H) 4p $^1I_6$	6	141539.69	0.59	0.29	0.19	6 (2)
$3d^5$ (^{4}F) 4p $^3F_4$	4	142046.880	0.120	0.22	0.022	9 (4)

Table of 4p levels continued

Designation	J	Energy (cm^{-1})	E_{rev} - E_{prev} (cm^{-1})	Level Unc. (cm^{-1})	Rel. Unc. (cm^{-1})	Lines
$3d^5$ (^{4}F) 4p $^3F_3$	3	142312.42	-0.15	0.26	0.16	13 (4)
$3d^5$ (^{4}F) 4p $^3F_2$	2	142534.6	0.0	0.24	0.1	8 (4)
$3d^5$ (a^{2}G) 4p $^3H_4$	4	142855.211	0.011	0.22	0.015	11 (6)
$3d^5$ (a^{2}G) 4p $^3H_5$	5	142908.155	0.055	0.22	0.011	10 (6)
$3d^5$ (a^{2}G) 4p $^3H_6$	6	143320.76	0.14	0.22	0.01	6 (5)
$3d^5$ (a^{2}G) 4p $^3G_5$	5	143883.594	0.064	0.22	0.013	8 (3)
$3d^5$ (a^{2}G) 4p $^3G_4$	4	144085.83	0.03	0.22	0.02	13 (5)
$3d^5$ (a^{2}G) 4p $^3G_3$	3	144116.242	-0.008	0.22	0.021	9 (4)
$3d^5$ (b^{2}F) 4p $^1G_4$	4	144332.114	0.144	0.23	0.019	12 (7)
$3d^5$ (b^{2}F) 4p $^3F_2$	2	144501.498	-0.052	0.23	0.056	12 (5)
$3d^5$ (b^{2}F) 4p $^3F_3$	3	144570.363	0.013	0.22	0.022	18 (12)
$3d^5$ (a^{2}G) 4p $^1H_5$	5	144586.503	0.003	0.23	0.013	9 (4)
$3d^5$ (^{2}H) 4p $^1H_5$	5	144842.95	0.18	0.27	0.25	3 (3)
$3d^5$ (b^{2}F) 4p $^3F_4$	4	144968.0	-0.2	0.24	0.1	9 (6)
$3d^5$ (a^{2}G) 4p $^1F_3$	3	145038.468	0.048	0.23	0.065	12 (9)
$3d^5$ (b^{2}F) 4p $^1D_2$	2	145618.203	0.073	0.23	0.015	9 (7)
$3d^5$ (b^{2}F) 4p $^3G_3$	3	146890.911	0.061	0.23	0.015	10 (9)
$3d^5$ (b^{2}F) 4p $^3G_4$	4	147161.102	0.032	0.22	0.012	7 (6)
$3d^5$ (b^{2}F) 4p $^3G_5$	5	147405.77	-0.05	0.22	0.02	6 (5)
$3d^5$ (b^{2}F) 4p $^3D_1$	1	147555.967	0.057	0.23	0.029	9 (6)
$3d^5$ (b^{2}F) 4p $^3D_2$	2	147614.39	0.06	0.24	0.13	10 (8)
$3d^5$ (b^{2}F) 4p $^3D_3$	3	147635.559	0.069	0.23	0.018	12 (5)
$3d^5$ (^{2}S) 4p $^3P_1$	1	148915.07	-0.09	0.25	0.11	4 (2)
$3d^5$ (^{2}H) 4p $^1G_4$	4	149012.999	0.019	0.23	0.021	8 (6)
$3d^5$ (^{2}S) 4p $^3P_2$	2	149524.64	-0.58	0.25	0.15	10 (6)
$3d^5$ (b^{2}F) 4p $^1F_3$	3	150654.262	-0.118	0.24	0.096	8 (6)
$3d^5$ (^{2}S) 4p $^1P_1$	1	151636.68	0.03	0.24	0.13	5 (3)

Table of 4p levels continued

Designation	J	Energy (cm^{-1})	E_{rev} - E_{prev} (cm^{-1})	Level Unc. (cm^{-1})	Rel. Unc. (cm^{-1})	Lines
$3d^5$ (b^2D) 4p $^3F_2$	2	157684.11	-0.10	0.25	0.12	5 (2)
$3d^5$ (b^2D) 4p $^3F_3$	3	157982.088	0.318	0.24	0.032	10 (4)
$3d^5$ (b^2D) 4p $^3D_1$	1	158256.67	-0.44	0.25	0.12	8 (5)
$3d^5$ (b^2D) 4p $^3F_4$	4	158562.484	0.434	0.24	0.016	5 (4)
$3d^5$ (b^2D) 4p $^3D_3$	3	158729.055	-0.065	0.23	0.024	12 (8)
$3d^5$ (b^2D) 4p $^1F_3$	3	159492.894	0.054	0.23	0.017	7 (4)
$3d^5$ (b^2D) 4p $^3P_2$	2	160037.448	0.118	0.23	0.031	7 (5)
$3d^5$ (b^2D) 4p $^3P_1$	1	160066.18	-0.09	0.25	0.13	9 (7)
$3d^5$ (b^2D) 4p $^3P_0$	0	160073.94	0.51	0.89	0.86	1 (1)
$3d^5$ (b^2D) 4p $^1P_1$	1	161018.385	0.235	0.25	0.082	4 (2)
$3d^5$ (b^2D) 4p $^1D_2$	2	162084.69	0.20	0.23	0.03	5 (5)
$3d^5$ (b^2G) 4p $^3H_4$	4	165719.277	0.107	0.27	0.021	4 (3)
$3d^5$ (b^2G) 4p $^3H_5$	5	165939.966	0.186	1.4	0.018	2 (1)
$3d^5$ (b^2G) 4p $^3H_6$	6	166188.45	0.76	0.26	0.17	3 (2)
$3d^5$ (b^2G) 4p $^3F_4$	4	166222.494	0.324	0.27	0.024	5 (5)
$3d^5$ (b^2G) 4p $^3F_3$	3	166498.02	-0.06	0.27	0.18	5 (4)
$3d^5$ (b^2G) 4p $^3G_4$	4	167208.01	0.70	0.36	0.27	1 (1)
$3d^5$ (b^2G) 4p $^1H_5$	5	168779.796	0.196	0.26	0.025	4 (2)
$3d^5$ (b^2G) 4p $^1G_4$	4	169277.54	0.11	0.26	0.03	1 (1)
$3d^5$ (b^2G) 4p $^1F_3$	3	170310.036	0.256	0.26	0.029	8 (7)
$3d^5$ (^2P) 4p $^3P_1$	1	178824.449	-1.321	0.45	0.034	1 (1)
$3d^5$ (^2P) 4p $^1D_2$	2	183722.96	-0.69	0.45	0.44	4 (2)
$3d^5$ (c^2D) 4p $^3F_3$	3	191118.463	-0.207	0.43	0.032	2 (1)
$3d^5$ (c^2D) 4p $^3F_4$	4	191632.01	0.22	0.33	0.19	1 (1)
$3d^5$ (c^2D) 4p $^3D_1$	1	192546.08	-0.58	0.45	0.11	3 (2)
$3d^5$ (c^2D) 4p $^1D_2$	2	193555.046	-0.364	0.43	0.039	4 (4)
$3d^5$ (c^2D) 4p $^1F_3$	3	194842.083	-0.057	0.43	0.025	3 (3)

Table of 4d, 5s and 5d levels

Designation	J	Energy (cm^{-1})	E_{rev} - E_{prev} (cm^{-1})	Level Unc. (cm^{-1})	Rel. Unc. (cm^{-1})	Lines
$3d^5$ (^6S) 4d $^7D_3$	3	147306.288	0.318	0.22	0.096	3 (2)
$3d^5$ (^6S) 4d $^7D_4$	4	147327.16	0.31	0.23	0.13	2 (2)
$3d^5$ (^6S) 4d $^7D_5$	5	147355.12	0.42	0.24	0.13	1 (1)
$3d^5$ (^6S) 5s $^7S_3$	3	149285.367	0.367	0.22	0.084	4 (4)
$3d^5$ (^6S) 4d $^5D_3$	3	151534.15	0.02	0.24	0.12	3 (2)
$3d^5$ (^6S) 4d $^5D_2$	2	151535.052	0.152	0.21	0.046	2 (2)
$3d^5$ (^6S) 5s $^5S_2$	2	151757.744	0.074	0.21	0.047	4 (4)
$3d^5$ (^4G) 4d $^5H_3$	3	179178.797	0.177	0.22	0.016	10 (7)
$3d^5$ (^4G) 4d $^5H_4$	4	179194.45	0.23	0.23	0.12	7 (6)
$3d^5$ (^4G) 4d $^5H_5$	5	179207.80	0.23	0.23	0.11	4 (3)
$3d^5$ (^4G) 4d $^5H_6$	6	179216.74	0.27	0.24	0.11	3 (2)
$3d^5$ (^4G) 4d $^5H_7$	7	179221.723	0.273	0.24	0.099	2 (2)
$3d^5$ (^4G) 4d $^5F_5$	5	179579.86	0.03	0.25	0.13	3 (3)
$3d^5$ (^4G) 4d $^5F_4$	4	179631.03	0.26	0.23	0.16	12 (6)
$3d^5$ (^4G) 4d $^5F_3$	3	179661.534	0.054	0.22	0.028	9 (7)
$3d^5$ (^4G) 4d $^5F_2$	2	179676.902	0.012	0.23	0.063	9 (7)
$3d^5$ (^4G) 4d $^5F_1$	1	179683.03	0.09	0.25	0.17	5 (2)
$3d^5$ (^6S) 5d $^5D_3$	3	193611.0	0.1	0.24	0.1	13 (6)
$3d^5$ (^6S) 5d $^5D_4$	4	193611.383	0.013	0.22	0.015	16 (8)

B Fe III Classified FTS Linelist

The classified FTS linelist is shown in the Table below. Lines with multiple Fe III identifications are listed for every identification. Lines weighted out of the energy level optimisation process, usually due to double-identifications, are indicated by an asterisk (*). The columns include:

ln (EW): The natural logarithm of the equivalent widths, a measure of the line intensities. The equivalent widths of the FTS lines have been intensity calibrated and placed on a common intensity scale (Section 3.1.2).

SNR: The observed signal-to-noise ratios.

FWHM: The FWHM of the observed spectral lines in $10^{-3}\cdot$ cm^{-1} (mK).

$\sigma_{\mathbf{obs}}$: The wavenumbers of the spectral lines in cm^{-1}.

Line Unc.: The total uncertainty of the spectral lines in cm^{-1}. Lines with an increased uncertainty for the energy level optimisation process are indicated by an asterisk (*).

$\sigma_{\mathbf{Ritz}}$: The Ritz wavenumber of the spectral lines in cm^{-1}.

Ritz Unc.: The uncertainties of the Ritz wavenumbers of the spectral lines in cm^{-1}.

Energy Levels: The energy levels of the identified transitions.

Fe III Classified FTS linelist

ln (EW)	SNR	FWHM	σ_{obs} (cm^{-1})	Unc. (cm^{-1})		σ_{Ritz} (cm^{-1})	Unc. (cm^{-1})	Energy Levels
10.2	2	312	34882.3258	0.0770		34882.328	0.065	(b^2D) 4p $^3D_3$ - (^{6}S) 5d $^5D_4$
10.5	4	282	35192.8485	0.0381	*	35192.698	0.079	(b^2F) 4s $^3F_2$ - (^{4}D) 4p $^3P_1$
8.2	3	253	38790.8526	0.0457	*	38790.933	0.047	(a^2D) 4s $^1D_2$ - (^{4}D) 4p $^3F_3$
9.0	3	225	39158.4741	0.0355	*	39158.522	0.056	(b^2F) 4s $^1F_3$ - (a^2D) 4p $^1F_3$
11.3	30	540	39553.7323	0.0092		39553.7321	0.011	(^{4}F) 4p $^3G_4$ - (^{4}G) 4d $^5H_3$
9.9	4	228	39963.4931	0.0270	*	39963.891	0.084	(a^2D) 4s $^3D_3$ - (^{4}P) 4p $^3D_3$
8.3	2	234	40515.8230	0.0558	*	40515.779	0.029	(a^2D) 4s $^3D_3$ - (^{4}D) 4p $^5D_2$
8.1	4	141	41542.7093	0.0192	*	41542.71	0.14	(b^2G) 4s $^1G_4$ - (b^2D) 4p $^1F_3$
8.9	3	422	41561.4960	0.0656	*	41561.401	0.038	(^{2}H) 4s $^3H_5$ - (^{2}I) 4p $^3I_5$
8.7	3	344	41684.2597	0.0643	*	41683.948	0.072	(b^2F) 4s $^3F_2$ - (^{4}F) 4p $^5G_3$
7.0	3	72	42065.8355	0.0125	*	42065.73	0.12	(b^2D) 4s $^1D_2$ - (^{2}S) 4p $^1P_1$
8.4	4	133	42823.1345	0.0163	*	42823.161	0.089	(b^2F) 4s $^3F_2$ - (^{4}F) 4p $^5F_1$
7.9	3	166	42948.0145	0.0283	*	42948.094	0.032	(^{4}G) 4s $^3G_4$ - (^{4}G) 4p $^5G_5$
7.7	3	243	43543.0346	0.0360	*	43543.063	0.042	(a^2F) 4s $^1F_3$ - (a^2D) 4p $^1D_2$
6.9	4	106	44148.2980	0.0141	*	44148.07	0.27	(b^2F) 4s $^3F_2$ - (^{4}F) 4p $^5D_1$
6.5	5	63	44245.5988	0.0072	*	44245.583	0.045	(a^2F) 4s $^3F_3$ - (^{4}D) 4p $^3P_2$

Fe III Classified FTS linelist continued

ln (EW)	SNR	FWHM	σ_{obs} (cm^{-1})	Unc. (cm^{-1})		σ_{Ritz} (cm^{-1})	Unc. (cm^{-1})	Energy Levels		
8.7	5	477	44541.7688	0.0509	*	44541.850	0.029	(a^2G) 4s $^1G_4$	-	(^{2}H) 4p $^3G_5$
7.8	6	143	44597.9131	0.0127	*	44597.927	0.042	(a^2D) 4s $^1D_2$	-	(a^2D) 4p $^1D_2$
6.9	3	138	44710.5895	0.0203	*	44710.552	0.027	(b^2F) 4s $^3F_3$	-	(^{2}H) 4p $^3G_4$
7.5	3	226	44780.1358	0.0370	*	44780.052	0.032	(^{4}G) 4s $^3G_5$	-	(^{4}G) 4p $^5H_6$
7.3	4	148	44993.6266	0.0219	*	44993.687	0.038	(^{4}P) 4s $^3P_2$	-	(^{4}P) 4p $^5P_2$
6.4	2	134	45145.8087	0.0280	*	45145.95	0.18	(^{2}S) 4s $^1S_0$	-	(b^2F) 4p $^3D_1$
6.5	2	208	45746.3082	0.0432	*	45746.485	0.032	(^{4}G) 4s $^3G_4$	-	(^{4}G) 4p $^5F_3$
7.9	4	392	45839.1190	0.0517		45839.131	0.05	(^{2}S) 4s $^3S_1$	-	(b^2F) 4p $^3F_2$
8.5	8	226	45848.2672	0.0139	*	45848.292	0.053	(^{4}P) 4s $^3P_1$	-	(^{4}P) 4p $^3P_2$
6.4	3	154	45941.6864	0.0250	*	45941.721	0.036	(^{4}D) 4s $^3D_3$	-	(^{4}D) 4p $^5D_2$
9.3	23	334	45969.5526	0.0076	*	45969.513	0.061	(^{4}P) 4s $^3P_2$	-	(^{4}P) 4p $^3P_2$
8.0	5	313	46314.3315	0.0300	*	46314.430	0.034	(a^2G) 4s $^1G_4$	-	(a^2G) 4p $^1G_4$
9.3	29	328	46458.3351	0.0061		46458.3350	0.008	(a^2F) 4s $^1F_3$	-	(a^2F) 4p $^1G_4$
7.1	3	237	46542.1081	0.0385	*	46542.075	0.012	(^{4}D) 4s $^5D_2$	-	(^{4}P) 4p $^5D_1$
7.6	4	241	46581.4907	0.0307		46581.458	0.019	(^{4}D) 4s $^5D_2$	-	(^{4}P) 4p $^5D_2$
7.5	5	337	46610.6936	0.0349	*	46610.681	0.016	(^{2}I) 4s $^1I_6$	-	(^{2}I) 4p $^3K_7$

Fe III Classified FTS linelist continued

ln (EW)	SNR	FWHM	σ_{obs} (cm^{-1})	Unc. (cm^{-1})		σ_{Ritz} (cm^{-1})	Unc. (cm^{-1})	Energy Levels		
8.1	5	244	46620.6566	0.0243	*	46620.6684	0.011	(^{4}D) 4s ^{5}D$_4$	-	(^{4}G) 4p ^{5}F$_5$
6.9	3	302	46630.4321	0.0466	*	46630.4530	0.011	(^{4}D) 4s ^{5}D$_3$	-	(^{4}G) 4p ^{5}F$_4$
8.2	6	281	46638.3978	0.0249		46638.3973	0.01	(^{4}D) 4s ^{5}D$_3$	-	(^{4}G) 4p ^{5}F$_3$
7.5	5	292	46771.4152	0.0310	*	46771.4640	0.01	(^{4}D) 4s ^{5}D$_4$	-	(^{4}G) 4p ^{5}F$_4$
7.6	3	406	46793.4981	0.1603	*	46793.456	0.039	(^{4}D) 4s ^{3}D$_3$	-	(^{4}D) 4p ^{5}P$_3$
8.0	8	283	46826.5455	0.0174	*	46826.524	0.014	(^{2}I) 4s ^{1}I$_6$	-	(^{2}I) 4p ^{3}I$_5$
6.3	4	135	46915.1713	0.0187	*	46915.110	0.033	(a^{2}G) 4s ^{3}G$_3$	-	(a^{2}F) 4p ^{3}F$_4$
8.0	9	296	47075.0513	0.0164	*	47075.023	0.042	(a^{2}F) 4s ^{3}F$_2$	-	(a^{2}D) 4p ^{1}D$_2$
7.4	5	312	47186.6562	0.0326	*	47186.707	0.017	(^{4}D) 4s ^{5}D$_1$	-	(^{4}G) 4p ^{5}F$_2$
7.9	10	363	47230.5449	0.0185		47230.5500	0.011	(^{4}D) 4s ^{5}D$_2$	-	(^{4}P) 4p ^{5}D$_3$
6.9	4	340	47231.5788	0.0826		47231.6071	0.01	(^{4}D) 4s ^{5}D$_3$	-	(^{4}P) 4p ^{5}D$_3$
7.9	6	236	47290.7457	0.0193	*	47290.953	0.023	(^{4}F) 4s ^{3}F$_4$	-	(^{2}H) 4p ^{3}H$_5$
7.9	6	236	47290.7457	0.0193	*	47290.729	0.056	(b^{2}F) 4s ^{1}F$_3$	-	(b^{2}F) 4p ^{1}G$_4$
7.9	6	294	47407.9131	0.0242	*	47407.913	0.038	(a^{2}F) 4s ^{3}F$_3$	-	(a^{2}D) 4p ^{3}F$_3$
10.0	56	332	47438.2610	0.0038		47438.2611	0.0057	(^{4}G) 4s ^{3}G$_3$	-	(^{4}G) 4p ^{3}F$_2$
7.4	6	435	47490.1392	0.0707	*	47490.157	0.031	(^{2}H) 4s ^{3}H$_5$	-	(^{4}F) 4p ^{5}F$_5$

Fe III Classified FTS linelist continued

ln (EW)	SNR	FWHM	σ_{obs} (cm^{-1})	Unc. (cm^{-1})		σ_{Ritz} (cm^{-1})	Unc. (cm^{-1})	Energy Levels		
7.4	6	435	47490.1392	0.0707	*	47490.166	0.043	(a^2G) 4s $^1G_4$	-	(a^2G) 4p $^3F_4$
10.2	70	338	47517.6266	0.0034		47517.6267	0.0053	(^{4}G) 4s $^3G_4$	-	(^{4}G) 4p $^3F_3$
7.8	7	356	47521.2821	0.0268	*	47521.266	0.018	(^{4}G) 4s $^3G_3$	-	(^{4}G) 4p $^3F_3$
8.1	9	340	47581.9598	0.0195	*	47581.923	0.02	(^{4}F) 4s $^3F_4$	-	(^{2}H) 4p $^3G_5$
8.3	11	336	47618.9330	0.0151	*	47618.923	0.026	(^{4}F) 4s $^3F_3$	-	(^{2}H) 4p $^3G_4$
8.0	8	322	47621.2885	0.0204	*	47621.279	0.022	(^{4}G) 4s $^3G_4$	-	(^{4}G) 4p $^3F_4$
10.4	95	329	47656.0046	0.0030		47656.0047	0.0049	(^{4}G) 4s $^3G_5$	-	(^{4}G) 4p $^3F_4$
11.1	174	333	47660.7730	0.0029		47660.7730	0.0048	(^{4}G) 4s $^3G_5$	-	(^{4}G) 4p $^3H_6$
8.2	13	405	47684.8350	0.0156		47684.8442	0.0095	(^{4}D) 4s $^5D_3$	-	(^{4}P) 4p $^5D_4$
7.5	6	481	47701.7604	0.0391		47701.804	0.019	(a^2D) 4s $^1D_2$	-	(a^2F) 4p $^3G_3$
6.5	4	295	47703.7307	0.0374		47703.723	0.025	(^{4}F) 4s $^3F_3$	-	(^{2}H) 4p $^3G_3$
6.3	3	321	47709.9109	0.1032		47709.874	0.039	(a^2F) 4s $^3F_2$	-	(a^2D) 4p $^3F_3$
6.9	4	206	47751.4453	0.0244	*	47751.45	0.11	(^{4}D) 4s $^3D_2$	-	(^{4}D) 4p $^3D_3$
8.5	13	228	47764.1047	0.0092	*	47764.077	0.07	(^{4}F) 4s $^3F_2$	-	(^{2}H) 4p $^3G_3$
6.5	3	348	47797.8637	0.0522	*	47797.529	0.087	(^{4}F) 4s $^5F_1$	-	(a^2D) 4p $^1D_2$
9.0	34	428	47801.3704	0.0076		47801.3711	0.0094	(^{4}D) 4s $^3D_2$	-	(^{4}D) 4p $^3D_2$

Fe III Classified FTS linelist continued

ln (EW)	SNR	FWHM	σ_{obs} (cm^{-1})	Unc. (cm^{-1})		σ_{Ritz} (cm^{-1})	Unc. (cm^{-1})	Energy Levels		
9.1	36	437	47825.8620	0.0075		47825.8552	0.0078	(^{4}D) 4s ^{5}D$_4$	-	(^{4}P) 4p ^{5}D$_4$
10.9	138	343	47828.2127	0.0029	*	47827.69	0.3	(^{4}G) 4s ^{3}G$_4$	-	(^{4}G) 4p ^{3}H$_5$
10.9	138	343	47828.2127	0.0029	*	47828.328	0.079	(^{4}D) 4s ^{3}D$_1$	-	(^{4}D) 4p ^{3}D$_2$
8.9	29	435	47830.3435	0.0086		47830.3357	0.0093	(a^{2}G) 4s ^{3}G$_3$	-	(^{2}H) 4p ^{3}H$_4$
7.5	7	256	47852.4572	0.0194	*	47852.413	0.079	(^{4}D) 4s ^{3}D$_2$	-	(^{4}D) 4p ^{3}D$_1$
7.9	9	416	47863.0000	0.0235	*	47862.42	0.3	(^{4}G) 4s ^{3}G$_5$	-	(^{4}G) 4p ^{3}H$_5$
8.7	16	357	47879.3708	0.0117		47879.370	0.014	(^{4}D) 4s ^{3}D$_1$	-	(^{4}D) 4p ^{3}D$_1$
9.7	41	315	47897.0537	0.0045	*	47897.01	0.11	(^{4}D) 4s ^{3}D$_3$	-	(^{4}D) 4p ^{3}D$_3$
7.9	4	376	47926.8370	0.0442	*	47926.607	0.099	(b^{2}F) 4s ^{1}F$_3$	-	(b^{2}F) 4p ^{3}F$_4$
8.1	15	379	47946.9363	0.0136		47946.935	0.015	(^{4}D) 4s ^{3}D$_3$	-	(^{4}D) 4p ^{3}D$_2$
7.3	9	298	47957.2871	0.0165		47957.286	0.018	(^{4}G) 4s ^{3}G$_4$	-	(^{4}G) 4p ^{3}H$_4$
10.6	110	323	47960.9256	0.0029		47960.9254	0.0048	(^{4}G) 4s ^{3}G$_3$	-	(^{4}G) 4p ^{3}H$_4$
7.9	9	485	47963.8296	0.0272		47963.830	0.029	(^{2}P) 4s ^{3}P$_1$	-	(^{2}P) 4p ^{3}P$_1$
8.7	27	424	47979.8203	0.0091	*	47979.804	0.014	(a^{2}G) 4s ^{3}G$_4$	-	(^{2}H) 4p ^{3}H$_5$
9.7	33	356	48056.0034	0.0059	*	48056.36	0.11	(b^{2}F) 4s ^{3}F$_2$	-	(^{4}F) 4p ^{3}D$_1$
6.4	5	263	48077.7988	0.0541		48077.783	0.039	(b^{2}F) 4s ^{3}F$_4$	-	(^{4}F) 4p ^{3}D$_3$

Fe III Classified FTS linelist continued

ln (EW)	SNR	FWHM	σ_{obs} (cm^{-1})	Unc. (cm^{-1})		σ_{Ritz} (cm^{-1})	Unc. (cm^{-1})	Energy Levels		
11.7	291	348	48084.7519	0.0030		48084.7518	0.0049	(^{6}S) 4s $^5S_2$	-	(^{6}S) 4p $^5P_3$
6.6	5	345	48194.9973	0.0734	*	48195.068	0.022	(a^{2}G) 4s $^3G_5$	-	(^{2}H) 4p $^3G_4$
9.8	43	325	48280.7773	0.0045		48280.7772	0.0064	(^{2}I) 4s $^1I_6$	-	(^{2}I) 4p $^1H_5$
11.3	186	362	48334.4927	0.0030		48334.4928	0.0049	(^{6}S) 4s $^5S_2$	-	(^{6}S) 4p $^5P_2$
8.7	32	429	48356.3761	0.0080	*	48356.401	0.024	(a^{2}G) 4s $^3G_5$	-	(^{2}H) 4p $^3H_6$
8.9	13	498	48403.5356	0.0393	*	48404.155	0.019	(a^{2}G) 4s $^3G_4$	-	(^{2}H) 4p $^3G_3$
10.0	55	325	48486.5985	0.0038		48486.5986	0.0057	(^{4}D) 4s $^3D_3$	-	(^{4}D) 4p $^3F_4$
10.8	108	359	48491.3696	0.0030		48491.3694	0.0049	(^{6}S) 4s $^5S_2$	-	(^{6}S) 4p $^5P_1$
9.7	39	341	48535.4085	0.0050		48535.4084	0.0069	(^{4}D) 4s $^3D_2$	-	(^{4}D) 4p $^3F_3$
10.5	92	336	48561.7536	0.0030		48561.7536	0.0049	(^{2}I) 4s $^1I_6$	-	(^{2}I) 4p $^1K_7$
7.4	6	159	48570.2525	0.0133	*	48570.238	0.079	(^{4}D) 4s $^3D_2$	-	(^{4}D) 4p $^3F_2$
8.5	25	409	48576.8191	0.0094		48576.8181	0.011	(b^{2}F) 4s $^1F_3$	-	(b^{2}F) 4p $^1D_2$
9.4	59	442	48597.1950	0.0058		48597.1949	0.0077	(^{4}D) 4s $^3D_1$	-	(^{4}D) 4p $^3F_2$
9.9	45	330	48618.6551	0.0044	*	48618.789	0.088	(^{4}P) 4s $^3P_2$	-	(^{4}P) 4p $^3D_3$
9.1	48	414	48625.6246	0.0062		48625.6215	0.0077	(a^{2}F) 4s $^3F_4$	-	(a^{2}D) 4p $^3F_4$
7.3	8	441	48658.1936	0.0561	*	48658.218	0.049	(c^{2}D) 4s $^1D_2$	-	(c^{2}D) 4p $^3F_3$

Fe III Classified FTS linelist continued

ln (EW)	SNR	FWHM	σ_{obs} (cm^{-1})	Unc. (cm^{-1})		σ_{Ritz} (cm^{-1})	Unc. (cm^{-1})	Energy Levels		
7.3	8	441	48658.1936	0.0561	*	48658.183	0.043	(b^2F) 4s $^3F_4$	-	(^{4}F) 4p $^3F_4$
7.3	7	483	48680.9755	0.0711		48680.972	0.018	(^{4}D) 4s $^3D_3$	-	(^{4}D) 4p $^3F_3$
7.4	9	442	48710.6252	0.0263	*	48710.696	0.039	(a^2F) 4s $^1F_3$	-	(a^2F) 4p $^3F_4$
8.7	27	443	48747.0063	0.0092		48747.0143	0.0087	(^{4}D) 4s $^5D_4$	-	(^{4}P) 4p $^5P_3$
9.0	42	426	48779.0825	0.0067	*	48779.134	0.041	(^{4}P) 4s $^3P_1$	-	(^{4}P) 4p $^3D_2$
8.8	35	447	48863.8589	0.0078		48863.8657	0.0089	(^{2}H) 4s $^3H_4$	-	(^{2}H) 4p $^3H_4$
6.6	5	371	48883.5021	0.0825	*	48883.562	0.012	(^{4}D) 4s $^5D_2$	-	(^{4}P) 4p $^5P_2$
8.0	16	381	48884.6198	0.0126		48884.6188	0.011	(^{4}D) 4s $^5D_3$	-	(^{4}P) 4p $^5P_2$
6.4	5	308	48894.6492	0.0656	*	48894.797	0.018	(a^2F) 4s $^1F_3$	-	(a^2F) 4p $^3F_3$
8.4	21	460	48900.3552	0.0118		48900.355	0.014	(^{4}P) 4s $^3P_2$	-	(^{4}P) 4p $^3D_2$
7.1	8	337	48920.1695	0.0207	*	48919.97	0.13	(b^2F) 4s $^3F_3$	-	(^{4}F) 4p $^3F_3$
6.8	4	547	48924.2504	0.1401	*	48923.72	0.13	(b^2F) 4s $^3F_4$	-	(^{4}F) 4p $^3F_3$
8.7	11	328	48990.6286	0.0154		48990.636	0.016	(^{4}F) 4s $^3F_4$	-	(^{4}F) 4p $^3G_5$
7.9	14	432	48993.9143	0.0158		48993.918	0.016	(^{4}P) 4s $^3P_1$	-	(^{4}P) 4p $^3D_1$
6.9	6	431	49029.7906	0.0750		49029.817	0.016	(^{4}D) 4s $^5D_2$	-	(^{4}P) 4p $^5P_1$
7.9	14	405	49033.9890	0.0155		49033.990	0.017	(a^2D) 4s $^3D_2$	-	(a^2D) 4p $^1D_2$

Fe III Classified FTS linelist continued

ln (EW)	SNR	FWHM	σ_{obs} (cm^{-1})	Unc. (cm^{-1})		σ_{Ritz} (cm^{-1})	Unc. (cm^{-1})	Energy Levels		
7.0	5	500	49036.7229	0.0912	*	49036.722	0.024	(^{4}F) 4s ^{3}F$_4$	-	(^{2}H) 4p ^{3}I$_5$
7.8	13	449	49049.4839	0.0350		49049.456	0.02	(^{4}P) 4s ^{3}P$_1$	-	(^{4}D) 4p ^{5}D$_2$
7.5	4	343	49062.0381	0.0437	*	49062.025	0.02	(a^{2}D) 4s ^{3}D$_3$	-	(a^{2}D) 4p ^{1}D$_2$
9.3	58	443	49068.6900	0.0059		49068.6899	0.0079	(^{2}H) 4s ^{3}H$_5$	-	(^{2}H) 4p ^{3}H$_5$
7.6	4	242	49072.2874	0.0289	*	49072.300	0.025	(^{4}P) 4s ^{3}P$_1$	-	(^{4}D) 4p ^{5}D$_1$
7.1	5	578	49079.3601	0.1084	*	49079.489	0.019	(^{4}D) 4s ^{5}D$_1$	-	(^{4}P) 4p ^{5}P$_1$
7.6	11	365	49099.4785	0.0174	*	49099.492	0.018	(^{2}H) 4s ^{3}H$_4$	-	(^{2}H) 4p ^{3}H$_5$
7.5	10	448	49101.4811	0.0221	*	49101.479	0.097	(^{4}P) 4s ^{3}P$_2$	-	(^{4}D) 4p ^{5}D$_3$
7.1	3	318	49120.1518	0.0564	*	49120.083	0.023	(^{4}D) 4s ^{5}D$_0$	-	(^{4}P) 4p ^{5}P$_1$
7.1	4	175	49121.8239	0.0248	*	49121.724	0.1	(b^{2}F) 4s ^{3}F$_2$	-	(^{4}F) 4p ^{3}F$_2$
8.8	36	434	49131.2568	0.0075		49131.2561	0.0093	(^{2}H) 4s ^{3}H$_6$	-	(^{2}H) 4p ^{3}G$_5$
8.3	20	493	49140.9851	0.0132		49140.988	0.015	(^{4}F) 4s ^{3}F$_3$	-	(^{4}F) 4p ^{3}G$_4$
7.2	6	555	49196.6669	0.0939	*	49196.160	0.074	(^{4}F) 4s ^{3}F$_3$	-	(^{4}F) 4p ^{3}G$_3$
7.9	3	437	49226.3694	0.0744	*	49226.66	0.2	(^{2}S) 4s ^{1}S$_0$	-	(^{2}S) 4p ^{1}P$_1$
7.6	10	495	49256.5146	0.0242		49256.514	0.026	(^{4}F) 4s ^{3}F$_2$	-	(^{4}F) 4p ^{3}G$_3$
6.2	3	371	49280.0938	0.1124	*	49279.70	0.52	(^{2}P) 4s ^{1}P$_1$	-	(^{2}P) 4p ^{1}D$_2$

Fe III Classified FTS linelist continued

ln (EW)	SNR	FWHM	σ_{obs} (cm^{-1})	Unc. (cm^{-1})		σ_{Ritz} (cm^{-1})	Unc. (cm^{-1})	Energy Levels		
9.3	61	451	49341.1383	0.0058	*	49341.171	0.023	(^{2}H) 4s ^{3}H$_6$	-	(^{2}H) 4p ^{3}H$_6$
8.7	33	438	49352.8698	0.0079		49352.8714	0.0096	(a^{2}D) 4s ^{1}D$_2$	-	(a^{2}D) 4p ^{1}F$_3$
7.2	8	302	49354.5159	0.0196		49354.503	0.019	(^{4}F) 4s ^{3}F$_4$	-	(a^{2}G) 4p ^{1}G$_4$
7.1	7	362	49359.6446	0.0271		49359.660	0.018	(^{2}H) 4s ^{3}H$_5$	-	(^{2}H) 4p ^{3}G$_5$
6.1	3	384	49395.5682	0.1345		49395.587	0.032	(a^{2}G) 4s ^{1}G$_4$	-	(a^{2}G) 4p ^{3}H$_5$
8.2	22	422	49408.2409	0.0106		49408.242	0.013	(^{2}H) 4s ^{3}H$_5$	-	(^{2}H) 4p ^{3}G$_4$
6.7	5	440	49439.1207	0.0935	*	49439.044	0.02	(^{2}H) 4s ^{3}H$_4$	-	(^{2}H) 4p ^{3}G$_4$
8.2	19	451	49523.8416	0.0125		49523.844	0.014	(^{2}H) 4s ^{3}H$_4$	-	(^{2}H) 4p ^{3}G$_3$
8.2	21	437	49555.1714	0.0212	*	49555.199	0.019	(a^{2}G) 4s ^{3}G$_5$	-	(^{4}F) 4p ^{3}G$_5$
8.0	16	442	49569.5735	0.0144		49569.575	0.016	(^{2}H) 4s ^{3}H$_5$	-	(^{2}H) 4p ^{3}H$_6$
7.0	5	131	49625.9842	0.0125	*	49625.922	0.037	(a^{2}F) 4s ^{1}F$_3$	-	(^{2}H) 4p ^{3}H$_4$
9.0	42	446	49668.8399	0.0069		49668.8408	0.0089	(a^{2}D) 4s ^{3}D$_2$	-	(a^{2}D) 4p ^{3}F$_3$
6.0	3	304	49679.5010	0.0930	*	49679.486	0.024	(a^{2}G) 4s ^{3}G$_4$	-	(^{4}F) 4p ^{3}G$_5$
8.3	22	407	49688.3330	0.0104		49688.334	0.012	(a^{2}F) 4s ^{3}F$_3$	-	(a^{2}F) 4p ^{1}G$_4$
8.8	36	456	49696.8768	0.0078		49696.8762	0.0097	(a^{2}D) 4s ^{3}D$_3$	-	(a^{2}D) 4p ^{3}F$_3$
10.5	176	475	49717.9344	0.0051	*	49717.133	0.027	(a^{2}G) 4s ^{3}G$_5$	-	(^{4}F) 4p ^{3}G$_4$

Fe III Classified FTS linelist continued

ln (EW)	SNR	FWHM	σ_{obs} (cm^{-1})	Unc. (cm^{-1})		σ_{Ritz} (cm^{-1})	Unc. (cm^{-1})	Energy Levels		
8.2	20	438	49725.5699	0.0117		49725.572	0.013	(a^2G) 4s $^3G_4$	-	(^{2}H) 4p $^3I_5$
8.8	36	470	49772.9742	0.0079		49772.9741	0.0099	(^{4}P) 4s $^5P_1$	-	(^{4}P) 4p $^5D_0$
9.2	54	477	49788.1992	0.0063		49788.2014	0.0076	(^{4}P) 4s $^5P_1$	-	(^{4}P) 4p $^5D_1$
8.4	9	209	49827.5648	0.0121	*	49827.584	0.019	(^{4}P) 4s $^5P_1$	-	(^{4}P) 4p $^5D_2$
8.2	20	437	49841.3861	0.0120	*	49841.420	0.027	(a^2G) 4s $^3G_4$	-	(^{4}F) 4p $^3G_4$
6.7	5	409	49847.7822	0.0794		49847.817	0.022	(^{4}P) 4s $^3P_1$	-	(^{4}D) 4p $^5P_2$
8.7	33	474	49856.9685	0.0086		49856.9643	0.0087	(^{4}P) 4s $^5P_2$	-	(^{4}P) 4p $^5D_1$
6.6	4	113	49859.3115	0.0143	*	49859.388	0.051	(^{4}D) 4s $^5D_2$	-	(^{4}P) 4p $^3P_2$
7.0	7	381	49860.4265	0.0534		49860.445	0.05	(^{4}D) 4s $^5D_3$	-	(^{4}P) 4p $^3P_2$
9.4	61	475	49896.3845	0.0060	*	49896.592	0.073	(a^2G) 4s $^3G_4$	-	(^{4}F) 4p $^3G_3$
9.4	61	475	49896.3845	0.0060	*	49896.347	0.019	(^{4}P) 4s $^5P_2$	-	(^{4}P) 4p $^5D_2$
7.3	8	444	49919.0400	0.0271		49919.066	0.021	(a^2G) 4s $^3G_5$	-	(a^2G) 4p $^1G_4$
8.4	23	472	49921.9426	0.0112		49921.943	0.013	(b^2D) 4s $^1D_2$	-	(b^2D) 4p $^1F_3$
8.9	38	431	49938.0878	0.0072	*	49938.093	0.019	(a^2G) 4s $^3G_5$	-	(^{2}H) 4p $^3I_6$
7.4	9	454	49949.6830	0.0260		49949.661	0.02	(a^2D) 4s $^1D_2$	-	(a^2F) 4p $^3F_3$
8.4	23	442	49952.2312	0.0106		49952.2294	0.0086	(^{4}P) 4s $^5P_2$	-	(^{4}G) 4p $^5F_3$

Fe III Classified FTS linelist continued

ln (EW)	SNR	FWHM	σ_{obs} (cm^{-1})	Unc. (cm^{-1})		σ_{Ritz} (cm^{-1})	Unc. (cm^{-1})	Energy Levels		
8.4	8	276	49954.6044	0.0179		49954.617	0.018	(^{4}P) 4s ^{5}P$_3$	-	(^{4}P) 4p ^{5}D$_2$
8.2	16	485	49982.7440	0.0156	*	49982.751	0.073	(a^{2}G) 4s ^{3}G$_3$	-	(^{4}F) 4p ^{3}G$_3$
7.9	13	368	50002.5649	0.0145		50002.5550	0.0088	(^{4}P) 4s ^{5}P$_3$	-	(^{4}G) 4p ^{5}F$_4$
8.7	35	433	50010.5037	0.0076	*	50010.4993	0.0094	(^{4}P) 4s ^{5}P$_3$	-	(^{4}G) 4p ^{5}F$_3$
6.7	4	457	50022.5005	0.1027	*	50022.412	0.04	(^{4}P) 4s ^{3}P$_2$	-	(^{4}D) 4p ^{5}P$_3$
10.5	194	470	50089.2751	0.0051		50089.2746	0.0071	(^{4}G) 4s ^{5}G$_2$	-	(^{4}G) 4p ^{5}G$_2$
8.6	40	357	50089.7541	0.0064	*	50089.694	0.064	(^{4}G) 4s ^{5}G$_3$	-	(^{4}G) 4p ^{5}G$_2$
7.2	3	238	50110.4682	0.0361	*	50110.570	0.064	(^{4}G) 4s ^{5}G$_2$	-	(^{4}G) 4p ^{5}G$_3$
10.7	75	350	50110.9890	0.0034		50110.9893	0.0053	(^{4}G) 4s ^{5}G$_3$	-	(^{4}G) 4p ^{5}G$_3$
9.6	77	453	50118.3865	0.0054		50118.3857	0.0069	(^{4}G) 4s ^{5}G$_4$	-	(^{4}G) 4p ^{5}G$_3$
5.8	3	291	50129.4312	0.0505	*	50129.512	0.029	(a^{2}G) 4s ^{3}G$_3$	-	(a^{2}G) 4p ^{1}G$_4$
7.4	10	398	50140.9238	0.0386	*	50140.9060	0.0083	(^{4}G) 4s ^{5}G$_3$	-	(^{4}G) 4p ^{5}G$_4$
11.0	100	353	50148.3021	0.0031		50148.3024	0.005	(^{4}G) 4s ^{5}G$_4$	-	(^{4}G) 4p ^{5}G$_4$
9.7	85	452	50168.7312	0.0053		50168.7299	0.0068	(^{4}G) 4s ^{5}G$_5$	-	(^{4}G) 4p ^{5}G$_4$
9.2	53	448	50178.9011	0.0062		50178.8999	0.0081	(a^{2}F) 4s ^{3}F$_2$	-	(a^{2}F) 4p ^{3}G$_3$
6.6	4	487	50189.8816	0.1271		50189.9001	0.0081	(^{4}G) 4s ^{5}G$_4$	-	(^{4}G) 4p ^{5}G$_5$

Fe III Classified FTS linelist continued

ln (EW)	SNR	FWHM	σ_{obs} (cm^{-1})	Unc. (cm^{-1})		σ_{Ritz} (cm^{-1})	Unc. (cm^{-1})	Energy Levels		
10.0	127	445	50195.5518	0.0051		50195.5519	0.0071	(^{2}I) 4s $^3I_6$	-	(^{2}I) 4p $^3K_7$
10.1	122	456	50200.1252	0.0051	*	50200.125	0.014	(^{2}I) 4s $^3I_7$	-	(^{2}I) 4p $^3K_7$
10.1	122	456	50200.1252	0.0051	*	50200.645	0.038	(a^{2}F) 4s $^3F_4$	-	(a^{2}F) 4p $^1G_4$
6.8	7	309	50209.0702	0.0426	*	50209.07	0.1	(^{4}F) 4s $^3F_3$	-	(a^{2}G) 4p $^3F_3$
11.3	136	353	50210.3269	0.0031		50210.3276	0.005	(^{4}G) 4s $^5G_5$	-	(^{4}G) 4p $^5G_5$
7.4	3	222	50220.7241	0.0377	*	50220.65	0.1	(^{4}F) 4s $^3F_4$	-	(a^{2}G) 4p $^3F_3$
9.4	64	452	50251.4006	0.0057		50251.3989	0.007	(^{4}G) 4s $^5G_6$	-	(^{4}G) 4p $^5G_5$
7.7	4	344	50252.4911	0.0464	*	50252.70	0.13	(^{2}S) 4s $^3S_1$	-	(^{2}S) 4p $^3P_1$
7.1	3	456	50275.7993	0.1793	*	50276.258	0.04	(a^{2}D) 4s $^3D_3$	-	(^{2}I) 4p $^3H_4$
8.4	26	404	50306.3346	0.0090		50306.3341	0.0086	(^{4}P) 4s $^5P_1$	-	(^{4}P) 4p $^5S_2$
11.6	181	353	50314.1304	0.0031		50314.1304	0.0051	(^{4}G) 4s $^5G_6$	-	(^{4}G) 4p $^5G_6$
6.8	8	284	50327.0888	0.0189	*	50326.957	0.071	(^{4}F) 4s $^3F_2$	-	(a^{2}G) 4p $^3F_2$
6.3	3	123	50371.0168	0.0242	*	50371.026	0.03	(a^{2}G) 4s $^1G_4$	-	(a^{2}G) 4p $^3G_5$
8.6	26	465	50375.0963	0.0099		50375.0970	0.0081	(^{4}P) 4s $^5P_2$	-	(^{4}P) 4p $^5S_2$
9.9	109	443	50395.6618	0.0051		50395.6610	0.0068	(^{2}I) 4s $^3I_5$	-	(^{2}I) 4p $^3I_5$
9.7	81	458	50402.2706	0.0054		50402.2732	0.0071	(a^{2}D) 4s $^3D_3$	-	(a^{2}D) 4p $^3F_4$

Fe III Classified FTS linelist continued

ln (EW)	SNR	FWHM	σ_{obs} (cm^{-1})	Unc. (cm^{-1})		σ_{Ritz} (cm^{-1})	Unc. (cm^{-1})	Energy Levels		
8.0	17	422	50411.3903	0.0133		50411.3955	0.0096	(^{2}I) 4s $^3I_6$	-	(^{2}I) 4p $^3I_5$
6.1	4	295	50424.9115	0.0798		50424.966	0.063	(a^{2}F) 4s $^3F_3$	-	(^{4}F) 4p $^5G_3$
9.7	83	451	50433.3669	0.0053		50433.3669	0.0067	(^{4}P) 4s $^5P_3$	-	(^{4}P) 4p $^5S_2$
8.8	35	475	50451.9236	0.0082		50451.9238	0.01	(^{4}P) 4s $^5P_2$	-	(^{4}G) 4p $^5F_2$
7.5	9	501	50494.9505	0.0279	*	50494.897	0.041	(b^{2}F) 4s $^3F_4$	-	(a^{2}G) 4p $^3G_5$
6.7	3	283	50530.3033	0.0474	*	50530.239	0.036	(^{4}F) 4s $^3F_4$	-	(a^{2}G) 4p $^3F_4$
7.6	10	457	50539.9886	0.0225		50539.969	0.019	(^{2}H) 4s $^3H_6$	-	(^{4}F) 4p $^3G_5$
8.6	28	423	50545.4351	0.0089		50545.4392	0.0083	(^{4}P) 4s $^5P_2$	-	(^{4}P) 4p $^5D_3$
9.3	60	460	50603.7038	0.0060	*	50603.7091	0.0093	(^{4}P) 4s $^5P_3$	-	(^{4}P) 4p $^5D_3$
9.3	60	460	50603.7038	0.0060	*	50603.674	0.037	(a^{2}G) 4s $^1G_4$	-	(a^{2}G) 4p $^3G_3$
5.2	2	186	50669.3269	0.0397	*	50669.205	0.078	(a^{2}G) 4s $^3G_4$	-	(a^{2}F) 4p $^1F_3$
7.2	7	476	50693.3859	0.0335	*	50693.382	0.029	(b^{2}F) 4s $^3F_3$	-	(a^{2}G) 4p $^3G_4$
6.9	6	398	50703.2867	0.0669	*	50703.323	0.036	(b^{2}F) 4s $^3F_2$	-	(a^{2}G) 4p $^3G_3$
6.9	6	398	50703.2867	0.0669	*	50703.228	0.033	(a^{2}G) 4p $^3H_5$	-	(^{6}S) 5d $^5D_4$
8.2	9	310	50829.6094	0.0182		50829.610	0.02	(b^{2}G) 4s $^1G_4$	-	(b^{2}G) 4p $^1H_5$
9.6	77	444	50845.2609	0.0054		50845.2606	0.0073	(^{2}H) 4s $^3H_4$	-	(^{2}H) 4p $^3I_5$

Fe III Classified FTS linelist continued

ln (EW)	SNR	FWHM	σ_{obs} (cm^{-1})	Unc. (cm^{-1})		σ_{Ritz} (cm^{-1})	Unc. (cm^{-1})	Energy Levels		
8.0	15	483	50859.4080	0.0171	*	50859.333	0.021	(^{4}D) 4s ^{5}D$_2$	-	(^{4}D) 4p ^{5}F$_1$
7.6	4	272	50862.5769	0.0325	*	50862.27	0.13	(^{2}S) 4s ^{3}S$_1$	-	(^{2}S) 4p ^{3}P$_2$
9.1	44	427	50882.3594	0.0067		50882.3591	0.0087	(a^{2}F) 4s ^{3}F$_3$	-	(a^{2}F) 4p ^{3}G$_4$
9.4	64	456	50896.1007	0.0058		50896.1021	0.0074	(^{2}I) 4s ^{3}I$_5$	-	(^{2}I) 4p ^{3}I$_6$
8.8	27	512	50909.0344	0.0104	*	50908.966	0.041	(a^{2}F) 4s ^{3}F$_2$	-	(a^{2}D) 4p ^{3}D$_2$
8.8	27	512	50909.0344	0.0104	*	50909.005	0.023	(^{4}D) 4s ^{5}D$_1$	-	(^{4}D) 4p ^{5}F$_1$
7.8	15	394	50909.6309	0.0141	*	50909.51	0.1	(a^{2}G) 4s ^{3}G$_4$	-	(a^{2}G) 4p ^{3}F$_3$
9.7	83	453	50911.8366	0.0053		50911.8366	0.0069	(^{2}I) 4s ^{3}I$_6$	-	(^{2}I) 4p ^{3}I$_6$
8.3	18	512	50915.0280	0.0149	*	50915.040	0.079	(^{4}F) 4s ^{3}F$_3$	-	(^{4}F) 4p ^{3}D$_2$
8.3	18	438	50916.4165	0.0132		50916.409	0.013	(^{2}I) 4s ^{3}I$_7$	-	(^{2}I) 4p ^{3}I$_6$
7.2	7	447	50930.3523	0.0658	*	50930.307	0.027	(^{2}H) 4s ^{3}H$_5$	-	(^{4}F) 4p ^{3}G$_4$
6.5	4	430	50937.3015	0.1210		50937.277	0.065	(a^{2}F) 4s ^{3}F$_4$	-	(^{4}F) 4p ^{5}G$_3$
6.4	3	219	50939.7030	0.0393	*	50939.666	0.045	(b^{2}F) 4s ^{3}F$_3$	-	(b^{2}F) 4p ^{1}G$_4$
8.4	20	506	50943.4176	0.0137		50943.417	0.015	(b^{2}F) 4s ^{3}F$_4$	-	(b^{2}F) 4p ^{1}G$_4$
8.7	30	440	50949.5994	0.0087		50949.5987	0.011	(^{4}D) 4s ^{5}D$_0$	-	(^{4}D) 4p ^{5}F$_1$
6.4	3	437	50961.2360	0.1272	*	50961.109	0.027	(^{2}H) 4s ^{3}H$_4$	-	(^{4}F) 4p ^{3}G$_4$

Fe III Classified FTS linelist continued

ln (EW)	SNR	FWHM	σ_{obs} (cm^{-1})	Unc. (cm^{-1})		σ_{Ritz} (cm^{-1})	Unc. (cm^{-1})	Energy Levels		
6.8	6	352	50975.3699	0.0566		50975.394	0.055	(^{4}F) 4s ^{3}F$_2$	-	(^{4}F) 4p ^{3}D$_2$
7.2	8	372	50982.4106	0.0251		50982.403	0.022	(^{4}F) 4s ^{3}F$_3$	-	(^{4}F) 4p ^{3}D$_3$
9.1	42	472	50988.0554	0.0073		50988.0555	0.0092	(^{4}D) 4s ^{5}D$_2$	-	(^{4}D) 4p ^{5}F$_2$
8.4	22	490	50993.9827	0.0118		50993.985	0.013	(^{4}F) 4s ^{3}F$_4$	-	(^{4}F) 4p ^{3}D$_3$
11.0	96	352	51011.8354	0.0032		51011.8354	0.0052	(^{2}I) 4s ^{3}I$_7$	-	(^{2}I) 4p ^{3}K$_8$
8.7	10	418	51016.6899	0.0218	*	51016.281	0.072	(^{2}H) 4s ^{3}H$_4$	-	(^{4}F) 4p ^{3}G$_3$
9.5	63	459	51037.7274	0.0059		51037.7276	0.0079	(^{4}D) 4s ^{5}D$_1$	-	(^{4}D) 4p ^{5}F$_2$
7.9	6	166	51045.6632	0.0137	*	51045.56	0.13	(^{4}F) 4s ^{3}F$_2$	-	(^{4}F) 4p ^{3}D$_1$
8.0	16	464	51053.1987	0.0156		51053.194	0.017	(a^{2}G) 4s ^{3}G$_3$	-	(a^{2}G) 4p ^{3}F$_2$
10.5	93	393	51056.9453	0.0037		51056.9462	0.0054	(^{4}P) 4s ^{5}P$_3$	-	(^{4}P) 4p ^{5}D$_4$
9.0	38	458	51073.9350	0.0076		51073.9348	0.0096	(a^{2}G) 4s ^{1}G$_4$	-	(a^{2}G) 4p ^{1}H$_5$
7.9	5	425	51088.6135	0.0390	*	51088.579	0.08	(b^{2}F) 4s ^{3}F$_2$	-	(b^{2}F) 4p ^{3}F$_2$
7.7	7	356	51094.8001	0.0243		51094.801	0.036	(c^{2}D) 4s ^{1}D$_2$	-	(c^{2}D) 4p ^{1}D$_2$
7.7	7	356	51094.8001	0.0243		51094.802	0.033	(a^{2}G) 4s ^{3}G$_5$	-	(a^{2}G) 4p ^{3}F$_4$
9.7	84	442	51151.2659	0.0053		51151.2658	0.0073	(^{2}H) 4s ^{3}H$_5$	-	(^{2}H) 4p ^{3}I$_6$
8.6	12	479	51156.8255	0.0200	*	51156.865	0.013	(a^{2}F) 4s ^{3}F$_4$	-	(a^{2}F) 4p ^{3}G$_5$

Fe III Classified FTS linelist continued

ln (EW)	SNR	FWHM	σ_{obs} (cm^{-1})	Unc. (cm^{-1})		σ_{Ritz} (cm^{-1})	Unc. (cm^{-1})	Energy Levels		
6.9	5	237	51157.3011	0.0255	*	51157.444	0.04	(b^2F) 4s $^3F_2$	-	(b^2F) 4p $^3F_3$
9.9	60	406	51170.6399	0.0046		51170.6409	0.0064	(^{4}D) 4s $^5D_2$	-	(^{4}D) 4p $^5F_3$
8.8	36	435	51171.7000	0.0077		51171.6980	0.0087	(^{4}D) 4s $^5D_3$	-	(^{4}D) 4p $^5F_3$
8.0	8	318	51177.9164	0.0190		51177.915	0.019	(b^2F) 4s $^3F_3$	-	(b^2F) 4p $^3F_3$
6.3	5	260	51181.6481	0.0277	*	51181.666	0.045	(b^2F) 4s $^3F_4$	-	(b^2F) 4p $^3F_3$
10.0	99	470	51190.2028	0.0052	*	51190.11	0.24	(^{2}I) 4s $^3I_6$	-	(^{2}I) 4p $^3I_7$
6.5	3	267	51190.7227	0.0447	*	51190.62	0.12	(^{4}G) 4s $^3G_4$	-	(^{4}G) 4p $^3G_3$
9.6	35	377	51194.3645	0.0061	*	51194.26	0.12	(^{4}G) 4s $^3G_3$	-	(^{4}G) 4p $^3G_3$
10.0	46	365	51194.7527	0.0049	*	51194.68	0.24	(^{2}I) 4s $^3I_7$	-	(^{2}I) 4p $^3I_7$
7.8	8	708	51197.9326	0.0872	*	51198.601	0.038	(^{4}F) 4s $^5F_4$	-	(a^2F) 4p $^1G_4$
7.8	8	708	51197.9326	0.0872	*	51197.806	0.048	(b^2F) 4s $^3F_4$	-	(a^2G) 4p $^1H_5$
9.9	57	426	51212.2412	0.0049		51212.2411	0.0069	(^{4}G) 4s $^3G_4$	-	(^{4}G) 4p $^3G_4$
7.9	9	691	51215.7992	0.0793	*	51215.881	0.019	(^{4}G) 4s $^3G_3$	-	(^{4}G) 4p $^3G_4$
7.1	5	621	51219.2214	0.1373	*	51219.089	0.037	(a^2G) 4s $^3G_4$	-	(a^2G) 4p $^3F_4$
7.2	5	245	51220.6442	0.0258	*	51220.620	0.022	(^{4}G) 4s $^3G_4$	-	(^{4}G) 4p $^3G_5$
6.6	6	258	51246.9723	0.0207		51246.967	0.021	(^{4}G) 4s $^3G_5$	-	(^{4}G) 4p $^3G_4$

Fe III Classified FTS linelist continued

ln (EW)	SNR	FWHM	σ_{obs} (cm^{-1})	Unc. (cm^{-1})		σ_{Ritz} (cm^{-1})	Unc. (cm^{-1})	Energy Levels		
10.2	76	418	51255.3460	0.0042		51255.3461	0.0063	(^{4}G) 4s ^{3}G$_5$	-	(^{4}G) 4p ^{3}G$_5$
10.2	81	417	51272.9580	0.0041		51272.9580	0.0062	(^{2}H) 4s ^{3}H$_6$	-	(^{2}H) 4p ^{3}I$_7$
7.7	12	434	51290.8704	0.0185		51290.868	0.02	(^{4}F) 4s ^{5}F$_1$	-	(^{4}F) 4p ^{5}G$_2$
7.2	7	453	51296.2411	0.0652	*	51296.23	0.14	(^{4}D) 4s ^{3}D$_1$	-	(^{4}D) 4p ^{3}P$_0$
7.5	2	483	51305.0906	0.1210	*	51305.248	0.039	(a^{2}G) 4s ^{3}G$_3$	-	(a^{2}G) 4p ^{3}F$_4$
7.7	7	328	51327.3524	0.0233		51327.352	0.025	(b^{2}G) 4s ^{1}G$_4$	-	(b^{2}G) 4p ^{1}G$_4$
8.3	19	500	51367.1111	0.0141		51367.112	0.016	(b^{2}G) 4s ^{3}G$_3$	-	(b^{2}G) 4p ^{3}H$_4$
6.9	4	353	51378.9910	0.0487	*	51379.0	1.4	(b^{2}G) 4s ^{3}G$_4$	-	(b^{2}G) 4p ^{3}H$_4$
7.8	10	401	51394.7213	0.0198	*	51394.671	0.038	(a^{2}F) 4s ^{3}F$_4$	-	(a^{2}F) 4p ^{3}G$_4$
10.4	88	398	51404.6266	0.0038		51404.6266	0.0058	(^{4}D) 4s ^{5}D$_3$	-	(^{4}D) 4p ^{5}F$_4$
7.2	6	497	51447.4373	0.0803		51447.434	0.08	(b^{2}D) 4s ^{1}D$_2$	-	(b^{2}D) 4p ^{1}P$_1$
10.9	130	389	51453.6462	0.0035		51453.6463	0.0056	(^{4}G) 4s ^{5}G$_2$	-	(^{4}G) 4p ^{5}H$_3$
7.6	6	304	51454.1868	0.0247	*	51454.066	0.064	(^{4}G) 4s ^{5}G$_3$	-	(^{4}G) 4p ^{5}H$_3$
7.6	7	404	51455.6068	0.0299	*	51455.424	0.093	(a^{2}G) 4s ^{1}G$_4$	-	(b^{2}F) 4p ^{3}F$_4$
8.2	13	300	51503.0768	0.0122	*	51503.057	0.079	(^{4}D) 4s ^{3}D$_2$	-	(^{4}D) 4p ^{3}P$_1$
8.3	10	409	51525.8309	0.0200	*	51525.900	0.062	(a^{2}G) 4s ^{1}G$_4$	-	(a^{2}G) 4p ^{1}F$_3$

Fe III Classified FTS linelist continued

ln (EW)	SNR	FWHM	σ_{obs} (cm^{-1})	Unc. (cm^{-1})		σ_{Ritz} (cm^{-1})	Unc. (cm^{-1})	Energy Levels		
7.6	8	391	51528.0251	0.0241		51528.006	0.02	(a^2F) 4s $^3F_3$	-	(a^2D) 4p $^1F_3$
7.6	5	454	51529.9952	0.0454	*	51530.014	0.1	(^{4}D) 4s $^3D_1$	-	(^{4}D) 4p $^3P_1$
9.5	53	534	51545.7439	0.0069	*	51545.71	0.11	(a^2F) 4s $^3F_4$	-	(a^2F) 4p $^3D_3$
9.5	53	534	51545.7439	0.0069	*	51545.6376	0.011	(^{4}D) 4s $^5D_4$	-	(^{4}D) 4p $^5F_4$
8.3	16	488	51574.3872	0.0158		51574.385	0.018	(^{4}F) 4s $^3F_4$	-	(^{4}F) 4p $^3F_4$
9.8	56	414	51575.6895	0.0049		51575.6909	0.0069	(a^2F) 4s $^3F_4$	-	(^{4}F) 4p $^5G_5$
7.5	6	278	51579.5598	0.0240	*	51579.295	0.094	(b^2F) 4s $^3F_4$	-	(b^2F) 4p $^3F_4$
8.5	22	466	51599.6878	0.0114		51599.687	0.013	(b^2G) 4s $^3G_4$	-	(b^2G) 4p $^3H_5$
7.3	6	530	51614.4078	0.0929	*	51614.4	1.4	(b^2G) 4s $^3G_5$	-	(b^2G) 4p $^3H_5$
11.2	104	358	51616.7392	0.0031	*	51616.743	0.022	(^{4}G) 4s $^5G_3$	-	(^{4}G) 4p $^5H_4$
7.8	9	350	51624.1302	0.0202		51624.140	0.022	(^{4}G) 4s $^5G_4$	-	(^{4}G) 4p $^5H_4$
8.6	22	487	51631.3890	0.0118	*	51631.76	0.18	(a^2G) 4s $^3G_5$	-	(^{2}H) 4p $^1I_6$
6.4	4	326	51649.8792	0.0871	*	51649.771	0.065	(b^2F) 4s $^3F_4$	-	(a^2G) 4p $^1F_3$
10.8	133	388	51772.8558	0.0035		51772.8562	0.0056	(^{4}D) 4s $^5D_4$	-	(^{4}D) 4p $^5F_5$
11.4	128	358	51802.8240	0.0032		51802.8239	0.0053	(^{4}G) 4s $^5G_4$	-	(^{4}G) 4p $^5H_5$
7.5	8	367	51814.9242	0.0238	*	51814.924	0.019	(^{4}D) 4s $^3D_2$	-	(^{4}D) 4p $^3P_2$

Fe III Classified FTS linelist continued

ln (EW)	SNR	FWHM	σ_{obs} (cm^{-1})	Unc. (cm^{-1})		σ_{Ritz} (cm^{-1})	Unc. (cm^{-1})	Energy Levels		
7.9	8	502	51828.4687	0.0326	*	51828.34	0.13	(^{4}F) 4s $^3F_3$	-	(^{4}F) 4p $^3F_3$
7.9	11	355	51829.9646	0.0165		51829.967	0.017	(a^{2}F) 4s $^3F_2$	-	(a^{2}D) 4p $^1F_3$
6.5	4	269	51840.0504	0.0363	*	51839.93	0.13	(^{4}F) 4s $^3F_4$	-	(^{4}F) 4p $^3F_3$
8.2	10	349	51844.6042	0.0182		51844.601	0.02	(a^{2}D) 4s $^1D_2$	-	(a^{2}D) 4p $^1P_1$
8.7	22	423	51849.9125	0.0108		51849.914	0.013	(^{2}I) 4s $^3I_5$	-	(^{2}I) 4p $^1H_5$
8.3	13	337	51860.2876	0.0135		51860.288	0.015	(a^{2}F) 4s $^3F_3$	-	(a^{2}F) 4p $^3F_2$
7.9	12	357	51862.4457	0.0155	*	51862.90	0.2	(b^{2}G) 4s $^3G_5$	-	(b^{2}G) 4p $^3H_6$
7.9	12	357	51862.4457	0.0155	*	51862.45	0.11	(a^{2}F) 4s $^1F_3$	-	(a^{2}F) 4p $^1D_2$
8.8	27	441	51882.3426	0.0094		51882.3427	0.011	(a^{2}D) 4s $^3D_3$	-	(a^{2}D) 4p $^3P_2$
7.6	9	284	51896.9427	0.0166		51896.942	0.019	(b^{2}G) 4s $^3G_5$	-	(b^{2}G) 4p $^3F_4$
6.8	3	352	51902.9269	0.0621	*	51903.014	0.046	(^{4}G) 4s $^3G_3$	-	(^{4}P) 4p $^3D_2$
12.3	286	376	51912.3705	0.0032		51912.3704	0.0053	(^{6}S) 4s $^7S_3$	-	(^{6}S) 4p $^7P_2$
9.0	29	426	51919.8343	0.0080		51919.8354	0.0084	(^{4}P) 4s $^5P_2$	-	(^{4}P) 4p $^5P_3$
7.0	6	269	51925.0830	0.0210	*	51925.098	0.04	(a^{2}F) 4s $^1F_3$	-	(a^{2}G) 4p $^1G_4$
8.2	11	305	51940.7195	0.0139	*	51940.695	0.038	(a^{2}F) 4s $^3F_3$	-	(a^{2}F) 4p $^3F_4$
8.9	26	409	51960.4880	0.0084		51960.4882	0.01	(^{4}D) 4s $^3D_3$	-	(^{4}D) 4p $^3P_2$

Fe III Classified FTS linelist continued

ln (EW)	SNR	FWHM	σ_{obs} (cm^{-1})	Unc. (cm^{-1})		σ_{Ritz} (cm^{-1})	Unc. (cm^{-1})	Energy Levels		
8.3	15	440	51971.6134	0.0154		51971.614	0.017	(b^2F) 4s $^1F_3$	-	(^{2}H) 4p $^1G_4$
7.0	2	262	51977.1775	0.0627	*	51977.297	0.038	(a^2D) 4s $^3D_3$	-	(a^2F) 4p $^1G_4$
8.7	19	373	51978.1169	0.0103		51978.1053	0.0085	(^{4}P) 4s $^5P_3$	-	(^{4}P) 4p $^5P_3$
11.6	148	366	52007.5599	0.0032		52007.5599	0.0053	(^{4}G) 4s $^5G_5$	-	(^{4}G) 4p $^5H_6$
6.9	4	454	52029.2830	0.0632	*	52029.19	0.1	(^{2}H) 4s $^3H_4$	-	(a^2G) 4p $^3F_3$
7.9	8	420	52052.7543	0.0256		52052.760	0.027	(b^2D) 4s $^3D_3$	-	(b^2D) 4p $^3F_3$
7.8	9	436	52075.7039	0.0256	*	52075.94	0.11	(b^2D) 4s $^3D_2$	-	(b^2D) 4p $^3F_3$
8.8	25	429	52078.1209	0.0092		52078.1236	0.011	(^{4}F) 4s $^5F_4$	-	(^{4}F) 4p $^5G_4$
8.0	11	394	52094.7634	0.0182		52094.766	0.02	(a^2F) 4s $^3F_2$	-	(a^2F) 4p $^3D_1$
6.5	4	263	52101.2747	0.0348	*	52101.257	0.012	(^{4}F) 4s $^5F_5$	-	(^{4}F) 4p $^5G_4$
7.4	7	395	52110.9921	0.0294	*	52110.92	0.11	(^{4}F) 4s $^3F_2$	-	(^{4}F) 4p $^3F_2$
6.1	3	227	52121.8241	0.0376	*	52121.808	0.029	(a^2F) 4s $^3F_3$	-	(a^2F) 4p $^3D_2$
8.5	17	394	52124.7907	0.0119		52124.796	0.013	(a^2F) 4s $^3F_3$	-	(a^2F) 4p $^3F_3$
8.9	29	400	52129.6914	0.0076		52129.6880	0.0088	(^{4}P) 4s $^5P_1$	-	(^{4}P) 4p $^5P_2$
8.7	14	658	52138.2584	0.0244	*	52138.40	0.16	(a^2D) 4s $^3D_2$	-	(a^2D) 4p $^3P_1$
7.3	7	328	52138.9847	0.0235	*	52138.948	0.024	(a^2G) 4s $^3G_5$	-	(^{4}F) 4p $^3F_4$

Fe III Classified FTS linelist continued

ln (EW)	SNR	FWHM	σ_{obs} (cm^{-1})	Unc. (cm^{-1})		σ_{Ritz} (cm^{-1})	Unc. (cm^{-1})	Energy Levels		
7.5	7	331	52146.5878	0.0229	*	52146.625	0.016	(^{2}I) 4s $^3I_6$	-	(^{2}I) 4p $^1K_7$
6.8	4	223	52151.1067	0.0296	*	52151.197	0.019	(^{2}I) 4s $^3I_7$	-	(^{2}I) 4p $^1K_7$
9.7	63	425	52152.1476	0.0046		52152.1475	0.0067	(^{2}I) 4s $^1I_6$	-	(^{2}I) 4p $^1I_6$
9.5	53	420	52154.8209	0.0051		52154.8214	0.0067	(^{4}F) 4s $^5F_4$	-	(a^{2}F) 4p $^3G_5$
7.2	5	478	52162.3182	0.0951	*	52162.249	0.028	(a^{2}F) 4s $^3F_2$	-	(a^{2}F) 4p $^3F_2$
8.9	21	349	52177.9568	0.0089		52177.9551	0.0083	(^{4}F) 4s $^5F_5$	-	(a^{2}F) 4p $^3G_5$
6.7	5	301	52198.4469	0.0329	*	52198.4509	0.011	(^{4}P) 4s $^5P_2$	-	(^{4}P) 4p $^5P_2$
11.7	376	397	52216.7440	0.0035		52216.7440	0.0056	(^{4}G) 4s $^5G_6$	-	(^{4}G) 4p $^5H_7$
6.4	4	211	52238.3043	0.0245		52238.304	0.026	(c^{2}D) 4s $^3D_2$	-	(c^{2}D) 4p $^3F_3$
12.6	372	383	52244.6916	0.0032		52244.6916	0.0053	(^{6}S) 4s $^7S_3$	-	(^{6}S) 4p $^7P_3$
6.8	4	407	52253.6058	0.1019		52253.543	0.032	(^{4}D) 4s $^5D_4$	-	(^{4}G) 4p $^3G_5$
7.8	10	432	52256.6920	0.0220		52256.7208	0.01	(^{4}P) 4s $^5P_3$	-	(^{4}P) 4p $^5P_2$
7.4	4	598	52263.2366	0.0678	*	52263.235	0.028	(a^{2}G) 4s $^3G_4$	-	(^{4}F) 4p $^3F_4$
7.6	9	371	52275.9432	0.0199		52275.943	0.014	(^{4}P) 4s $^5P_1$	-	(^{4}P) 4p $^5P_1$
7.1	3	551	52307.9888	0.0927	*	52307.976	0.036	(^{2}H) 4s $^3H_5$	-	(a^{2}G) 4p $^3F_4$
7.8	8	449	52309.7422	0.0277	*	52309.828	0.041	(^{2}I) 4s $^1I_6$	-	(^{4}F) 4p $^5G_6$

Fe III Classified FTS linelist continued

ln (EW)	SNR	FWHM	σ_{obs} (cm^{-1})	Unc. (cm^{-1})		σ_{Ritz} (cm^{-1})	Unc. (cm^{-1})	Energy Levels		
7.1	5	120	52338.7192	0.0130	*	52338.778	0.038	(^{2}H) 4s $^3H_4$	-	(a^2G) 4p $^3F_4$
8.5	13	349	52344.7064	0.0134		52344.706	0.013	(^{4}P) 4s $^5P_2$	-	(^{4}P) 4p $^5P_1$
7.7	8	345	52359.8500	0.0218		52359.850	0.024	(b^2G) 4s $^1G_4$	-	(b^2G) 4p $^1F_3$
6.0	4	135	52381.8383	0.0193		52381.838	0.021	(c^2D) 4s $^1D_2$	-	(c^2D) 4p $^1F_3$
8.0	11	411	52417.6045	0.0185		52417.594	0.013	(^{2}I) 4s $^3I_6$	-	(^{2}I) 4p $^3H_6$
9.8	68	442	52422.1666	0.0046		52422.1672	0.0066	(^{2}I) 4s $^3I_7$	-	(^{2}I) 4p $^3H_6$
7.8	11	335	52423.7686	0.0149		52423.769	0.017	(a^2F) 4s $^3F_2$	-	(a^2F) 4p $^3D_2$
6.6	3	398	52435.6620	0.0623	*	52435.660	0.023	(^{4}F) 4s $^3F_4$	-	(a^2G) 4p $^3H_5$
7.3	4	417	52443.4294	0.0509	*	52443.282	0.041	(^{4}F) 4s $^5F_5$	-	(^{2}I) 4p $^1I_6$
8.6	22	388	52453.0038	0.0094		52453.0063	0.011	(a^2F) 4s $^3F_4$	-	(a^2F) 4p $^3F_4$
8.2	14	326	52509.5323	0.0122	*	52509.721	0.081	(^{4}D) 4s $^5D_3$	-	(^{4}P) 4p $^3D_3$
7.6	8	370	52513.7356	0.0244		52513.735	0.026	(b^2D) 4s $^1D_2$	-	(b^2D) 4p $^1D_2$
6.9	4	478	52528.9504	0.0661	*	52528.78	0.13	(a^2G) 4s $^3G_4$	-	(^{4}F) 4p $^3F_3$
7.8	5	600	52541.1639	0.0606	*	52541.20	0.11	(^{4}P) 4s $^3P_1$	-	(^{4}P) 4p $^3S_1$
6.7	3	498	52543.7444	0.0806	*	52543.67	0.11	(^{4}F) 4s $^5F_4$	-	(a^2F) 4p $^3D_3$
8.1	13	364	52551.0349	0.0149	*	52550.950	0.075	(a^2F) 4s $^1F_3$	-	(a^2F) 4p $^1F_3$

Fe III Classified FTS linelist continued

ln (EW)	SNR	FWHM	σ_{obs} (cm^{-1})	Unc. (cm^{-1})		σ_{Ritz} (cm^{-1})	Unc. (cm^{-1})	Energy Levels		
8.6	23	410	52573.6511	0.0097		52573.6468	0.011	(^{4}F) 4s ^{5}F$_4$	-	(^{4}F) 4p ^{5}G$_5$
7.7	10	379	52588.6451	0.0187		52588.646	0.021	(^{4}F) 4s ^{5}F$_1$	-	(^{4}F) 4p ^{5}F$_1$
10.4	111	401	52600.9632	0.0035		52600.9632	0.0056	(^{4}F) 4s ^{5}F$_5$	-	(^{4}F) 4p ^{5}G$_6$
6.5	4	328	52615.8957	0.0457	*	52616.53	0.18	(^{2}H) 4s ^{3}H$_6$	-	(^{2}H) 4p ^{1}I$_6$
8.6	24	437	52633.1566	0.0097		52633.1558	0.012	(b^{2}D) 4s ^{3}D$_3$	-	(b^{2}D) 4p ^{3}F$_4$
8.4	6	62	52650.1768	0.1765	*	52650.732	0.081	(^{4}D) 4s ^{5}D$_4$	-	(^{4}P) 4p ^{3}D$_3$
8.2	17	362	52662.5626	0.0111	*	52662.42	0.11	(^{4}P) 4s ^{3}P$_2$	-	(^{4}P) 4p ^{3}S$_1$
5.7	4	130	52704.2125	0.0172	*	52704.1915	0.01	(^{2}I) 4s ^{3}I$_5$	-	(^{2}I) 4p ^{3}H$_5$
7.9	12	316	52713.8963	0.0132	*	52713.929	0.065	(a^{2}D) 4s ^{3}D$_3$	-	(^{4}F) 4p ^{5}G$_3$
9.5	62	410	52719.9259	0.0046		52719.9260	0.0067	(^{2}I) 4s ^{3}I$_6$	-	(^{2}I) 4p ^{3}H$_5$
7.6	7	520	52755.5434	0.0366	*	52755.280	0.041	(^{2}I) 4s ^{1}I$_6$	-	(^{4}F) 4p ^{5}F$_5$
12.8	1291	409	52757.2956	0.0036		52757.2956	0.0057	(^{6}S) 4s ^{7}S$_3$	-	(^{6}S) 4p ^{7}P$_4$
7.1	5	254	52790.2610	0.0248	*	52790.230	0.038	(^{4}D) 4s ^{5}D$_2$	-	(^{4}P) 4p ^{3}D$_2$
8.5	8	190	52791.3212	0.0122	*	52791.287	0.038	(^{4}D) 4s ^{5}D$_3$	-	(^{4}P) 4p ^{3}D$_2$
8.5	8	190	52791.3212	0.0122	*	52791.25	0.1	(a^{2}F) 4s ^{1}F$_3$	-	(a^{2}G) 4p ^{3}F$_3$
9.6	52	385	52798.6979	0.0047		52798.6980	0.0068	(^{2}I) 4s ^{3}I$_5$	-	(^{2}I) 4p ^{3}H$_4$

Fe III Classified FTS linelist continued

ln (EW)	SNR	FWHM	σ_{obs} (cm^{-1})	Unc. (cm^{-1})		σ_{Ritz} (cm^{-1})	Unc. (cm^{-1})	Energy Levels		
8.4	11	524	52799.8859	0.0233	*	52799.73	0.11	(b^2D) 4s $^3D_3$	-	(b^2D) 4p $^3D_3$
7.2	3	716	52805.8976	0.1187	*	52806.22	0.16	(a^2D) 4s $^3D_2$	-	(a^2D) 4p $^3D_1$
7.3	7	266	52822.9053	0.0182		52822.906	0.02	(b^2D) 4s $^3D_2$	-	(b^2D) 4p $^3D_3$
8.5	14	437	52828.9583	0.0167	*	52828.9716	0.011	(^{4}F) 4s $^5F_4$	-	(^{4}F) 4p $^5F_4$
7.2	4	431	52829.4197	0.0544	*	52829.5513	0.01	(^{4}G) 4s $^5G_4$	-	(^{4}G) 4p $^5F_5$
7.0	5	452	52837.1865	0.0477	*	52837.157	0.097	(a^2G) 4s $^3G_3$	-	(^{4}F) 4p $^3F_2$
7.4	6	547	52844.4309	0.0452	*	52844.93	0.18	(^{2}H) 4s $^3H_5$	-	(^{2}H) 4p $^1I_6$
8.8	28	445	52847.1675	0.0086		52847.1674	0.011	(^{4}F) 4s $^5F_4$	-	(^{4}F) 4p $^5F_3$
8.4	19	402	52849.9900	0.0109		52849.9788	0.0081	(^{4}G) 4s $^5G_5$	-	(^{4}G) 4p $^5F_5$
9.0	34	433	52852.1051	0.0071		52852.1053	0.0092	(^{4}F) 4s $^5F_5$	-	(^{4}F) 4p $^5F_4$
7.1	3	203	52855.9069	0.0786	*	52855.921	0.036	(a^2F) 4s $^3F_3$	-	(^{2}H) 4p $^3H_4$
7.3	7	257	52856.8300	0.0178		52856.819	0.014	(a^2D) 4s $^3D_3$	-	(^{4}F) 4p $^5G_4$
7.9	10	512	52866.5171	0.0508	*	52866.90	0.52	(^{2}P) 4s $^3P_2$	-	(^{2}P) 4p $^1D_2$
8.3	19	419	52867.9339	0.0114		52867.933	0.013	(a^2D) 4s $^3D_2$	-	(a^2D) 4p $^3D_2$
6.7	4	399	52872.6217	0.0477	*	52872.525	0.078	(a^2F) 4s $^3F_3$	-	(^{4}F) 4p $^5D_2$
7.6	8	478	52885.1892	0.0316	*	52885.210	0.064	(^{4}G) 4s $^5G_2$	-	(^{4}P) 4p $^5D_1$

Fe III Classified FTS linelist continued

ln (EW)	SNR	FWHM	σ_{obs} (cm^{-1})	Unc. (cm^{-1})		σ_{Ritz} (cm^{-1})	Unc. (cm^{-1})	Energy Levels		
7.6	8	478	52885.1892	0.0316	*	52884.755	0.089	(^{4}F) 4s ^{5}F$_1$	-	(a^{2}F) 4p ^{3}F$_2$
10.5	139	397	52891.0491	0.0035		52891.0501	0.0055	(^{4}G) 4s ^{5}G$_6$	-	(^{4}G) 4p ^{5}F$_5$
7.9	9	308	52917.2831	0.0166	*	52917.31	0.1	(a^{2}D) 4s ^{1}D$_2$	-	(a^{2}F) 4p ^{1}D$_2$
8.7	12	608	52924.9851	0.0530	*	52925.012	0.02	(^{4}G) 4s ^{5}G$_3$	-	(^{4}P) 4p ^{5}D$_2$
8.7	12	608	52924.9851	0.0530	*	52924.593	0.066	(^{4}G) 4s ^{5}G$_2$	-	(^{4}P) 4p ^{5}D$_2$
8.5	16	495	52973.1232	0.0157	*	52972.9505	0.01	(^{4}G) 4s ^{5}G$_3$	-	(^{4}G) 4p ^{5}F$_4$
8.7	28	444	52980.3736	0.0084	*	52980.476	0.064	(^{4}G) 4s ^{5}G$_2$	-	(^{4}G) 4p ^{5}F$_3$
8.7	28	444	52980.3736	0.0084	*	52980.3469	0.0084	(^{4}G) 4s ^{5}G$_4$	-	(^{4}G) 4p ^{5}F$_4$
8.4	20	412	52980.8990	0.0106		52980.8948	0.0083	(^{4}G) 4s ^{5}G$_3$	-	(^{4}G) 4p ^{5}F$_3$
9.5	57	396	52988.2902	0.0046		52988.2912	0.0062	(^{4}G) 4s ^{5}G$_4$	-	(^{4}G) 4p ^{5}F$_3$
6.8	5	226	52991.3222	0.0248	*	52991.354	0.091	(^{4}D) 4s ^{5}D$_2$	-	(^{4}D) 4p ^{5}D$_3$
10.2	101	402	53000.7739	0.0036		53000.7744	0.0056	(^{4}G) 4s ^{5}G$_5$	-	(^{4}G) 4p ^{5}F$_4$
8.1	15	366	53005.0128	0.0125		53005.014	0.012	(^{4}D) 4s ^{5}D$_2$	-	(^{4}P) 4p ^{3}D$_1$
8.8	28	438	53023.2792	0.0084		53023.2815	0.0081	(^{4}F) 4s ^{5}F$_4$	-	(^{4}F) 4p ^{5}F$_5$
9.7	65	409	53046.4159	0.0043		53046.4152	0.0061	(^{4}F) 4s ^{5}F$_5$	-	(^{4}F) 4p ^{5}F$_5$
6.7	3	405	53060.5266	0.1204	*	53060.5515	0.011	(^{4}D) 4s ^{5}D$_2$	-	(^{4}D) 4p ^{5}D$_2$

Fe III Classified FTS linelist continued

ln (EW)	SNR	FWHM	σ_{obs} (cm^{-1})	Unc. (cm^{-1})		σ_{Ritz} (cm^{-1})	Unc. (cm^{-1})	Energy Levels		
9.3	47	428	53061.6079	0.0056		53061.6086	0.0076	(^{4}D) 4s ^{5}D$_3$	-	(^{4}D) 4p ^{5}D$_2$
6.8	5	198	53071.5883	0.0189	*	53071.566	0.016	(a^{2}G) 4s ^{3}G$_4$	-	(a^{2}G) 4p ^{3}H$_4$
7.6	11	386	53083.3984	0.0177		53083.396	0.018	(^{4}D) 4s ^{5}D$_2$	-	(^{4}D) 4p ^{5}D$_1$
7.3	8	322	53095.2829	0.0211		53095.280	0.018	(^{4}D) 4s ^{5}D$_0$	-	(^{4}P) 4p ^{3}D$_1$
7.3	4	418	53100.8045	0.0477	*	53100.834	0.047	(a^{2}F) 4s ^{1}F$_3$	-	(a^{2}G) 4p ^{3}F$_4$
8.0	12	353	53106.9976	0.0156		53106.9919	0.011	(^{4}D) 4s ^{5}D$_3$	-	(^{4}D) 4p ^{5}D$_4$
8.7	28	403	53124.5107	0.0079		53124.5105	0.0098	(a^{2}G) 4s ^{3}G$_4$	-	(a^{2}G) 4p ^{3}H$_5$
9.7	68	470	53133.3064	0.0048	*	53133.422	0.091	(^{4}D) 4s ^{5}D$_4$	-	(^{4}D) 4p ^{5}D$_3$
8.6	25	427	53157.7145	0.0091		53157.7246	0.0098	(a^{2}G) 4s ^{3}G$_3$	-	(a^{2}G) 4p ^{3}H$_4$
8.3	19	432	53171.2979	0.0121	*	53171.322	0.038	(a^{2}D) 4s ^{3}D$_3$	-	(a^{2}F) 4p ^{3}G$_4$
7.8	4	601	53173.5708	0.1614	*	53173.662	0.025	(^{4}D) 4s ^{5}D$_0$	-	(^{4}D) 4p ^{5}D$_1$
6.9	5	261	53232.5260	0.0273	*	53232.547	0.051	(^{4}P) 4s ^{5}P$_3$	-	(^{4}P) 4p ^{3}P$_2$
9.7	67	406	53248.0026	0.0042		53248.0029	0.0062	(^{4}D) 4s ^{5}D$_4$	-	(^{4}D) 4p ^{5}D$_4$
8.3	14	485	53403.7357	0.0179	*	53403.7624	0.011	(^{4}G) 4s ^{5}G$_3$	-	(^{4}P) 4p ^{5}S$_2$
8.3	14	485	53403.7357	0.0179	*	53403.343	0.064	(^{4}G) 4s ^{5}G$_2$	-	(^{4}P) 4p ^{5}S$_2$
7.2	7	408	53411.0991	0.0293		53411.099	0.019	(^{4}F) 4s ^{3}F$_4$	-	(a^{2}G) 4p ^{3}G$_5$

Fe III Classified FTS linelist continued

ln (EW)	SNR	FWHM	σ_{obs} (cm^{-1})	Unc. (cm^{-1})		σ_{Ritz} (cm^{-1})	Unc. (cm^{-1})	Energy Levels		
8.9	32	392	53412.8283	0.0068		53412.8268	0.0087	(a^2G) 4s $^3G_5$	-	(a^2G) 4p $^3H_6$
9.3	46	402	53442.7838	0.0053		53442.7837	0.0074	(^{4}G) 4s $^5G_2$	-	(^{4}G) 4p $^5F_1$
8.9	2	251	53450.8996	0.0550	*	53450.962	0.014	(^{4}F) 4s $^5F_4$	-	(a^2F) 4p $^3F_4$
8.6	26	426	53477.9925	0.0089		53477.9917	0.011	(b^2F) 4s $^3F_2$	-	(b^2F) 4p $^3G_3$
9.6	54	520	53480.5545	0.0058	*	53480.589	0.013	(^{4}G) 4s $^5G_3$	-	(^{4}G) 4p $^5F_2$
9.6	54	520	53480.5545	0.0058	*	53480.170	0.065	(^{4}G) 4s $^5G_2$	-	(^{4}G) 4p $^5F_2$
6.4	4	267	53563.7441	0.0340	*	53563.57	0.11	(b^2D) 4s $^3D_3$	-	(b^2D) 4p $^1F_3$
8.3	14	381	53574.0981	0.0137	*	53574.1046	0.0093	(^{4}G) 4s $^5G_3$	-	(^{4}P) 4p $^5D_3$
9.3	55	429	53581.5026	0.0051		53581.5010	0.0067	(^{4}G) 4s $^5G_4$	-	(^{4}P) 4p $^5D_3$
7.5	4	714	53601.7245	0.0960	*	53601.753	0.028	(^{4}F) 4s $^3F_3$	-	(a^2G) 4p $^3G_4$
6.7	4	438	53605.9051	0.0513	*	53605.815	0.076	(a^2D) 4s $^1D_2$	-	(a^2F) 4p $^1F_3$
8.6	21	566	53613.0126	0.0140	*	53612.877	0.095	(b^2F) 4s $^1F_3$	-	(b^2F) 4p $^1F_3$
8.6	21	566	53613.0126	0.0140	*	53613.335	0.027	(^{4}F) 4s $^3F_4$	-	(a^2G) 4p $^3G_4$
6.3	4	164	53632.3022	0.0186	*	53632.165	0.03	(^{4}F) 4s $^3F_3$	-	(a^2G) 4p $^3G_3$
7.9	12	458	53667.2757	0.0187		53667.276	0.021	(^{4}D) 4s $^5D_1$	-	(^{4}D) 4p $^5D_0$
6.9	5	429	53692.5383	0.0456	*	53692.519	0.071	(^{4}F) 4s $^3F_2$	-	(a^2G) 4p $^3G_3$

Fe III Classified FTS linelist continued

ln (EW)	SNR	FWHM	σ_{obs} (cm^{-1})	Unc. (cm^{-1})		σ_{Ritz} (cm^{-1})	Unc. (cm^{-1})	Energy Levels		
7.5	10	392	53714.9169	0.0207		53714.911	0.018	(^{4}D) 4s ^{5}D$_2$	-	(^{4}D) 4p ^{5}P$_1$
8.0	12	402	53764.6101	0.0171	*	53764.583	0.02	(^{4}D) 4s ^{5}D$_1$	-	(^{4}D) 4p ^{5}P$_1$
9.0	34	378	53768.6539	0.0064		53768.6540	0.0085	(b^{2}F) 4s ^{3}F$_3$	-	(b^{2}F) 4p ^{3}G$_4$
5.8	3	250	53788.8945	0.0471	*	53788.934	0.039	(a^{2}D) 4s ^{3}D$_2$	-	(a^{2}D) 4p ^{1}F$_3$
8.1	16	362	53805.1749	0.0115		53805.177	0.013	(^{4}D) 4s ^{5}D$_0$	-	(^{4}D) 4p ^{5}P$_1$
7.3	7	317	53816.9394	0.0229	*	53816.969	0.038	(a^{2}D) 4s ^{3}D$_3$	-	(a^{2}D) 4p ^{1}F$_3$
9.0	38	432	53858.9021	0.0065	*	53858.913	0.014	(^{4}D) 4s ^{5}D$_2$	-	(^{4}D) 4p ^{5}P$_2$
9.0	38	432	53858.9021	0.0065	*	53859.619	0.041	(^{4}F) 4s ^{3}F$_4$	-	(b^{2}F) 4p ^{1}G$_4$
7.7	12	436	53893.2019	0.0190		53893.201	0.02	(a^{2}G) 4s ^{1}G$_4$	-	(b^{2}F) 4p ^{3}G$_5$
8.7	29	430	53908.5852	0.0081		53908.5848	0.01	(^{4}D) 4s ^{5}D$_1$	-	(^{4}D) 4p ^{5}P$_2$
8.4	23	364	53912.3021	0.0085	*	53912.287	0.019	(^{4}D) 4s ^{5}D$_2$	-	(^{4}D) 4p ^{5}P$_3$
9.7	64	436	53913.3711	0.0045	*	53913.344	0.018	(^{4}D) 4s ^{5}D$_3$	-	(^{4}D) 4p ^{5}P$_3$
9.7	64	436	53913.3711	0.0045	*	53913.56	0.28	(^{4}F) 4s ^{5}F$_1$	-	(^{4}F) 4p ^{5}D$_1$
7.1	6	356	53925.9938	0.0311	*	53925.91	0.16	(^{4}F) 4s ^{5}F$_1$	-	(^{4}F) 4p ^{5}D$_0$
8.7	28	403	53975.6630	0.0078		53975.6621	0.0097	(a^{2}G) 4s ^{3}G$_5$	-	(a^{2}G) 4p ^{3}G$_5$
7.2	4	781	53985.2013	0.1048	*	53984.993	0.019	(^{2}H) 4s ^{3}H$_6$	-	(a^{2}G) 4p ^{3}H$_5$

Fe III Classified FTS linelist continued

ln (EW)	SNR	FWHM	σ_{obs} (cm^{-1})	Unc. (cm^{-1})		σ_{Ritz} (cm^{-1})	Unc. (cm^{-1})	Energy Levels		
9.3	46	456	54017.1522	0.0060	*	54017.072	0.045	(b^2F) 4s $^3F_4$	-	(b^2F) 4p $^3G_5$
9.3	46	456	54017.1522	0.0060	*	54017.421	0.076	(^{4}F) 4s $^3F_3$	-	(b^2F) 4p $^3F_2$
7.3	8	304	54034.7106	0.0204	*	54034.7381	0.0089	(^{4}G) 4s $^5G_4$	-	(^{4}P) 4p $^5D_4$
8.7	30	441	54048.0970	0.0082		54048.0936	0.0084	(^{4}F) 4s $^5F_4$	-	(^{4}F) 4p $^5D_4$
6.8	6	284	54054.3523	0.0231	*	54054.355	0.018	(^{4}D) 4s $^5D_4$	-	(^{4}D) 4p $^5P_3$
8.6	26	401	54055.1644	0.0084		54055.1656	0.0082	(^{4}G) 4s $^5G_5$	-	(^{4}P) 4p $^5D_4$
8.9	38	449	54071.2248	0.0068		54071.2273	0.0079	(^{4}F) 4s $^5F_5$	-	(^{4}F) 4p $^5D_4$
6.8	3	542	54077.9223	0.0906	*	54077.775	0.099	(^{4}F) 4s $^3F_2$	-	(b^2F) 4p $^3F_2$
6.8	6	341	54086.2792	0.0310		54086.286	0.026	(^{4}F) 4s $^3F_3$	-	(b^2F) 4p $^3F_3$
6.8	4	494	54097.8309	0.0619	*	54097.868	0.029	(^{4}F) 4s $^3F_4$	-	(b^2F) 4p $^3F_3$
6.2	3	344	54099.9956	0.0588	*	54099.949	0.022	(a^2G) 4s $^3G_4$	-	(a^2G) 4p $^3G_5$
7.4	9	382	54108.3080	0.0219	*	54108.12	0.11	(b^2D) 4s $^3D_3$	-	(b^2D) 4p $^3P_2$
7.0	6	354	54122.9506	0.0296	*	54122.991	0.048	(a^2G) 4s $^1G_4$	-	(b^2F) 4p $^3D_3$
7.2	6	312	54131.2998	0.0252		54131.299	0.027	(b^2D) 4s $^3D_2$	-	(b^2D) 4p $^3P_2$
7.6	10	435	54143.0445	0.0220		54143.048	0.024	(b^2F) 4s $^3F_2$	-	(b^2F) 4p $^3D_1$
6.7	9	136	54160.2079	0.0083	*	54160.03	0.12	(b^2D) 4s $^3D_2$	-	(b^2D) 4p $^3P_1$

Fe III Classified FTS linelist continued

ln (EW)	SNR	FWHM	σ_{obs} (cm^{-1})	Unc. (cm^{-1})		σ_{Ritz} (cm^{-1})	Unc. (cm^{-1})	Energy Levels		
6.1	2	261	54177.9479	0.0567	*	54177.898	0.025	(a^2G) 4s $^3G_5$	-	(a^2G) 4p $^3G_4$
8.6	27	420	54191.2632	0.0085		54191.2546	0.0095	(^{2}H) 4s $^3H_4$	-	(a^2G) 4p $^3H_4$
8.8	30	434	54213.3964	0.0077		54213.3966	0.0097	(^{2}H) 4s $^3H_5$	-	(a^2G) 4p $^3H_5$
8.2	17	338	54221.9250	0.0107	*	54221.942	0.086	(b^2F) 4s $^3F_3$	-	(b^2F) 4p $^3D_2$
7.6	11	391	54229.6681	0.0183		54229.658	0.012	(a^2D) 4s $^3D_3$	-	(a^2F) 4p $^3F_4$
7.3	2	121	54243.1271	0.0250	*	54243.111	0.046	(b^2F) 4s $^3F_3$	-	(b^2F) 4p $^3D_3$
7.5	11	395	54244.1733	0.0190	*	54244.199	0.016	(^{2}H) 4s $^3H_4$	-	(a^2G) 4p $^3H_5$
8.2	17	387	54246.8596	0.0119		54246.862	0.014	(b^2F) 4s $^3F_4$	-	(b^2F) 4p $^3D_3$
8.3	20	382	54261.0889	0.0100		54261.0915	0.012	(^{4}F) 4s $^5F_4$	-	(^{4}F) 4p $^5D_3$
8.3	18	476	54302.1856	0.0138		54302.185	0.016	(a^2G) 4s $^3G_4$	-	(a^2G) 4p $^3G_4$
6.5	5	240	54385.5927	0.0267	*	54385.724	0.039	(a^2D) 4s $^3D_2$	-	(a^2F) 4p $^3F_3$
6.9	3	447	54388.3967	0.0690	*	54388.344	0.022	(a^2G) 4s $^3G_3$	-	(a^2G) 4p $^3G_4$
9.1	43	466	54397.5949	0.0063		54397.5964	0.0083	(^{2}H) 4s $^3H_6$	-	(a^2G) 4p $^3H_6$
7.9	13	376	54418.7585	0.0148		54418.756	0.017	(a^2G) 4s $^3G_3$	-	(a^2G) 4p $^3G_3$
6.4	3	355	54424.1993	0.0551	*	54424.182	0.041	(a^2G) 4s $^3G_5$	-	(b^2F) 4p $^1G_4$
6.7	4	466	54499.7202	0.0615	*	54499.737	0.047	(^{2}I) 4s $^3I_5$	-	(a^2F) 4p $^1G_4$

Fe III Classified FTS linelist continued

ln (EW)	SNR	FWHM	σ_{obs} (cm^{-1})	Unc. (cm^{-1})		σ_{Ritz} (cm^{-1})	Unc. (cm^{-1})	Energy Levels		
6.9	5	355	54522.4800	0.0337	*	54522.57	0.13	(^{4}P) 4s ^{3}P$_1$	-	(^{4}D) 4p ^{3}P$_0$
6.4	4	195	54548.5274	0.0232	*	54548.469	0.042	(a^{2}G) 4s ^{3}G$_4$	-	(b^{2}F) 4p ^{1}G$_4$
7.8	10	462	54626.0004	0.0232		54626.000	0.018	(^{2}H) 4s ^{3}H$_5$	-	(a^{2}G) 4p ^{3}H$_6$
7.3	7	460	54669.1642	0.0355	*	54669.031	0.033	(^{4}G) 4s ^{5}G$_3$	-	(^{4}G) 4p ^{3}F$_2$
6.2	3	303	54678.6121	0.0438	*	54678.571	0.03	(a^{2}G) 4s ^{3}G$_5$	-	(a^{2}G) 4p ^{1}H$_5$
6.6	4	346	54756.3170	0.0395	*	54756.356	0.074	(^{4}P) 4s ^{3}P$_1$	-	(^{4}D) 4p ^{3}P$_1$
6.8	6	228	54759.4037	0.0208	*	54759.433	0.032	(^{4}G) 4s ^{5}G$_4$	-	(^{4}G) 4p ^{3}F$_3$
7.1	4	395	54804.0728	0.0472	*	54804.012	0.076	(a^{2}G) 4s ^{3}G$_3$	-	(b^{2}F) 4p ^{3}F$_2$
5.7	4	144	54877.5407	0.0194	*	54877.577	0.079	(^{4}P) 4s ^{3}P$_2$	-	(^{4}D) 4p ^{3}P$_1$
6.8	5	249	54929.3969	0.0229	*	54929.352	0.032	(^{4}G) 4s ^{5}G$_6$	-	(^{4}G) 4p ^{3}H$_6$
6.9	4	516	54953.3615	0.0697	*	54953.311	0.037	(a^{2}F) 4s ^{1}F$_3$	-	(a^{2}G) 4p ^{3}H$_4$
7.1	5	310	54955.8133	0.0296	*	54955.8972	0.01	(^{4}G) 4s ^{5}G$_4$	-	(^{4}P) 4p ^{5}P$_3$
7.3	5	494	54960.3965	0.0497		54960.432	0.013	(^{2}H) 4s ^{3}H$_6$	-	(a^{2}G) 4p ^{3}G$_5$
7.0	4	326	55068.2045	0.0392	*	55068.223	0.039	(^{4}P) 4s ^{3}P$_1$	-	(^{4}D) 4p ^{3}P$_2$
6.6	5	277	55070.0377	0.0280	*	55069.50	0.3	(^{4}G) 4s ^{5}G$_4$	-	(^{4}G) 4p ^{3}H$_5$
8.2	2	609	55112.4648	0.2518	*	55112.24	0.12	(b^{2}D) 4s ^{3}D$_2$	-	(b^{2}D) 4p ^{1}P$_1$

Fe III Classified FTS linelist continued

ln (EW)	SNR	FWHM	σ_{obs} (cm^{-1})	Unc. (cm^{-1})		σ_{Ritz} (cm^{-1})	Unc. (cm^{-1})	Energy Levels		
6.7	2	660	55125.7634	0.1492	*	55125.833	0.034	(^{4}F) 4s $^5F_5$	-	(^{2}H) 4p $^3H_6$
7.0	6	361	55157.8887	0.0306	*	55157.91	0.11	(^{4}D) 4s $^5D_4$	-	(^{4}D) 4p $^3D_3$
7.6	9	395	55189.4532	0.0220		55189.444	0.023	(^{4}P) 4s $^3P_2$	-	(^{4}D) 4p $^3P_2$
7.5	4	279	55747.4553	0.0401	*	55747.497	0.036	(^{4}D) 4s $^5D_4$	-	(^{4}D) 4p $^3F_4$
7.2	4	276	55961.9246	0.0347		55961.924	0.037	(c^{2}D) 4s $^3D_2$	-	(c^{2}D) 4p $^1F_3$
7.8	4	63	56188.6567	0.0077		56188.6577	0.0099	(^{4}F) 4p $^5D_3$	-	(^{6}S) 5d $^5D_4$
7.2	5	286	56251.1285	0.0307		56251.140	0.015	(^{4}P) 4s $^5P_1$	-	(^{4}P) 4p $^3D_1$
9.0	30	433	56306.1661	0.0078	*	56306.243	0.091	(^{4}P) 4s $^5P_2$	-	(^{4}D) 4p $^5D_3$
8.6	17	474	56306.7066	0.0139	*	56306.678	0.012	(^{4}P) 4s $^5P_1$	-	(^{4}D) 4p $^5D_2$
7.0	5	385	56398.2689	0.0401		56398.285	0.02	(^{4}P) 4s $^5P_2$	-	(^{4}D) 4p $^5D_1$
6.7	4	202	56433.7006	0.0292	*	56433.7106	0.012	(^{4}P) 4s $^5P_3$	-	(^{4}D) 4p $^5D_2$
9.0	28	460	56479.1071	0.0088	*	56479.0939	0.0096	(^{4}P) 4s $^5P_3$	-	(^{4}D) 4p $^5D_4$
6.9	4	200	57029.7704	0.0228	*	57029.800	0.02	(^{4}P) 4s $^5P_2$	-	(^{4}D) 4p $^5P_1$
7.7	4	501	57173.7561	0.0674	*	57173.802	0.017	(^{4}P) 4s $^5P_2$	-	(^{4}D) 4p $^5P_2$
7.9	7	494	57202.4824	0.0364	*	57202.468	0.067	(^{4}G) 4s $^5G_2$	-	(^{4}D) 4p $^5F_1$
7.2	5	283	57232.0714	0.0274	*	57232.072	0.017	(^{4}P) 4s $^5P_3$	-	(^{4}D) 4p $^5P_2$

Fe III Classified FTS linelist continued

ln (EW)	SNR	FWHM	σ_{obs} (cm^{-1})	Unc. (cm^{-1})		σ_{Ritz} (cm^{-1})	Unc. (cm^{-1})	Energy Levels		
8.5	13	375	57285.4455	0.0146		57285.446	0.016	(^{4}P) 4s $^5P_3$	-	(^{4}D) 4p $^5P_3$
8.3	9	518	57331.5662	0.0587	*	57331.610	0.015	(^{4}G) 4s $^5G_3$	-	(^{4}D) 4p $^5F_2$
8.3	9	518	57331.5662	0.0587	*	57331.191	0.064	(^{4}G) 4s $^5G_2$	-	(^{4}D) 4p $^5F_2$
8.0	9	383	57521.5887	0.0222		57521.5919	0.011	(^{4}G) 4s $^5G_4$	-	(^{4}D) 4p $^5F_3$
7.3	5	117	57681.6462	0.0147	*	57681.390	0.079	(^{4}G) 4p $^3G_5$	-	(^{4}G) 4d $^5F_4$
8.7	10	429	57774.9436	0.0219		57774.9480	0.011	(^{4}G) 4s $^5G_5$	-	(^{4}D) 4p $^5F_4$
8.7	10	491	58043.2540	0.0246		58043.2379	0.012	(^{4}G) 4s $^5G_6$	-	(^{4}D) 4p $^5F_5$
8.7	9	581	58226.9355	0.0318		58226.955	0.03	(^{2}H) 4s $^3H_4$	-	(b^{2}F) 4p $^3G_3$
8.3	8	453	58466.3517	0.0288		58466.343	0.024	(^{2}H) 4s $^3H_5$	-	(b^{2}F) 4p $^3G_4$
8.8	12	490	58482.6051	0.0214		58482.607	0.022	(^{2}H) 4s $^3H_6$	-	(b^{2}F) 4p $^3G_5$
7.0	4	175	58771.0308	0.0237	*	58771.167	0.056	(a^{2}D) 4s $^1D_2$	-	(b^{2}F) 4p $^1D_2$
6.6	3	226	58906.2639	0.0403	*	58906.241	0.042	(^{4}D) 4s $^3D_2$	-	(^{4}F) 4p $^5F_3$
6.7	3	213	59429.4404	0.0351	*	59429.629	0.049	(^{4}D) 4s $^3D_2$	-	(a^{2}F) 4p $^3F_2$
6.7	4	155	59693.2335	0.0223	*	59693.577	0.031	(^{4}F) 4s $^5F_4$	-	(a^{2}G) 4p $^3H_4$
7.0	3	258	59694.3801	0.0405	*	59694.137	0.047	(^{4}D) 4s $^3D_2$	-	(a^{2}F) 4p $^3F_3$
7.0	2	347	60568.8454	0.0913	*	60568.69	0.17	(b^{2}D) 4s $^3D_3$	-	(b^{2}G) 4p $^3F_3$

Fe III Classified FTS linelist continued

ln (EW)	SNR	FWHM	σ_{obs} (cm^{-1})	Unc. (cm^{-1})		σ_{Ritz} (cm^{-1})	Unc. (cm^{-1})	Energy Levels		
6.9	4	153	61311.2342	0.0217		61311.235	0.023	(^{4}G) 4p ^{3}F$_4$	-	(^{4}G) 4d ^{5}F$_3$
7.3	4	212	61350.5669	0.0286	*	61350.793	0.036	(^{4}G) 4s ^{3}G$_4$	-	(a^{2}D) 4p ^{3}F$_3$
6.3	2	134	61531.5362	0.0299	*	61531.569	0.02	(a^{2}D) 4p ^{3}F$_3$	-	(^{6}S) 5d ^{5}D$_4$
6.5	2	160	61685.4616	0.0349		61685.461	0.037	(^{2}P) 4s ^{3}P$_1$	-	(c^{2}D) 4p ^{3}D$_1$
7.9	4	355	62199.5806	0.0506	*	62199.32	0.11	(^{6}S) 4p ^{5}P$_2$	-	(^{6}S) 4d ^{5}D$_3$
7.6	3	225	62200.2216	0.0401		62200.222	0.042	(^{6}S) 4p ^{5}P$_2$	-	(^{6}S) 4d ^{5}D$_2$
8.3	3	550	62266.1520	0.0923		62266.037	0.037	(^{6}S) 4p ^{5}P$_1$	-	(^{6}S) 5s ^{5}S$_2$
8.4	5	383	62672.6395	0.0404		62672.655	0.038	(^{6}S) 4p ^{5}P$_3$	-	(^{6}S) 5s ^{5}S$_2$
6.9	2	162	62963.5969	0.0339	*	62963.658	0.048	(a^{2}F) 4s ^{3}F$_3$	-	(b^{2}F) 4p ^{3}D$_3$

C Fe III Classified Grating Linelist

The classified grating linelist is shown below and lines with multiple Fe III identifications are listed for every identification. Lines weighted out of the energy level optimisation process are indicated by an asterisk (*) and are usually due to badly observed lines or doubly-identified lines. The columns include:

Exp. Cat. : Exposure time category. The Q ("quick") category is data from the 5-minute exposure linelists and R is data from the 45-minute exposure linelists.

Int. : The intensity of the observed grating lines.

$\sigma_{\mathbf{obs}}$: The wavenumbers of the spectral lines in cm^{-1}.

Line Unc.: The total uncertainty of the spectral lines in cm^{-1}. Lines with an increased uncertainty for the energy level optimisation process are indicated by an asterisk (*).

$\sigma_{\mathbf{Ritz}}$: The Ritz wavenumber of the spectral lines in cm^{-1}.

Ritz Unc.: The uncertainties of the Ritz wavenumbers of the spectral lines in cm^{-1}.

Transition: The energy levels of the identified transitions.

Fe III Classified grating linelist

Exp.	Cat.	Int.	σ_{obs} (cm^{-1})	Unc. (cm^{-1})		σ_{Ritz} (cm^{-1})	Unc. (cm^{-1})	Transition		
	R	216	55090.23	0.21	*	55089.92	0.3	(^{4}G) 4s ^{5}G$_5$	-	(^{4}G) 4p ^{3}H$_5$
	R	196	55133.51	0.21		55133.453	0.072	(a^{2}D) 4s ^{3}D$_2$	-	(^{4}F) 4p ^{5}D$_2$
	R	145	55149.867	0.091	*	55150.02	0.27	(a^{2}D) 4s ^{3}D$_2$	-	(^{4}F) 4p ^{5}D$_1$
	R	106	55161.518	0.091		55161.488	0.071	(a^{2}D) 4s ^{3}D$_3$	-	(^{4}F) 4p ^{5}D$_2$
	R	169	55191.598	0.091		55191.696	0.033	(^{4}G) 4s ^{5}G$_3$	-	(^{4}G) 4p ^{3}H$_4$
	R	69	55194.34	0.21		55194.480	0.081	(^{4}F) 4s ^{3}F$_2$	-	(b^{2}F) 4p ^{1}D$_2$
	R	106	55199.062	0.091		55199.092	0.033	(^{4}G) 4s ^{5}G$_4$	-	(^{4}G) 4p ^{3}H$_4$
	R	107	55254.908	0.092		55254.823	0.056	(a^{2}G) 4s ^{3}G$_4$	-	(a^{2}G) 4p ^{1}F$_3$
	R	188	55303.556	0.092		55303.541	0.032	(a^{2}F) 4s ^{3}F$_4$	-	(^{4}F) 4p ^{3}G$_5$
	R	93	55310.19	0.21		55310.297	0.077	(a^{2}F) 4s ^{3}F$_2$	-	(^{4}F) 4p ^{3}G$_3$
	R	73	55340.99	0.21		55340.982	0.056	(a^{2}G) 4s ^{3}G$_3$	-	(a^{2}G) 4p ^{1}F$_3$
	R	190	55379.418	0.092	*	55379.259	0.04	(^{2}I) 4s ^{3}I$_5$	-	(^{4}F) 4p ^{5}G$_4$
	R	216	55391.136	0.092		55391.071	0.019	(^{2}H) 4s ^{3}H$_5$	-	(a^{2}G) 4p ^{3}G$_4$
	R	67	55394.42	0.21		55394.41	0.1	(a^{2}F) 4s ^{3}F$_2$	-	(a^{2}F) 4p ^{1}D$_2$
	R	211	55452.48	0.22		55452.286	0.019	(^{2}H) 4s ^{3}H$_4$	-	(a^{2}G) 4p ^{3}G$_3$
	R	53	55465.7	0.22	*	55465.475	0.033	(a^{2}F) 4s ^{3}F$_4$	-	(^{4}F) 4p ^{3}G$_4$

Fe III Classified grating linelist continued

Exp.	Cat.	Int.	σ_{obs} (cm^{-1})	Unc. (cm^{-1})		σ_{Ritz} (cm^{-1})	Unc. (cm^{-1})	Transition		
	R	99	55471.701	0.092		55471.691	0.039	(^{2}I) 4s ^{3}I$_6$	-	(a^{2}F) 4p ^{3}G$_5$
	Q	72	55500.394	0.092		55500.431	0.052	(a^{2}G) 4s ^{1}G$_4$	-	(^{2}H) 4p ^{1}G$_4$
	R	88	55606.559	0.093		55606.486	0.036	(^{4}D) 4s ^{5}D$_3$	-	(^{4}D) 4p ^{3}F$_4$
	R	202	55624.344	0.093		55624.302	0.055	(b^{2}F) 4s ^{3}F$_4$	-	(^{2}H) 4p ^{1}G$_4$
	R	175	55637.56	0.22		55637.356	0.042	(^{2}H) 4s ^{3}H$_5$	-	(b^{2}F) 4p ^{1}G$_4$
	R	56	55663.79	0.22	*	55663.341	0.029	(^{2}H) 4s ^{3}H$_6$	-	(a^{2}G) 4p ^{1}H$_5$
	R	92	55721.389	0.093		55721.284	0.014	(^{2}I) 4s ^{3}I$_5$	-	(^{2}I) 4p ^{1}I$_6$
	R	157	55741.484	0.093		55741.591	0.019	(^{2}I) 4s ^{3}I$_7$	-	(^{2}I) 4p ^{1}I$_6$
	R	106	55781.066	0.093		55780.949	0.074	(a^{2}F) 4s ^{3}F$_3$	-	(a^{2}F) 4p ^{1}F$_3$
	R	226	55823.508	0.093		55823.553	0.081	(^{4}P) 4s ^{5}P$_2$	-	(^{4}P) 4p ^{3}D$_3$
	R	87	55894.31	0.22	*	55894.699	0.04	(^{2}I) 4s ^{3}I$_6$	-	(^{4}F) 4p ^{5}G$_6$
	R	105	55899.274	0.094		55899.272	0.04	(^{2}I) 4s ^{3}I$_7$	-	(^{4}F) 4p ^{5}G$_6$
	R	193	55906.431	0.094		55906.407	0.028	(^{2}H) 4s ^{3}H$_4$	-	(b^{2}F) 4p ^{3}F$_3$
	R	157	55920.655	0.094		55920.717	0.05	(a^{2}G) 4s ^{3}G$_3$	-	(b^{2}F) 4p ^{1}D$_2$
	R	195	55922.69	0.22		55922.547	0.034	(^{2}H) 4s ^{3}H$_4$	-	(a^{2}G) 4p ^{1}H$_5$
	R	103	55957.96	0.22		55957.87	0.16	(b^{2}G) 4s ^{3}G$_3$	-	(b^{2}G) 4p ^{1}F$_3$

Fe III Classified grating linelist continued

Exp.	Cat.	Int.	σ_{obs} (cm^{-1})	Unc. (cm^{-1})		σ_{Ritz} (cm^{-1})	Unc. (cm^{-1})	Transition		
	Q	76	55979.82	0.094		55979.824	0.053	(^{4}D) 4p $^5P_2$	-	(^{4}G) 4d $^5F_2$
	Q	149	56021.75	0.22		56021.25	0.1	(a^{2}F) 4s $^3F_3$	-	(a^{2}G) 4p $^3F_3$
	R	137	56033.365	0.094	*	56033.496	0.042	(^{2}I) 4s $^1I_6$	-	(^{4}F) 4p $^3G_5$
	R	234	56036.41	0.094		56036.356	0.038	(^{4}P) 4s $^5P_1$	-	(^{4}P) 4p $^3D_2$
	R	110	56066.603	0.094		56066.552	0.085	(^{4}F) 4p $^5D_2$	-	(^{6}S) 5d $^5D_3$
	R	175	56082.953	0.094	*	56082.910	0.077	(a^{2}F) 4s $^3F_2$	-	(a^{2}F) 4p $^1F_3$
	R	175	56082.953	0.094	*	56083.156	0.1	(^{2}H) 4p $^3H_4$	-	(^{6}S) 5d $^5D_3$
	R	249	56105.33	0.22		56105.119	0.038	(^{4}P) 4s $^5P_2$	-	(^{4}P) 4p $^3D_2$
	R	114	56163.431	0.095		56163.389	0.038	(^{4}P) 4s $^5P_3$	-	(^{4}P) 4p $^3D_2$
	R	58	56214.32	0.22		56214.342	0.04	(a^{2}F) 4s $^1F_3$	-	(a^{2}G) 4p $^3G_3$
	R	63	56234.4	0.22		56234.697	0.033	(^{4}D) 4p $^5D_4$	-	(^{4}G) 4d $^5H_3$
	R	199	56320.037	0.095		56319.903	0.015	(^{4}P) 4s $^5P_2$	-	(^{4}P) 4p $^3D_1$
	R	184	56322.8	0.22		56323.21	0.1	(a^{2}F) 4s $^3F_2$	-	(a^{2}G) 4p $^3F_3$
	R	173	56324.61	0.22		56324.631	0.032	(^{4}F) 4s $^5F_5$	-	(^{4}F) 4p $^3G_5$
	Q	49	56329.587	0.095		56329.522	0.02	(^{4}P) 4s $^5P_1$	-	(^{4}D) 4p $^5D_1$
	R	150	56364.48	0.095		56364.513	0.091	(^{4}P) 4s $^5P_3$	-	(^{4}D) 4p $^5D_3$

Fe III Classified grating linelist continued

Exp.	Cat.	Int.	σ_{obs} (cm^{-1})	Unc. (cm^{-1})		σ_{Ritz} (cm^{-1})	Unc. (cm^{-1})	Transition		
	R	136	56375.411	0.095		56375.4407	0.012	(^{4}P) 4s ^{5}P$_2$	-	(^{4}D) 4p ^{5}D$_2$
	R	94	56380.687	0.095		56380.740	0.04	(a^{2}F) 4s ^{3}F$_2$	-	(a^{2}G) 4p ^{3}F$_2$
	R	95	56402.088	0.095	*	56401.656	0.016	(^{4}F) 4p ^{5}D$_4$	-	(^{6}S) 5d ^{5}D$_4$
	R	95	56402.088	0.095	*	56401.251	0.098	(^{4}F) 4p ^{5}D$_4$	-	(^{6}S) 5d ^{5}D$_3$
	R	105	56406.86	0.096		56406.834	0.036	(^{4}F) 4s ^{3}F$_3$	-	(b^{2}F) 4p ^{3}G$_3$
	R	172	56430.16	0.096		56430.214	0.047	(a^{2}F) 4s ^{1}F$_3$	-	(b^{2}F) 4p ^{1}G$_4$
	R	89	56463.552	0.096		56463.431	0.033	(^{4}F) 4s ^{5}F$_4$	-	(^{4}F) 4p ^{3}G$_4$
	R	164	56467.283	0.096		56467.188	0.068	(^{4}F) 4s ^{3}F$_2$	-	(b^{2}F) 4p ^{3}G$_3$
	R	153	56599.534	0.096		56599.598	0.073	(a^{2}F) 4s ^{1}F$_3$	-	(b^{2}F) 4p ^{3}F$_2$
	R	81	56668.69	0.22		56668.463	0.04	(a^{2}F) 4s ^{1}F$_3$	-	(b^{2}F) 4p ^{3}F$_3$
	R	100	56677.13	0.22		56677.025	0.027	(^{4}F) 4s ^{3}F$_3$	-	(b^{2}F) 4p ^{3}G$_4$
	R	143	56688.51	0.23	*	56688.607	0.029	(^{4}F) 4s ^{3}F$_4$	-	(b^{2}F) 4p ^{3}G$_4$
	R	143	56688.51	0.23	*	56688.498	0.034	(^{4}F) 4s ^{5}F$_5$	-	(a^{2}G) 4p ^{1}G$_4$
	Q	37	56766.41	0.23		56766.485	0.041	(^{2}I) 4s ^{1}I$_6$	-	(^{2}H) 4p ^{3}I$_7$
	R	119	56794.657	0.097		56794.579	0.036	(a^{2}F) 4s ^{3}F$_3$	-	(^{4}F) 4p ^{3}D$_3$
	R	191	56839.53	0.23		56839.85	0.12	(^{4}P) 4p ^{3}D$_1$	-	(^{4}G) 4d ^{5}F$_1$

Fe III Classified grating linelist continued

Exp.	Cat.	Int.	σ_{obs} (cm^{-1})	Unc. (cm^{-1})		σ_{Ritz} (cm^{-1})	Unc. (cm^{-1})	Transition		
	R	105	56842.99	0.23		56843.144	0.041	(a^2F) 4s $^3F_4$	-	(a^2G) 4p $^3F_4$
	R	170	56863.87	0.23		56863.730	0.025	(^{4}P) 4s $^5P_1$	-	(^{4}D) 4p $^5D_0$
	R	133	56927.18	0.23		56927.07	0.15	(b^2D) 4s $^1D_2$	-	(b^2G) 4p $^3F_3$
	R	154	56961.037	0.097		56961.037	0.02	(^{4}P) 4s $^5P_1$	-	(^{4}D) 4p $^5P_1$
	R	125	57066.29	0.23		57066.092	0.091	(a^2F) 4s $^1F_3$	-	(b^2F) 4p $^3F_4$
	R	170	57107.39	0.23		57107.266	0.032	(a^2G) 4s $^3G_4$	-	(b^2F) 4p $^3G_3$
	R	164	57130.35	0.23		57130.313	0.084	(^{4}F) 4s $^3F_3$	-	(b^2F) 4p $^3D_2$
	R	177	57132.25	0.23		57132.244	0.071	(^{4}F) 4s $^3F_2$	-	(b^2F) 4p $^3D_1$
	R	174	57136.556	0.098		57136.568	0.055	(a^2F) 4s $^1F_3$	-	(a^2G) 4p $^1F_3$
	R	115	57141.649	0.098		57141.694	0.083	(a^2G) 4s $^1G_4$	-	(b^2F) 4p $^1F_3$
	R	114	57189.69	0.23		57189.678	0.075	(^{4}D) 4s $^3D_1$	-	(a^2D) 4p $^3P_2$
	Q	33	57193.25	0.23		57193.425	0.031	(a^2G) 4s $^3G_3$	-	(b^2F) 4p $^3G_3$
	R	55	57227.13	0.23		57227.176	0.018	(^{4}P) 4s $^5P_2$	-	(^{4}D) 4p $^5P_3$
	Q	39	57253.077	0.098		57253.170	0.028	(a^2G) 4s $^3G_5$	-	(b^2F) 4p $^3G_4$
	Q	72	57265.995	0.098	*	57265.565	0.091	(b^2F) 4s $^3F_4$	-	(b^2F) 4p $^1F_3$
	R	218	57377.449	0.099		57377.457	0.025	(a^2G) 4s $^3G_4$	-	(b^2F) 4p $^3G_4$

Fe III Classified grating linelist continued

Exp.	Cat.	Int.	σ_{obs} (cm^{-1})	Unc. (cm^{-1})		σ_{Ritz} (cm^{-1})	Unc. (cm^{-1})	Transition		
	Q	159	57381.565	0.099	*	57381.41	0.1	(a^2D) 4s $^3D_3$	-	(a^2F) 4p $^1D_2$
	R	73	57403.21	0.23		57403.239	0.046	(^{4}D) 4s $^3D_3$	-	(a^2F) 4p $^1G_4$
	R	81	57426.58	0.23		57426.468	0.016	(^{4}F) 4p $^5F_5$	-	(^{6}S) 5d $^5D_4$
	R	139	57473.577	0.099	*	57473.77	0.18	(^{4}D) 4s $^3D_1$	-	(a^2D) 4p $^3P_1$
	R	216	57497.87	0.23		57497.837	0.024	(a^2G) 4s $^3G_5$	-	(b^2F) 4p $^3G_5$
	R	215	57514.17	0.23	*	57513.776	0.064	(^{4}G) 4s $^5G_2$	-	(^{4}D) 4p $^5F_3$
	R	215	57514.17	0.23	*	57514.196	0.012	(^{4}G) 4s $^5G_3$	-	(^{4}D) 4p $^5F_3$
	R	92	57591.51	0.23	*	57591.844	0.047	(^{4}D) 4s $^3D_3$	-	(a^2F) 4p $^3G_3$
	R	223	57620.5	0.1	*	57620.373	0.098	(^{4}F) 4p $^5F_4$	-	(^{6}S) 5d $^5D_3$
	R	223	57620.5	0.1	*	57620.778	0.017	(^{4}F) 4p $^5F_4$	-	(^{6}S) 5d $^5D_4$
	R	60	57640.51	0.23		57640.52	0.13	(a^2F) 4s $^3F_3$	-	(^{4}F) 4p $^3F_3$
	R	231	57654.73	0.23	*	57654.462	0.075	(a^2D) 4s $^1D_2$	-	(b^2F) 4p $^3F_2$
	R	156	57656.19	0.23		57656.16	0.18	(^{2}S) 4s $^1S_0$	-	(b^2D) 4p $^3P_1$
	R	249	57667.53	0.23		57667.324	0.039	(^{2}I) 4s $^3I_5$	-	(^{2}H) 4p $^3H_4$
	R	97	57723.4	0.1		57723.328	0.039	(a^2D) 4s $^1D_2$	-	(b^2F) 4p $^3F_3$
	R	75	57746.92	0.23		57747.124	0.012	(^{4}G) 4s $^5G_3$	-	(^{4}D) 4p $^5F_4$

Fe III Classified grating linelist continued

Exp.	Cat.	Int.	σ_{obs} (cm^{-1})	Unc. (cm^{-1})		σ_{Ritz} (cm^{-1})	Unc. (cm^{-1})	Transition		
	R	208	57754.6	0.1		57754.5205	0.011	(^{4}G) 4s ^{5}G$_4$	-	(^{4}D) 4p ^{5}F$_4$
	R	85	57851.59	0.23	*	57851.914	0.042	(a^{2}G) 4s ^{3}G$_4$	-	(b^{2}F) 4p ^{3}D$_3$
	R	68	57864.21	0.23		57864.234	0.041	(^{4}F) 4s ^{5}F$_5$	-	(a^{2}G) 4p ^{3}F$_4$
	R	58	57875.9	0.23		57876.102	0.017	(^{4}F) 4p ^{5}G$_5$	-	(^{6}S) 5d ^{5}D$_4$
	R	65	57902.97	0.23		57902.950	0.038	(^{2}I) 4s ^{3}I$_5$	-	(^{2}H) 4p ^{3}H$_5$
	R	213	57916.79	0.23		57916.904	0.084	(a^{2}G) 4s ^{3}G$_3$	-	(b^{2}F) 4p ^{3}D$_2$
	R	235	57918.0	0.1	*	57918.685	0.038	(^{2}I) 4s ^{3}I$_6$	-	(^{2}H) 4p ^{3}H$_5$
	R	235	57937.7	0.1	*	57938.073	0.043	(a^{2}G) 4s ^{3}G$_3$	-	(b^{2}F) 4p ^{3}D$_3$
	R	72	57942.46	0.23	*	57942.48	0.13	(a^{2}F) 4s ^{3}F$_2$	-	(^{4}F) 4p ^{3}F$_3$
	Q	101	58002.32	0.24		58002.1666	0.011	(^{4}G) 4s ^{5}G$_5$	-	(^{4}D) 4p ^{5}F$_5$
	R	154	58013.12	0.24		58013.12	0.24	(^{4}D) 4s ^{3}D$_1$	-	(a^{2}D) 4p ^{3}P$_0$
	Q	52	58057.3	0.1	*	58057.123	0.04	(a^{2}F) 4p ^{3}G$_4$	-	(^{6}S) 5d ^{5}D$_4$
	R	79	58070.29	0.24	*	58069.912	0.078	(a^{2}D) 4s ^{3}D$_3$	-	(a^{2}F) 4p ^{1}F$_3$
	Q	91	58102.8	0.1		58102.82	0.1	(^{2}P) 4s ^{1}P$_1$	-	(c^{2}D) 4p ^{3}D$_1$
	R	206	58109.8	0.24	*	58110.06	0.18	(^{2}I) 4s ^{1}I$_6$	-	(^{2}H) 4p ^{1}I$_6$
	R	190	58114.67	0.24		58114.63	0.16	(^{4}D) 4s ^{3}D$_2$	-	(a^{2}D) 4p ^{3}D$_1$

Fe III Classified grating linelist continued

Exp.	Cat.	Int.	σ_{obs} (cm^{-1})	Unc. (cm^{-1})		σ_{Ritz} (cm^{-1})	Unc. (cm^{-1})	Transition		
	R	116	58141.73	0.24		58141.59	0.16	(^{4}D) 4s ^{3}D$_1$	-	(a^{2}D) 4p ^{3}D$_1$
	Q	58	58162.0	0.1	*	58162.077	0.073	(^{4}D) 4p ^{5}F$_5$	-	(^{4}G) 4d ^{5}F$_4$
	Q	73	58164.7	0.1		58164.703	0.092	(a^{2}F) 4s ^{3}F$_2$	-	(^{4}F) 4p ^{3}F$_2$
	R	94	58169.7	0.1	*	58169.991	0.033	(^{4}D) 4p ^{5}F$_3$	-	(^{4}G) 4d ^{5}H$_3$
	Q	69	58191.5	0.1		58191.432	0.055	(a^{2}D) 4s ^{1}D$_2$	-	(a^{2}G) 4p ^{1}F$_3$
	R	74	58282.22	0.24		58282.18	0.1	(a^{2}D) 4s ^{3}D$_2$	-	(a^{2}G) 4p ^{3}F$_3$
	R	103	58304.62	0.24		58304.846	0.032	(^{4}F) 4s ^{5}F$_4$	-	(^{4}F) 4p ^{3}D$_3$
	R	128	58321.52	0.24	*	58321.910	0.042	(^{4}D) 4s ^{3}D$_3$	-	(a^{2}D) 4p ^{3}D$_2$
	R	161	58352.6	0.1		58352.576	0.034	(^{4}D) 4p ^{5}F$_2$	-	(^{4}G) 4d ^{5}H$_3$
	R	228	58389.0	0.1	*	58389.295	0.073	(^{4}D) 4p ^{5}F$_4$	-	(^{4}G) 4d ^{5}F$_4$
	R	228	58389.0	0.1	*	58389.00	0.11	(^{4}P) 4s ^{5}P$_3$	-	(^{4}D) 4p ^{3}D$_3$
	R	89	58401.22	0.24		58401.19	0.18	(^{4}F) 4s ^{5}F$_5$	-	(^{2}H) 4p ^{1}I$_6$
	R	126	58403.81	0.24		58403.835	0.04	(^{2}I) 4s ^{3}I$_5$	-	(^{2}H) 4p ^{3}H$_6$
	R	136	58419.88	0.24	*	58419.569	0.04	(^{2}I) 4s ^{3}I$_6$	-	(^{2}H) 4p ^{3}H$_6$
	R	136	58419.88	0.24	*	58419.799	0.036	(^{4}D) 4p ^{5}F$_4$	-	(^{4}G) 4d ^{5}F$_3$
	R	192	58424.22	0.24		58424.142	0.041	(^{2}I) 4s ^{3}I$_7$	-	(^{2}H) 4p ^{3}H$_6$

Fe III Classified grating linelist continued

Exp.	Cat.	Int.	σ_{obs} (cm^{-1})	Unc. (cm^{-1})		σ_{Ritz} (cm^{-1})	Unc. (cm^{-1})	Transition		
	R	79	58474.44	0.24		58474.475	0.032	(^{4}G) 4s ^{5}G$_5$	-	(^{4}G) 4p ^{3}G$_4$
	R	77	58513.89	0.24		58514.11	0.11	(^{4}F) 4p ^{5}G$_3$	-	(^{6}S) 5d ^{5}D$_3$
	R	58	58583.37	0.24		58583.34	0.13	(^{4}D) 4s ^{5}D$_1$	-	(^{4}D) 4p ^{3}P$_0$
	R	203	58608.33	0.24		58608.37	0.18	(^{2}S) 4s ^{1}S$_0$	-	(b^{2}D) 4p ^{1}P$_1$
	R	106	58619.8	0.1		58619.796	0.041	(a^{2}D) 4s ^{3}D$_3$	-	(a^{2}G) 4p ^{3}F$_4$
	R	92	58767.4	0.1		58767.452	0.073	(^{4}D) 4s ^{5}D$_2$	-	(^{4}D) 4p ^{3}P$_1$
	R	134	58775.5	0.1	*	58775.84	0.11	3d^6 ^{3}D$_2$	-	(^{6}S) 4p ^{5}P$_1$
	R	42	58835.23	0.24		58835.313	0.036	(^{4}D) 4p ^{5}F$_2$	-	(^{4}G) 4d ^{5}F$_3$
	R	126	58978.9	0.1	*	58978.588	0.036	(^{4}P) 4s ^{5}P$_3$	-	(^{4}D) 4p ^{3}F$_4$
	Q	62	58995.3	0.1		58995.445	0.072	(^{6}S) 4s ^{7}S$_3$	-	(^{6}S) 4p ^{5}P$_3$
	R	101	59111.8	0.1		59111.78	0.1	(^{2}P) 4s ^{1}P$_1$	-	(c^{2}D) 4p ^{1}D$_2$
	Q	29	59245.5	0.25		59245.186	0.073	(^{6}S) 4s ^{7}S$_3$	-	(^{6}S) 4p ^{5}P$_2$
	R	133	59251.15	0.25		59251.148	0.04	(a^{2}F) 4p ^{1}G$_4$	-	(^{6}S) 5d ^{5}D$_4$
	R	48	59362.08	0.25		59362.146	0.05	(^{4}D) 4s ^{3}D$_2$	-	(a^{2}F) 4p ^{3}D$_1$
	R	223	59404.15	0.11	*	59403.687	0.064	(^{4}G) 4s ^{5}G$_2$	-	(^{4}D) 4p ^{5}D$_2$
	R	223	59404.15	0.11	*	59404.106	0.013	(^{4}G) 4s ^{5}G$_3$	-	(^{4}D) 4p ^{5}D$_2$

Fe III Classified grating linelist continued

Exp.	Cat.	Int.	σ_{obs} (cm^{-1})	Unc. (cm^{-1})		σ_{Ritz} (cm^{-1})	Unc. (cm^{-1})	Transition		
	R	78	59456.64	0.25		59456.586	0.079	(^{4}D) 4s ^{3}D$_1$	-	(a^{2}F) 4p ^{3}F$_2$
	R	78	59456.64	0.25		59456.8858	0.011	(^{4}G) 4s ^{5}G$_4$	-	(^{4}D) 4p ^{5}D$_4$
	R	189	59594.22	0.11		59594.303	0.093	(^{2}S) 4s ^{3}S$_1$	-	(b^{2}D) 4p ^{3}D$_1$
	R	222	59648.75	0.11		59648.718	0.038	(^{2}I) 4s ^{3}I$_5$	-	(^{2}H) 4p ^{3}I$_5$
	R	138	59655.58	0.11		59655.600	0.04	(^{4}D) 4s ^{3}D$_3$	-	(a^{2}F) 4p ^{3}F$_4$
	R	133	59717.93	0.11	*	59718.106	0.08	(^{4}D) 4s ^{3}D$_1$	-	(a^{2}F) 4p ^{3}D$_2$
	Q	32	59898.03	0.25		59898.462	0.039	(a^{2}F) 4s ^{3}F$_3$	-	(b^{2}F) 4p ^{3}F$_3$
	R	69	59901.58	0.25		59901.45	0.13	(a^{2}D) 4s ^{3}D$_2$	-	(^{4}F) 4p ^{3}F$_3$
	R	51	59966.06	0.25	*	59966.500	0.042	(^{2}I) 4s ^{3}I$_5$	-	(a^{2}G) 4p ^{1}G$_4$
	R	100	59979.22	0.25		59979.349	0.07	(^{4}P) 4p ^{3}P$_2$	-	(^{4}G) 4d ^{5}F$_2$
	R	134	59985.48	0.11		59985.526	0.038	(^{2}I) 4s ^{3}I$_5$	-	(^{2}H) 4p ^{3}I$_6$
	R	242	60001.07	0.25		60001.260	0.038	(^{2}I) 4s ^{3}I$_6$	-	(^{2}H) 4p ^{3}I$_6$
	R	96	60062.22	0.25	*	60062.306	0.042	(^{4}G) 4s ^{3}G$_5$	-	(^{2}I) 4p ^{3}I$_6$
	R	190	60172.56	0.11		60172.524	0.043	(a^{2}F) 4s ^{3}F$_4$	-	(b^{2}F) 4p ^{1}G$_4$
	R	65	60200.35	0.25		60200.28	0.1	(^{6}S) 4p ^{5}P$_3$	-	(^{6}S) 5s ^{7}S$_3$
	R	65	60200.35	0.25		60200.423	0.04	(a^{2}F) 4s ^{3}F$_2$	-	(b^{2}F) 4p ^{3}F$_3$

Fe III Classified grating linelist continued

Exp.	Cat.	Int.	σ_{obs} (cm^{-1})	Unc. (cm^{-1})		σ_{Ritz} (cm^{-1})	Unc. (cm^{-1})	Transition		
	R	98	60253.05	0.25		60252.731	0.039	(^{4}D) 4s ^{3}D$_3$	-	(^{4}F) 4p ^{5}D$_4$
	Q	65	60355.86	0.11	*	60355.929	0.04	(^{2}I) 4s ^{3}I$_7$	-	(^{2}H) 4p ^{3}I$_7$
	R	79	60366.28	0.26		60366.567	0.054	(a^{2}F) 4s ^{3}F$_3$	-	(a^{2}G) 4p ^{1}F$_3$
	Q	57	60457.12	0.26		60457.070	0.033	(^{4}P) 4p ^{5}P$_2$	-	(^{4}G) 4d ^{5}H$_3$
	R	129	60472.25	0.11		60472.273	0.032	(a^{2}D) 4s ^{3}D$_3$	-	(a^{2}G) 4p ^{3}H$_4$
	R	129	60537.08	0.11	*	60537.241	0.042	(^{4}P) 4s ^{3}P$_2$	-	(a^{2}D) 4p ^{3}P$_2$
	R	145	60642.7	0.11		60642.73	0.11	(b^{2}F) 4s ^{1}F$_3$	-	(b^{2}D) 4p ^{3}F$_2$
	R	64	60668.35	0.26		60668.528	0.056	(a^{2}F) 4s ^{3}F$_2$	-	(a^{2}G) 4p ^{1}F$_3$
	R	107	60699.87	0.26		60700.11	0.16	(^{4}P) 4s ^{3}P$_1$	-	(a^{2}D) 4p ^{3}P$_1$
	R	91	60719.59	0.11		60719.582	0.04	(^{4}G) 4s ^{3}G$_3$	-	(a^{2}D) 4p ^{1}D$_2$
	R	188	60808.39	0.11		60808.402	0.087	(a^{2}F) 4s ^{3}F$_4$	-	(b^{2}F) 4p ^{3}F$_4$
	R	61	60821.07	0.26	*	60821.33	0.17	(^{4}P) 4s ^{3}P$_2$	-	(a^{2}D) 4p ^{3}P$_1$
	R	61	60821.07	0.26	*	60820.800	0.048	(^{4}P) 4s ^{3}P$_2$	-	(a^{2}F) 4p ^{3}G$_3$
	R	223	60871.72	0.11	*	60871.97	0.16	3d^6 a^{3}F$_4$	-	(^{6}S) 4p ^{7}P$_3$
	R	202	60947.07	0.26	*	60947.803	0.075	(^{4}G) 4p ^{3}F$_3$	-	(^{4}G) 4d ^{5}H$_4$
	R	202	60947.07	0.26	*	60947.330	0.034	(^{4}F) 4s ^{5}F$_5$	-	(a^{2}G) 4p ^{3}G$_4$

Fe III Classified grating linelist continued

Exp.	Cat.	Int.	σ_{obs} (cm^{-1})	Unc. (cm^{-1})		σ_{Ritz} (cm^{-1})	Unc. (cm^{-1})	Transition		
	R	199	60955.2	0.11		60955.175	0.052	(^{4}P) 4p ^{5}P$_2$	-	(^{4}G) 4d ^{5}F$_2$
	R	161	60956.65	0.26		60956.776	0.086	(a^{2}G) 4s ^{3}G$_3$	-	(b^{2}F) 4p ^{1}F$_3$
	R	108	61016.2	0.11		61016.118	0.043	(^{4}G) 4s ^{3}G$_5$	-	(^{2}I) 4p ^{1}H$_5$
	R	220	61156.58	0.26	*	61156.868	0.048	(^{2}I) 4s ^{1}I$_6$	-	(a^{2}G) 4p ^{1}H$_5$
	R	182	61193.63	0.26		61193.614	0.044	(^{4}F) 4s ^{5}F$_5$	-	(b^{2}F) 4p ^{1}G$_4$
	R	145	61278.68	0.26		61278.68	0.26	(b^{2}D) 4s ^{3}D$_3$	-	(b^{2}G) 4p ^{3}G$_4$
	R	143	61280.18	0.26	*	61280.731	0.079	(^{4}G) 4p ^{3}F$_4$	-	(^{4}G) 4d ^{5}F$_4$
	R	111	61354.7	0.26	*	61354.433	0.037	(^{4}G) 4s ^{3}G$_3$	-	(a^{2}D) 4p ^{3}F$_3$
	R	84	61358.92	0.26	*	61359.40	0.11	(^{4}G) 4s ^{5}G$_3$	-	(^{4}D) 4p ^{3}D$_3$
	R	84	61358.92	0.26	*	61358.98	0.12	(^{4}G) 4s ^{5}G$_2$	-	(^{4}D) 4p ^{3}D$_3$
	R	214	61368.63	0.26		61368.827	0.071	(^{4}P) 4s ^{3}P$_2$	-	(^{4}F) 4p ^{5}G$_3$
	Q	67	61404.02	0.26		61403.81	0.12	(^{2}S) 4s ^{3}S$_1$	-	(b^{2}D) 4p ^{3}P$_1$
	Q	58	61412.91	0.26		61413.32	0.15	(^{2}I) 4s ^{1}I$_6$	-	(^{2}H) 4p ^{1}H$_5$
	R	72	61550.58	0.27		61550.866	0.043	(^{4}P) 4s ^{3}P$_2$	-	(a^{2}D) 4p ^{3}D$_2$
	R	209	61567.98	0.11		61568.064	0.043	(^{4}G) 4s ^{3}G$_5$	-	(^{2}I) 4p ^{3}H$_6$
	R	158	61588.72	0.27	*	61589.077	0.051	(^{4}D) 4s ^{3}D$_2$	-	(a^{2}D) 4p ^{1}P$_1$

Fe III Classified grating linelist continued

Exp.	Cat.	Int.	σ_{obs} (cm^{-1})	Unc. (cm^{-1})		σ_{Ritz} (cm^{-1})	Unc. (cm^{-1})	Transition		
	R	123	61623.9	0.27	*	61622.74	0.11	(a^2F) 4s $^1F_3$	-	(^{2}S) 4p $^3P_2$
	Q	86	61657.03	0.11	*	61656.845	0.033	(^{4}P) 4p $^5D_4$	-	(^{4}G) 4d $^5H_3$
	R	141	61687.65	0.27		61687.670	0.081	(b^2F) 4s $^1F_3$	-	(b^2D) 4p $^3D_3$
	R	94	61699.49	0.27		61699.50	0.18	(^{2}I) 4s $^3I_7$	-	(^{2}H) 4p $^1I_6$
	R	88	61929.93	0.27	*	61930.176	0.043	(^{4}G) 4s $^3G_4$	-	(^{2}I) 4p $^3H_4$
	Q	28	61933.58	0.27	*	61933.815	0.044	(^{4}G) 4s $^3G_3$	-	(^{2}I) 4p $^3H_4$
	R	135	61977.22	0.12		61977.26	0.11	(^{4}P) 4s $^3P_2$	-	(a^2F) 4p $^3D_3$
	Q	118	62043.36	0.27		62043.345	0.042	(^{6}S) 4p $^5P_1$	-	(^{6}S) 4d $^5D_2$
	R	134	62055.99	0.27		62056.190	0.035	(^{4}G) 4s $^3G_4$	-	(a^2D) 4p $^3F_4$
	R	133	62108.91	0.27		62109.078	0.073	(^{4}P) 4p $^5D_4$	-	(^{4}G) 4d $^5F_4$
	R	168	62110.14	0.12		62110.082	0.033	(^{4}P) 4p $^5D_3$	-	(^{4}G) 4d $^5H_3$
	R	133	62159.33	0.27	*	62159.390	0.037	(a^2D) 4s $^3D_2$	-	(b^2F) 4p $^3F_3$
	R	167	62187.47	0.27	*	62187.425	0.036	(a^2D) 4s $^3D_3$	-	(b^2F) 4p $^3F_3$
	R	163	62325.29	0.12		62325.445	0.036	(^{4}P) 4s $^5P_1$	-	(^{4}D) 4p $^3P_2$
	Q	103	62422.79	0.12		62422.914	0.037	(^{6}S) 4p $^5P_2$	-	(^{6}S) 5s $^5S_2$
	Q	135	62449.07	0.12		62449.06	0.11	(^{6}S) 4p $^5P_3$	-	(^{6}S) 4d $^5D_3$

Fe III Classified grating linelist continued

Exp.	Cat.	Int.	σ_{obs} (cm^{-1})	Unc. (cm^{-1})		σ_{Ritz} (cm^{-1})	Unc. (cm^{-1})	Transition		
	R	216	62471.93	0.12	*	62471.867	0.047	(^{4}P) 4s ^{3}P$_2$	-	(a^{2}D) 4p ^{1}F$_3$
	R	192	62592.75	0.12		62592.819	0.036	(^{4}P) 4p ^{5}D$_3$	-	(^{4}G) 4d ^{5}F$_3$
	R	125	62608.08	0.12		62608.187	0.053	(^{4}P) 4p ^{5}D$_3$	-	(^{4}G) 4d ^{5}F$_2$
	R	109	62682.56	0.12	*	62682.928	0.044	(^{4}P) 4s ^{3}P$_1$	-	(a^{2}F) 4p ^{3}F$_2$
	R	101	62686.26	0.12		62686.334	0.037	(^{4}G) 4p ^{5}F$_2$	-	(^{4}G) 4d ^{5}F$_3$
	R	146	62698.99	0.12		62698.99	0.12	(^{2}P) 4s ^{3}P$_2$	-	(c^{2}D) 4p ^{1}D$_2$
	R	171	62701.66	0.12		62701.702	0.053	(^{4}G) 4p ^{5}F$_2$	-	(^{4}G) 4d ^{5}F$_2$
	R	144	62708.19	0.28	*	62707.83	0.12	(^{4}G) 4p ^{5}F$_2$	-	(^{4}G) 4d ^{5}F$_1$
	R	132	62719.16	0.28		62718.945	0.07	(^{4}G) 4p ^{5}F$_3$	-	(^{4}G) 4d ^{5}H$_4$
	R	192	62739.35	0.28		62739.088	0.074	(^{4}G) 4p ^{5}F$_1$	-	(^{4}G) 4d ^{5}F$_2$
	R	228	62745.96	0.28	*	62745.22	0.11	(^{4}G) 4p ^{5}F$_1$	-	(^{4}G) 4d ^{5}F$_1$
	R	225	62752.66	0.28		62752.362	0.09	(a^{2}F) 4s ^{1}F$_3$	-	(b^{2}F) 4p ^{1}F$_3$
	Q	41	62804.41	0.12	*	62804.149	0.05	(^{4}P) 4s ^{3}P$_2$	-	(a^{2}F) 4p ^{3}F$_2$
	R	174	62868.49	0.28	*	62868.593	0.042	(^{4}D) 4s ^{5}D$_4$	-	(^{2}I) 4p ^{3}H$_5$
	R	218	62870.19	0.28		62870.002	0.044	(^{4}D) 4s ^{3}D$_3$	-	(a^{2}G) 4p ^{1}G$_4$
	R	131	62877.58	0.28		62877.684	0.07	(^{4}G) 4p ^{5}F$_5$	-	(^{4}G) 4d ^{5}H$_4$

Fe III Classified grating linelist continued

Exp.	Cat.	Int.	σ_{obs} (cm^{-1})	Unc. (cm^{-1})		σ_{Ritz} (cm^{-1})	Unc. (cm^{-1})	Transition		
	R	201	62942.53	0.28		62942.489	0.087	(a^2F) 4s $^3F_3$	-	(b^2F) 4p $^3D_2$
	R	203	62995.06	0.28		62994.712	0.04	(^{2}I) 4s $^3I_5$	-	(a^2G) 4p $^3H_4$
	R	212	63063.43	0.12		63063.391	0.039	(^{2}I) 4s $^3I_6$	-	(a^2G) 4p $^3H_5$
	R	132	63112.11	0.28		63112.30	0.11	(^{4}G) 4p $^5F_4$	-	(^{4}G) 4d $^5F_5$
	R	162	63155.91	0.28		63155.524	0.074	(^{4}G) 4p $^5F_3$	-	(^{4}G) 4d $^5F_4$
	R	228	63163.37	0.28		63163.469	0.074	(^{4}G) 4p $^5F_4$	-	(^{4}G) 4d $^5F_4$
	R	179	63186.08	0.12	*	63186.029	0.036	(^{4}G) 4p $^5F_3$	-	(^{4}G) 4d $^5F_3$
	R	179	63186.08	0.12	*	63186.027	0.051	(a^2F) 4s $^3F_2$	-	(b^2F) 4p $^3D_1$
	R	144	63194.15	0.12		63193.973	0.036	(^{4}G) 4p $^5F_4$	-	(^{4}G) 4d $^5F_3$
	R	112	63201.74	0.12	*	63201.397	0.053	(^{4}G) 4p $^5F_3$	-	(^{4}G) 4d $^5F_2$
	Q	87	63263.07	0.28		63263.09	0.11	(^{4}G) 4p $^5F_5$	-	(^{4}G) 4d $^5F_5$
	R	137	63314.5	0.12		63314.264	0.074	(^{4}G) 4p $^5F_5$	-	(^{4}G) 4d $^5F_4$
	R	143	63318.51	0.28	*	63318.02	0.12	(^{4}P) 4p $^5D_0$	-	(^{4}G) 4d $^5F_1$
	Q	68	63422.44	0.12		63422.319	0.086	(^{2}S) 4s $^3S_1$	-	(b^2D) 4p $^1D_2$
	R	244	63475.74	0.12	*	63475.969	0.045	(a^2F) 4s $^3F_4$	-	(b^2F) 4p $^3D_3$
	R	244	63475.74	0.12	*	63475.995	0.04	(^{2}I) 4s $^3I_6$	-	(a^2G) 4p $^3H_6$

Fe III Classified grating linelist continued

Exp.	Cat.	Int.	σ_{obs} (cm^{-1})	Unc. (cm^{-1})		σ_{Ritz} (cm^{-1})	Unc. (cm^{-1})	Transition		
	R	246	63480.58	0.28		63480.567	0.041	(^{2}I) 4s ^{3}I$_7$	-	(a^{2}G) 4p ^{3}H$_6$
	R	193	63574.97	0.28	*	63574.283	0.092	(^{4}G) 4p ^{5}H$_7$	-	(^{4}G) 4d ^{5}H$_6$
	Q	82	63579.3	0.12		63579.264	0.091	(^{4}G) 4p ^{5}H$_7$	-	(^{4}G) 4d ^{5}H$_7$
	R	215	63590.46	0.28		63590.59	0.1	(^{4}D) 4s ^{3}D$_2$	-	(a^{2}G) 4p ^{3}F$_3$
	R	157	63631.73	0.28	*	63631.214	0.044	(^{4}G) 4s ^{3}G$_4$	-	(a^{2}F) 4p ^{1}G$_4$
	R	203	63648.34	0.12	*	63648.120	0.046	(^{4}D) 4s ^{3}D$_2$	-	(a^{2}G) 4p ^{3}F$_2$
	R	234	63674.76	0.28		63675.077	0.078	(^{4}D) 4s ^{3}D$_1$	-	(a^{2}G) 4p ^{3}F$_2$
	Q	44	63742.34	0.12		63742.396	0.092	(^{4}G) 4p ^{5}H$_6$	-	(^{4}G) 4d ^{5}H$_6$
	Q	249	63823.42	0.29	*	63823.459	0.046	(^{4}G) 4s ^{3}G$_3$	-	(a^{2}F) 4p ^{3}G$_3$
	R	112	63904.75	0.29		63904.412	0.07	(^{4}G) 4p ^{5}H$_5$	-	(^{4}G) 4d ^{5}H$_4$
	R	134	63908.67	0.29		63908.533	0.091	(^{4}F) 4s ^{5}F$_1$	-	(b^{2}F) 4p ^{3}D$_1$
	R	221	63917.86	0.12		63917.762	0.076	(^{4}G) 4p ^{5}H$_5$	-	(^{4}G) 4d ^{5}H$_5$
	R	180	63966.92	0.29		63966.96	0.11	(^{4}F) 4s ^{5}F$_1$	-	(b^{2}F) 4p ^{3}D$_2$
	R	215	64045.95	0.29		64045.738	0.051	(^{4}D) 4s ^{3}D$_3$	-	(a^{2}G) 4p ^{3}F$_4$
	R	237	64067.37	0.12		64067.443	0.039	(^{4}G) 4p ^{5}H$_4$	-	(^{4}G) 4d ^{5}H$_3$
	R	229	64082.85	0.12		64083.096	0.071	(^{4}G) 4p ^{5}H$_4$	-	(^{4}G) 4d ^{5}H$_4$

Fe III Classified grating linelist continued

Exp.	Cat.	Int.	σ_{obs} (cm^{-1})	Unc. (cm^{-1})		σ_{Ritz} (cm^{-1})	Unc. (cm^{-1})	Transition		
	R	162	64095.78	0.29	*	64096.446	0.079	(^{4}G) 4p ^{5}H$_4$	-	(^{4}G) 4d ^{5}H$_5$
	R	249	64230.61	0.29	*	64230.121	0.067	(^{4}G) 4p ^{5}H$_3$	-	(^{4}G) 4d ^{5}H$_3$
	R	124	64291.4	0.12	*	64291.66	0.12	(b^{2}F) 4s ^{3}F$_3$	-	(b^{2}D) 4p ^{3}F$_2$
	R	250	64296.73	0.29		64296.557	0.084	(^{4}D) 4s ^{3}D$_2$	-	(^{4}F) 4p ^{3}D$_2$
	R	127	64341.08	0.12		64340.992	0.074	(^{4}G) 4p ^{5}H$_5$	-	(^{4}G) 4d ^{5}F$_4$
	R	127	64341.08	0.12		64341.098	0.056	(a^{2}F) 4s ^{3}F$_3$	-	(^{2}H) 4p ^{1}G$_4$
	R	225	64393.57	0.12		64393.68	0.1	(^{4}D) 4s ^{3}D$_1$	-	(^{4}F) 4p ^{3}D$_1$
	R	236	64403.94	0.29	*	64403.89	0.14	(b^{2}D) 4s ^{3}D$_2$	-	(b^{2}G) 4p ^{1}F$_3$
	R	227	64458.91	0.12	*	64459.348	0.093	(^{6}S) 4p ^{7}P$_4$	-	(^{6}S) 4d ^{7}D$_3$
	Q	128	64480.23	0.12		64480.22	0.11	(^{6}S) 4p ^{7}P$_4$	-	(^{6}S) 4d ^{7}D$_4$
	Q	217	64508.18	0.12		64508.18	0.12	(^{6}S) 4p ^{7}P$_4$	-	(^{6}S) 4d ^{7}D$_5$
	R	92	64550.28	0.29		64550.180	0.041	(^{4}G) 4p ^{5}H$_4$	-	(^{4}G) 4d ^{5}F$_3$
	R	157	64593.68	0.29		64593.391	0.093	(b^{2}F) 4s ^{3}F$_4$	-	(b^{2}D) 4p ^{3}F$_3$
	R	191	64622.11	0.13		64622.161	0.036	(^{4}G) 4s ^{3}G$_5$	-	(a^{2}F) 4p ^{3}G$_5$
	R	103	64673.14	0.29		64672.753	0.09	3d^6 b^{3}F$_4$	-	(^{4}G) 4p ^{5}H$_3$
	R	136	64680.96	0.29	*	64682.354	0.097	(^{4}G) 4p ^{5}H$_3$	-	(^{4}G) 4d ^{5}F$_4$

Fe III Classified grating linelist continued

Exp.	Cat.	Int.	σ_{obs} (cm^{-1})	Unc. (cm^{-1})		σ_{Ritz} (cm^{-1})	Unc. (cm^{-1})	Transition		
	R	154	64719.89	0.29	*	64720.107	0.086	$3d^6\ b^1G_4$	-	$(^4G)\ 4p\ ^3G_4$
	R	104	64728.69	0.13	*	64728.485	0.086	$3d^6\ b^1G_4$	-	$(^4G)\ 4p\ ^3G_5$
	R	150	64741.97	0.13	*	64741.739	0.048	$(^2I)\ 4s\ ^3I_6$	-	$(a^2G)\ 4p\ ^1H_5$
	R	101	64789.75	0.13		64789.644	0.095	$(a^2D)\ 4s\ ^1D_2$	-	$(^2S)\ 4p\ ^1P_1$
	R	204	64825.03	0.13	*	64825.240	0.044	$(^4G)\ 4s\ ^3G_4$	-	$(a^2F)\ 4p\ ^3G_4$
	Q	92	64843.95	0.29		64843.75	0.11	$(b^2F)\ 4s\ ^3F_2$	-	$(b^2D)\ 4p\ ^3D_1$
	Q	142	64971.94	0.13		64971.952	0.093	$(^6S)\ 4p\ ^7P_3$	-	$(^6S)\ 4d\ ^7D_3$
	Q	159	64992.8	0.3		64992.82	0.12	$(^6S)\ 4p\ ^7P_3$	-	$(^6S)\ 4d\ ^7D_4$
	R	247	65005.9	0.3	*	65006.260	0.036	$(^4G)\ 4s\ ^3G_4$	-	$(^4F)\ 4p\ ^5G_5$
	R	148	65014.6	0.3	*	65014.115	0.07	$3d^6\ b^3F_4$	-	$(^4G)\ 4p\ ^5H_5$
	Q	43	65043.19	0.13		65043.301	0.076	$(b^2F)\ 4s\ ^1F_3$	-	$(b^2D)\ 4p\ ^1D_2$
	R	141	65089.4	0.3		65089.884	0.045	$(^4D)\ 4s\ ^3D_3$	-	$(^4F)\ 4p\ ^3F_4$
	R	147	65110.4	0.3		65110.587	0.093	$(^4G)\ 4s\ ^5G_2$	-	$(^4D)\ 4p\ ^3P_1$
	R	161	65173.2	0.3		65173.787	0.093	$(b^2F)\ 4s\ ^3F_4$	-	$(b^2D)\ 4p\ ^3F_4$
	R	163	65224.76	0.13		65224.586	0.046	$(a^2D)\ 4s\ ^3D_2$	-	$(b^2F)\ 4p\ ^3D_3$
	R	170	65231.61	0.13		65231.452	0.084	$(a^2D)\ 4s\ ^3D_3$	-	$(b^2F)\ 4p\ ^3D_2$

Fe III Classified grating linelist continued

Exp.	Cat.	Int.	σ_{obs} (cm^{-1})	Unc. (cm^{-1})		σ_{Ritz} (cm^{-1})	Unc. (cm^{-1})	Transition		
	Q	117	65280.03	0.13	*	65279.781	0.037	(^{4}G) 4s ^{3}G$_4$	-	(^{4}F) 4p ^{5}F$_3$
	Q	84	65304.29	0.13		65304.273	0.093	(^{6}S) 4p ^{7}P$_2$	-	(^{6}S) 4d ^{7}D$_3$
	R	87	65402.99	0.13	*	65402.649	0.03	(^{4}D) 4s ^{5}D$_3$	-	(^{4}F) 4p ^{5}G$_4$
	R	190	65456.04	0.13	*	65455.895	0.036	(^{4}G) 4s ^{3}G$_4$	-	(^{4}F) 4p ^{5}F$_5$
	Q	81	65481.84	0.13		65481.877	0.091	(^{4}G) 4p ^{5}G$_6$	-	(^{4}G) 4d ^{5}H$_7$
	R	186	65530.5	0.13		65530.686	0.076	(^{4}G) 4p ^{5}G$_5$	-	(^{4}G) 4d ^{5}H$_5$
	Q	58	65539.69	0.13		65539.629	0.092	(^{4}G) 4p ^{5}G$_5$	-	(^{4}G) 4d ^{5}H$_6$
	R	183	65559.11	0.13		65558.933	0.07	(^{4}G) 4p ^{5}G$_4$	-	(^{4}G) 4d ^{5}H$_4$
	Q	55	65572.35	0.13		65572.283	0.076	(^{4}G) 4p ^{5}G$_4$	-	(^{4}G) 4d ^{5}H$_5$
	R	224	65588.87	0.13		65588.850	0.07	(^{4}G) 4p ^{5}G$_3$	-	(^{4}G) 4d ^{5}H$_4$
	R	207	65594.59	0.13		65594.493	0.067	(^{4}G) 4p ^{5}G$_2$	-	(^{4}G) 4d ^{5}H$_3$
	R	122	65807.2	0.3	*	65806.808	0.046	(^{4}G) 4s ^{3}G$_3$	-	(a^{2}F) 4p ^{3}F$_2$
	R	223	65840.07	0.13		65840.01	0.11	(^{4}G) 4p ^{5}G$_6$	-	(^{4}G) 4d ^{5}F$_5$
	R	120	65877.06	0.13		65877.21	0.1	(^{4}F) 4s ^{5}F$_1$	-	(^{2}S) 4p ^{3}P$_2$
	R	214	65915.15	0.13		65915.09	0.1	(^{4}P) 4s ^{3}P$_1$	-	(a^{2}F) 4p ^{1}D$_2$
	R	200	65918.32	0.13		65918.301	0.037	(^{4}G) 4s ^{3}G$_5$	-	(a^{2}F) 4p ^{3}F$_4$

Fe III Classified grating linelist continued

Exp.	Cat.	Int.	σ_{obs} (cm^{-1})	Unc. (cm^{-1})		σ_{Ritz} (cm^{-1})	Unc. (cm^{-1})	Transition		
	Q	59	65953.58	0.13		65953.916	0.074	(^{4}G) 4p ^{5}G$_5$	-	(^{4}G) 4d ^{5}F$_4$
	R	112	65980.38	0.13		65980.326	0.071	(a^{2}G) 4s ^{1}G$_4$	-	(b^{2}D) 4p ^{1}F$_3$
	R	61	65995.7	0.3	*	65995.513	0.074	(^{4}G) 4p ^{5}G$_4$	-	(^{4}G) 4d ^{5}F$_4$
	R	212	66025.99	0.13		66026.017	0.036	(^{4}G) 4p ^{5}G$_4$	-	(^{4}G) 4d ^{5}F$_3$
	R	75	66040.56	0.13	*	66040.843	0.07	3d^6 b^{3}F$_4$	-	(^{4}G) 4p ^{5}F$_5$
	Q	57	66071.36	0.13	*	66071.302	0.053	(^{4}G) 4p ^{5}G$_3$	-	(^{4}G) 4d ^{5}F$_2$
	Q	57	66071.36	0.13	*	66071.316	0.045	(^{4}G) 4s ^{3}G$_3$	-	(a^{2}F) 4p ^{3}F$_3$
	R	70	66092.72	0.13		66092.598	0.074	(^{4}G) 4p ^{5}G$_2$	-	(^{4}G) 4d ^{5}F$_2$
	R	215	66098.83	0.13		66098.73	0.11	(^{4}G) 4p ^{5}G$_2$	-	(^{4}G) 4d ^{5}F$_1$
	R	241	66153.8	0.13	*	66153.497	0.03	(^{4}D) 4s ^{5}D$_3$	-	(^{4}F) 4p ^{5}F$_4$
	R	232	66170.61	0.13		66170.636	0.031	(^{4}D) 4s ^{5}D$_2$	-	(^{4}F) 4p ^{5}F$_3$
	Q	130	66438.43	0.13		66438.427	0.079	(^{6}S) 4p ^{7}P$_4$	-	(^{6}S) 5s ^{7}S$_3$
	R	144	66447.57	0.13		66447.587	0.084	(^{4}D) 4s ^{5}D$_1$	-	(^{4}F) 4p ^{5}F$_1$
	Q	57	66488.79	0.13		66488.818	0.03	(^{4}D) 4s ^{5}D$_4$	-	(^{4}F) 4p ^{5}F$_5$
	R	122	66504.09	0.13		66504.10	0.1	(a^{2}D) 4s ^{3}D$_2$	-	(^{2}S) 4p ^{3}P$_1$
	R	100	66563.05	0.13		66563.272	0.063	3d^6 b^{3}P$_2$	-	(^{4}G) 4p ^{5}F$_2$

Fe III Classified grating linelist continued

Exp.	Cat.	Int.	σ_{obs} (cm^{-1})	Unc. (cm^{-1})		σ_{Ritz} (cm^{-1})	Unc. (cm^{-1})	Transition		
	R	87	66626.69	0.13		66626.541	0.043	(^{4}D) 4s $^5D_2$	-	(a^2F) 4p $^3D_1$
	R	144	66653.16	0.13		66653.26	0.1	(b^2F) 4s $^3F_2$	-	(b^2D) 4p $^3P_1$
	R	190	66713.86	0.13	*	66713.493	0.078	3d^6 b^3F_2	-	(^{4}P) 4p $^5S_2$
	R	50	66724.49	0.31		66724.810	0.083	(^{4}P) 4s $^3P_2$	-	(a^2F) 4p $^1F_3$
	R	105	66802.45	0.13		66802.441	0.037	(^{4}G) 4s $^3G_3$	-	(^{2}H) 4p $^3H_4$
	Q	116	66950.99	0.13		66951.031	0.079	(^{6}S) 4p $^7P_3$	-	(^{6}S) 5s $^7S_3$
	R	170	67034.15	0.31		67034.428	0.036	(^{4}G) 4s $^3G_4$	-	(^{2}H) 4p $^3H_5$
	R	129	67266.64	0.14		67266.740	0.095	(a^2F) 4s $^3F_2$	-	(^{2}S) 4p $^1P_1$
	Q	81	67283.39	0.14		67283.352	0.079	(^{6}S) 4p $^7P_2$	-	(^{6}S) 5s $^7S_3$
	Q	34	67360.3	0.32		67360.124	0.037	(^{4}G) 4s $^3G_5$	-	(^{2}H) 4p $^3G_5$
	R	175	67374.05	0.14		67373.979	0.037	(^{4}G) 4s $^3G_4$	-	(^{2}H) 4p $^3G_4$
	R	66	67384.49	0.32	*	67385.01	0.11	3d^6 a^3F_3	-	(^{6}S) 4p $^5P_3$
	R	85	67458.86	0.32		67458.779	0.037	(^{4}G) 4s $^3G_4$	-	(^{2}H) 4p $^3G_3$
	R	165	67462.5	0.14		67462.419	0.038	(^{4}G) 4s $^3G_3$	-	(^{2}H) 4p $^3G_3$
	R	74	67476.93	0.14	*	67477.33	0.11	3d^6 a^3F_2	-	(^{6}S) 4p $^5P_2$
	R	71	67497.61	0.32	*	67498.011	0.089	(^{4}F) 4s $^3F_3$	-	(b^2D) 4p $^3F_3$

Fe III Classified grating linelist continued

Exp.	Cat.	Int.	σ_{obs} (cm^{-1})	Unc. (cm^{-1})		σ_{Ritz} (cm^{-1})	Unc. (cm^{-1})	Transition		
	R	104	67509.64	0.14		67509.593	0.088	(^{4}F) 4s ^{3}F$_4$	-	(b^2D) 4p ^{3}F$_3$
	R	192	67513.65	0.14		67513.630	0.03	(^{4}D) 4s ^{5}D$_4$	-	(^{4}F) 4p ^{5}D$_4$
	R	66	67549.81	0.32		67549.856	0.081	(^{4}P) 4s ^{3}P$_1$	-	(^{4}F) 4p ^{3}D$_2$
	R	120	67570.31	0.32		67570.039	0.039	(^{4}G) 4s ^{3}G$_5$	-	(^{2}H) 4p ^{3}H$_6$
	R	172	67585.65	0.14		67585.617	0.03	(^{4}D) 4s ^{5}D$_3$	-	(^{4}F) 4p ^{5}D$_3$
	R	59	67608.77	0.32		67609.15	0.24	(^{4}G) 4s ^{5}G$_6$	-	(^{2}I) 4p ^{3}I$_7$
	R	125	67707.14	0.32	*	67707.318	0.074	(^{4}D) 4s ^{5}D$_3$	-	(^{4}F) 4p ^{5}D$_2$
	R	95	67723.06	0.32		67722.82	0.27	(^{4}D) 4s ^{5}D$_2$	-	(^{4}F) 4p ^{5}D$_1$
	R	102	67726.77	0.14		67726.628	0.03	(^{4}D) 4s ^{5}D$_4$	-	(^{4}F) 4p ^{5}D$_3$
	R	87	67738.61	0.32		67738.440	0.044	(^{4}P) 4s ^{3}P$_2$	-	(^{4}F) 4p ^{3}D$_3$
	R	84	67784.85	0.14		67784.85	0.14	(^{4}D) 4s ^{5}D$_1$	-	(^{4}F) 4p ^{5}D$_0$
	R	80	67868.67	0.14		67868.545	0.064	3d^6 b^{3}F$_3$	-	(^{4}G) 4p ^{3}F$_2$
	R	111	67971.45	0.14	*	67970.724	0.072	3d^6 b^{3}F$_4$	-	(^{4}G) 4p ^{3}F$_3$
	R	173	67979.21	0.32	*	67978.762	0.081	3d^6 b^{3}F$_2$	-	(^{4}G) 4p ^{3}F$_2$
	R	144	67987.39	0.32	*	67986.62	0.12	(a^2G) 4s ^{3}G$_3$	-	(b^2D) 4p ^{3}F$_2$
	R	143	68062.31	0.14	*	68061.767	0.081	3d^6 b^{3}F$_2$	-	(^{4}G) 4p ^{3}F$_3$

Fe III Classified grating linelist continued

Exp.	Cat.	Int.	σ_{obs} (cm^{-1})	Unc. (cm^{-1})		σ_{Ritz} (cm^{-1})	Unc. (cm^{-1})	Transition		
	R	191	68074.68	0.32		68074.376	0.071	$3d^6\ b^3F_4$	-	$(^4G)\ 4p\ ^3F_4$
	R	153	68167.3	0.14	*	68167.188	0.07	$3d^6\ b^3F_4$	-	$(^4P)\ 4p\ ^5P_3$
	R	153	68167.3	0.14	*	68167.38	0.1	$(^4D)\ 4p\ ^3F_4$	-	$(^6S)\ 5d\ ^5D_3$
	R	102	68198.73	0.33		68198.443	0.088	$(a^2G)\ 4s\ ^3G_4$	-	$(b^2D)\ 4p\ ^3F_3$
	R	136	68259.48	0.33	*	68258.231	0.078	$3d^6\ b^3F_2$	-	$(^4P)\ 4p\ ^5P_3$
	R	129	68305.73	0.33	*	68305.332	0.096	$(^4F)\ 4s\ ^3F_2$	-	$(b^2D)\ 4p\ ^3D_3$
	R	97	68358.4	0.14		68358.321	0.032	$(^4D)\ 4s\ ^5D_4$	-	$(^2H)\ 4p\ ^3G_5$
	R	50	68566.55	0.33	*	68565.673	0.043	$(^4G)\ 4s\ ^5G_6$	-	$(^2I)\ 4p\ ^1K_7$
	R	61	68645.72	0.33	*	68646.19	0.15	$3d^6\ a^3P_1$	-	$(^6S)\ 4p\ ^5P_2$
	R	144	68654.16	0.33		68654.553	0.089	$(a^2G)\ 4s\ ^3G_5$	-	$(b^2D)\ 4p\ ^3F_4$
	R	49	68677.88	0.33		68677.89	0.16	$(b^2F)\ 4s\ ^1F_3$	-	$(b^2G)\ 4p\ ^3H_4$
	R	53	68768.41	0.33		68768.837	0.038	$(^4G)\ 4s\ ^3G_5$	-	$(^4F)\ 4p\ ^3G_5$
	R	42	68896.19	0.33		68896.044	0.039	$(^4G)\ 4s\ ^3G_4$	-	$(^4F)\ 4p\ ^3G_4$
	R	175	69020.45	0.14		69020.399	0.07	$(^4F)\ 4s\ ^3F_4$	-	$(b^2D)\ 4p\ ^1F_3$
	R	50	69077.33	0.33		69077.476	0.042	$(^4G)\ 4s\ ^5G_4$	-	$(^2I)\ 4p\ ^3H_5$
	R	185	69132.39	0.14	*	69132.704	0.04	$(^4G)\ 4s\ ^3G_5$	-	$(a^2G)\ 4p\ ^1G_4$

Fe III Classified grating linelist continued

Exp.	Cat.	Int.	σ_{obs} (cm^{-1})	Unc. (cm^{-1})		σ_{Ritz} (cm^{-1})	Unc. (cm^{-1})	Transition		
	R	124	69532.13	0.34		69532.14	0.13	(^{6}S) 4p $^7P_2$	-	(^{6}S) 4d $^5D_3$
	R	59	69676.36	0.34	*	69676.631	0.039	(^{4}P) 4s $^5P_2$	-	(a^{2}D) 4p $^1F_3$
	R	62	69680.83	0.15	*	69680.45	0.14	3d^6 a$^3P_2$	-	(^{6}S) 4p $^5P_3$
	R	79	69723.87	0.15	*	69723.829	0.081	(^{4}G) 4s $^3G_4$	-	(a^{2}F) 4p $^1F_3$
	R	58	69755.83	0.15		69755.729	0.078	(^{6}S) 4p $^7P_2$	-	(^{6}S) 5s $^5S_2$
	R	44	69766.87	0.34		69767.034	0.033	(^{4}D) 4s $^5D_4$	-	(^{4}F) 4p $^3G_5$
	R	67	69842.35	0.34		69842.072	0.075	(^{4}D) 4s $^5D_2$	-	(^{4}F) 4p $^3G_3$
	R	164	69859.77	0.34	*	69860.526	0.1	(^{4}D) 4p $^5P_3$	-	(^{6}S) 5d $^5D_3$
	R	148	69861.09	0.34	*	69860.931	0.035	(^{4}D) 4p $^5P_3$	-	(^{6}S) 5d $^5D_4$
	R	82	69867.78	0.15		69867.726	0.088	(^{2}H) 4s $^3H_5$	-	(b^{2}D) 4p $^3F_4$
	R	102	69913.89	0.34		69913.900	0.1	(^{4}D) 4p $^5P_2$	-	(^{6}S) 5d $^5D_3$
	R	115	69964.42	0.34		69964.13	0.1	(^{4}G) 4s $^3G_4$	-	(a^{2}G) 4p $^3F_3$
	R	88	70025.07	0.15		70025.299	0.04	(^{4}G) 4s $^3G_3$	-	(a^{2}G) 4p $^3F_2$
	R	51	70131.0	0.34		70130.901	0.035	(^{4}D) 4s $^5D_4$	-	(a^{2}G) 4p $^1G_4$
	R	101	70285.48	0.15		70285.570	0.064	3d^6 b$^3P_2$	-	(^{4}D) 4p $^5F_1$
	R	81	70308.31	0.15	*	70308.440	0.047	(^{4}G) 4s $^3G_5$	-	(a^{2}G) 4p $^3F_4$

Fe III Classified grating linelist continued

Exp.	Cat.	Int.	σ_{obs} (cm^{-1})	Unc. (cm^{-1})		σ_{Ritz} (cm^{-1})	Unc. (cm^{-1})	Transition		
	R	151	70667.53	0.15		70667.283	0.031	(^{4}D) 4p ^{5}D$_4$	-	(^{6}S) 5d ^{5}D$_4$
	R	200	70824.29	0.15		70823.926	0.078	3d^6 b^{3}F$_2$	-	(^{4}D) 4p ^{5}F$_3$
	R	88	70965.92	0.15	*	70965.812	0.07	3d^6 b^{3}F$_4$	-	(^{4}D) 4p ^{5}F$_4$
	R	126	71306.69	0.15		71306.637	0.043	(^{4}D) 4s ^{5}D$_4$	-	(a^{2}G) 4p ^{3}F$_4$
	R	96	71318.13	0.15	*	71317.859	0.041	(^{4}G) 4s ^{3}G$_4$	-	(^{4}F) 4p ^{3}F$_4$
	R	64	71352.33	0.36		71352.586	0.041	(^{4}G) 4s ^{3}G$_5$	-	(^{4}F) 4p ^{3}F$_4$
	R	164	71443.01	0.15		71443.272	0.094	(^{4}G) 4s ^{5}G$_2$	-	(^{4}F) 4p ^{5}G$_2$
	R	81	71583.5	0.15	*	71583.40	0.13	(^{4}G) 4s ^{3}G$_4$	-	(^{4}F) 4p ^{3}F$_3$
	R	135	71602.16	0.15	*	71601.837	0.09	(^{4}G) 4s ^{5}G$_2$	-	(^{4}F) 4p ^{5}G$_3$
	R	135	71602.16	0.15	*	71602.256	0.067	(^{4}G) 4s ^{5}G$_3$	-	(^{4}F) 4p ^{5}G$_3$
	R	199	71646.07	0.15		71646.165	0.064	3d^6 b^{3}F$_3$	-	(^{4}G) 4p ^{3}G$_4$
	R	218	71673.8	0.15		71673.717	0.071	3d^6 b^{3}F$_4$	-	(^{4}G) 4p ^{3}G$_5$
	R	64	71722.63	0.36	*	71722.794	0.033	(^{4}P) 4s ^{5}P$_3$	-	(^{2}H) 4p ^{3}G$_3$
	R	183	71734.88	0.15		71734.76	0.12	3d^6 b^{3}F$_2$	-	(^{4}G) 4p ^{3}G$_3$
	R	117	71745.28	0.36		71745.147	0.03	(^{4}G) 4s ^{5}G$_3$	-	(^{4}F) 4p ^{5}G$_4$
	R	216	71752.48	0.15		71752.543	0.03	(^{4}G) 4s ^{5}G$_4$	-	(^{4}F) 4p ^{5}G$_4$

Fe III Classified grating linelist continued

Exp.	Cat.	Int.	σ_{obs} (cm^{-1})	Unc. (cm^{-1})		σ_{Ritz} (cm^{-1})	Unc. (cm^{-1})	Transition		
	R	105	71783.85	0.15		71783.876	0.068	(^{4}G) 4s $^5G_2$	-	(a^{2}D) 4p $^3D_2$
	R	72	71809.26	0.15	*	71809.262	0.1	(^{4}G) 4s $^3G_3$	-	(^{4}F) 4p $^3F_2$
	R	80	71812.51	0.15		71812.51	0.1	(^{4}D) 4s $^3D_2$	-	(^{2}S) 4p $^3P_1$
	R	195	71849.66	0.15		71849.668	0.029	(^{4}G) 4s $^5G_5$	-	(a^{2}F) 4p $^3G_5$
	R	125	71935.05	0.16		71934.901	0.092	3d^6 b^{3}P$_2$	-	(^{4}P) 4p $^3D_3$
	R	167	72052.65	0.36	*	72051.732	0.1	3d^6 b^{3}F$_3$	-	(^{4}P) 4p $^3D_3$
	R	219	72070.62	0.36		72070.91	0.1	3d^6 b^{3}F$_4$	-	(^{4}P) 4p $^3D_3$
	Q	211	72087.61	0.36	*	72087.473	0.039	(^{4}G) 4s $^5G_5$	-	(a^{2}F) 4p $^3G_4$
	R	143	72126.03	0.16	*	72126.190	0.037	(^{4}G) 4s $^3G_4$	-	(a^{2}G) 4p $^3H_4$
	R	72	72155.75	0.36		72156.067	0.043	(^{4}G) 4s $^5G_6$	-	(^{2}I) 4p $^1I_6$
	R	163	72268.64	0.16		72268.494	0.029	(^{4}G) 4s $^5G_5$	-	(^{4}F) 4p $^5G_5$
	R	136	72309.66	0.37		72309.565	0.03	(^{4}G) 4s $^5G_6$	-	(^{4}F) 4p $^5G_5$
	R	235	72313.74	0.16		72313.748	0.03	(^{4}G) 4s $^5G_6$	-	(^{4}F) 4p $^5G_6$
	R	215	72333.25	0.16		72333.298	0.067	3d^6 b^{3}F$_3$	-	(^{4}P) 4p $^3D_2$
	R	191	72368.95	0.37		72369.243	0.099	(^{4}D) 4p $^5F_4$	-	(^{6}S) 5d $^5D_3$
	R	91	72422.47	0.37		72422.08	0.11	(^{4}D) 4s $^3D_2$	-	(^{2}S) 4p $^3P_2$

Fe III Classified grating linelist continued

Exp.	Cat.	Int.	σ_{obs} (cm^{-1})	Unc. (cm^{-1})		σ_{Ritz} (cm^{-1})	Unc. (cm^{-1})	Transition		
	R	72	72503.7	0.37		72503.391	0.03	(^{4}G) 4s ^{5}G$_4$	-	(^{4}F) 4p ^{5}F$_4$
	R	83	72513.9	0.16	*	72514.190	0.031	(^{4}G) 4s ^{5}G$_3$	-	(^{4}F) 4p ^{5}F$_3$
	R	83	72513.9	0.16	*	72513.771	0.067	(^{4}G) 4s ^{5}G$_2$	-	(^{4}F) 4p ^{5}F$_3$
	R	186	72553.99	0.37		72553.60	0.11	3d^6 b^{3}F$_4$	-	(^{4}D) 4p ^{5}D$_3$
	R	65	72705.7	0.37	*	72705.296	0.039	(^{4}G) 4s ^{5}G$_3$	-	(a^{2}D) 4p ^{1}F$_3$
	R	65	72705.7	0.37	*	72704.877	0.071	(^{4}G) 4s ^{5}G$_2$	-	(a^{2}D) 4p ^{1}F$_3$
	Q	179	72718.12	0.16	*	72718.128	0.029	(^{4}G) 4s ^{5}G$_5$	-	(^{4}F) 4p ^{5}F$_5$
	R	206	72759.23	0.16		72759.200	0.03	(^{4}G) 4s ^{5}G$_6$	-	(^{4}F) 4p ^{5}F$_5$
	R	64	72834.17	0.37		72833.80	0.15	(b^{2}F) 4s ^{3}F$_4$	-	(b^{2}G) 4p ^{3}F$_4$
	R	55	73018.23	0.37		73018.103	0.032	(^{4}D) 4s ^{5}D$_3$	-	(a^{2}G) 4p ^{3}H$_4$
	R	141	73034.34	0.37		73035.004	0.084	3d^6 b^{1}G$_4$	-	(^{2}I) 4p ^{3}I$_5$
	R	101	73051.14	0.16		73051.241	0.07	3d^6 b^{3}P$_1$	-	(^{4}P) 4p ^{3}D$_2$
	R	67	73266.62	0.38	*	73266.025	0.068	3d^6 b^{3}P$_1$	-	(^{4}P) 4p ^{3}D$_1$
	R	152	73301.53	0.16	*	73302.086	0.04	(^{4}G) 4s ^{5}G$_3$	-	(a^{2}F) 4p ^{3}F$_3$
	R	152	73301.53	0.16	*	73301.667	0.072	(^{4}G) 4s ^{5}G$_2$	-	(a^{2}F) 4p ^{3}F$_3$
	R	117	73344.22	0.16		73344.407	0.069	3d^6 b^{3}P$_1$	-	(^{4}D) 4p ^{5}D$_1$

Fe III Classified grating linelist continued

Exp.	Cat.	Int.	σ_{obs} (cm^{-1})	Unc. (cm^{-1})		σ_{Ritz} (cm^{-1})	Unc. (cm^{-1})	Transition		
	R	63	73401.07	0.38	*	73401.981	0.065	$3d^6\ b^3F_3$	-	$(^4D)\ 4p\ ^5P_2$
	Q	192	73455.42	0.16	*	73455.355	0.065	$3d^6\ b^3F_3$	-	$(^4D)\ 4p\ ^5P_3$
	R	109	73637.65	0.16		73637.820	0.049	$(^4G)\ 4s\ ^3G_5$	-	$(b^2F)\ 4p\ ^1G_4$
	R	76	73694.14	0.16	*	73693.72	0.11	$3d^6\ b^3P_0$	-	$(^4P)\ 4p\ ^3D_1$
	R	62	73742.83	0.16		73742.940	0.029	$(^4G)\ 4s\ ^5G_5$	-	$(^4F)\ 4p\ ^5D_4$
	R	99	73841.23	0.16		73841.342	0.04	$(^4G)\ 4s\ ^3G_4$	-	$(b^2F)\ 4p\ ^3F_3$
	R	108	73914.15	0.38	*	73913.43	0.11	$(^4P)\ 4p\ ^3P_2$	-	$(^6S)\ 5d\ ^5D_3$
	R	36	74033.49	0.38		74033.211	0.032	$(^4G)\ 4s\ ^5G_3$	-	$(^2H)\ 4p\ ^3H_4$
	R	44	74040.29	0.38		74040.608	0.032	$(^4G)\ 4s\ ^5G_4$	-	$(^2H)\ 4p\ ^3H_4$
	R	49	74049.83	0.16		74049.815	0.074	$(^4G)\ 4s\ ^5G_3$	-	$(^4F)\ 4p\ ^5D_2$
	R	38	74120.69	0.38	*	74119.924	0.069	$3d^6\ b^3P_1$	-	$(^4D)\ 4p\ ^5P_2$
	R	127	74248.53	0.17		74248.722	0.034	$(^4D)\ 4s\ ^5D_3$	-	$(a^2G)\ 4p\ ^3G_4$
	R	171	74441.82	0.39		74442.08	0.12	$3d^6\ b^3P_2$	-	$(^4D)\ 4p\ ^3D_3$
	R	202	74489.34	0.17		74489.257	0.085	$3d^6\ b^1G_4$	-	$(^2I)\ 4p\ ^1H_5$
	R	121	74569.55	0.39		74569.465	0.068	$(a^2F)\ 4s\ ^3F_4$	-	$(b^2D)\ 4p\ ^3D_3$
	R	71	74609.55	0.39	*	74608.834	0.067	$3d^6\ b^3F_3$	-	$(^4D)\ 4p\ ^3D_2$

Fe III Classified grating linelist continued

Exp.	Cat.	Int.	σ_{obs} (cm^{-1})	Unc. (cm^{-1})		σ_{Ritz} (cm^{-1})	Unc. (cm^{-1})	Transition		
	R	105	74615.34	0.39		74615.786	0.033	(^{4}G) 4s ^{5}G$_4$	-	(^{2}H) 4p ^{3}G$_4$
	R	123	74890.27	0.39		74890.406	0.041	(^{4}D) 4s ^{5}D$_4$	-	(a^{2}G) 4p ^{1}H$_5$
	R	198	75167.57	0.17		75167.671	0.073	3d^6 b^{3}F$_4$	-	(^{4}D) 4p ^{3}F$_4$
	R	39	75200.2	0.4		75200.303	0.06	(^{4}D) 4s ^{5}D$_2$	-	(a^{2}G) 4p ^{1}F$_3$
	R	134	75237.2	0.4		75237.650	0.074	(a^{2}D) 4s ^{1}D$_2$	-	(b^{2}D) 4p ^{1}D$_2$
	R	70	75326.79	0.17		75326.777	0.069	3d^6 b^{3}P$_1$	-	(^{4}D) 4p ^{3}D$_2$
	R	146	75342.73	0.17		75342.871	0.067	3d^6 b^{3}F$_3$	-	(^{4}D) 4p ^{3}F$_3$
	R	132	75487.88	0.17		75487.918	0.093	3d^6 b^{3}F$_2$	-	(^{4}D) 4p ^{3}F$_2$
	R	204	75570.82	0.17	*	75571.115	0.092	(a^{2}D) 4s ^{3}D$_2$	-	(b^{2}D) 4p ^{3}F$_3$
	R	44	75750.3	0.4		75750.00	0.15	(^{4}F) 4s ^{3}F$_4$	-	(b^{2}G) 4p ^{3}F$_4$
	R	48	75796.8	0.4		75796.60	0.11	(^{4}P) 4s ^{3}P$_2$	-	(^{2}S) 4p ^{3}P$_2$
	R	188	75978.37	0.17	*	75978.53	0.12	3d^6 b^{3}P$_2$	-	(^{4}P) 4p ^{3}S$_1$
	R	97	75996.39	0.17		75996.344	0.033	(^{4}G) 4s ^{5}G$_5$	-	(^{4}F) 4p ^{3}G$_5$
	R	57	76068.01	0.41		76068.378	0.077	(^{6}S) 4s ^{5}S$_2$	-	(^{4}P) 4p ^{5}D$_3$
	R	28	76083.64	0.41	*	76083.501	0.032	(^{4}G) 4s ^{5}G$_6$	-	(^{2}H) 4p ^{3}I$_5$
	R	33	76089.6	0.41		76089.026	0.099	(^{4}P) 4p ^{5}D$_4$	-	(^{6}S) 5d ^{5}D$_3$

Fe III Classified grating linelist continued

Exp.	Cat.	Int.	σ_{obs} (cm^{-1})	Unc. (cm^{-1})		σ_{Ritz} (cm^{-1})	Unc. (cm^{-1})	Transition		
	R	33	76089.6	0.41		76089.431	0.031	(^{4}P) 4p ^{5}D$_4$	-	(^{6}S) 5d ^{5}D$_4$
	R	155	76280.62	0.17		76280.52	0.14	(a^{2}G) 4s ^{3}G$_5$	-	(b^{2}G) 4p ^{3}H$_6$
	R	67	76339.96	0.41		76339.784	0.035	(^{4}G) 4s ^{5}G$_4$	-	(a^{2}G) 4p ^{1}G$_4$
	R	204	76379.61	0.41		76379.237	0.031	(^{4}G) 4s ^{5}G$_5$	-	(^{2}H) 4p ^{3}I$_6$
	R	153	76418.6	0.41		76418.75	0.13	(^{4}F) 4s ^{5}F$_1$	-	(b^{2}D) 4p ^{3}P$_1$
	R	40	76438.75	0.41		76438.85	0.15	(a^{2}G) 4s ^{3}G$_4$	-	(b^{2}G) 4p ^{3}F$_4$
	R	59	76542.02	0.41		76542.263	0.099	(^{4}P) 4p ^{5}D$_3$	-	(^{6}S) 5d ^{5}D$_3$
	R	189	76813.41	0.18		76813.31	0.11	3d^6 b^{3}P$_1$	-	(^{4}P) 4p ^{3}S$_1$
	R	45	76891.79	0.41		76891.90	0.35	(b^{2}G) 4s ^{1}G$_4$	-	(c^{2}D) 4p ^{1}F$_3$
	R	82	76965.41	0.18		76965.636	0.078	(^{4}G) 4s ^{5}G$_4$	-	(a^{2}F) 4p ^{1}F$_3$
	R	73	77136.09	0.18		77135.877	0.031	(^{4}G) 4p ^{5}F$_3$	-	(^{6}S) 5d ^{5}D$_4$
	R	152	77241.01	0.18		77241.00	0.13	3d^6 b^{3}P$_0$	-	(^{4}P) 4p ^{3}S$_1$
	R	131	77294.93	0.18	*	77294.617	0.032	(^{4}G) 4p ^{5}F$_5$	-	(^{6}S) 5d ^{5}D$_4$
	R	156	77306.46	0.18		77306.46	0.18	(b^{2}G) 4s ^{3}G$_5$	-	(c^{2}D) 4p ^{3}F$_4$
	R	54	77327.2	0.42		77327.685	0.086	3d^6 b^{1}G$_4$	-	(a^{2}F) 4p ^{3}G$_3$
	R	219	77442.84	0.18		77442.774	0.077	(^{6}S) 4s ^{5}S$_2$	-	(^{4}P) 4p ^{5}P$_3$

Fe III Classified grating linelist continued

Exp.	Cat.	Int.	σ_{obs} (cm^{-1})	Unc. (cm^{-1})		σ_{Ritz} (cm^{-1})	Unc. (cm^{-1})	Transition		
	R	54	77654.94	0.42	*	77654.510	0.072	(a^2D) 4s ^{3}D$_3$	-	(b^2D) 4p ^{3}P$_2$
	R	54	77654.94	0.42	*	77655.21	0.11	(a^2D) 4s ^{3}D$_2$	-	(b^2D) 4p ^{3}P$_1$
	R	191	77721.33	0.18		77721.389	0.077	(^{6}S) 4s ^{5}S$_2$	-	(^{4}P) 4p ^{5}P$_2$
	R	174	77867.73	0.18		77867.644	0.077	(^{6}S) 4s ^{5}S$_2$	-	(^{4}P) 4p ^{5}P$_1$
	R	211	77909.9	0.18	*	77909.459	0.078	(^{4}P) 4s ^{5}P$_1$	-	(b^2F) 4p ^{3}F$_2$
	R	206	78193.79	0.18		78193.689	0.089	3d^6 b^{3}P$_2$	-	(^{4}D) 4p ^{3}P$_1$
	R	50	78283.65	0.43	*	78283.978	0.057	(^{4}G) 4s ^{3}G$_4$	-	(^{2}H) 4p ^{1}G$_4$
	R	68	78307.31	0.43		78307.30	0.13	(^{4}F) 4s ^{3}F$_4$	-	(b^2G) 4p ^{1}H$_5$
	Q	68	78505.44	0.18		78505.556	0.068	3d^6 b^{3}P$_2$	-	(^{4}D) 4p ^{3}P$_2$
	R	98	78697.52	0.43		78697.215	0.088	(^{6}S) 4s ^{5}S$_2$	-	(^{4}P) 4p ^{3}P$_2$
	R	187	78794.82	0.19		78794.68	0.13	3d^6 b^{3}P$_1$	-	(^{4}D) 4p ^{3}P$_0$
	R	148	79028.52	0.19		79028.463	0.09	3d^6 b^{3}P$_1$	-	(^{4}D) 4p ^{3}P$_1$
	R	223	79340.4	0.19		79340.330	0.069	3d^6 b^{3}P$_1$	-	(^{4}D) 4p ^{3}P$_2$
	R	183	79456.2	0.19		79456.16	0.12	3d^6 b^{3}P$_0$	-	(^{4}D) 4p ^{3}P$_1$
	R	142	79696.96	0.19		79697.160	0.079	(^{6}S) 4s ^{5}S$_2$	-	(^{4}D) 4p ^{5}F$_1$
	R	60	79737.0	0.45	*	79736.15	0.11	(^{4}D) 4s ^{5}D$_1$	-	(^{2}S) 4p ^{3}P$_2$

Fe III Classified grating linelist continued

Exp.	Cat.	Int.	σ_{obs} (cm^{-1})	Unc. (cm^{-1})		σ_{Ritz} (cm^{-1})	Unc. (cm^{-1})	Transition		
	R	105	79825.34	0.45		79825.96	0.13	(^{4}F) 4s ^{3}F$_3$	-	(b^{2}G) 4p ^{1}F$_3$
	R	65	79837.83	0.45		79837.54	0.13	(^{4}F) 4s ^{3}F$_4$	-	(b^{2}G) 4p ^{1}F$_3$
	R	64	79895.31	0.45		79895.043	0.032	(^{4}G) 4s ^{5}G$_6$	-	(a^{2}G) 4p ^{3}H$_6$
	R	169	80305.93	0.19	*	80306.667	0.082	3d^6 b^{1}G$_4$	-	(^{2}H) 4p ^{3}H$_4$
	R	59	80577.71	0.45	*	80577.050	0.095	3d^6 a^{1}D$_2$	-	(^{4}P) 4p ^{5}D$_1$
	R	46	80599.08	0.45		80598.616	0.034	(^{4}G) 4s ^{5}G$_4$	-	(a^{2}G) 4p ^{3}G$_4$
	R	60	80727.7	0.2	*	80727.11	0.12	(^{4}D) 4s ^{3}D$_3$	-	(b^{2}D) 4p ^{3}F$_2$
	R	64	80833.56	0.46		80833.263	0.082	3d^6 b^{1}G$_4$	-	(^{2}H) 4p ^{3}G$_5$
	R	38	80919.7	0.46		80919.30	0.14	(^{6}S) 4s ^{5}S$_2$	-	(^{4}G) 4p ^{3}G$_3$
	R	76	80965.8	0.2	*	80966.645	0.083	3d^6 b^{1}G$_4$	-	(^{2}H) 4p ^{3}G$_3$
	R	127	81069.5	0.2		81069.54	0.13	3d^6 ^{5}D$_1$	-	(^{6}S) 4p ^{7}P$_2$
	R	141	81154.87	0.46		81154.11	0.11	(^{4}D) 4s ^{3}D$_2$	-	(b^{2}D) 4p ^{3}D$_1$
	R	142	81160.6	0.2		81160.788	0.041	(^{4}G) 4s ^{5}G$_6$	-	(a^{2}G) 4p ^{1}H$_5$
	R	185	81172.1	0.2		81172.010	0.095	3d^6 a^{1}D$_2$	-	(^{4}G) 4p ^{5}F$_2$
	R	106	81181.0	0.2		81181.07	0.11	(^{4}D) 4s ^{3}D$_1$	-	(b^{2}D) 4p ^{3}D$_1$
	R	197	81417.4	0.2		81417.23	0.15	(^{4}G) 4s ^{5}G$_6$	-	(^{2}H) 4p ^{1}H$_5$

Fe III Classified grating linelist continued

Exp.	Cat.	Int.	σ_{obs} (cm^{-1})	Unc. (cm^{-1})		σ_{Ritz} (cm^{-1})	Unc. (cm^{-1})	Transition		
	R	105	81434.02	0.46	*	81434.489	0.076	$3d^6\ b^3F_4$	-	$(^2I)\ 4p\ ^1H_5$
	R	126	81550.4	0.2		81550.59	0.15	$(a^2F)\ 4s\ ^3F_3$	-	$(b^2G)\ 4p\ ^3F_4$
	R	210	81565.8	0.2	*	81565.93	0.51	$3d^6\ ^5D_3$	-	$(^6S)\ 4p\ ^7P_2$
	R	64	81668.52	0.47		81667.886	0.066	$3d^6\ b^3P_2$	-	$(a^2D)\ 4p\ ^3F_3$
	R	128	81784.7	0.2	*	81784.717	0.064	$3d^6\ b^3F_3$	-	$(a^2D)\ 4p\ ^3F_3$
	R	216	81826.0	0.2		81826.12	0.14	$(a^2F)\ 4s\ ^3F_3$	-	$(b^2G)\ 4p\ ^3F_3$
	R	154	81828.71	0.47	*	81829.18	0.12	$(^6S)\ 4s\ ^5S_2$	-	$(^4D)\ 4p\ ^5D_3$
	R	221	81898.0	0.2	*	81898.379	0.077	$(^6S)\ 4s\ ^5S_2$	-	$(^4D)\ 4p\ ^5D_2$
	R	221	81898.0	0.2	*	81898.26	0.51	$3d^6\ ^5D_3$	-	$(^6S)\ 4p\ ^7P_3$
	R	137	81920.9	0.2	*	81921.223	0.079	$(^6S)\ 4s\ ^5S_2$	-	$(^4D)\ 4p\ ^5D_1$
	R	149	81957.7	0.2		81957.53	0.12	$3d^6\ ^1F_3$	-	$(^4D)\ 4p\ ^3D_3$
	Q	185	82128.44	0.47		82128.08	0.14	$(a^2F)\ 4s\ ^3F_2$	-	$(b^2G)\ 4p\ ^3F_3$
	R	192	82287.9	0.2		82288.062	0.082	$3d^6\ b^1G_4$	-	$(^2H)\ 4p\ ^3I_5$
	Q	79	82334.3	0.2		82334.34	0.19	$3d^6\ ^5D_4$	-	$(^6S)\ 4p\ ^7P_3$
	R	93	82404.1	0.2		82403.910	0.083	$3d^6\ b^1G_4$	-	$(^4F)\ 4p\ ^3G_4$
	Q	54	82509.2	0.2	*	82509.288	0.071	$3d^6\ b^3F_4$	-	$(a^2D)\ 4p\ ^3F_4$

Fe III Classified grating linelist continued

Exp.	Cat.	Int.	σ_{obs} (cm^{-1})	Unc. (cm^{-1})		σ_{Ritz} (cm^{-1})	Unc. (cm^{-1})	Transition		
	R	151	82605.6	0.2	*	82605.843	0.084	$3d^6\ b^1G_4$	-	$(a^2G)\ 4p\ ^1G_4$
	R	82	82697.12	0.48		82696.740	0.078	$(^6S)\ 4s\ ^5S_2$	-	$(^4D)\ 4p\ ^5P_2$
	R	92	82750.08	0.21		82750.114	0.078	$(^6S)\ 4s\ ^5S_2$	-	$(^4D)\ 4p\ ^5P_3$
	R	96	82777.69	0.21		82777.829	0.074	$3d^6\ ^3D_3$	-	$(^4G)\ 4p\ ^5G_4$
	R	153	82858.35	0.21		82858.42	0.11	$3d^6\ ^3D_1$	-	$(^4G)\ 4p\ ^5G_2$
	R	176	82889.12	0.48		82889.730	0.081	$3d^6\ ^3D_2$	-	$(^4G)\ 4p\ ^5G_3$
	R	107	82962.01	0.21		82961.845	0.096	$(^4D)\ 4s\ ^3D_1$	-	$(b^2D)\ 4p\ ^3P_2$
	R	161	82976.26	0.48	*	82975.13	0.39	$(b^2D)\ 4s\ ^1D_2$	-	$(c^2D)\ 4p\ ^3D_1$
	R	137	83059.93	0.21		83059.63	0.11	$(^4P)\ 4s\ ^5P_3$	-	$(^2S)\ 4p\ ^3P_2$
	R	49	83080.22	0.48		83080.452	0.077	$(^4D)\ 4s\ ^3D_3$	-	$(b^2D)\ 4p\ ^3P_2$
	R	182	83232.55	0.48	*	83231.70	0.11	$3d^6\ b^1G_4$	-	$(a^2F)\ 4p\ ^1F_3$
	R	165	83462.35	0.49		83463.00	0.13	$(a^2D)\ 4s\ ^1D_2$	-	$(b^2G)\ 4p\ ^1F_3$
	R	133	83471.62	0.49		83471.99	0.12	$3d^6\ b^1G_4$	-	$(a^2G)\ 4p\ ^3F_3$
	R	197	83781.92	0.21	*	83781.579	0.087	$3d^6\ b^1G_4$	-	$(a^2G)\ 4p\ ^3F_4$
	R	150	83853.08	0.21	*	83853.67	0.13	$(^6S)\ 4s\ ^5S_2$	-	$(^4D)\ 4p\ ^3D_3$
	R	150	83853.08	0.21	*	83853.353	0.066	$3d^6\ b^3P_2$	-	$(a^2D)\ 4p\ ^3P_2$

Fe III Classified grating linelist continued

Exp.	Cat.	Int.	σ_{obs} (cm^{-1})	Unc. (cm^{-1})		σ_{Ritz} (cm^{-1})	Unc. (cm^{-1})	Transition		
	Q	47	83894.52	0.49	*	83894.36	0.1	$3d^6\ a^1D_2$	-	$(^4P)\ 4p\ ^3P_2$
	R	203	83903.67	0.49		83903.593	0.084	$(^6S)\ 4s\ ^5S_2$	-	$(^4D)\ 4p\ ^3D_2$
	R	151	83918.95	0.49		83918.555	0.037	$(^4G)\ 4s\ ^5G_4$	-	$(b^2F)\ 4p\ ^3G_5$
	R	111	84062.36	0.49	*	84062.33	0.13	$3d^6\ a^1G_4$	-	$(^4G)\ 4p\ ^5H_3$
	R	115	84064.98	0.49	*	84065.138	0.067	$3d^6\ b^3F_3$	-	$(a^2F)\ 4p\ ^1G_4$
	R	180	84137.62	0.21		84137.44	0.16	$3d^6\ b^3P_2$	-	$(a^2D)\ 4p\ ^3P_1$
	R	233	84254.1	0.5	*	84253.743	0.068	$3d^6\ b^3F_3$	-	$(a^2F)\ 4p\ ^3G_3$
	R	233	84254.1	0.5	*	84253.666	0.077	$3d^6\ ^3D_3$	-	$(^4G)\ 4p\ ^5H_4$
	R	233	84254.1	0.5	*	84254.048	0.096	$(^4P)\ 4s\ ^3P_2$	-	$(b^2D)\ 4p\ ^3F_3$
	R	97	84271.4	0.5	*	84272.917	0.074	$3d^6\ b^3F_4$	-	$(a^2F)\ 4p\ ^3G_3$
	R	151	84365.05	0.21	*	84364.49	0.18	$3d^6\ b^3F_2$	-	$(a^2D)\ 4p\ ^3P_1$
	R	151	84365.05	0.21	*	84363.960	0.082	$3d^6\ b^3F_2$	-	$(a^2F)\ 4p\ ^3G_3$
	R	186	84688.35	0.22	*	84688.127	0.071	$3d^6\ b^3P_1$	-	$(a^2D)\ 4p\ ^3P_2$
	R	93	84801.5	0.5		84801.770	0.086	$3d^6\ b^3F_3$	-	$(^4F)\ 4p\ ^5G_3$
	R	59	84804.7	0.5		84805.26	0.16	$3d^6\ b^3P_2$	-	$(a^2D)\ 4p\ ^3D_1$
	R	170	84821.6	0.5		84820.944	0.091	$3d^6\ b^3F_4$	-	$(^4F)\ 4p\ ^5G_3$

Fe III Classified grating linelist continued

Exp.	Cat.	Int.	σ_{obs} (cm^{-1})	Unc. (cm^{-1})		σ_{Ritz} (cm^{-1})	Unc. (cm^{-1})	Transition		
	Q	123	84912.3	0.5		84911.987	0.097	$3d^6\ b^3F_2$	-	$(^4F)\ 4p\ ^5G_3$
	R	137	84963.21	0.22	*	84963.834	0.071	$3d^6\ b^3F_4$	-	$(^4F)\ 4p\ ^5G_4$
	R	114	85205.87	0.22	*	85205.616	0.095	$3d^6\ a^1D_2$	-	$(^4D)\ 4p\ ^5F_3$
	R	110	85278.32	0.22	*	85278.337	0.074	$3d^6\ b^3F_4$	-	$(a^2F)\ 4p\ ^3G_4$
	R	102	85293.45	0.51	*	85293.37	0.12	$3d^6\ b^3P_2$	-	$(a^2F)\ 4p\ ^3D_3$
	R	68	85362.25	0.51		85361.15	0.1	$3d^6\ b^3P_1$	-	$(^4F)\ 4p\ ^5G_2$
	R	195	85429.12	0.22	*	85429.38	0.13	$3d^6\ b^3F_4$	-	$(a^2F)\ 4p\ ^3D_3$
	R	182	85546.13	0.22	*	85546.212	0.054	$(^4G)\ 4s\ ^5G_5$	-	$(^2H)\ 4p\ ^1G_4$
	R	147	85610.35	0.22	*	85609.873	0.074	$3d^6\ ^3D_3$	-	$(^4G)\ 4p\ ^5F_4$
	R	169	85617.1	0.51		85617.818	0.074	$3d^6\ ^3D_3$	-	$(^4G)\ 4p\ ^5F_3$
	R	122	85687.31	0.51		85687.000	0.082	$3d^6\ b^1G_4$	-	$(a^2G)\ 4p\ ^3H_5$
	R	117	85732.12	0.51	*	85732.878	0.071	$3d^6\ b^3F_4$	-	$(^4F)\ 4p\ ^5F_3$
	R	156	85858.87	0.22		85858.78	0.15	$(^2I)\ 4s\ ^3I_5$	-	$(b^2G)\ 4p\ ^3H_4$
	R	195	85924.97	0.52	*	85923.984	0.074	$3d^6\ b^3F_4$	-	$(a^2D)\ 4p\ ^1F_3$
	R	178	85940.19	0.22		85940.10	0.13	$(a^2F)\ 4s\ ^3F_2$	-	$(b^2G)\ 4p\ ^1F_3$
	R	200	86238.42	0.52	*	86237.092	0.068	$3d^6\ b^3F_3$	-	$(a^2F)\ 4p\ ^3F_2$

Fe III Classified grating linelist continued

Exp.	Cat.	Int.	σ_{obs} (cm^{-1})	Unc. (cm^{-1})		σ_{Ritz} (cm^{-1})	Unc. (cm^{-1})	Transition		
	R	167	86278.97	0.52	*	86279.826	0.083	$3d^6\ b^3F_2$	-	$(a^2F)\ 4p\ ^3D_1$
	R	95	86309.13	0.22		86309.408	0.078	$(^4P)\ 4s\ ^3P_2$	-	$(b^2D)\ 4p\ ^3P_2$
	R	220	86335.88	0.22	*	86336.673	0.071	$3d^6\ b^3F_4$	-	$(a^2F)\ 4p\ ^3F_4$
	R	197	86348.11	0.22		86348.26	0.14	$(^2I)\ 4s\ ^3I_7$	-	$(b^2G)\ 4p\ ^3H_6$
	R	190	86663.3	0.53	*	86662.439	0.083	$3d^6\ b^1G_4$	-	$(a^2G)\ 4p\ ^3G_5$
	R	190	86663.3	0.53	*	86664.264	0.074	$3d^6\ ^3D_3$	-	$(^4P)\ 4p\ ^5D_4$
	R	116	86681.33	0.53		86681.58	0.38	$(b^2F)\ 4s\ ^1F_3$	-	$(^2P)\ 4p\ ^1D_2$
	R	93	86954.48	0.53	*	86955.035	0.075	$3d^6\ b^3P_1$	-	$(a^2F)\ 4p\ ^3F_2$
	R	92	86959.09	0.53		86958.73	0.12	$(^4G)\ 4s\ ^3G_3$	-	$(b^2D)\ 4p\ ^3F_2$
	R	213	87010.92	0.53		87010.797	0.066	$3d^6\ b^3P_2$	-	$(^4F)\ 4p\ ^5D_3$
	R	180	87026.82	0.53		87026.33	0.13	$3d^6\ a^1D_2$	-	$(^4D)\ 4p\ ^5D_3$
	R	237	87110.97	0.23		87110.959	0.087	$3d^6\ b^1G_4$	-	$(b^2F)\ 4p\ ^1G_4$
	R	116	87253.41	0.53	*	87253.067	0.093	$(^4G)\ 4s\ ^3G_4$	-	$(b^2D)\ 4p\ ^3F_3$
	Q	134	87438.35	0.23	*	87437.76	0.11	$3d^6\ ^3D_1$	-	$(^4G)\ 4p\ ^3F_2$
	R	228	87448.06	0.23		87447.772	0.083	$3d^6\ ^3D_2$	-	$(^4G)\ 4p\ ^3F_2$
	Q	165	87493.12	0.54		87492.611	0.078	$3d^6\ ^3D_3$	-	$(^4G)\ 4p\ ^3F_4$

Fe III Classified grating linelist continued

Exp.	Cat.	Int.	σ_{obs} (cm^{-1})	Unc. (cm^{-1})		σ_{Ritz} (cm^{-1})	Unc. (cm^{-1})	Transition		
	Q	166	87530.95	0.23		87530.777	0.083	$3d^6\ ^3D_2$	-	$(^4G)\ 4p\ ^3F_3$
	Q	92	87621.91	0.54		87621.80	0.17	$3d^6\ b^1G_4$	-	$(^2H)\ 4p\ ^1H_5$
	R	112	87727.76	0.23	*	87727.242	0.082	$3d^6\ ^3D_2$	-	$(^4P)\ 4p\ ^5P_3$
	R	213	87747.39	0.54		87746.84	0.11	$3d^6\ b^1G_4$	-	$(b^2F)\ 4p\ ^3F_4$
	R	165	87777.89	0.54	*	87778.495	0.071	$3d^6\ b^3F_4$	-	$(^2H)\ 4p\ ^3G_5$
	R	137	87808.03	0.54		87807.903	0.065	$3d^6\ b^3F_3$	-	$(^2H)\ 4p\ ^3G_4$
	R	225	87832.79	0.54	*	87833.463	0.094	$(^4G)\ 4s\ ^3G_4$	-	$(b^2D)\ 4p\ ^3F_4$
	R	251	87893.16	0.54		87892.703	0.065	$3d^6\ b^3F_3$	-	$(^2H)\ 4p\ ^3G_3$
	R	98	87947.65	0.54		87947.262	0.097	$3d^6\ a^1D_2$	-	$(^4D)\ 4p\ ^5P_3$
	R	124	88002.53	0.54		88002.920	0.08	$3d^6\ b^3F_2$	-	$(^2H)\ 4p\ ^3G_3$
	R	146	88031.27	0.23		88031.04	0.18	$3d^6\ a^1S_0$	-	$(^4P)\ 4p\ ^3D_1$
	Q	126	88346.25	0.23		88346.31	0.14	$3d^6\ ^5D_2$	-	$(^6S)\ 4p\ ^5P_3$
	Q	172	88402.24	0.23		88402.36	0.13	$3d^6\ ^5D_1$	-	$(^6S)\ 4p\ ^5P_2$
	R	169	88441.02	0.55	*	88441.79	0.12	$3d^6\ ^3G_3$	-	$(^4G)\ 4p\ ^5G_2$
	Q	202	88464.42	0.23		88464.42	0.23	$3d^6\ ^5D_0$	-	$(^6S)\ 4p\ ^5P_1$
	R	197	88508.89	0.55	*	88506.757	0.084	$3d^6\ b^3F_2$	-	$(a^2D)\ 4p\ ^1P_1$

Fe III Classified grating linelist continued

Exp.	Cat.	Int.	σ_{obs} (cm^{-1})	Unc. (cm^{-1})		σ_{Ritz} (cm^{-1})	Unc. (cm^{-1})	Transition		
	R	197	88508.89	0.55	*	88508.77	0.11	(^{4}D) 4s ^{5}D$_0$	-	(b^{2}D) 4p ^{3}D$_1$
	Q	222	88559.37	0.24		88559.24	0.13	3d^6 ^{5}D$_1$	-	(^{6}S) 4p ^{5}P$_1$
	Q	234	88596.17	0.24		88596.05	0.14	3d^6 ^{5}D$_2$	-	(^{6}S) 4p ^{5}P$_2$
	Q	235	88649.02	0.24	*	88649.01	0.51	3d^6 ^{5}D$_3$	-	(^{6}S) 4p ^{5}P$_3$
	R	202	88694.39	0.24	*	88694.367	0.1	3d^6 ^{3}G$_4$	-	(^{4}G) 4p ^{5}G$_4$
	Q	214	88752.88	0.24		88752.93	0.14	3d^6 ^{5}D$_2$	-	(^{6}S) 4p ^{5}P$_1$
	R	191	88840.09	0.24		88839.865	0.088	3d^6 ^{3}D$_3$	-	(^{4}P) 4p ^{3}P$_2$
	Q	254	88898.77	0.55		88898.75	0.51	3d^6 ^{5}D$_3$	-	(^{6}S) 4p ^{5}P$_2$
	R	186	88934.66	0.55	*	88935.03	0.13	(^{2}I) 4s ^{3}I$_6$	-	(b^{2}G) 4p ^{1}H$_5$
	R	149	88972.01	0.55	*	88971.67	0.11	3d^6 ^{3}D$_1$	-	(^{4}P) 4p ^{3}P$_2$
	R	207	88981.75	0.55		88981.683	0.094	3d^6 ^{3}D$_2$	-	(^{4}P) 4p ^{3}P$_2$
	R	179	89033.56	0.55		89032.958	0.071	(^{4}D) 4s ^{5}D$_4$	-	(b^{2}D) 4p ^{3}D$_3$
	Q	255	89085.03	0.56		89085.09	0.2	3d^6 ^{5}D$_4$	-	(^{6}S) 4p ^{5}P$_3$
	R	127	89181.24	0.56		89181.19	0.11	3d^6 ^{3}G$_5$	-	(^{4}G) 4p ^{5}G$_6$
	Q	46	89186.97	0.24		89187.208	0.071	3d^6 b^{3}F$_4$	-	(^{4}F) 4p ^{3}G$_5$
	R	99	89233.61	0.24		89233.294	0.071	3d^6 b^{3}F$_4$	-	(^{2}H) 4p ^{3}I$_5$

Fe III Classified grating linelist continued

Exp.	Cat.	Int.	σ_{obs} (cm^{-1})	Unc. (cm^{-1})		σ_{Ritz} (cm^{-1})	Unc. (cm^{-1})	Transition		
	R	220	89329.42	0.56		89329.968	0.066	$3d^6\ b^3F_3$	-	$(^4F)\ 4p\ ^3G_4$
	Q	41	89349.46	0.56	*	89349.142	0.072	$3d^6\ b^3F_4$	-	$(^4F)\ 4p\ ^3G_4$
	R	243	89492.91	0.24	*	89495.36	0.1	$3d^6\ b^3F_2$	-	$(^4F)\ 4p\ ^3G_3$
	Q	28	89531.77	0.56		89531.901	0.067	$3d^6\ b^3F_3$	-	$(a^2G)\ 4p\ ^1G_4$
	R	218	89550.93	0.24		89551.075	0.072	$3d^6\ b^3F_4$	-	$(a^2G)\ 4p\ ^1G_4$
	R	110	89607.9	0.24		89607.91	0.1	$(^6S)\ 4s\ ^7S_3$	-	$(^4P)\ 4p\ ^3P_2$
	R	178	89835.15	0.24		89834.778	0.099	$3d^6\ a^1D_2$	-	$(^4D)\ 4p\ ^3F_3$
	R	224	89889.26	0.24		89888.731	0.086	$3d^6\ ^1F_3$	-	$(a^2D)\ 4p\ ^3F_4$
	R	131	90176.77	0.24		90176.927	0.098	$3d^6\ b^3F_4$	-	$(a^2F)\ 4p\ ^1F_3$
	R	199	90281.06	0.57		90281.22	0.11	$3d^6\ b^3P_2$	-	$(a^2G)\ 4p\ ^3F_3$
	R	201	90338.32	0.57		90338.752	0.069	$3d^6\ b^3P_2$	-	$(a^2G)\ 4p\ ^3F_2$
	R	133	90348.36	0.57		90348.888	0.1	$3d^6\ ^3G_4$	-	$(^4G)\ 4p\ ^5H_5$
	R	179	90415.01	0.57	*	90414.404	0.088	$3d^6\ b^1G_4$	-	$(b^2F)\ 4p\ ^3D_3$
	Q	51	90419.1	0.57	*	90417.23	0.12	$3d^6\ b^3F_4$	-	$(a^2G)\ 4p\ ^3F_3$
	R	192	90509.04	0.57	*	90508.27	0.12	$3d^6\ b^3F_2$	-	$(a^2G)\ 4p\ ^3F_3$
	Q	67	90553.3	0.57		90552.69	0.11	$3d^6\ ^3G_5$	-	$(^4G)\ 4p\ ^5H_4$

Fe III Classified grating linelist continued

Exp.	Cat.	Int.	σ_{obs} (cm^{-1})	Unc. (cm^{-1})		σ_{Ritz} (cm^{-1})	Unc. (cm^{-1})	Transition		
	Q	47	90565.68	0.57		90565.800	0.081	$3d^6\ b^3F_2$	-	$(a^2G)\ 4p\ ^3F_2$
	Q	42	90726.98	0.58		90726.811	0.076	$3d^6\ b^3F_4$	-	$(a^2G)\ 4p\ ^3F_4$
	Q	55	90730.76	0.58		90731.38	0.11	$3d^6\ ^3G_5$	-	$(^4G)\ 4p\ ^5H_5$
	Q	83	90987.51	0.25		90987.189	0.096	$3d^6\ b^3P_2$	-	$(^4F)\ 4p\ ^3D_2$
	Q	176	91053.87	0.58		91054.552	0.067	$3d^6\ b^3P_2$	-	$(^4F)\ 4p\ ^3D_3$
	Q	94	91057.1	0.58	*	91057.35	0.12	$3d^6\ b^3P_2$	-	$(^4F)\ 4p\ ^3D_1$
	R	220	91082.23	0.58	*	91083.574	0.079	$3d^6\ ^3D_3$	-	$(^4G)\ 4p\ ^3G_4$
	Q	126	91104.05	0.25		91104.020	0.095	$3d^6\ b^3F_3$	-	$(^4F)\ 4p\ ^3D_2$
	Q	178	91190.37	0.25	*	91190.557	0.071	$3d^6\ b^3F_4$	-	$(^4F)\ 4p\ ^3D_3$
	R	201	91213.91	0.58		91214.24	0.1	$3d^6\ b^3F_2$	-	$(^4F)\ 4p\ ^3D_2$
	Q	94	91284.52	0.25		91284.40	0.12	$3d^6\ b^3F_2$	-	$(^4F)\ 4p\ ^3D_1$
	R	198	91370.01	0.58	*	91368.801	0.087	$3d^6\ ^1F_3$	-	$(a^2D)\ 4p\ ^3P_2$
	Q	74	91463.94	0.25		91463.755	0.087	$3d^6\ ^1F_3$	-	$(a^2F)\ 4p\ ^1G_4$
	R	82	91526.65	0.59	*	91526.411	0.1	$3d^6\ ^3G_4$	-	$(^4G)\ 4p\ ^5F_4$
	R	141	91534.86	0.59		91534.356	0.1	$3d^6\ ^3G_4$	-	$(^4G)\ 4p\ ^5F_3$
	R	77	91577.86	0.59		91578.32	0.2	$3d^6\ a^1S_0$	-	$(^4P)\ 4p\ ^3S_1$

Fe III Classified grating linelist continued

Exp.	Cat.	Int.	σ_{obs} (cm^{-1})	Unc. (cm^{-1})		σ_{Ritz} (cm^{-1})	Unc. (cm^{-1})	Transition		
	R	131	91652.31	0.25		91652.360	0.088	$3d^6\ ^1F_3$	-	$(a^2F)\ 4p\ ^3G_3$
	R	156	91726.96	0.59		91726.81	0.11	$3d^6\ a^3F_2$	-	$(^4G)\ 4p\ ^5G_2$
	R	208	91751.96	0.59		91751.783	0.067	$3d^6\ b^3F_3$	-	$(^4F)\ 4p\ ^3F_4$
	R	232	91757.85	0.59		91758.11	0.11	$3d^6\ ^3G_5$	-	$(^4G)\ 4p\ ^5F_5$
	Q	176	91769.98	0.25	*	91770.707	0.08	$3d^6\ ^3D_3$	-	$(^4P)\ 4p\ ^3D_2$
	Q	176	91769.98	0.25	*	91770.957	0.073	$3d^6\ b^3F_4$	-	$(^4F)\ 4p\ ^3F_4$
	Q	125	91791.79	0.25		91791.844	0.092	$3d^6\ b^1G_4$	-	$(^2H)\ 4p\ ^1G_4$
	Q	86	91822.05	0.25		91821.963	0.098	$3d^6\ b^3P_1$	-	$(^4F)\ 4p\ ^3D_2$
	R	170	91884.23	0.59	*	91884.226	0.1	$3d^6\ a^3F_3$	-	$(^4G)\ 4p\ ^5G_2$
	Q	46	91892.25	0.25		91892.13	0.12	$3d^6\ b^3P_1$	-	$(^4F)\ 4p\ ^3D_1$
	R	215	91903.06	0.59	*	91902.51	0.11	$3d^6\ ^3D_1$	-	$(^4P)\ 4p\ ^3D_2$
	R	222	91971.28	0.59		91971.83	0.11	$3d^6\ ^3D_3$	-	$(^4D)\ 4p\ ^5D_3$
	Q	117	92017.48	0.25		92017.32	0.13	$3d^6\ b^3F_3$	-	$(^4F)\ 4p\ ^3F_3$
	R	223	92036.79	0.59	*	92036.50	0.14	$3d^6\ b^3F_4$	-	$(^4F)\ 4p\ ^3F_3$
	R	233	92041.71	0.59	*	92041.82	0.11	$3d^6\ ^1F_3$	-	$(^4F)\ 4p\ ^5G_2$
	R	233	92041.71	0.59	*	92041.029	0.076	$3d^6\ ^3D_3$	-	$(^4D)\ 4p\ ^5D_2$

Fe III Classified grating linelist continued

Exp.	Cat.	Int.	σ_{obs} (cm^{-1})	Unc. (cm^{-1})		σ_{Ritz} (cm^{-1})	Unc. (cm^{-1})	Transition		
	R	251	92127.77	0.59	*	92127.54	0.15	$3d^6\ b^3F_2$	-	$(^4F)\ 4p\ ^3F_3$
	R	251	92127.77	0.59	*	92127.565	0.1	$3d^6\ ^3G_4$	-	$(^4P)\ 4p\ ^5D_3$
	R	251	92127.77	0.59	*	92127.309	0.082	$3d^6\ ^3D_2$	-	$(^4P)\ 4p\ ^3D_1$
	R	192	92182.98	0.25		92182.847	0.082	$3d^6\ ^3D_2$	-	$(^4D)\ 4p\ ^5D_2$
	Q	126	92238.7	0.6		92239.55	0.11	$3d^6\ b^3F_3$	-	$(^4F)\ 4p\ ^3F_2$
	Q	54	92319.99	0.26		92319.82	0.14	$3d^6\ b^3P_0$	-	$(^4F)\ 4p\ ^3D_1$
	R	210	92342.4	0.6		92343.277	0.086	$3d^6\ ^1F_3$	-	$(^4F)\ 4p\ ^5G_4$
	Q	93	92349.92	0.26		92349.76	0.11	$3d^6\ b^3F_2$	-	$(^4F)\ 4p\ ^3F_2$
	R	101	92559.9	0.6		92560.114	0.065	$3d^6\ b^3F_3$	-	$(a^2G)\ 4p\ ^3H_4$
	R	121	92632.13	0.26		92632.232	0.071	$3d^6\ b^3F_4$	-	$(a^2G)\ 4p\ ^3H_5$
	R	96	92802.2	0.6		92802.43	0.11	$3d^6\ a^1D_2$	-	$(^4D)\ 4p\ ^3P_1$
	R	80	92827.58	0.26	*	92827.20	0.11	$3d^6\ ^3D_1$	-	$(^4D)\ 4p\ ^5P_1$
	R	93	92837.41	0.26		92837.206	0.083	$3d^6\ ^3D_2$	-	$(^4D)\ 4p\ ^5P_1$
	Q	37	92892.86	0.26		92892.764	0.077	$3d^6\ ^3D_3$	-	$(^4D)\ 4p\ ^5P_3$
	Q	121	93021.35	0.26		93021.132	0.1	$3d^6\ ^3G_3$	-	$(^4G)\ 4p\ ^3F_2$
	R	247	93091.41	0.61	*	93091.18	0.11	$3d^6\ a^3F_2$	-	$(^4G)\ 4p\ ^5H_3$

Fe III Classified grating linelist continued

Exp.	Cat.	Int.	σ_{obs} (cm^{-1})	Unc. (cm^{-1})		σ_{Ritz} (cm^{-1})	Unc. (cm^{-1})	Transition		
	R	227	93104.23	0.26		93104.137	0.1	$3d^6\ ^3G_3$	-	$(^4G)\ 4p\ ^3F_3$
	R	137	93207.5	0.26		93207.48	0.13	$(^4D)\ 4s\ ^3D_2$	-	$(b^2G)\ 4p\ ^1F_3$
	R	137	93207.5	0.26		93207.789	0.1	$3d^6\ ^3G_3$	-	$(^4G)\ 4p\ ^3F_4$
	R	126	93239.22	0.61		93238.88	0.38	$(^4F)\ 4s\ ^3F_3$	-	$(^2P)\ 4p\ ^1D_2$
	R	119	93248.87	0.26		93248.597	0.1	$3d^6\ a^3F_3$	-	$(^4G)\ 4p\ ^5H_3$
	Q	64	93265.14	0.26	*	93264.943	0.083	$(^6S)\ 4s\ ^5S_2$	-	$(a^2D)\ 4p\ ^3P_2$
	Q	136	93305.6	0.26		93305.497	0.1	$3d^6\ ^3G_4$	-	$(^4G)\ 4p\ ^3F_3$
	R	119	93333.82	0.61	*	93335.07	0.22	$3d^6\ ^3H_5$	-	$(^4G)\ 4p\ ^5G_4$
	R	134	93376.7	0.61		93376.66	0.22	$3d^6\ ^3H_5$	-	$(^4G)\ 4p\ ^5G_5$
	Q	70	93409.23	0.26		93409.149	0.1	$3d^6\ ^3G_4$	-	$(^4G)\ 4p\ ^3F_4$
	Q	59	93433.14	0.26		93433.11	0.11	$3d^6\ b^1G_4$	-	$(b^2F)\ 4p\ ^1F_3$
	R	167	93439.78	0.61		93439.40	0.22	$3d^6\ ^3H_5$	-	$(^4G)\ 4p\ ^5G_6$
	Q	171	93543.27	0.26	*	93543.796	0.1	$3d^6\ ^3G_3$	-	$(^4G)\ 4p\ ^3H_4$
	Q	95	93606.84	0.61	*	93607.671	0.071	$3d^6\ b^3F_4$	-	$(a^2G)\ 4p\ ^3G_5$
	Q	185	93616.65	0.26	*	93615.56	0.32	$3d^6\ ^3G_4$	-	$(^4G)\ 4p\ ^3H_5$
	R	194	93717.29	0.61	*	93716.116	0.086	$3d^6\ ^1F_3$	-	$(a^2F)\ 4p\ ^3F_4$

Fe III Classified grating linelist continued

Exp.	Cat.	Int.	σ_{obs} (cm^{-1})	Unc. (cm^{-1})		σ_{Ritz} (cm^{-1})	Unc. (cm^{-1})	Transition		
	Q	189	93792.09	0.62	*	93790.733	0.066	$3d^6\ b^3F_3$	-	$(a^2G)\ 4p\ ^3G_4$
	Q	189	93792.09	0.62	*	93791.64	0.11	$3d^6\ ^3G_5$	-	$(^4G)\ 4p\ ^3F_4$
	Q	181	93796.14	0.62		93796.41	0.11	$3d^6\ ^3G_5$	-	$(^4G)\ 4p\ ^3H_6$
	R	188	93809.33	0.62	*	93809.907	0.072	$3d^6\ b^3F_4$	-	$(a^2G)\ 4p\ ^3G_4$
	R	226	93930.41	0.26		93931.362	0.081	$3d^6\ b^3F_2$	-	$(a^2G)\ 4p\ ^3G_3$
	Q	175	93996.36	0.27		93996.32	0.12	$3d^6\ ^3D_3$	-	$(^4D)\ 4p\ ^3D_3$
	Q	87	94046.3	0.27		94046.243	0.079	$3d^6\ ^3D_3$	-	$(^4D)\ 4p\ ^3D_2$
	Q	61	94138.03	0.27		94138.14	0.13	$3d^6\ ^3D_2$	-	$(^4D)\ 4p\ ^3D_3$
	R	133	94158.77	0.62		94158.435	0.069	$3d^6\ b^3P_2$	-	$(b^2F)\ 4p\ ^3F_3$
	Q	79	94178.28	0.27		94178.05	0.11	$3d^6\ ^3D_1$	-	$(^4D)\ 4p\ ^3D_2$
	Q	151	94187.86	0.27		94188.061	0.086	$3d^6\ ^3D_2$	-	$(^4D)\ 4p\ ^3D_2$
	R	104	94206.84	0.62		94206.401	0.095	$3d^6\ b^3F_3$	-	$(b^2F)\ 4p\ ^3F_2$
	Q	125	94229.21	0.27		94229.09	0.12	$3d^6\ ^3D_1$	-	$(^4D)\ 4p\ ^3D_1$
	Q	80	94239.07	0.27		94239.103	0.1	$3d^6\ ^3D_2$	-	$(^4D)\ 4p\ ^3D_1$
	Q	67	94275.14	0.27		94275.266	0.067	$3d^6\ b^3F_3$	-	$(b^2F)\ 4p\ ^3F_3$
	Q	74	94316.76	0.27		94316.618	0.1	$3d^6\ b^3F_2$	-	$(b^2F)\ 4p\ ^3F_2$

Fe III Classified grating linelist continued

Exp.	Cat.	Int.	σ_{obs} (cm^{-1})	Unc. (cm^{-1})		σ_{Ritz} (cm^{-1})	Unc. (cm^{-1})	Transition		
	Q	34	94385.03	0.62		94385.483	0.082	$3d^6\ b^3F_2$	-	$(b^2F)\ 4p\ ^3F_3$
	R	155	94466.35	0.62		94466.44	0.13	$3d^6\ ^3H_4$	-	$(^4G)\ 4p\ ^5H_3$
	R	130	94556.03	0.63	*	94557.24	0.12	$3d^6\ a^1G_4$	-	$(^4D)\ 4p\ ^3F_4$
	R	130	94556.03	0.63	*	94555.04	0.11	$3d^6\ ^3G_3$	-	$(^4P)\ 4p\ ^3P_2$
	R	103	94562.74	0.63		94562.125	0.093	$3d^6\ a^3F_2$	-	$(^4P)\ 4p\ ^5D_2$
	R	193	94629.94	0.63	*	94631.342	0.086	$3d^6\ ^1F_3$	-	$(^2H)\ 4p\ ^3H_4$
	R	193	94629.94	0.63	*	94629.11	0.12	$3d^6\ ^3H_4$	-	$(^4G)\ 4p\ ^5H_4$
	Q	96	94672.49	0.27		94672.895	0.1	$3d^6\ b^3F_3$	-	$(b^2F)\ 4p\ ^3F_4$
	Q	67	94692.04	0.27		94692.07	0.1	$3d^6\ b^3F_4$	-	$(b^2F)\ 4p\ ^3F_4$
	R	170	94743.09	0.27		94743.371	0.081	$3d^6\ b^3F_3$	-	$(a^2G)\ 4p\ ^1F_3$
	R	228	94776.13	0.63	*	94775.427	0.087	$3d^6\ a^3F_3$	-	$(^4G)\ 4p\ ^5F_3$
	R	242	94779.18	0.63	*	94780.280	0.08	$3d^6\ ^3D_3$	-	$(^4D)\ 4p\ ^3F_3$
	R	145	94810.99	0.63		94810.90	0.22	$3d^6\ ^3H_5$	-	$(^4G)\ 4p\ ^5H_4$
	R	123	94814.14	0.63	*	94814.29	0.1	$(^6S)\ 4s\ ^7S_3$	-	$(^4D)\ 4p\ ^3D_2$
	R	123	94814.14	0.63	*	94815.110	0.1	$3d^6\ ^3D_3$	-	$(^4D)\ 4p\ ^3F_2$
	R	144	94922.95	0.27	*	94922.098	0.086	$3d^6\ ^3D_2$	-	$(^4D)\ 4p\ ^3F_3$

Fe III Classified grating linelist continued

Exp.	Cat.	Int.	σ_{obs} (cm^{-1})	Unc. (cm^{-1})		σ_{Ritz} (cm^{-1})	Unc. (cm^{-1})	Transition		
	R	144	94922.95	0.27	*	94924.344	0.1	$3d^6\ b^3P_1$	-	$(b^2F)\ 4p\ ^3F_2$
	R	208	94989.76	0.63	*	94989.59	0.22	$3d^6\ ^3H_5$	-	$(^4G)\ 4p\ ^5H_5$
	R	69	95041.5	0.63		95040.875	0.091	$3d^6\ a^3F_2$	-	$(^4P)\ 4p\ ^5S_2$
	Q	38	95172.47	0.27	*	95171.65	0.15	$3d^6\ a^3P_0$	-	$(^4P)\ 4p\ ^5D_1$
	Q	38	95172.47	0.27	*	95173.90	0.22	$3d^6\ ^3H_5$	-	$(^4G)\ 4p\ ^5H_6$
	R	157	95241.81	0.64		95241.841	0.071	$(^4G)\ 4s\ ^5G_4$	-	$(b^2D)\ 4p\ ^3D_3$
	R	128	95322.98	0.64		95323.106	0.078	$3d^6\ b^3F_3$	-	$(b^2F)\ 4p\ ^1D_2$
	R	73	95367.7	0.64	*	95368.636	0.087	$3d^6\ a^3F_3$	-	$(^4P)\ 4p\ ^5D_3$
	R	169	95422.76	0.27		95422.89	0.12	$3d^6\ ^3H_6$	-	$(^4G)\ 4p\ ^5H_6$
	R	143	95434.14	0.27	*	95433.323	0.091	$3d^6\ b^3F_2$	-	$(b^2F)\ 4p\ ^1D_2$
	R	106	95544.38	0.64		95544.04	0.13	$3d^6\ a^3P_2$	-	$(^4G)\ 4p\ ^5H_3$
	R	107	95607.78	0.64	*	95606.35	0.13	$3d^6\ a^3F_4$	-	$(^4P)\ 4p\ ^5D_3$
	R	62	95619.85	0.64		95619.680	0.074	$(^4P)\ 4s\ ^5P_3$	-	$(b^2D)\ 4p\ ^1D_2$
	R	71	95674.19	0.27		95674.59	0.13	$3d^6\ ^3D_2$	-	$(^4P)\ 4p\ ^3S_1$
	R	54	95683.71	0.64		95683.711	0.1	$3d^6\ ^3G_3$	-	$(^4D)\ 4p\ ^5F_2$
	R	110	95993.89	0.28		95993.27	0.12	$3d^6\ ^3H_4$	-	$(^4G)\ 4p\ ^5F_3$

Fe III Classified grating linelist continued

Exp.	Cat.	Int.	σ_{obs} (cm^{-1})	Unc. (cm^{-1})		σ_{Ritz} (cm^{-1})	Unc. (cm^{-1})	Transition		
	R	76	96040.91	0.65		96041.049	0.084	$3d^6\ b^3P_1$	-	$(b^2F)\ 4p\ ^1D_2$
	R	109	96067.39	0.28	*	96067.656	0.1	$3d^6\ ^3G_4$	-	$(^4D)\ 4p\ ^5F_3$
	R	146	96211.11	0.65	*	96209.73	0.13	$3d^6\ a^3P_1$	-	$(^4P)\ 4p\ ^5S_2$
	R	139	96265.29	0.28		96265.31	0.12	$3d^6\ ^3H_6$	-	$(^4G)\ 4p\ ^5F_5$
	R	218	96299.78	0.65	*	96300.585	0.1	$3d^6\ ^3G_4$	-	$(^4D)\ 4p\ ^5F_4$
	Q	169	96306.08	0.28		96306.144	0.094	$3d^6\ a^3F_2$	-	$(^4G)\ 4p\ ^3F_2$
	Q	55	96389.07	0.28		96389.149	0.094	$3d^6\ a^3F_2$	-	$(^4G)\ 4p\ ^3F_3$
	Q	80	96463.46	0.28		96463.563	0.088	$3d^6\ a^3F_3$	-	$(^4G)\ 4p\ ^3F_2$
	Q	180	96546.53	0.28		96546.568	0.088	$3d^6\ a^3F_3$	-	$(^4G)\ 4p\ ^3F_3$
	R	171	96595.87	0.28		96595.814	0.069	$3d^6\ b^3F_3$	-	$(b^2F)\ 4p\ ^3G_3$
	Q	62	96650.01	0.28		96650.220	0.088	$3d^6\ a^3F_3$	-	$(^4G)\ 4p\ ^3F_4$
	R	155	96683.09	0.28		96683.07	0.11	$3d^6\ ^3G_5$	-	$(^4D)\ 4p\ ^5F_4$
	Q	58	96705.81	0.28		96706.031	0.083	$3d^6\ b^3F_2$	-	$(b^2F)\ 4p\ ^3G_3$
	R	126	96728.26	0.65		96728.585	0.087	$3d^6\ ^1F_3$	-	$(^4F)\ 4p\ ^3G_4$
	Q	141	96777.13	0.66		96777.13	0.15	$3d^6\ ^3G_3$	-	$(^4G)\ 4p\ ^3G_3$
	Q	95	96783.97	0.66		96784.28	0.13	$3d^6\ a^3F_4$	-	$(^4G)\ 4p\ ^3F_3$

Fe III Classified grating linelist continued

Exp.	Cat.	Int.	σ_{obs} (cm^{-1})	Unc. (cm^{-1})		σ_{Ritz} (cm^{-1})	Unc. (cm^{-1})	Transition		
	Q	54	96798.58	0.28		96798.752	0.1	$3d^6\ ^3G_3$	-	$(^4G)\ 4p\ ^3G_4$
	Q	122	96866.47	0.66		96866.005	0.067	$3d^6\ b^3F_3$	-	$(b^2F)\ 4p\ ^3G_4$
	Q	212	96887.96	0.28		96887.93	0.13	$3d^6\ a^3F_4$	-	$(^4G)\ 4p\ ^3F_4$
	Q	34	96930.13	0.28		96930.518	0.087	$3d^6\ ^1F_3$	-	$(a^2G)\ 4p\ ^1G_4$
	R	163	96974.87	0.66	*	96975.60	0.12	$3d^6\ a^3P_2$	-	$(^4P)\ 4p\ ^5D_1$
	R	152	96978.63	0.66		96978.49	0.15	$3d^6\ ^3G_4$	-	$(^4G)\ 4p\ ^3G_3$
	R	187	96986.72	0.66		96986.227	0.088	$3d^6\ a^3F_3$	-	$(^4G)\ 4p\ ^3H_4$
	Q	156	96999.8	0.28		97000.112	0.1	$3d^6\ ^3G_4$	-	$(^4G)\ 4p\ ^3G_4$
	Q	68	97007.98	0.28	*	97008.490	0.1	$3d^6\ ^3G_4$	-	$(^4G)\ 4p\ ^3G_5$
	R	196	97095.11	0.28	*	97094.34	0.33	$3d^6\ a^3F_4$	-	$(^4G)\ 4p\ ^3H_5$
	R	244	97129.63	0.28		97129.846	0.073	$3d^6\ b^3F_4$	-	$(b^2F)\ 4p\ ^3G_5$
	R	126	97144.91	0.28		97144.039	0.074	$3d^6\ b^3P_2$	-	$(b^2F)\ 4p\ ^3D_1$
	R	211	97201.09	0.28	*	97202.462	0.1	$3d^6\ b^3P_2$	-	$(b^2F)\ 4p\ ^3D_2$
	Q	82	97223.3	0.28		97223.631	0.074	$3d^6\ b^3P_2$	-	$(b^2F)\ 4p\ ^3D_3$
	R	201	97319.72	0.28		97319.293	0.1	$3d^6\ b^3F_3$	-	$(b^2F)\ 4p\ ^3D_2$
	R	177	97341.13	0.28		97340.462	0.072	$3d^6\ b^3F_3$	-	$(b^2F)\ 4p\ ^3D_3$

Fe III Classified grating linelist continued

Exp.	Cat.	Int.	σ_{obs} (cm^{-1})	Unc. (cm^{-1})		σ_{Ritz} (cm^{-1})	Unc. (cm^{-1})	Transition		
	R	203	97359.32	0.66		97359.636	0.078	$3d^6\ b^3F_4$	-	$(b^2F)\ 4p\ ^3D_3$
	R	178	97370.23	0.66	*	97371.087	0.086	$3d^6\ b^3F_2$	-	$(b^2F)\ 4p\ ^3D_1$
	Q	175	97390.71	0.28		97390.98	0.11	$3d^6\ ^3G_5$	-	$(^4G)\ 4p\ ^3G_5$
	R	94	97428.95	0.28		97429.51	0.1	$3d^6\ b^3F_2$	-	$(b^2F)\ 4p\ ^3D_2$
	R	182	97474.15	0.28	*	97475.00	0.14	$3d^6\ a^3P_1$	-	$(^4G)\ 4p\ ^3F_2$
	R	65	97533.1	0.67	*	97533.17	0.13	$3d^6\ a^3P_2$	-	$(^4G)\ 4p\ ^5F_1$
	R	124	97570.88	0.29		97570.56	0.12	$3d^6\ a^3P_2$	-	$(^4G)\ 4p\ ^5F_2$
	Q	78	97645.57	0.29		97645.95	0.15	$3d^6\ ^3D_1$	-	$(^4D)\ 4p\ ^3P_0$
	R	88	97659.3	0.29		97659.39	0.15	$3d^6\ a^3P_0$	-	$(^4P)\ 4p\ ^5P_1$
	R	192	97764.71	0.29		97764.41	0.12	$3d^6\ ^3H_4$	-	$(^4G)\ 4p\ ^3F_3$
	R	74	97840.18	0.29		97840.055	0.1	$3d^6\ a^3F_2$	-	$(^4P)\ 4p\ ^3P_2$
	R	150	97868.14	0.29		97868.06	0.12	$3d^6\ ^3H_4$	-	$(^4G)\ 4p\ ^3F_4$
	Q	65	97879.73	0.29		97879.74	0.12	$3d^6\ ^3D_1$	-	$(^4D)\ 4p\ ^3P_1$
	Q	124	97889.21	0.67		97889.75	0.1	$3d^6\ ^3D_2$	-	$(^4D)\ 4p\ ^3P_1$
	R	158	97978.7	0.29		97978.813	0.077	$3d^6\ b^3P_1$	-	$(b^2F)\ 4p\ ^3D_1$
	Q	51	98036.72	0.29		98037.236	0.1	$3d^6\ b^3P_1$	-	$(b^2F)\ 4p\ ^3D_2$

Fe III Classified grating linelist continued

Exp.	Cat.	Int.	σ_{obs} (cm^{-1})	Unc. (cm^{-1})		σ_{Ritz} (cm^{-1})	Unc. (cm^{-1})	Transition		
	Q	157	98059.5	0.29		98059.796	0.079	$3d^6\ ^3D_3$	-	$(^4D)\ 4p\ ^3P_2$
	R	192	98074.7	0.67		98074.47	0.32	$3d^6\ ^3H_4$	-	$(^4G)\ 4p\ ^3H_5$
	R	158	98105.87	0.29		98106.254	0.09	$3d^6\ ^1F_3$	-	$(a^2G)\ 4p\ ^3F_4$
	R	142	98180.62	0.67	*	98179.34	0.13	$3d^6\ a^3P_1$	-	$(^4P)\ 4p\ ^5P_1$
	Q	226	98203.47	0.29		98204.07	0.12	$3d^6\ ^3H_4$	-	$(^4G)\ 4p\ ^3H_4$
	Q	219	98256.15	0.29		98256.26	0.26	$3d^6\ ^3H_5$	-	$(^4G)\ 4p\ ^3H_5$
	Q	227	98303.38	0.29		98303.61	0.12	$3d^6\ ^3H_6$	-	$(^4G)\ 4p\ ^3H_6$
	Q	54	98385.01	0.29	*	98385.44	0.11	$3d^6\ ^3G_5$	-	$(^4D)\ 4p\ ^5D_4$
	R	184	98406.12	0.29		98406.51	0.12	$3d^6\ b^3P_0$	-	$(b^2F)\ 4p\ ^3D_1$
	Q	43	98504.89	0.68	*	98503.14	0.12	$3d^6\ b^3P_2$	-	$(^2S)\ 4p\ ^3P_1$
	Q	43	98504.89	0.68	*	98505.25	0.33	$3d^6\ ^3H_6$	-	$(^4G)\ 4p\ ^3H_5$
	R	81	98554.21	0.29		98554.57	0.1	$3d^6\ ^3G_3$	-	$(^4D)\ 4p\ ^5P_2$
	R	179	98568.88	0.29	*	98570.000	0.086	$3d^6\ ^1F_3$	-	$(^4F)\ 4p\ ^3D_3$
	R	147	98842.94	0.29	*	98842.01	0.12	$3d^6\ a^3P_2$	-	$(^4G)\ 4p\ ^3F_3$
	R	68	98968.84	0.29		98968.723	0.092	$3d^6\ a^3F_2$	-	$(^4D)\ 4p\ ^5F_2$
	Q	104	99008.72	0.29		99008.91	0.14	$3d^6\ a^3P_1$	-	$(^4P)\ 4p\ ^3P_2$

Fe III Classified grating linelist continued

Exp.	Cat.	Int.	σ_{obs} (cm^{-1})	Unc. (cm^{-1})		σ_{Ritz} (cm^{-1})	Unc. (cm^{-1})	Transition		
	R	111	99083.58	0.69	*	99083.70	0.13	(^{4}D) 4s ^{5}D$_4$	-	(b^{2}G) 4p ^{1}H$_5$
	Q	24	99112.45	0.29		99112.71	0.12	3d^6 b^{3}P$_2$	-	(^{2}S) 4p ^{3}P$_2$
	R	119	99125.91	0.69		99126.142	0.087	3d^6 a^{3}F$_3$	-	(^{4}D) 4p ^{5}F$_2$
	Q	96	99293.3	0.3	*	99293.68	0.11	3d^6 a^{1}D$_2$	-	(^{4}F) 4p ^{5}G$_3$
	R	117	99308.22	0.69		99308.727	0.087	3d^6 a^{3}F$_3$	-	(^{4}D) 4p ^{5}F$_3$
	Q	29	99317.0	0.69		99317.09	0.12	3d^6 a^{3}P$_2$	-	(^{4}P) 4p ^{5}P$_2$
	Q	77	99369.11	0.69		99369.81	0.12	3d^6 a^{1}G$_4$	-	(^{2}I) 4p ^{3}I$_5$
	R	160	99415.5	0.3		99415.94	0.14	3d^6 ^{1}F$_3$	-	(^{4}F) 4p ^{3}F$_3$
	R	217	99462.5	0.69		99463.34	0.12	3d^6 a^{3}P$_2$	-	(^{4}P) 4p ^{5}P$_1$
	R	144	99547.36	0.69	*	99546.44	0.13	3d^6 a^{3}F$_4$	-	(^{4}D) 4p ^{5}F$_3$
	R	173	99684.1	0.3		99684.23	0.13	3d^6 ^{1}I$_6$	-	(^{2}I) 4p ^{3}K$_7$
	R	127	99762.2	0.7		99761.42	0.1	3d^6 ^{3}G$_3$	-	(^{4}D) 4p ^{3}D$_2$
	R	201	99900.3	0.3		99900.07	0.13	3d^6 ^{1}I$_6$	-	(^{2}I) 4p ^{3}I$_5$
	R	110	99947.4	0.7		99947.49	0.12	3d^6 b^{3}P$_1$	-	(^{2}S) 4p ^{3}P$_2$
	R	139	99959.9	0.7	*	99958.731	0.086	3d^6 ^{1}F$_3$	-	(a^{2}G) 4p ^{3}H$_4$
	R	84	100008.7	0.7	*	100008.86	0.13	3d^6 a^{3}P$_1$	-	(^{4}D) 4p ^{5}F$_1$

Fe III Classified grating linelist continued

Exp.	Cat.	Int.	σ_{obs} (cm^{-1})	Unc. (cm^{-1})		σ_{Ritz} (cm^{-1})	Unc. (cm^{-1})	Transition		
	Q	137	100062.0	0.3		100062.14	0.14	$3d^6\ a^3F_2$	-	$(^4G)\ 4p\ ^3G_3$
	Q	52	100219.5	0.3		100219.56	0.14	$3d^6\ a^3F_3$	-	$(^4G)\ 4p\ ^3G_3$
	Q	147	100240.9	0.3		100241.183	0.088	$3d^6\ a^3F_3$	-	$(^4G)\ 4p\ ^3G_4$
	Q	185	100292.6	0.7		100292.91	0.13	$3d^6\ a^3P_2$	-	$(^4P)\ 4p\ ^3P_2$
	R	119	100359.1	0.7		100359.16	0.1	$3d^6\ b^3F_3$	-	$(b^2F)\ 4p\ ^1F_3$
	R	150	100401.86	0.71	*	100400.51	0.13	$3d^6\ ^1I_6$	-	$(^2I)\ 4p\ ^3I_6$
	Q	79	100478.8	0.3		100478.89	0.13	$3d^6\ a^3F_4$	-	$(^4G)\ 4p\ ^3G_4$
	Q	166	100487.2	0.3		100487.27	0.13	$3d^6\ a^3F_4$	-	$(^4G)\ 4p\ ^3G_5$
	Q	68	100494.94	0.71		100495.46	0.1	$3d^6\ ^3G_3$	-	$(^4D)\ 4p\ ^3F_3$
	Q	59	100501.91	0.71	*	100502.445	0.1	$3d^6\ ^3G_4$	-	$(^4D)\ 4p\ ^3F_4$
	Q	185	100530.1	0.3		100530.29	0.12	$3d^6\ ^3G_3$	-	$(^4D)\ 4p\ ^3F_2$
	Q	40	100646.65	0.71	*	100646.75	0.11	$3d^6\ a^3F_3$	-	$(^4P)\ 4p\ ^3D_3$
	R	189	100661.27	0.71		100661.516	0.099	$3d^6\ a^1D_2$	-	$(a^2F)\ 4p\ ^3D_1$
	R	219	100680.52	0.71	*	100678.78	0.27	$3d^6\ ^1I_6$	-	$(^2I)\ 4p\ ^3I_7$
	Q	199	100696.4	0.3		100696.818	0.1	$3d^6\ ^3G_4$	-	$(^4D)\ 4p\ ^3F_3$
	Q	64	100718.73	0.71		100719.08	0.11	$3d^6\ ^3D_1$	-	$(a^2D)\ 4p\ ^1D_2$

Fe III Classified grating linelist continued

Exp. Cat.	Int.	σ_{obs} (cm^{-1})	Unc. (cm^{-1})		σ_{Ritz} (cm^{-1})	Unc. (cm^{-1})	Transition		
R	200	100760.54	0.71	*	100759.49	0.12	$3d^6\ ^3H_4$	-	$(^4D)\ 4p\ ^5F_4$
R	200	100760.54	0.71	*	100760.93	0.11	$3d^6\ b^1G_4$	-	$(b^2D)\ 4p\ ^3F_3$
Q	66	100770.5	0.3		100770.897	0.096	$3d^6\ a^3F_2$	-	$(^4P)\ 4p\ ^3D_2$
Q	186	100823.7	0.3		100824.06	0.12	$3d^6\ a^1G_4$	-	$(^2I)\ 4p\ ^1H_5$
Q	237	100884.45	0.31	*	100884.93	0.11	$3d^6\ ^3G_5$	-	$(^4D)\ 4p\ ^3F_4$
Q	237	100884.45	0.31	*	100884.46	0.15	$3d^6\ a^3F_4$	-	$(^4P)\ 4p\ ^3D_3$
Q	167	100928.03	0.31		100928.316	0.091	$3d^6\ a^3F_3$	-	$(^4P)\ 4p\ ^3D_2$
Q	127	100985.62	0.31		100985.681	0.092	$3d^6\ a^3F_2$	-	$(^4P)\ 4p\ ^3D_1$
R	244	101040.43	0.71	*	101041.219	0.092	$3d^6\ a^3F_2$	-	$(^4D)\ 4p\ ^5D_2$
Q	118	101064.0	0.31		101064.063	0.092	$3d^6\ a^3F_2$	-	$(^4D)\ 4p\ ^5D_1$
R	205	101130.01	0.72		101129.44	0.12	$3d^6\ a^3F_3$	-	$(^4D)\ 4p\ ^5D_3$
R	194	101189.09	0.31		101189.350	0.087	$3d^6\ ^1F_3$	-	$(a^2G)\ 4p\ ^3G_4$
Q	86	101198.7	0.31		101198.638	0.087	$3d^6\ a^3F_3$	-	$(^4D)\ 4p\ ^5D_2$
R	209	101218.66	0.31	*	101219.762	0.087	$3d^6\ ^1F_3$	-	$(a^2G)\ 4p\ ^3G_3$
Q	124	101354.09	0.31		101354.32	0.13	$3d^6\ ^1I_6$	-	$(^2I)\ 4p\ ^1H_5$
Q	124	101364.98	0.72	*	101363.944	0.083	$3d^6\ ^3D_2$	-	$(a^2D)\ 4p\ ^3F_3$

Fe III Classified grating linelist continued

Exp.	Cat.	Int.	σ_{obs} (cm^{-1})	Unc. (cm^{-1})		σ_{Ritz} (cm^{-1})	Unc. (cm^{-1})	Transition		
	Q	124	101364.98	0.72	*	101367.15	0.16	$3d^6\ a^3F_4$	-	$(^4D)\ 4p\ ^5D_3$
	Q	231	101436.96	0.31		101437.40	0.16	$3d^6\ ^3H_4$	-	$(^4G)\ 4p\ ^3G_3$
	R	197	101466.9	0.72		101467.40	0.12	$3d^6\ ^3H_4$	-	$(^4G)\ 4p\ ^3G_5$
	R	125	101507.0	0.31	*	101507.90	0.1	$3d^6\ b^1G_4$	-	$(b^2D)\ 4p\ ^3D_3$
	Q	244	101637.89	0.72	*	101640.81	0.22	$3d^6\ ^3H_5$	-	$(^4G)\ 4p\ ^3G_4$
	Q	71	101649.98	0.72		101649.19	0.22	$3d^6\ ^3H_5$	-	$(^4G)\ 4p\ ^3G_5$
	Q	54	101674.58	0.72		101673.883	0.088	$3d^6\ ^1F_3$	-	$(b^2F)\ 4p\ ^3F_3$
	R	211	101695.52	0.31		101695.578	0.092	$3d^6\ a^3F_2$	-	$(^4D)\ 4p\ ^5P_1$
	R	122	101712.98	0.31		101712.97	0.15	$3d^6\ a^3P_0$	-	$(^4D)\ 4p\ ^5D_1$
	Q	50	101864.63	0.73	*	101864.59	0.14	$3d^6\ ^3H_4$	-	$(^4P)\ 4p\ ^3D_3$
	Q	236	101897.85	0.31		101898.18	0.12	$3d^6\ ^3H_6$	-	$(^4G)\ 4p\ ^3G_5$
	Q	82	101927.55	0.31		101927.523	0.076	$3d^6\ ^3D_3$	-	$(a^2D)\ 4p\ ^3F_4$
	Q	49	101997.21	0.31		101996.999	0.088	$3d^6\ a^3F_3$	-	$(^4D)\ 4p\ ^5P_2$
	R	163	102050.18	0.73	*	102050.373	0.088	$3d^6\ a^3F_3$	-	$(^4D)\ 4p\ ^5P_3$
	Q	71	102071.65	0.31		102071.51	0.11	$3d^6\ ^1F_3$	-	$(b^2F)\ 4p\ ^3F_4$
	Q	251	102143.27	0.73	*	102141.988	0.099	$3d^6\ ^1F_3$	-	$(a^2G)\ 4p\ ^1F_3$

Fe III Classified grating linelist continued

Exp.	Cat.	Int.	σ_{obs} (cm^{-1})	Unc. (cm^{-1})		σ_{Ritz} (cm^{-1})	Unc. (cm^{-1})	Transition		
	Q	71	102210.92	0.31	*	102210.08	0.13	$3d^6\ a^3P_1$	-	$(^4D)\ 4p\ ^5D_2$
	Q	154	102273.23	0.73	*	102271.74	0.1	$3d^6\ b^1G_4$	-	$(b^2D)\ 4p\ ^1F_3$
	R	168	102346.78	0.73	*	102347.28	0.15	$3d^6\ ^3H_4$	-	$(^4D)\ 4p\ ^5D_3$
	R	97	102486.6	0.74		102487.22	0.15	$3d^6\ b^3P_0$	-	$(^2S)\ 4p\ ^1P_1$
	Q	94	102721.61	0.32		102721.723	0.094	$3d^6\ ^1F_3$	-	$(b^2F)\ 4p\ ^1D_2$
	R	90	102748.49	0.74		102748.85	0.31	$3d^6\ a^1S_0$	-	$(^4F)\ 4p\ ^5D_1$
	R	68	102766.99	0.32		102767.13	0.13	$3d^6\ a^3P_1$	-	$(^4D)\ 4p\ ^5D_0$
	R	213	102887.94	0.32		102888.447	0.098	$3d^6\ a^1D_2$	-	$(a^2D)\ 4p\ ^1P_1$
	R	163	102942.97	0.74		102942.19	0.14	$3d^6\ a^3P_2$	-	$(^4P)\ 4p\ ^3D_3$
	R	84	102996.54	0.74		102996.51	0.14	$3d^6\ a^3F_2$	-	$(^4D)\ 4p\ ^3D_3$
	R	211	103046.56	0.32		103046.433	0.095	$3d^6\ a^3F_2$	-	$(^4D)\ 4p\ ^3D_2$
	Q	84	103097.46	0.32		103097.48	0.11	$3d^6\ a^3F_2$	-	$(^4D)\ 4p\ ^3D_1$
	Q	60	103154.14	0.32		103153.93	0.13	$3d^6\ a^3F_3$	-	$(^4D)\ 4p\ ^3D_3$
	Q	120	103203.86	0.32		103203.852	0.09	$3d^6\ a^3F_3$	-	$(^4D)\ 4p\ ^3D_2$
	R	138	103223.72	0.75		103223.76	0.12	$3d^6\ a^3P_2$	-	$(^4P)\ 4p\ ^3D_2$
	Q	112	103391.66	0.32		103391.64	0.16	$3d^6\ a^3F_4$	-	$(^4D)\ 4p\ ^3D_3$

Fe III Classified grating linelist continued

Exp.	Cat.	Int.	σ_{obs} (cm^{-1})	Unc. (cm^{-1})		σ_{Ritz} (cm^{-1})	Unc. (cm^{-1})	Transition		
	R	138	103408.21	0.75		103407.593	0.077	$3d^6\ ^3D_3$	-	$(a^2D)\ 4p\ ^3P_2$
	R	154	103502.71	0.75		103502.547	0.079	$3d^6\ ^3D_3$	-	$(a^2F)\ 4p\ ^1G_4$
	R	133	103549.35	0.75		103549.411	0.084	$3d^6\ ^3D_2$	-	$(a^2D)\ 4p\ ^3P_2$
	R	222	103662.87	0.75		103662.49	0.12	$3d^6\ a^1G_4$	-	$(a^2F)\ 4p\ ^3G_3$
	Q	68	103746.71	0.32		103746.38	0.15	$3d^6\ a^3P_0$	-	$(^4D)\ 4p\ ^3D_1$
	Q	33	103816.07	0.75		103815.30	0.11	$3d^6\ a^3F_2$	-	$(^4D)\ 4p\ ^3F_2$
	Q	39	103823.4	0.75		103823.49	0.19	$3d^6\ ^3D_1$	-	$(a^2D)\ 4p\ ^3P_1$
	Q	37	103833.21	0.75	*	103833.50	0.18	$3d^6\ ^3D_2$	-	$(a^2D)\ 4p\ ^3P_1$
	Q	37	103833.21	0.75	*	103832.970	0.086	$3d^6\ ^3D_2$	-	$(a^2F)\ 4p\ ^3G_3$
	Q	121	103879.27	0.32		103879.50	0.18	$3d^6\ a^1S_0$	-	$(a^2D)\ 4p\ ^1P_1$
	R	220	103937.85	0.32		103937.889	0.09	$3d^6\ a^3F_3$	-	$(^4D)\ 4p\ ^3F_3$
	Q	150	103960.59	0.32		103961.16	0.13	$3d^6\ a^1D_2$	-	$(a^2F)\ 4p\ ^1D_2$
	Q	74	103981.67	0.76		103981.22	0.13	$3d^6\ a^3F_4$	-	$(^4D)\ 4p\ ^3F_4$
	R	174	103993.82	0.76		103994.431	0.09	$3d^6\ ^1F_3$	-	$(b^2F)\ 4p\ ^3G_3$
	R	147	104080.05	0.76		104080.61	0.11	$3d^6\ ^3D_3$	-	$(^4F)\ 4p\ ^5G_2$
	R	81	104148.87	0.76		104148.44	0.12	$3d^6\ a^3P_2$	-	$(^4D)\ 4p\ ^5P_1$

Fe III Classified grating linelist continued

Exp.	Cat.	Int.	σ_{obs} (cm^{-1})	Unc. (cm^{-1})		σ_{Ritz} (cm^{-1})	Unc. (cm^{-1})	Transition		
	R	184	104175.37	0.76		104175.60	0.13	$3d^6\ a^3F_4$	-	$(^4D)\ 4p\ ^3F_3$
	Q	107	104215.19	0.33		104215.29	0.14	$3d^6\ a^3P_1$	-	$(^4D)\ 4p\ ^3D_2$
	R	189	104239.03	0.33		104239.179	0.095	$3d^6\ ^3D_3$	-	$(^4F)\ 4p\ ^5G_3$
	Q	39	104266.37	0.76	*	104266.33	0.15	$3d^6\ a^3P_1$	-	$(^4D)\ 4p\ ^3D_1$
	R	136	104345.84	0.33		104345.81	0.12	$3d^6\ a^3P_2$	-	$(^4D)\ 4p\ ^5P_3$
	R	143	104371.79	0.76		104371.77	0.16	$3d^6\ ^3H_4$	-	$(^4D)\ 4p\ ^3D_3$
	R	87	104381.41	0.33		104380.997	0.1	$3d^6\ ^3D_2$	-	$(^4F)\ 4p\ ^5G_3$
	R	133	104421.01	0.33		104421.218	0.078	$3d^6\ ^3D_3$	-	$(a^2D)\ 4p\ ^3D_2$
	R	147	104491.18	0.76		104491.31	0.18	$3d^6\ ^3D_1$	-	$(a^2D)\ 4p\ ^3D_1$
	R	172	104500.9	0.76		104501.32	0.17	$3d^6\ ^3D_2$	-	$(a^2D)\ 4p\ ^3D_1$
	R	156	104526.19	0.33	*	104525.89	0.12	$(^6S)\ 4p\ ^5P_3$	-	$(^6S)\ 5d\ ^5D_3$
	R	156	104526.19	0.33	*	104526.293	0.083	$(^6S)\ 4p\ ^5P_3$	-	$(^6S)\ 5d\ ^5D_4$
	R	181	104562.57	0.77		104563.036	0.084	$3d^6\ ^3D_2$	-	$(a^2D)\ 4p\ ^3D_2$
	Q	88	104649.36	0.33		104649.66	0.11	$3d^6\ a^1D_2$	-	$(a^2F)\ 4p\ ^1F_3$
	R	210	104696.0	0.33		104696.572	0.079	$3d^6\ ^3D_3$	-	$(a^2F)\ 4p\ ^3G_4$
	R	153	104820.03	0.77	*	104818.95	0.16	$3d^6\ a^1G_4$	-	$(a^2F)\ 4p\ ^3D_3$

Fe III Classified grating linelist continued

Exp.	Cat.	Int.	σ_{obs} (cm^{-1})	Unc. (cm^{-1})		σ_{Ritz} (cm^{-1})	Unc. (cm^{-1})	Transition		
	R	170	104847.87	0.33		104847.61	0.13	$3d^6\ ^3D_3$	-	$(a^2F)\ 4p\ ^3D_3$
	Q	71	104889.64	0.33		104889.96	0.13	$3d^6\ a^1D_2$	-	$(a^2G)\ 4p\ ^3F_3$
	R	133	104960.02	0.77	*	104961.35	0.13	$3d^6\ ^3H_4$	-	$(^4D)\ 4p\ ^3F_4$
	R	133	104960.02	0.77	*	104960.37	0.13	$3d^6\ ^1I_6$	-	$(a^2F)\ 4p\ ^3G_5$
	R	120	104989.97	0.77		104989.43	0.13	$3d^6\ ^3D_2$	-	$(a^2F)\ 4p\ ^3D_3$
	R	172	105105.93	0.33	*	105104.26	0.12	$3d^6\ a^1G_4$	-	$(^4F)\ 4p\ ^5F_4$
	R	122	105133.84	0.77		105132.917	0.077	$3d^6\ ^3D_3$	-	$(^4F)\ 4p\ ^5F_4$
	R	158	105155.7	0.77		105155.73	0.13	$3d^6\ ^3H_4$	-	$(^4D)\ 4p\ ^3F_3$
	Q	68	105181.89	0.33		105181.87	0.17	$3d^6\ a^3P_0$	-	$(^4P)\ 4p\ ^3S_1$
	Q	219	105225.72	0.33		105225.69	0.13	$3d^6\ ^1I_6$	-	$(^2I)\ 4p\ ^1I_6$
	R	187	105292.45	0.33	*	105292.931	0.083	$3d^6\ ^3D_2$	-	$(^4F)\ 4p\ ^5F_3$
	R	207	105313.87	0.33		105313.56	0.12	$3d^6\ a^1G_4$	-	$(a^2D)\ 4p\ ^1F_3$
	Q	111	105383.18	0.33		105383.37	0.13	$3d^6\ ^1I_6$	-	$(^4F)\ 4p\ ^5G_6$
	Q	120	105449.08	0.33		105449.37	0.15	$3d^6\ a^3P_2$	-	$(^4D)\ 4p\ ^3D_3$
	R	128	105483.55	0.33		105484.037	0.085	$3d^6\ ^3D_2$	-	$(a^2D)\ 4p\ ^1F_3$
	Q	41	105499.03	0.78	*	105499.29	0.12	$3d^6\ a^3P_2$	-	$(^4D)\ 4p\ ^3D_2$

Fe III Classified grating linelist continued

Exp. Cat.	Int.	σ_{obs} (cm^{-1})	Unc. (cm^{-1})		σ_{Ritz} (cm^{-1})	Unc. (cm^{-1})	Transition		
R	156	105510.81	0.78		105510.20	0.13	$3d^6\ ^3D_1$	-	$(^4F)\ 4p\ ^5F_1$
R	164	105549.61	0.33		105550.33	0.13	$3d^6\ a^3P_2$	-	$(^4D)\ 4p\ ^3D_1$
R	198	105653.36	0.78		105653.15	0.36	$(a^2F)\ 4s\ ^1F_3$	-	$(c^2D)\ 4p\ ^1D_2$
R	177	105663.13	0.78		105663.290	0.097	$3d^6\ a^1D_2$	-	$(^4F)\ 4p\ ^3D_3$
R	124	105674.45	0.78		105674.501	0.08	$3d^6\ ^3D_3$	-	$(a^2F)\ 4p\ ^3F_2$
Q	120	105701.88	0.34		105701.82	0.16	$3d^6\ a^3P_1$	-	$(^4P)\ 4p\ ^3S_1$
R	122	105749.28	0.78		105748.836	0.087	$3d^6\ ^3D_2$	-	$(a^2F)\ 4p\ ^3D_1$
R	183	105754.75	0.34		105754.908	0.077	$3d^6\ ^3D_3$	-	$(a^2F)\ 4p\ ^3F_4$
R	191	105910.11	0.34		105910.35	0.12	$3d^6\ a^1G_4$	-	$(a^2F)\ 4p\ ^3F_3$
R	235	105939.5	0.34		105939.009	0.079	$3d^6\ ^3D_3$	-	$(a^2F)\ 4p\ ^3F_3$
R	174	106067.66	0.34	*	106067.83	0.11	$3d^6\ ^3D_1$	-	$(a^2F)\ 4p\ ^3D_2$
R	217	106079.59	0.34	*	106080.827	0.085	$3d^6\ ^3D_2$	-	$(a^2F)\ 4p\ ^3F_3$
Q	92	106116.78	0.34		106116.519	0.094	$3d^6\ ^1F_3$	-	$(^2H)\ 4p\ ^1G_4$
Q	35	106197.7	0.34		106197.94	0.11	$3d^6\ ^3G_5$	-	$(^2I)\ 4p\ ^3I_6$
R	184	106234.16	0.79	*	106233.33	0.12	$3d^6\ a^3P_2$	-	$(^4D)\ 4p\ ^3F_3$
Q	34	106303.25	0.79		106302.45	0.1	$3d^6\ ^3G_3$	-	$(a^2D)\ 4p\ ^1D_2$

Fe III Classified grating linelist continued

Exp.	Cat.	Int.	σ_{obs} (cm^{-1})	Unc. (cm^{-1})		σ_{Ritz} (cm^{-1})	Unc. (cm^{-1})	Transition		
	R	107	106324.43	0.79	*	106323.38	0.12	$3d^6\ a^1G_4$	-	$(^4F)\ 4p\ ^5D_4$
	R	87	106535.99	0.79		106536.38	0.12	$3d^6\ a^1G_4$	-	$(^4F)\ 4p\ ^5D_3$
	R	115	106565.25	0.34	*	106565.037	0.077	$3d^6\ ^3D_3$	-	$(^4F)\ 4p\ ^5D_3$
	R	115	106628.1	0.8	*	106628.16	0.13	$3d^6\ ^1F_3$	-	$(^2S)\ 4p\ ^3P_2$
	R	212	106642.4	0.8	*	106641.47	0.12	$3d^6\ a^1G_4$	-	$(^2H)\ 4p\ ^3H_4$
	R	169	106731.18	0.34		106731.45	0.12	$3d^6\ a^1D_2$	-	$(^4F)\ 4p\ ^3F_2$
	R	200	106769.47	0.34		106769.262	0.1	$3d^6\ ^3G_4$	-	$(^2I)\ 4p\ ^1H_5$
	R	108	106828.8	0.8		106828.56	0.1	$3d^6\ ^3D_2$	-	$(^4F)\ 4p\ ^5D_2$
	R	131	106834.1	0.8		106835.11	0.29	$3d^6\ ^3D_1$	-	$(^4F)\ 4p\ ^5D_1$
	R	178	106937.9	0.8	*	106937.30	0.1	$3d^6\ ^3G_3$	-	$(a^2D)\ 4p\ ^3F_3$
	Q	165	106986.08	0.34		106985.82	0.15	$3d^6\ a^3P_2$	-	$(^4P)\ 4p\ ^3S_1$
	R	179	107168.3	0.8		107168.07	0.12	$3d^6\ a^1G_4$	-	$(^2H)\ 4p\ ^3G_5$
	R	154	107330.11	0.35		107330.112	0.078	$3d^6\ ^3D_3$	-	$(^2H)\ 4p\ ^3G_3$
	Q	56	107396.74	0.35		107397.03	0.15	$3d^6\ a^3P_0$	-	$(^4D)\ 4p\ ^3P_1$
	R	122	107406.77	0.81	*	107407.36	0.13	$3d^6\ ^1I_6$	-	$(^2H)\ 4p\ ^3H_5$
	Q	166	107517.05	0.35		107516.69	0.1	$3d^6\ ^3G_3$	-	$(^2I)\ 4p\ ^3H_4$

Fe III Classified grating linelist continued

Exp.	Cat.	Int.	σ_{obs} (cm^{-1})	Unc. (cm^{-1})		σ_{Ritz} (cm^{-1})	Unc. (cm^{-1})	Transition		
	Q	154	107623.74	0.35		107623.540	0.1	$3d^6\ ^3G_4$	-	$(^2I)\ 4p\ ^3H_5$
	R	159	107642.28	0.81		107642.70	0.1	$3d^6\ ^3G_3$	-	$(a^2D)\ 4p\ ^3F_4$
	Q	52	107683.2	0.35		107683.19	0.17	$3d^6\ a^3P_1$	-	$(^4D)\ 4p\ ^3P_0$
	Q	183	107704.07	0.35		107703.70	0.11	$3d^6\ ^3G_5$	-	$(^2I)\ 4p\ ^3H_6$
	R	240	107717.96	0.81		107718.046	0.1	$3d^6\ ^3G_4$	-	$(^2I)\ 4p\ ^3H_4$
	Q	158	107758.04	0.35		107757.78	0.11	$3d^6\ ^1F_3$	-	$(b^2F)\ 4p\ ^1F_3$
	R	228	107844.59	0.81	*	107844.74	0.12	$3d^6\ b^3P_2$	-	$(b^2D)\ 4p\ ^3D_1$
	R	228	107844.59	0.81	*	107844.061	0.1	$3d^6\ ^3G_4$	-	$(a^2D)\ 4p\ ^3F_4$
	Q	93	107908.39	0.35		107908.24	0.13	$3d^6\ ^1I_6$	-	$(^2H)\ 4p\ ^3H_6$
	Q	73	107917.47	0.35		107916.98	0.14	$3d^6\ a^3P_1$	-	$(^4D)\ 4p\ ^3P_1$
	Q	61	108006.17	0.35		108006.03	0.11	$3d^6\ ^3G_5$	-	$(^2I)\ 4p\ ^3H_5$
	R	246	108073.4	0.82	*	108071.79	0.12	$3d^6\ b^3F_2$	-	$(b^2D)\ 4p\ ^3D_1$
	R	241	108228.51	0.82		108228.84	0.14	$3d^6\ a^3P_1$	-	$(^4D)\ 4p\ ^3P_2$
	R	251	108316.42	0.82		108317.127	0.09	$3d^6\ b^3P_2$	-	$(b^2D)\ 4p\ ^3D_3$
	Q	63	108453.87	0.82		108453.132	0.095	$3d^6\ b^3F_4$	-	$(b^2D)\ 4p\ ^3D_3$
	Q	172	108544.28	0.82	*	108544.175	0.1	$3d^6\ b^3F_2$	-	$(b^2D)\ 4p\ ^3D_3$

Fe III Classified grating linelist continued

Exp.	Cat.	Int.	σ_{obs} (cm^{-1})	Unc. (cm^{-1})		σ_{Ritz} (cm^{-1})	Unc. (cm^{-1})	Transition		
	R	213	108699.37	0.35		108698.31	0.11	$3d^6\ a^1D_2$	-	$(b^2F)\ 4p\ ^3F_2$
	R	227	108767.31	0.35	*	108767.173	0.098	$3d^6\ a^1D_2$	-	$(b^2F)\ 4p\ ^3F_3$
	R	227	108767.31	0.35	*	108767.377	0.078	$3d^6\ ^3D_3$	-	$(^4F)\ 4p\ ^3G_4$
	Q	60	108793.92	0.36	*	108793.89	0.14	$3d^6\ a^1G_4$	-	$(^4F)\ 4p\ ^3G_3$
	Q	60	108793.92	0.36	*	108793.79	0.13	$3d^6\ a^3F_4$	-	$(^2I)\ 4p\ ^3I_5$
	R	180	108907.42	0.83		108906.66	0.12	$3d^6\ ^3D_3$	-	$(a^2F)\ 4p\ ^1D_2$
	Q	183	108940.89	0.36		108940.65	0.12	$3d^6\ a^1G_4$	-	$(a^2G)\ 4p\ ^1G_4$
	Q	117	108969.62	0.36		108969.310	0.078	$3d^6\ ^3D_3$	-	$(a^2G)\ 4p\ ^1G_4$
	R	161	109038.55	0.36		109038.47	0.14	$3d^6\ ^3D_1$	-	$(a^2F)\ 4p\ ^1D_2$
	R	150	109049.54	0.83	*	109048.48	0.13	$3d^6\ ^3D_2$	-	$(a^2F)\ 4p\ ^1D_2$
	R	221	109108.19	0.83		109107.21	0.15	$3d^6\ b^3P_0$	-	$(b^2D)\ 4p\ ^3D_1$
	Q	86	109216.69	0.36		109216.971	0.095	$3d^6\ b^3F_4$	-	$(b^2D)\ 4p\ ^1F_3$
	Q	115	109235.18	0.36		109235.28	0.1	$3d^6\ a^1D_2$	-	$(a^2G)\ 4p\ ^1F_3$
	R	117	109276.72	0.84		109276.86	0.16	$3d^6\ b^1G_4$	-	$(b^2G)\ 4p\ ^3F_3$
	Q	51	109406.68	0.36	*	109406.33	0.1	$3d^6\ ^3G_3$	-	$(a^2F)\ 4p\ ^3G_3$
	Q	113	109419.13	0.36		109419.085	0.1	$3d^6\ ^3G_4$	-	$(a^2F)\ 4p\ ^1G_4$

Fe III Classified grating linelist continued

Exp.	Cat.	Int.	σ_{obs} (cm^{-1})	Unc. (cm^{-1})		σ_{Ritz} (cm^{-1})	Unc. (cm^{-1})	Transition		
	R	228	109490.71	0.84		109489.93	0.13	$3d^6\ ^1I_6$	-	$(^2H)\ 4p\ ^3I_6$
	R	227	109513.14	0.36		109512.84	0.12	$3d^6\ a^3P_2$	-	$(^4D)\ 4p\ ^3P_2$
	Q	150	109553.98	0.36		109553.98	0.36	$3d^6\ ^3H_5$	-	$(^2I)\ 4p\ ^3K_6$
	Q	179	109566.59	0.36		109566.50	0.13	$3d^6\ a^1G_4$	-	$(a^2F)\ 4p\ ^1F_3$
	R	203	109595.54	0.36	*	109595.16	0.1	$3d^6\ ^3D_3$	-	$(a^2F)\ 4p\ ^1F_3$
	Q	55	109607.78	0.36		109607.690	0.1	$3d^6\ ^3G_4$	-	$(a^2F)\ 4p\ ^3G_3$
	Q	89	109625.56	0.36		109625.520	0.093	$3d^6\ b^3P_2$	-	$(b^2D)\ 4p\ ^3P_2$
	R	204	109654.64	0.36		109654.25	0.12	$3d^6\ b^3P_2$	-	$(b^2D)\ 4p\ ^3P_1$
	Q	81	109737.2	0.36		109736.98	0.1	$3d^6\ ^3D_2$	-	$(a^2F)\ 4p\ ^1F_3$
	Q	94	109745.15	0.36		109744.884	0.09	$3d^6\ a^3F_3$	-	$(a^2D)\ 4p\ ^1D_2$
	Q	194	109774.67	0.36	*	109773.92	0.13	$3d^6\ ^3H_4$	-	$(^2I)\ 4p\ ^3I_5$
	Q	106	109802.03	0.36		109801.57	0.11	$3d^6\ ^3G_5$	-	$(a^2F)\ 4p\ ^1G_4$
	Q	153	109806.85	0.36		109806.80	0.15	$3d^6\ a^1G_4$	-	$(a^2G)\ 4p\ ^3F_3$
	Q	146	109815.05	0.36		109815.01	0.1	$3d^6\ a^1D_2$	-	$(b^2F)\ 4p\ ^1D_2$
	R	125	109893.25	0.85		109892.992	0.079	$3d^6\ ^3D_3$	-	$(a^2G)\ 4p\ ^3F_2$
	R	214	109954.9	0.85		109954.36	0.12	$3d^6\ ^3G_3$	-	$(^4F)\ 4p\ ^5G_3$

Fe III Classified grating linelist continued

Exp.	Cat.	Int.	σ_{obs} (cm^{-1})	Unc. (cm^{-1})		σ_{Ritz} (cm^{-1})	Unc. (cm^{-1})	Transition		
	Q	179	109989.22	0.36		109988.86	0.12	$3d^6\ ^3H_6$	-	$(^2I)\ 4p\ ^3K_7$
	Q	108	110025.04	0.36		110024.80	0.11	$3d^6\ ^3D_1$	-	$(a^2G)\ 4p\ ^3F_2$
	R	216	110034.56	0.85	*	110034.810	0.085	$3d^6\ ^3D_2$	-	$(a^2G)\ 4p\ ^3F_2$
	R	137	110097.82	0.85	*	110097.25	0.1	$3d^6\ ^3G_3$	-	$(^4F)\ 4p\ ^5G_4$
	Q	132	110116.39	0.36		110116.38	0.12	$3d^6\ a^1G_4$	-	$(a^2G)\ 4p\ ^3F_4$
	Q	124	110145.14	0.36		110145.046	0.082	$3d^6\ ^3D_3$	-	$(a^2G)\ 4p\ ^3F_4$
	R	174	110155.21	0.85	*	110155.72	0.11	$3d^6\ ^3G_4$	-	$(^4F)\ 4p\ ^5G_3$
	R	150	110204.96	0.36		110204.70	0.12	$3d^6\ ^3H_6$	-	$(^2I)\ 4p\ ^3I_5$
	R	173	110222.72	0.85		110222.316	0.094	$3d^6\ a^3F_2$	-	$(a^2D)\ 4p\ ^3F_3$
	Q	77	110248.11	0.36	*	110248.04	0.13	$3d^6\ a^3F_4$	-	$(^2I)\ 4p\ ^1H_5$
	R	195	110298.83	0.36		110298.607	0.1	$3d^6\ ^3G_4$	-	$(^4F)\ 4p\ ^5G_4$
	R	213	110380.21	0.85		110379.735	0.088	$3d^6\ a^3F_3$	-	$(a^2D)\ 4p\ ^3F_3$
	R	163	110411.71	0.85		110411.75	0.1	$3d^6\ ^3G_3$	-	$(a^2F)\ 4p\ ^3G_4$
	Q	192	110456.11	0.37		110456.15	0.22	$3d^6\ ^3H_5$	-	$(^2I)\ 4p\ ^3I_6$
	R	205	110489.19	0.85		110489.03	0.12	$3d^6\ b^3P_1$	-	$(b^2D)\ 4p\ ^3P_1$
	R	209	110496.79	0.85		110496.79	0.85	$3d^6\ b^3P_1$	-	$(b^2D)\ 4p\ ^3P_0$

Fe III Classified grating linelist continued

Exp.	Cat.	Int.	σ_{obs} (cm^{-1})	Unc. (cm^{-1})		σ_{Ritz} (cm^{-1})	Unc. (cm^{-1})	Transition		
	Q	82	110580.08	0.37		110580.13	0.12	$3d^6\ a^1G_4$	-	$(^4F)\ 4p\ ^3D_3$
	R	160	110606.51	0.86	*	110606.46	0.12	$3d^6\ b^3P_2$	-	$(b^2D)\ 4p\ ^1P_1$
	R	211	110613.19	0.86	*	110613.110	0.1	$3d^6\ ^3G_4$	-	$(a^2F)\ 4p\ ^3G_4$
	Q	102	110617.63	0.37		110617.44	0.13	$3d^6\ a^3F_4$	-	$(a^2D)\ 4p\ ^3F_3$
	R	192	110673.91	0.86	*	110673.24	0.13	$3d^6\ ^3D_1$	-	$(^4F)\ 4p\ ^3D_2$
	R	122	110682.78	0.86	*	110683.25	0.11	$3d^6\ ^3D_2$	-	$(^4F)\ 4p\ ^3D_2$
	R	195	110704.74	0.86	*	110705.14	0.12	$3d^6\ ^3H_6$	-	$(^2I)\ 4p\ ^3I_6$
	Q	52	110750.43	0.37		110750.610	0.084	$3d^6\ ^3D_2$	-	$(^4F)\ 4p\ ^3D_3$
	Q	121	110757.79	0.37		110757.80	0.11	$3d^6\ ^3G_5$	-	$(a^2F)\ 4p\ ^3G_5$
	R	207	110762.93	0.86	*	110764.15	0.15	$3d^6\ ^3G_4$	-	$(a^2F)\ 4p\ ^3D_3$
	R	173	110794.1	0.37		110794.130	0.1	$3d^6\ ^3G_4$	-	$(^4F)\ 4p\ ^5G_5$
	R	155	110866.4	0.86		110866.29	0.1	$3d^6\ ^3G_3$	-	$(^4F)\ 4p\ ^5F_3$
	R	172	110916.76	0.37		110916.72	0.14	$3d^6\ b^3P_0$	-	$(b^2D)\ 4p\ ^3P_1$
	Q	191	110983.85	0.37		110983.41	0.25	$3d^6\ ^3H_6$	-	$(^2I)\ 4p\ ^3I_7$
	Q	134	110995.55	0.37		110995.60	0.11	$3d^6\ ^3G_5$	-	$(a^2F)\ 4p\ ^3G_4$
	R	192	111022.87	0.86		111023.12	0.11	$3d^6\ ^3G_5$	-	$(^2I)\ 4p\ ^1I_6$

Fe III Classified grating linelist continued

Exp.	Cat.	Int.	σ_{obs} (cm^{-1})	Unc. (cm^{-1})		σ_{Ritz} (cm^{-1})	Unc. (cm^{-1})	Transition		
	R	180	111049.59	0.86		111049.455	0.1	$3d^6\ ^3G_4$	-	$(^4F)\ 4p\ ^5F_4$
	Q	86	111057.56	0.37		111057.40	0.1	$3d^6\ ^3G_3$	-	$(a^2D)\ 4p\ ^1F_3$
	R	203	111067.38	0.86	*	111067.651	0.1	$3d^6\ ^3G_4$	-	$(^4F)\ 4p\ ^5F_3$
	R	190	111085.71	0.86	*	111087.721	0.1	$3d^6\ a^1D_2$	-	$(b^2F)\ 4p\ ^3G_3$
	R	190	111085.71	0.86	*	111085.132	0.088	$3d^6\ a^3F_3$	-	$(a^2D)\ 4p\ ^3F_4$
	R	173	111102.69	0.86		111102.32	0.13	$3d^6\ a^3F_4$	-	$(^2I)\ 4p\ ^3H_5$

D Parity-forbidden Fe III Transitions

The calculated parity-forbidden transitions for Fe III are listed below. The columns include:

$\sigma_{\mathbf{calc}}$: The wavenumbers of the transition in cm^{-1}.

Line Unc.: The uncertainty of the transition lines in cm^{-1}.

Transition: The parity-forbidden transition.

Transition Type: The radiation type of transition, which can be listed as either or both magnetic dipole (M1) or electric quadrupole (E2) radiation.

Fe III parity-forbidden transition linelist

σ_{calc} (cm^{-1})	Unc. (cm^{-1})	Transition			Type
302.7	0.52	$3d^6\ ^5D_3$	-	$3d^6\ ^5D_2$	M1
436.08	0.54	$3d^6\ ^5D_4$	-	$3d^6\ ^5D_3$	M1
1284.0	0.18	$3d^6\ a^3P_2$	-	$3d^6\ a^3P_1$	M1
3096.3	0.17	$3d^6\ a^3F_4$	-	$3d^6\ ^3G_5$	M1
3285.0	0.13	$3d^6\ a^3F_2$	-	$3d^6\ ^3G_3$	M1
3442.42	0.13	$3d^6\ a^3F_3$	-	$3d^6\ ^3G_3$	M1
3478.79	0.16	$3d^6\ a^3F_4$	-	$3d^6\ ^3G_4$	M1
4258.2	0.24	$3d^6\ ^3H_5$	-	$3d^6\ ^3G_5$	M1
4458.91	0.15	$3d^6\ ^3H_4$	-	$3d^6\ ^3G_4$	M1
4507.19	0.16	$3d^6\ ^3H_6$	-	$3d^6\ ^3G_5$	M1
4660.27	0.15	$3d^6\ ^3H_4$	-	$3d^6\ ^3G_3$	M1
4945.5	0.11	$3d^6\ ^3D_3$	-	$3d^6\ a^1D_2$	M1
5077.28	0.14	$3d^6\ ^3D_1$	-	$3d^6\ a^1D_2$	M1
9186.28	0.14	$3d^6\ a^3F_3$	-	$3d^6\ a^1G_4$	M1
9424.01	0.18	$3d^6\ a^3F_4$	-	$3d^6\ a^1G_4$	M1
9517.31	0.18	$3d^6\ a^3P_0$	-	$3d^6\ ^3D_1$	M1
10037.26	0.17	$3d^6\ a^3P_1$	-	$3d^6\ ^3D_1$	M1
10055.64	0.25	$3d^6\ ^3H_5$	-	$3d^6\ ^1I_6$	M1
10304.63	0.18	$3d^6\ ^3H_6$	-	$3d^6\ ^1I_6$	M1
10404.13	0.17	$3d^6\ ^3H_4$	-	$3d^6\ a^1G_4$	M1
10585.91	0.25	$3d^6\ ^3H_5$	-	$3d^6\ a^1G_4$	M1
11311.22	0.14	$3d^6\ a^3P_2$	-	$3d^6\ ^3D_2$	M1
11321.26	0.16	$3d^6\ a^3P_2$	-	$3d^6\ ^3D_1$	M1, E2
11453.04	0.14	$3d^6\ a^3P_2$	-	$3d^6\ ^3D_3$	M1
12038.8	0.11	$3d^6\ ^3D_3$	-	$3d^6\ ^1F_3$	M1
12180.62	0.11	$3d^6\ ^3D_2$	-	$3d^6\ ^1F_3$	M1
13945.69	0.13	$3d^6\ a^3F_2$	-	$3d^6\ a^1D_2$	M1
14103.11	0.12	$3d^6\ a^3F_3$	-	$3d^6\ a^1D_2$	M1

Fe III parity-forbidden transition linelist continued

σ_{calc} (cm^{-1})	Unc. (cm^{-1})	Transition			Type
14123.5	0.22	$3d^6\ a^3P_1$	-	$3d^6\ a^1S_0$	M1
14608.75	0.11	$3d^6\ a^1D_2$	-	$3d^6\ b^3P_2$	M1
14765.01	0.19	$3d^6\ a^1S_0$	-	$3d^6\ b^3P_1$	M1
15114.54	0.16	$3d^6\ a^3P_1$	-	$3d^6\ a^1D_2$	M1
16398.54	0.15	$3d^6\ a^3P_2$	-	$3d^6\ a^1D_2$	M1
17753.99	0.13	$3d^6\ ^3G_3$	-	$3d^6\ ^1F_3$	M1
17955.35	0.12	$3d^6\ ^3G_4$	-	$3d^6\ ^1F_3$	M1
18423.55	0.15	$3d^6\ ^3D_1$	-	$3d^6\ b^3P_0$	M1
18433.59	0.13	$3d^6\ ^3D_2$	-	$3d^6\ b^3P_0$	E2
18472.16	0.19	$3d^6\ ^5D_1$	-	$3d^6\ a^3P_2$	M1
18719.47	0.095	$3d^6\ ^3D_3$	-	$3d^6\ b^3P_1$	E2
18851.25	0.12	$3d^6\ ^3D_1$	-	$3d^6\ b^3P_1$	M1, E2
18968.55	0.53	$3d^6\ ^5D_3$	-	$3d^6\ a^3P_2$	M1
19437.401	0.092	$3d^6\ ^3D_3$	-	$3d^6\ b^3F_3$	M1, E2
19469.0	0.1	$3d^6\ ^3D_2$	-	$3d^6\ b^3F_2$	M1, E2
19554.243	0.092	$3d^6\ ^3D_3$	-	$3d^6\ b^3P_2$	M1, E2
19661.34	0.28	$3d^6\ ^5D_0$	-	$3d^6\ a^3P_1$	M1
19696.067	0.097	$3d^6\ ^3D_2$	-	$3d^6\ b^3P_2$	M1, E2
19756.2	0.2	$3d^6\ ^5D_1$	-	$3d^6\ a^3P_1$	M1, E2
19949.8	0.2	$3d^6\ ^5D_2$	-	$3d^6\ a^3P_1$	M1
20046.13	0.53	$3d^6\ ^5D_3$	-	$3d^6\ ^3H_4$	M1
20276.11	0.21	$3d^6\ ^5D_1$	-	$3d^6\ a^3P_0$	M1
20482.21	0.24	$3d^6\ ^5D_4$	-	$3d^6\ ^3H_4$	M1
20925.01	0.17	$3d^6\ ^5D_1$	-	$3d^6\ a^3F_2$	M1
20961.28	0.17	$3d^6\ ^5D_2$	-	$3d^6\ a^3F_3$	M1
21026.25	0.53	$3d^6\ ^5D_3$	-	$3d^6\ a^3F_4$	M1
21118.7	0.18	$3d^6\ ^5D_2$	-	$3d^6\ a^3F_2$	M1
21263.98	0.52	$3d^6\ ^5D_3$	-	$3d^6\ a^3F_3$	M1

Fe III parity-forbidden transition linelist continued

σ_{calc} (cm^{-1})	Unc. (cm^{-1})	Transition			Type
21421.4	0.52	$3d^6\ ^5D_3$	-	$3d^6\ a^3F_2$	M1
21462.33	0.25	$3d^6\ ^5D_4$	-	$3d^6\ a^3F_4$	M1
21700.06	0.23	$3d^6\ ^5D_4$	-	$3d^6\ a^3F_3$	M1
24403.7	0.18	$3d^6\ ^5D_2$	-	$3d^6\ ^3G_3$	M1, E2
24505.04	0.52	$3d^6\ ^5D_3$	-	$3d^6\ ^3G_4$	M1, E2
24706.4	0.52	$3d^6\ ^5D_3$	-	$3d^6\ ^3G_3$	M1, E2
24941.12	0.23	$3d^6\ ^5D_4$	-	$3d^6\ ^3G_4$	M1, E2
25042.38	0.12	$3d^6\ ^3G_3$	-	$3d^6\ b^3F_2$	M1, E2
25152.59	0.11	$3d^6\ ^3G_3$	-	$3d^6\ b^3F_3$	M1, E2
25353.95	0.11	$3d^6\ ^3G_4$	-	$3d^6\ b^3F_3$	E2
25717.27	0.12	$3d^6\ ^3G_5$	-	$3d^6\ b^3F_4$	M1, E2
26334.8	0.14	$3d^6\ a^1G_4$	-	$3d^6\ b^1G_4$	E2
26865.07	0.15	$3d^6\ ^1I_6$	-	$3d^6\ b^1G_4$	E2
27291.96	0.14	$3d^6\ a^3F_2$	-	$3d^6\ b^3P_0$	E2
27877.1	0.1	$3d^6\ a^3F_3$	-	$3d^6\ b^3P_1$	E2
28327.38	0.11	$3d^6\ a^3F_2$	-	$3d^6\ b^3F_2$	E2
28437.6	0.1	$3d^6\ a^3F_2$	-	$3d^6\ b^3F_3$	M1, E2
28484.8	0.11	$3d^6\ a^3F_3$	-	$3d^6\ b^3F_2$	M1, E2
28575.8	0.1	$3d^6\ a^3F_3$	-	$3d^6\ b^3F_4$	M1, E2
28595.0	0.1	$3d^6\ a^3F_3$	-	$3d^6\ b^3F_3$	E2
28813.57	0.15	$3d^6\ a^3F_4$	-	$3d^6\ b^3F_4$	E2
28832.74	0.14	$3d^6\ a^3F_4$	-	$3d^6\ b^3F_3$	M1, E2
28888.51	0.14	$3d^6\ a^3P_1$	-	$3d^6\ b^3P_1$	E2
28949.59	0.14	$3d^6\ a^3F_4$	-	$3d^6\ b^3P_2$	E2
29203.34	0.16	$3d^6\ a^3P_0$	-	$3d^6\ b^3P_2$	E2
29606.44	0.15	$3d^6\ a^3P_1$	-	$3d^6\ b^3F_3$	E2
29698.6	0.27	$3d^6\ ^5D_0$	-	$3d^6\ ^3D_1$	M1
29702.65	0.14	$3d^6\ ^3H_4$	-	$3d^6\ b^3F_2$	E2

Fe III parity-forbidden transition linelist continued

σ_{calc} (cm^{-1})	Unc. (cm^{-1})	Transition			Type
29723.29	0.14	$3d^6\ a^3P_1$	-	$3d^6\ b^3P_2$	M1, E2
29744.81	0.16	$3d^6\ a^3P_2$	-	$3d^6\ b^3P_0$	E2
29783.38	0.17	$3d^6\ ^5D_1$	-	$3d^6\ ^3D_2$	M1
29793.42	0.18	$3d^6\ ^5D_1$	-	$3d^6\ ^3D_1$	M1
29812.86	0.13	$3d^6\ ^3H_4$	-	$3d^6\ b^3F_3$	E2
29977.07	0.17	$3d^6\ ^5D_2$	-	$3d^6\ ^3D_2$	M1
29987.11	0.19	$3d^6\ ^5D_2$	-	$3d^6\ ^3D_1$	M1, E2
29994.64	0.23	$3d^6\ ^3H_5$	-	$3d^6\ b^3F_3$	E2
30118.89	0.17	$3d^6\ ^5D_2$	-	$3d^6\ ^3D_3$	M1
30172.51	0.13	$3d^6\ a^3P_2$	-	$3d^6\ b^3P_1$	M1, E2
30224.46	0.14	$3d^6\ ^3H_6$	-	$3d^6\ b^3F_4$	E2
30279.77	0.52	$3d^6\ ^5D_3$	-	$3d^6\ ^3D_2$	M1
30421.59	0.52	$3d^6\ ^5D_3$	-	$3d^6\ ^3D_3$	M1
30857.67	0.22	$3d^6\ ^5D_4$	-	$3d^6\ ^3D_3$	M1
30871.27	0.14	$3d^6\ a^3P_2$	-	$3d^6\ b^3F_4$	E2
30886.34	0.24	$3d^6\ ^5D_4$	-	$3d^6\ a^1G_4$	M1
31007.29	0.13	$3d^6\ a^3P_2$	-	$3d^6\ b^3P_2$	E2
32078.66	0.13	$3d^6\ ^3G_3$	-	$3d^6\ b^1G_4$	M1
32662.51	0.13	$3d^6\ ^3G_5$	-	$3d^6\ b^1G_4$	M1, E2
35758.81	0.15	$3d^6\ a^3F_4$	-	$3d^6\ b^1G_4$	M1
36920.71	0.23	$3d^6\ ^3H_5$	-	$3d^6\ b^1G_4$	M1
39973.05	0.23	$3d^6\ ^5D_0$	-	$(^6S)\ 4s\ ^5S_2$	E2
40067.87	0.13	$3d^6\ ^5D_1$	-	$(^6S)\ 4s\ ^5S_2$	E2
40188.988	0.063	$3d^6\ b^3F_3$	-	$(^4F)\ 4s\ ^3F_3$	E2
40196.577	0.069	$3d^6\ b^3F_4$	-	$(^4F)\ 4s\ ^3F_4$	E2
40238.8	0.1	$3d^6\ b^3F_2$	-	$(^4F)\ 4s\ ^3F_2$	E2
40261.56	0.14	$3d^6\ ^5D_2$	-	$(^6S)\ 4s\ ^5S_2$	E2
40564.26	0.51	$3d^6\ ^5D_3$	-	$(^6S)\ 4s\ ^5S_2$	E2

Fe III parity-forbidden transition linelist continued

σ_{calc} (cm^{-1})	Unc. (cm^{-1})	Transition			Type
41000.3	0.2	$3d^6\ ^5D_4$	-	$(^6S)\ 4s\ ^5S_2$	E2
43012.177	0.084	$3d^6\ ^3D_2$	-	$(^4P)\ 4s\ ^3P_2$	E2
43123.4	0.1	$3d^6\ ^3D_1$	-	$(^4P)\ 4s\ ^3P_1$	E2
43950.552	0.086	$3d^6\ ^1F_3$	-	$(a^2D)\ 4s\ ^1D_2$	E2
45005.417	0.086	$3d^6\ ^1F_3$	-	$(a^2F)\ 4s\ ^1F_3$	E2
45582.9	0.1	$3d^6\ ^3G_3$	-	$(^4G)\ 4s\ ^3G_3$	E2
45586.5	0.1	$3d^6\ ^3G_3$	-	$(^4G)\ 4s\ ^3G_4$	E2
45753.123	0.098	$3d^6\ ^3G_4$	-	$(^4G)\ 4s\ ^3G_5$	E2
45787.861	0.098	$3d^6\ ^3G_4$	-	$(^4G)\ 4s\ ^3G_4$	E2
46099.309	0.077	$3d^6\ ^3D_3$	-	$(^4D)\ 4s\ ^3D_3$	E2
46135.61	0.11	$3d^6\ ^3G_5$	-	$(^4G)\ 4s\ ^3G_5$	E2
46241.133	0.083	$3d^6\ ^3D_2$	-	$(^4D)\ 4s\ ^3D_3$	E2
46244.873	0.078	$3d^6\ ^3D_3$	-	$(^4D)\ 4s\ ^3D_2$	E2
46349.7	0.12	$3d^6\ ^3D_1$	-	$(^4D)\ 4s\ ^3D_1$	E2
46359.7	0.1	$3d^6\ ^3D_2$	-	$(^4D)\ 4s\ ^3D_1$	E2
46376.66	0.11	$3d^6\ ^3D_1$	-	$(^4D)\ 4s\ ^3D_2$	E2
48216.97	0.19	$3d^6\ ^5D_1$	-	$3d^6\ b^3P_0$	M1
48838.36	0.17	$3d^6\ ^5D_2$	-	$3d^6\ b^3P_1$	M1, E2
48867.861	0.092	$3d^6\ a^3F_2$	-	$(^4G)\ 4s\ ^3G_3$	E2
49025.281	0.086	$3d^6\ a^3F_3$	-	$(^4G)\ 4s\ ^3G_3$	E2
49028.918	0.086	$3d^6\ a^3F_3$	-	$(^4G)\ 4s\ ^3G_4$	E2
49231.91	0.13	$3d^6\ a^3F_4$	-	$(^4G)\ 4s\ ^3G_5$	E2
49266.65	0.13	$3d^6\ a^3F_4$	-	$(^4G)\ 4s\ ^3G_4$	E2
49975.84	0.52	$3d^6\ ^5D_3$	-	$3d^6\ b^3P_2$	M1, E2
50243.13	0.12	$3d^6\ ^3H_4$	-	$(^4G)\ 4s\ ^3G_3$	E2
50246.77	0.12	$3d^6\ ^3H_4$	-	$(^4G)\ 4s\ ^3G_4$	E2
50393.81	0.22	$3d^6\ ^3H_5$	-	$(^4G)\ 4s\ ^3G_5$	E2
50424.91	0.22	$3d^6\ ^3H_5$	-	$(^4G)\ 4s\ ^3G_3$	E2

Fe III parity-forbidden transition linelist continued

σ_{calc} (cm^{-1})	Unc. (cm^{-1})	Transition			Type
50428.55	0.22	$3d^6\ ^3H_5$	-	$(^4G)\ 4s\ ^3G_4$	E2
50616.084	0.087	$3d^6\ ^1F_3$	-	$(a^2G)\ 4s\ ^1G_4$	E2
50642.8	0.12	$3d^6\ ^3H_6$	-	$(^4G)\ 4s\ ^3G_5$	E2
50677.54	0.12	$3d^6\ ^3H_6$	-	$(^4G)\ 4s\ ^3G_4$	E2
51043.852	0.095	$3d^6\ a^1D_2$	-	$(a^2D)\ 4s\ ^1D_2$	E2
51933.11	0.12	$3d^6\ ^3G_3$	-	$(^4D)\ 4s\ ^3D_1$	E2
51960.1	0.1	$3d^6\ ^3G_3$	-	$(^4D)\ 4s\ ^3D_2$	E2
51991.77	0.091	$3d^6\ a^3F_2$	-	$(^4P)\ 4s\ ^3P_1$	E2
52027.964	0.088	$3d^6\ a^3F_3$	-	$(^4P)\ 4s\ ^3P_2$	E2
52034.89	0.18	$3d^6\ a^1S_0$	-	$(a^2D)\ 4s\ ^1D_2$	E2
52098.717	0.095	$3d^6\ a^1D_2$	-	$(a^2F)\ 4s\ ^1F_3$	E2
52149.19	0.086	$3d^6\ a^3F_3$	-	$(^4P)\ 4s\ ^3P_1$	E2
52161.4	0.1	$3d^6\ ^3G_4$	-	$(^4D)\ 4s\ ^3D_2$	E2
52265.7	0.13	$3d^6\ a^3F_4$	-	$(^4P)\ 4s\ ^3P_2$	E2
52349.8	0.1	$3d^6\ b^1G_4$	-	$(b^2D)\ 4s\ ^1D_2$	E2
52398.35	0.11	$3d^6\ ^3G_5$	-	$(^4D)\ 4s\ ^3D_3$	E2
52519.45	0.15	$3d^6\ a^3P_0$	-	$(^4P)\ 4s\ ^3P_2$	E2
52543.27	0.12	$3d^6\ a^1G_4$	-	$(^2I)\ 4s\ ^1I_6$	E2
53039.4	0.14	$3d^6\ a^3P_1$	-	$(^4P)\ 4s\ ^3P_2$	E2
53073.54	0.13	$3d^6\ ^1I_6$	-	$(^2I)\ 4s\ ^1I_6$	E2
53160.62	0.13	$3d^6\ a^3P_1$	-	$(^4P)\ 4s\ ^3P_1$	E2
53483.59	0.12	$3d^6\ a^1G_4$	-	$(a^2F)\ 4s\ ^3F_2$	E2
54144.898	0.092	$3d^6\ ^1F_3$	-	$(b^2F)\ 4s\ ^1F_3$	E2
54323.4	0.12	$3d^6\ a^3P_2$	-	$(^4P)\ 4s\ ^3P_2$	E2
54444.62	0.12	$3d^6\ a^3P_2$	-	$(^4P)\ 4s\ ^3P_1$	E2
54718.0	0.1	$3d^6\ ^3G_3$	-	$(^2I)\ 4s\ ^3I_5$	E2
54903.6	0.1	$3d^6\ ^3G_4$	-	$(^2I)\ 4s\ ^3I_6$	E2
54919.4	0.1	$3d^6\ ^3G_4$	-	$(^2I)\ 4s\ ^3I_5$	E2

Fe III parity-forbidden transition linelist continued

σ_{calc} (cm^{-1})	Unc. (cm^{-1})	Transition			Type
55218.11	0.11	$3d^6\ a^3F_2$	-	$(^4D)\ 4s\ ^3D_1$	E2
55245.064	0.094	$3d^6\ a^3F_2$	-	$(^4D)\ 4s\ ^3D_2$	E2
55256.92	0.088	$3d^6\ a^3F_3$	-	$(^4D)\ 4s\ ^3D_3$	E2
55281.54	0.11	$3d^6\ ^3G_5$	-	$(^2I)\ 4s\ ^3I_7$	E2
55286.11	0.11	$3d^6\ ^3G_5$	-	$(^2I)\ 4s\ ^3I_6$	E2
55375.53	0.11	$3d^6\ a^3F_3$	-	$(^4D)\ 4s\ ^3D_1$	E2
55402.484	0.088	$3d^6\ a^3F_3$	-	$(^4D)\ 4s\ ^3D_2$	E2
55494.218	0.089	$3d^6\ b^3P_2$	-	$(b^2D)\ 4s\ ^3D_2$	E2
55494.65	0.13	$3d^6\ a^3F_4$	-	$(^4D)\ 4s\ ^3D_3$	E2
55517.4	0.1	$3d^6\ b^3P_2$	-	$(b^2D)\ 4s\ ^3D_3$	E2
55640.22	0.13	$3d^6\ a^3F_4$	-	$(^4D)\ 4s\ ^3D_2$	E2
55893.97	0.15	$3d^6\ a^3P_0$	-	$(^4D)\ 4s\ ^3D_2$	E2
55960.68	0.12	$3d^6\ a^1G_4$	-	$(a^2D)\ 4s\ ^1D_2$	E2
56268.35	0.14	$3d^6\ a^3P_1$	-	$(^4D)\ 4s\ ^3D_3$	E2
56386.96	0.15	$3d^6\ a^3P_1$	-	$(^4D)\ 4s\ ^3D_1$	E2
56413.92	0.14	$3d^6\ a^3P_1$	-	$(^4D)\ 4s\ ^3D_2$	E2
57015.55	0.12	$3d^6\ a^1G_4$	-	$(a^2F)\ 4s\ ^1F_3$	E2
57552.35	0.12	$3d^6\ a^3P_2$	-	$(^4D)\ 4s\ ^3D_3$	E2
57585.51	0.099	$3d^6\ a^1D_2$	-	$(b^2F)\ 4s\ ^3F_4$	E2
57670.96	0.13	$3d^6\ a^3P_2$	-	$(^4D)\ 4s\ ^3D_1$	E2
57697.92	0.12	$3d^6\ a^3P_2$	-	$(^4D)\ 4s\ ^3D_2$	E2
57709.384	0.098	$3d^6\ a^1D_2$	-	$(a^2G)\ 4s\ ^1G_4$	E2
57824.29	0.11	$3d^6\ ^3G_5$	-	$(a^2D)\ 4s\ ^3D_3$	E2
58971.58	0.11	$3d^6\ ^3D_1$	-	$(a^2G)\ 4s\ ^3G_3$	E2
59050.244	0.075	$3d^6\ ^3D_3$	-	$(a^2G)\ 4s\ ^3G_5$	E2
59067.784	0.081	$3d^6\ ^3D_2$	-	$(a^2G)\ 4s\ ^3G_4$	E2
59218.451	0.098	$3d^6\ ^3G_4$	-	$(a^2F)\ 4s\ ^3F_4$	E2
59227.4	0.1	$3d^6\ ^3G_3$	-	$(a^2F)\ 4s\ ^3F_2$	E2

Fe III parity-forbidden transition linelist continued

σ_{calc} (cm^{-1})	Unc. (cm^{-1})	Transition			Type
59362.53	0.13	$3d^6\ ^3H_4$	-	$(^2I)\ 4s\ ^3I_6$	E2
59378.27	0.13	$3d^6\ ^3H_4$	-	$(^2I)\ 4s\ ^3I_5$	E2
59529.4	0.1	$3d^6\ ^3G_3$	-	$(a^2F)\ 4s\ ^3F_3$	E2
59539.74	0.22	$3d^6\ ^3H_5$	-	$(^2I)\ 4s\ ^3I_7$	E2
59544.31	0.22	$3d^6\ ^3H_5$	-	$(^2I)\ 4s\ ^3I_6$	E2
59560.05	0.22	$3d^6\ ^3H_5$	-	$(^2I)\ 4s\ ^3I_5$	E2
59600.94	0.11	$3d^6\ ^3G_5$	-	$(a^2F)\ 4s\ ^3F_4$	E2
59697.82	0.12	$3d^6\ ^3D_1$	-	$(^4F)\ 4s\ ^3F_2$	E2
59730.8	0.1	$3d^6\ ^3G_4$	-	$(a^2F)\ 4s\ ^3F_3$	E2
59768.213	0.082	$3d^6\ ^3D_2$	-	$(^4F)\ 4s\ ^3F_3$	E2
59788.73	0.12	$3d^6\ ^3H_6$	-	$(^2I)\ 4s\ ^3I_7$	E2
59793.3	0.12	$3d^6\ ^3H_6$	-	$(^2I)\ 4s\ ^3I_6$	E2
60553.473	0.092	$3d^6\ a^3F_2$	-	$(a^2D)\ 4s\ ^3D_2$	E2
60682.857	0.086	$3d^6\ a^3F_3$	-	$(a^2D)\ 4s\ ^3D_3$	E2
60710.893	0.087	$3d^6\ a^3F_3$	-	$(a^2D)\ 4s\ ^3D_2$	E2
60729.07	0.15	$3d^6\ b^1G_4$	-	$(b^2G)\ 4s\ ^1G_4$	E2
60920.59	0.13	$3d^6\ a^3F_4$	-	$(a^2D)\ 4s\ ^3D_3$	E2
60948.63	0.13	$3d^6\ a^3F_4$	-	$(a^2D)\ 4s\ ^3D_2$	E2
61238.2	0.1	$3d^6\ a^1D_2$	-	$(b^2F)\ 4s\ ^1F_3$	E2
61704.5	0.1	$3d^6\ ^3G_3$	-	$(a^2D)\ 4s\ ^1D_2$	E2
61722.33	0.14	$3d^6\ a^3P_1$	-	$(a^2D)\ 4s\ ^3D_2$	E2
61789.96	0.12	$3d^6\ a^3F_2$	-	$(^4F)\ 4s\ ^5F_1$	E2
61947.38	0.11	$3d^6\ a^3F_3$	-	$(^4F)\ 4s\ ^5F_1$	E2
62459.508	0.086	$3d^6\ a^3F_3$	-	$(a^2F)\ 4s\ ^3F_4$	E2
62467.79	0.25	$3d^6\ ^5D_0$	-	$(^4G)\ 4s\ ^5G_2$	E2
62502.34	0.12	$3d^6\ a^1G_4$	-	$(b^2F)\ 4s\ ^3F_4$	E2
62512.444	0.096	$3d^6\ a^3F_2$	-	$(a^2F)\ 4s\ ^3F_2$	E2
62531.006	0.082	$3d^6\ ^3D_3$	-	$(b^2F)\ 4s\ ^3F_4$	E2

Fe III parity-forbidden transition linelist continued

σ_{calc} (cm^{-1})	Unc. (cm^{-1})	Transition			Type
62534.76	0.078	$3d^6\ ^3D_3$	-	$(b^2F)\ 4s\ ^3F_3$	E2
62562.13	0.15	$3d^6\ ^5D_1$	-	$(^4G)\ 4s\ ^5G_3$	E2
62562.61	0.16	$3d^6\ ^5D_1$	-	$(^4G)\ 4s\ ^5G_2$	E2
62626.21	0.12	$3d^6\ a^1G_4$	-	$(a^2G)\ 4s\ ^1G_4$	E2
62654.88	0.08	$3d^6\ ^3D_3$	-	$(a^2G)\ 4s\ ^1G_4$	E2
62666.54	0.11	$3d^6\ ^3D_1$	-	$(b^2F)\ 4s\ ^3F_3$	E2
62676.584	0.084	$3d^6\ ^3D_2$	-	$(b^2F)\ 4s\ ^3F_3$	E2
62687.01	0.11	$3d^6\ ^3D_1$	-	$(b^2F)\ 4s\ ^3F_2$	E2
62697.051	0.086	$3d^6\ ^3D_2$	-	$(b^2F)\ 4s\ ^3F_2$	E2
62697.24	0.13	$3d^6\ a^3F_4$	-	$(a^2F)\ 4s\ ^3F_4$	E2
62748.43	0.15	$3d^6\ ^5D_2$	-	$(^4G)\ 4s\ ^5G_4$	E2
62755.82	0.15	$3d^6\ ^5D_2$	-	$(^4G)\ 4s\ ^5G_3$	E2
62756.3	0.16	$3d^6\ ^5D_2$	-	$(^4G)\ 4s\ ^5G_2$	E2
62814.405	0.095	$3d^6\ a^3F_2$	-	$(a^2F)\ 4s\ ^3F_3$	E2
62958.81	0.15	$3d^6\ a^3P_1$	-	$(^4F)\ 4s\ ^5F_1$	E2
62971.82	0.09	$3d^6\ a^3F_3$	-	$(a^2F)\ 4s\ ^3F_3$	E2
62978.29	0.12	$3d^6\ a^3P_2$	-	$(a^2D)\ 4s\ ^3D_3$	E2
63006.33	0.12	$3d^6\ a^3P_2$	-	$(a^2D)\ 4s\ ^3D_2$	E2
63030.7	0.51	$3d^6\ ^5D_3$	-	$(^4G)\ 4s\ ^5G_5$	E2
63032.61	0.13	$3d^6\ ^1I_6$	-	$(b^2F)\ 4s\ ^3F_4$	E2
63051.13	0.51	$3d^6\ ^5D_3$	-	$(^4G)\ 4s\ ^5G_4$	E2
63058.52	0.51	$3d^6\ ^5D_3$	-	$(^4G)\ 4s\ ^5G_3$	E2
63156.48	0.13	$3d^6\ ^1I_6$	-	$(a^2G)\ 4s\ ^1G_4$	E2
63161.35	0.15	$3d^6\ a^3P_0$	-	$(a^2F)\ 4s\ ^3F_2$	E2
63425.71	0.21	$3d^6\ ^5D_4$	-	$(^4G)\ 4s\ ^5G_6$	E2
63466.78	0.21	$3d^6\ ^5D_4$	-	$(^4G)\ 4s\ ^5G_5$	E2
63487.21	0.21	$3d^6\ ^5D_4$	-	$(^4G)\ 4s\ ^5G_4$	E2
63521.5	0.1	$3d^6\ ^3G_3$	-	$(^2H)\ 4s\ ^3H_4$	E2

Fe III parity-forbidden transition linelist continued

σ_{calc} (cm^{-1})	Unc. (cm^{-1})	Transition			Type
63681.3	0.14	$3d^6\ a^3P_1$	-	$(a^2F)\ 4s\ ^3F_2$	E2
63722.8	0.1	$3d^6\ ^3G_4$	-	$(^2H)\ 4s\ ^3H_4$	E2
63753.626	0.099	$3d^6\ ^3G_4$	-	$(^2H)\ 4s\ ^3H_5$	E2
63887.72	0.13	$3d^6\ ^3H_4$	-	$(a^2F)\ 4s\ ^3F_2$	E2
63983.26	0.14	$3d^6\ a^3P_1$	-	$(a^2F)\ 4s\ ^3F_3$	E2
64045.2	1.4	$3d^6\ b^3F_3$	-	$(b^2G)\ 4s\ ^3G_4$	E2
64049.63	0.16	$3d^6\ b^3F_4$	-	$(b^2G)\ 4s\ ^3G_5$	E2
64057.09	0.16	$3d^6\ b^3F_3$	-	$(b^2G)\ 4s\ ^3G_3$	E2
64108.13	0.12	$3d^6\ ^3H_6$	-	$(a^2F)\ 4s\ ^3F_4$	E2
64136.12	0.11	$3d^6\ ^3G_5$	-	$(^2H)\ 4s\ ^3H_5$	E2
64167.3	0.17	$3d^6\ b^3F_2$	-	$(b^2G)\ 4s\ ^3G_3$	E2
64364.52	0.11	$3d^6\ ^3G_5$	-	$(^2H)\ 4s\ ^3H_6$	E2
64371.46	0.22	$3d^6\ ^3H_5$	-	$(a^2F)\ 4s\ ^3F_3$	E2
64555.0	0.1	$3d^6\ ^3G_3$	-	$(a^2G)\ 4s\ ^3G_3$	E2
64641.2	0.1	$3d^6\ ^3G_3$	-	$(a^2G)\ 4s\ ^3G_4$	E2
64754.94	0.12	$3d^6\ a^3P_2$	-	$(a^2F)\ 4s\ ^3F_4$	E2
64756.3	0.1	$3d^6\ ^3G_4$	-	$(a^2G)\ 4s\ ^3G_3$	E2
64842.514	0.099	$3d^6\ ^3G_4$	-	$(a^2G)\ 4s\ ^3G_4$	E2
64966.8	0.1	$3d^6\ ^3G_4$	-	$(a^2G)\ 4s\ ^3G_5$	E2
65225.0	0.11	$3d^6\ ^3G_5$	-	$(a^2G)\ 4s\ ^3G_4$	E2
65281.23	0.12	$3d^6\ ^3G_3$	-	$(^4F)\ 4s\ ^3F_2$	E2
65341.6	0.1	$3d^6\ ^3G_3$	-	$(^4F)\ 4s\ ^3F_3$	E2
65349.29	0.11	$3d^6\ ^3G_5$	-	$(a^2G)\ 4s\ ^3G_5$	E2
65482.59	0.12	$3d^6\ ^3G_4$	-	$(^4F)\ 4s\ ^3F_2$	E2
65495.98	0.25	$3d^6\ ^5D_0$	-	$(^4P)\ 4s\ ^5P_2$	E2
65531.4	0.1	$3d^6\ ^3G_4$	-	$(^4F)\ 4s\ ^3F_4$	E2
65542.9	0.1	$3d^6\ ^3G_4$	-	$(^4F)\ 4s\ ^3F_3$	E2
65590.8	0.15	$3d^6\ ^5D_1$	-	$(^4P)\ 4s\ ^5P_2$	E2

Fe III parity-forbidden transition linelist continued

σ_{calc} (cm^{-1})	Unc. (cm^{-1})	Transition			Type
65659.56	0.15	$3d^6\ ^5D_1$	-	$(^4P)\ 4s\ ^5P_1$	E2
65726.22	0.15	$3d^6\ ^5D_2$	-	$(^4P)\ 4s\ ^5P_3$	E2
65784.49	0.15	$3d^6\ ^5D_2$	-	$(^4P)\ 4s\ ^5P_2$	E2
65853.25	0.15	$3d^6\ ^5D_2$	-	$(^4P)\ 4s\ ^5P_1$	E2
65913.85	0.11	$3d^6\ ^3G_5$	-	$(^4F)\ 4s\ ^3F_4$	E2
65925.43	0.11	$3d^6\ ^3G_5$	-	$(^4F)\ 4s\ ^3F_3$	E2
66028.92	0.51	$3d^6\ ^5D_3$	-	$(^4P)\ 4s\ ^5P_3$	E2
66155.03	0.13	$3d^6\ a^1G_4$	-	$(b^2F)\ 4s\ ^1F_3$	E2
66155.95	0.51	$3d^6\ ^5D_3$	-	$(^4P)\ 4s\ ^5P_1$	E2
66465.0	0.21	$3d^6\ ^5D_4$	-	$(^4P)\ 4s\ ^5P_3$	E2
66523.27	0.21	$3d^6\ ^5D_4$	-	$(^4P)\ 4s\ ^5P_2$	E2
66606.8	0.2	$3d^6\ a^1D_2$	-	$(^2S)\ 4s\ ^1S_0$	E2
66674.5	0.1	$3d^6\ ^1F_3$	-	$(b^2D)\ 4s\ ^1D_2$	E2
66806.454	0.093	$3d^6\ a^3F_2$	-	$(^2H)\ 4s\ ^3H_4$	E2
66963.874	0.088	$3d^6\ a^3F_3$	-	$(^2H)\ 4s\ ^3H_4$	E2
66994.683	0.088	$3d^6\ a^3F_3$	-	$(^2H)\ 4s\ ^3H_5$	E2
67232.42	0.13	$3d^6\ a^3F_4$	-	$(^2H)\ 4s\ ^3H_5$	E2
67460.82	0.13	$3d^6\ a^3F_4$	-	$(^2H)\ 4s\ ^3H_6$	E2
67804.7	0.1	$3d^6\ ^3D_3$	-	$(^2S)\ 4s\ ^3S_1$	E2
67839.984	0.093	$3d^6\ a^3F_2$	-	$(a^2G)\ 4s\ ^3G_3$	E2
67926.151	0.093	$3d^6\ a^3F_2$	-	$(a^2G)\ 4s\ ^3G_4$	E2
67936.46	0.13	$3d^6\ ^3D_1$	-	$(^2S)\ 4s\ ^3S_1$	E2
67946.5	0.11	$3d^6\ ^3D_2$	-	$(^2S)\ 4s\ ^3S_1$	E2
68083.571	0.088	$3d^6\ a^3F_3$	-	$(a^2G)\ 4s\ ^3G_4$	E2
68181.73	0.12	$3d^6\ ^3H_4$	-	$(^2H)\ 4s\ ^3H_4$	E2
68207.855	0.088	$3d^6\ a^3F_3$	-	$(a^2G)\ 4s\ ^3G_5$	E2
68212.54	0.12	$3d^6\ ^3H_4$	-	$(^2H)\ 4s\ ^3H_5$	E2
68363.51	0.22	$3d^6\ ^3H_5$	-	$(^2H)\ 4s\ ^3H_4$	E2

Fe III parity-forbidden transition linelist continued

σ_{calc} (cm^{-1})	Unc. (cm^{-1})	Transition	Type
68394.32	0.22	$3d^6\ ^3H_5$ - $(^2H)\ 4s\ ^3H_5$	E2
68445.59	0.13	$3d^6\ a^3F_4$ - $(a^2G)\ 4s\ ^3G_5$	E2
68622.72	0.22	$3d^6\ ^3H_5$ - $(^2H)\ 4s\ ^3H_6$	E2
68810.87	0.25	$3d^6\ ^5D_0$ - $(^4D)\ 4s\ ^5D_2$	E2
68856.02	0.15	$3d^6\ ^5D_1$ - $(^4D)\ 4s\ ^5D_1$	E2
68871.71	0.12	$3d^6\ ^3H_6$ - $(^2H)\ 4s\ ^3H_6$	E2
68904.63	0.15	$3d^6\ ^5D_1$ - $(^4D)\ 4s\ ^5D_3$	E2
68905.69	0.15	$3d^6\ ^5D_1$ - $(^4D)\ 4s\ ^5D_2$	E2
68957.31	0.15	$3d^6\ ^5D_2$ - $(^4D)\ 4s\ ^5D_4$	E2
69009.11	0.15	$3d^6\ ^5D_2$ - $(^4D)\ 4s\ ^5D_0$	E2
69010.15	0.13	$3d^6\ a^3F_4$ - $(^4F)\ 4s\ ^3F_4$	E2
69049.71	0.15	$3d^6\ ^5D_2$ - $(^4D)\ 4s\ ^5D_1$	E2
69098.32	0.15	$3d^6\ ^5D_2$ - $(^4D)\ 4s\ ^5D_3$	E2
69260.01	0.51	$3d^6\ ^5D_3$ - $(^4D)\ 4s\ ^5D_4$	E2
69301.42	0.12	$3d^6\ ^3H_4$ - $(a^2G)\ 4s\ ^3G_4$	E2
69352.41	0.51	$3d^6\ ^5D_3$ - $(^4D)\ 4s\ ^5D_1$	E2
69397.04	0.22	$3d^6\ ^3H_5$ - $(a^2G)\ 4s\ ^3G_3$	E2
69401.02	0.51	$3d^6\ ^5D_3$ - $(^4D)\ 4s\ ^5D_3$	E2
69402.08	0.51	$3d^6\ ^5D_3$ - $(^4D)\ 4s\ ^5D_2$	E2
69696.09	0.21	$3d^6\ ^5D_4$ - $(^4D)\ 4s\ ^5D_4$	E2
69732.19	0.12	$3d^6\ ^3H_6$ - $(a^2G)\ 4s\ ^3G_4$	E2
69837.1	0.21	$3d^6\ ^5D_4$ - $(^4D)\ 4s\ ^5D_3$	E2
69838.16	0.21	$3d^6\ ^5D_4$ - $(^4D)\ 4s\ ^5D_2$	E2
69856.48	0.12	$3d^6\ ^3H_6$ - $(a^2G)\ 4s\ ^3G_5$	E2
69941.5	0.14	$3d^6\ ^3H_4$ - $(^4F)\ 4s\ ^3F_2$	E2
70001.85	0.12	$3d^6\ ^3H_4$ - $(^4F)\ 4s\ ^3F_3$	E2
70172.05	0.22	$3d^6\ ^3H_5$ - $(^4F)\ 4s\ ^3F_4$	E2
70183.63	0.22	$3d^6\ ^3H_5$ - $(^4F)\ 4s\ ^3F_3$	E2

Fe III parity-forbidden transition linelist continued

σ_{calc} (cm^{-1})	Unc. (cm^{-1})	Transition			Type
70421.04	0.12	$3d^6\ ^3H_6$	-	$(^4F)\ 4s\ ^3F_4$	E2
71534.951	0.095	$3d^6\ a^3F_2$	-	$(b^2F)\ 4s\ ^3F_3$	E2
71555.418	0.097	$3d^6\ a^3F_2$	-	$(b^2F)\ 4s\ ^3F_2$	E2
71688.617	0.093	$3d^6\ a^3F_3$	-	$(b^2F)\ 4s\ ^3F_4$	E2
71692.37	0.09	$3d^6\ a^3F_3$	-	$(b^2F)\ 4s\ ^3F_3$	E2
71712.838	0.092	$3d^6\ a^3F_3$	-	$(b^2F)\ 4s\ ^3F_2$	E2
71926.35	0.14	$3d^6\ a^3F_4$	-	$(b^2F)\ 4s\ ^3F_4$	E2
71930.1	0.13	$3d^6\ a^3F_4$	-	$(b^2F)\ 4s\ ^3F_3$	E2
72050.22	0.13	$3d^6\ a^3F_4$	-	$(a^2G)\ 4s\ ^1G_4$	E2
72204.32	0.15	$3d^6\ a^3P_0$	-	$(b^2F)\ 4s\ ^3F_2$	E2
72703.8	0.14	$3d^6\ a^3P_1$	-	$(b^2F)\ 4s\ ^3F_3$	E2
72724.27	0.14	$3d^6\ a^3P_1$	-	$(b^2F)\ 4s\ ^3F_2$	E2
72910.22	0.12	$3d^6\ ^3H_4$	-	$(b^2F)\ 4s\ ^3F_3$	E2
72930.69	0.13	$3d^6\ ^3H_4$	-	$(b^2F)\ 4s\ ^3F_2$	E2
73088.25	0.22	$3d^6\ ^3H_5$	-	$(b^2F)\ 4s\ ^3F_4$	E2
73092.0	0.22	$3d^6\ ^3H_5$	-	$(b^2F)\ 4s\ ^3F_3$	E2
73337.24	0.13	$3d^6\ ^3H_6$	-	$(b^2F)\ 4s\ ^3F_4$	E2
73767.76	0.11	$3d^6\ a^1D_2$	-	$(b^2D)\ 4s\ ^1D_2$	E2
73984.05	0.13	$3d^6\ a^3P_2$	-	$(b^2F)\ 4s\ ^3F_4$	E2
73987.8	0.12	$3d^6\ a^3P_2$	-	$(b^2F)\ 4s\ ^3F_3$	E2
74758.8	0.19	$3d^6\ a^1S_0$	-	$(b^2D)\ 4s\ ^1D_2$	E2
75048.461	0.099	$3d^6\ ^3D_3$	-	$(b^2D)\ 4s\ ^3D_2$	E2
75071.64	0.11	$3d^6\ ^3D_3$	-	$(b^2D)\ 4s\ ^3D_3$	E2
75180.24	0.12	$3d^6\ ^3D_1$	-	$(b^2D)\ 4s\ ^3D_2$	E2
75190.3	0.1	$3d^6\ ^3D_2$	-	$(b^2D)\ 4s\ ^3D_2$	E2
75213.46	0.12	$3d^6\ ^3D_2$	-	$(b^2D)\ 4s\ ^3D_3$	E2
80444.49	0.33	$3d^6\ b^3P_2$	-	$(^2P)\ 4s\ ^3P_2$	E2
80449.11	0.33	$3d^6\ b^3P_2$	-	$(^2P)\ 4s\ ^3P_1$	E2

Fe III parity-forbidden transition linelist continued

σ_{calc} (cm^{-1})	Unc. (cm^{-1})	Transition			Type
80561.34	0.33	$3d^6\ b^3F_3$	-	$(^2P)\ 4s\ ^3P_2$	E2
80565.96	0.33	$3d^6\ b^3F_3$	-	$(^2P)\ 4s\ ^3P_1$	E2
80580.51	0.33	$3d^6\ b^3F_4$	-	$(^2P)\ 4s\ ^3P_2$	E2
80676.17	0.33	$3d^6\ b^3F_2$	-	$(^2P)\ 4s\ ^3P_1$	E2
80763.65	0.12	$3d^6\ ^3G_3$	-	$(b^2D)\ 4s\ ^3D_2$	E2
80965.01	0.12	$3d^6\ ^3G_4$	-	$(b^2D)\ 4s\ ^3D_2$	E2
81279.27	0.33	$3d^6\ b^3P_1$	-	$(^2P)\ 4s\ ^3P_2$	E2
81283.89	0.33	$3d^6\ b^3P_1$	-	$(^2P)\ 4s\ ^3P_1$	E2
81370.68	0.14	$3d^6\ ^3G_5$	-	$(b^2D)\ 4s\ ^3D_3$	E2
81383.67	0.25	$3d^6\ ^5D_0$	-	$(a^2D)\ 4s\ ^3D_2$	E2
81450.45	0.15	$3d^6\ ^5D_1$	-	$(a^2D)\ 4s\ ^3D_3$	E2
81672.18	0.16	$3d^6\ ^5D_2$	-	$(a^2D)\ 4s\ ^3D_2$	E2
81706.97	0.34	$3d^6\ b^3P_0$	-	$(^2P)\ 4s\ ^3P_2$	E2
81946.84	0.51	$3d^6\ ^5D_3$	-	$(a^2D)\ 4s\ ^3D_3$	E2
81974.88	0.51	$3d^6\ ^5D_3$	-	$(a^2D)\ 4s\ ^3D_2$	E2
82422.83	0.16	$3d^6\ ^5D_2$	-	$(^4F)\ 4s\ ^5F_4$	E2
82702.4	0.51	$3d^6\ ^5D_3$	-	$(^4F)\ 4s\ ^5F_5$	E2
82714.97	0.17	$3d^6\ ^5D_1$	-	$(^4F)\ 4s\ ^5F_1$	E2
82725.53	0.51	$3d^6\ ^5D_3$	-	$(^4F)\ 4s\ ^5F_4$	E2
82908.66	0.17	$3d^6\ ^5D_2$	-	$(^4F)\ 4s\ ^5F_1$	E2
83138.48	0.21	$3d^6\ ^5D_4$	-	$(^4F)\ 4s\ ^5F_5$	E2
83161.61	0.21	$3d^6\ ^5D_4$	-	$(^4F)\ 4s\ ^5F_4$	E2
83467.86	0.17	$3d^6\ ^3D_3$	-	$(b^2G)\ 4s\ ^3G_5$	E2
83624.4	1.4	$3d^6\ ^3D_2$	-	$(b^2G)\ 4s\ ^3G_4$	E2
83626.27	0.18	$3d^6\ ^3D_1$	-	$(b^2G)\ 4s\ ^3G_3$	E2
83631.15	0.16	$3d^6\ ^5D_2$	-	$(a^2F)\ 4s\ ^3F_2$	E2
84048.65	0.11	$3d^6\ a^3F_2$	-	$(b^2D)\ 4s\ ^3D_2$	E2
84206.07	0.11	$3d^6\ a^3F_3$	-	$(b^2D)\ 4s\ ^3D_2$	E2

Fe III parity-forbidden transition linelist continued

σ_{calc} (cm^{-1})	Unc. (cm^{-1})	Transition			Type
84229.25	0.12	$3d^6$ a^3F_3	-	(b^2D) 4s $^3D_3$	E2
84466.98	0.16	$3d^6$ a^3F_4	-	(b^2D) 4s $^3D_3$	E2
85239.46	0.31	$3d^6$ b^1G_4	-	(c^2D) 4s $^1D_2$	E2
87063.86	0.17	$3d^6$ a^1G_4	-	(b^2G) 4s $^1G_4$	E2
87594.13	0.18	$3d^6$ $^1I_6$	-	(b^2G) 4s $^1G_4$	E2
88468.59	0.32	$3d^6$ b^3P_2	-	(c^2D) 4s $^3D_2$	E2
88585.43	0.32	$3d^6$ b^3F_3	-	(c^2D) 4s $^3D_2$	E2
88604.6	0.32	$3d^6$ b^3F_4	-	(c^2D) 4s $^3D_2$	E2
88695.65	0.32	$3d^6$ b^3F_2	-	(c^2D) 4s $^3D_2$	E2
89197.8	1.4	$3d^6$ $^3G_3$	-	(b^2G) 4s $^3G_4$	E2
89209.68	0.18	$3d^6$ $^3G_3$	-	(b^2G) 4s $^3G_3$	E2
89384.42	0.18	$3d^6$ $^3G_4$	-	(b^2G) 4s $^3G_5$	E2
89399.1	1.4	$3d^6$ $^3G_4$	-	(b^2G) 4s $^3G_4$	E2
89411.04	0.18	$3d^6$ $^3G_4$	-	(b^2G) 4s $^3G_3$	E2
89731.07	0.33	$3d^6$ b^3P_0	-	(c^2D) 4s $^3D_2$	E2
89766.91	0.18	$3d^6$ $^3G_5$	-	(b^2G) 4s $^3G_5$	E2
89781.6	1.4	$3d^6$ $^3G_5$	-	(b^2G) 4s $^3G_4$	E2
91547.17	0.31	$3d^6$ $^1F_3$	-	(^2P) 4s $^1P_1$	E2
93858.1	1.4	$3d^6$ $^3H_4$	-	(b^2G) 4s $^3G_4$	E2
93869.95	0.19	$3d^6$ $^3H_4$	-	(b^2G) 4s $^3G_3$	E2
94025.11	0.27	$3d^6$ $^3H_5$	-	(b^2G) 4s $^3G_5$	E2
94039.8	1.4	$3d^6$ $^3H_5$	-	(b^2G) 4s $^3G_4$	E2
94051.73	0.27	$3d^6$ $^3H_5$	-	(b^2G) 4s $^3G_3$	E2
94274.1	0.19	$3d^6$ $^3H_6$	-	(b^2G) 4s $^3G_5$	E2
98640.47	0.32	$3d^6$ a^1D_2	-	(^2P) 4s $^1P_1$	E2
99564.12	0.31	$3d^6$ $^1F_3$	-	(c^2D) 4s $^1D_2$	E2
99998.74	0.33	$3d^6$ $^3D_3$	-	(^2P) 4s $^3P_2$	E2
100003.36	0.33	$3d^6$ $^3D_3$	-	(^2P) 4s $^3P_1$	E2

Fe III parity-forbidden transition linelist continued

σ_{calc} (cm^{-1})	Unc. (cm^{-1})	Transition			Type
100135.14	0.34	$3d^6\ ^3D_1$	-	$(^2P)\ 4s\ ^3P_1$	E2
100140.56	0.33	$3d^6\ ^3D_2$	-	$(^2P)\ 4s\ ^3P_2$	E2
108022.83	0.32	$3d^6\ ^3D_3$	-	$(c^2D)\ 4s\ ^3D_2$	E2
109003.55	0.33	$3d^6\ a^3F_2$	-	$(^2P)\ 4s\ ^3P_1$	E2
109156.35	0.33	$3d^6\ a^3F_3$	-	$(^2P)\ 4s\ ^3P_2$	E2
109160.97	0.33	$3d^6\ a^3F_3$	-	$(^2P)\ 4s\ ^3P_1$	E2
109394.08	0.35	$3d^6\ a^3F_4$	-	$(^2P)\ 4s\ ^3P_2$	E2
110167.78	0.35	$3d^6\ a^3P_1$	-	$(^2P)\ 4s\ ^3P_2$	E2
111451.78	0.34	$3d^6\ a^3P_2$	-	$(^2P)\ 4s\ ^3P_2$	E2
111456.4	0.34	$3d^6\ a^3P_2$	-	$(^2P)\ 4s\ ^3P_1$	E2
111574.26	0.32	$3d^6\ a^1G_4$	-	$(c^2D)\ 4s\ ^1D_2$	E2
113939.39	0.33	$3d^6\ ^3G_4$	-	$(c^2D)\ 4s\ ^3D_2$	E2

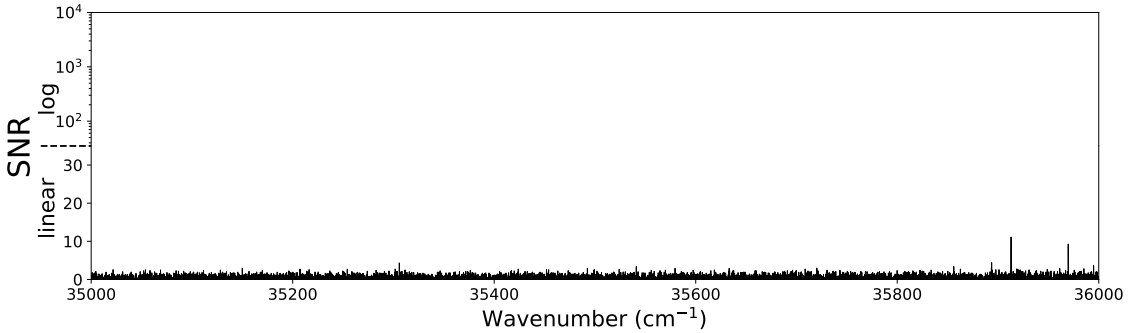
E FTS Spectral Plots

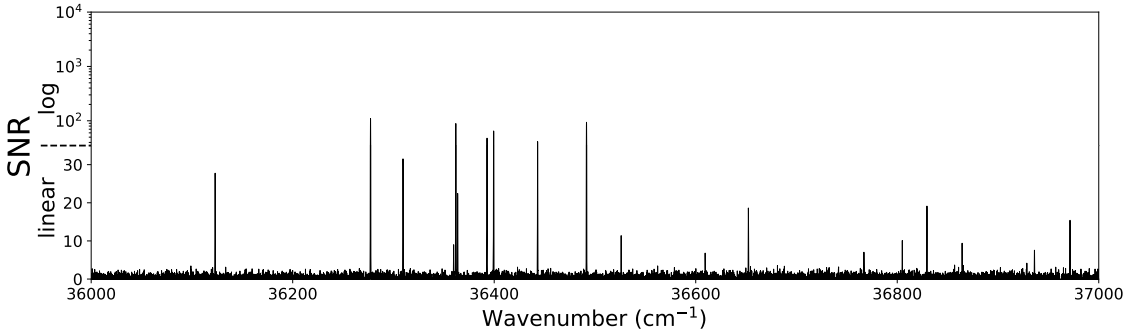
In this section, the plots of the FTS spectra used in this project are shown:

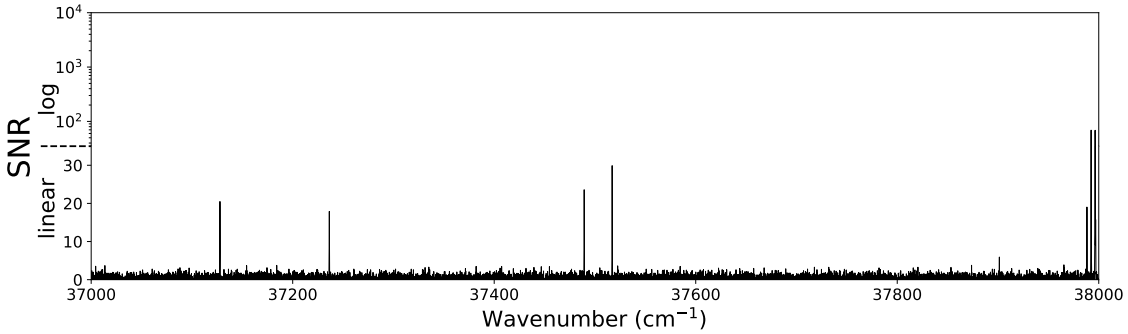
- Fe327,
- Fe116,
- Fe831,
- Fe832,
- Fe903,
- Fe103,
- Fe121, and
- Fe203.

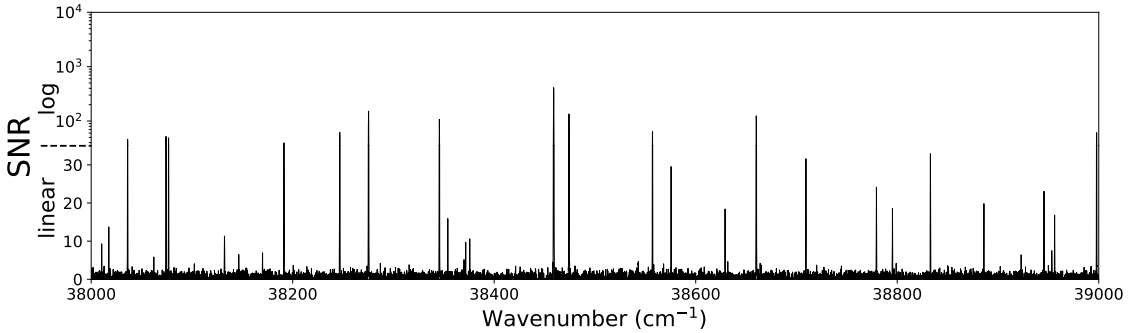
They are displayed in $1,000$ cm^{-1} segments and the y scale is split into a linear and log scale at the SNR of 35, to ensure visibility of the weakest lines. The wavenumbers are not calibrated.

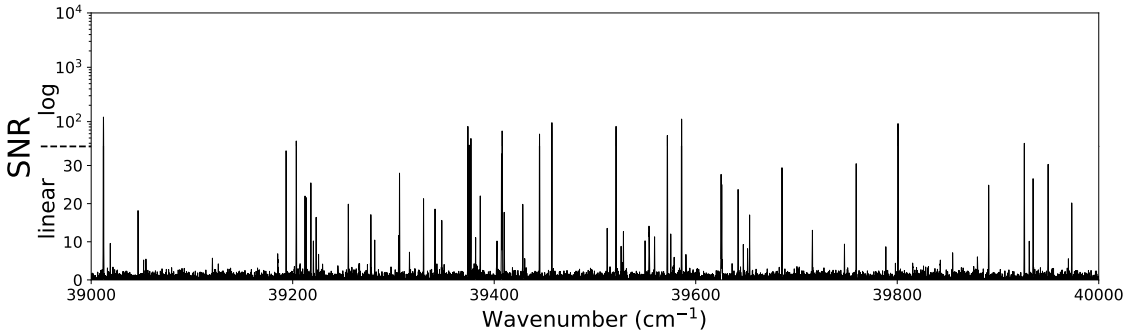
E.1 Fe327


SNR
log
linear
Wavenumber (cm^{-1})

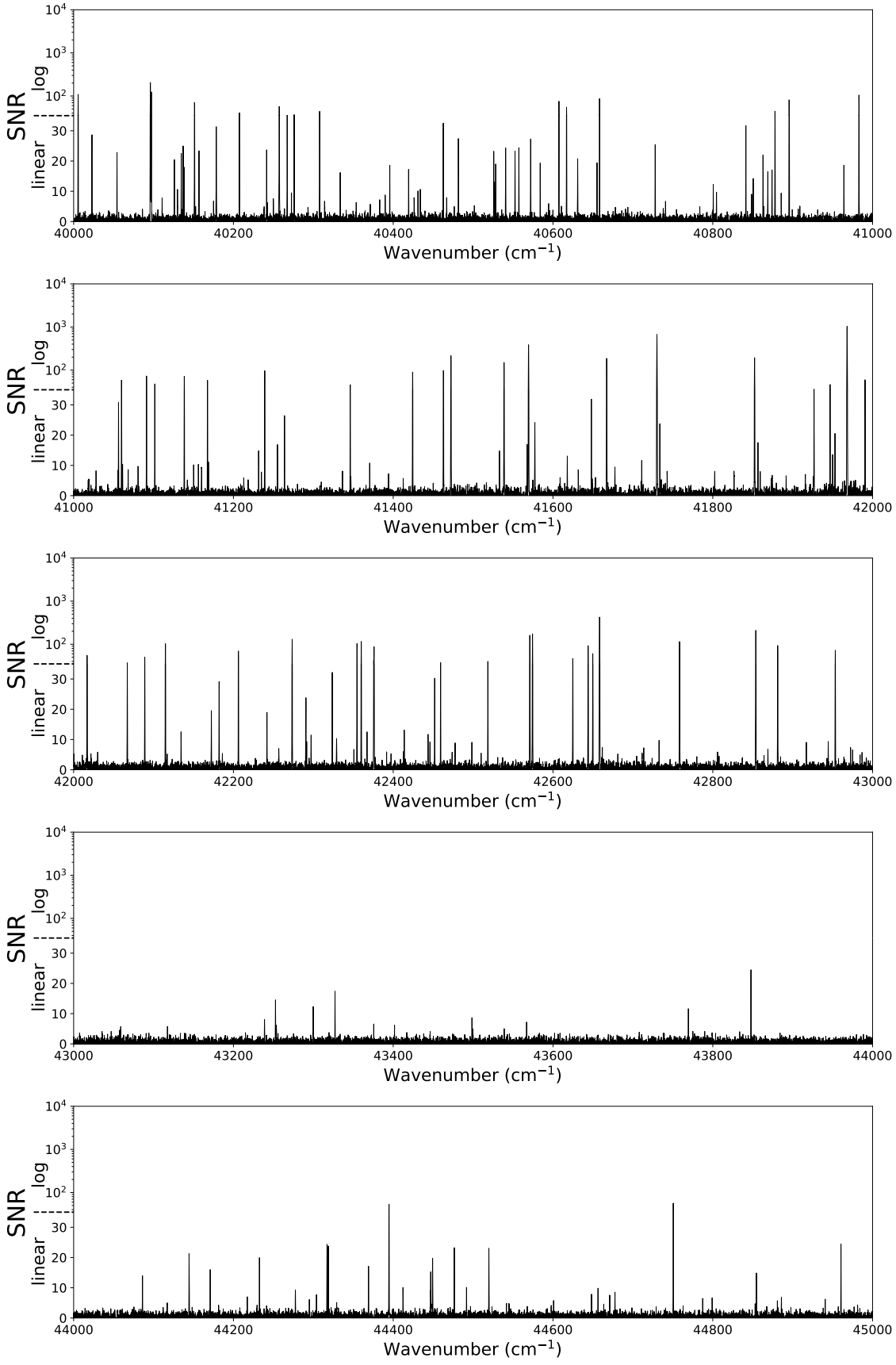

SNR
log
linear
Wavenumber (cm^{-1})


SNR
log
linear
Wavenumber (cm^{-1})

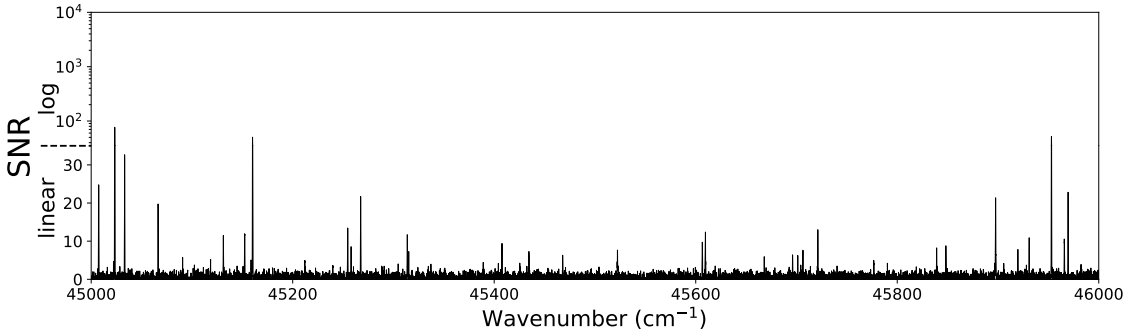

SNR
log
linear
Wavenumber (cm^{-1})

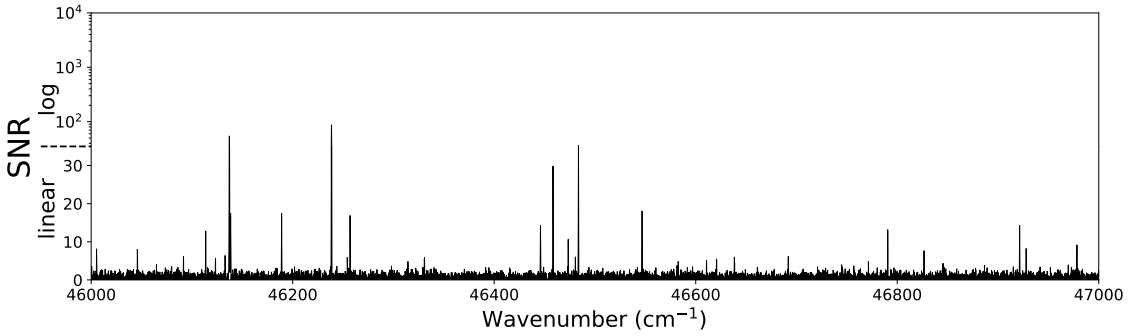

SNR
log
linear
Wavenumber (cm^{-1})

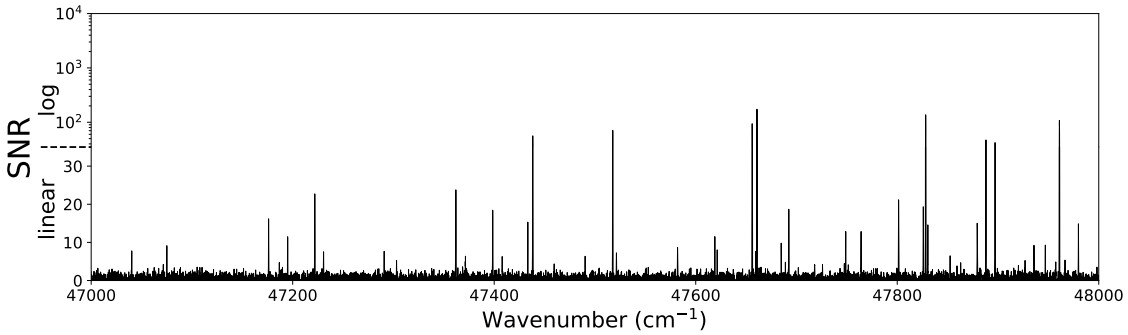
Fe327 (continued)

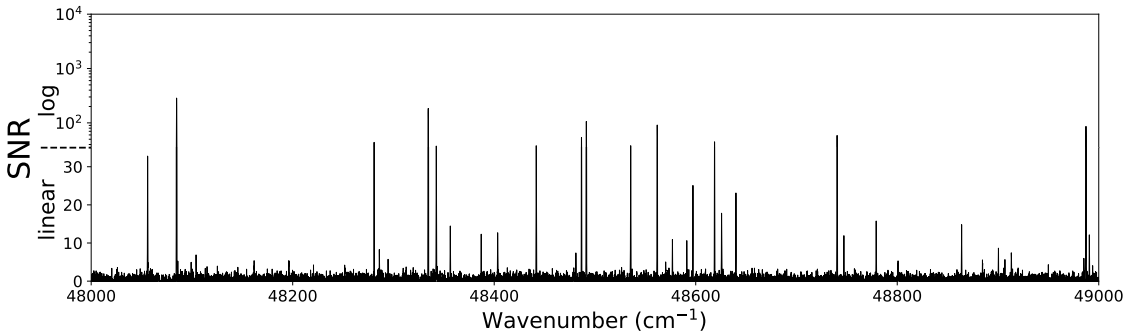


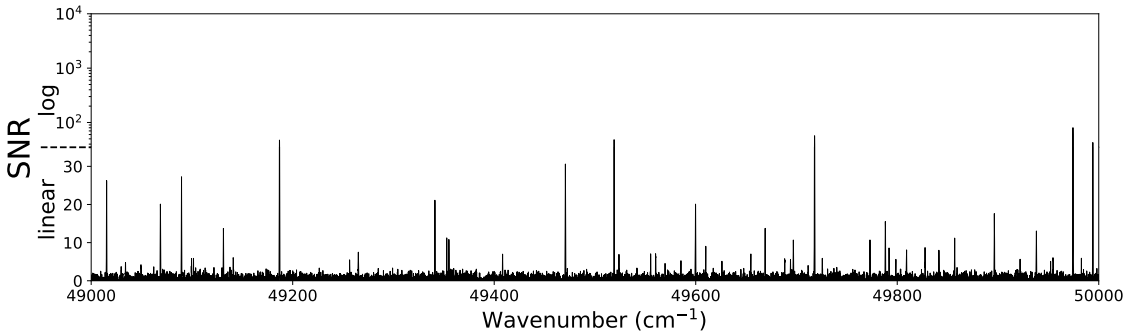
Fe327 (continued)



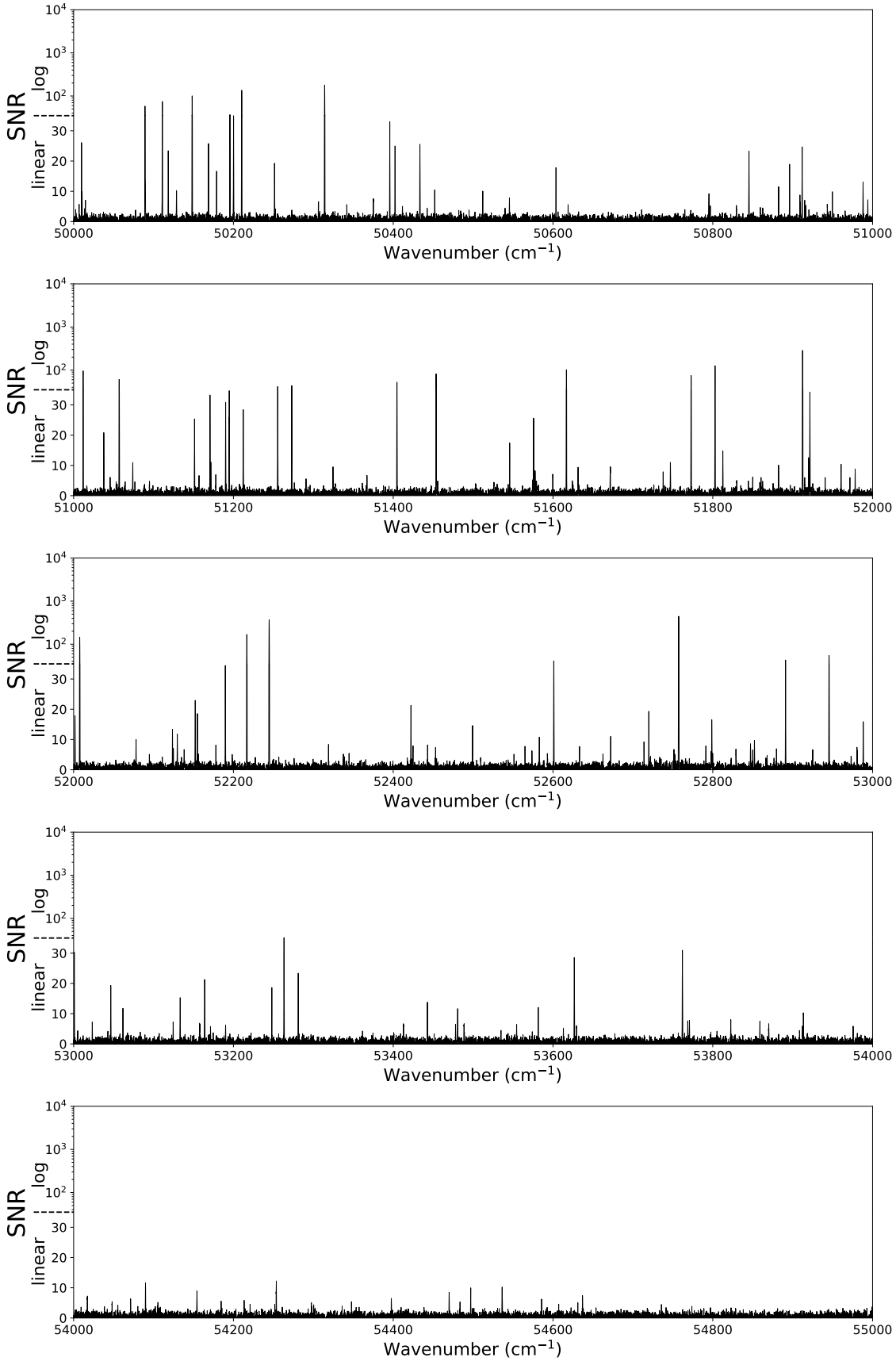




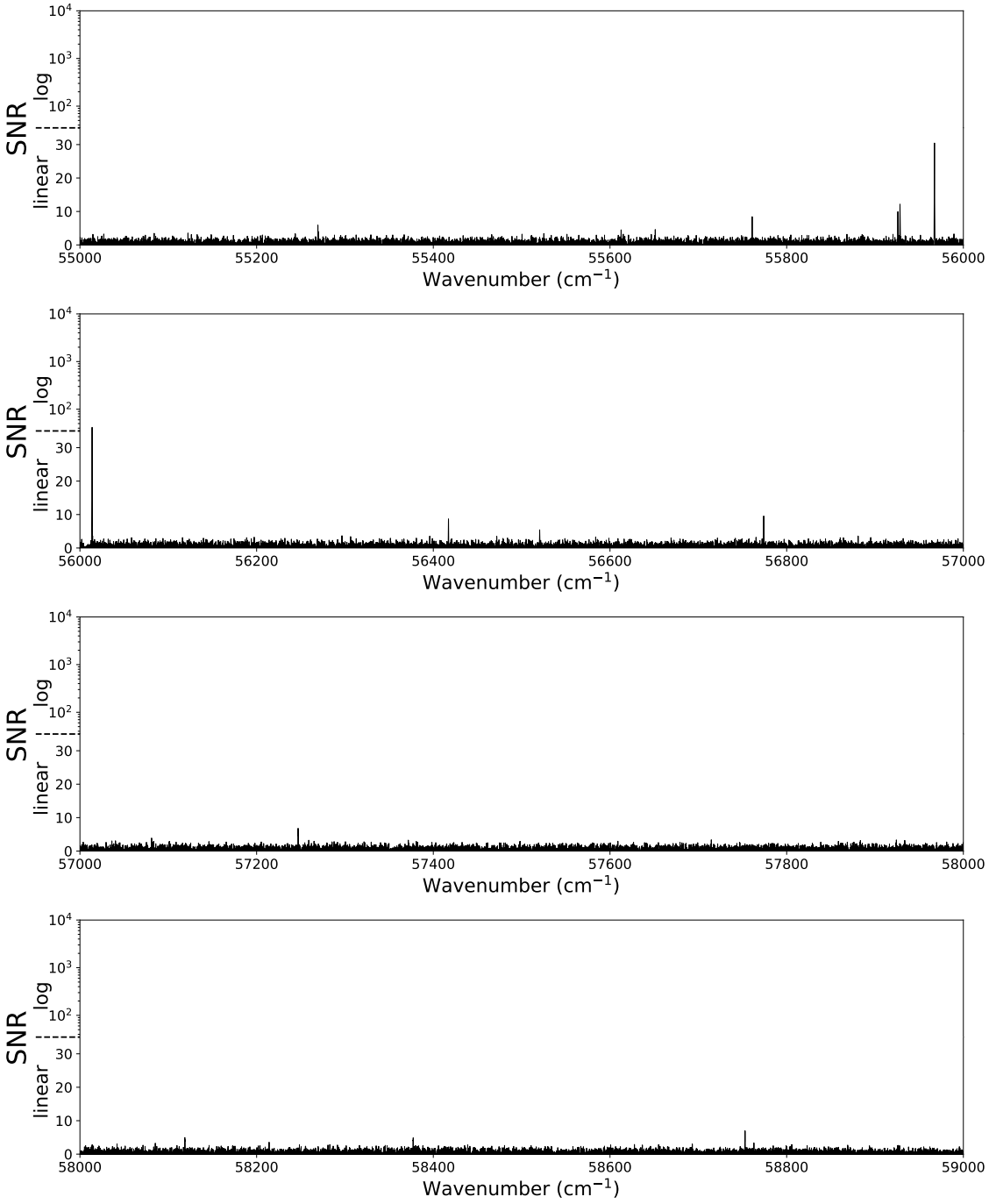




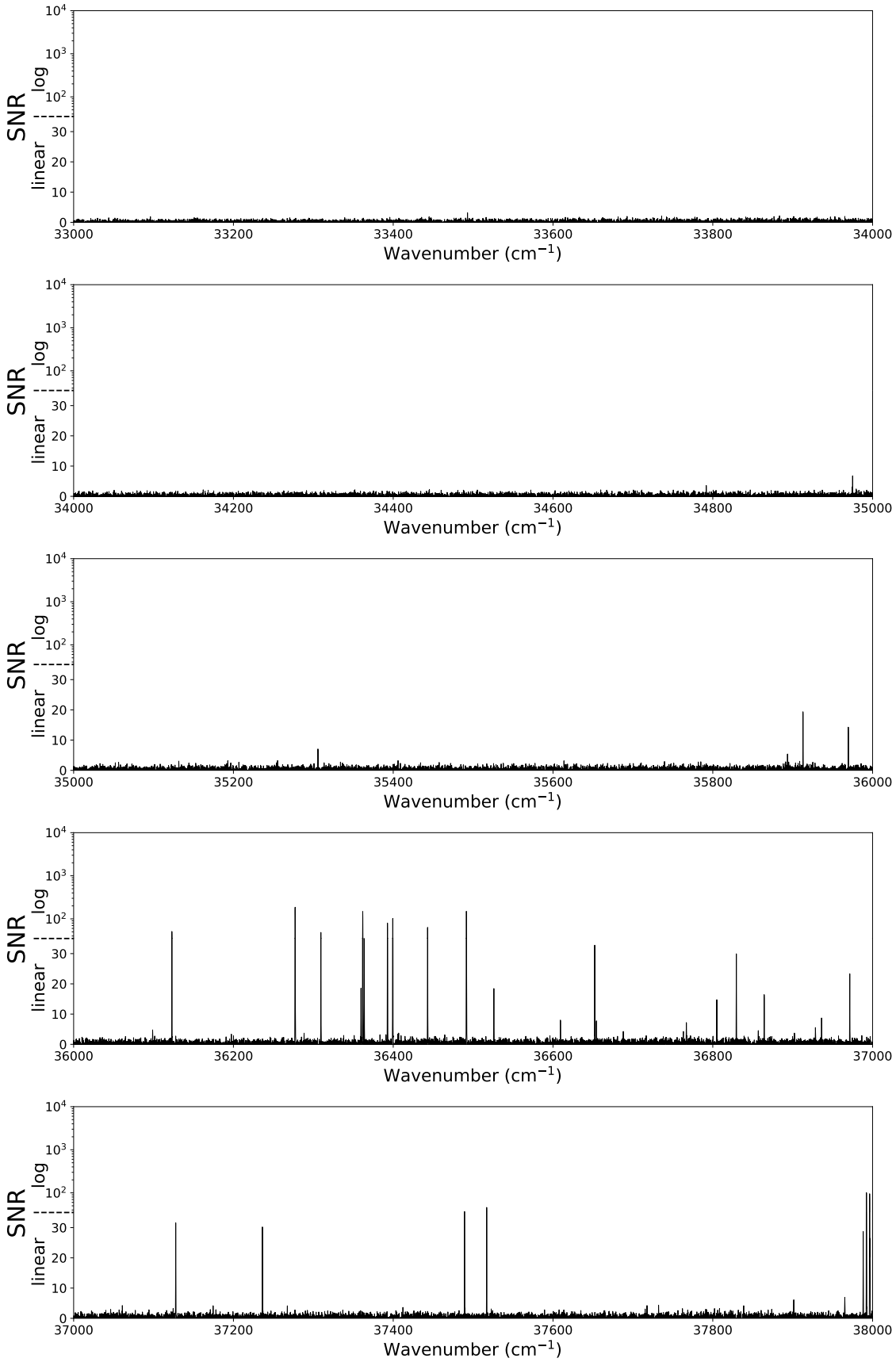
Fe327 (continued)



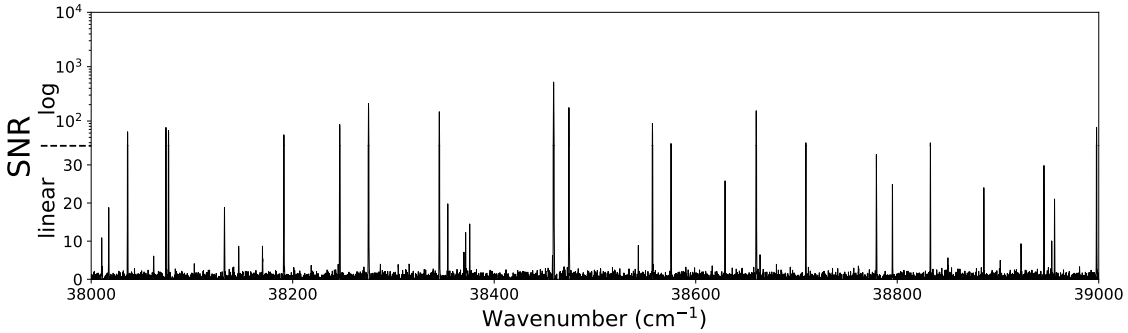
Fe327 (continued)

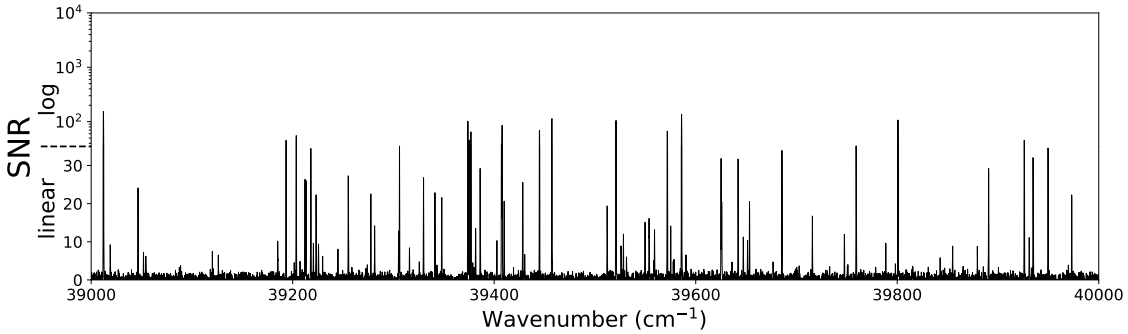


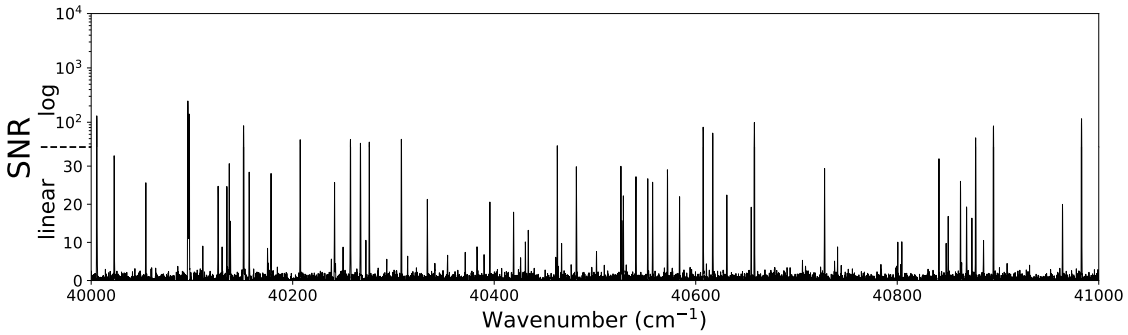
E.2 Fe116

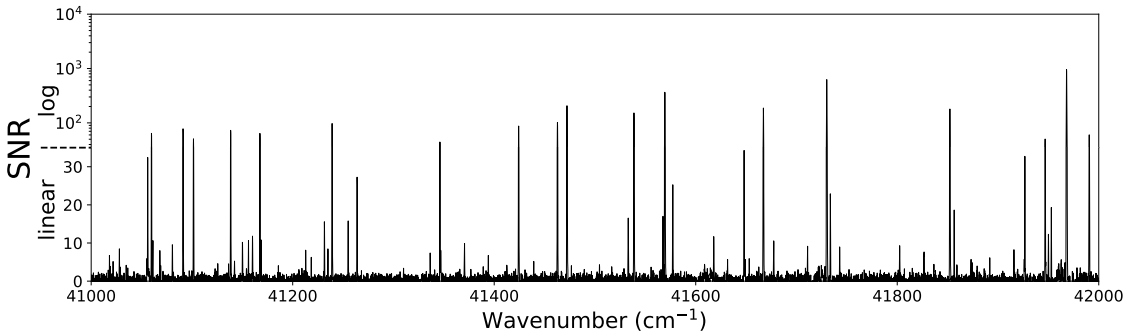

SNR
log
linear
Wavenumber (cm^{-1})
33000
33200
33400
33600
33800
34000
34200
34400
34600
34800
35000
35200
35400
35600
35800
36000
36200
36400
36600
36800
37000
37200
37400
37600
37800
38000

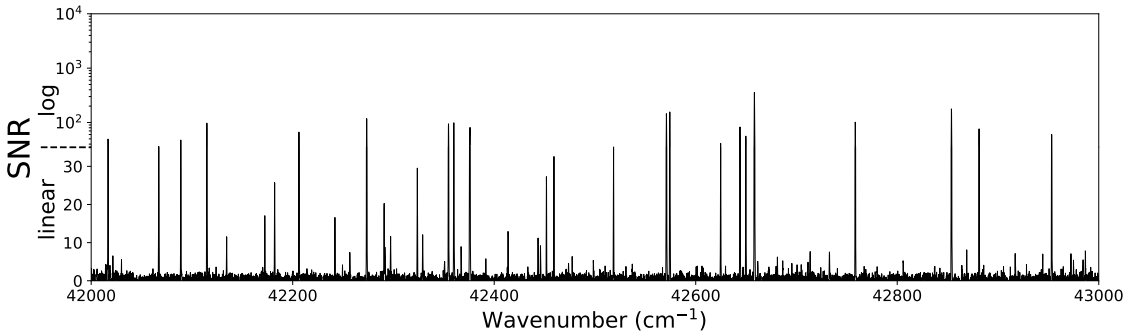
Fe116 (continued)



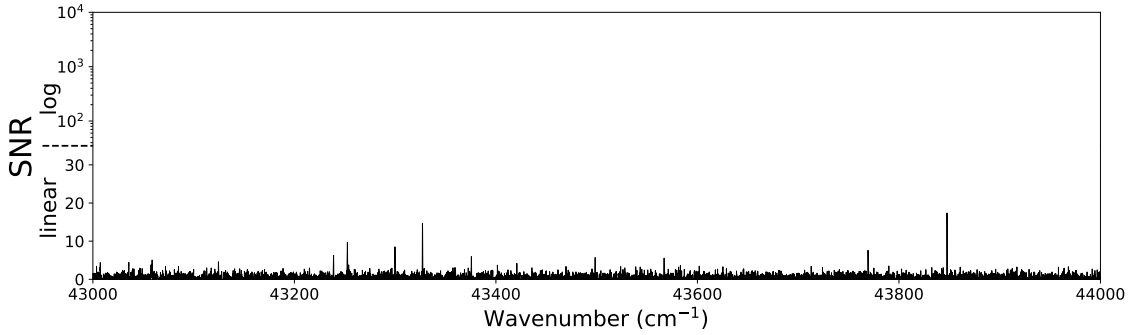


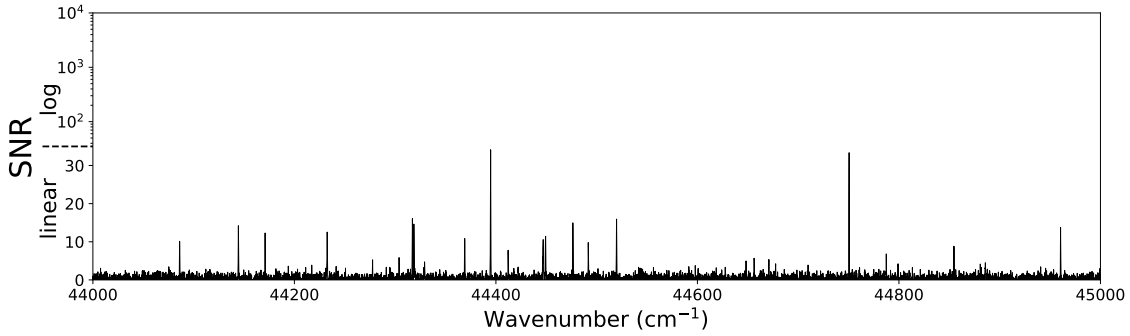


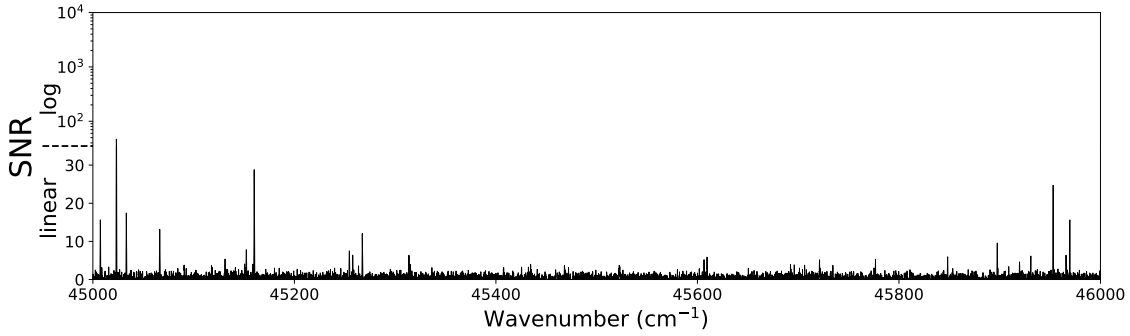


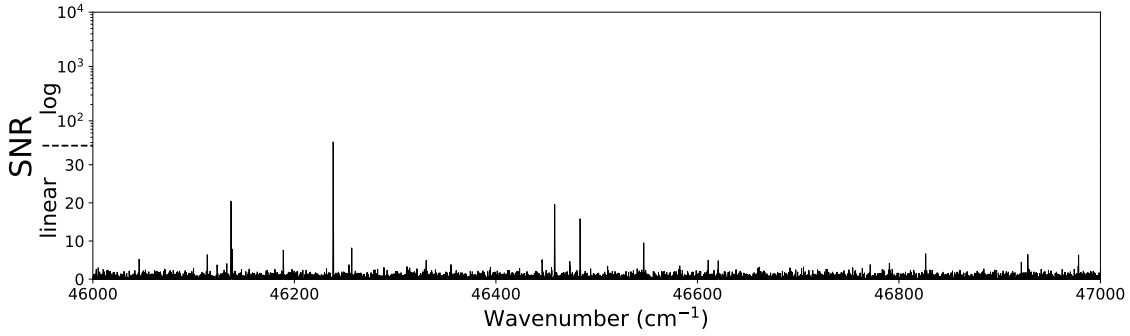


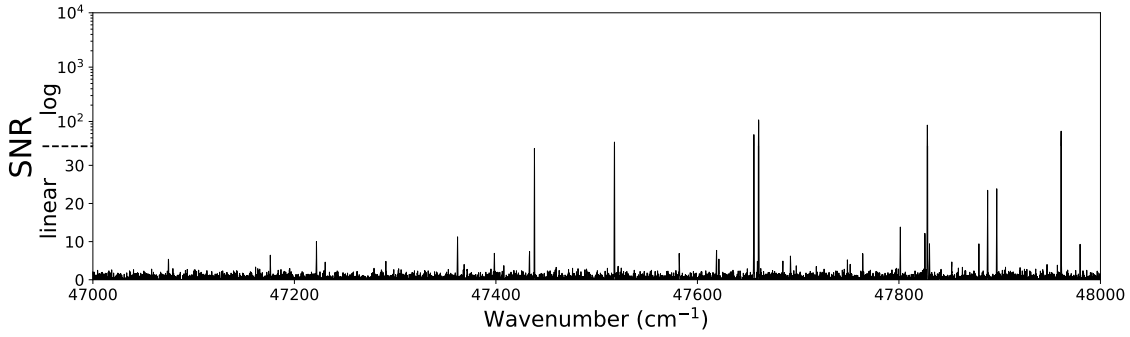
Fe116 (continued)



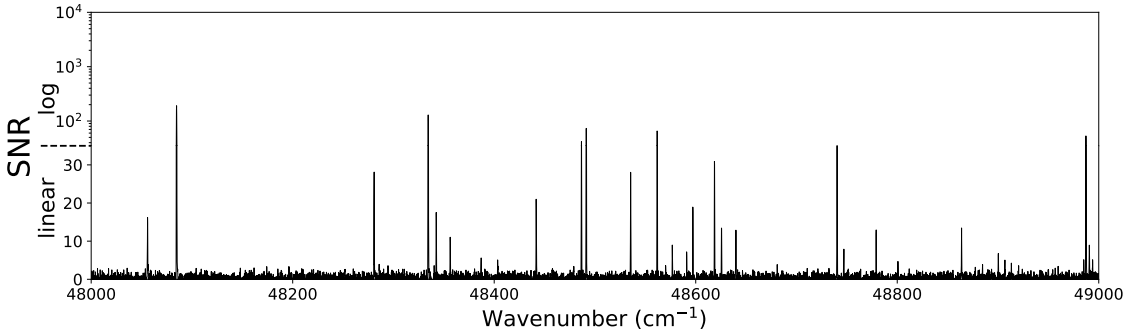


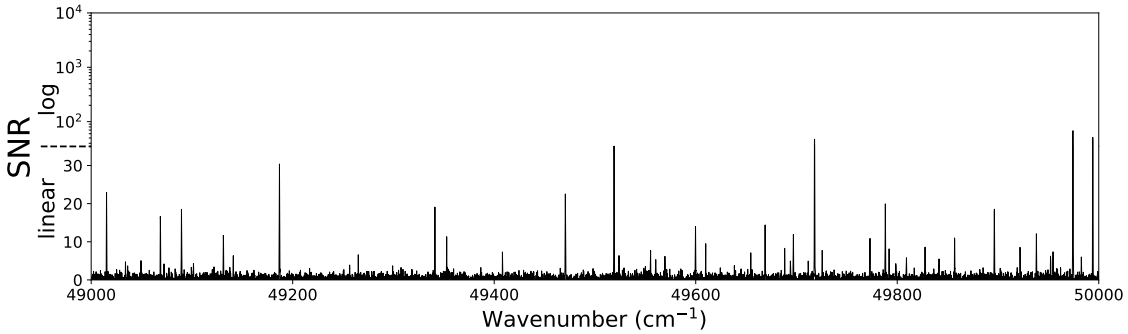


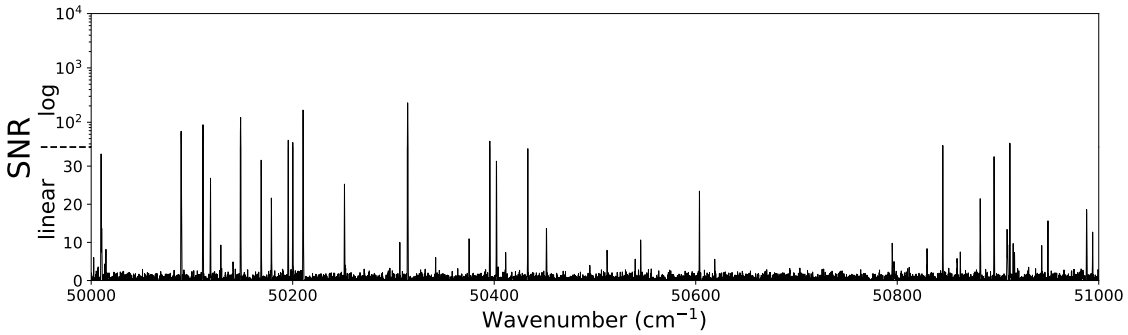


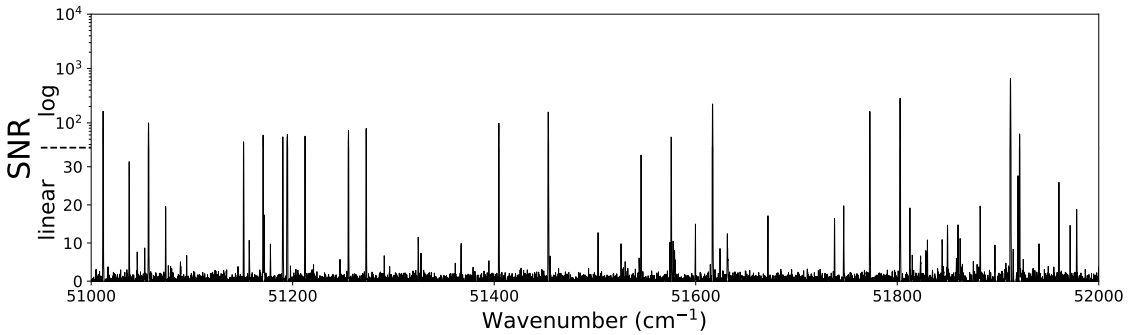


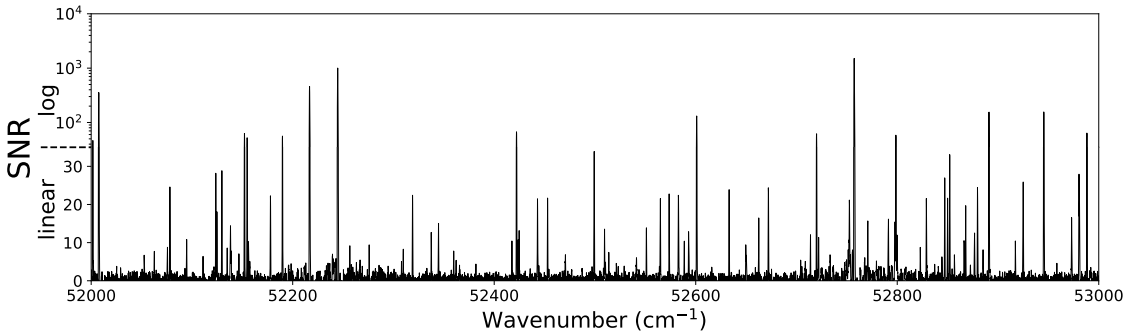
Fe116 (continued)



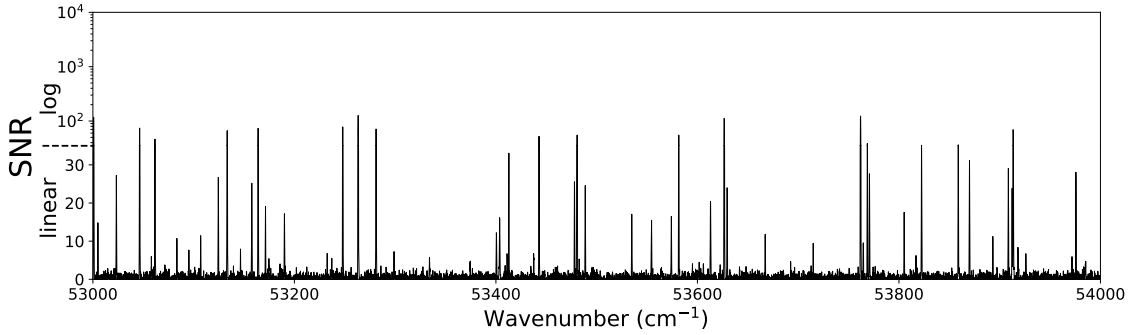


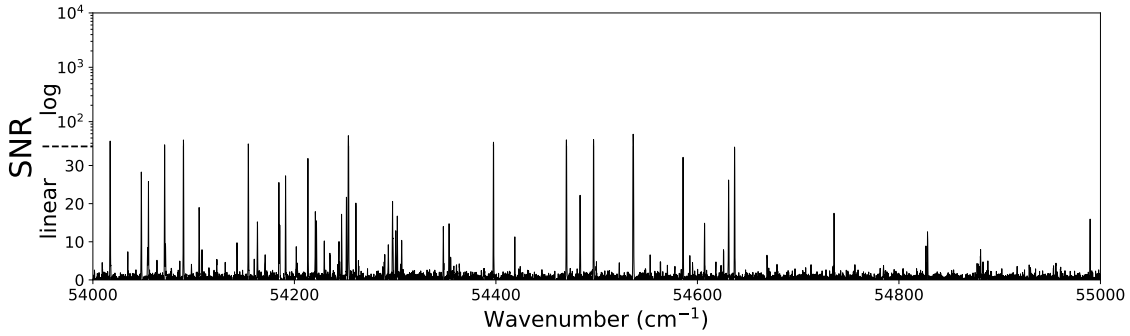


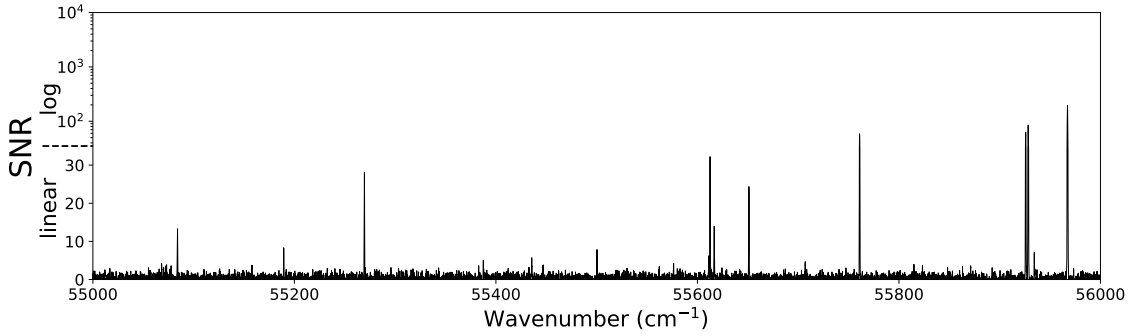


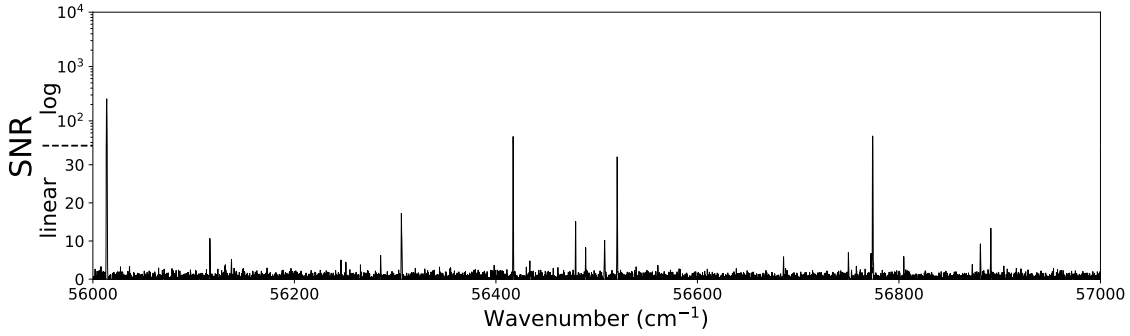


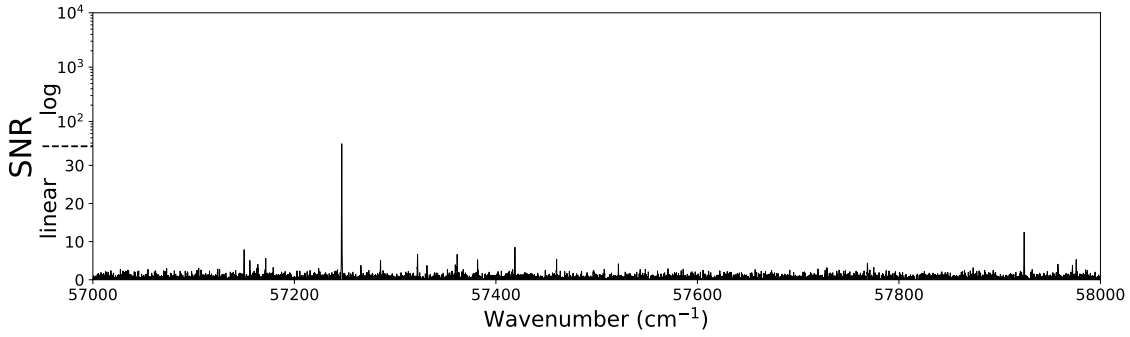
Fe116 (continued)



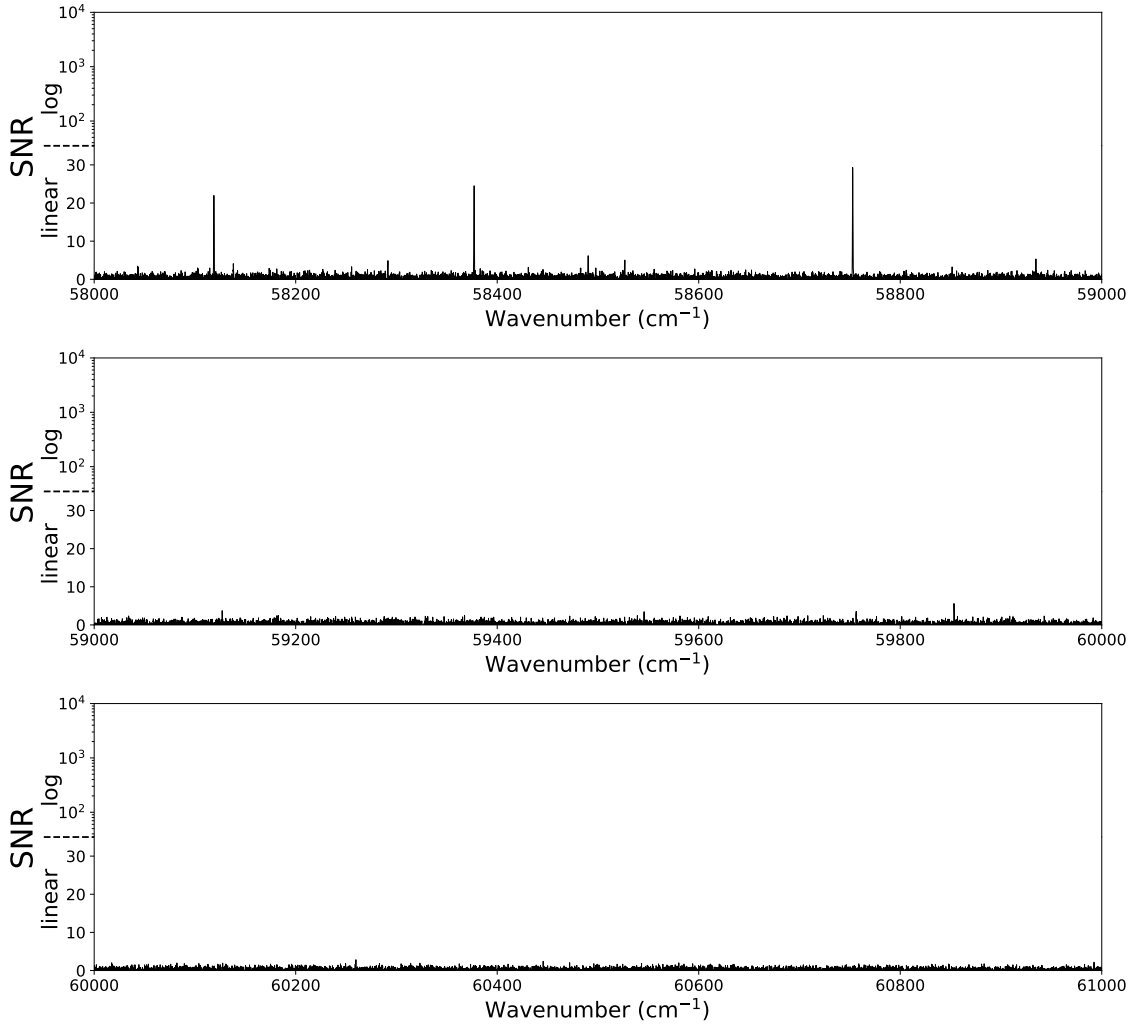




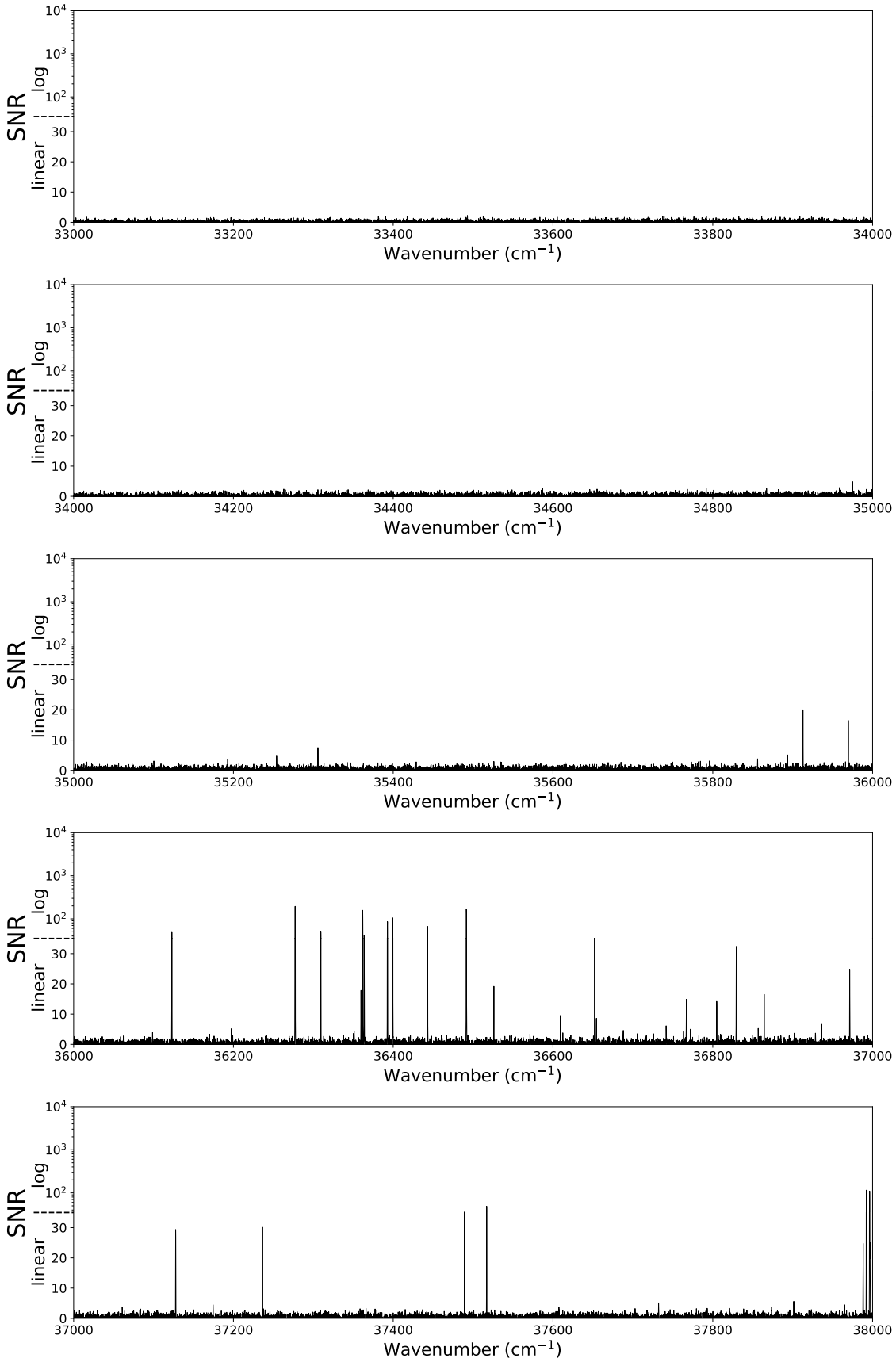




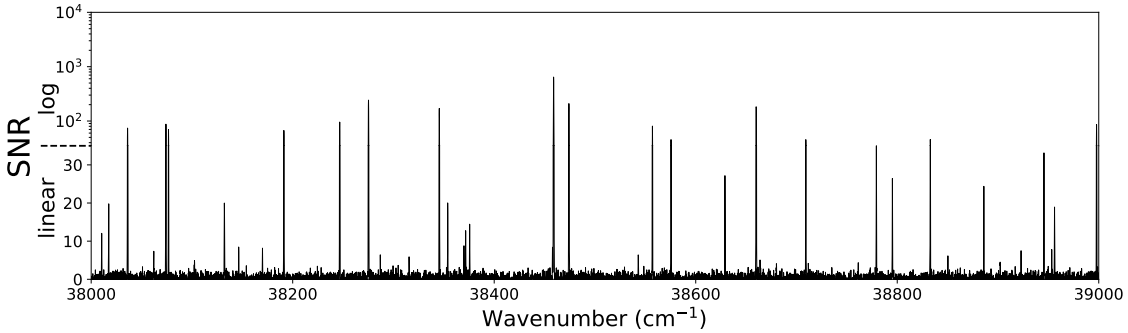
Fe116 (continued)

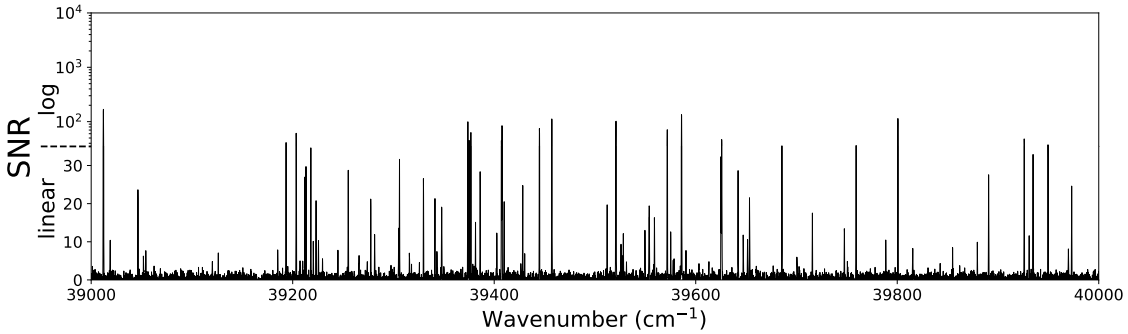


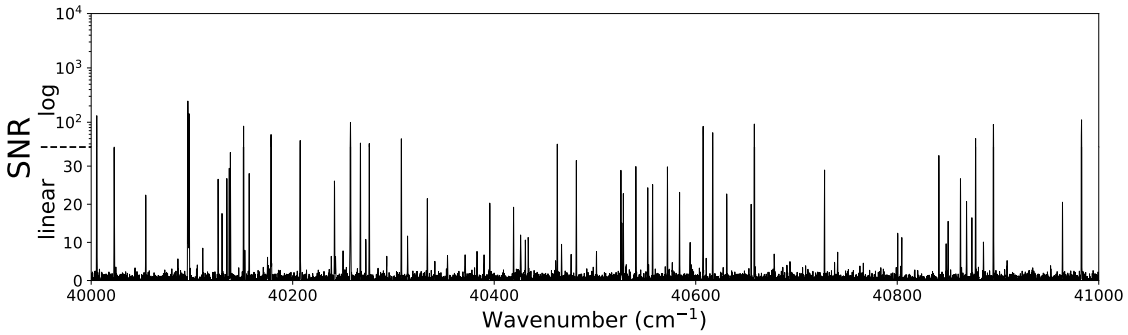
E.3 Fe831

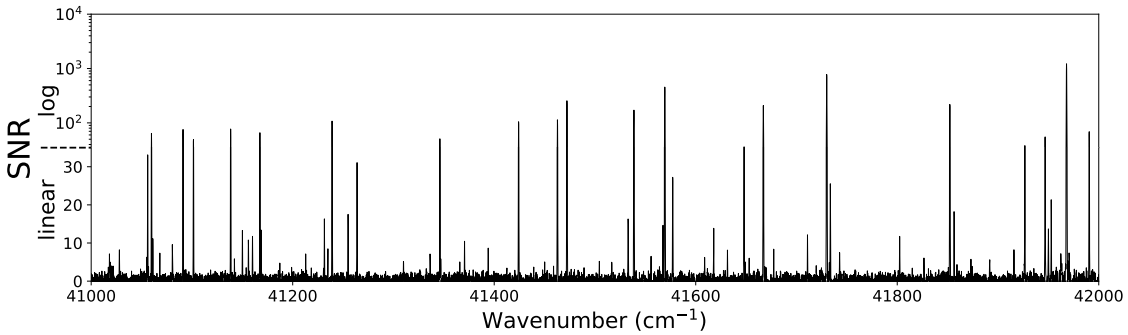

SNR
log
linear
Wavenumber (cm^{-1})
33000
33200
33400
33600
33800
34000
34000
34200
34400
34600
34800
35000
35000
35200
35400
35600
35800
36000
36000
36200
36400
36600
36800
37000
37000
37200
37400
37600
37800
38000

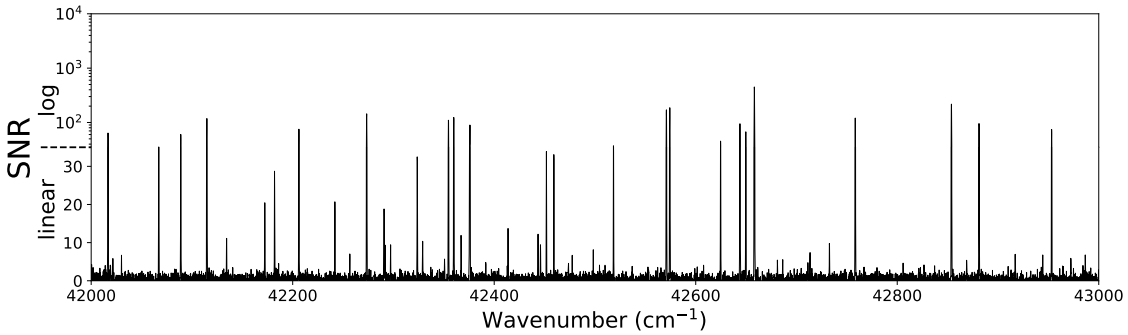
Fe831 (continued)



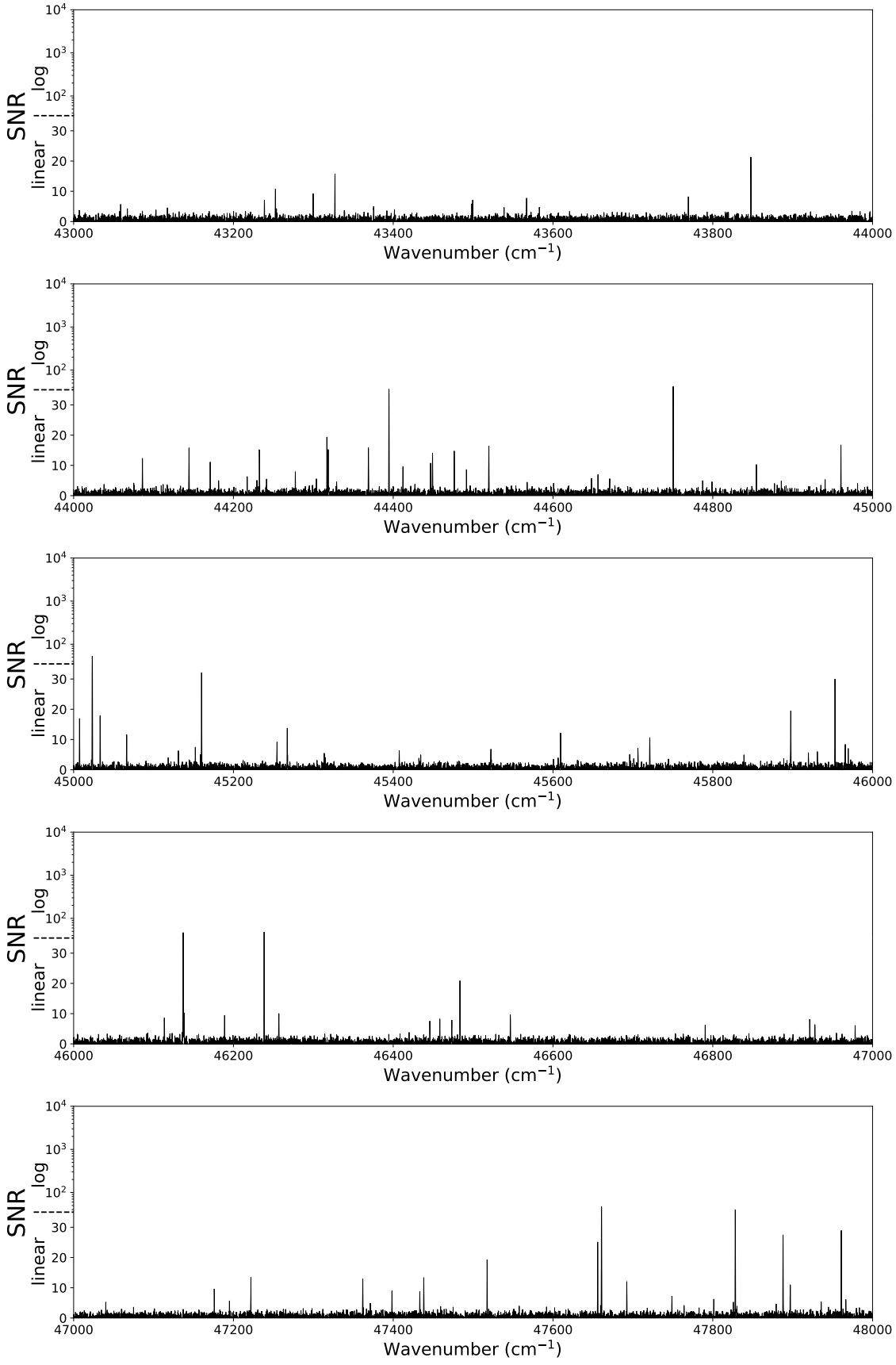




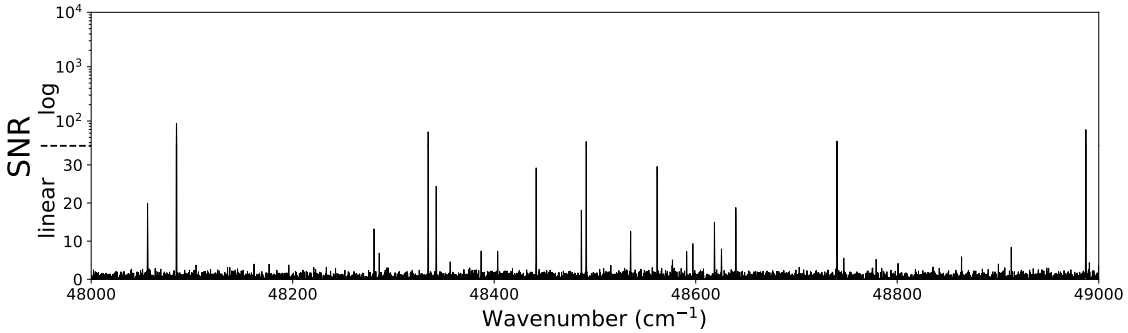


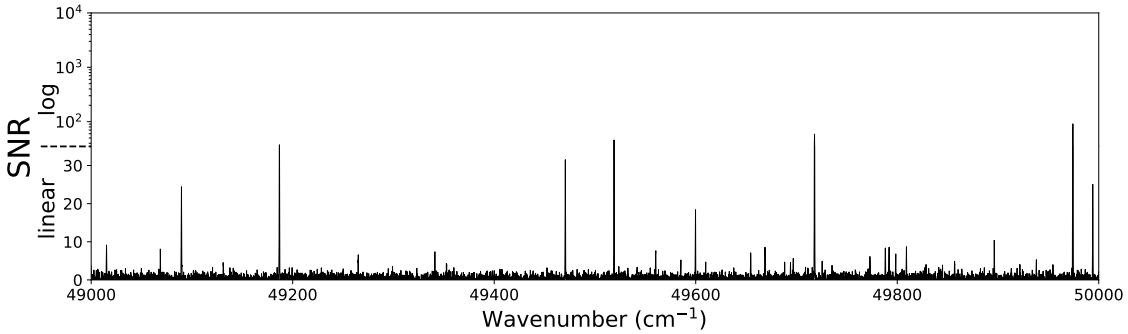


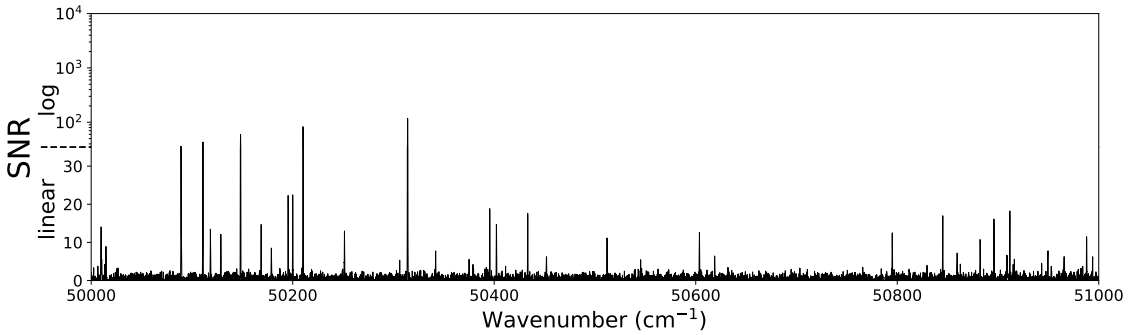
Fe831 (continued)

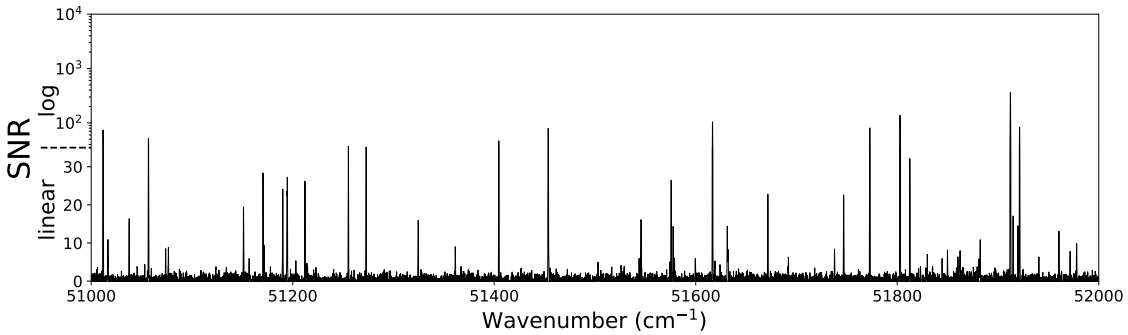


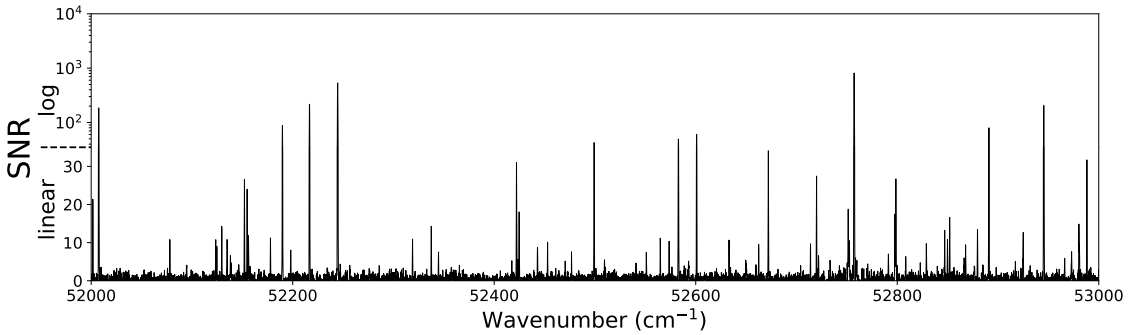
Fe831 (continued)



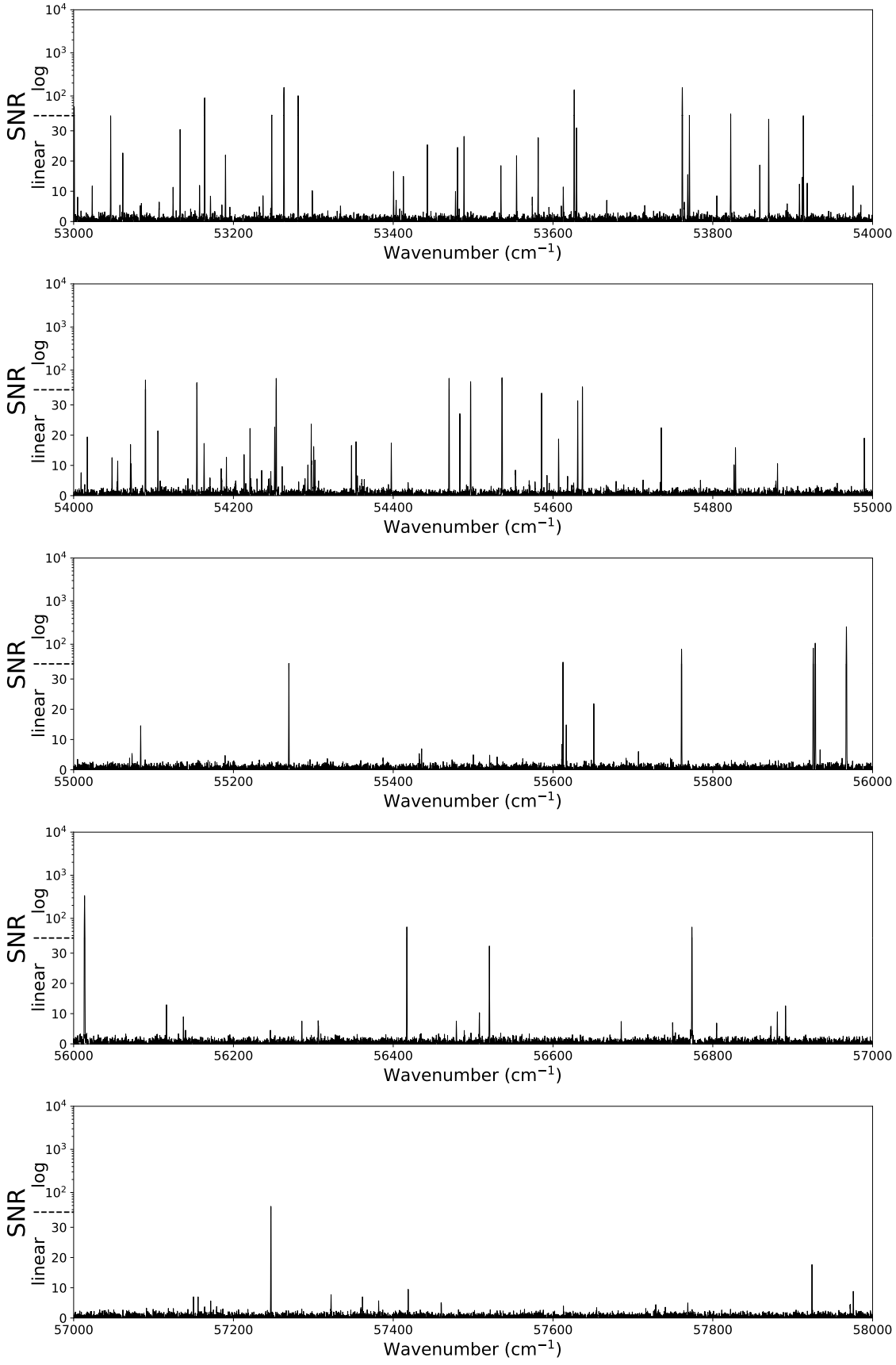




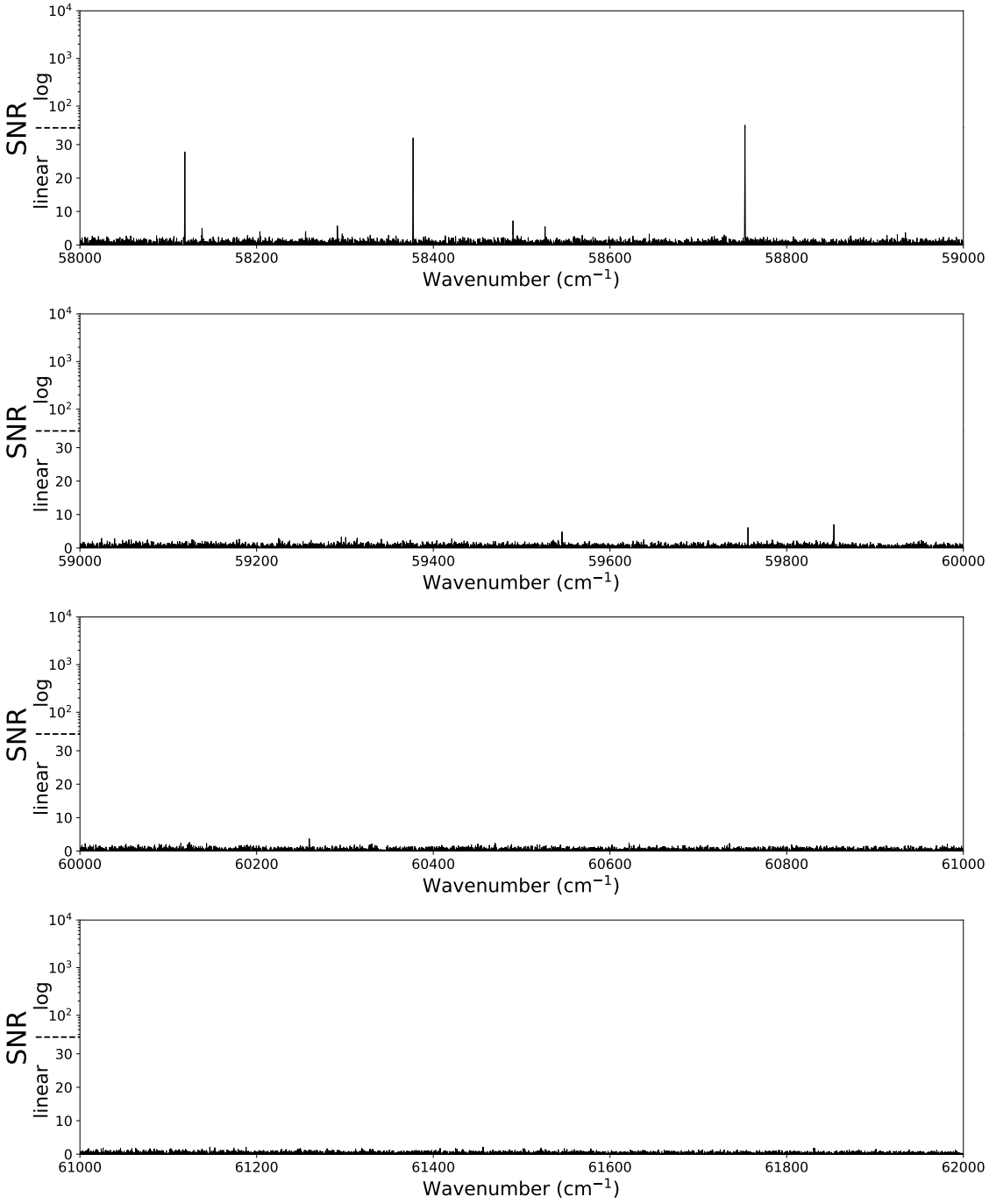




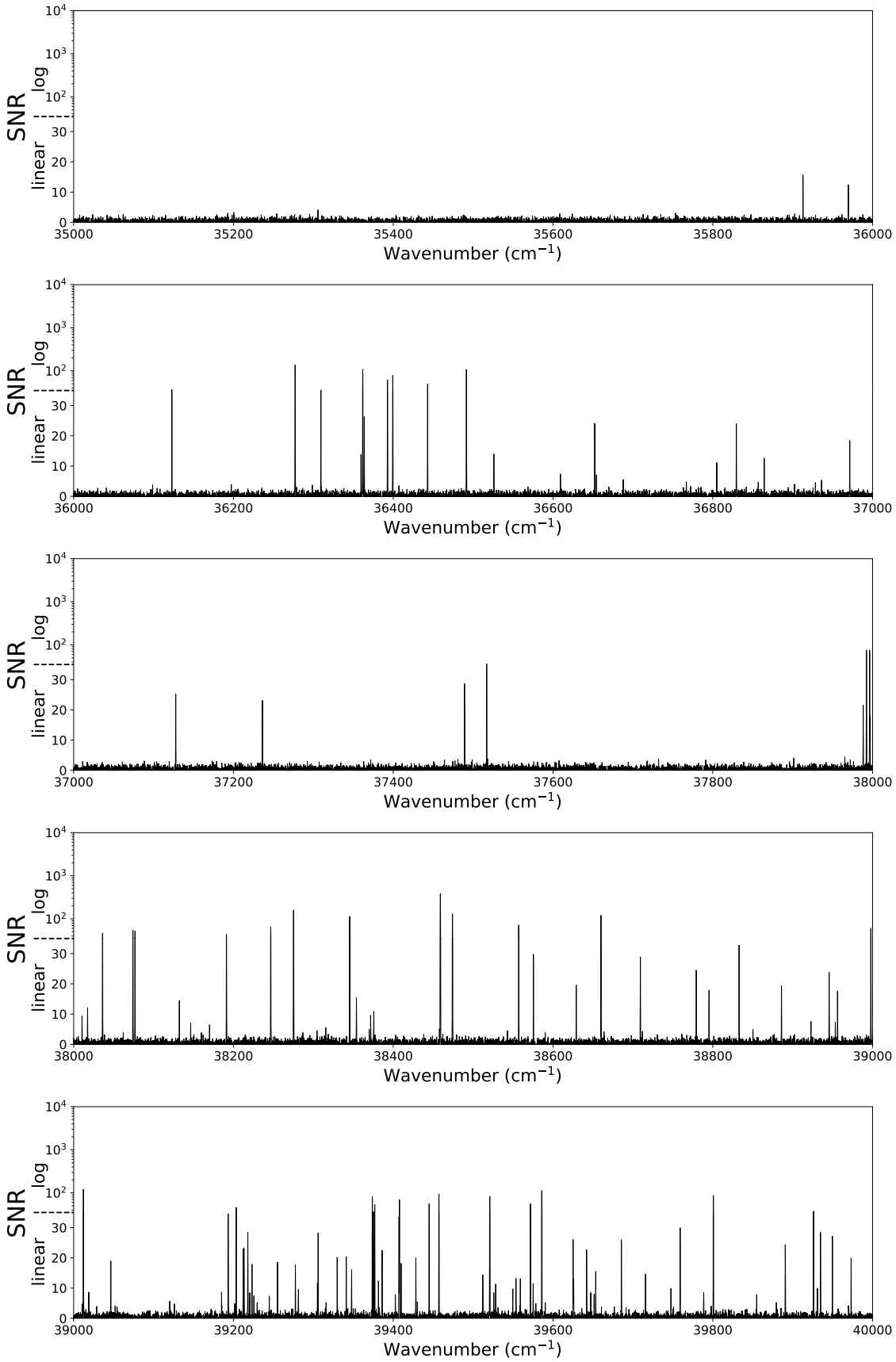
Fe831 (continued)



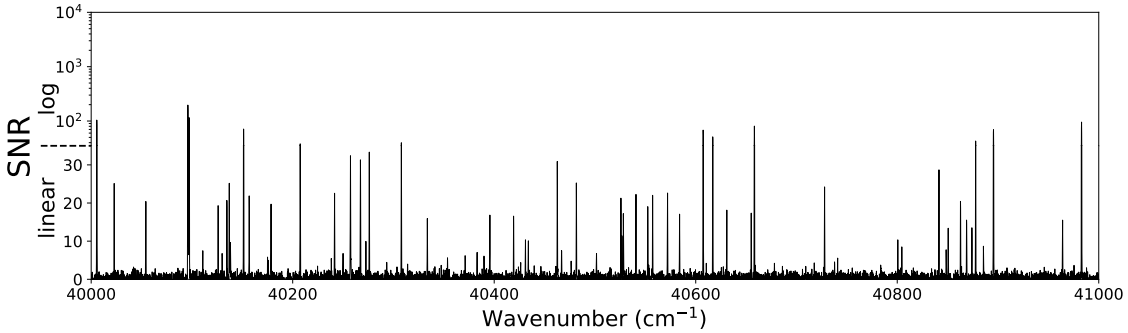
Fe831 (continued)

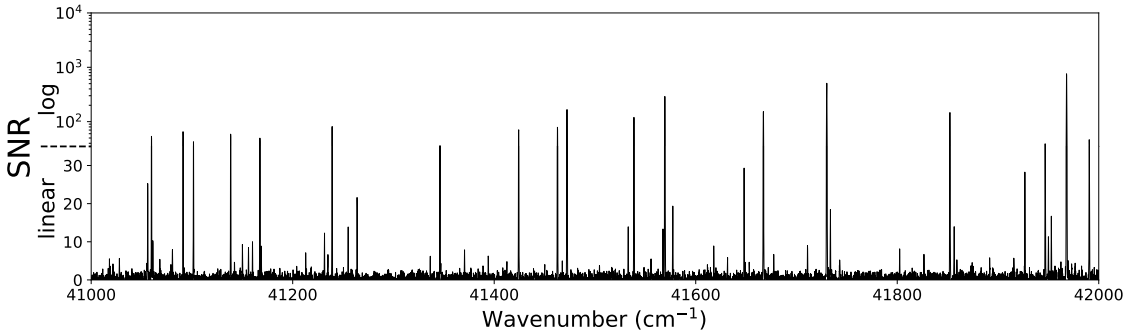


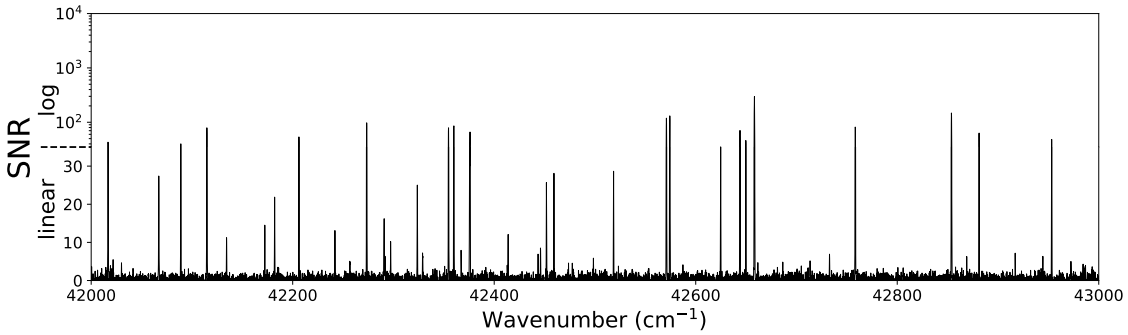
E.4 Fe832

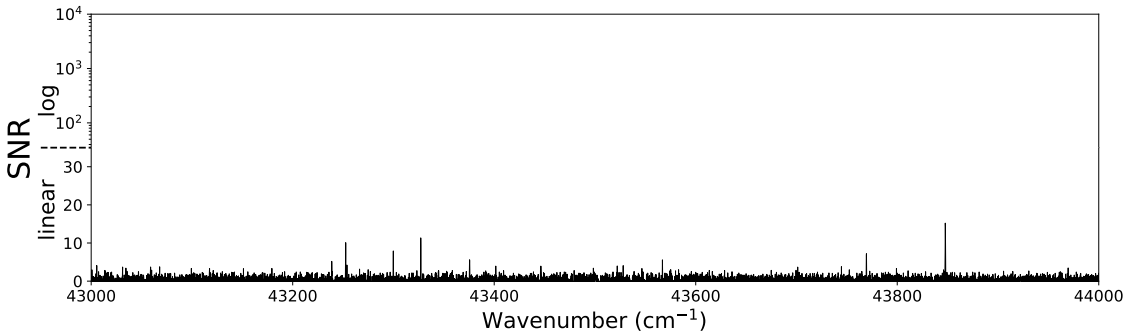

SNR
log
linear
Wavenumber (cm^{-1})
35000
35200
35400
35600
35800
36000
36000
36200
36400
36600
36800
37000
37000
37200
37400
37600
37800
38000
38000
38200
38400
38600
38800
39000
39000
39200
39400
39600
39800
40000

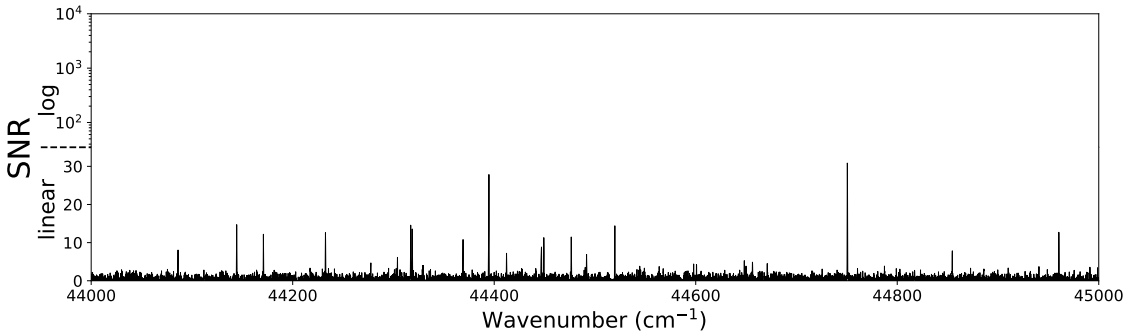
Fe832 (continued)



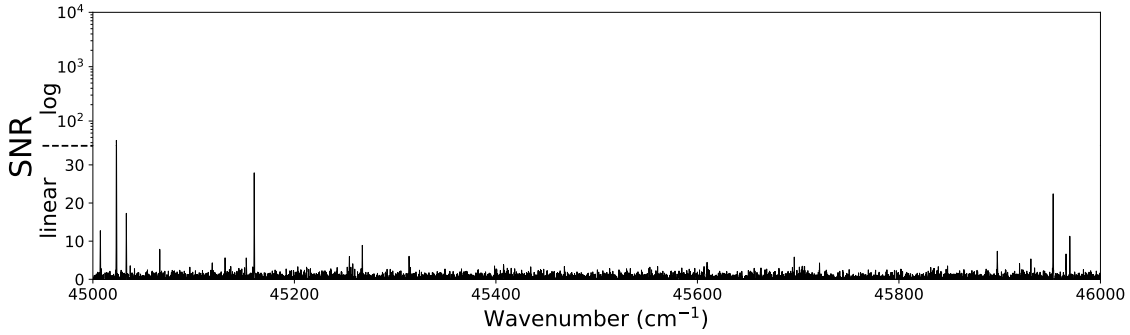


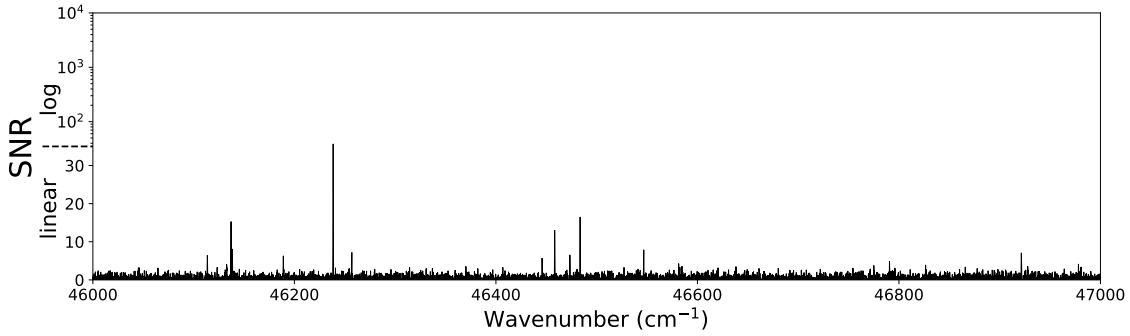


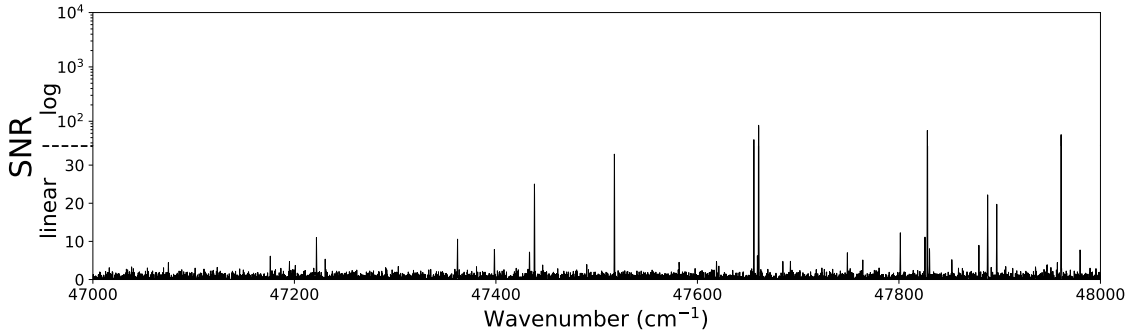


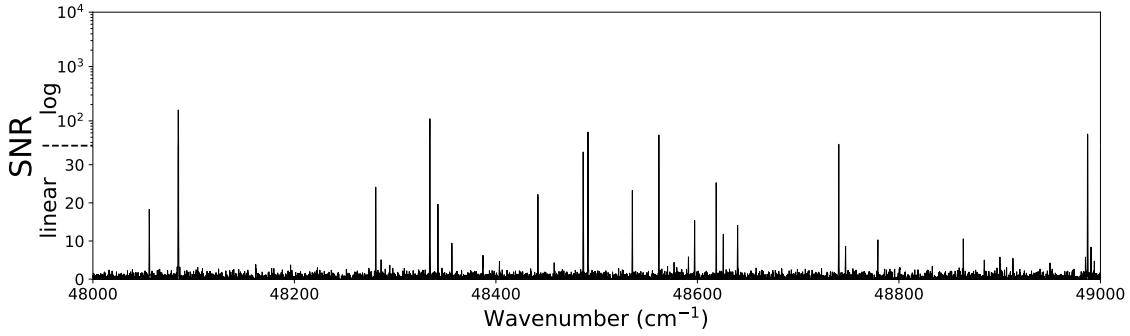


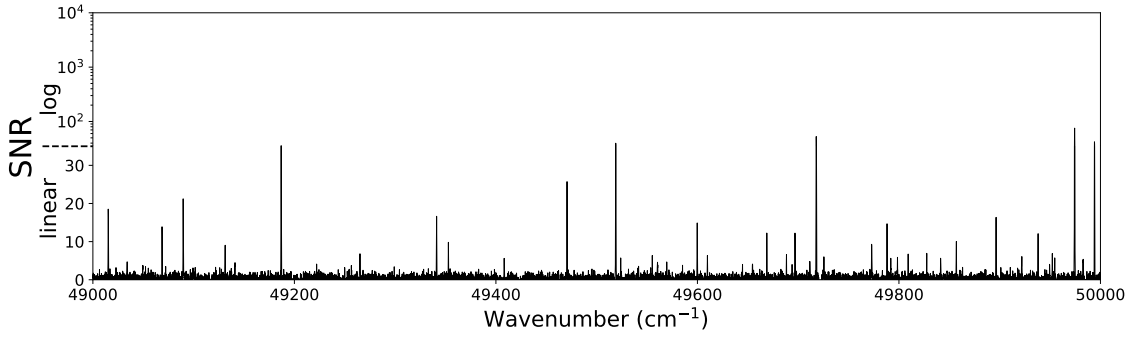
Fe832 (continued)



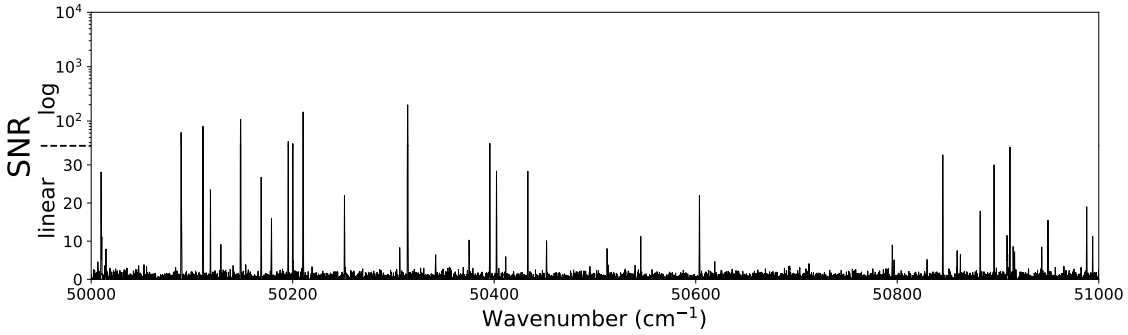


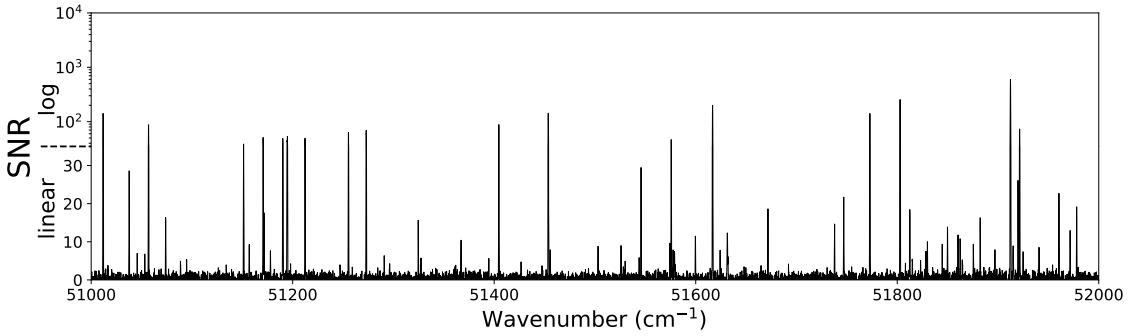


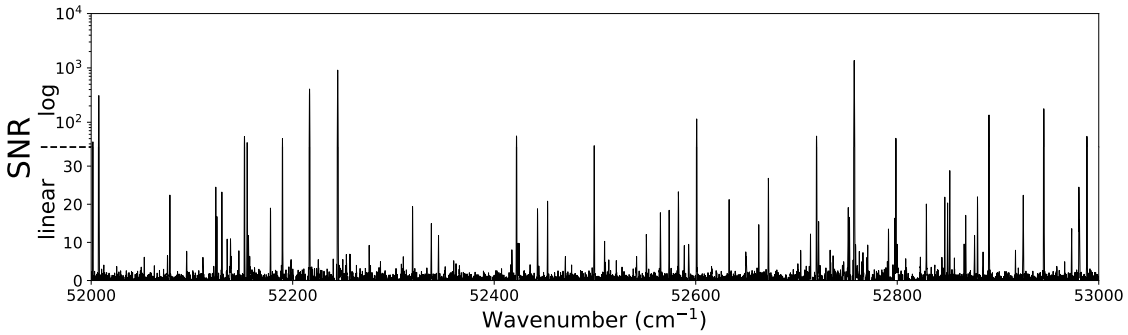


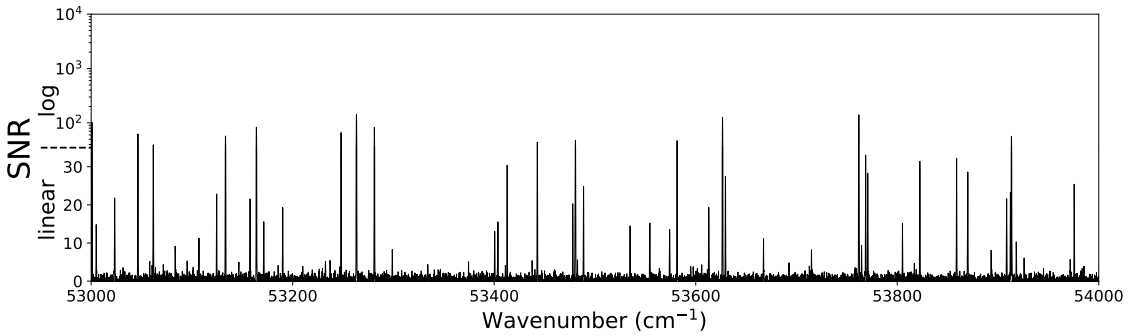


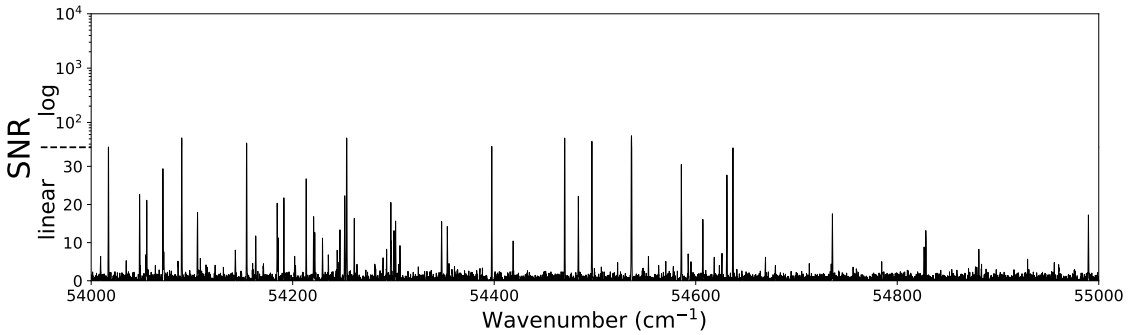
Fe832 (continued)



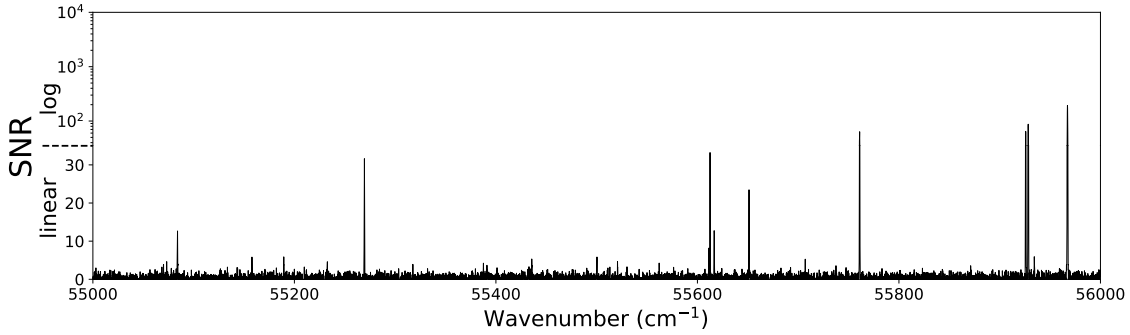


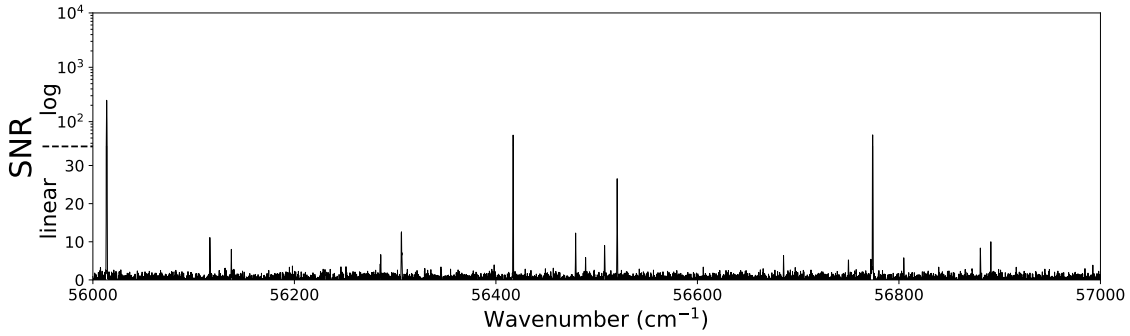


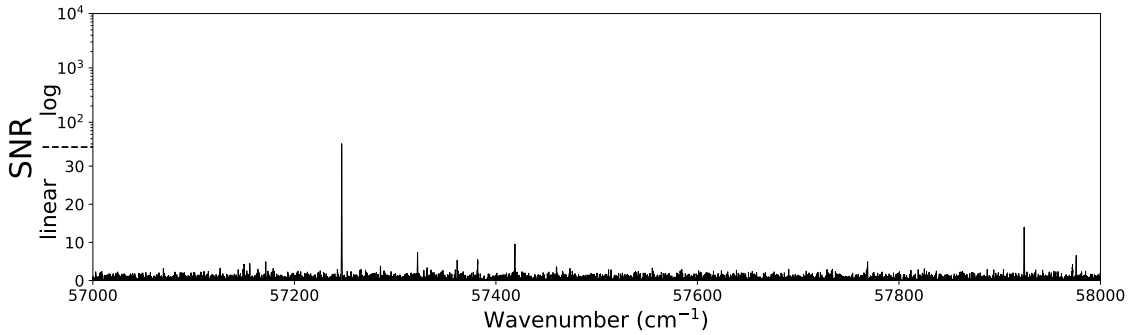


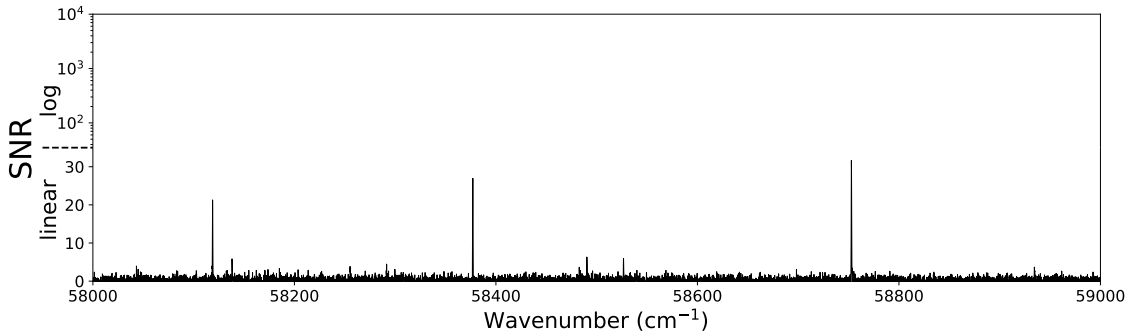


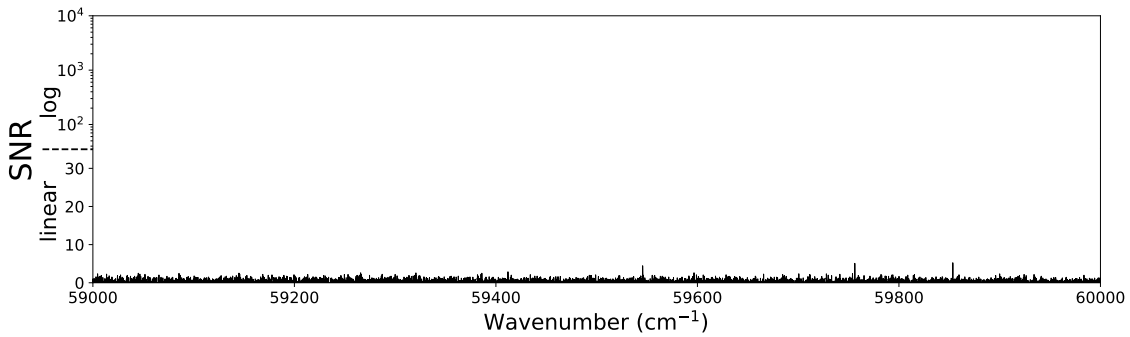
Fe832 (continued)



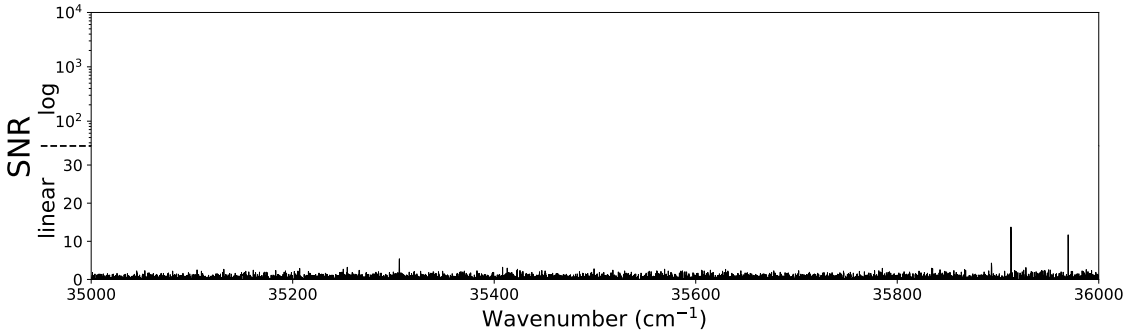


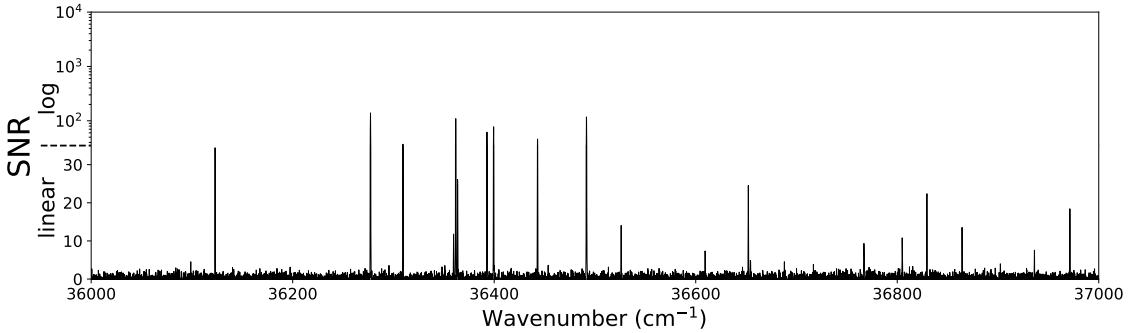


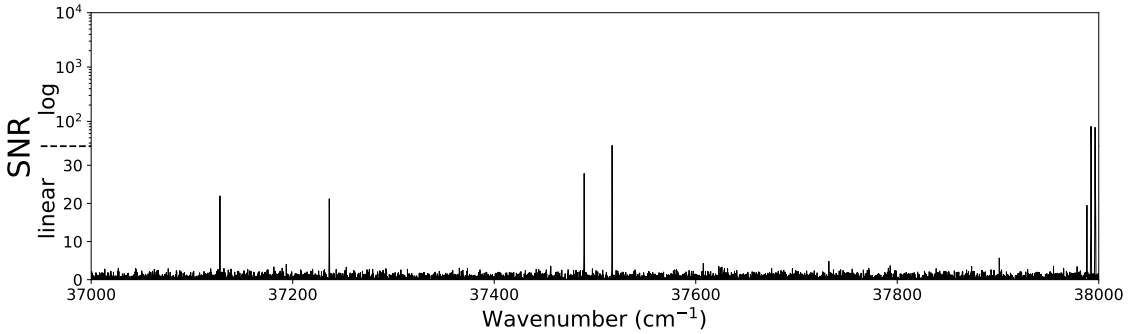


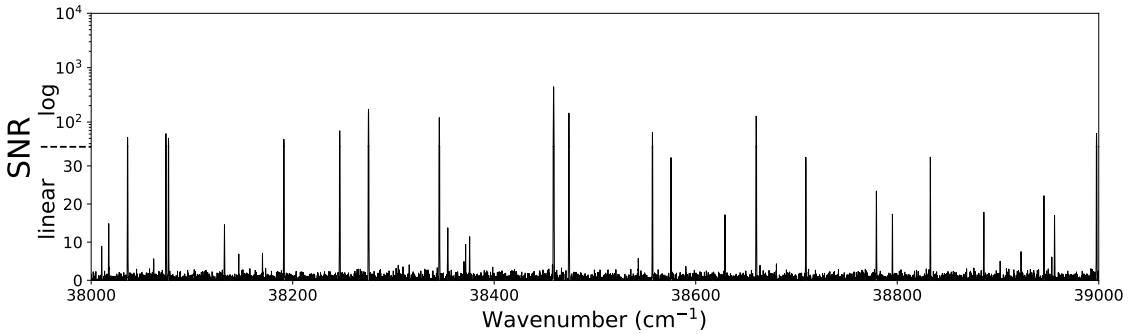


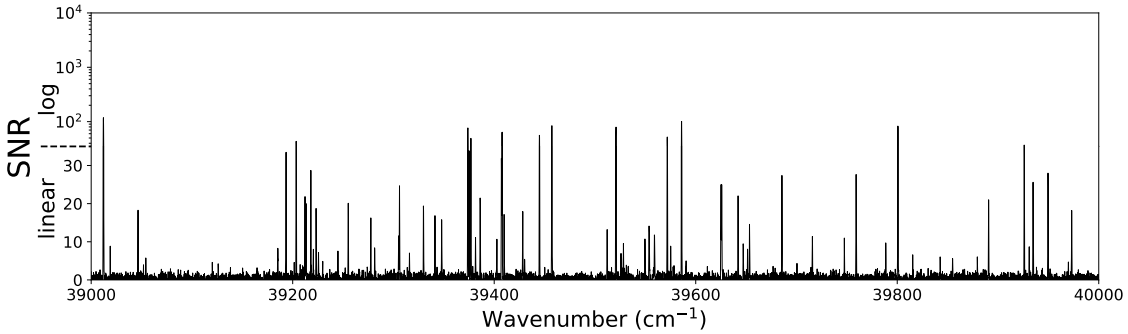
E.5 Fe903


SNR
log
linear
Wavenumber (cm^{-1})

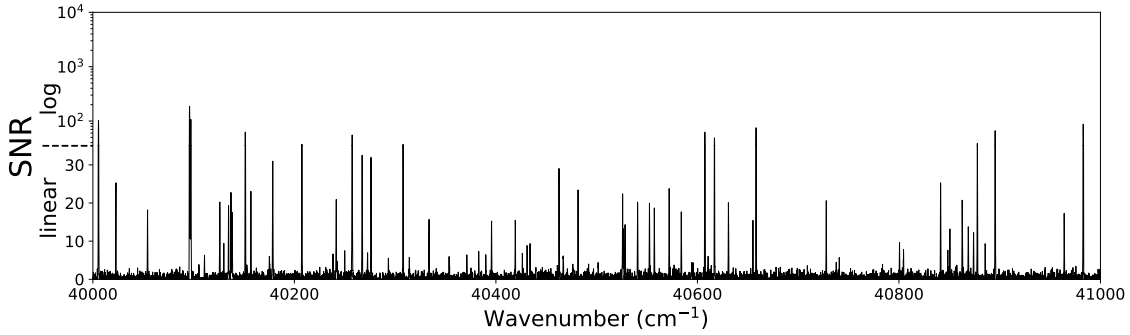

SNR
log
linear
Wavenumber (cm^{-1})

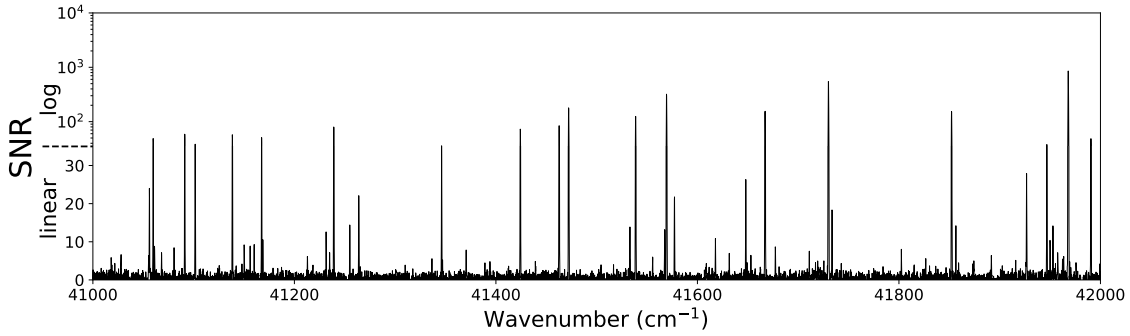

SNR
log
linear
Wavenumber (cm^{-1})

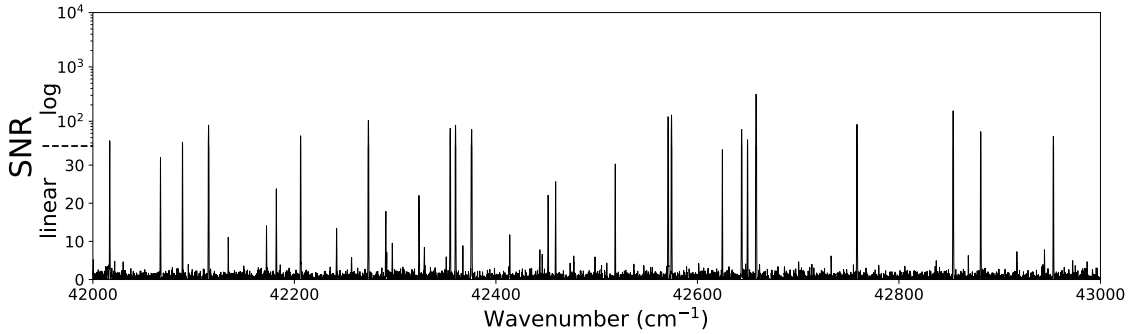

SNR
log
linear
Wavenumber (cm^{-1})

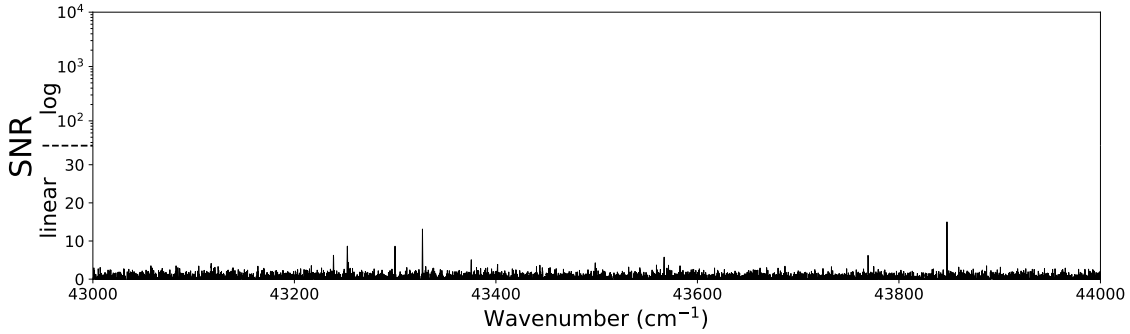

SNR
log
linear
Wavenumber (cm^{-1})

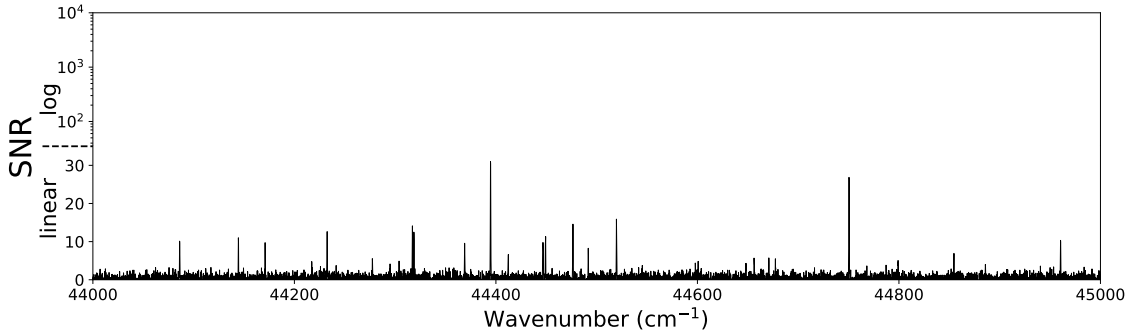
Fe903 (continued)



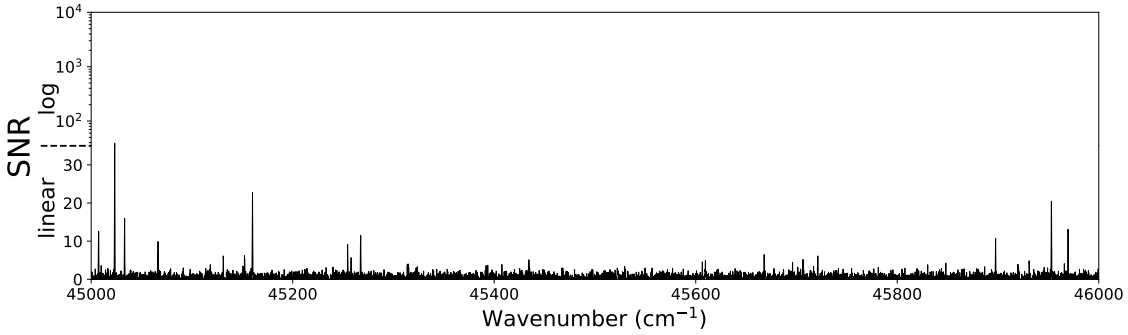


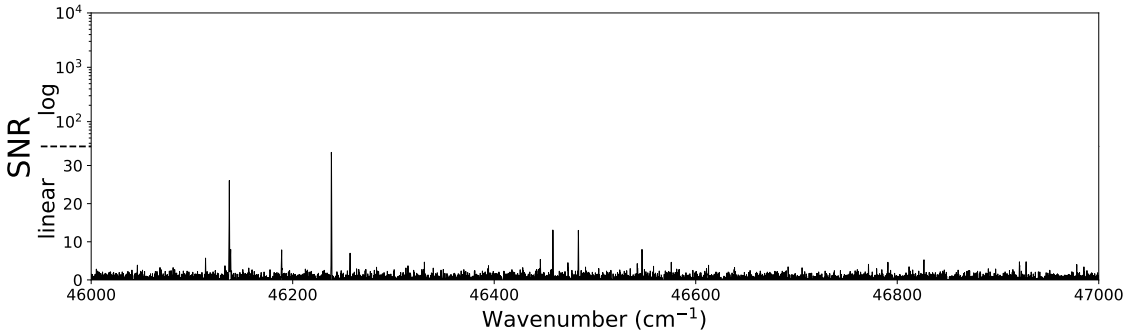


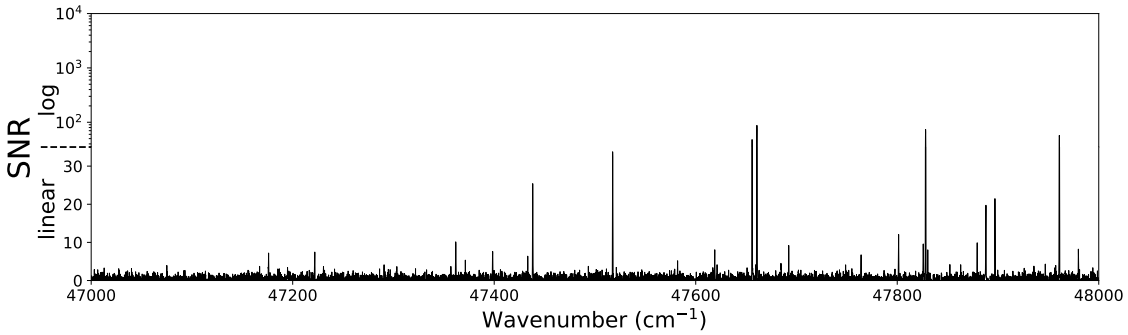


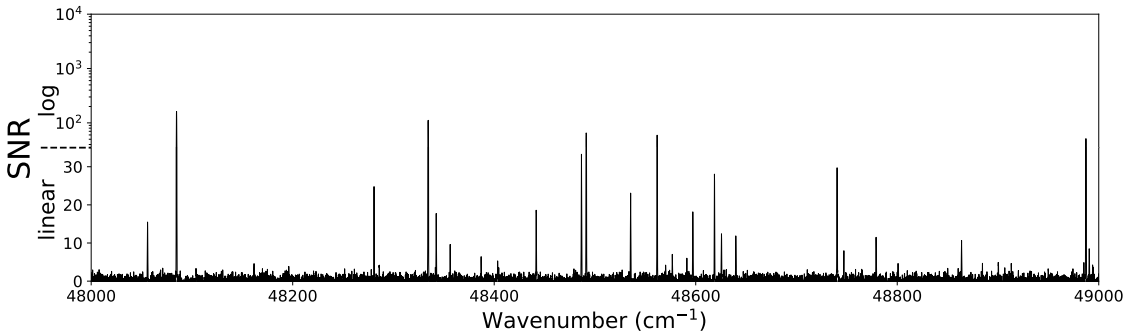


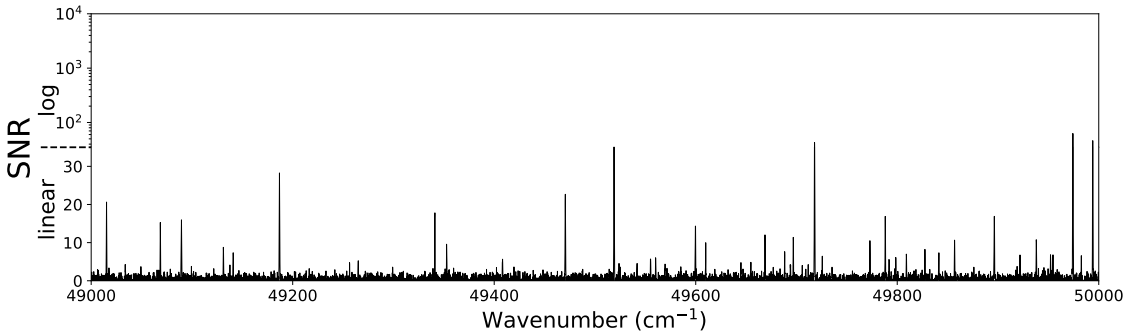
Fe903 (continued)



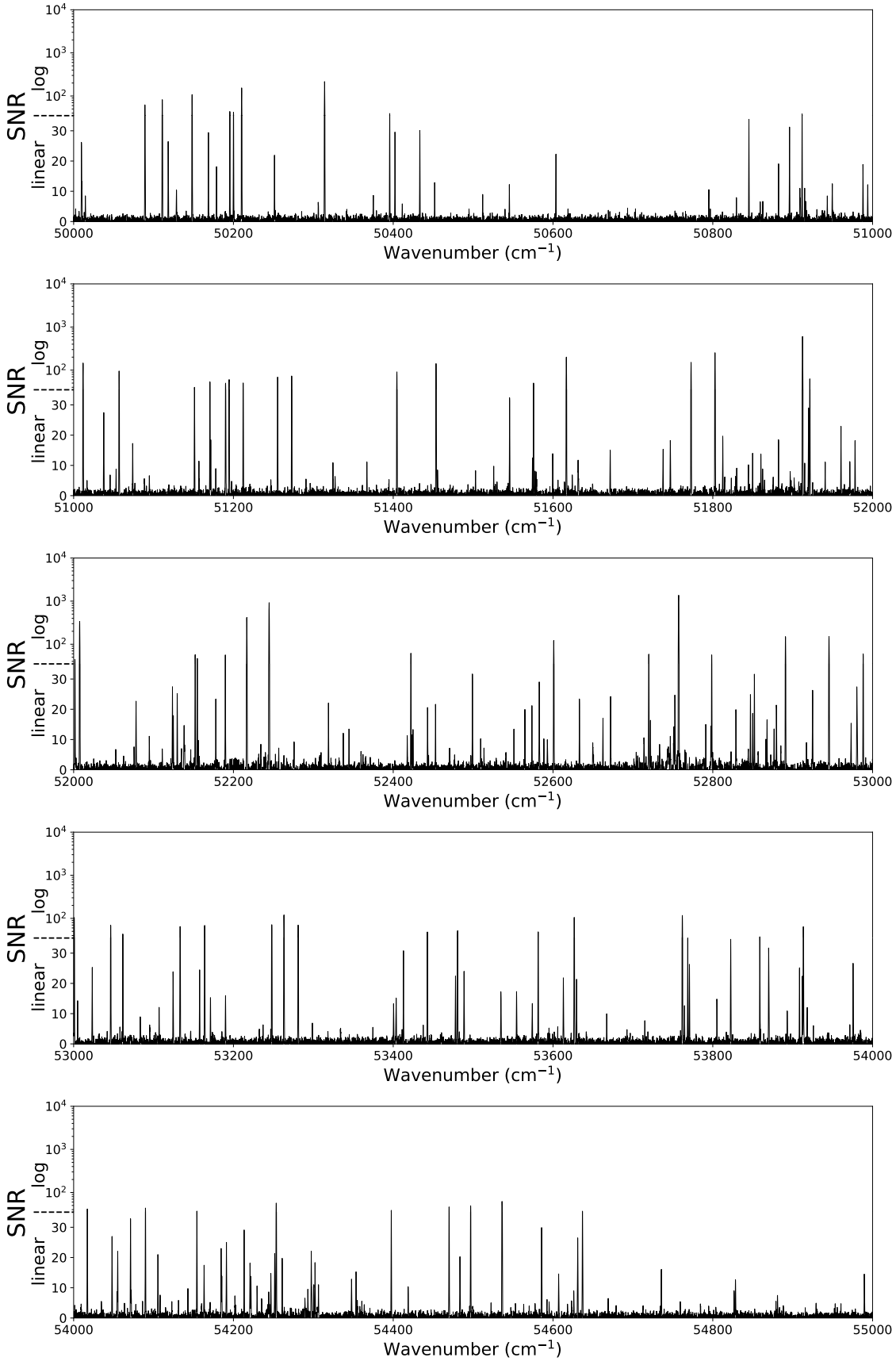




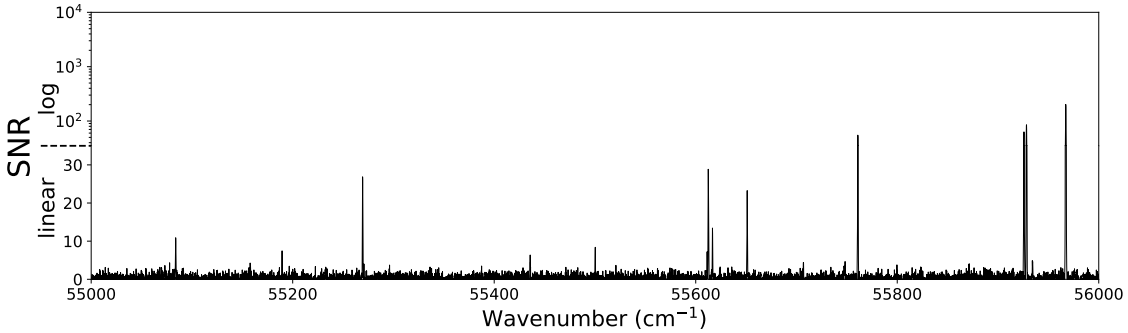


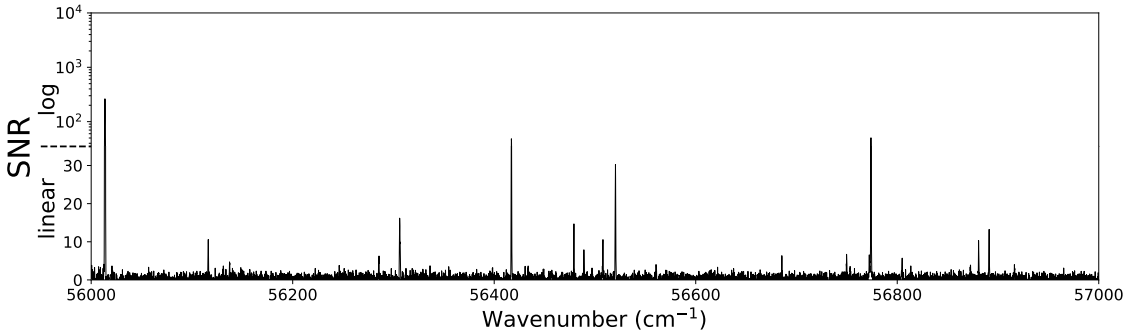


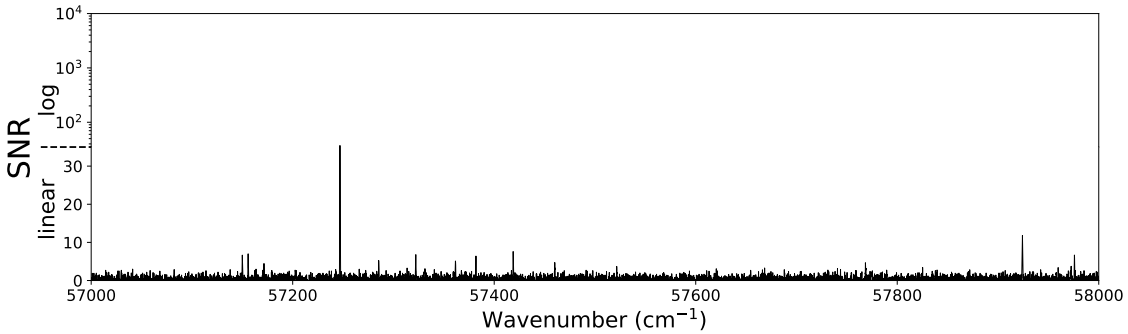
Fe903 (continued)

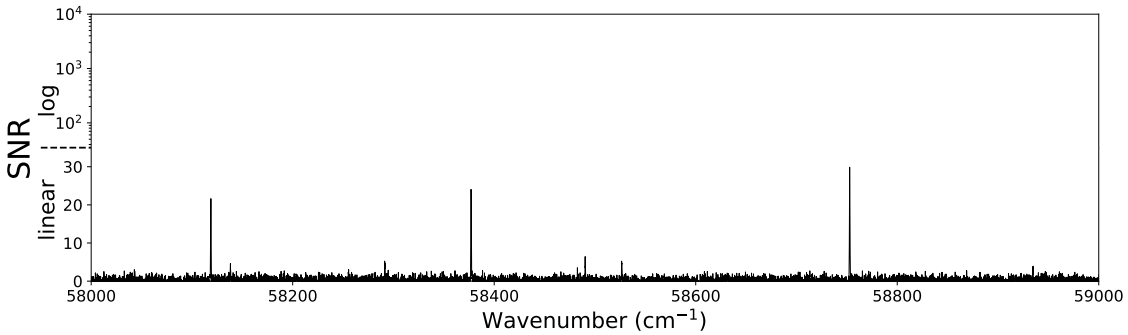


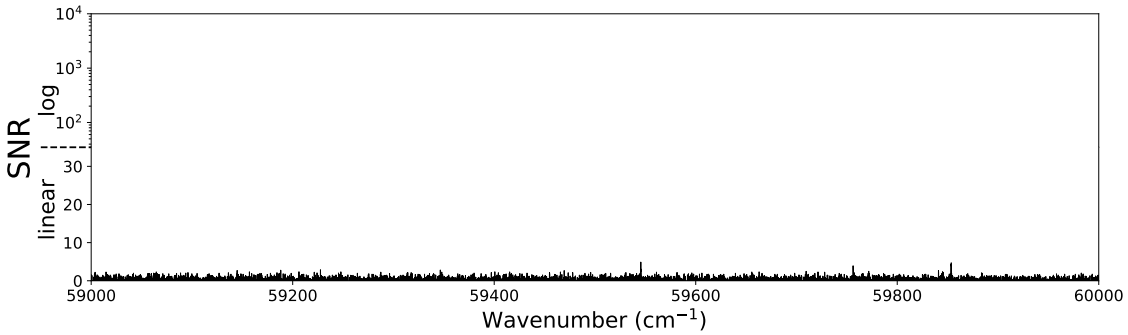
Fe903 (continued)



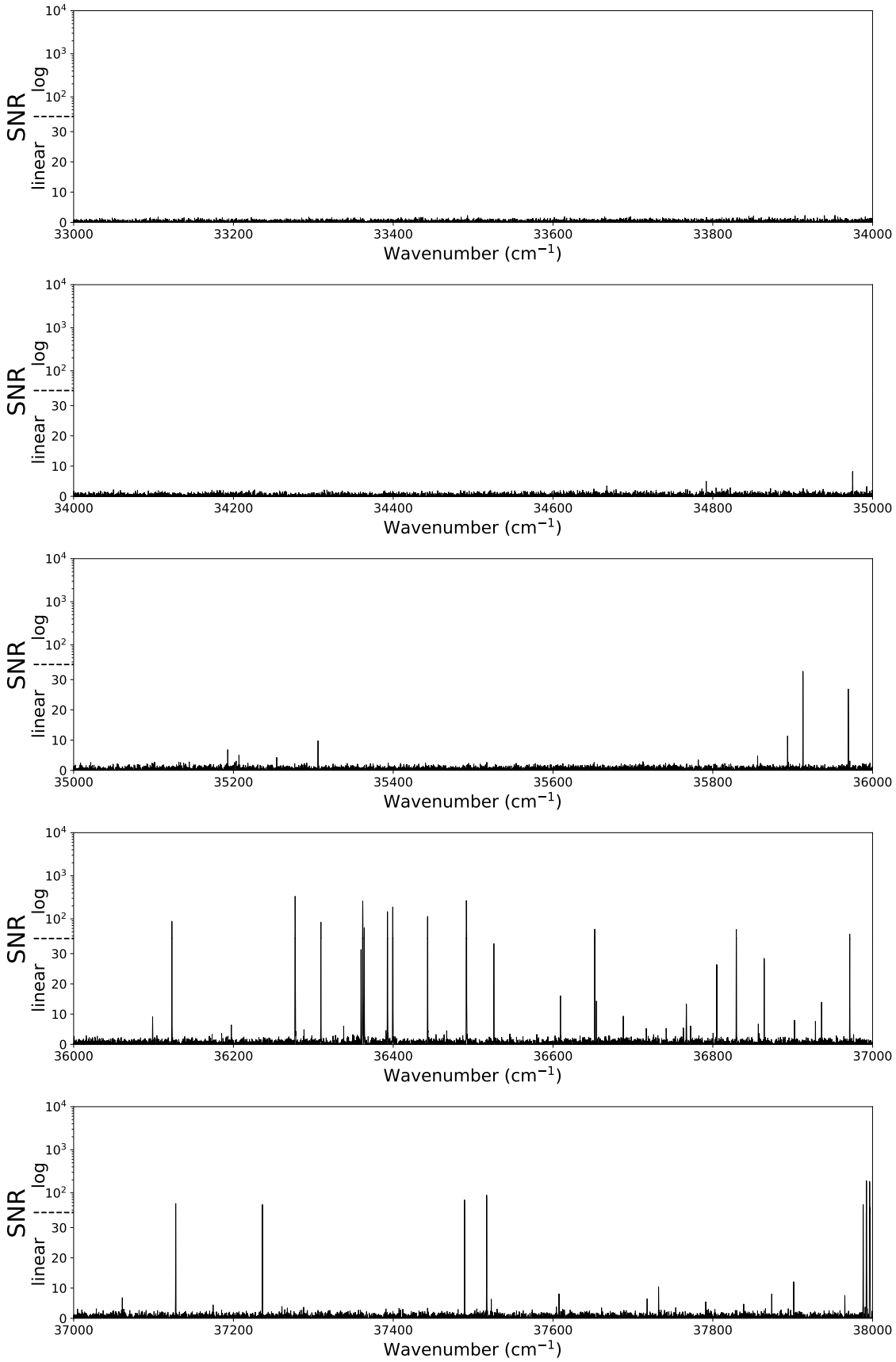




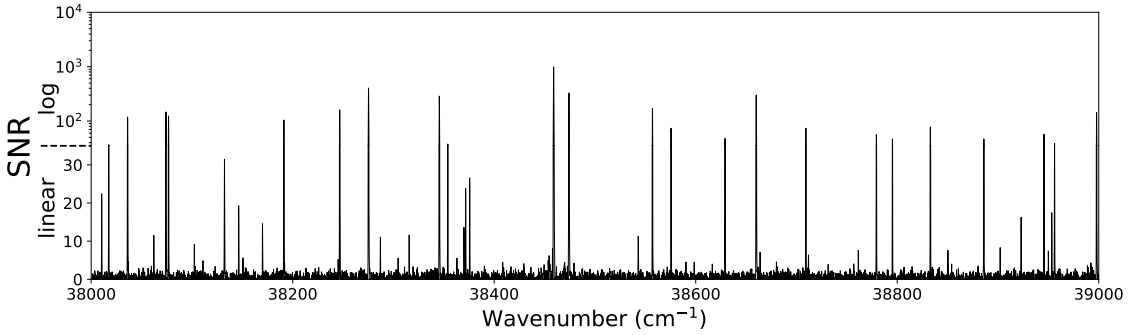


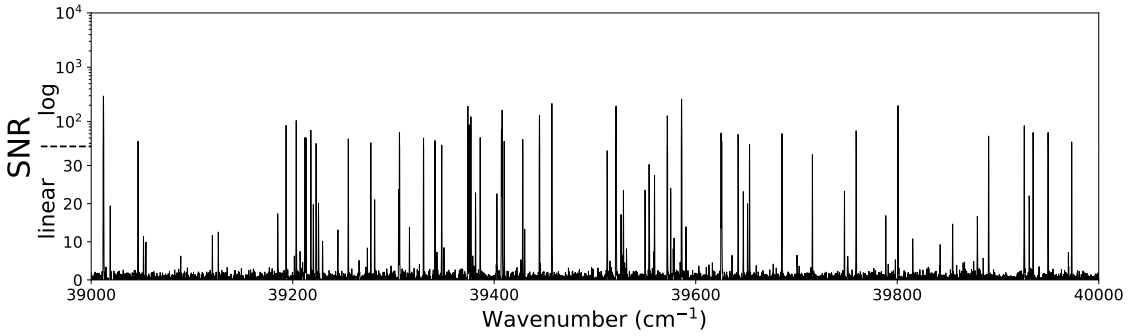


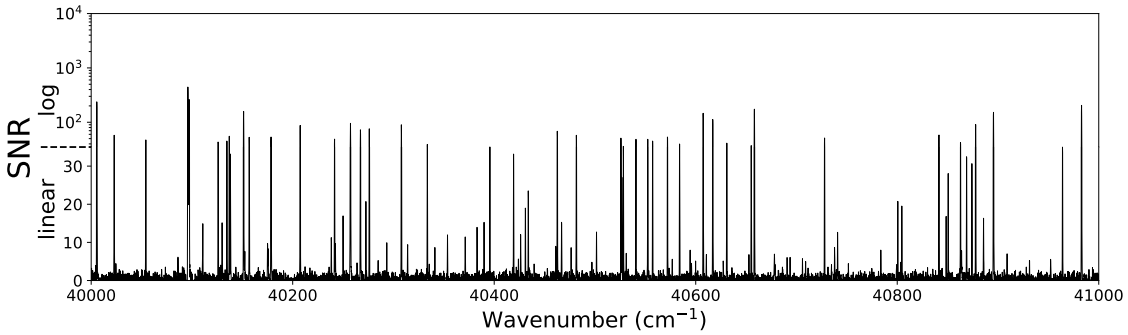
E.6 Fe103

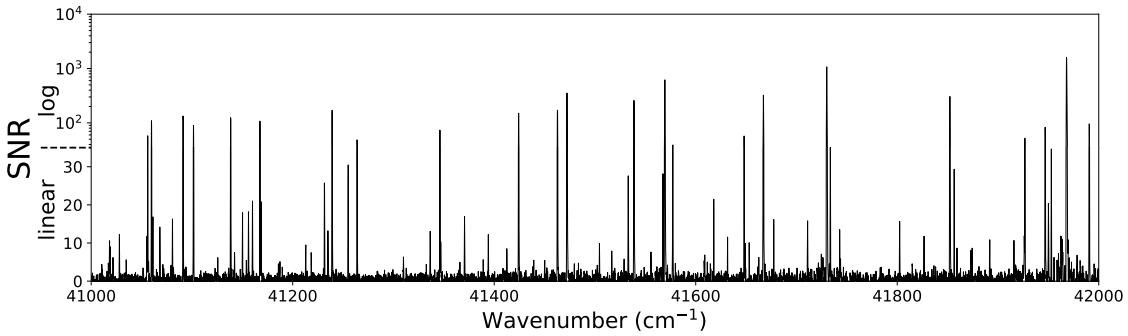

SNR
log
linear
Wavenumber (cm^{-1})
33000
33200
33400
33600
33800
34000
34200
34400
34600
34800
35000
35200
35400
35600
35800
36000
36200
36400
36600
36800
37000
37200
37400
37600
37800
38000

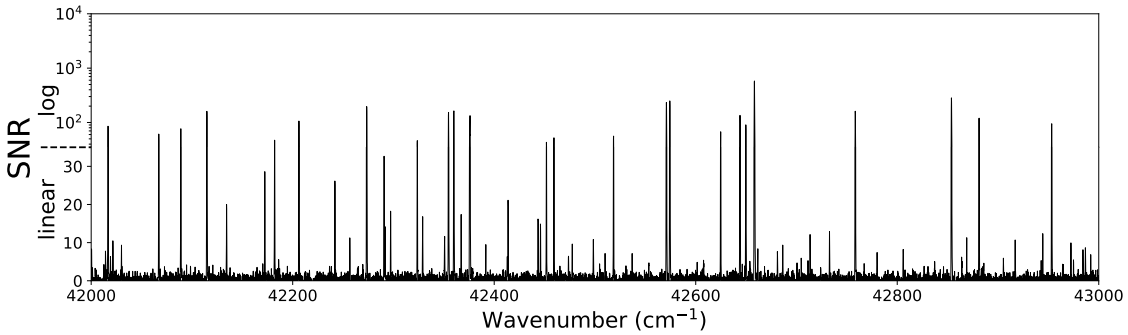
Fe103 (continued)



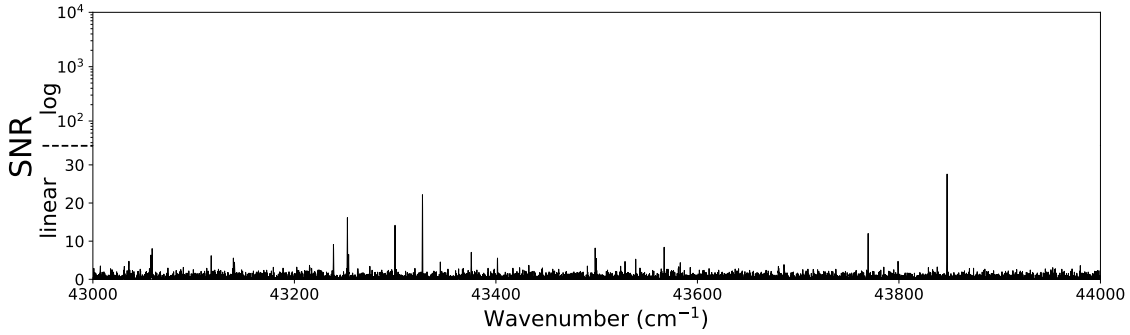


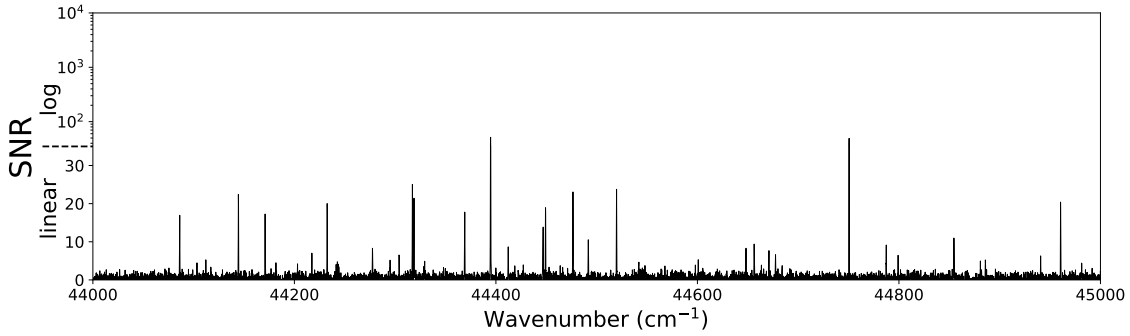


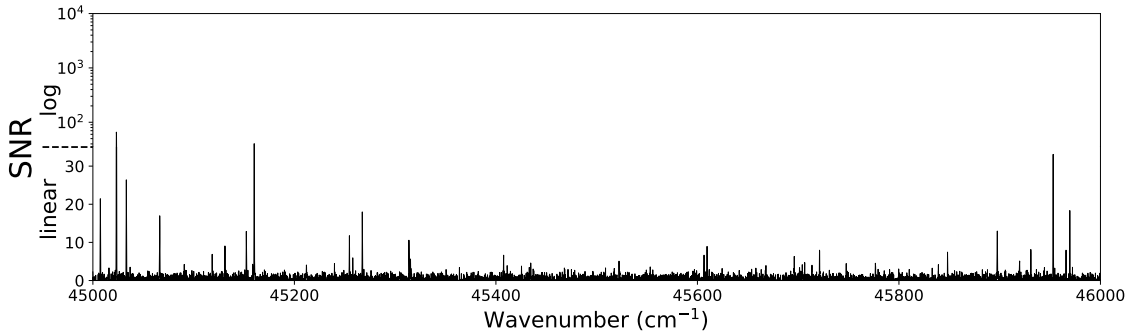


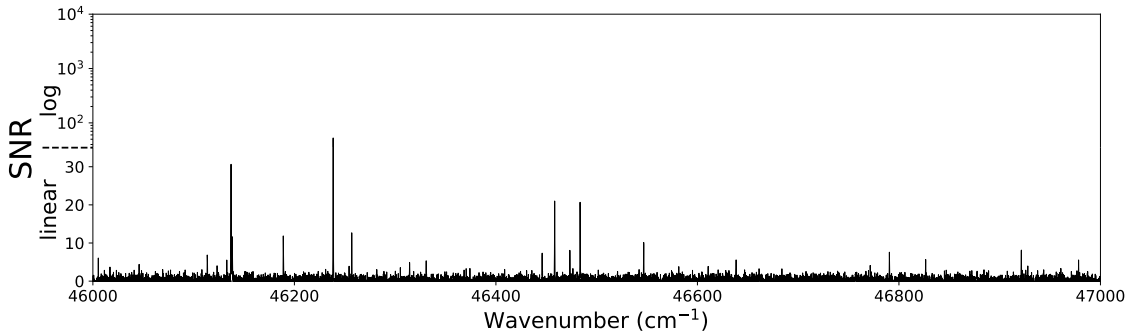


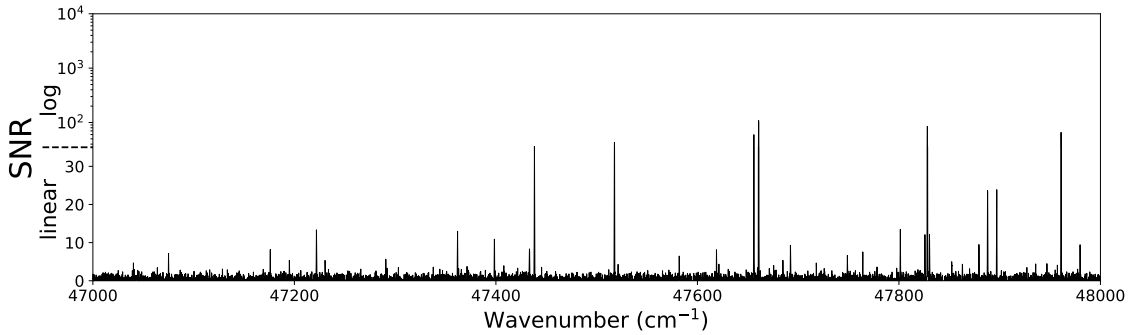
Fe103 (continued)



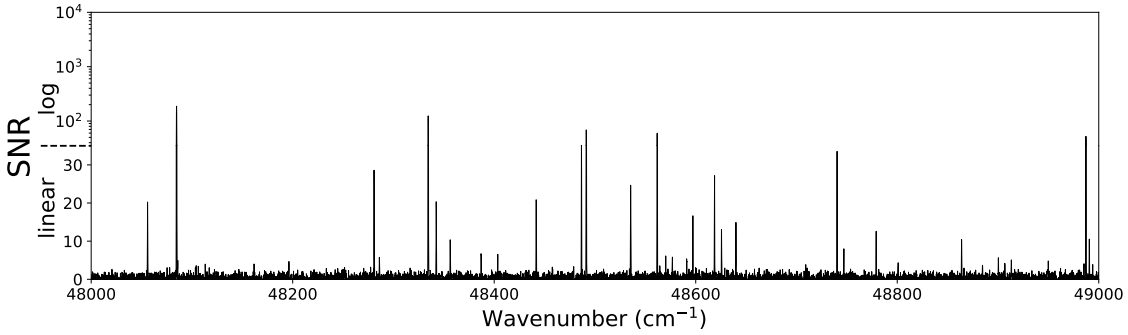


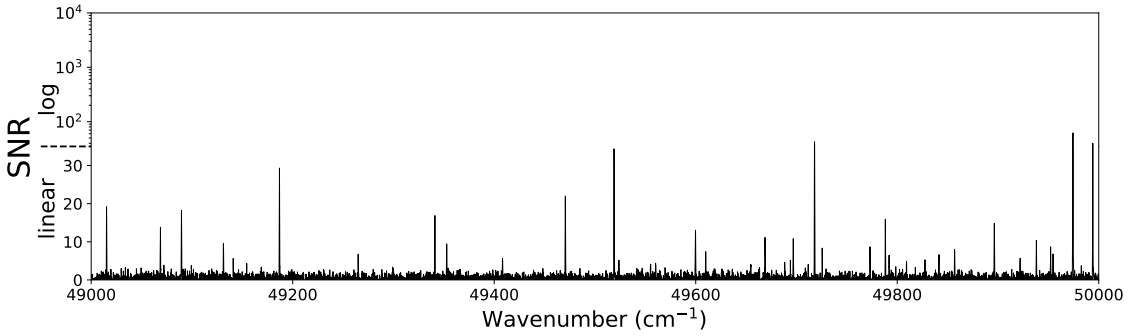


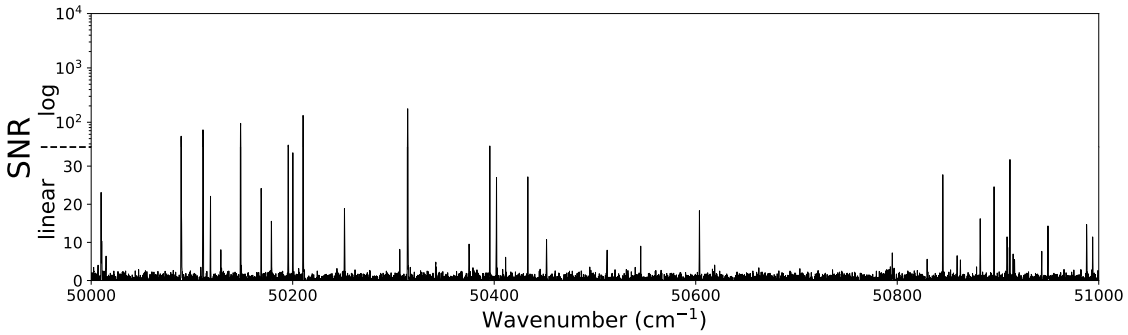


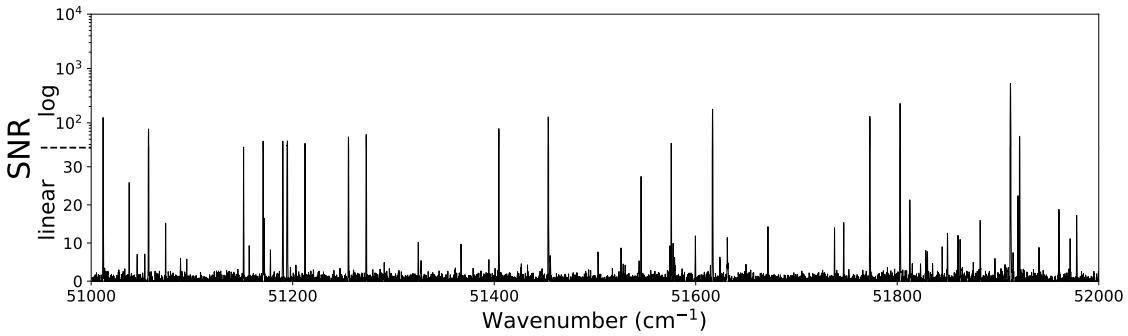


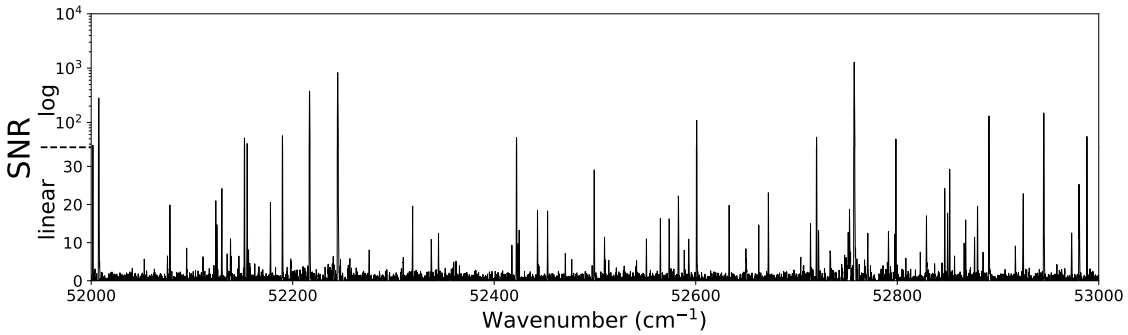
Fe103 (continued)



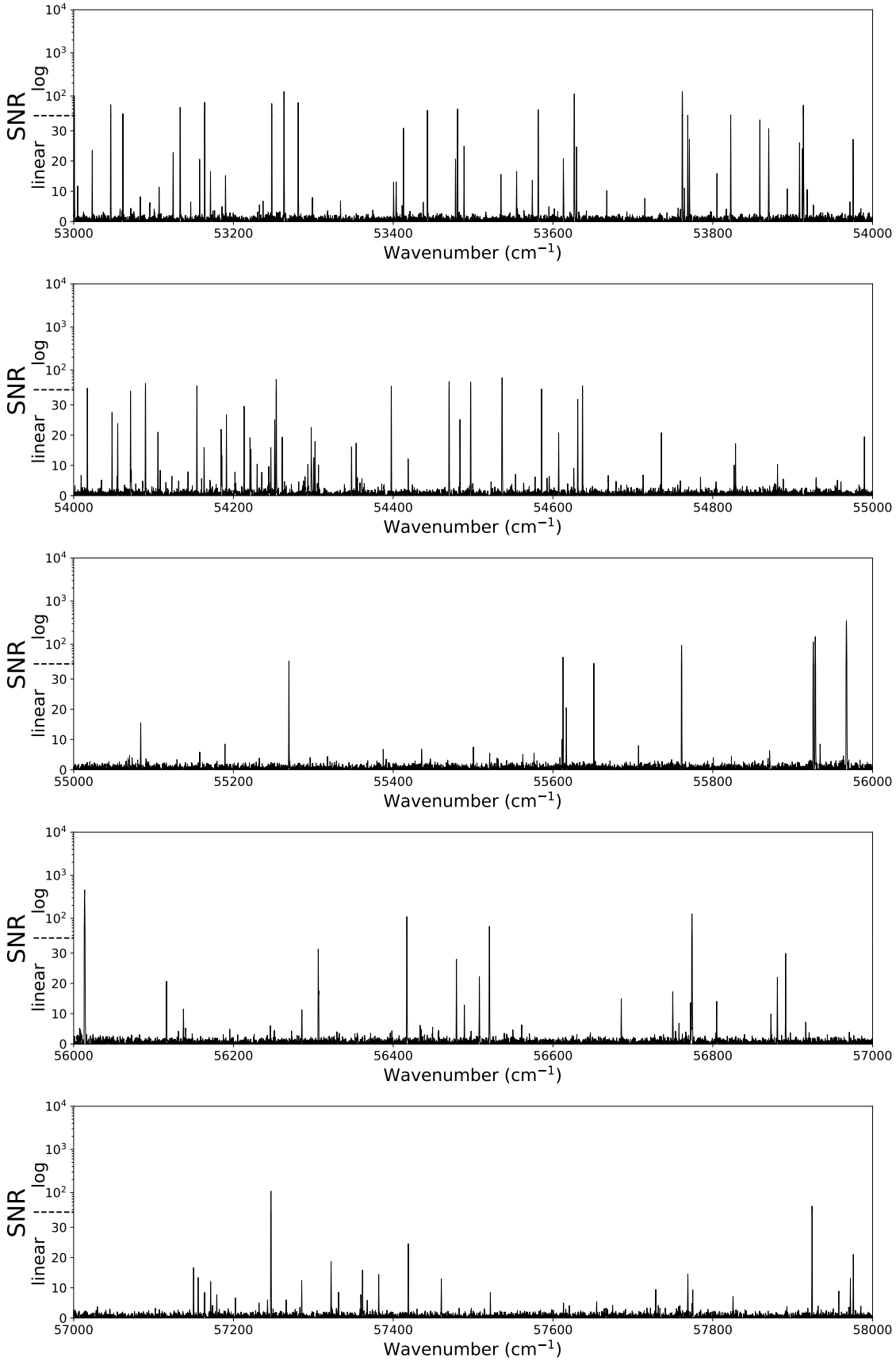




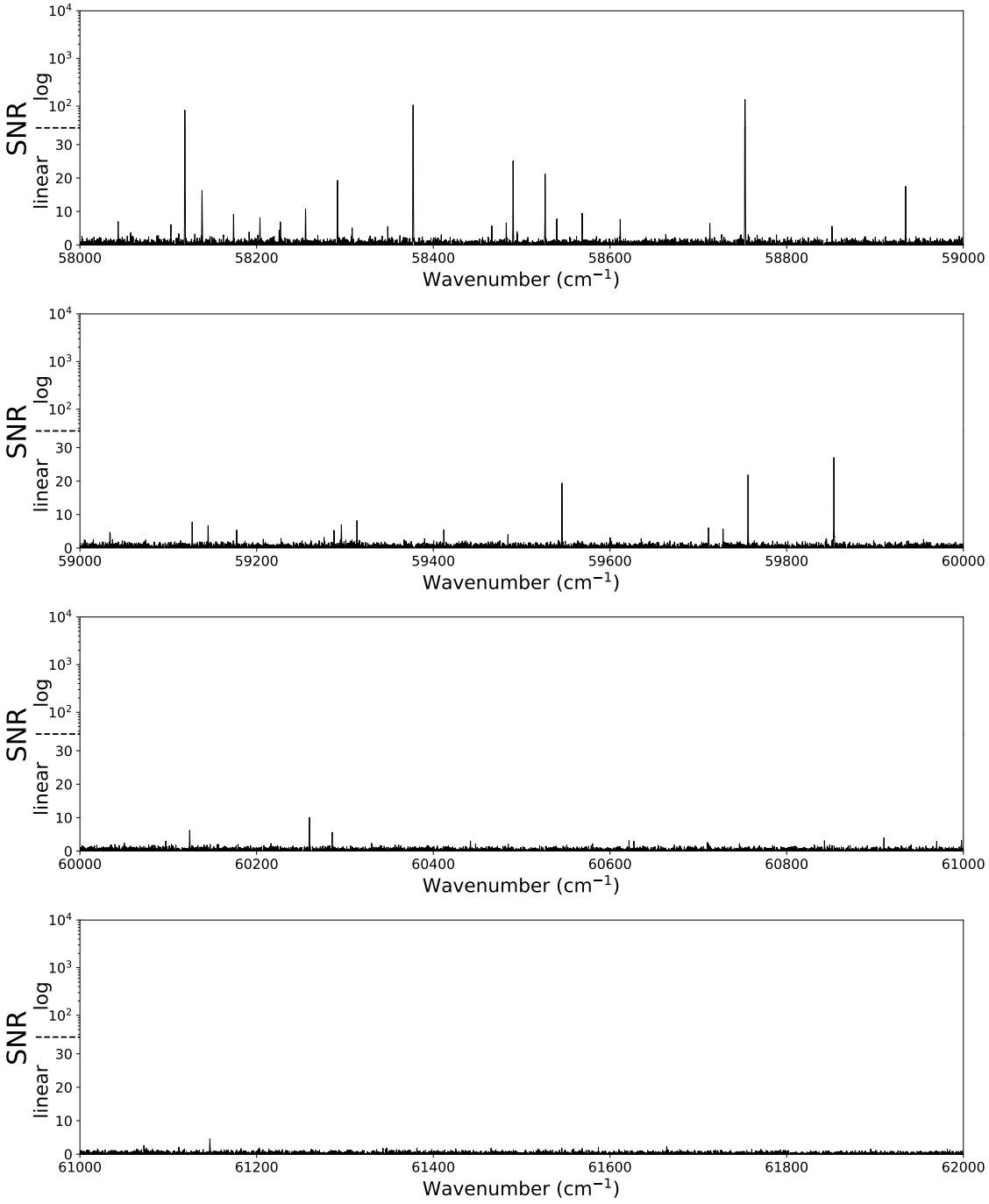




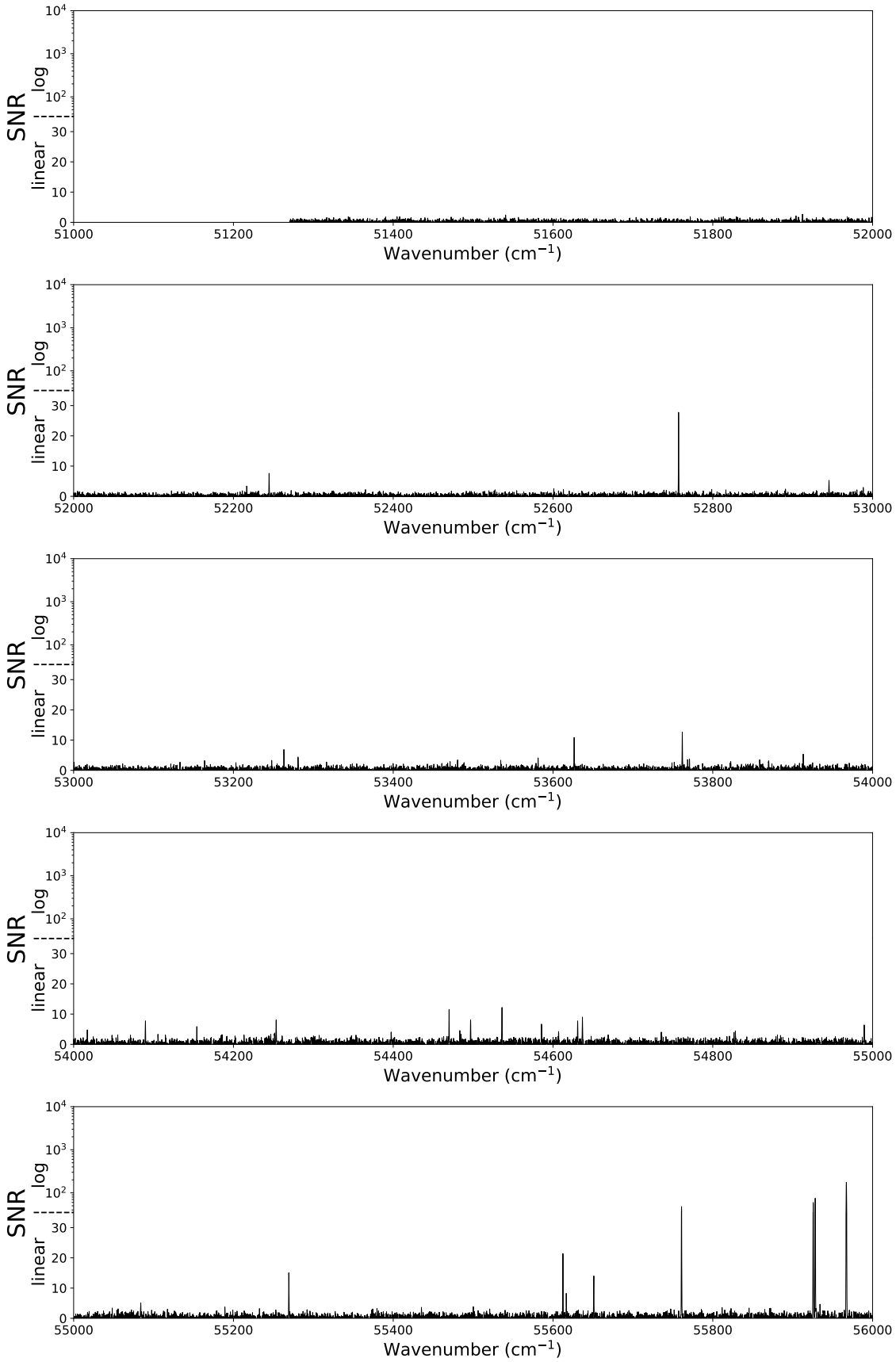
Fe103 (continued)



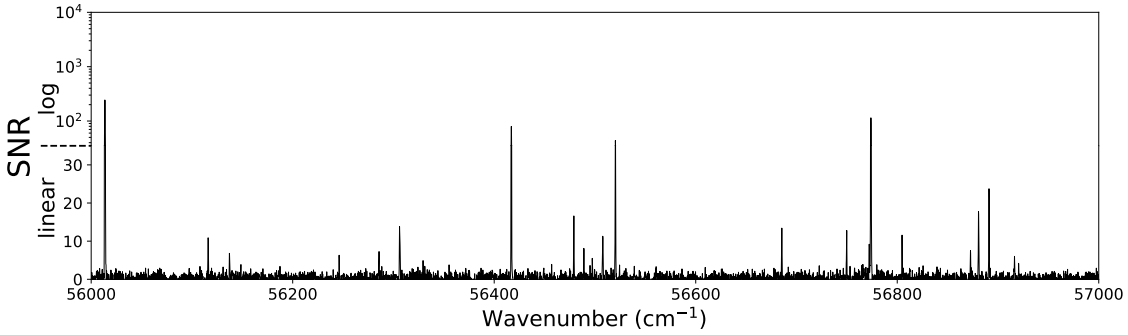
Fe103 (continued)

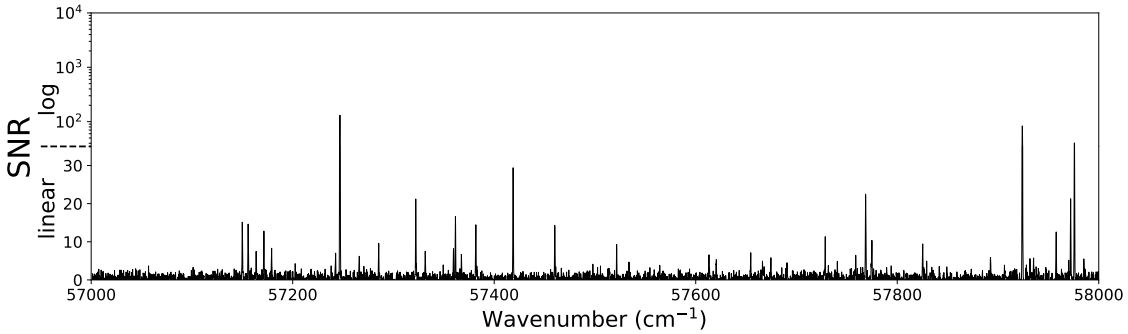


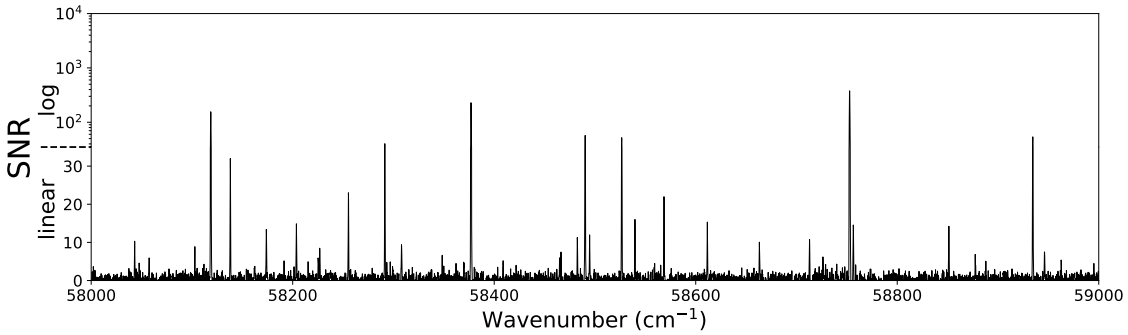
E.7 Fe121

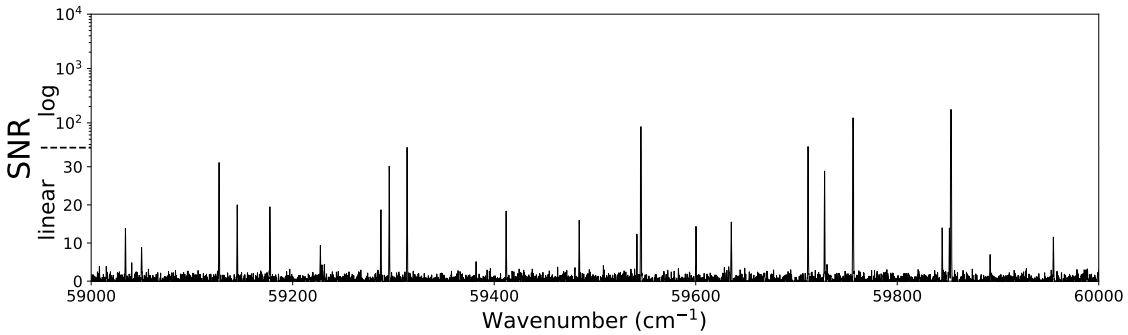


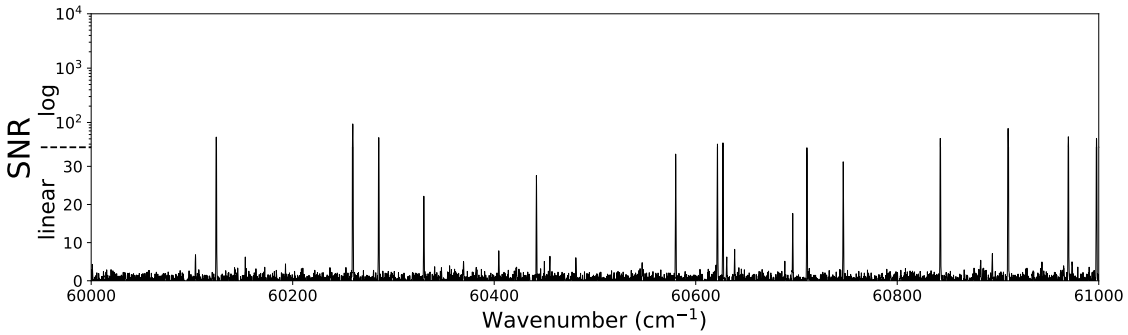
Fe121 (continued)



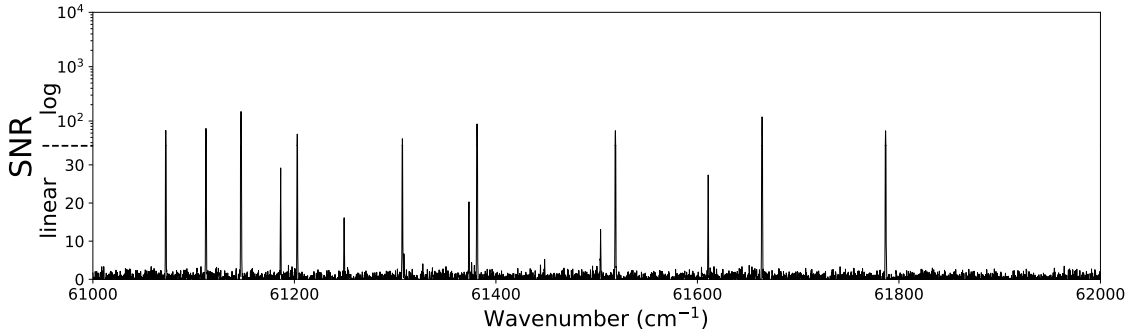


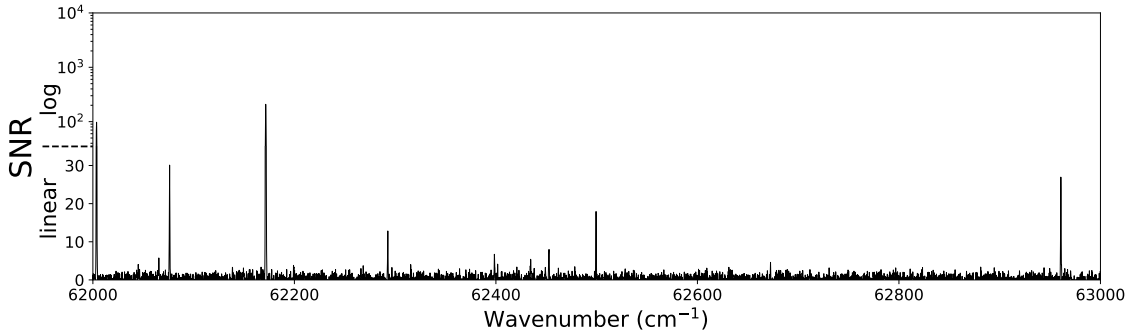


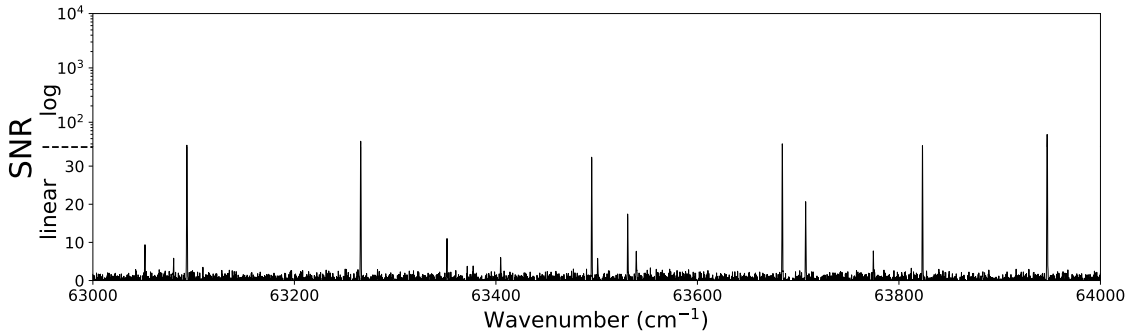


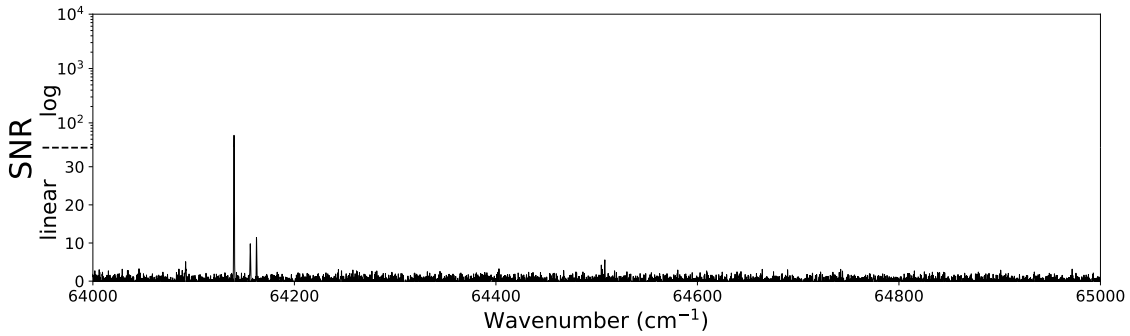


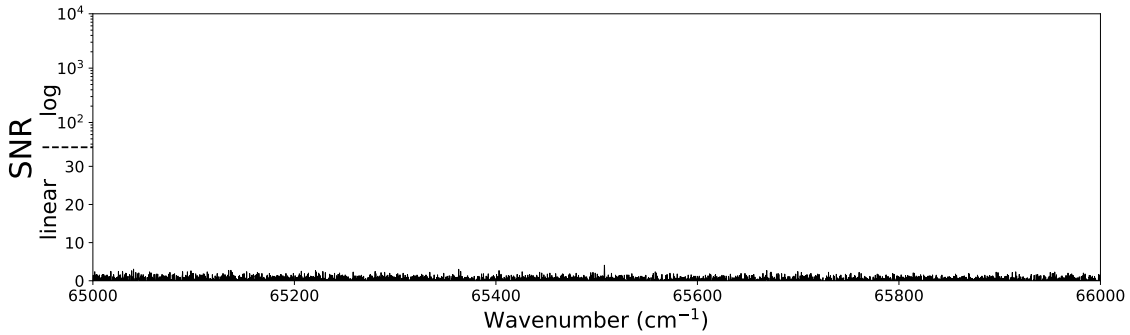
Fe121 (continued)



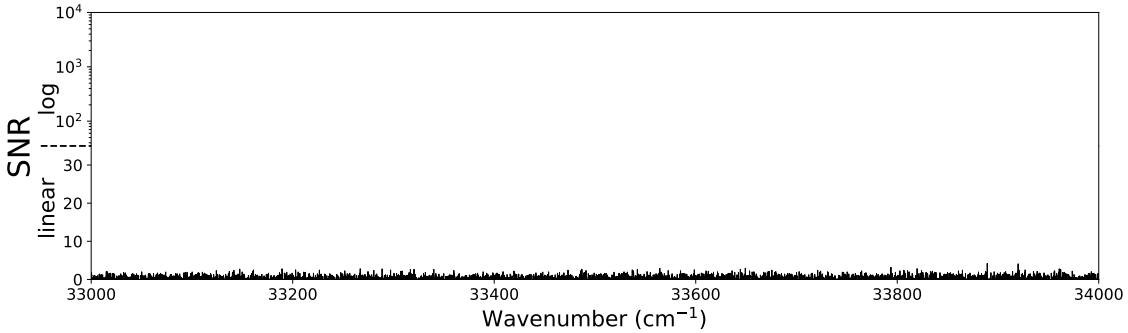


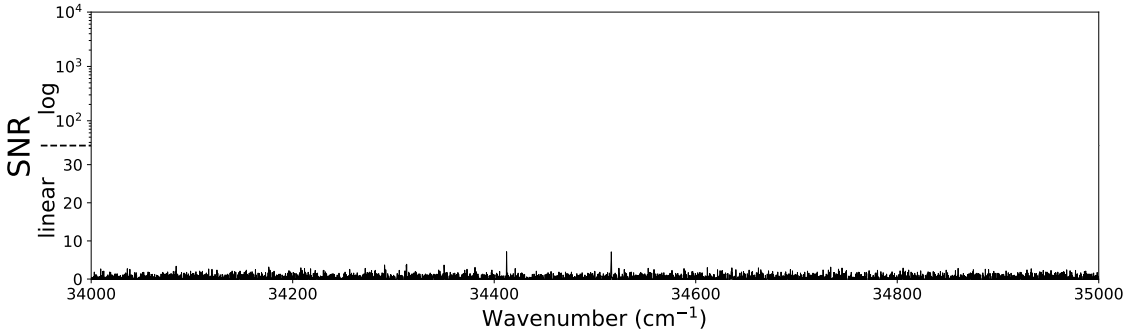


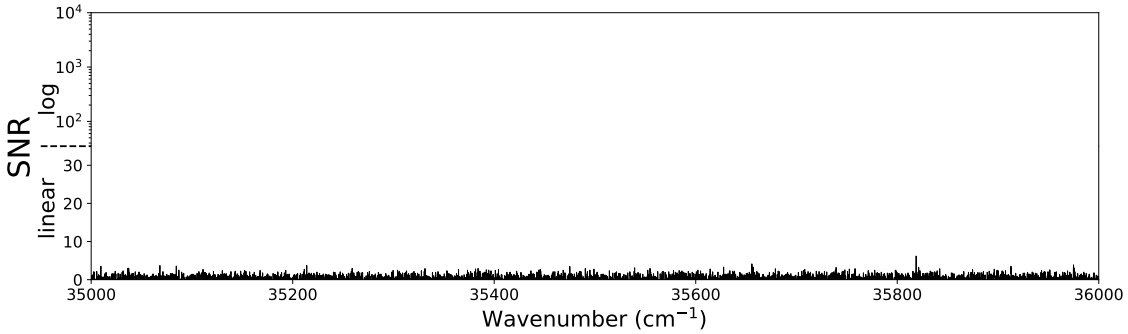


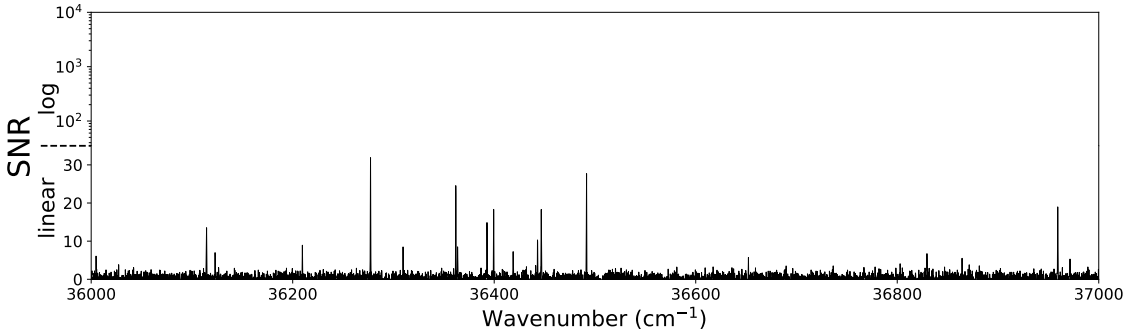


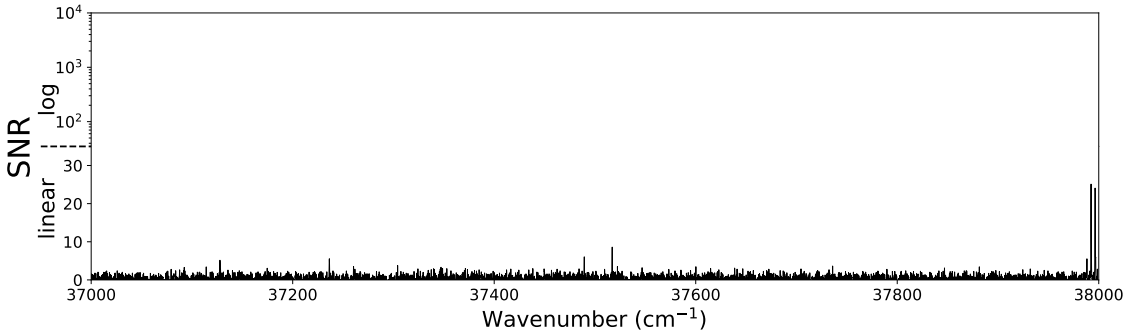
E.8 Fe203


SNR
log
linear
10^4
10^3
10^2
30
20
10
0
33000
33200
33400
33600
33800
34000
Wavenumber (cm^{-1})

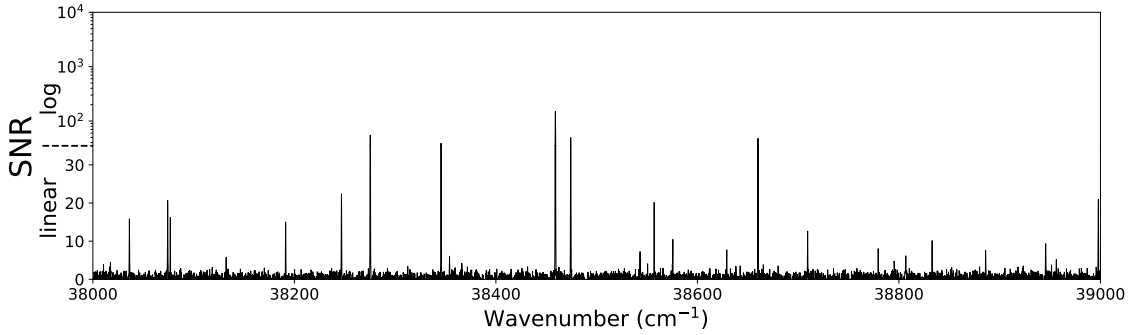

SNR
log
linear
10^4
10^3
10^2
30
20
10
0
34000
34200
34400
34600
34800
35000
Wavenumber (cm^{-1})

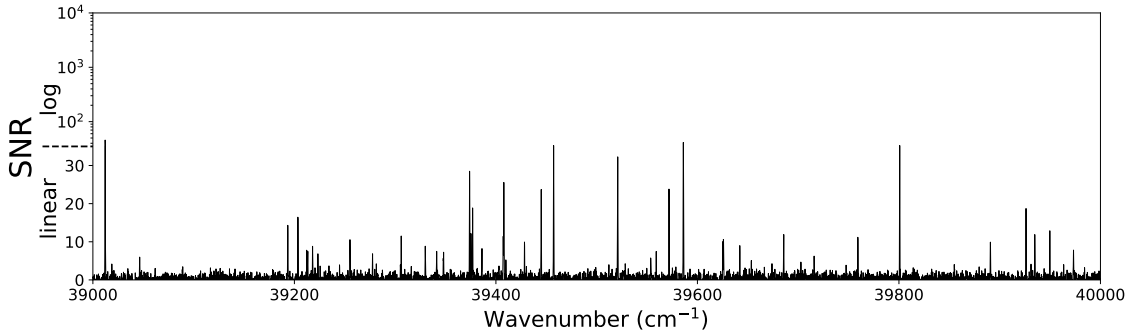

SNR
log
linear
10^4
10^3
10^2
30
20
10
0
35000
35200
35400
35600
35800
36000
Wavenumber (cm^{-1})

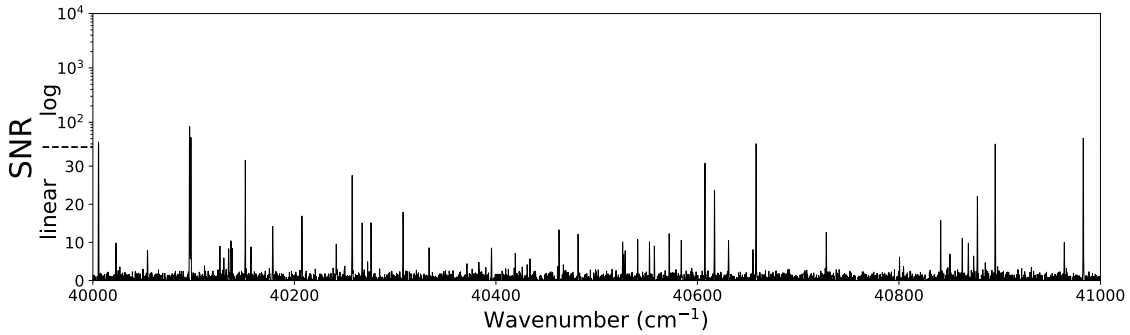

SNR
log
linear
10^4
10^3
10^2
30
20
10
0
36000
36200
36400
36600
36800
37000
Wavenumber (cm^{-1})

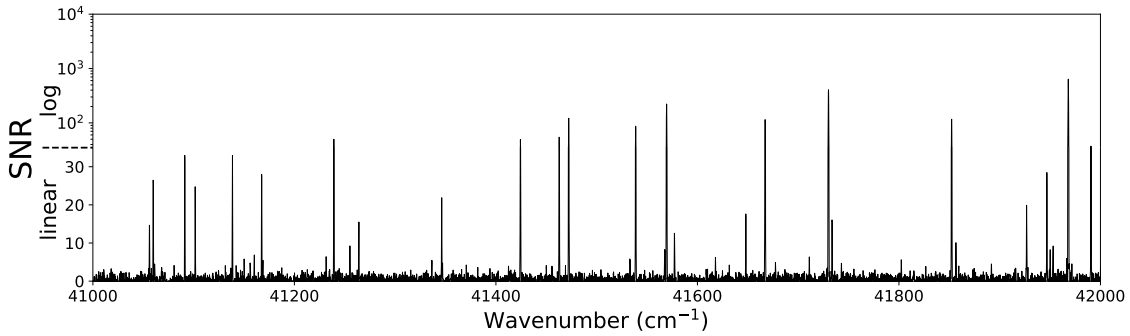

SNR
log
linear
10^4
10^3
10^2
30
20
10
0
37000
37200
37400
37600
37800
38000
Wavenumber (cm^{-1})

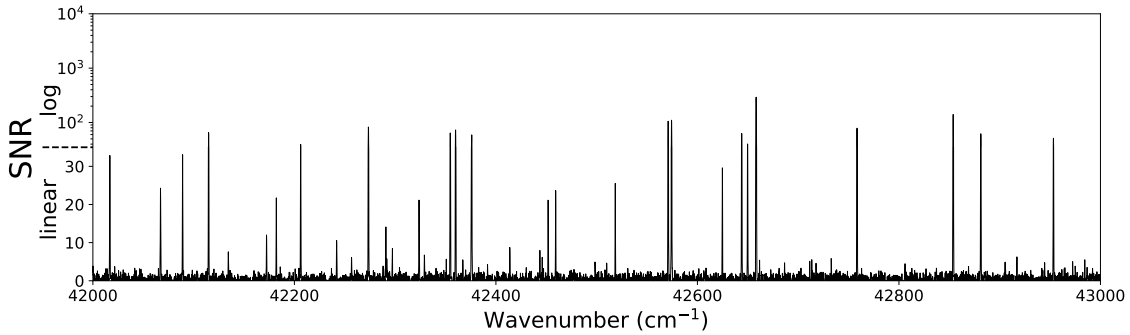
Fe203 (continued)



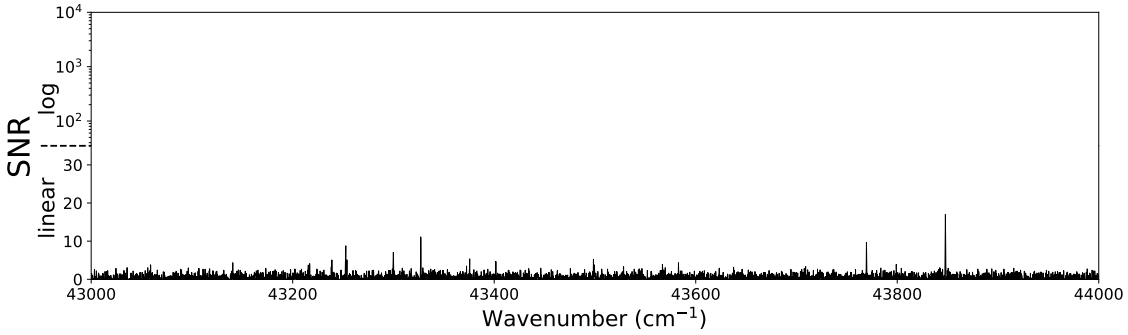


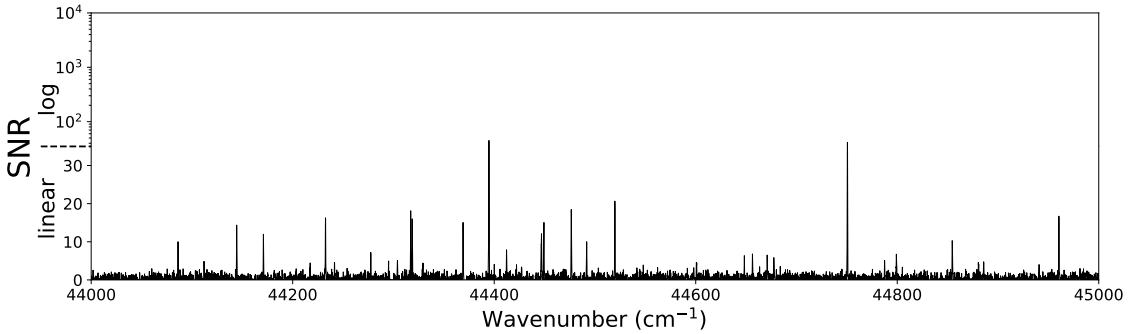


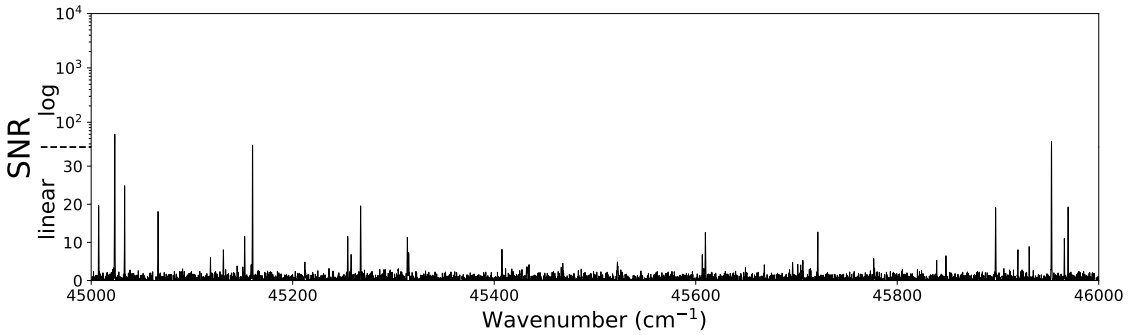


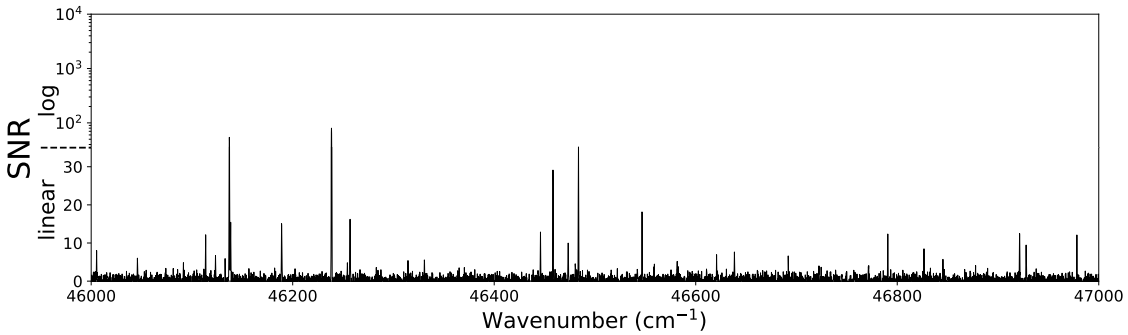


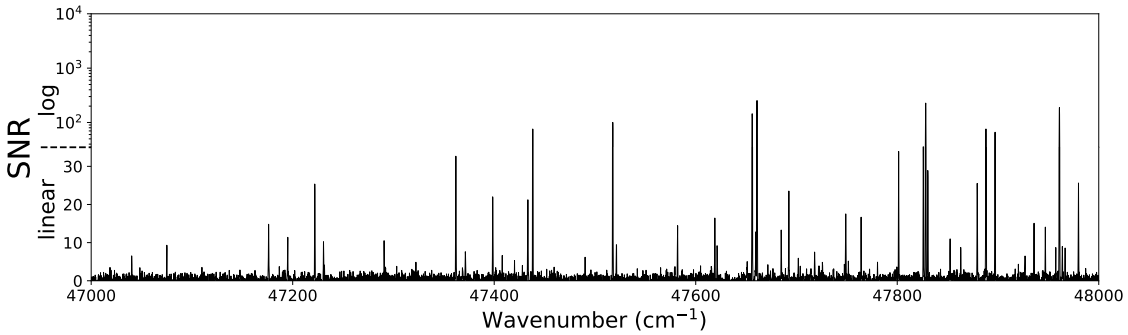
Fe203 (continued)



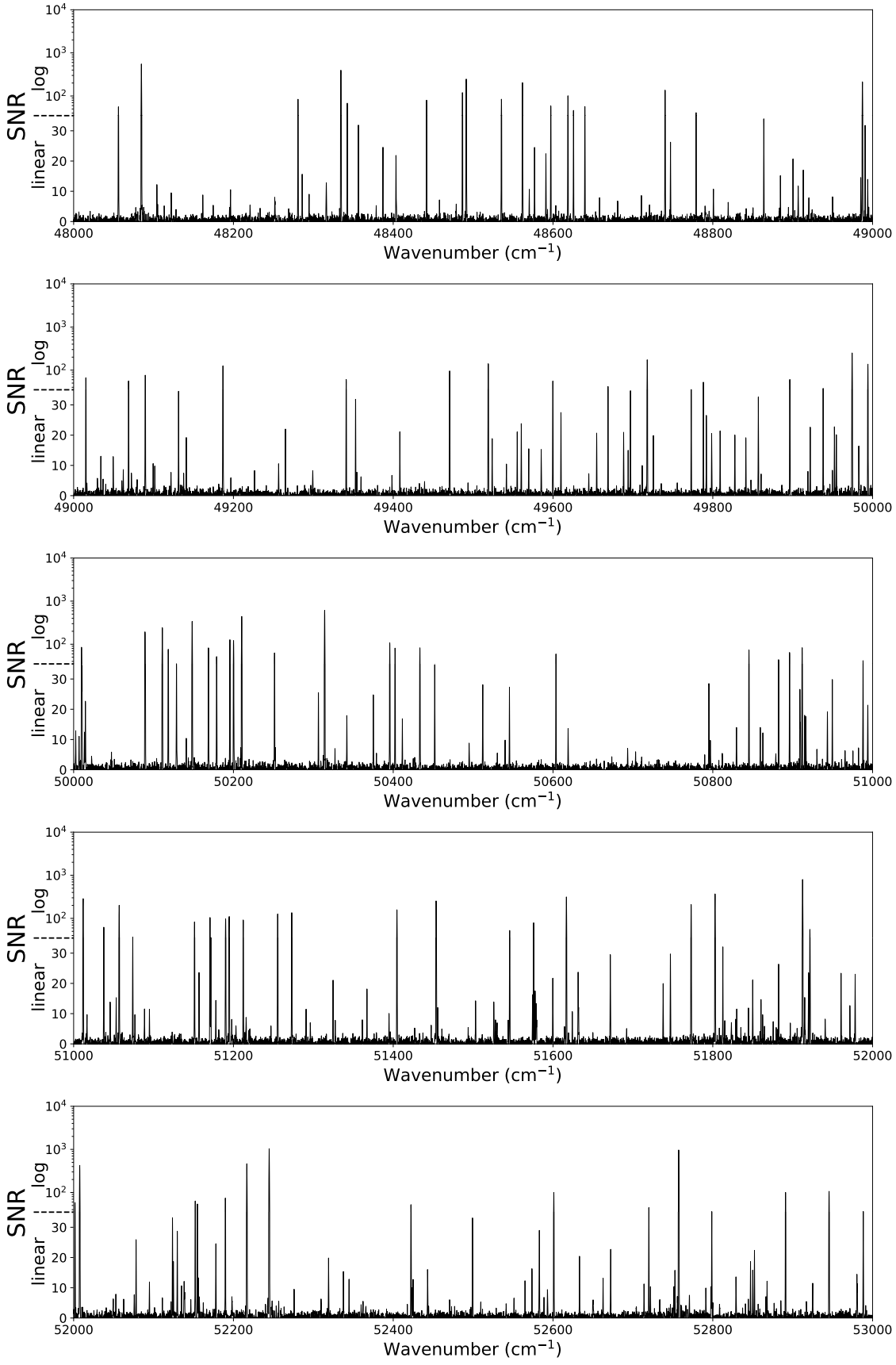




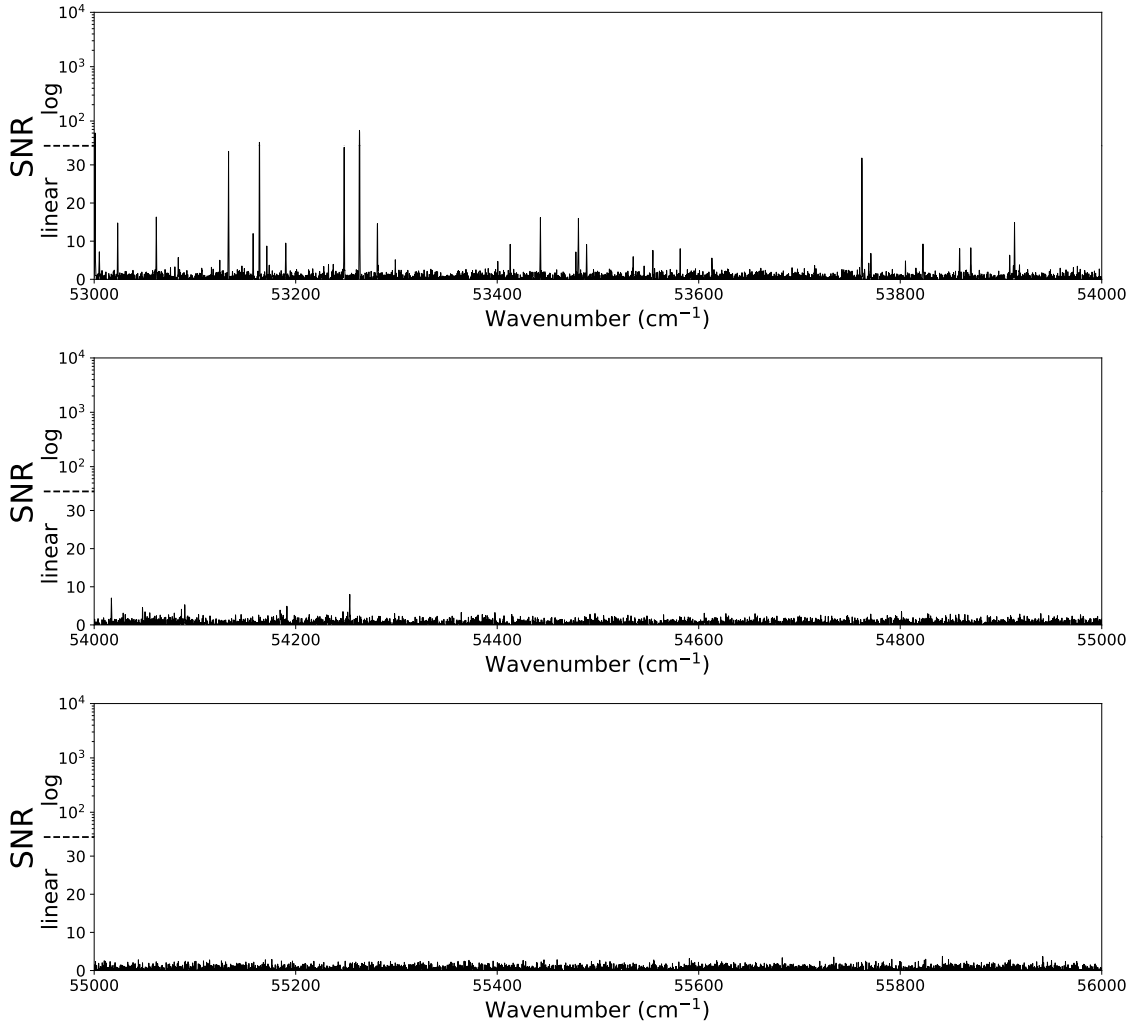




Fe203 (continued)



Fe203 (continued)



F Grating Plates and Spectral Plots

In this section, the grating plates and spectral plots used in this PhD thesis are presented. The images used in this PhD are:

- Image x1015_plate2a, Track 5.1, 5-minute exposure;
- Image x1015_plate2a, Track 5.1, 45-minute exposure;
- Image x1015_plate2b, Track 5.1, 5-minute exposure;
- Image x1015_plate2b, Track 5.1, 45-minute exposure;
- Image x1015_plate1b, Track 5.3, 5-minute exposure;
- Image x1015_plate1b, Track 5.3, 45-minute exposure;
- Image x1015_plate2a, Track 5.3, 5-minute exposure;
- Image x1015_plate2a, Track 5.3, 45-minute exposure;
- Image x1015_plate2b, Track 5.3, 5-minute exposure; and
- Image x1015_plate2b, Track 5.3, 45-minute exposure

Each image is approximately 240 Å and are shown here in ~ 10 Å segments with their spectral plots underneath. The line profiles are the cubic interpolation of the average intensity of each column of the uploaded bitmap image file. The wavelengths displayed here are not calibrated.

F.1 Image x1015_plate2a, Track 5.1, 5-minute exposure

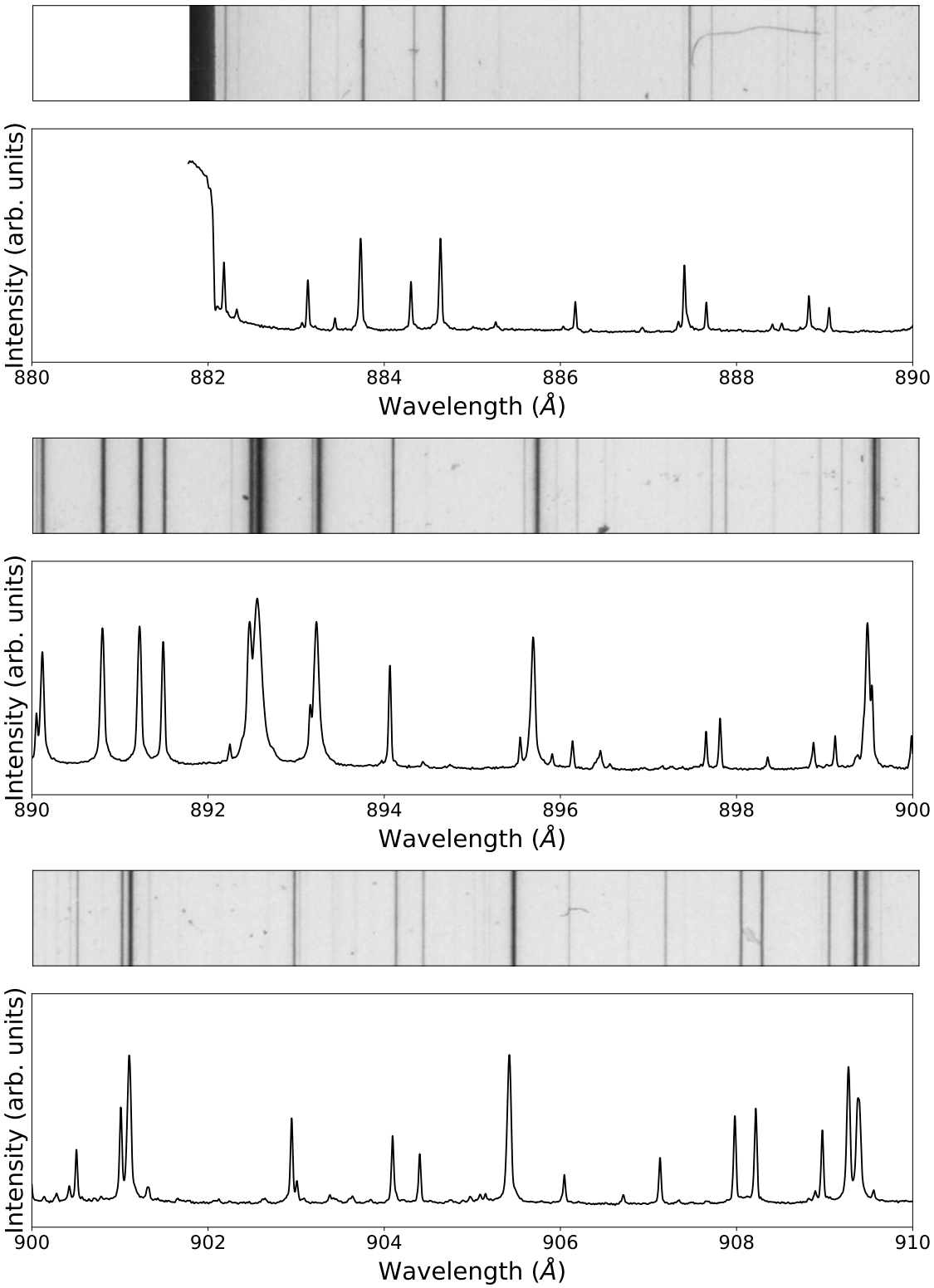


Image x1015_plate2a, Track 5.1, 5-minute exposure (continued)

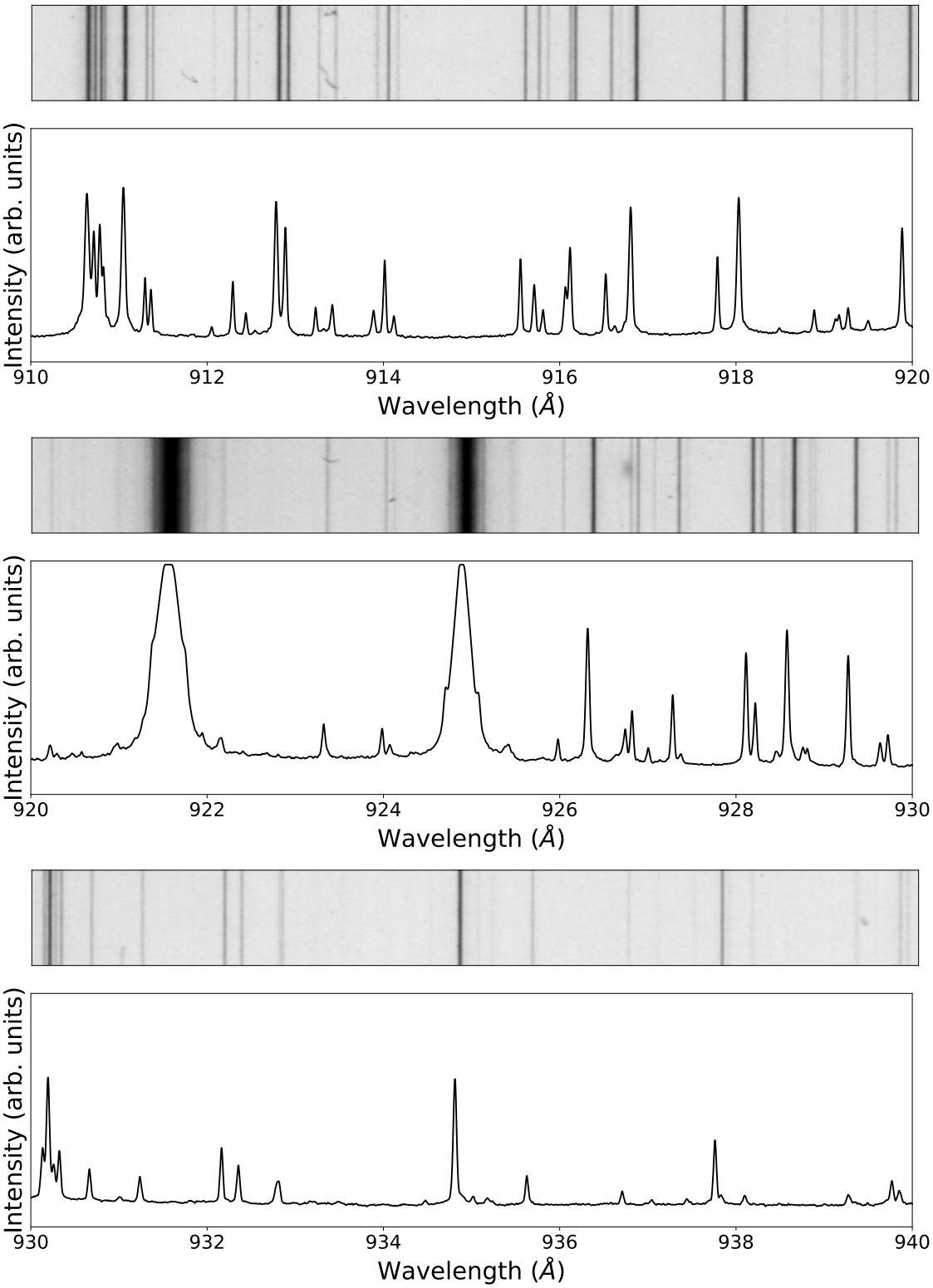
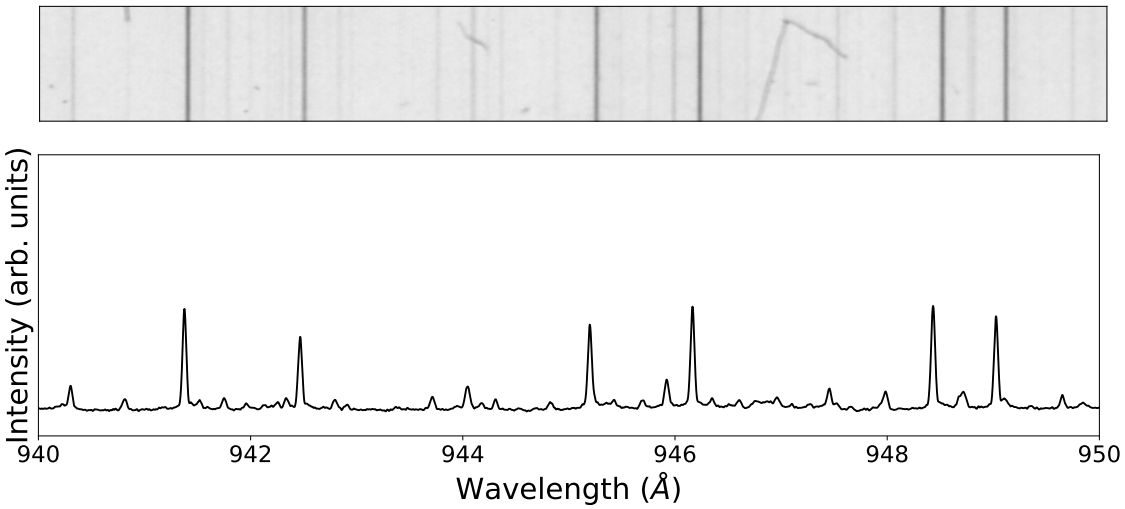
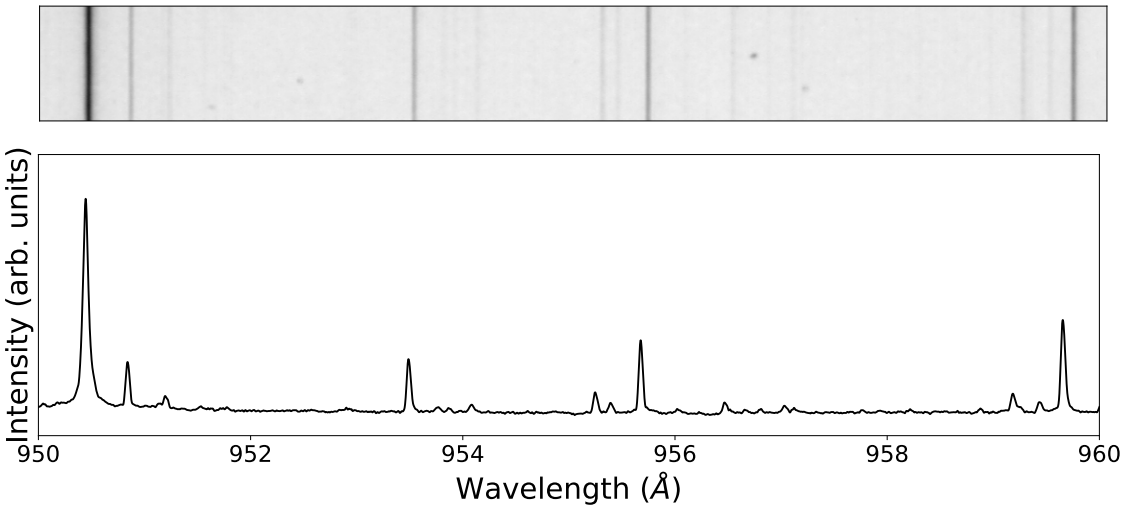


Image x1015_plate2a, Track 5.1, 5-minute exposure (continued)





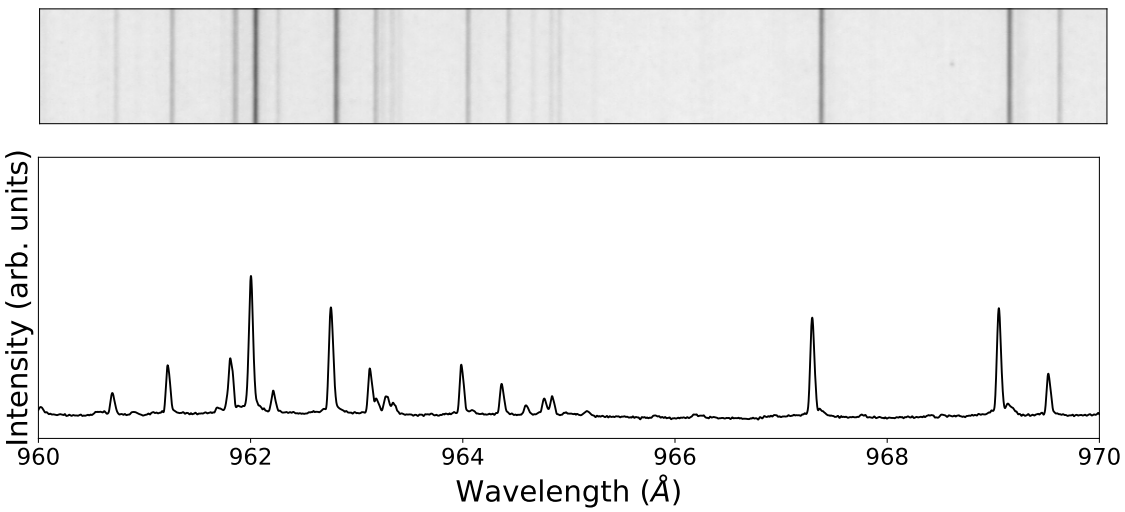


Image x1015_plate2a, Track 5.1, 5-minute exposure (continued)

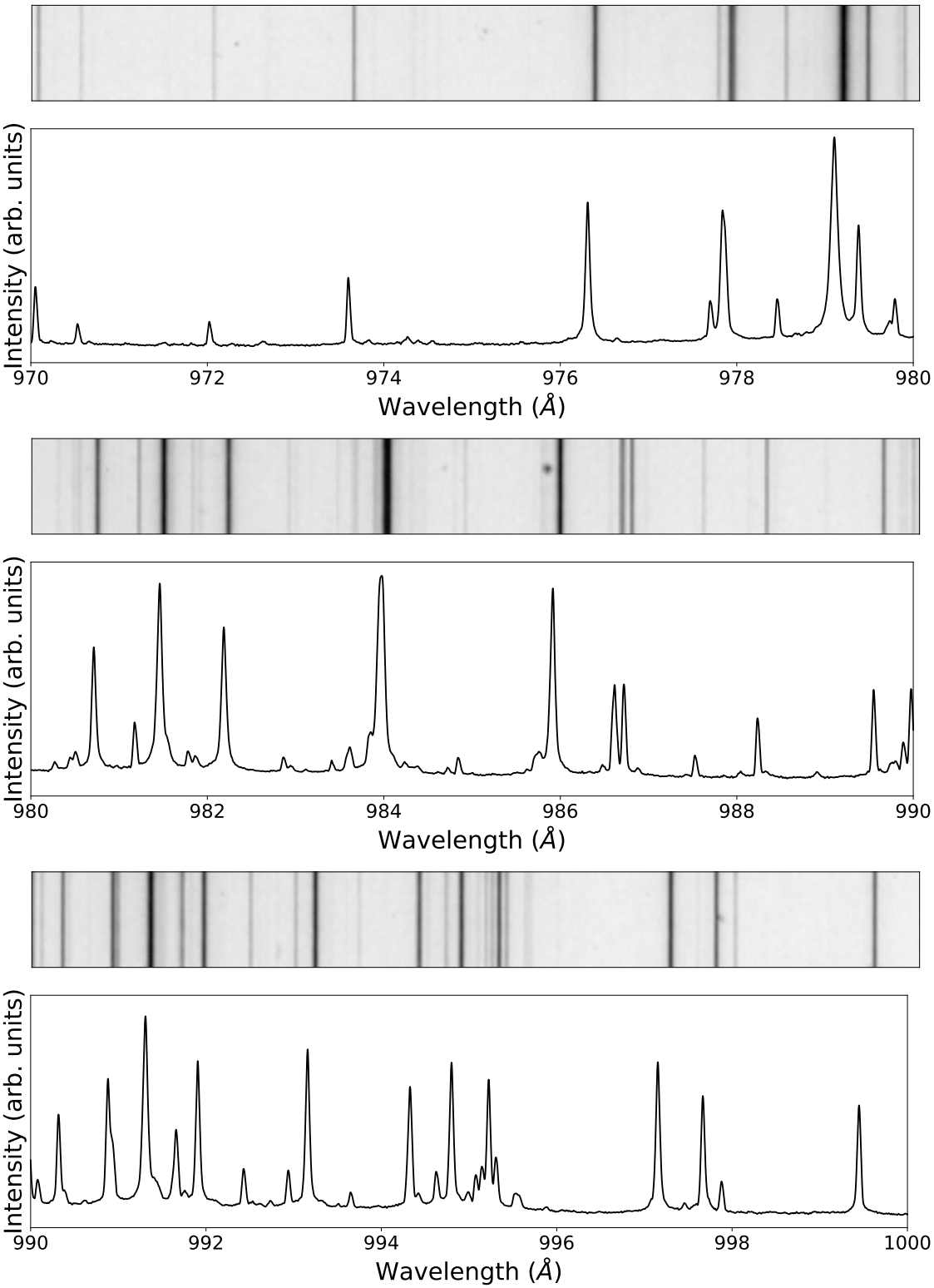


Image x1015_plate2a, Track 5.1, 5-minute exposure (continued)

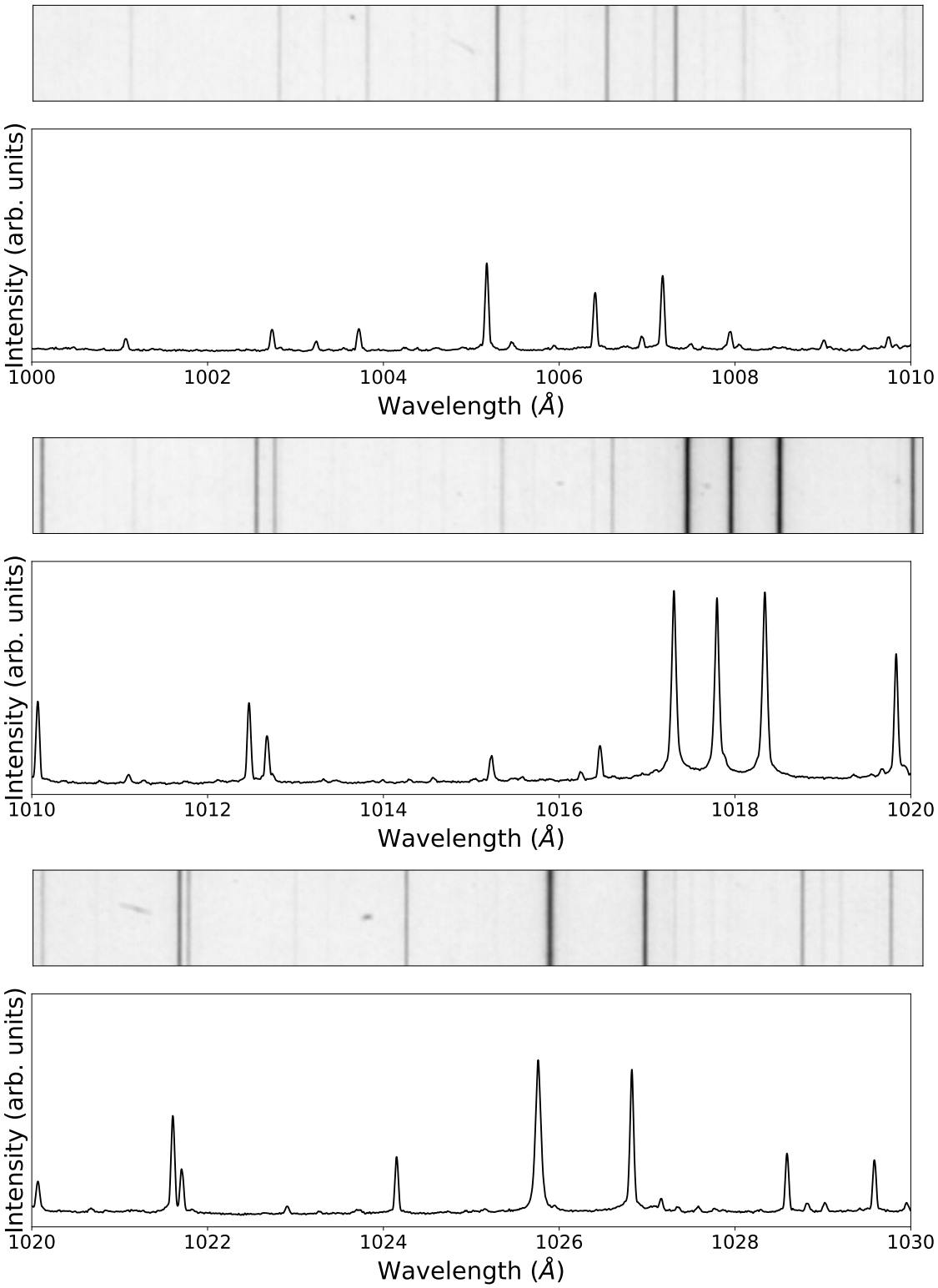


Image x1015_plate2a, Track 5.1, 5-minute exposure (continued)

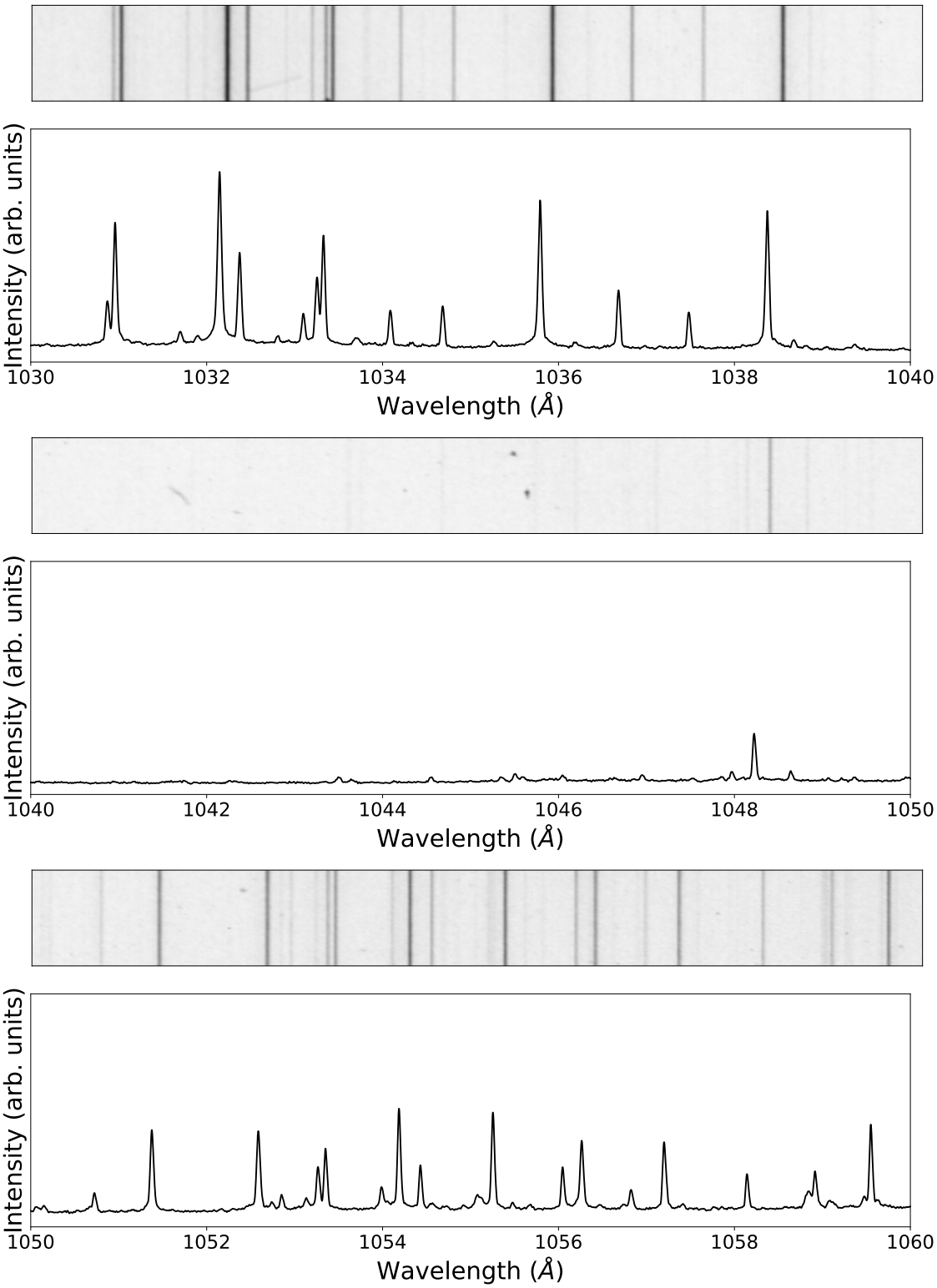


Image x1015_plate2a, Track 5.1, 5-minute exposure (continued)

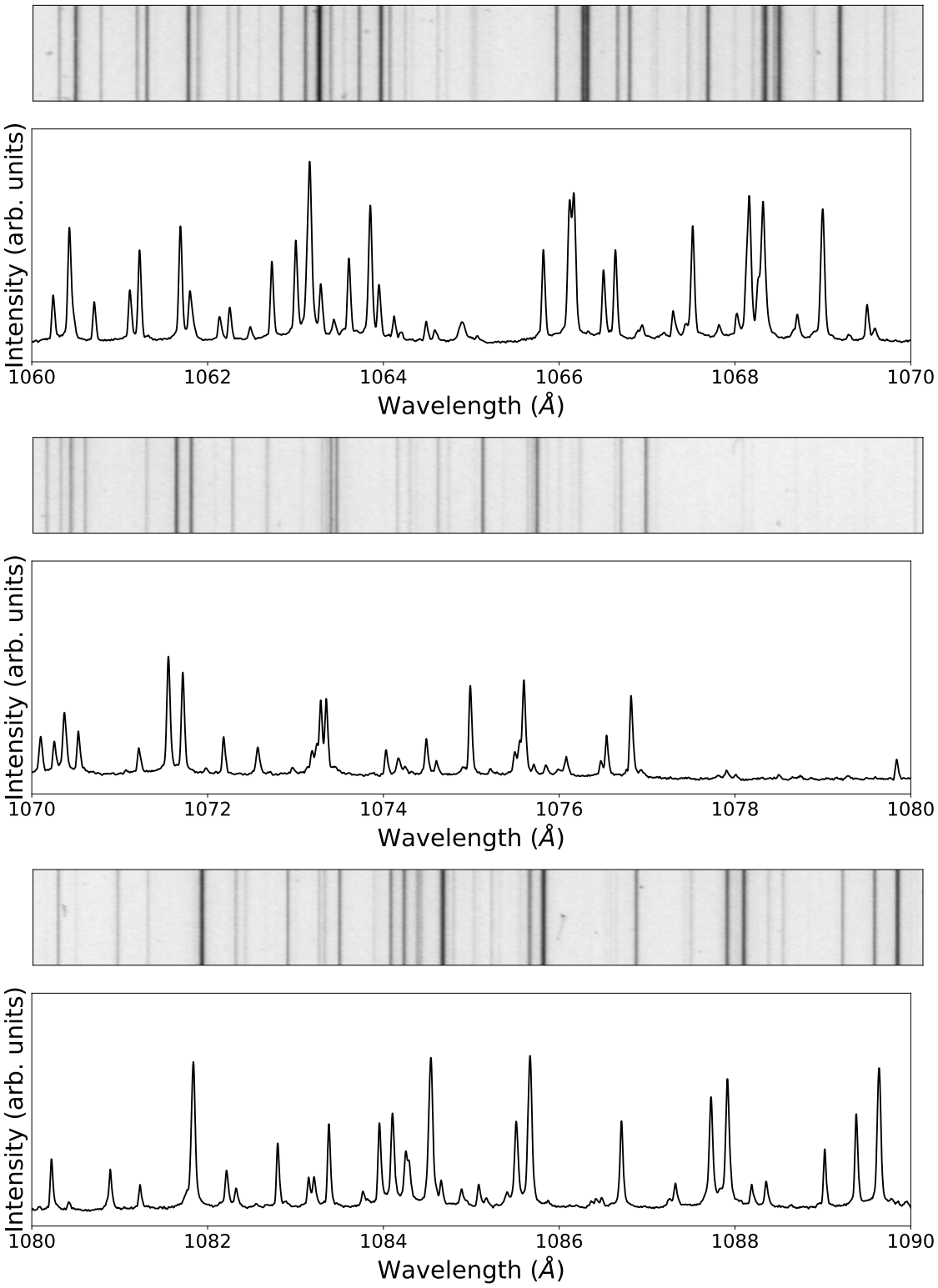
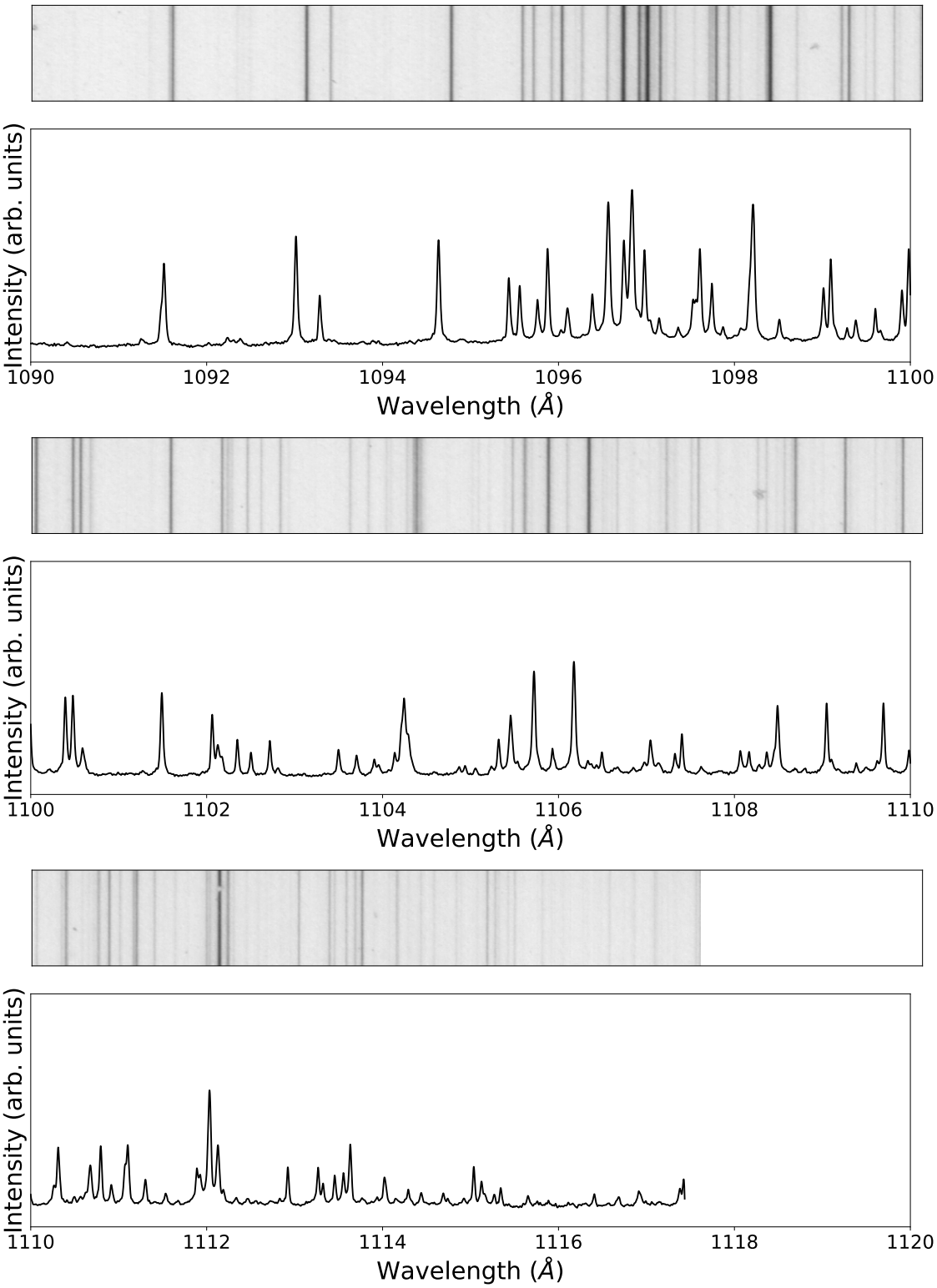


Image x1015_plate2a, Track 5.1, 5-minute exposure (continued)



F.2 Image x1015_plate2a, Track 5.1, 45-minute exposure

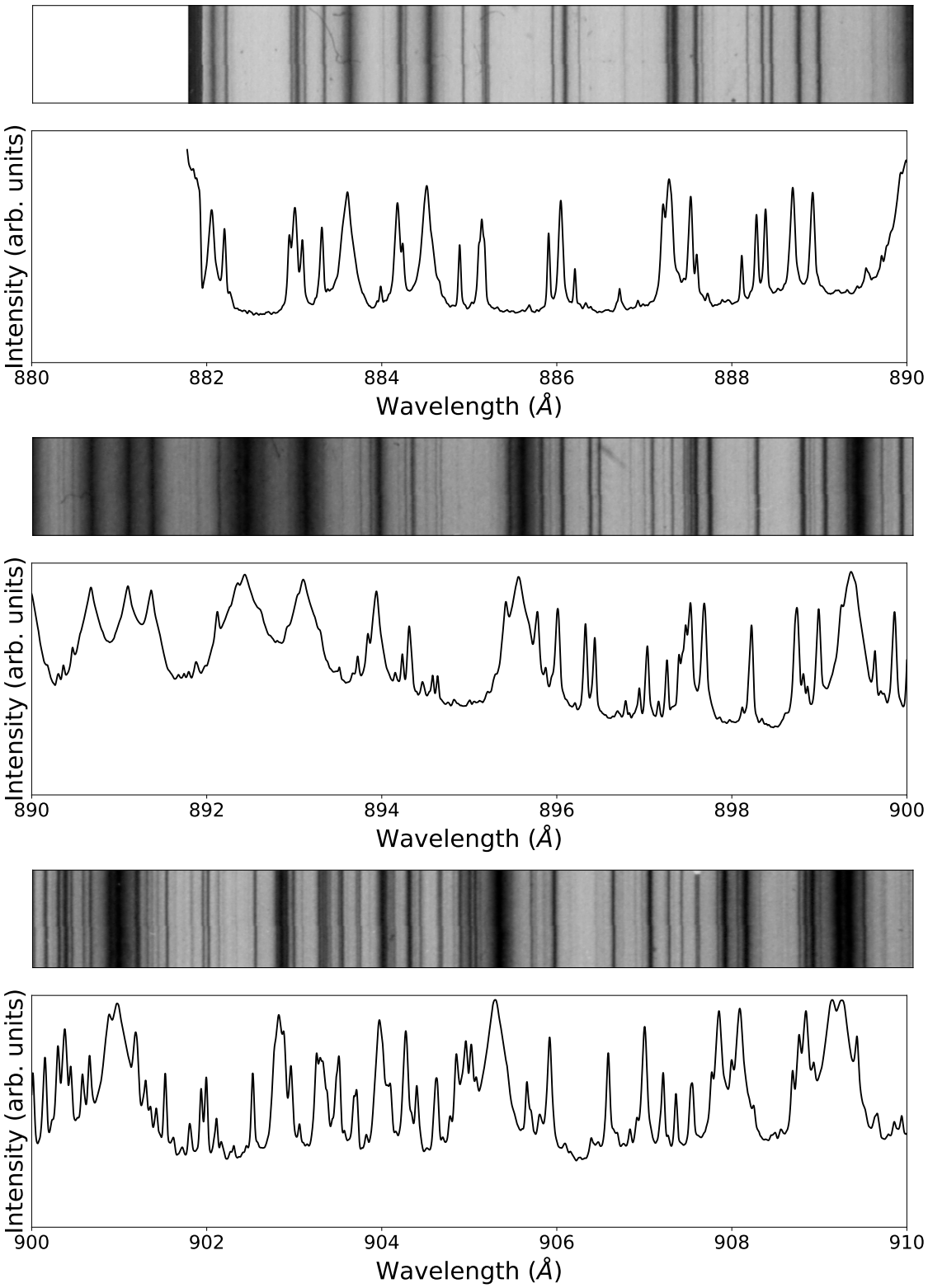


Image x1015_plate2a, Track 5.1, 45-minute exposure (continued)

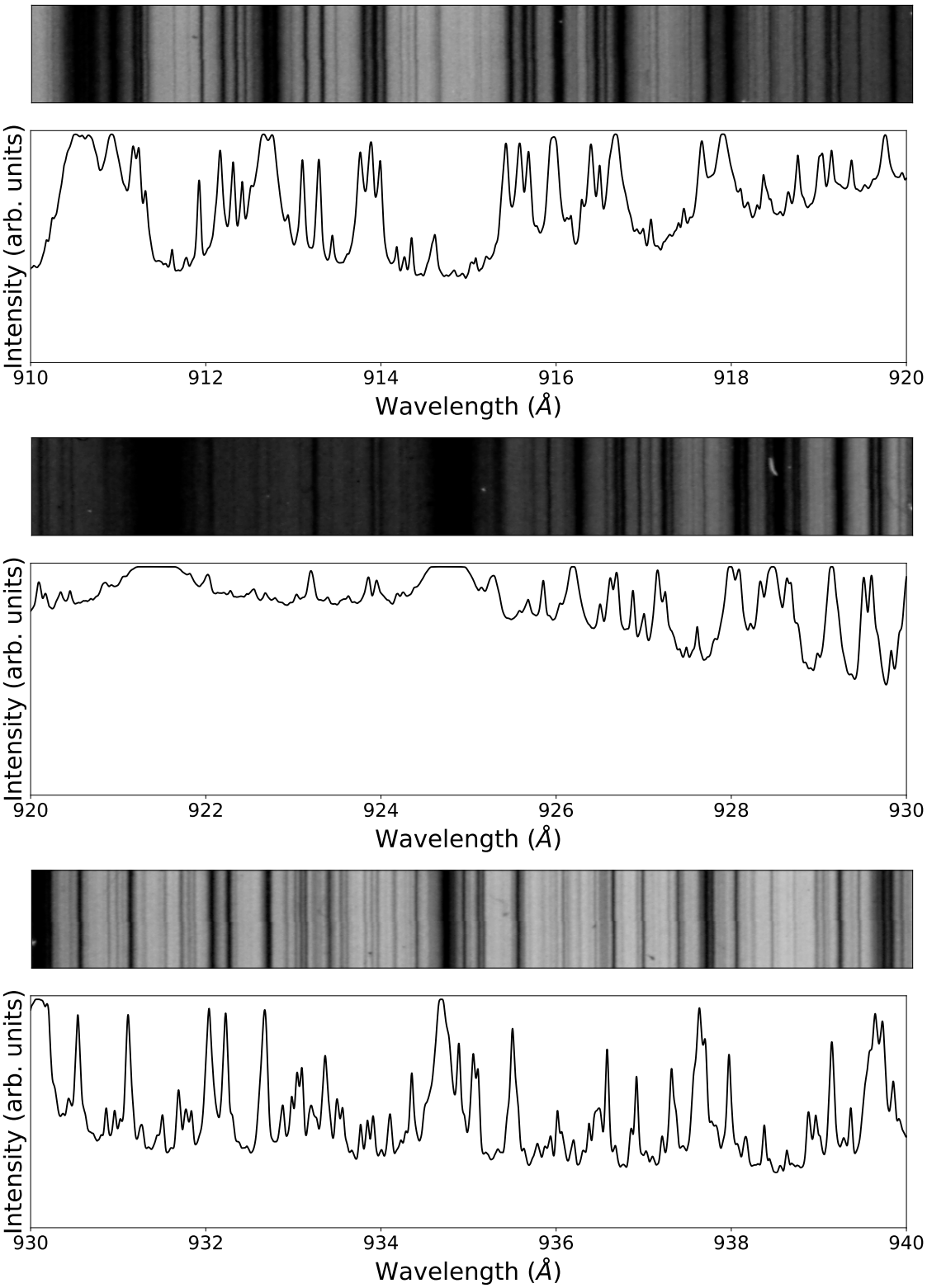


Image x1015_plate2a, Track 5.1, 45-minute exposure (continued)

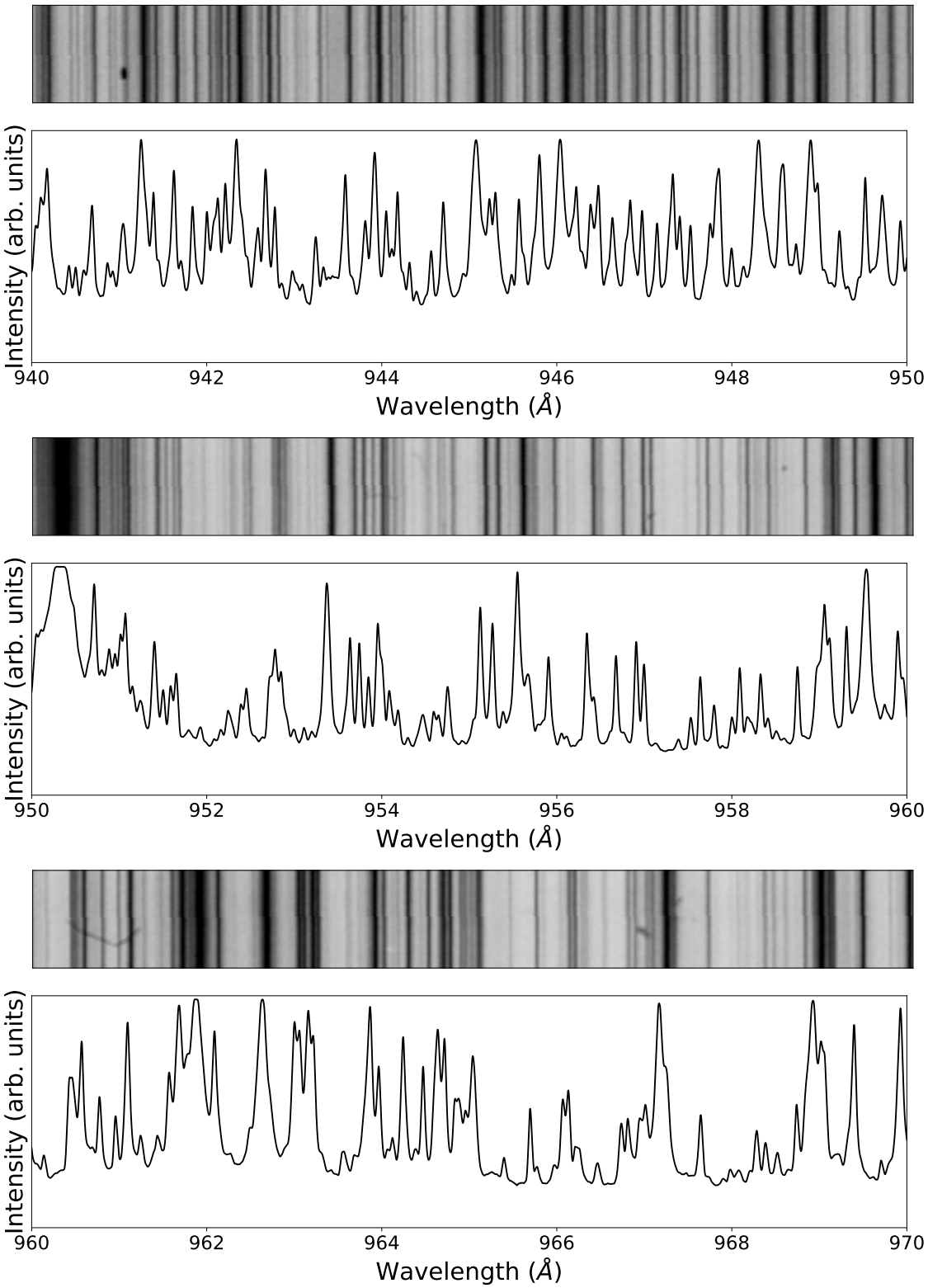


Image x1015_plate2a, Track 5.1, 45-minute exposure (continued)

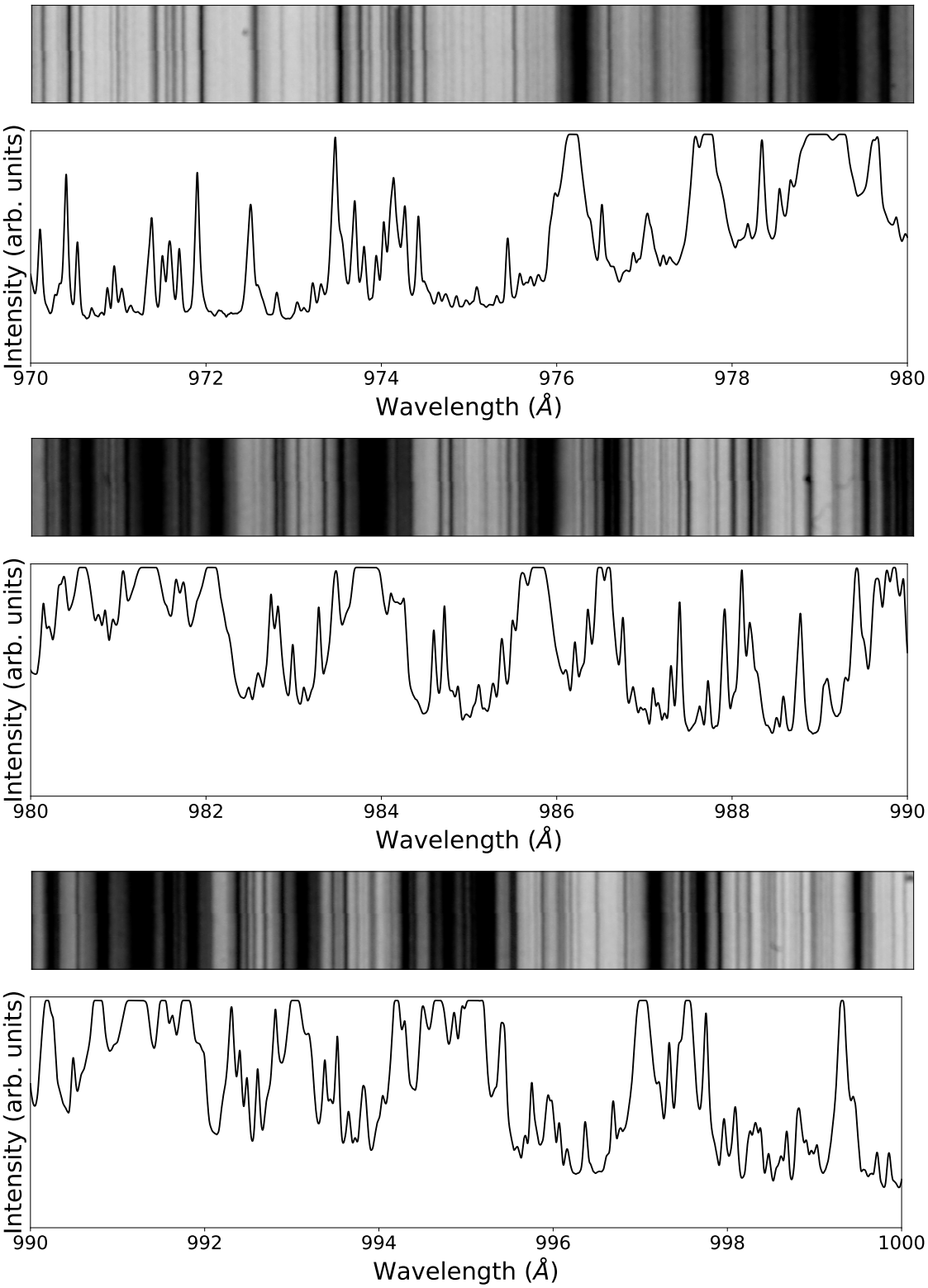


Image x1015_plate2a, Track 5.1, 45-minute exposure (continued)

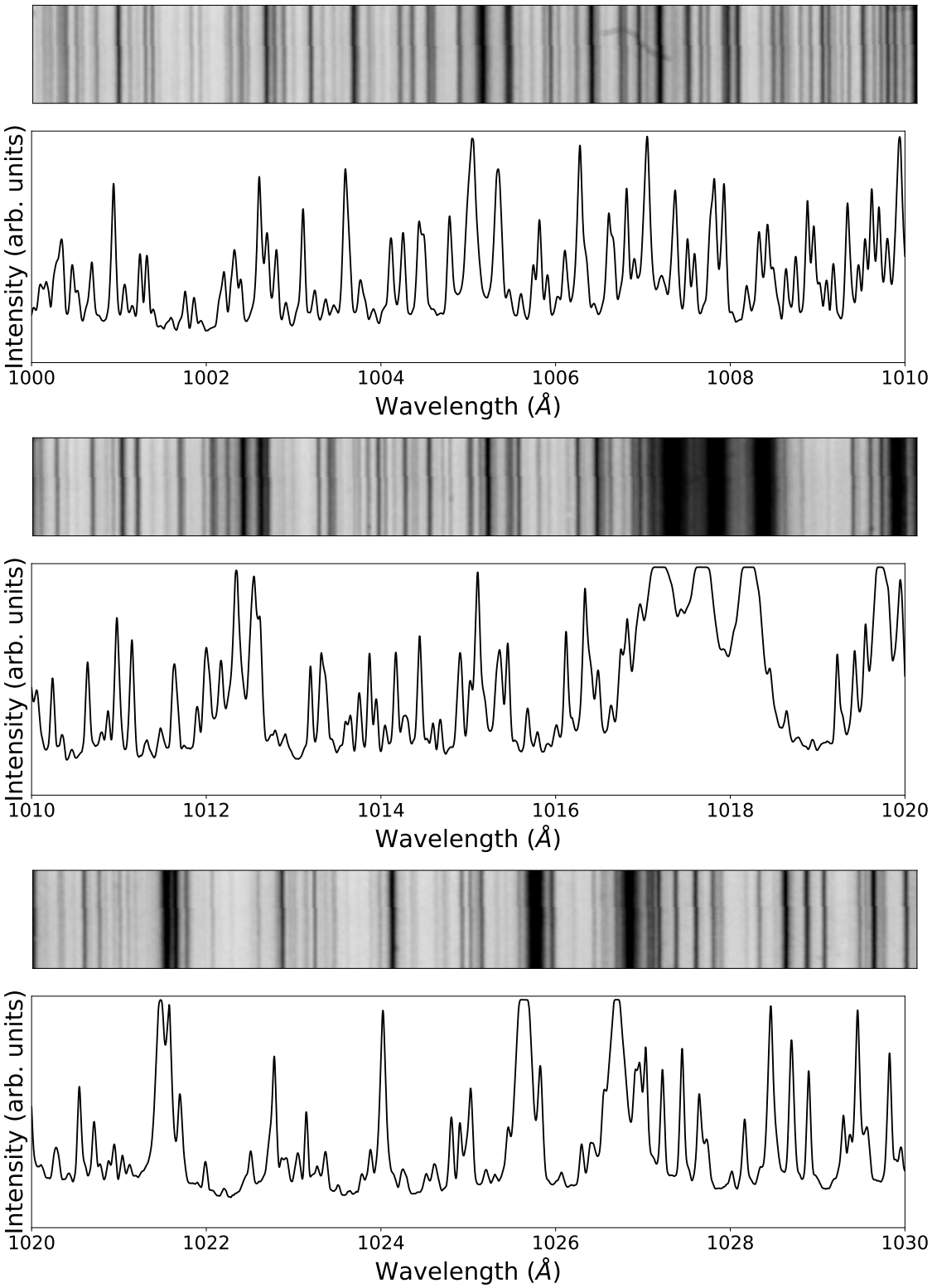


Image x1015_plate2a, Track 5.1, 45-minute exposure (continued)

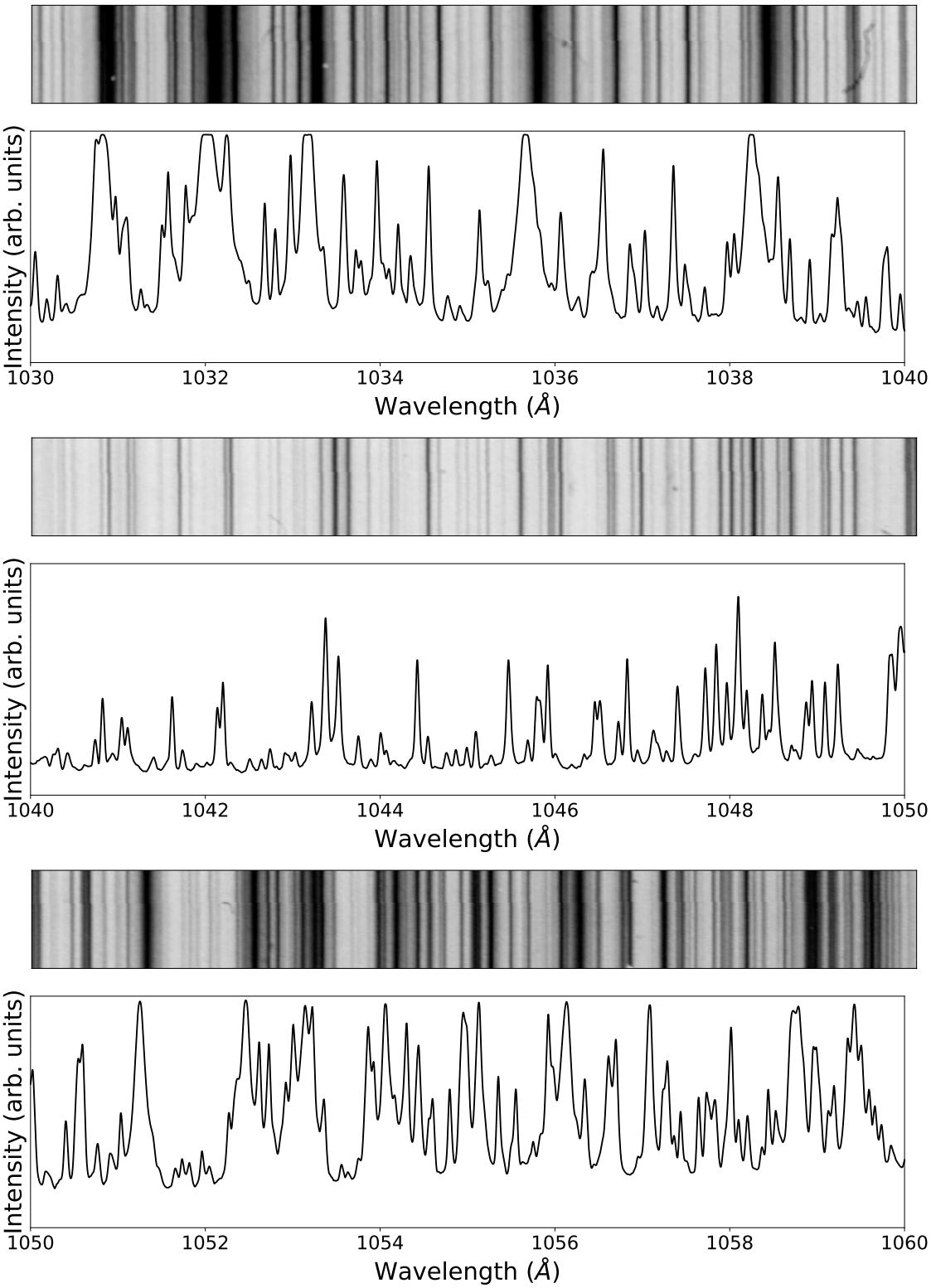


Image x1015_plate2a, Track 5.1, 45-minute exposure (continued)

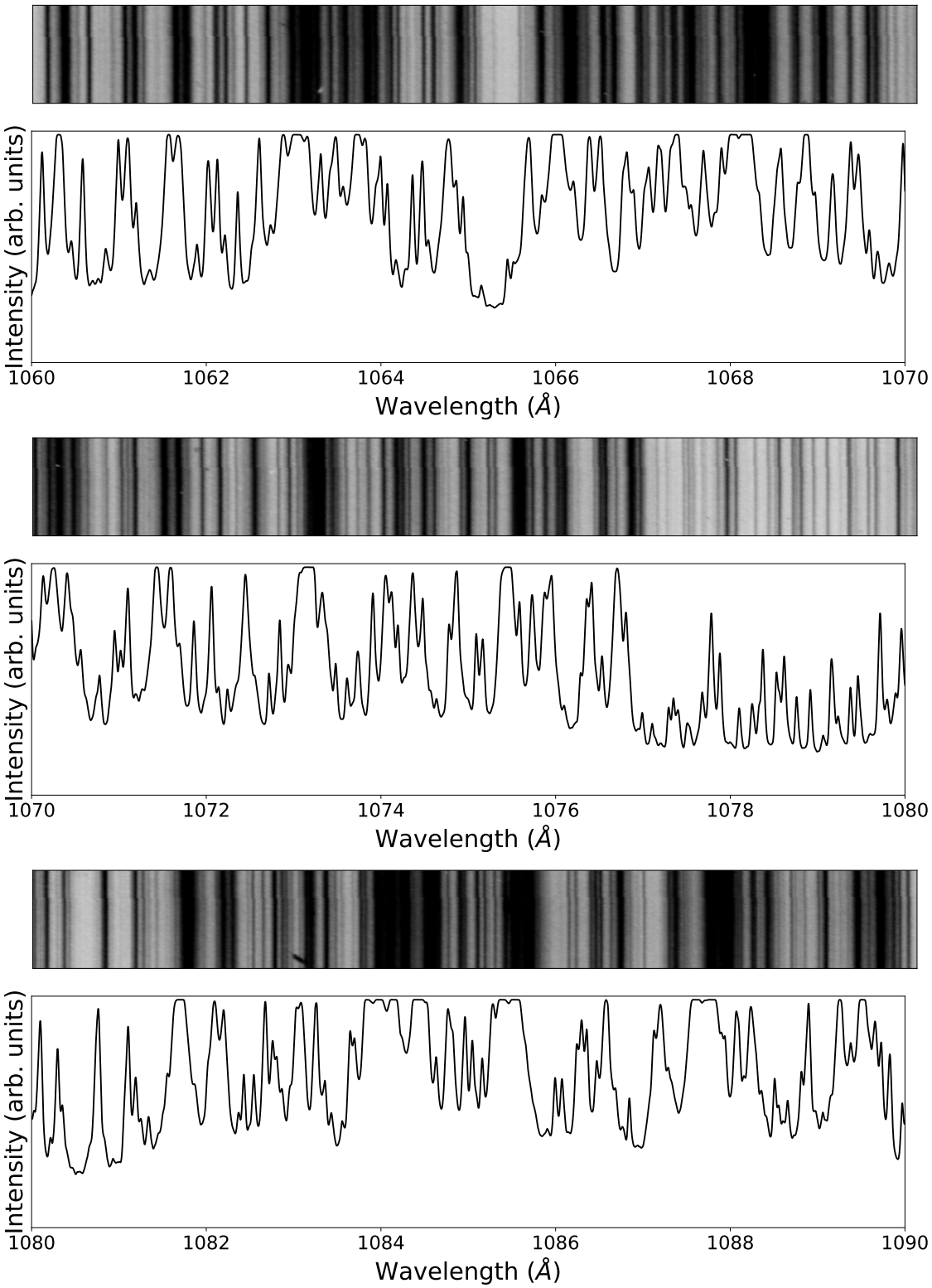
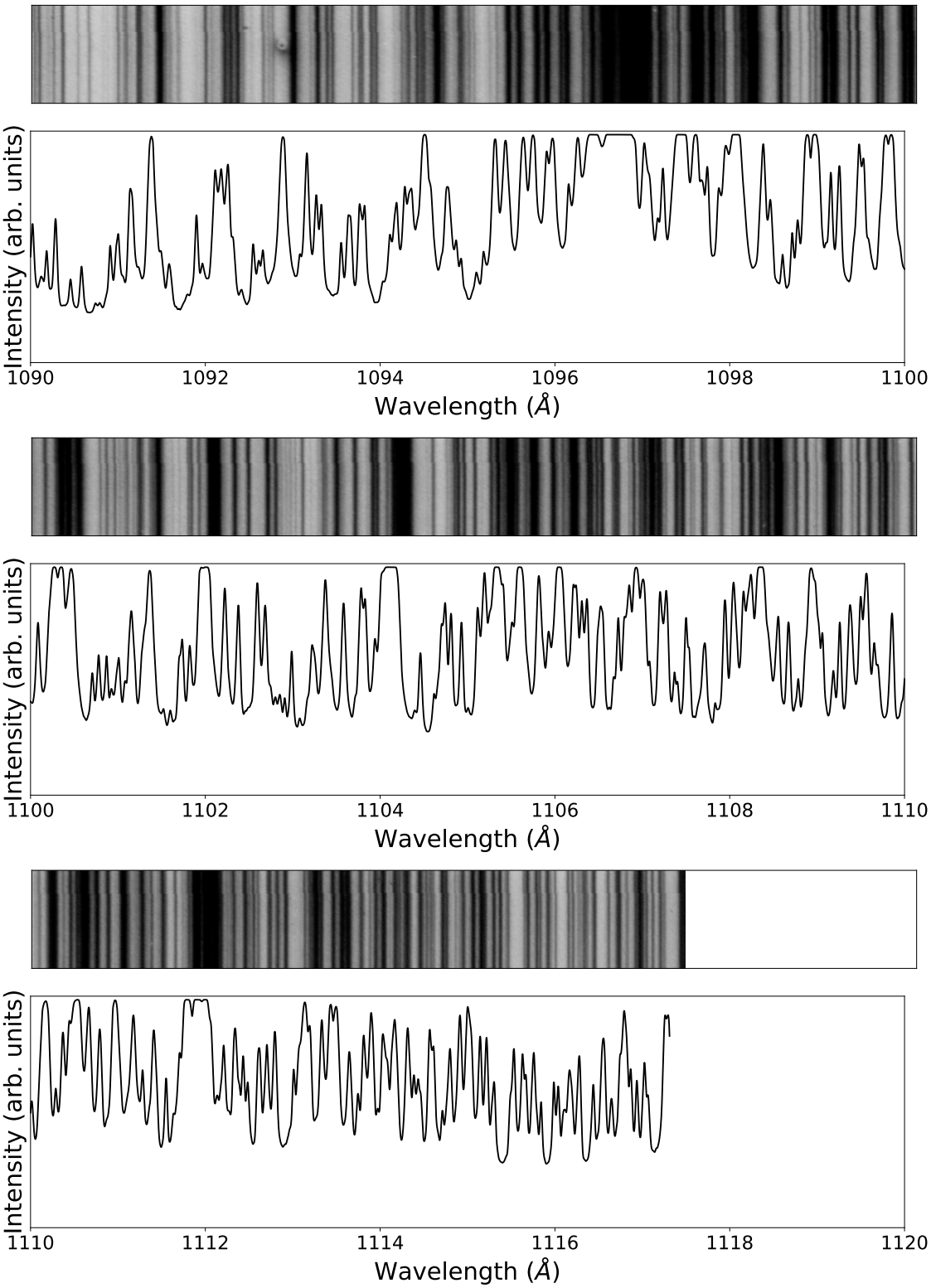


Image x1015_plate2a, Track 5.1, 45-minute exposure (continued)



F.3 Image x1015_plate2b, Track 5.1, 5-minute exposure

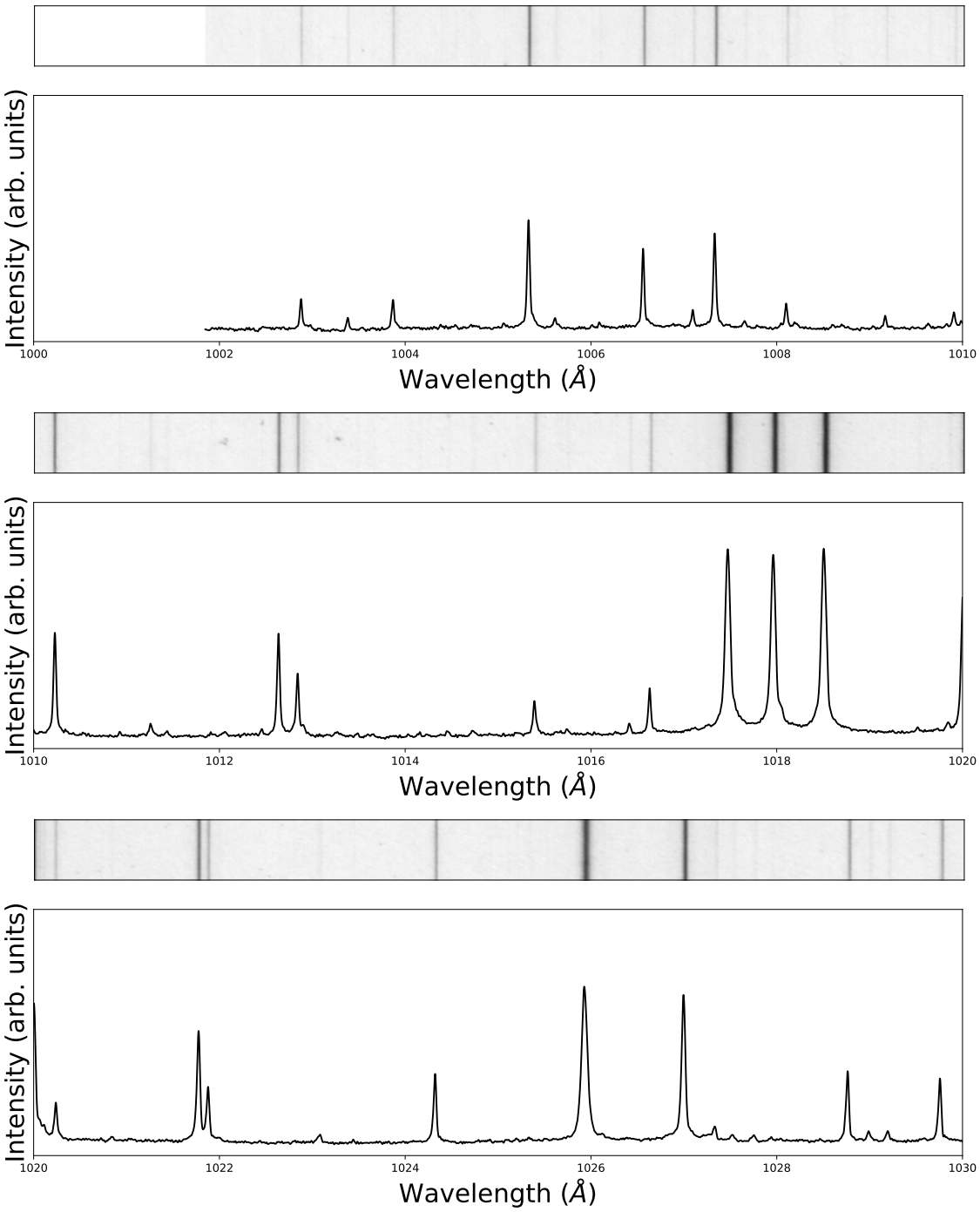


Image x1015_plate2b, Track 5.1, 5-minute exposure (continued)

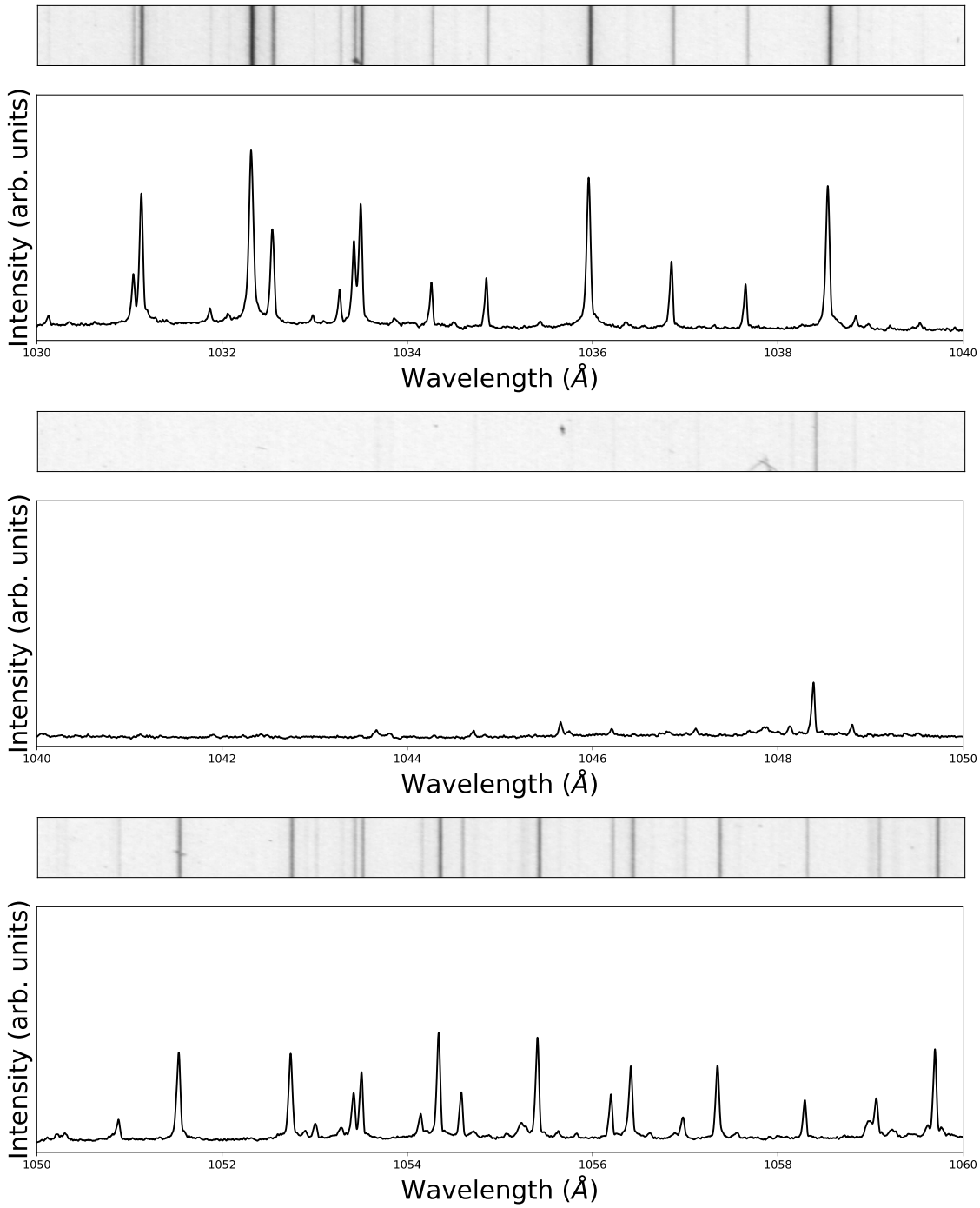


Image x1015_plate2b, Track 5.1, 5-minute exposure (continued)

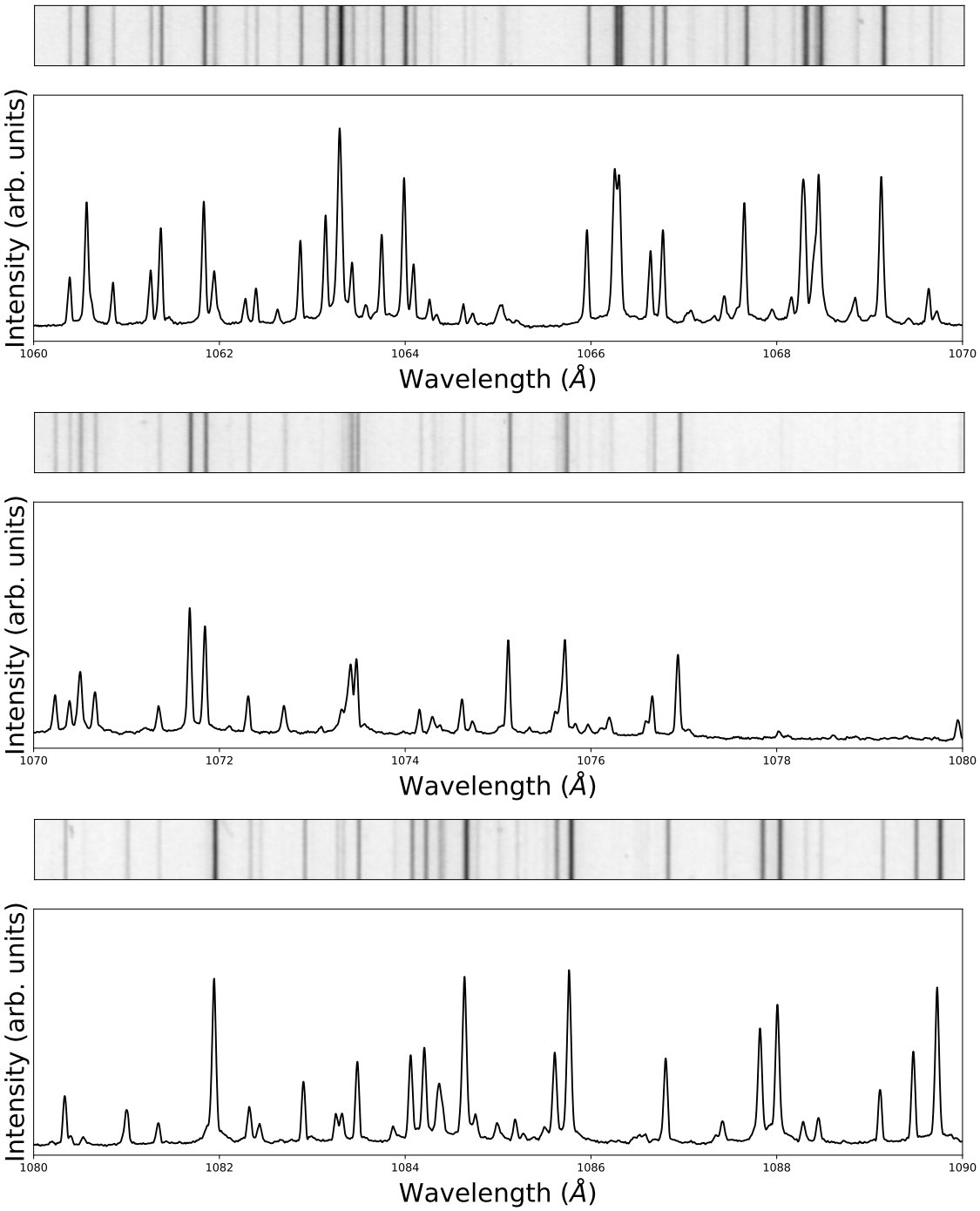


Image x1015_plate2b, Track 5.1, 5-minute exposure (continued)

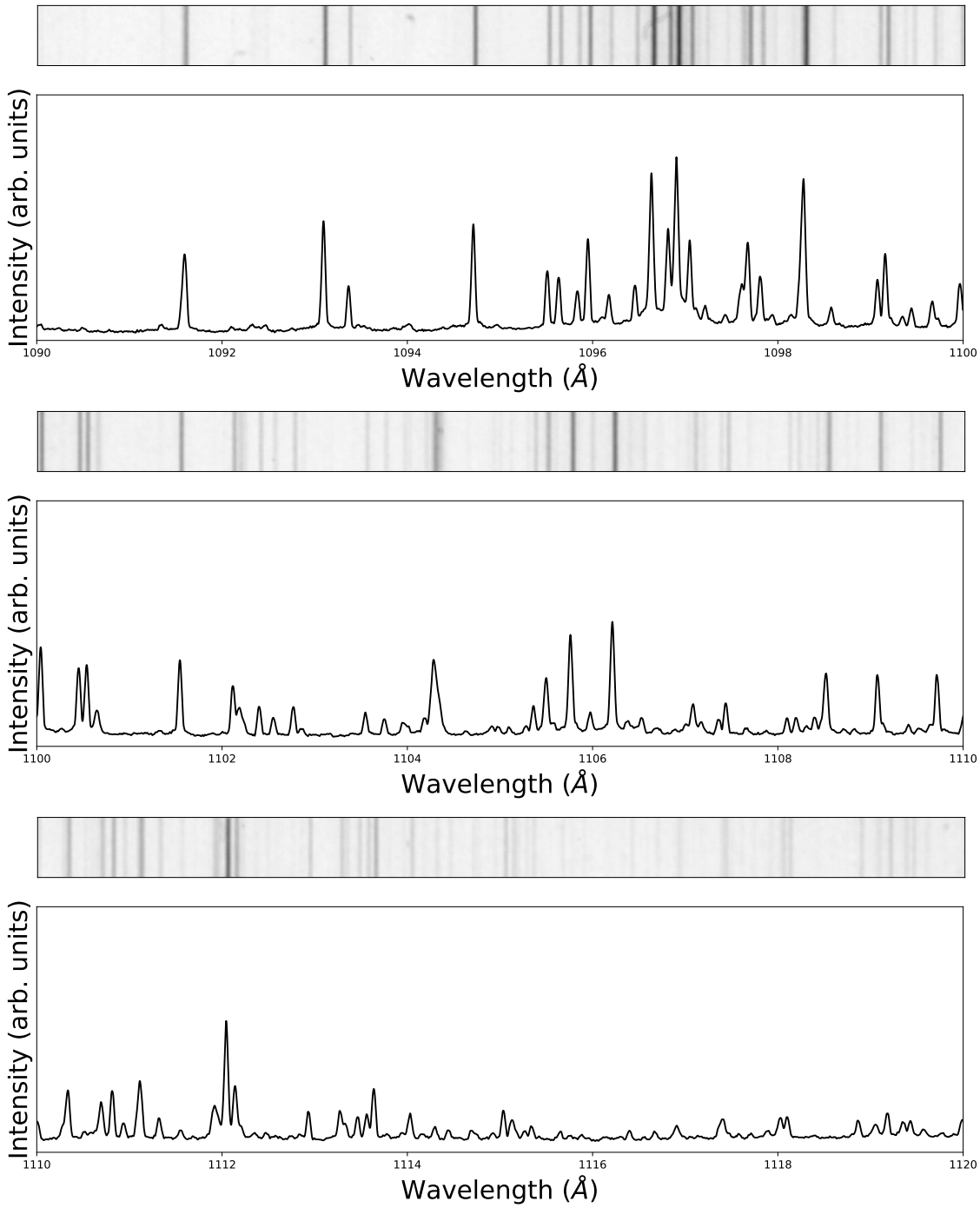


Image x1015_plate2b, Track 5.1, 5-minute exposure (continued)

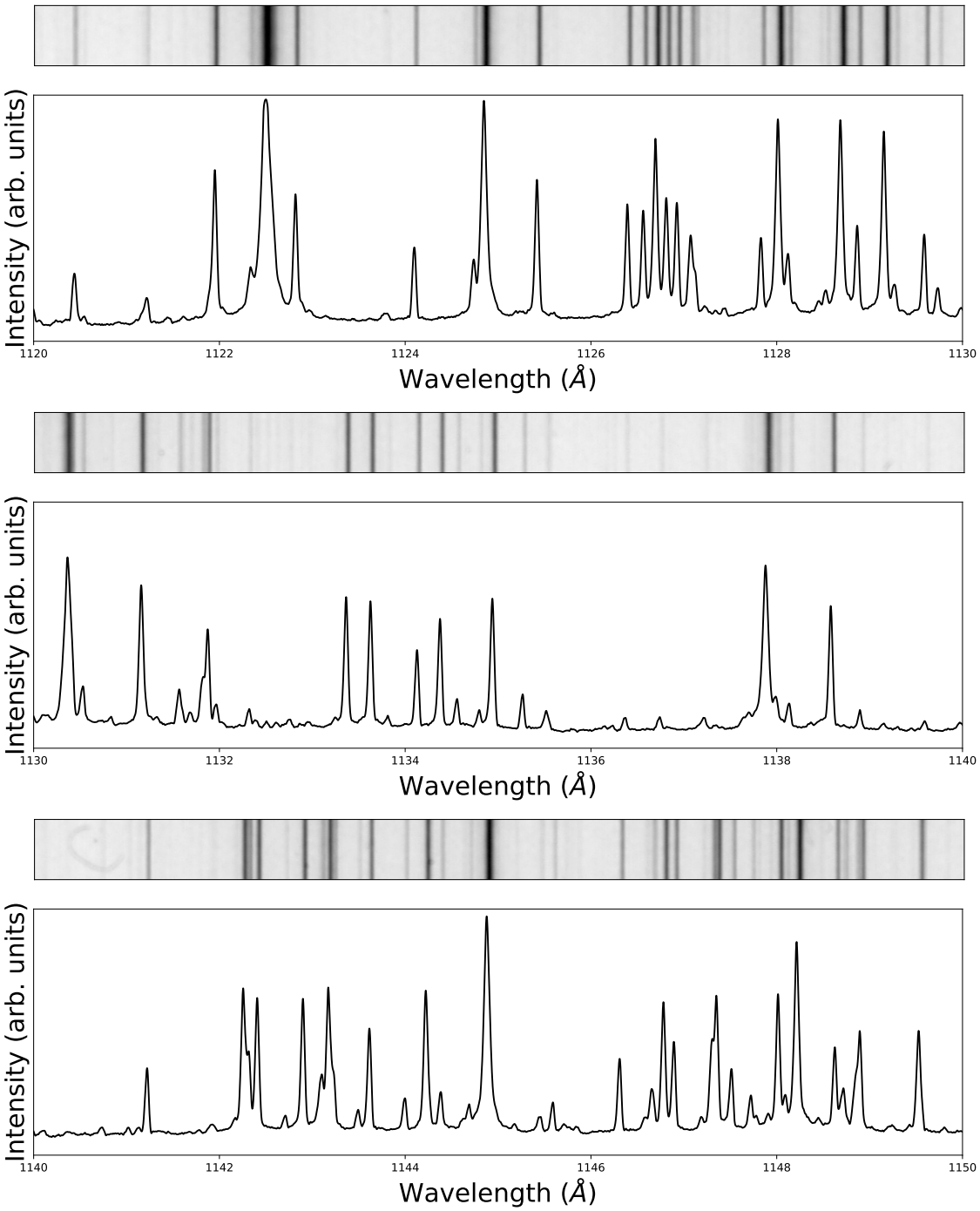


Image x1015_plate2b, Track 5.1, 5-minute exposure (continued)

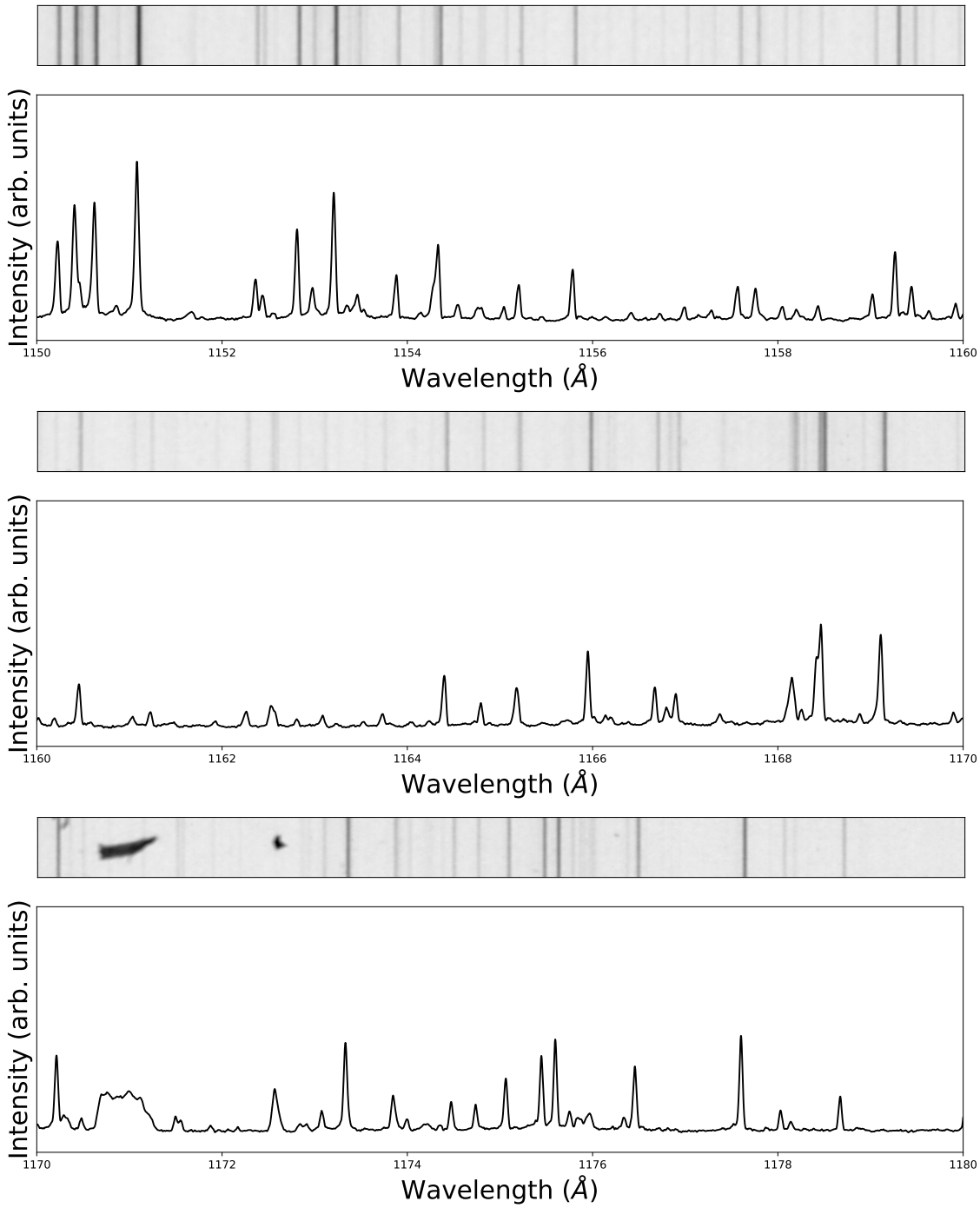


Image x1015_plate2b, Track 5.1, 5-minute exposure (continued)

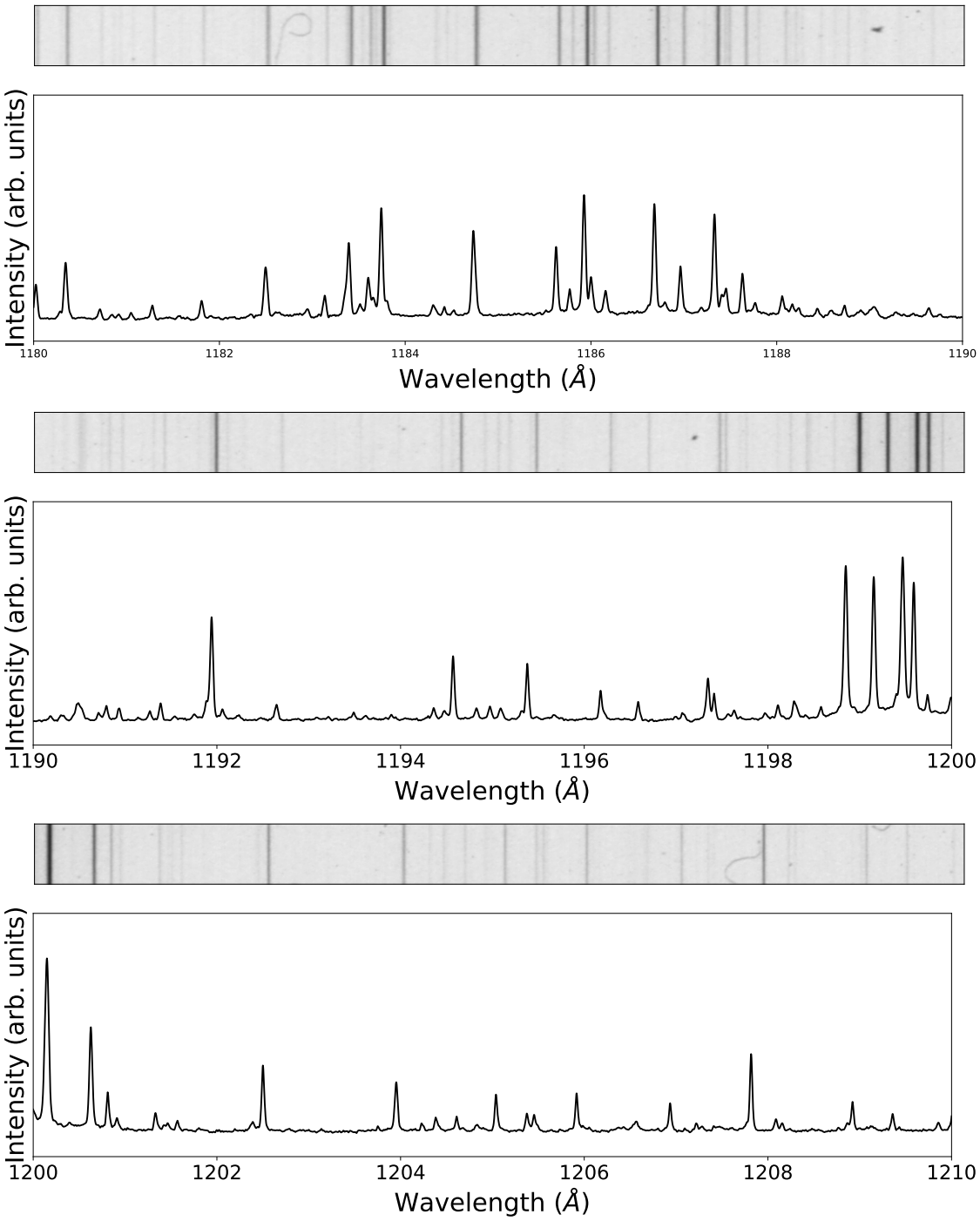
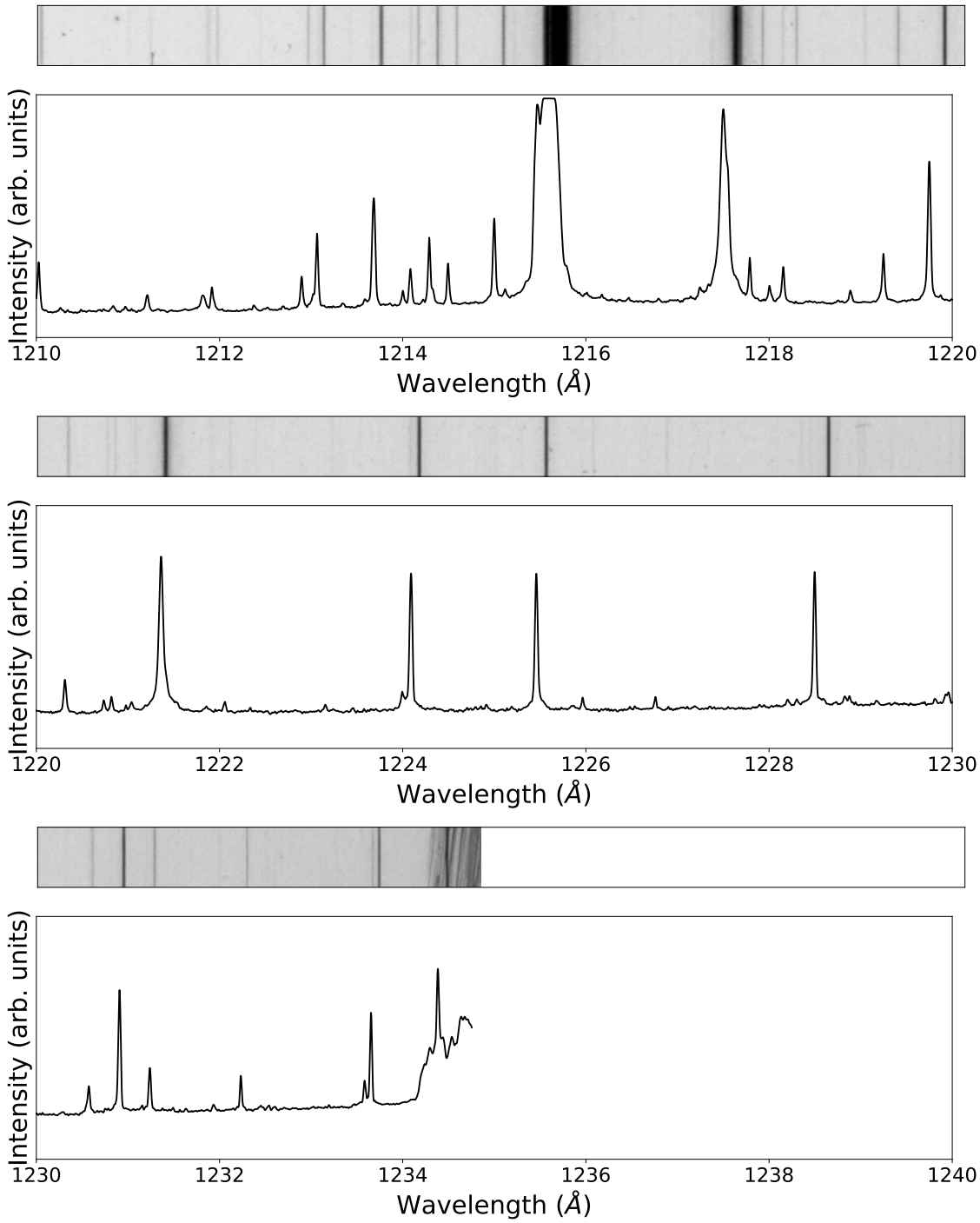


Image x1015_plate2b, Track 5.1, 5-minute exposure (continued)



F.4 Image x1015_plate2b, Track 5.1, 45-minute exposure

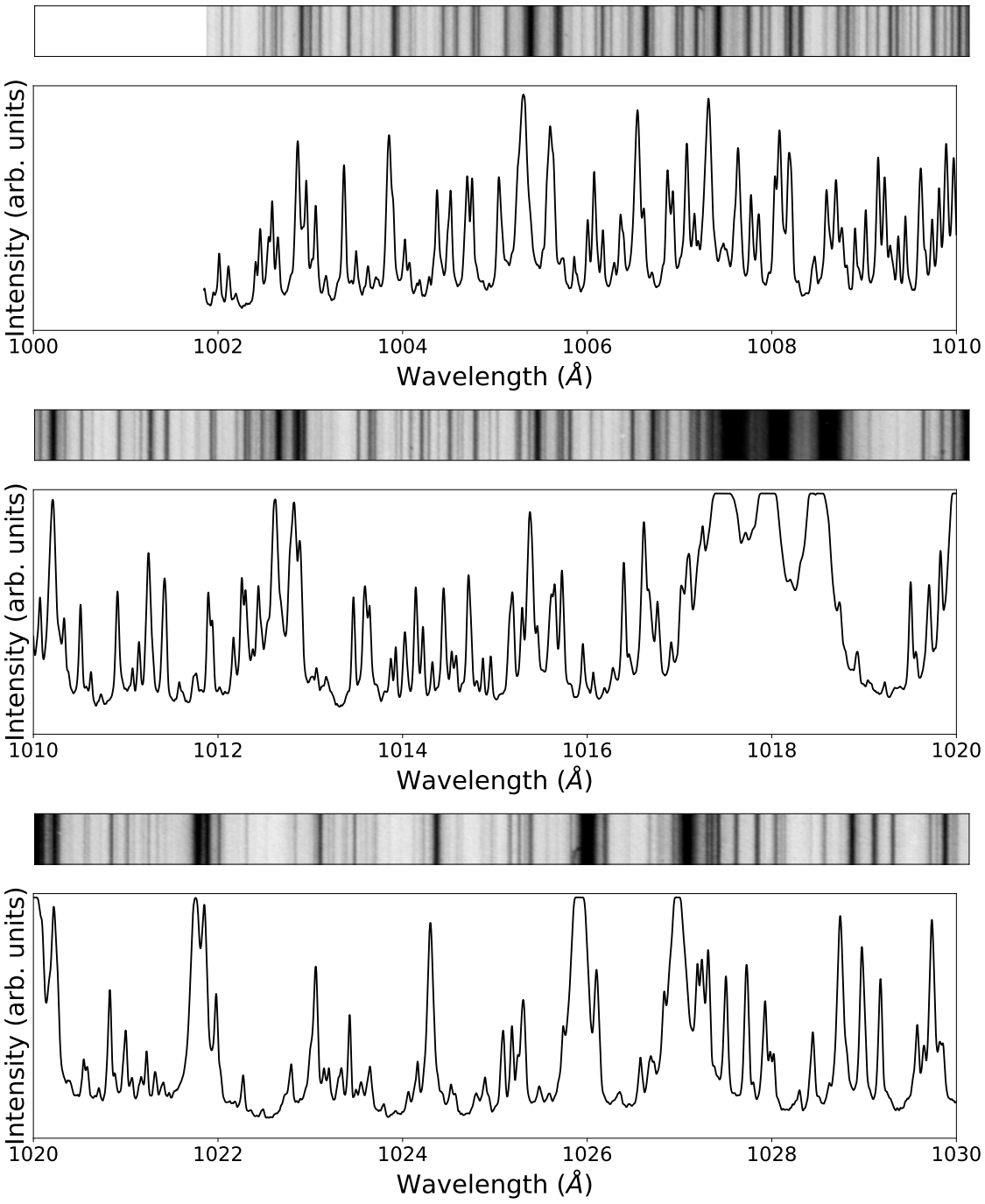


Image x1015_plate2b, Track 5.1, 45-minute exposure (continued)

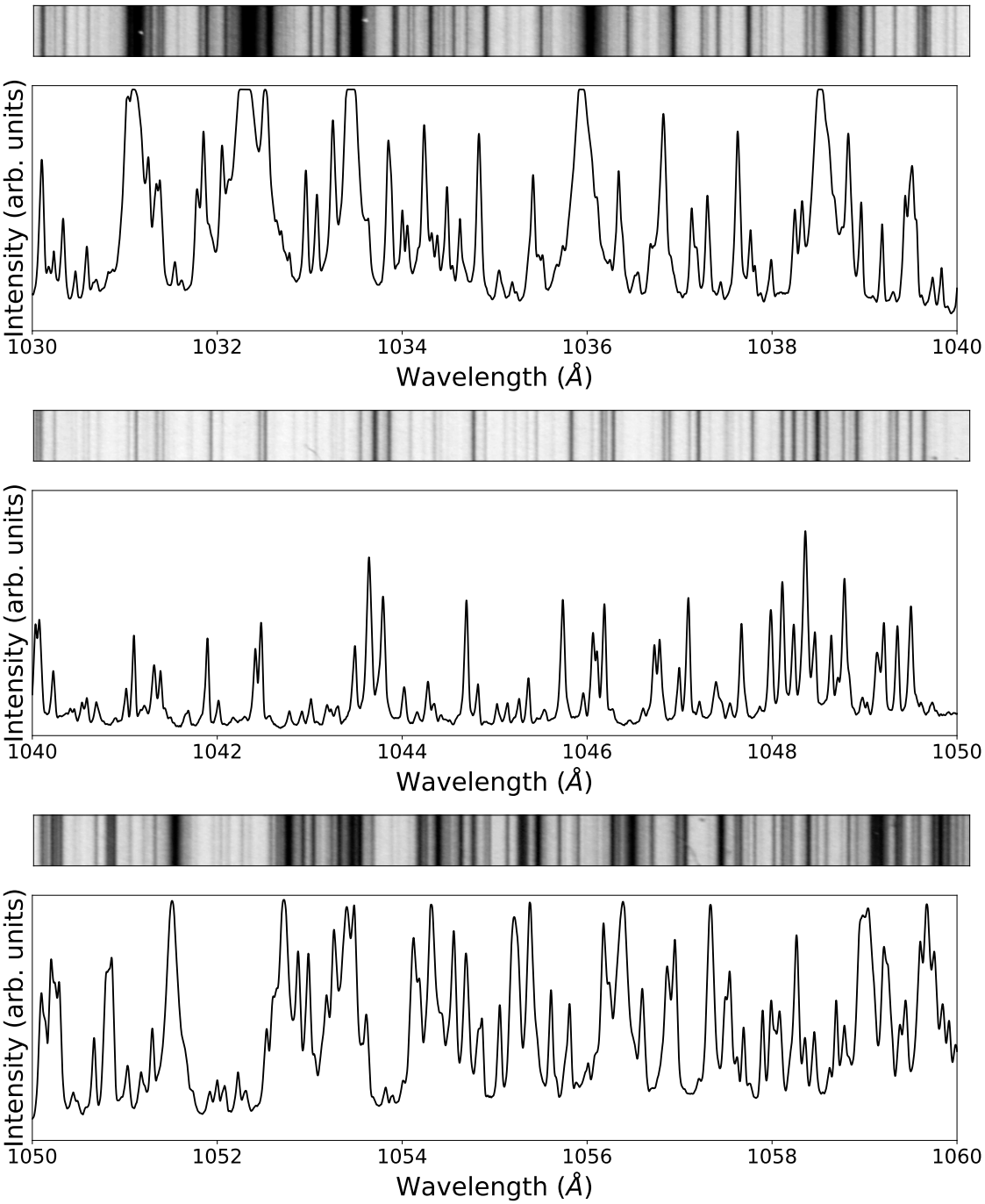


Image x1015_plate2b, Track 5.1, 45-minute exposure (continued)

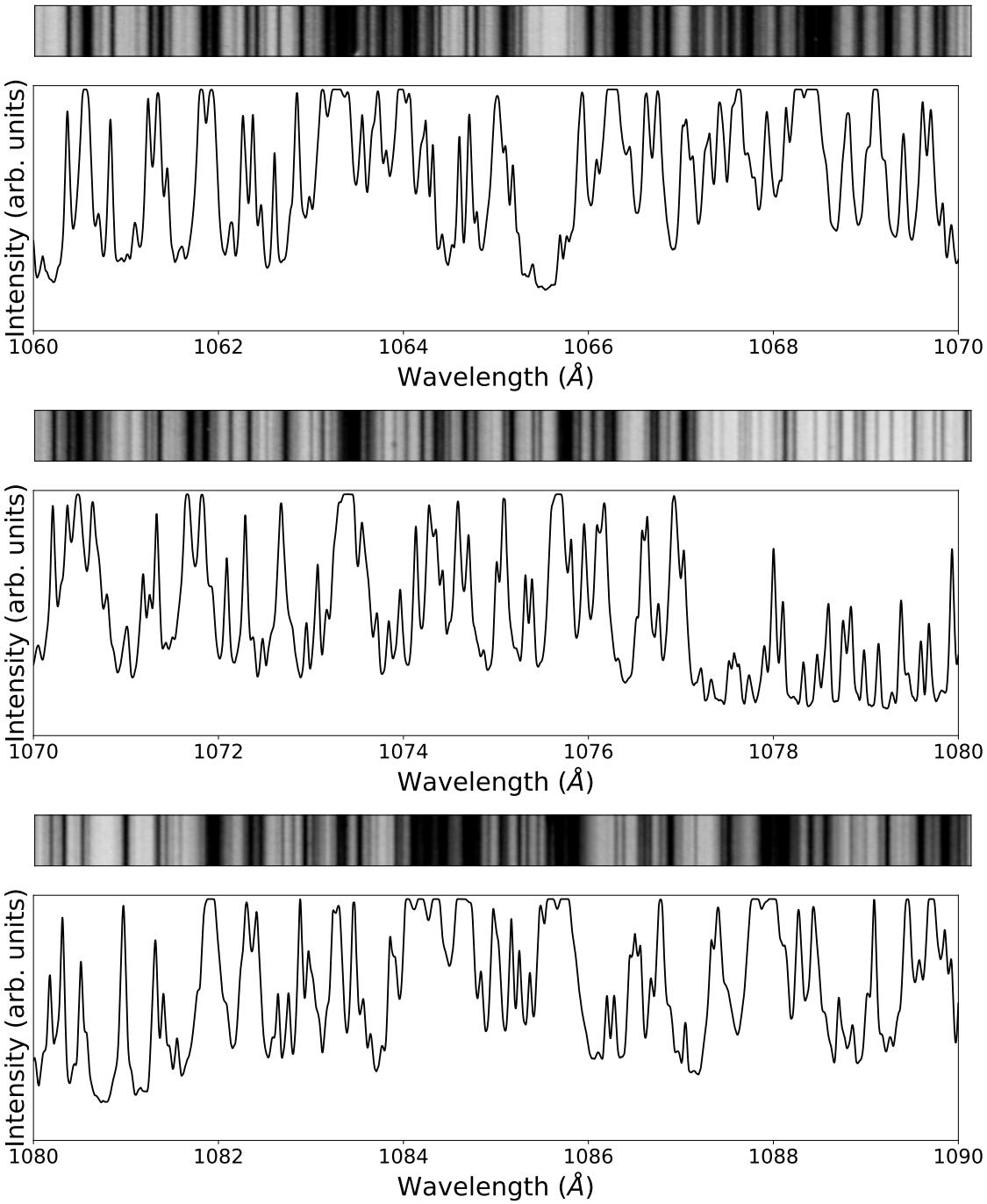


Image x1015_plate2b, Track 5.1, 45-minute exposure (continued)

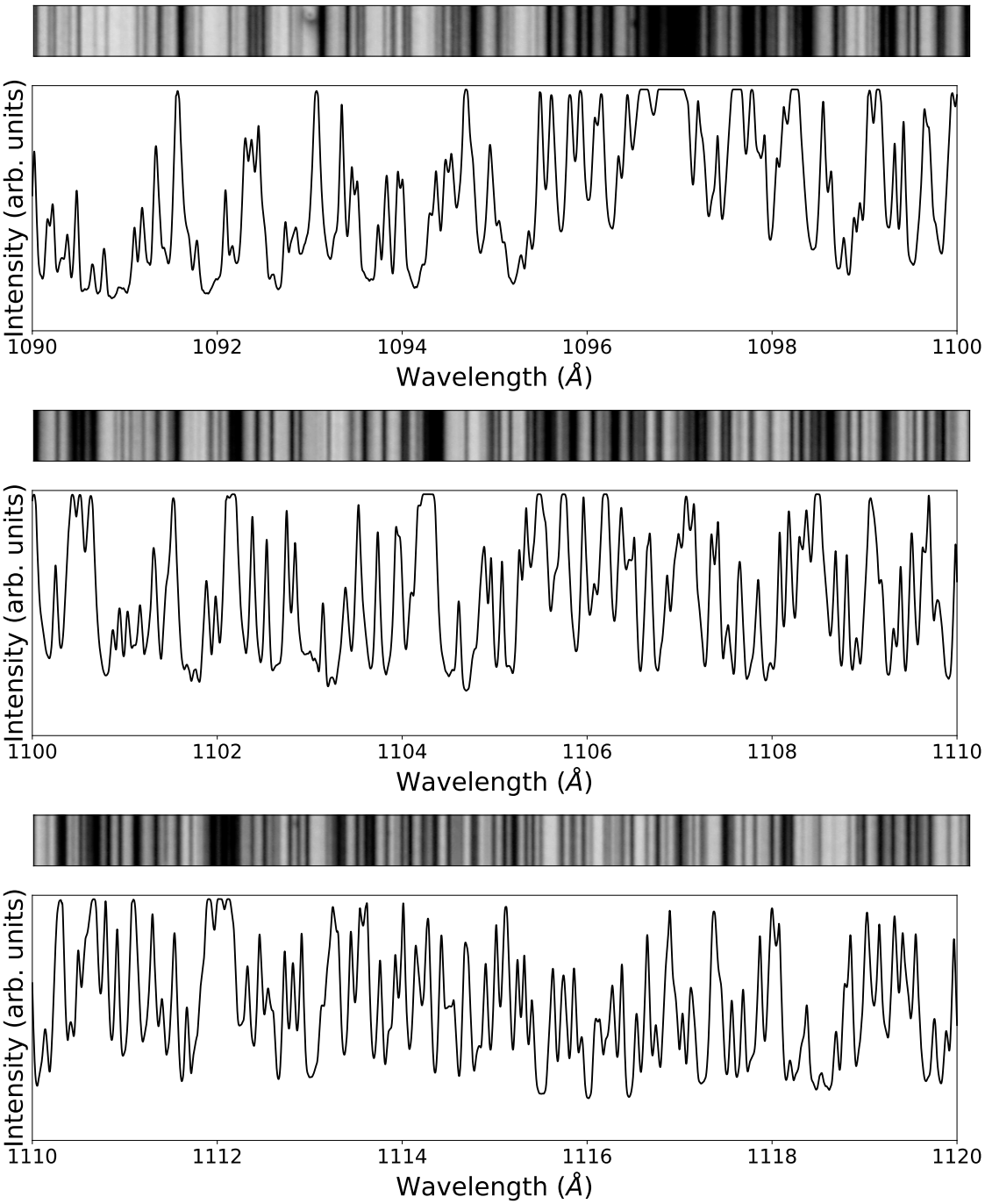


Image x1015_plate2b, Track 5.1, 45-minute exposure (continued)

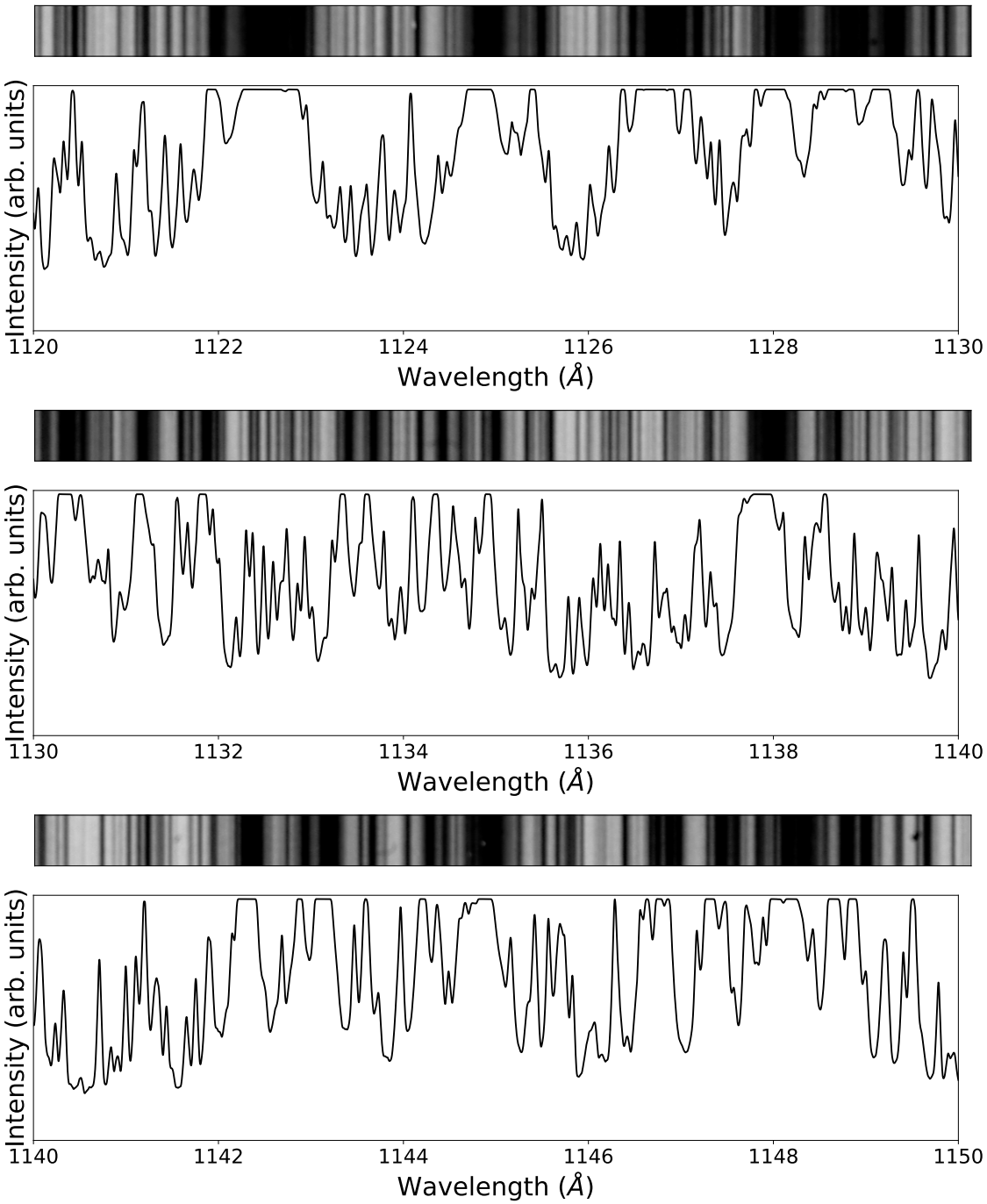


Image x1015_plate2b, Track 5.1, 45-minute exposure (continued)

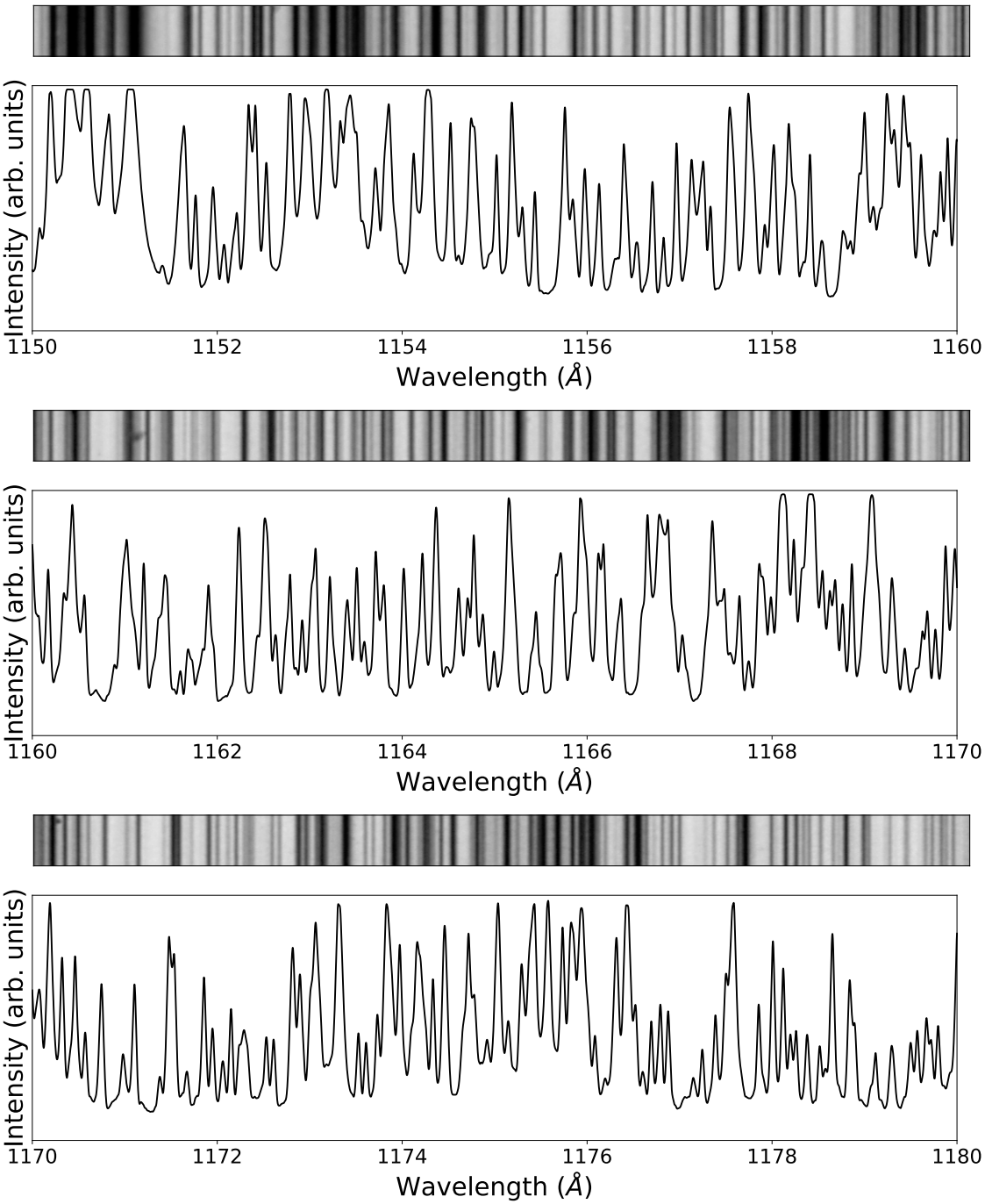


Image x1015_plate2b, Track 5.1, 45-minute exposure (continued)

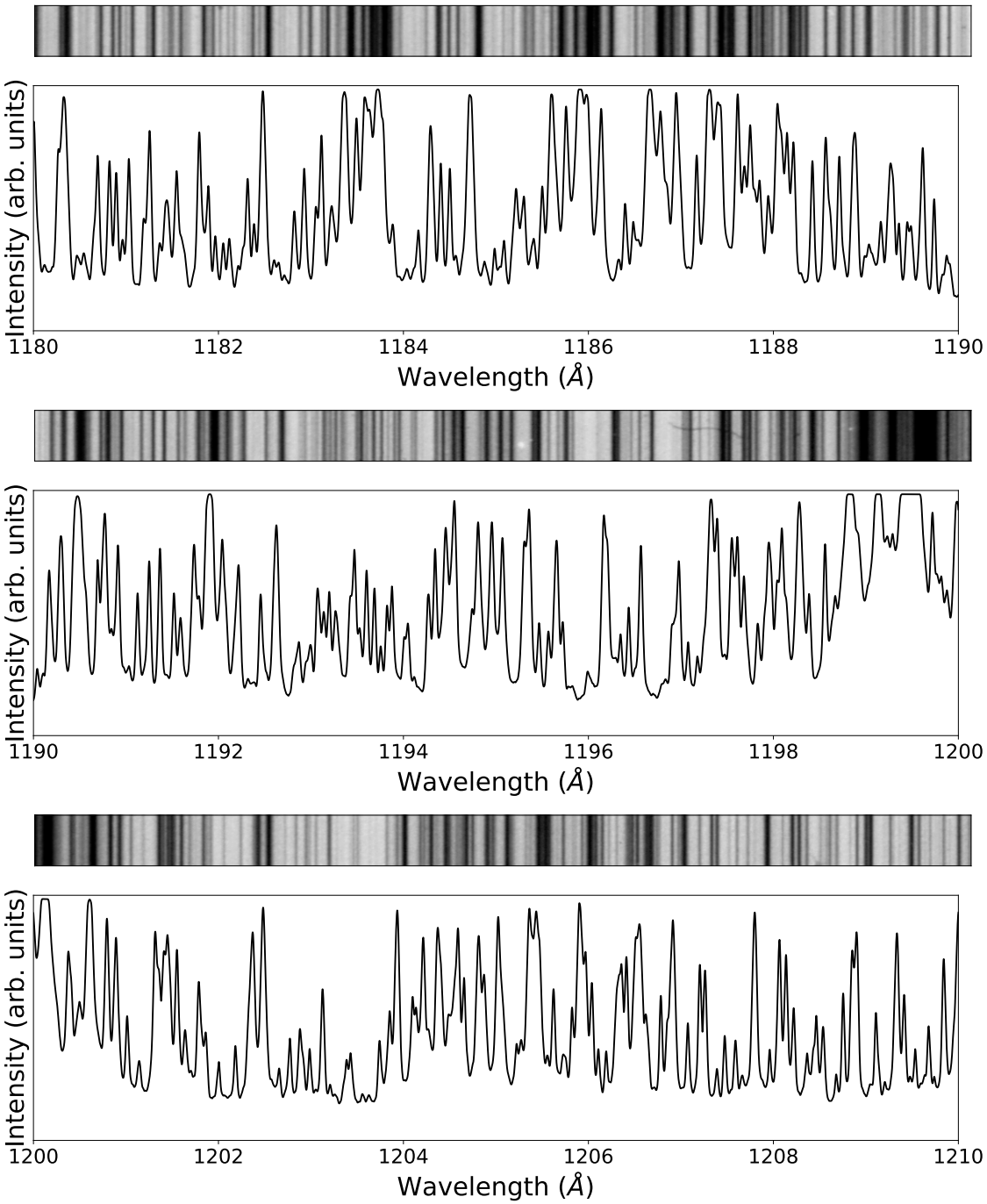
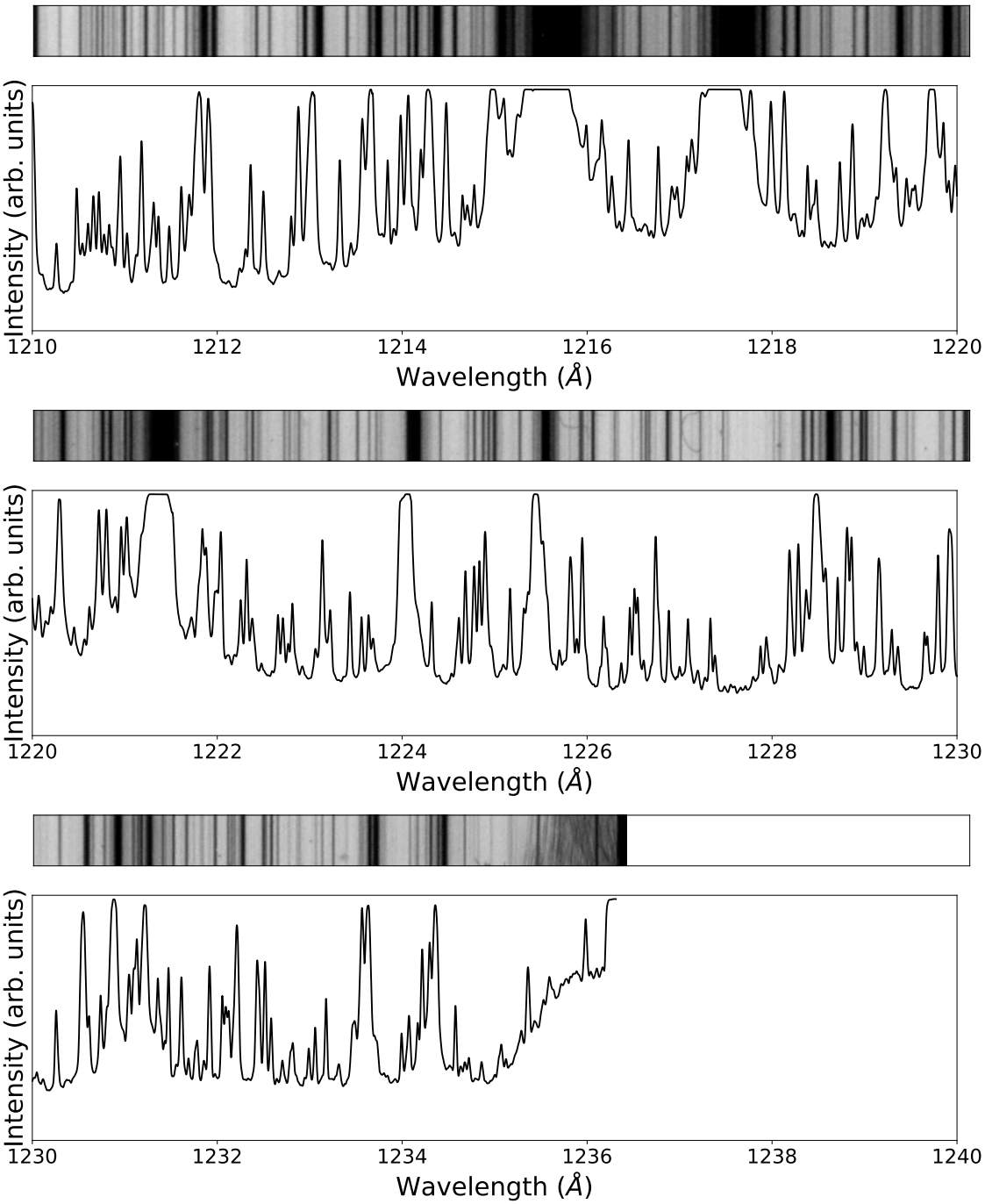


Image x1015_plate2b, Track 5.1, 45-minute exposure (continued)



F.5 Image x1015_plate1b, Track 5.3, 5-minute exposure

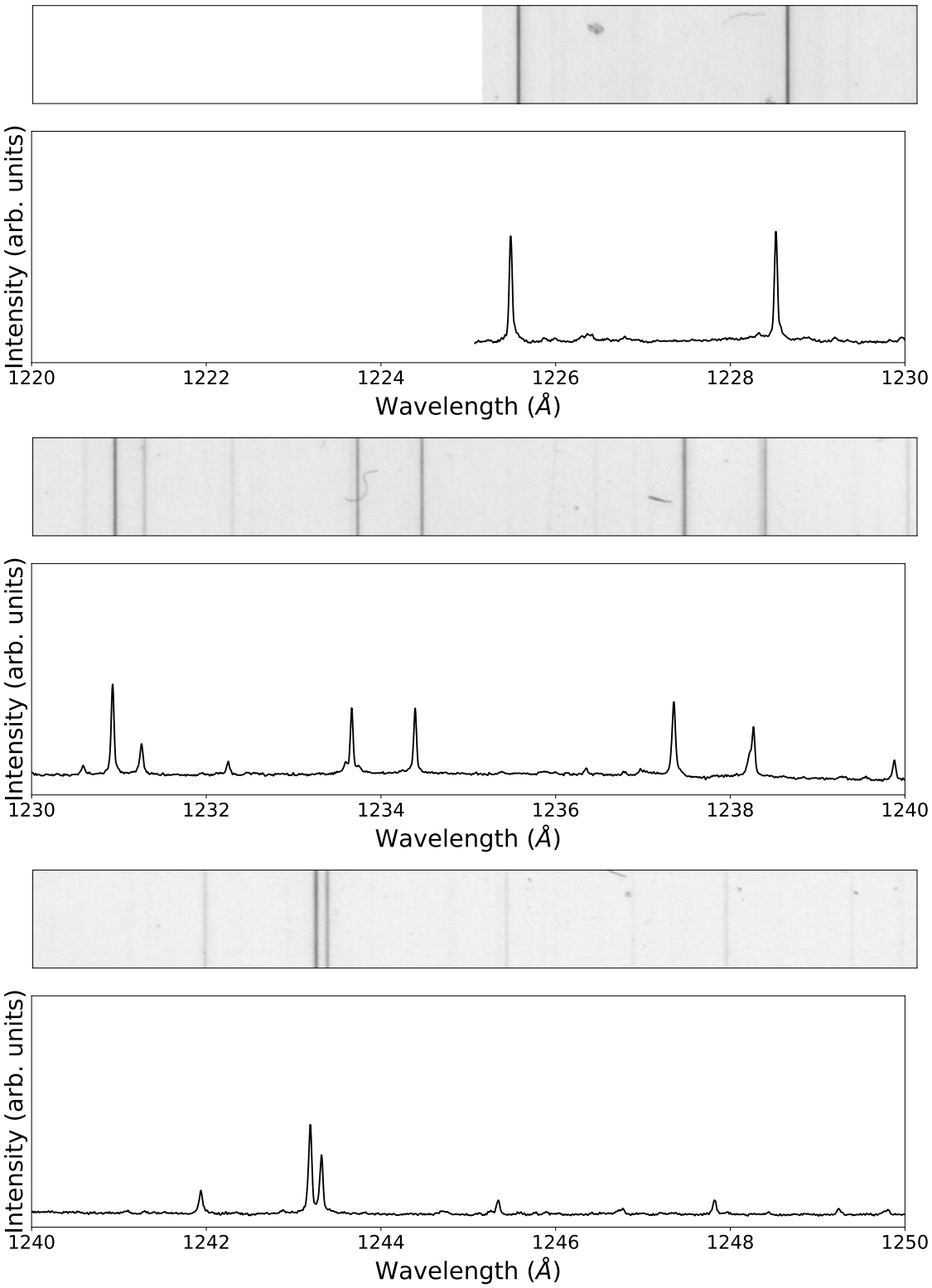


Image x1015_plate1b, Track 5.3, 5-minute exposure (continued)

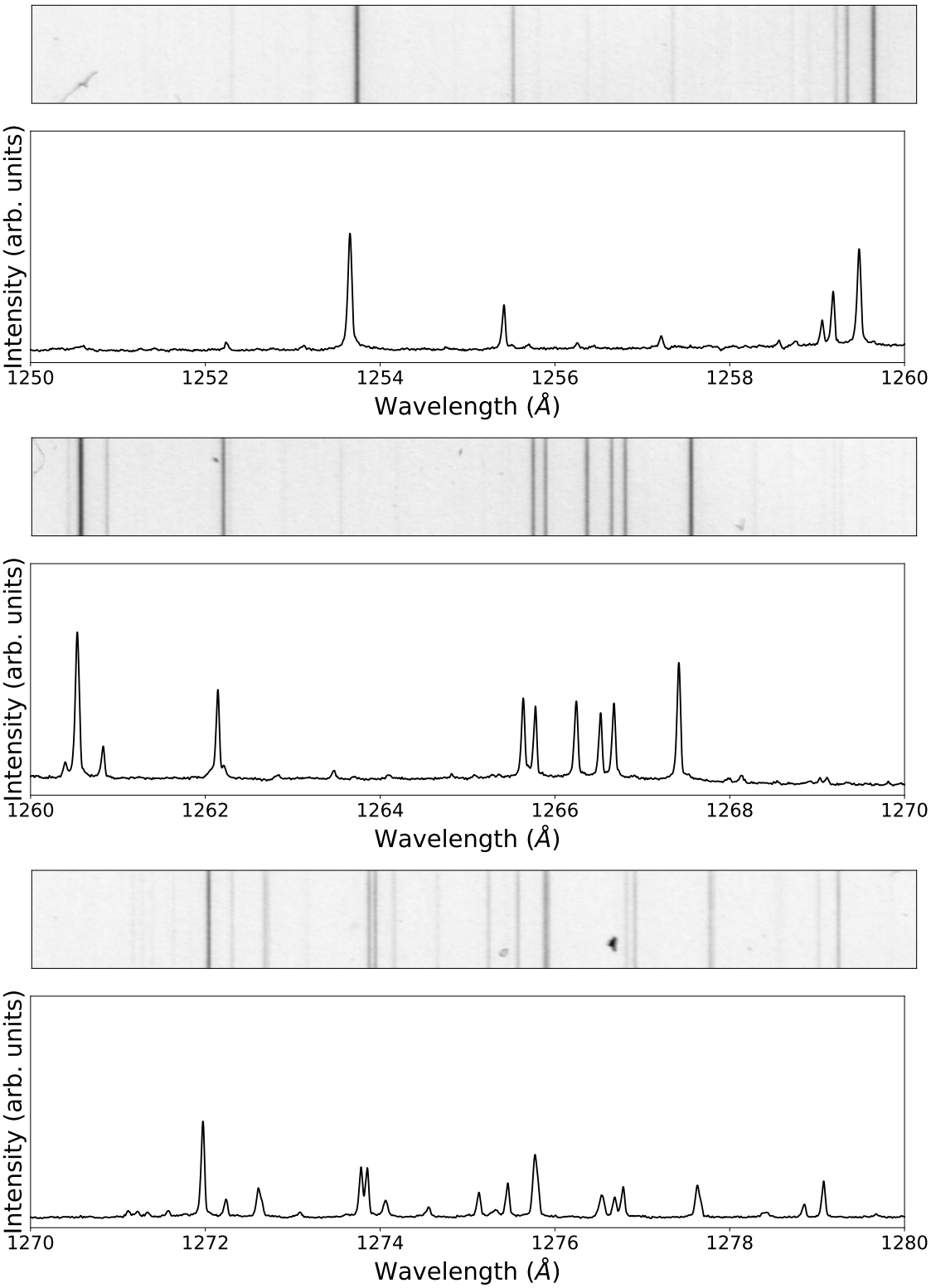


Image x1015_plate1b, Track 5.3, 5-minute exposure (continued)

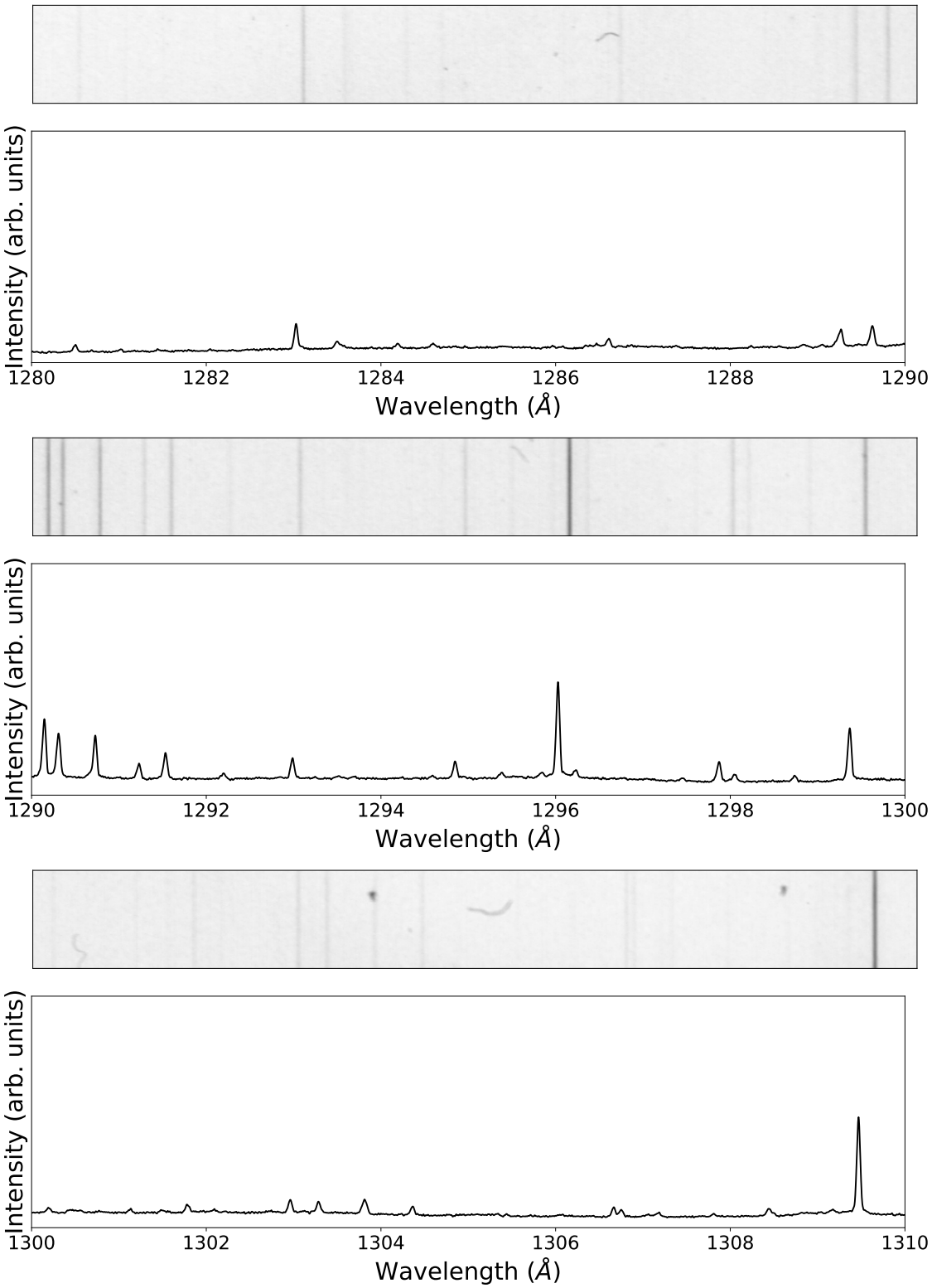


Image x1015_plate1b, Track 5.3, 5-minute exposure (continued)

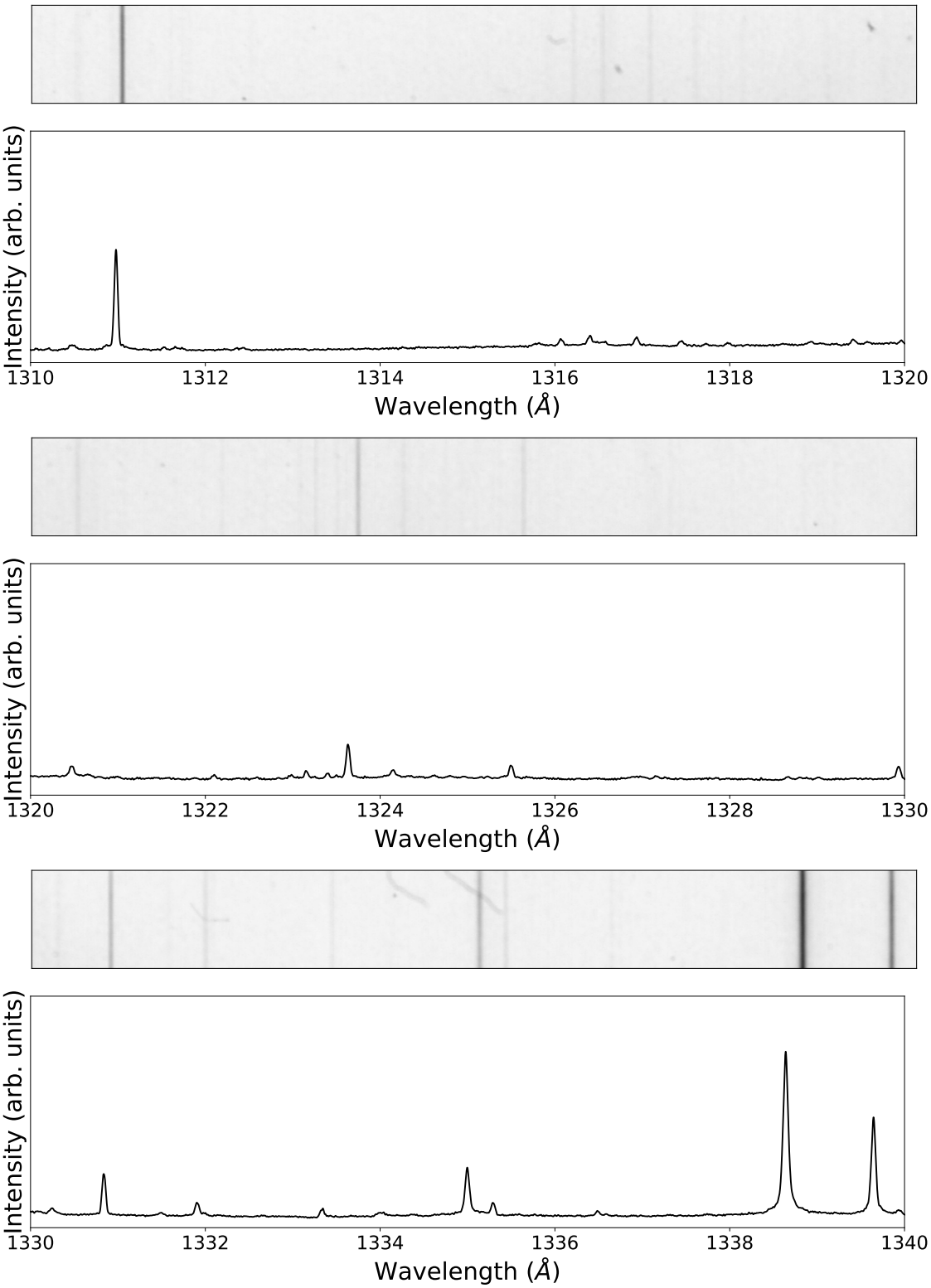


Image x1015_plate1b, Track 5.3, 5-minute exposure (continued)

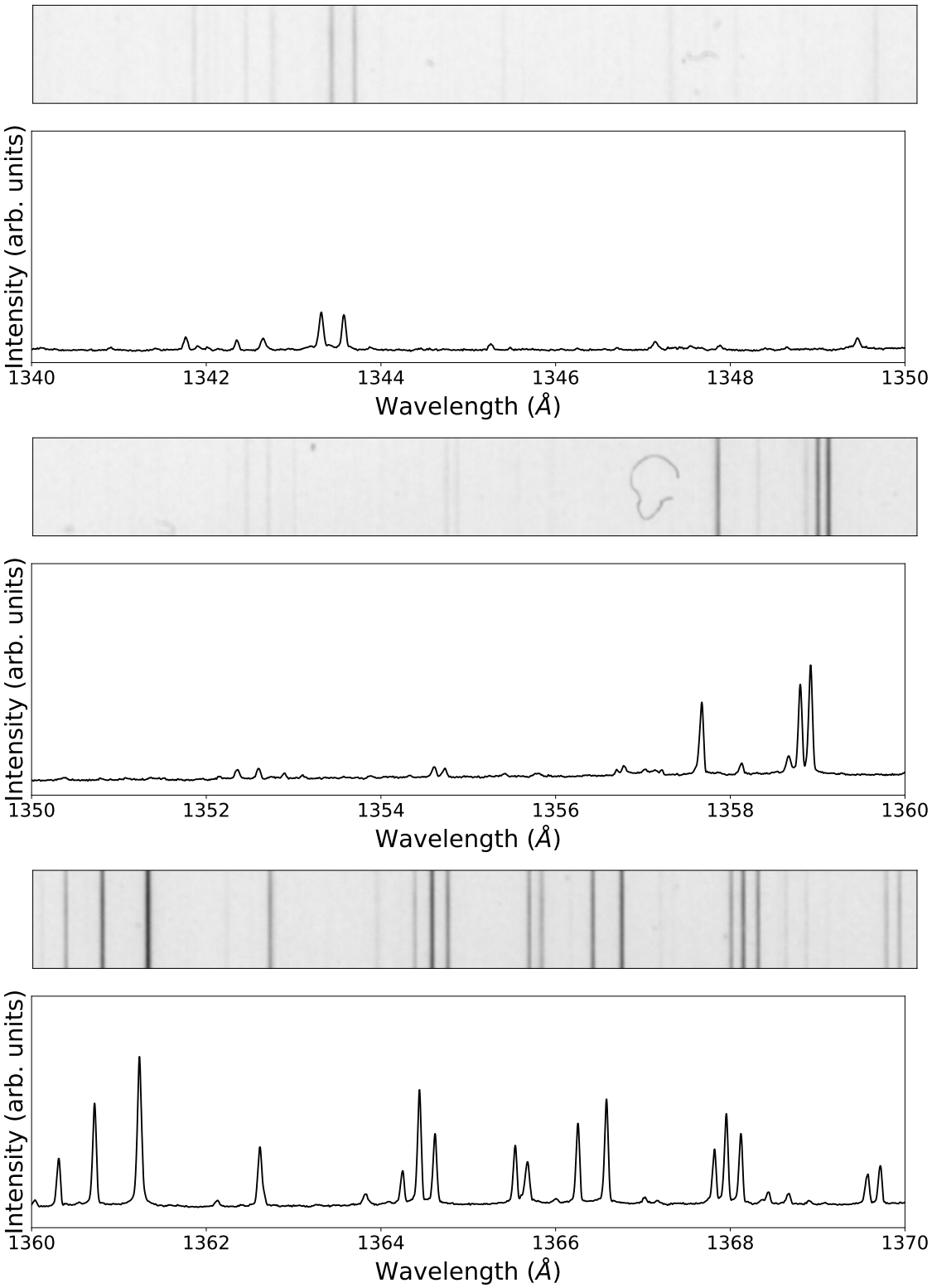


Image x1015_plate1b, Track 5.3, 5-minute exposure (continued)

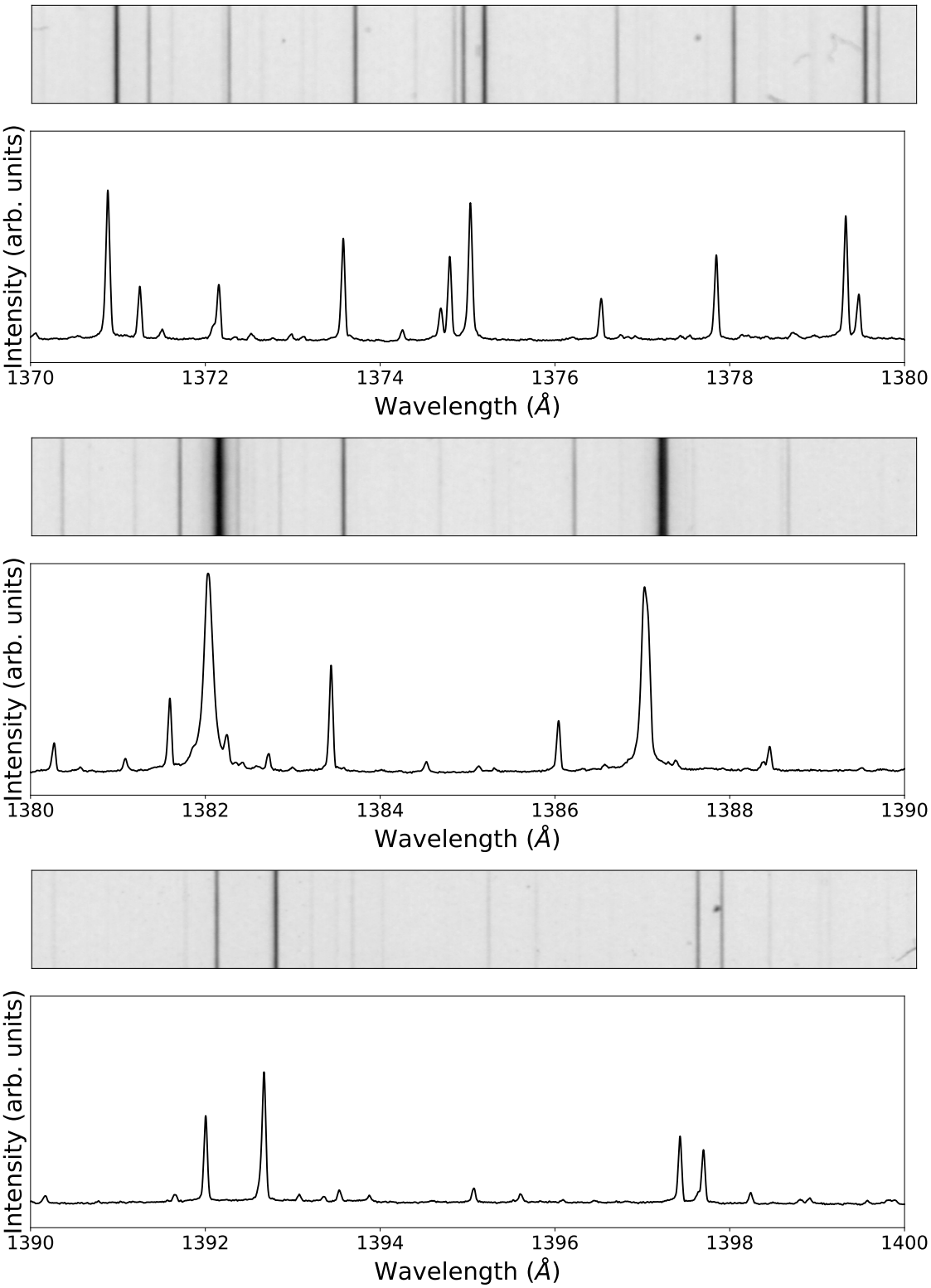


Image x1015_plate1b, Track 5.3, 5-minute exposure (continued)

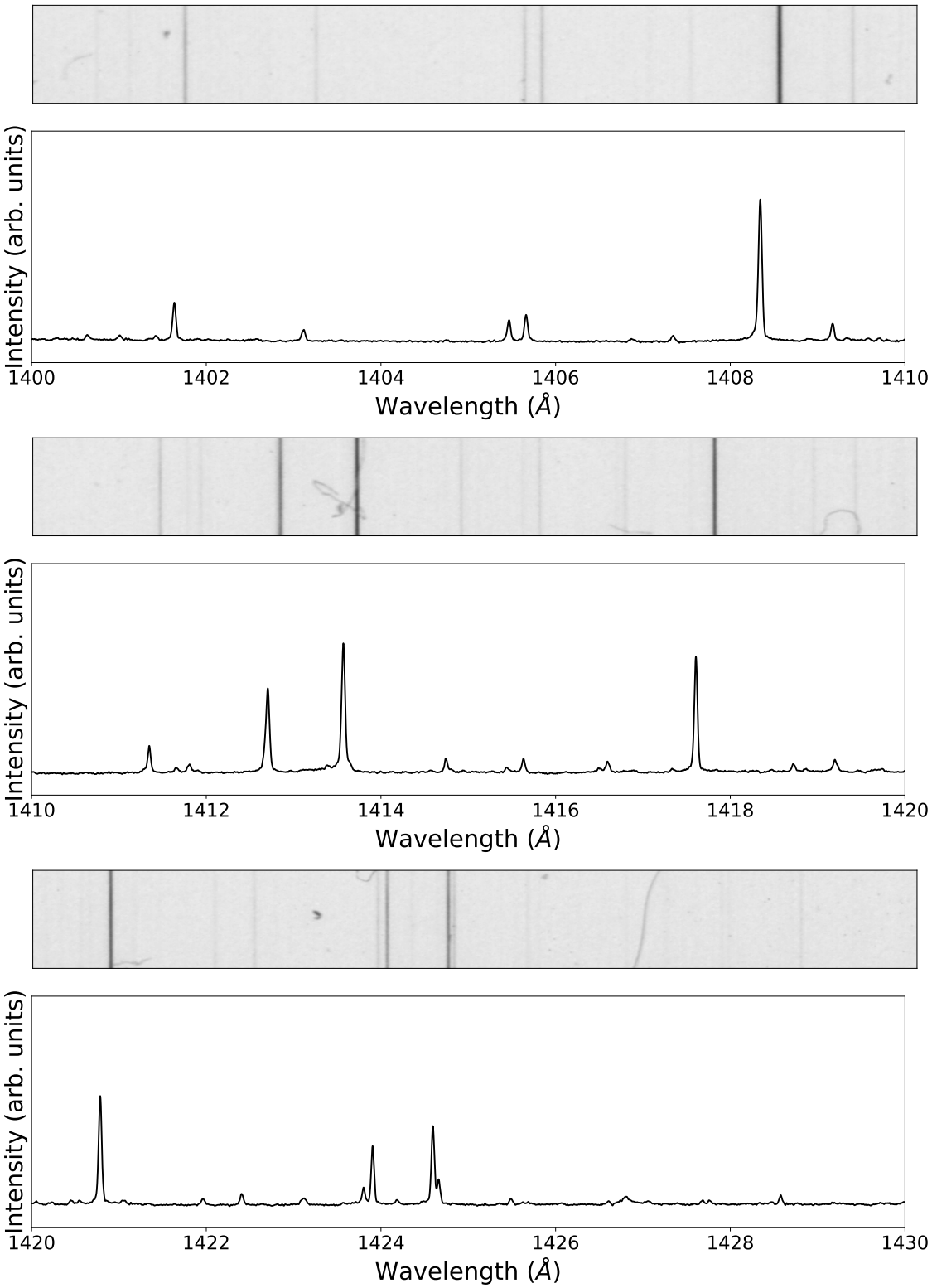


Image x1015_plate1b, Track 5.3, 5-minute exposure (continued)

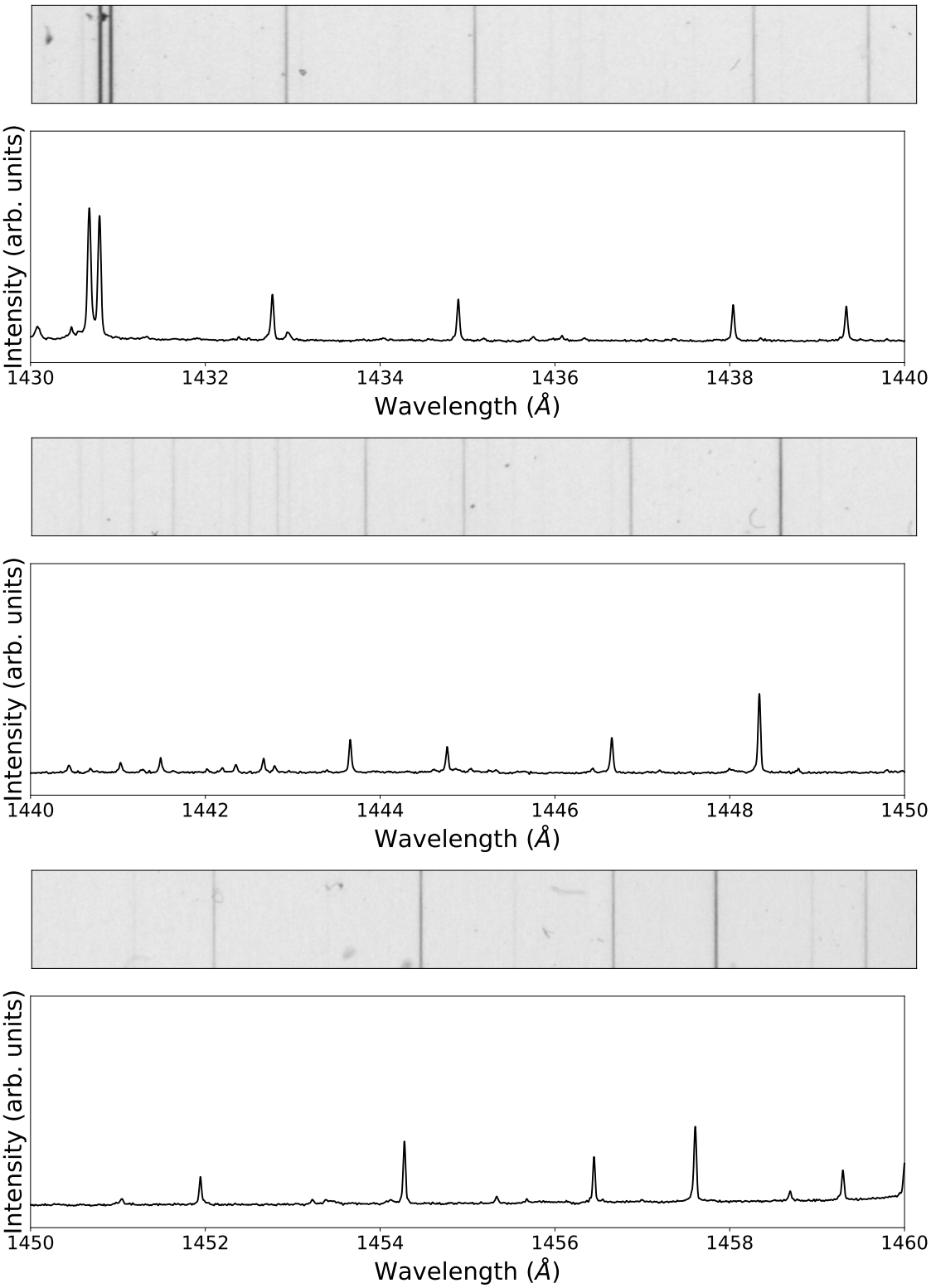
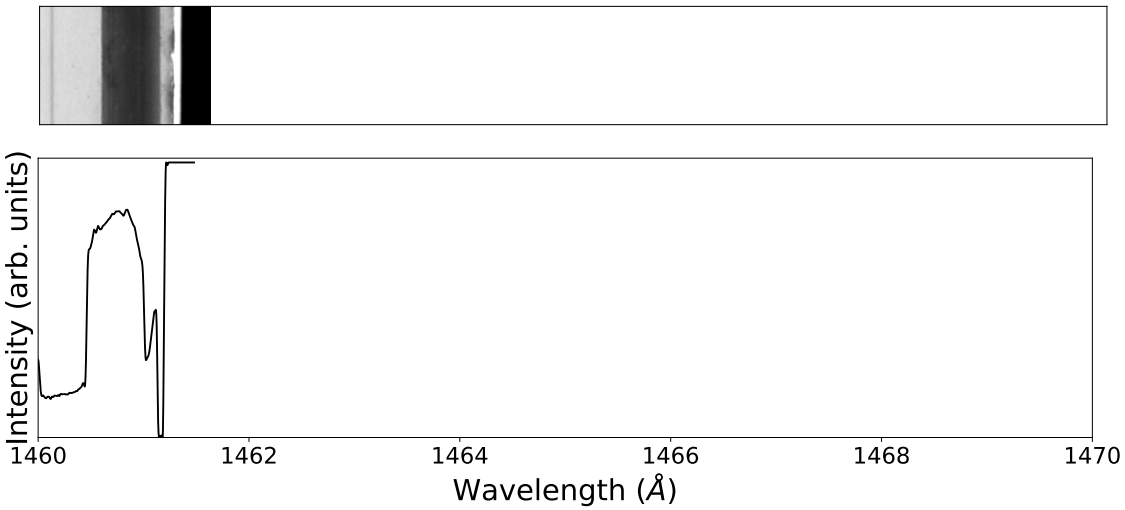


Image x1015_plate1b, Track 5.3, 5-minute exposure (continued)



F.6 Image x1015_plate1b, Track 5.3, 45-minute exposure

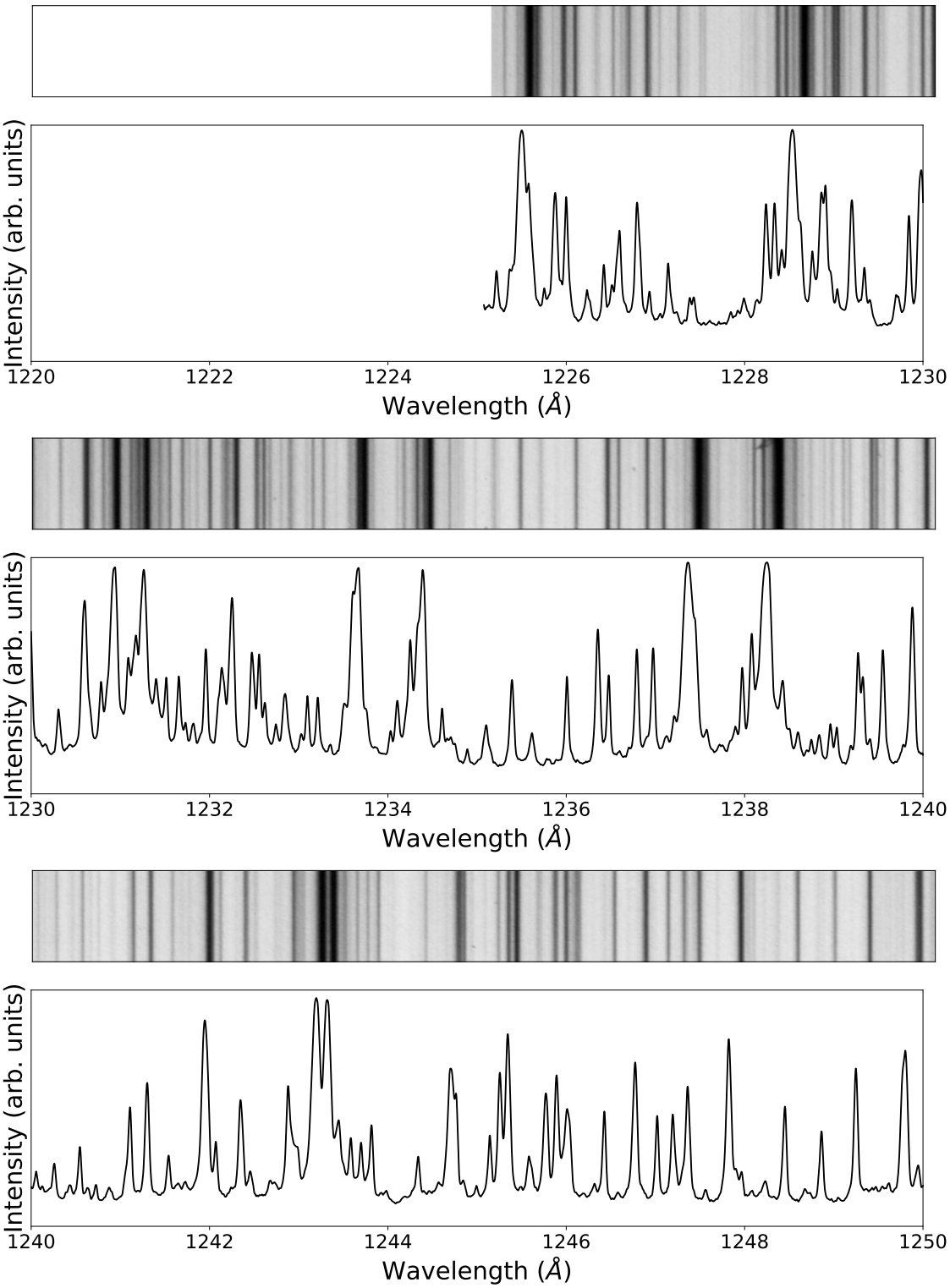


Image x1015_plate1b, Track 5.3, 45-minute exposure (continued)

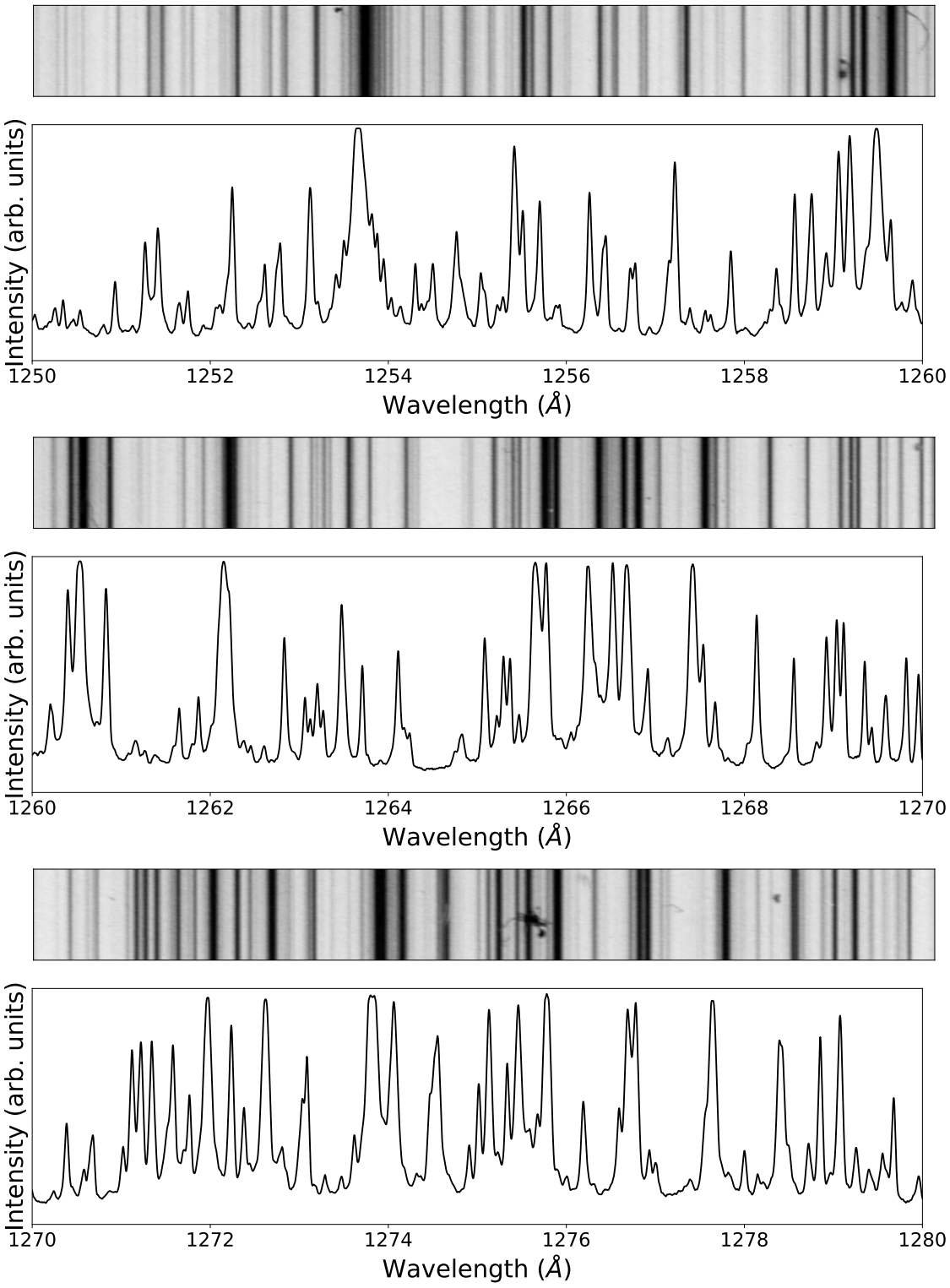


Image x1015_plate1b, Track 5.3, 45-minute exposure (continued)

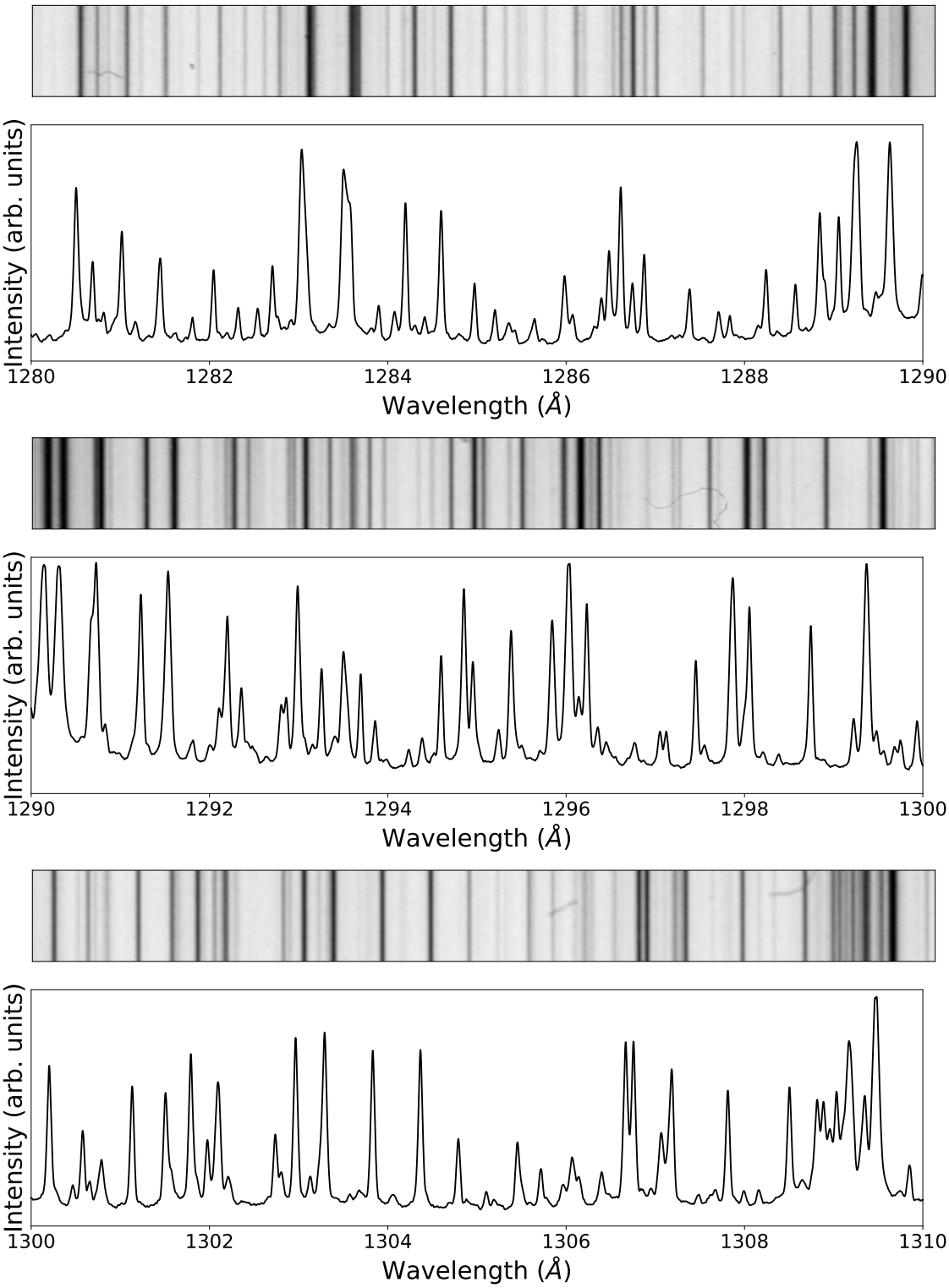


Image x1015_plate1b, Track 5.3, 45-minute exposure (continued)

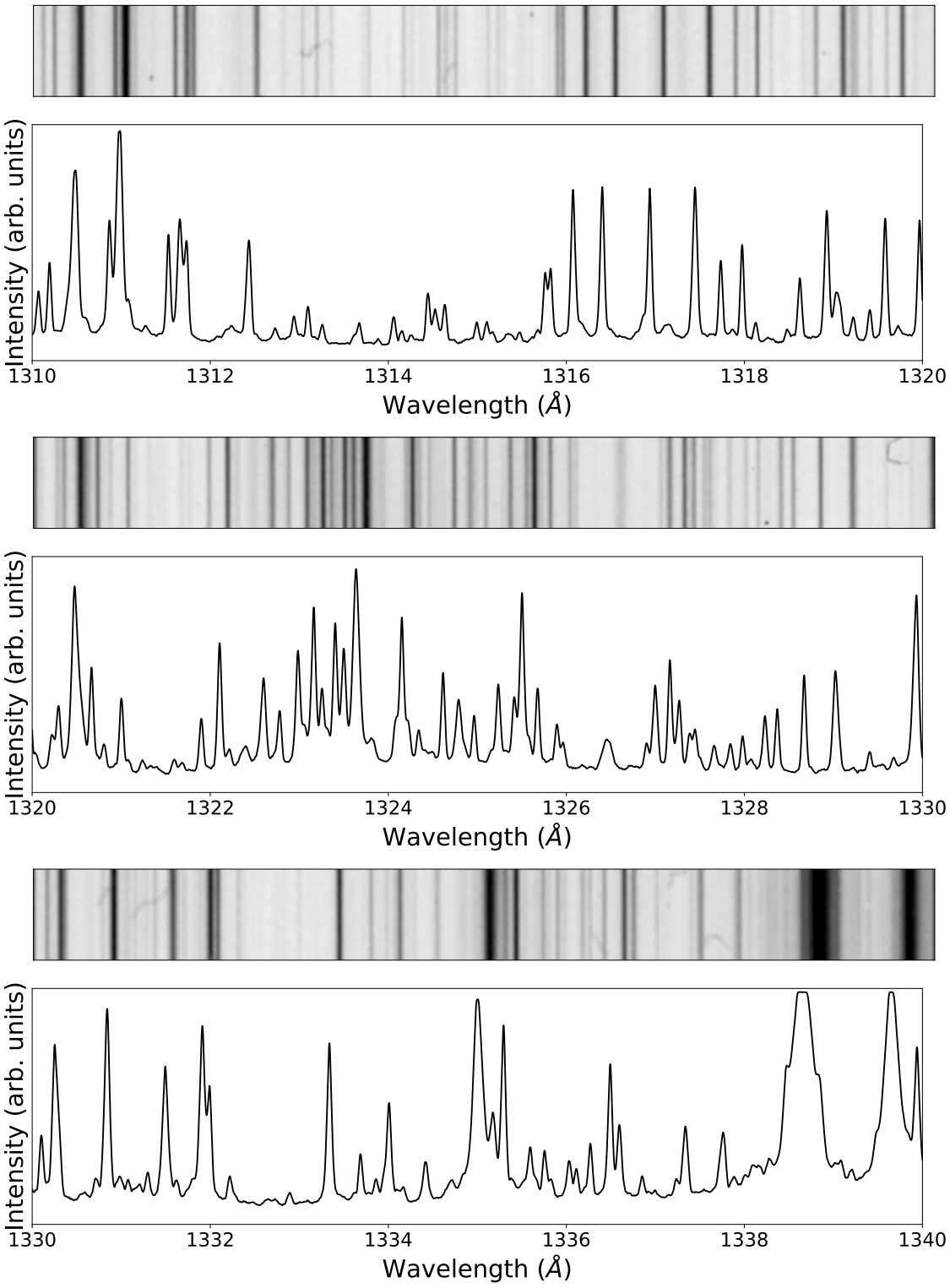


Image x1015_plate1b, Track 5.3, 45-minute exposure (continued)

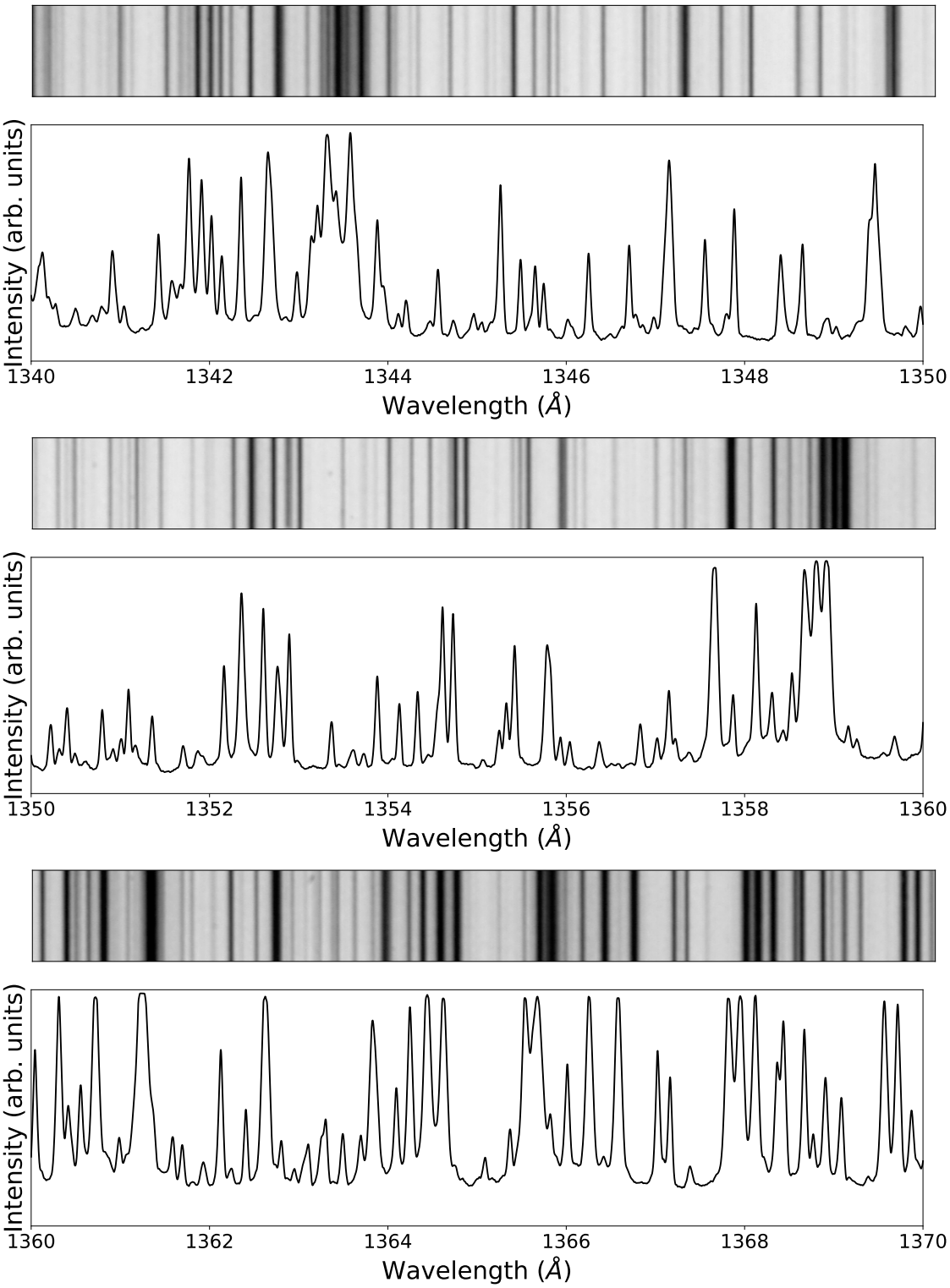


Image x1015_plate1b, Track 5.3, 45-minute exposure (continued)

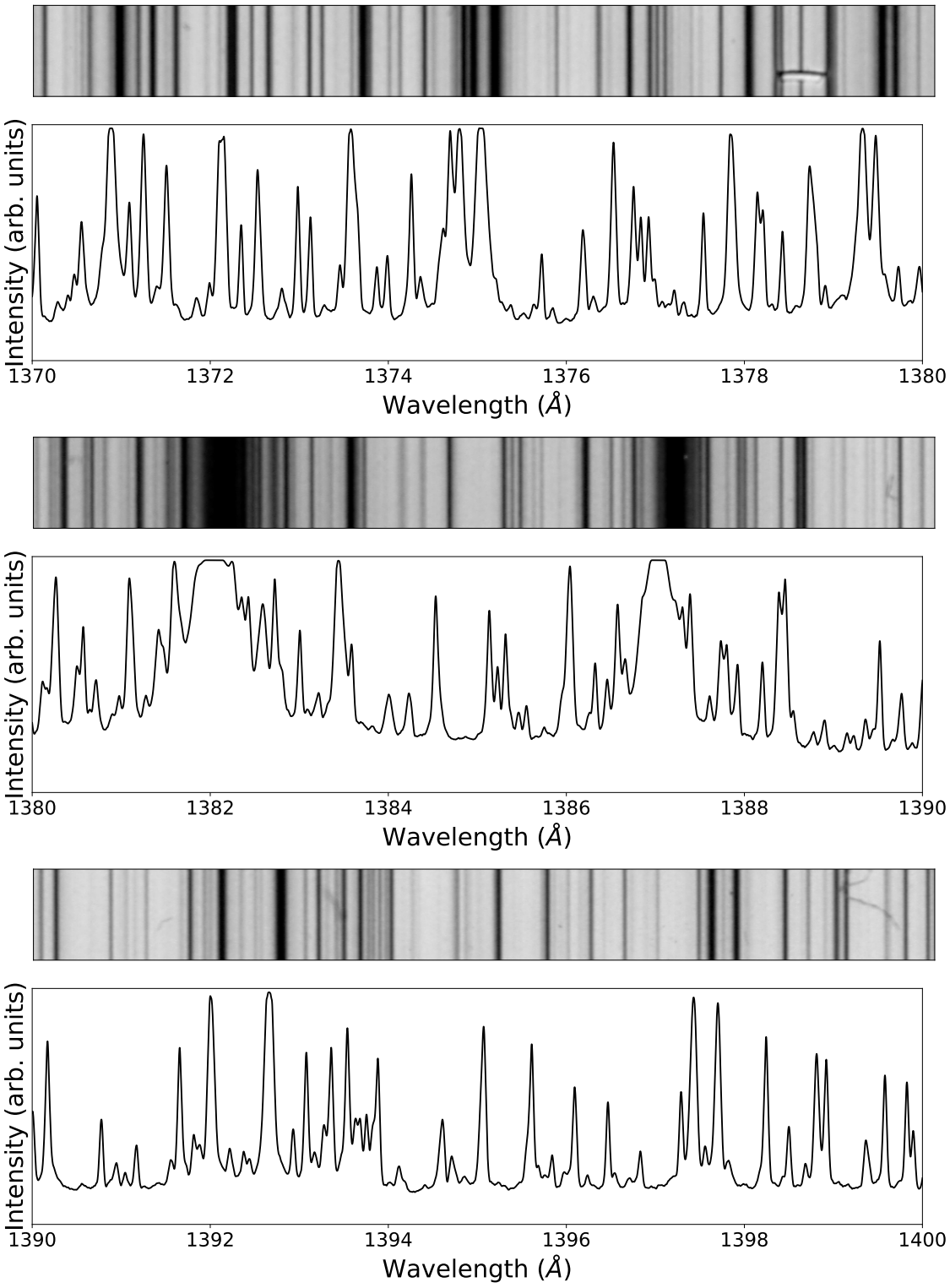


Image x1015_plate1b, Track 5.3, 45-minute exposure (continued)

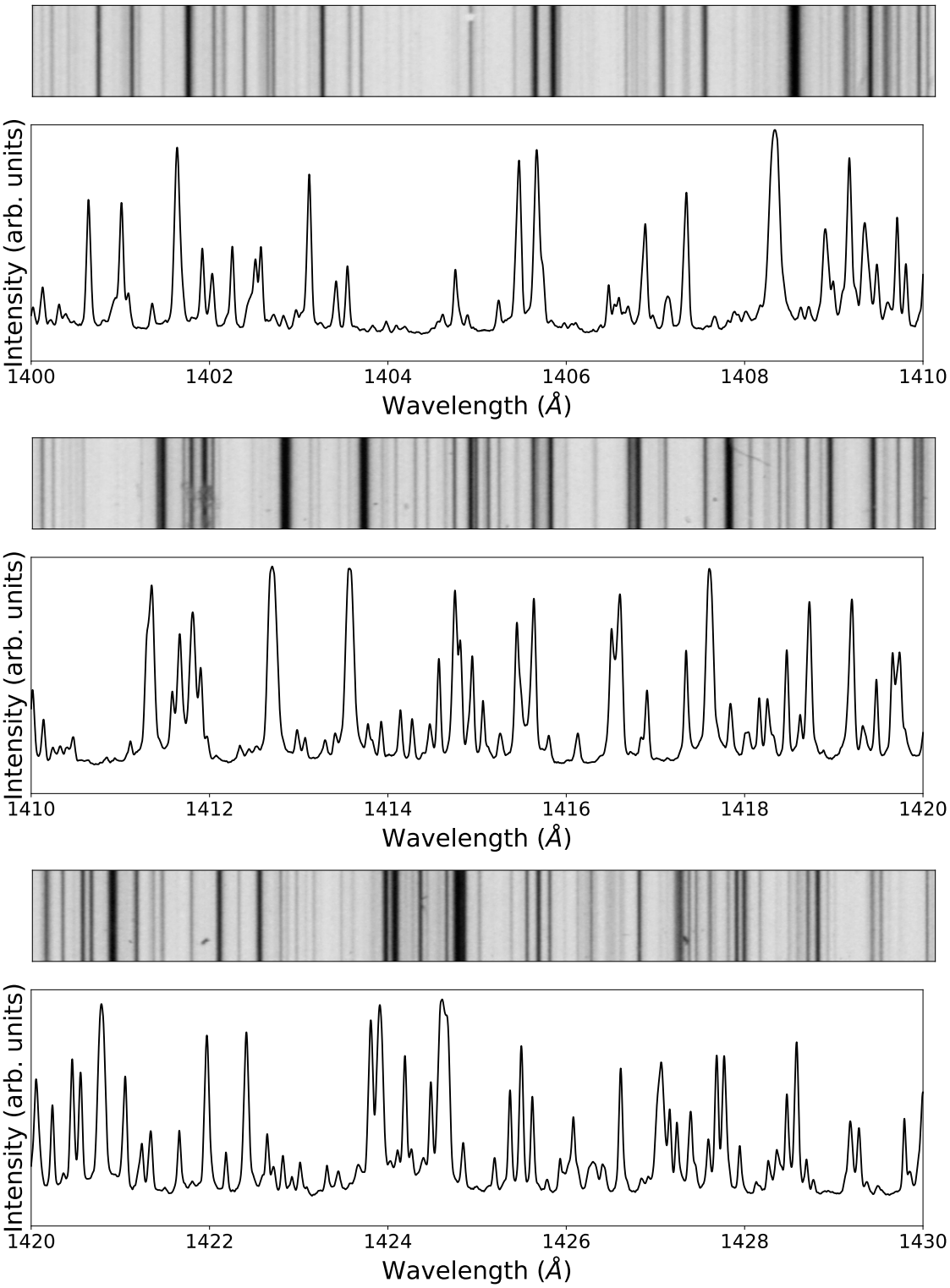


Image x1015_plate1b, Track 5.3, 45-minute exposure (continued)

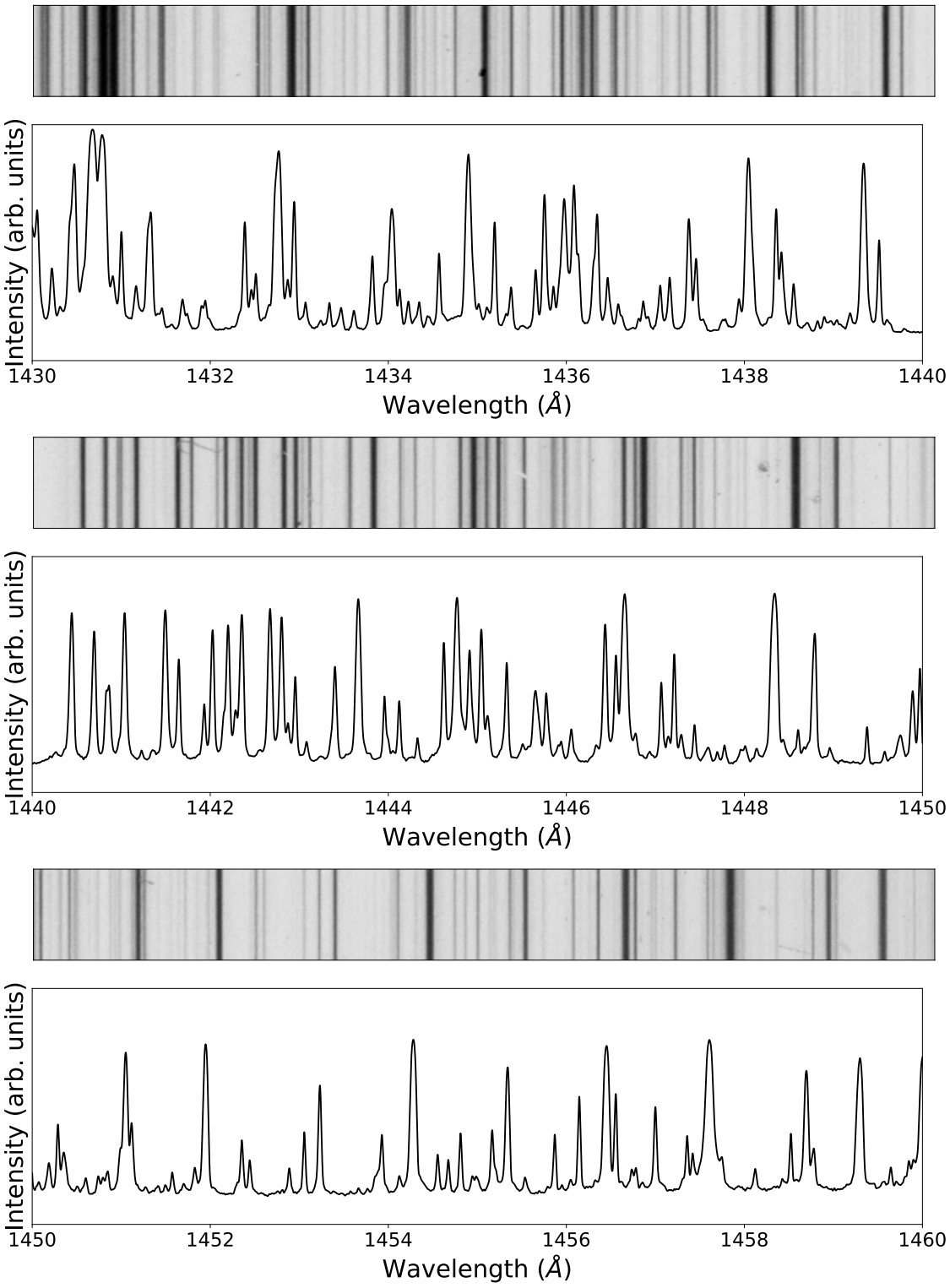
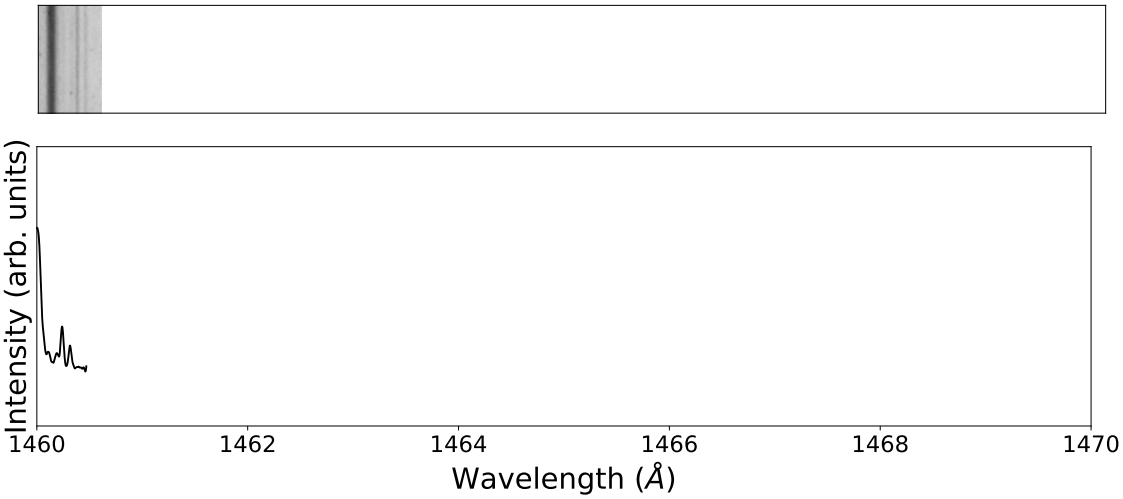


Image x1015_plate1b, Track 5.3, 45-minute exposure (continued)



F.7 Image x1015_plate2a, Track 5.3, 5-minute exposure

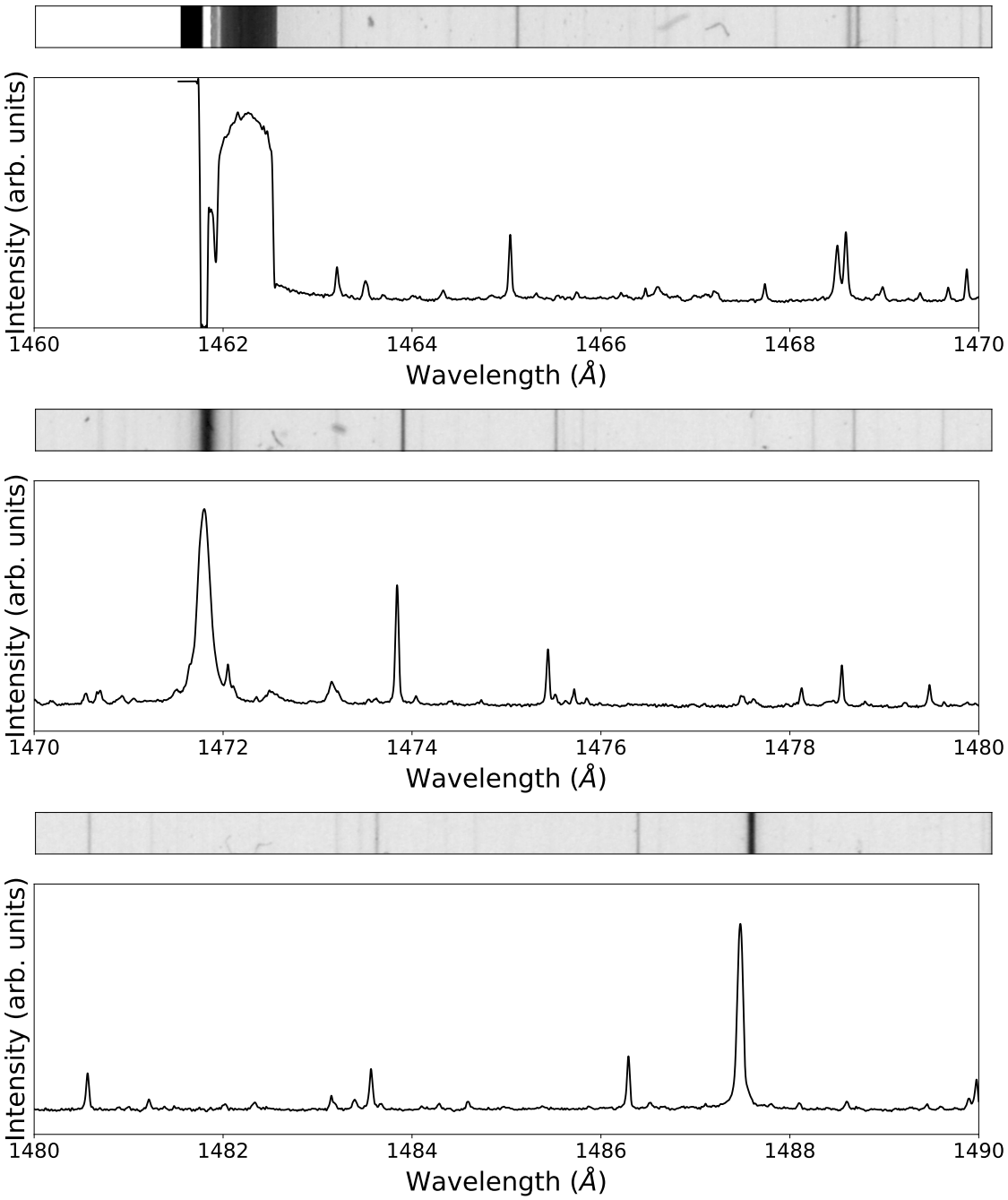


Image x1015_plate2a, Track 5.3, 5-minute exposure (continued)

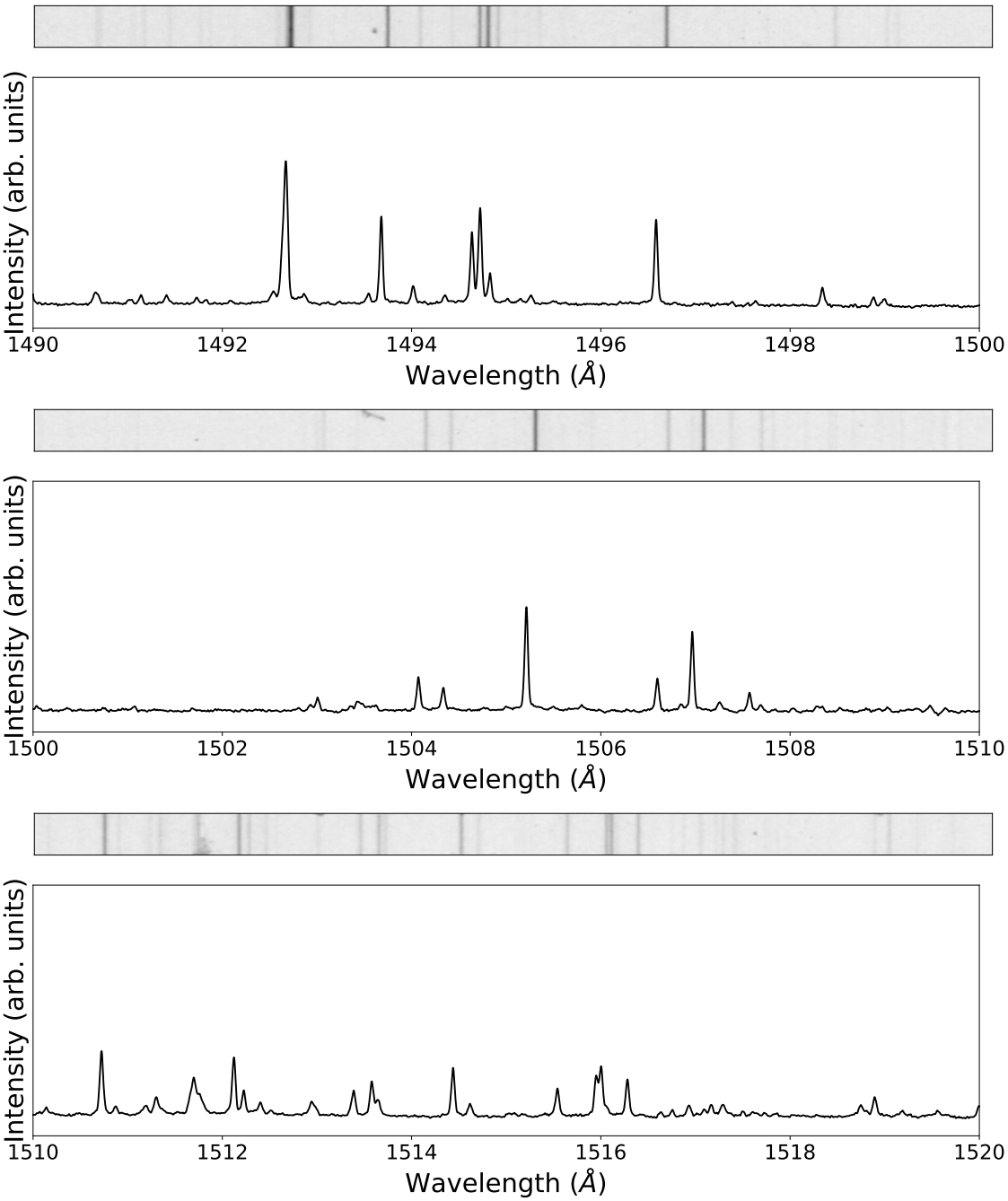
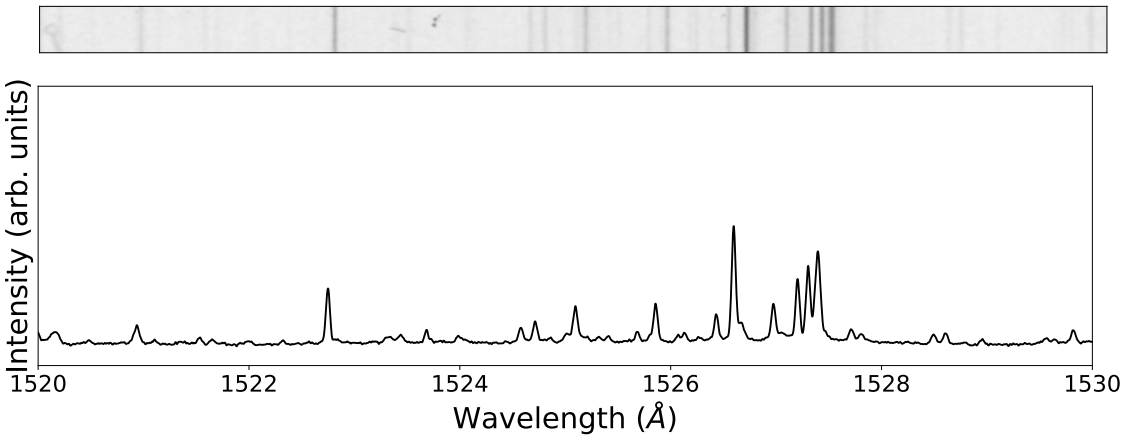
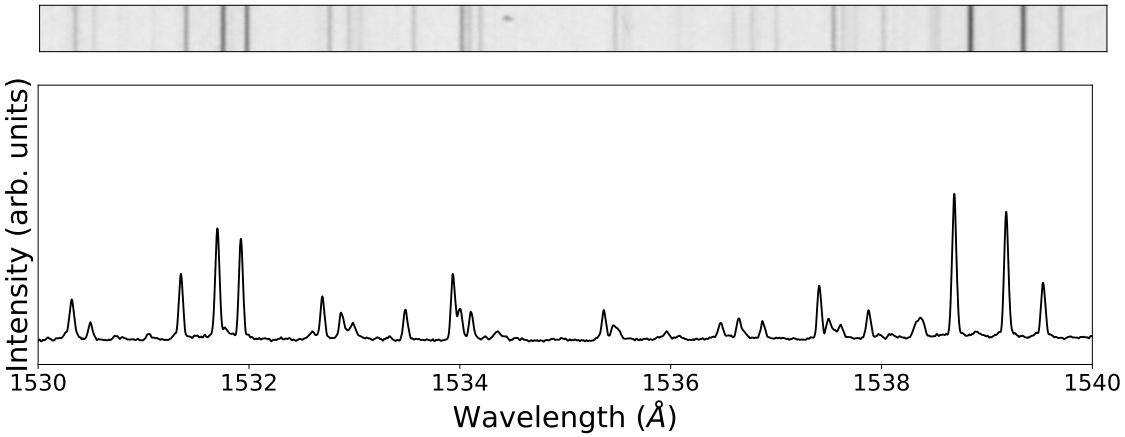


Image x1015_plate2a, Track 5.3, 5-minute exposure (continued)





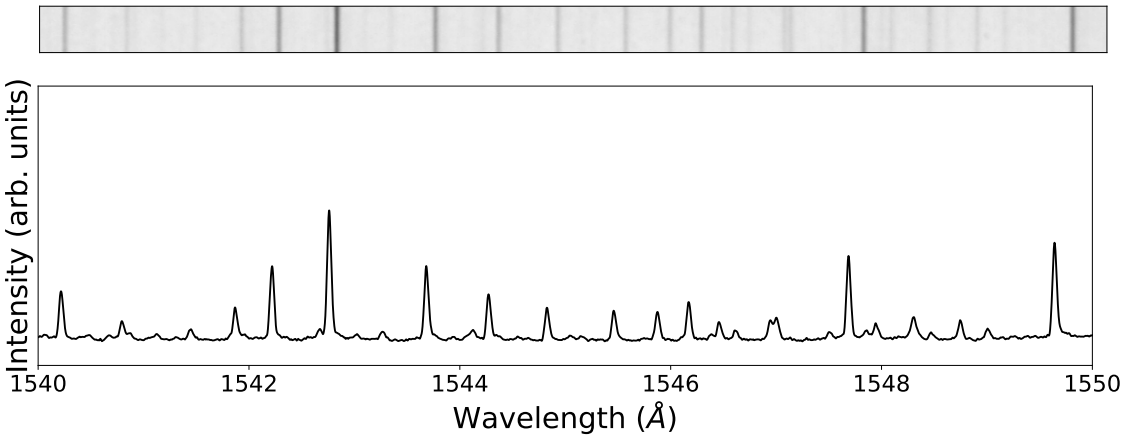


Image x1015_plate2a, Track 5.3, 5-minute exposure (continued)

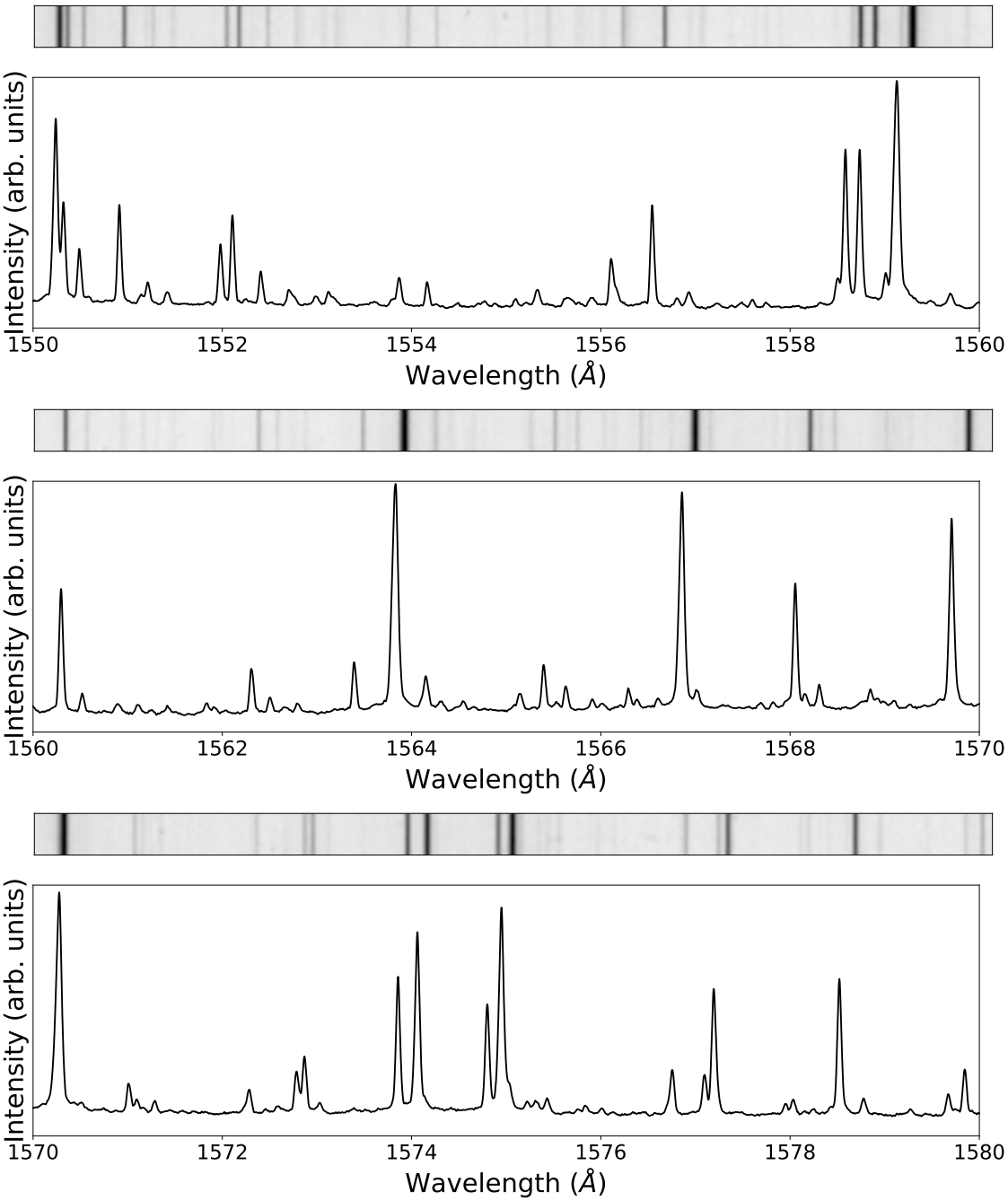


Image x1015_plate2a, Track 5.3, 5-minute exposure (continued)

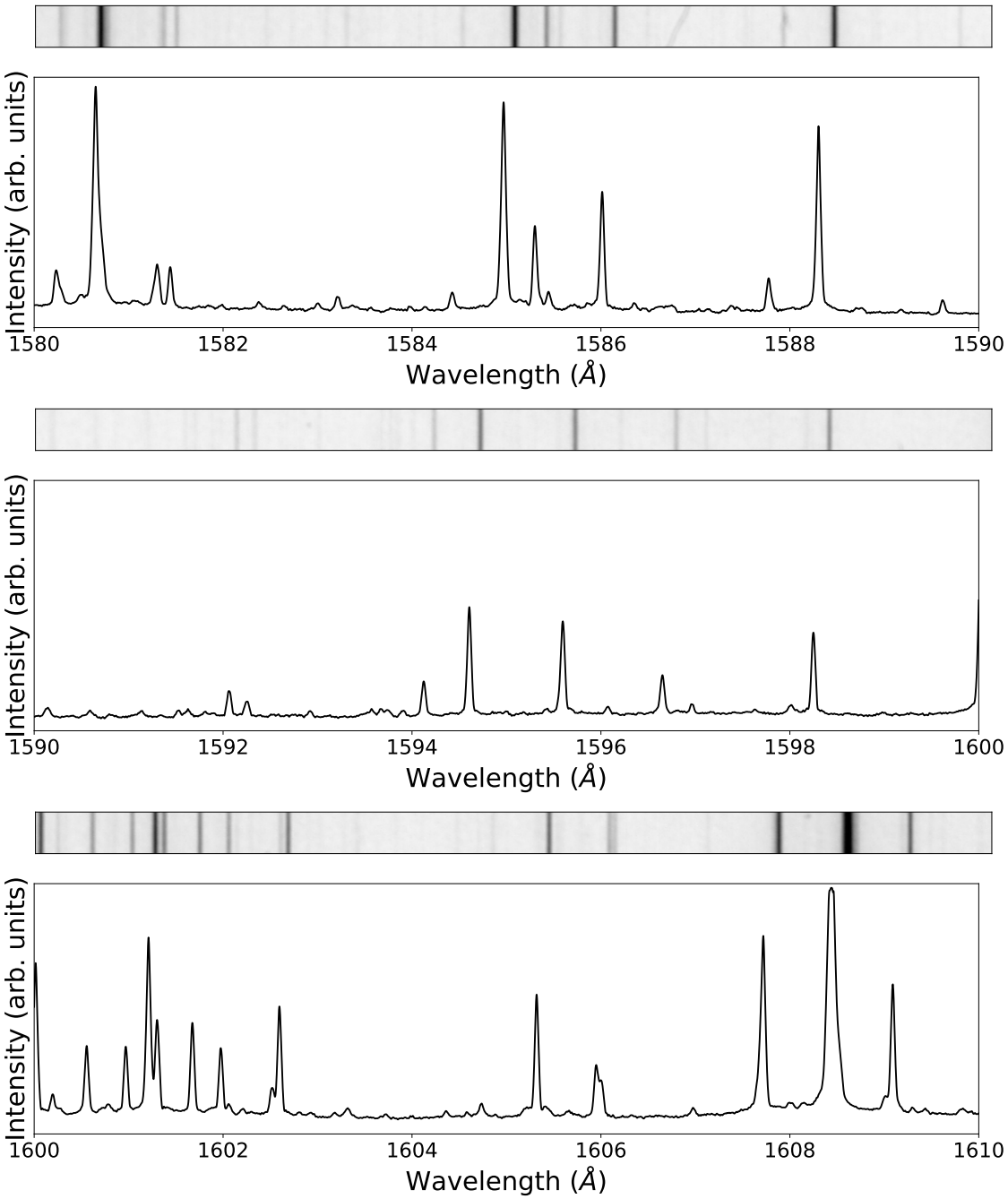


Image x1015_plate2a, Track 5.3, 5-minute exposure (continued)

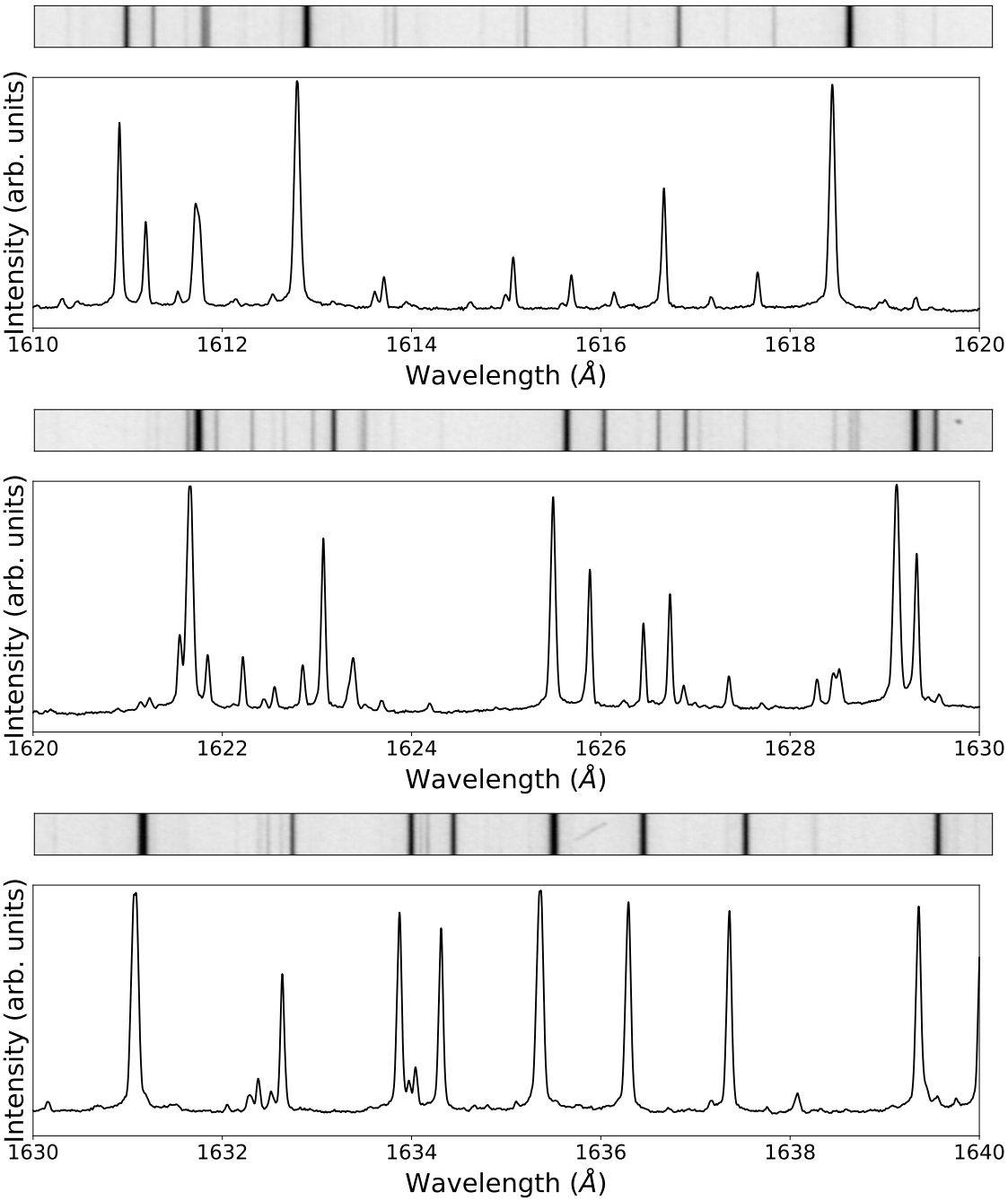


Image x1015_plate2a, Track 5.3, 5-minute exposure (continued)

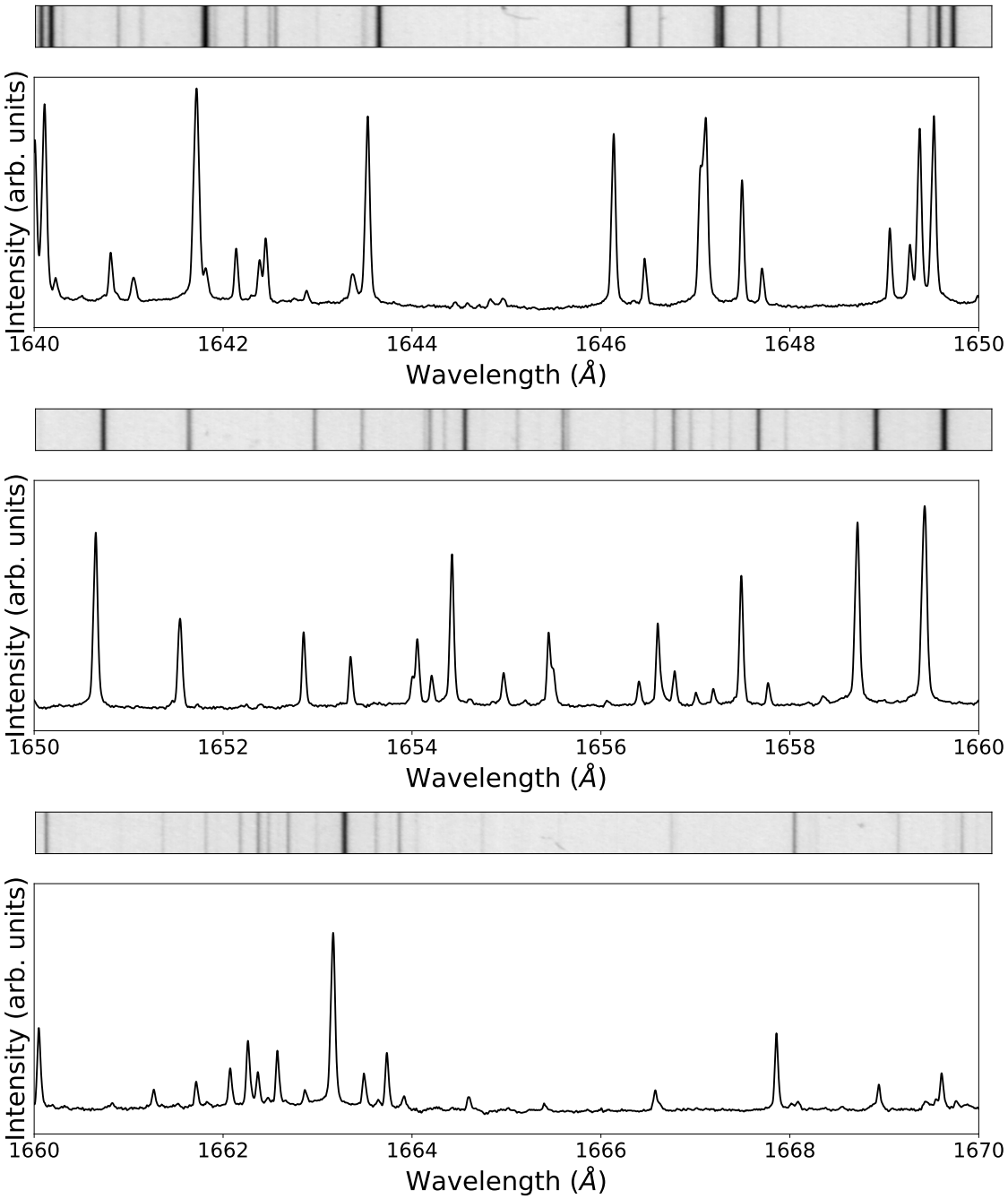
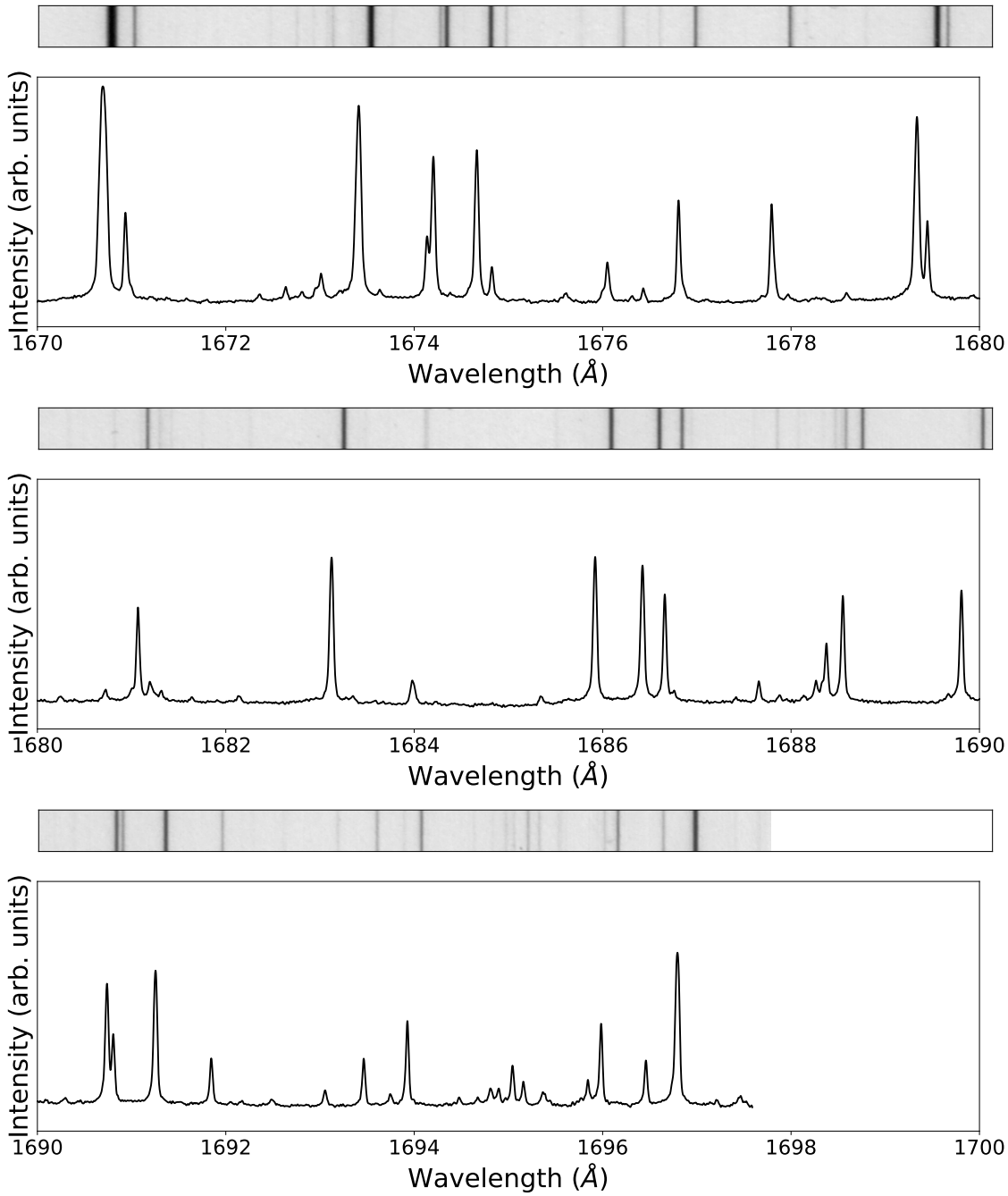


Image x1015_plate2a, Track 5.3, 5-minute exposure (continued)



F.8 Image x1015_plate2a, Track 5.3, 45-minute exposure

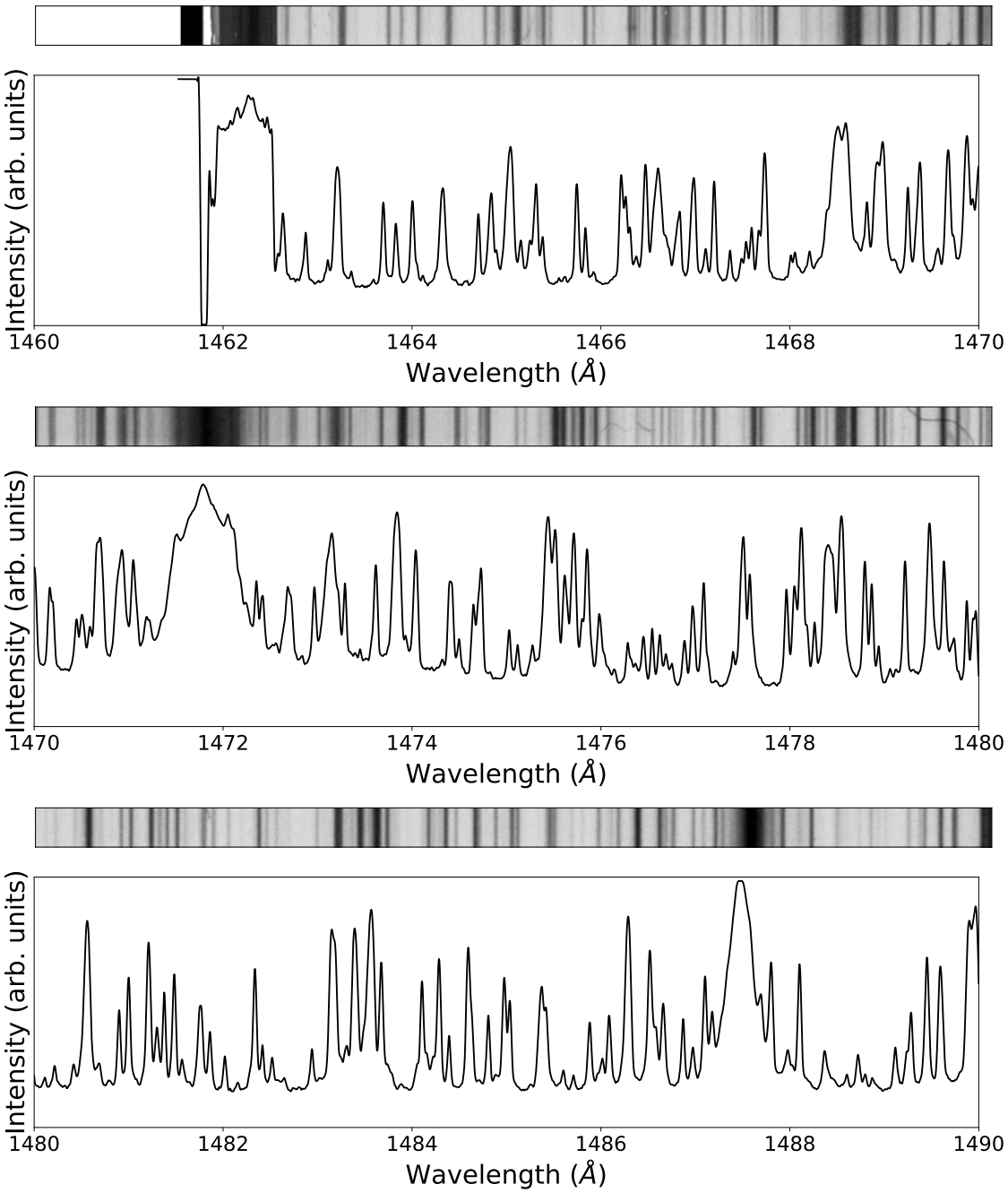


Image x1015_plate2a, Track 5.3, 45-minute exposure (continued)

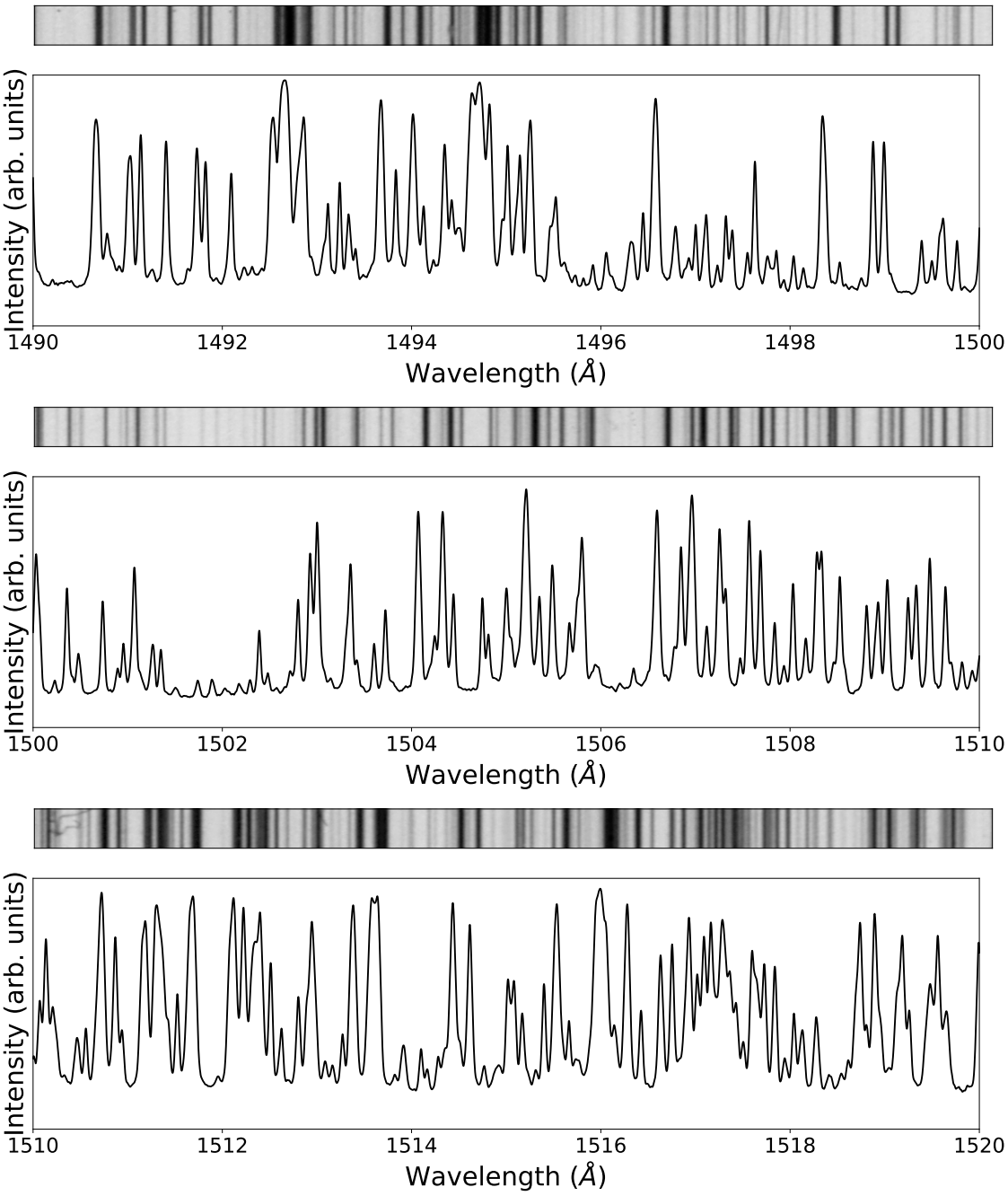


Image x1015_plate2a, Track 5.3, 45-minute exposure (continued)

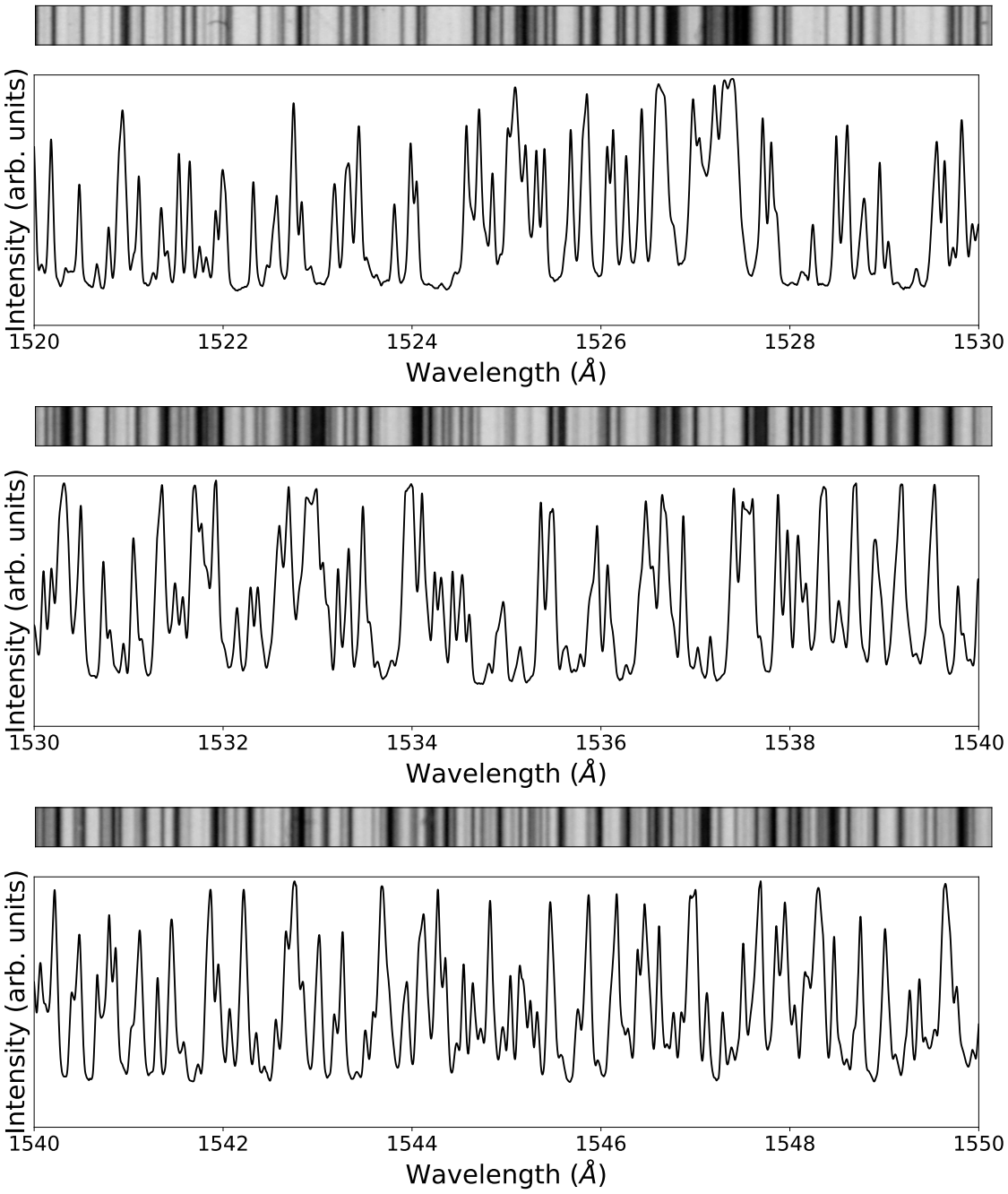


Image x1015_plate2a, Track 5.3, 45-minute exposure (continued)

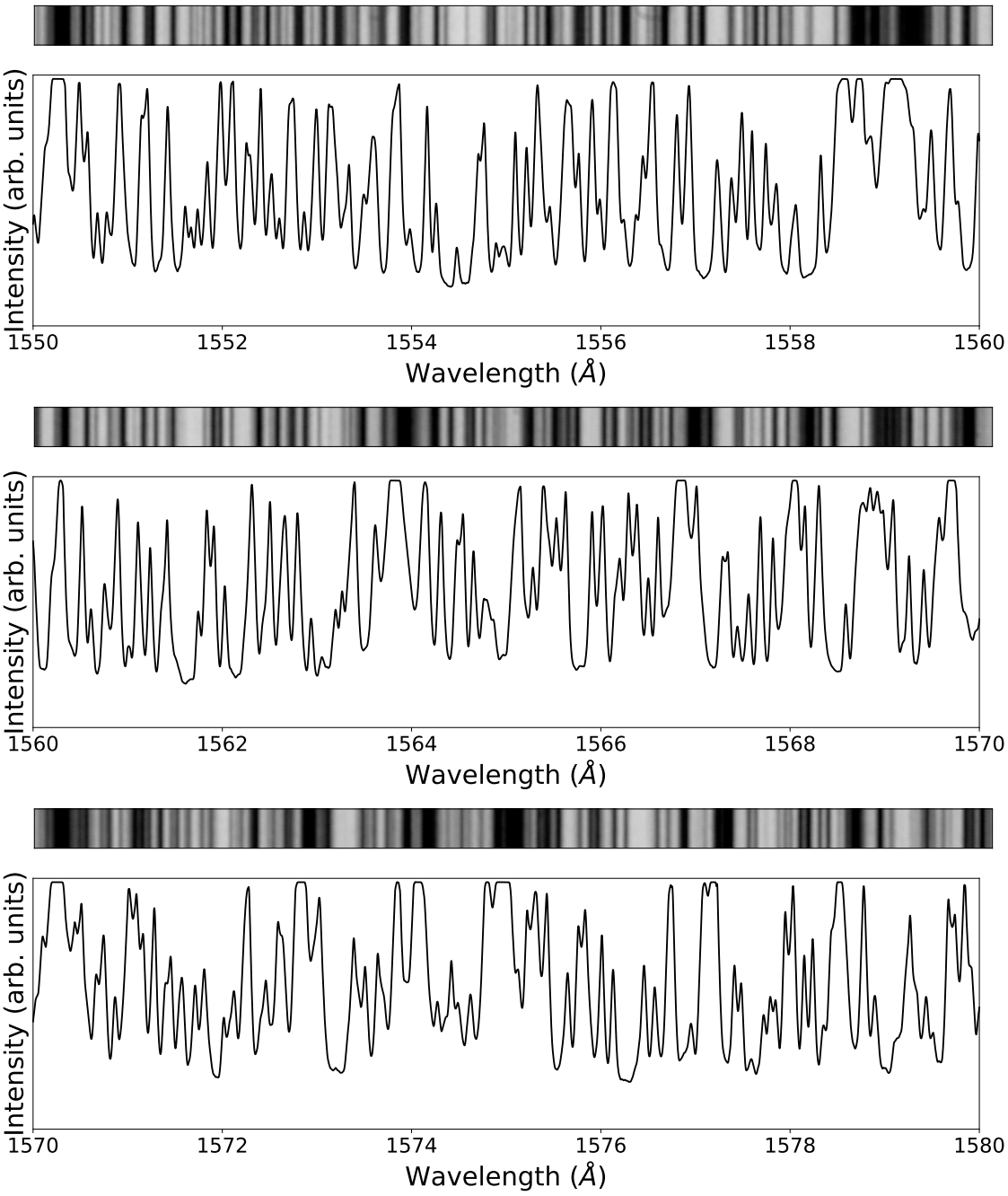


Image x1015_plate2a, Track 5.3, 45-minute exposure (continued)

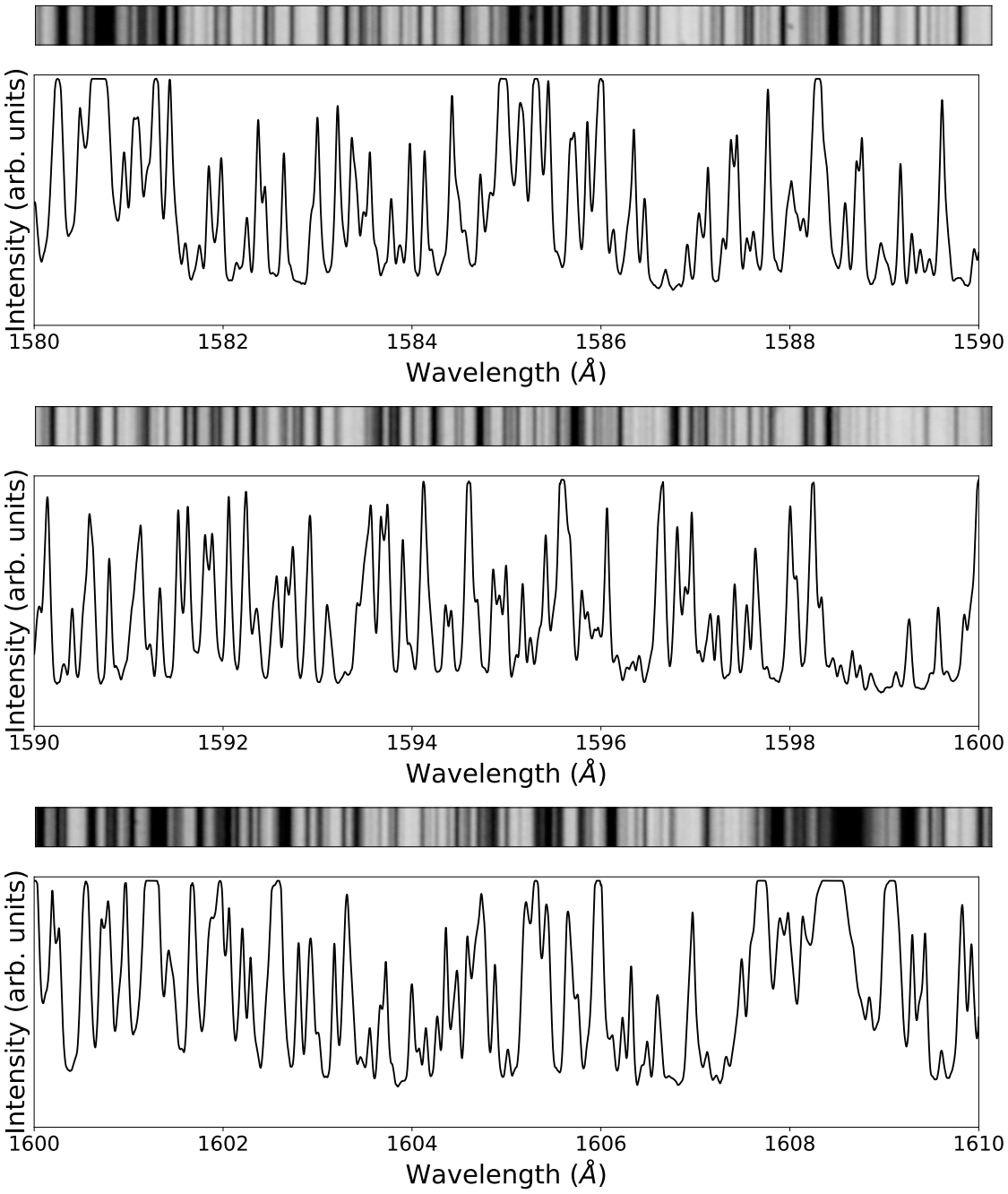


Image x1015_plate2a, Track 5.3, 45-minute exposure (continued)

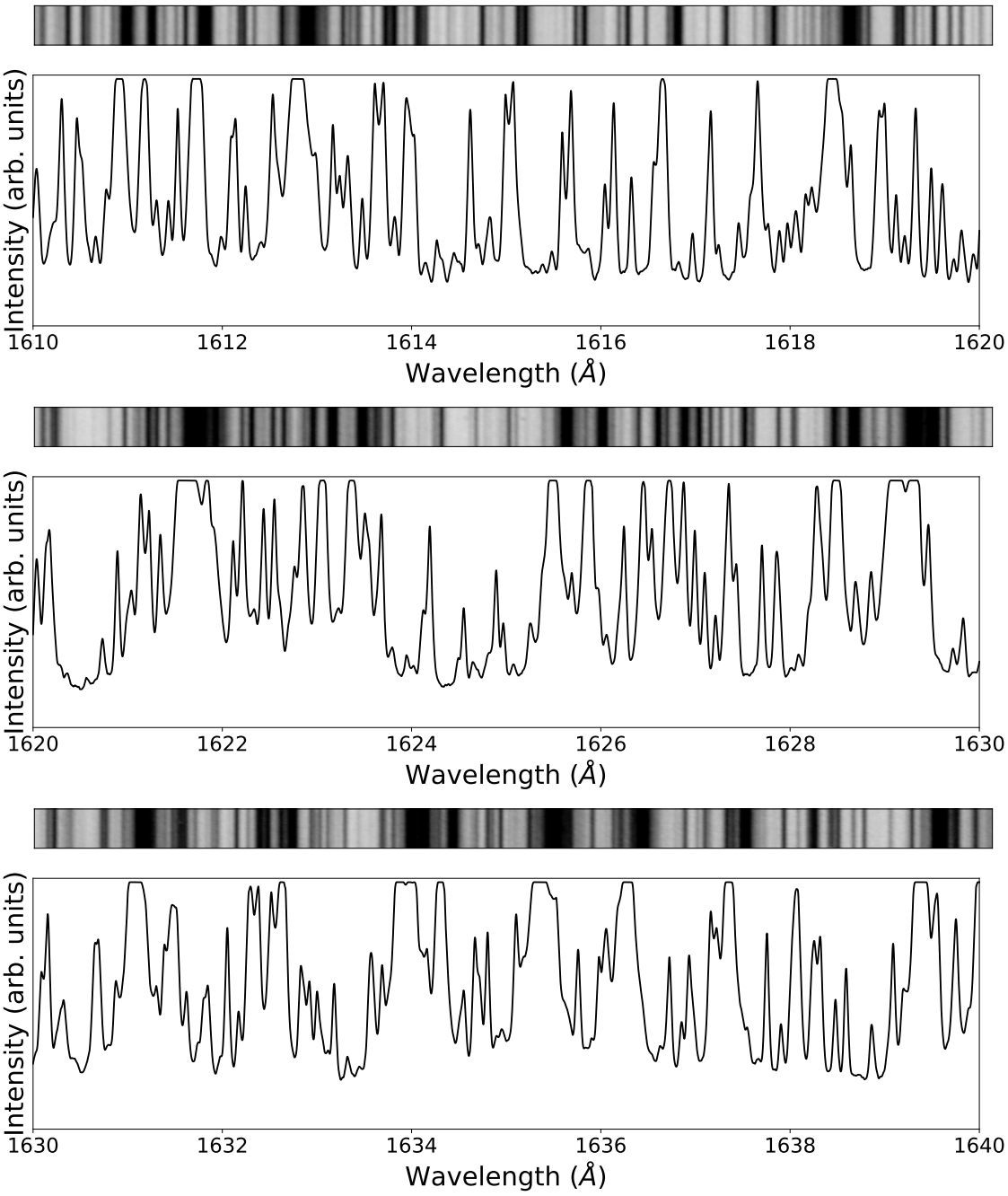


Image x1015_plate2a, Track 5.3, 45-minute exposure (continued)

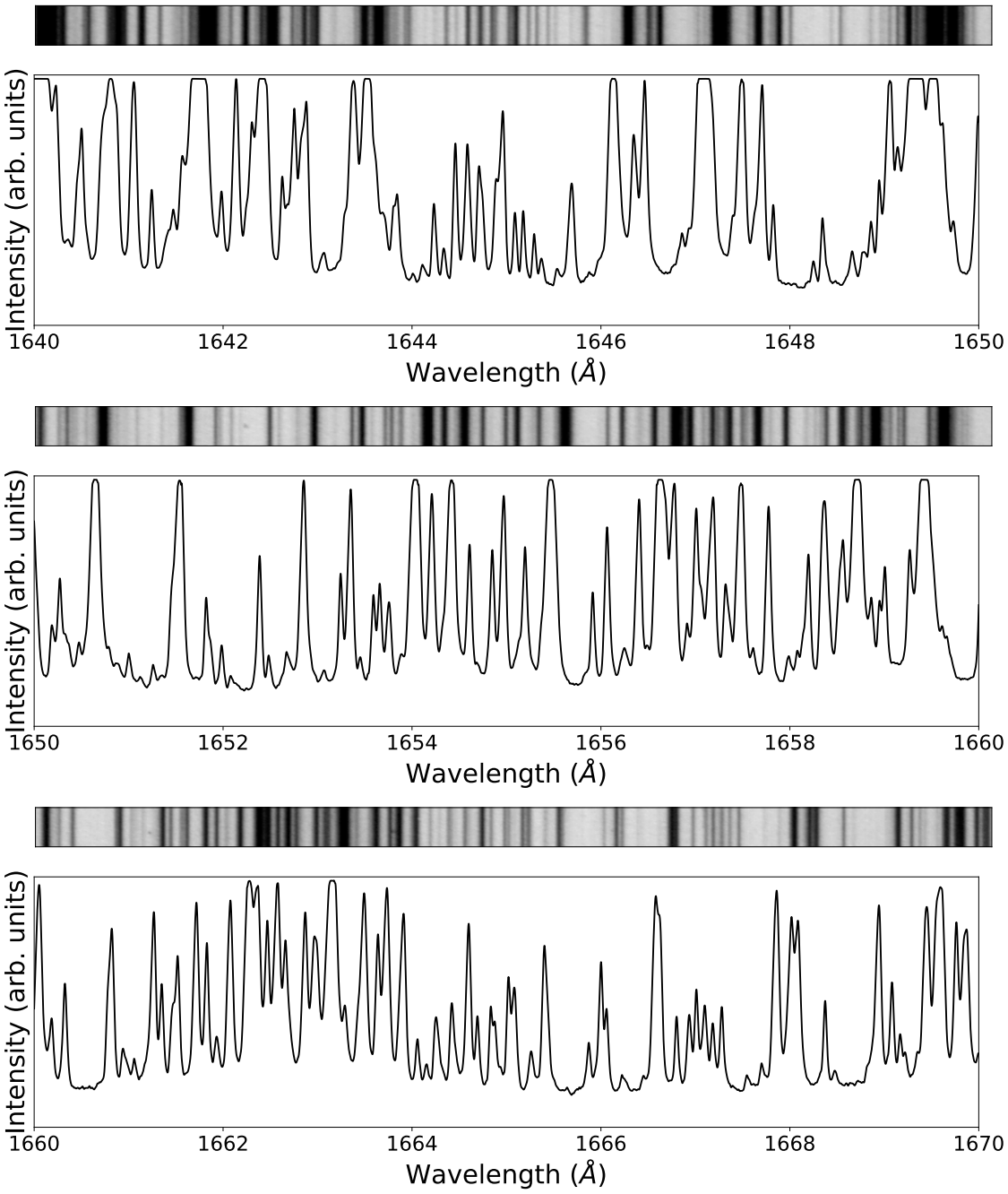
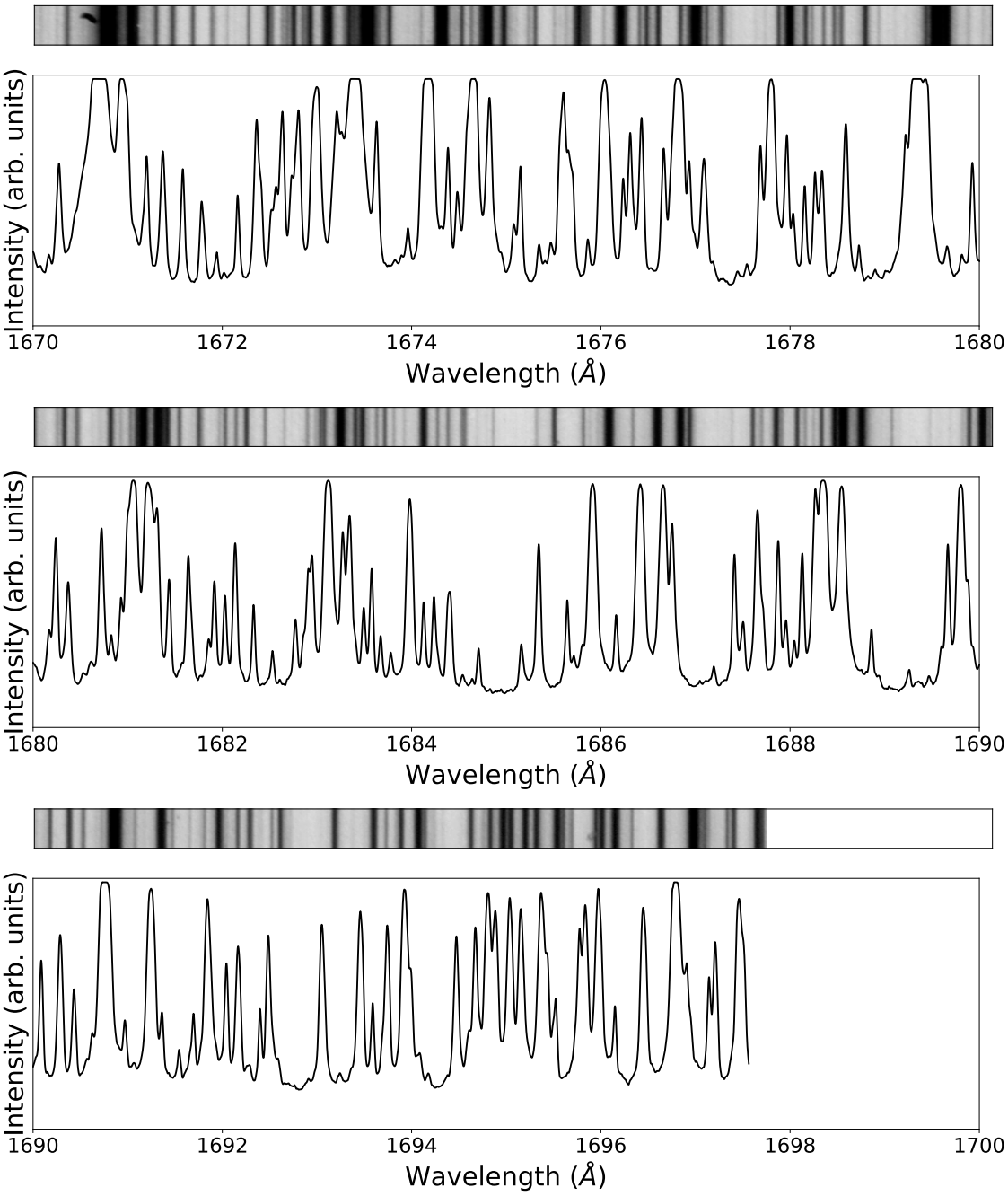


Image x1015_plate2a, Track 5.3, 45-minute exposure (continued)



F.9 Image x1015_plate2b, Track 5.3, 5-minute exposure

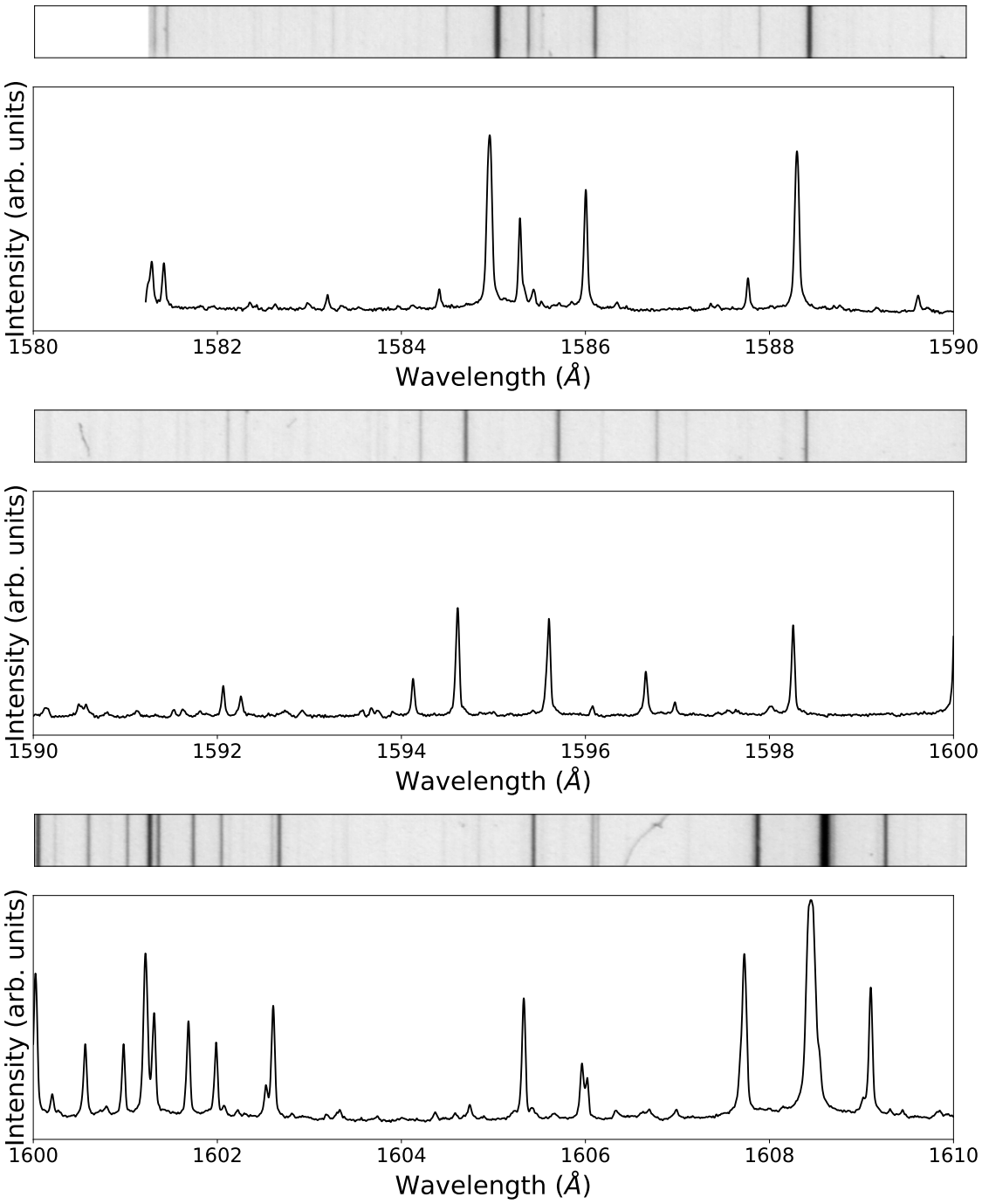


Image x1015_plate2b, Track 5.3, 5-minute exposure (continued)

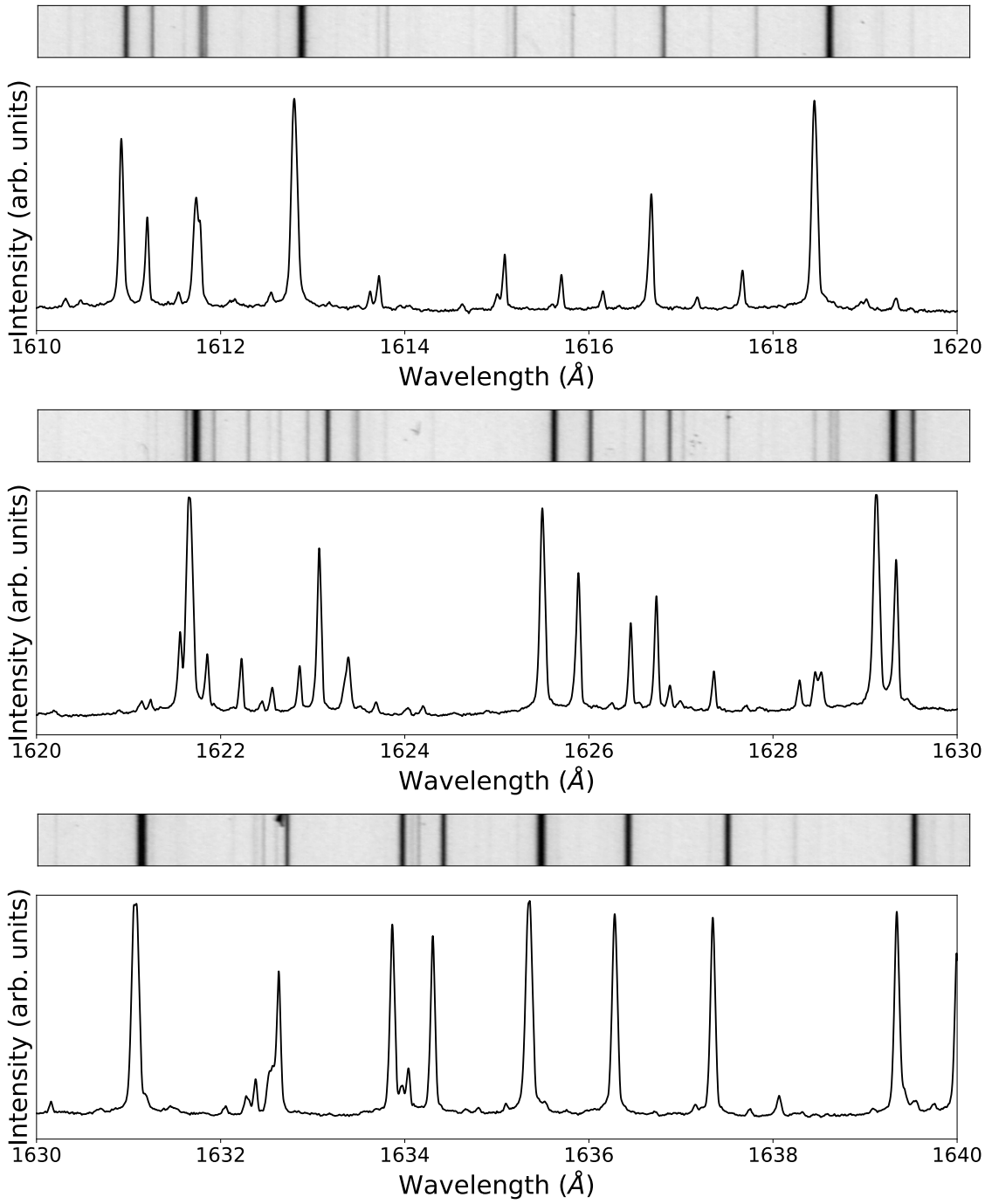


Image x1015_plate2b, Track 5.3, 5-minute exposure (continued)

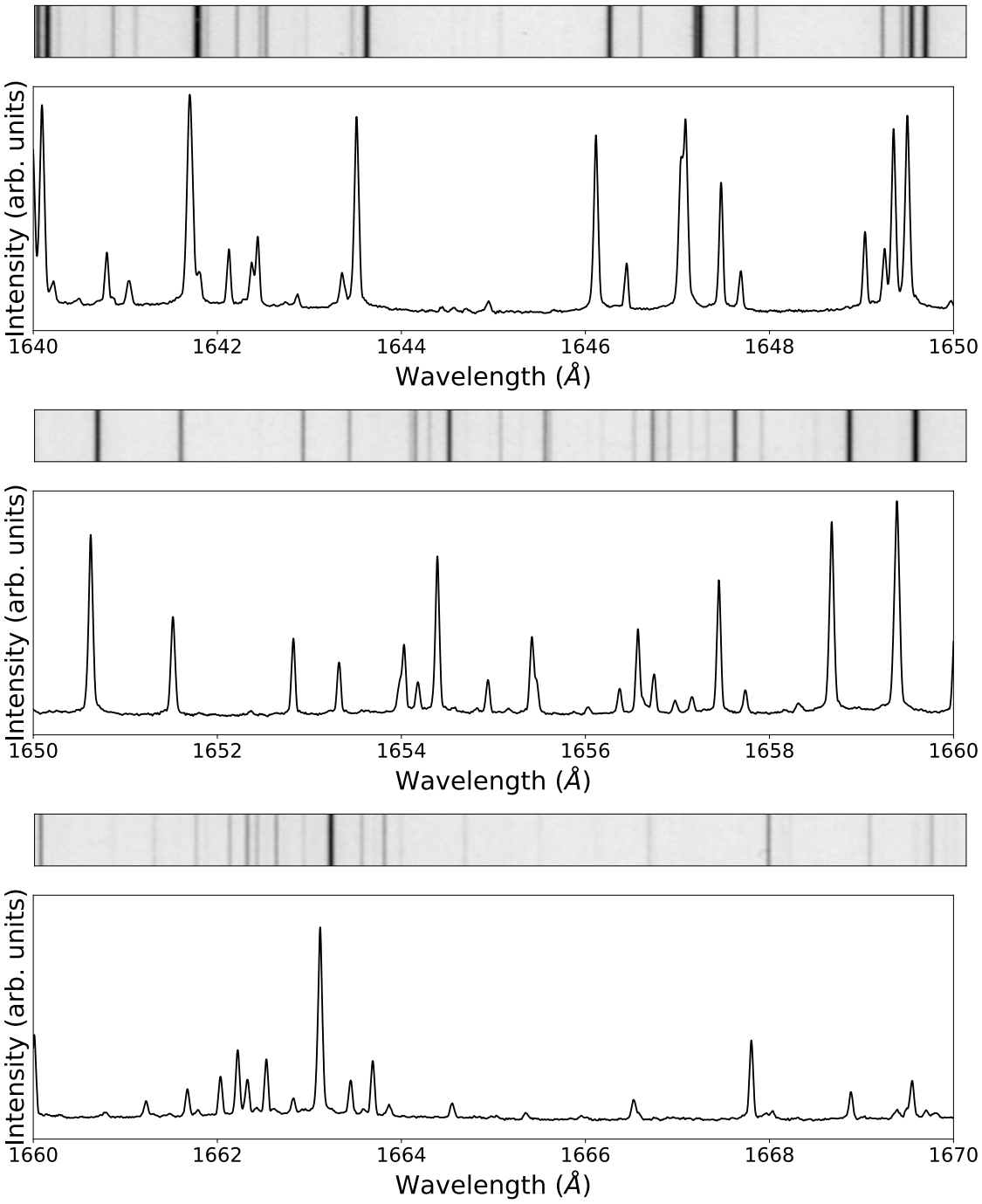


Image x1015_plate2b, Track 5.3, 5-minute exposure (continued)

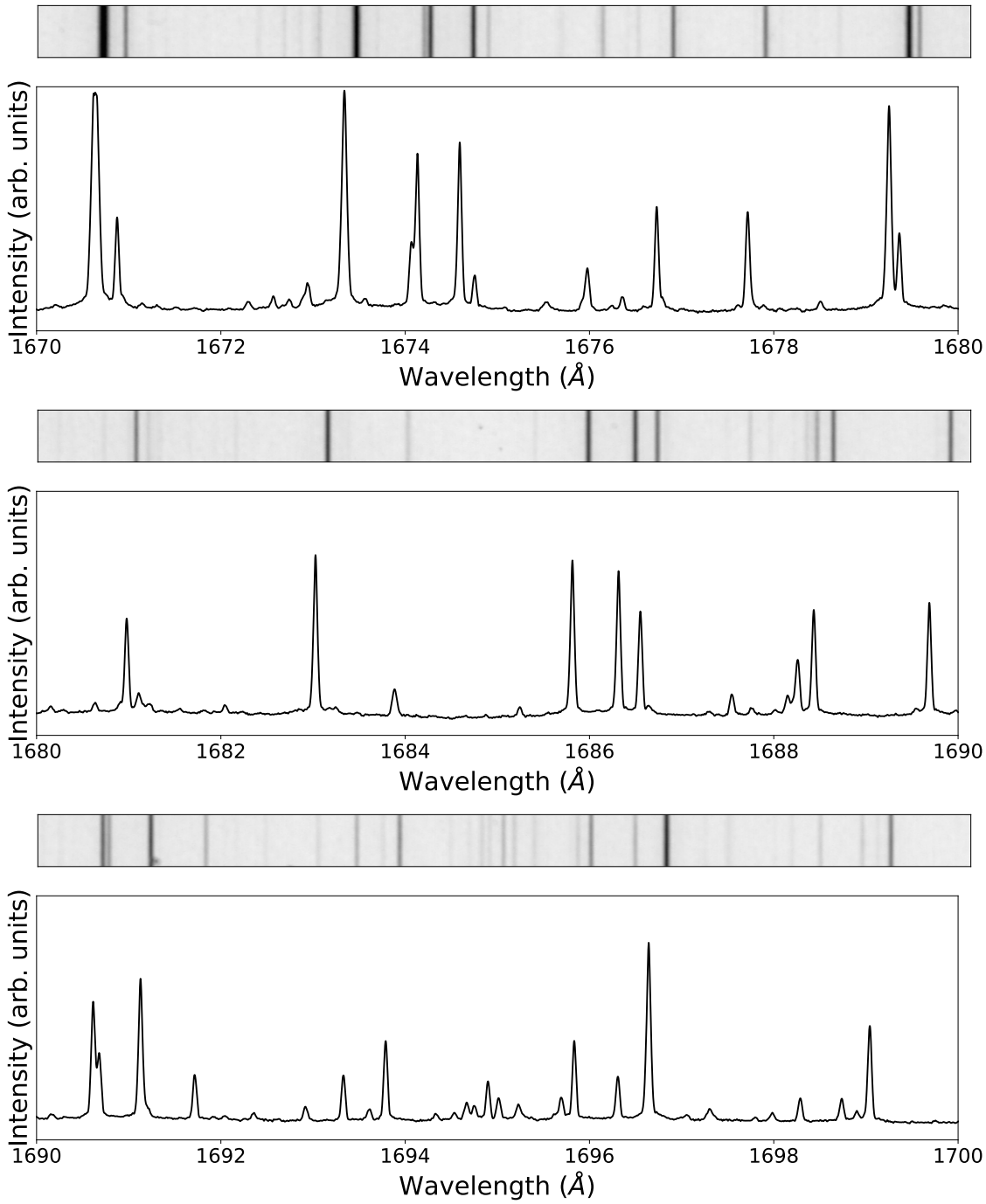


Image x1015_plate2b, Track 5.3, 5-minute exposure (continued)

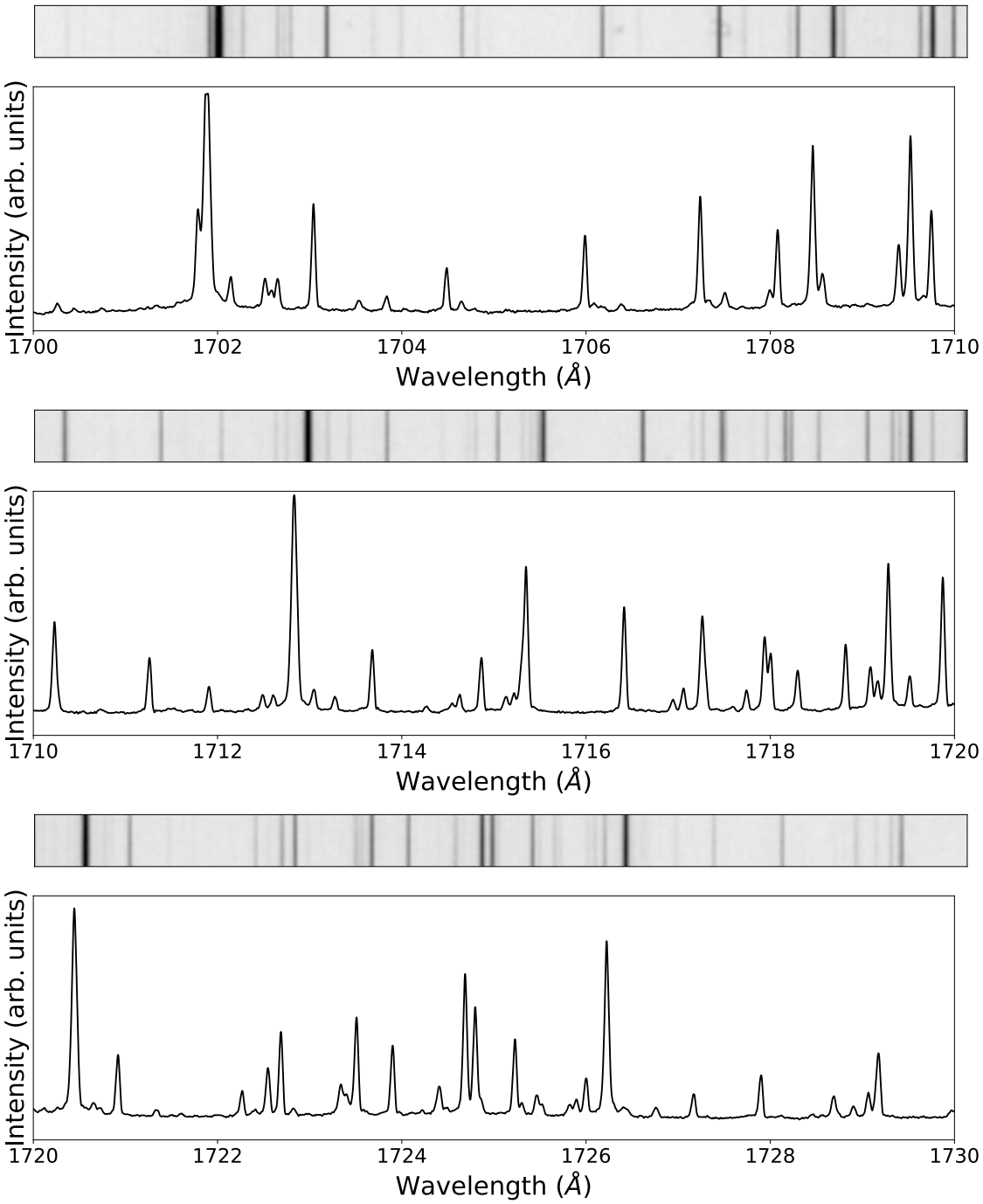


Image x1015_plate2b, Track 5.3, 5-minute exposure (continued)

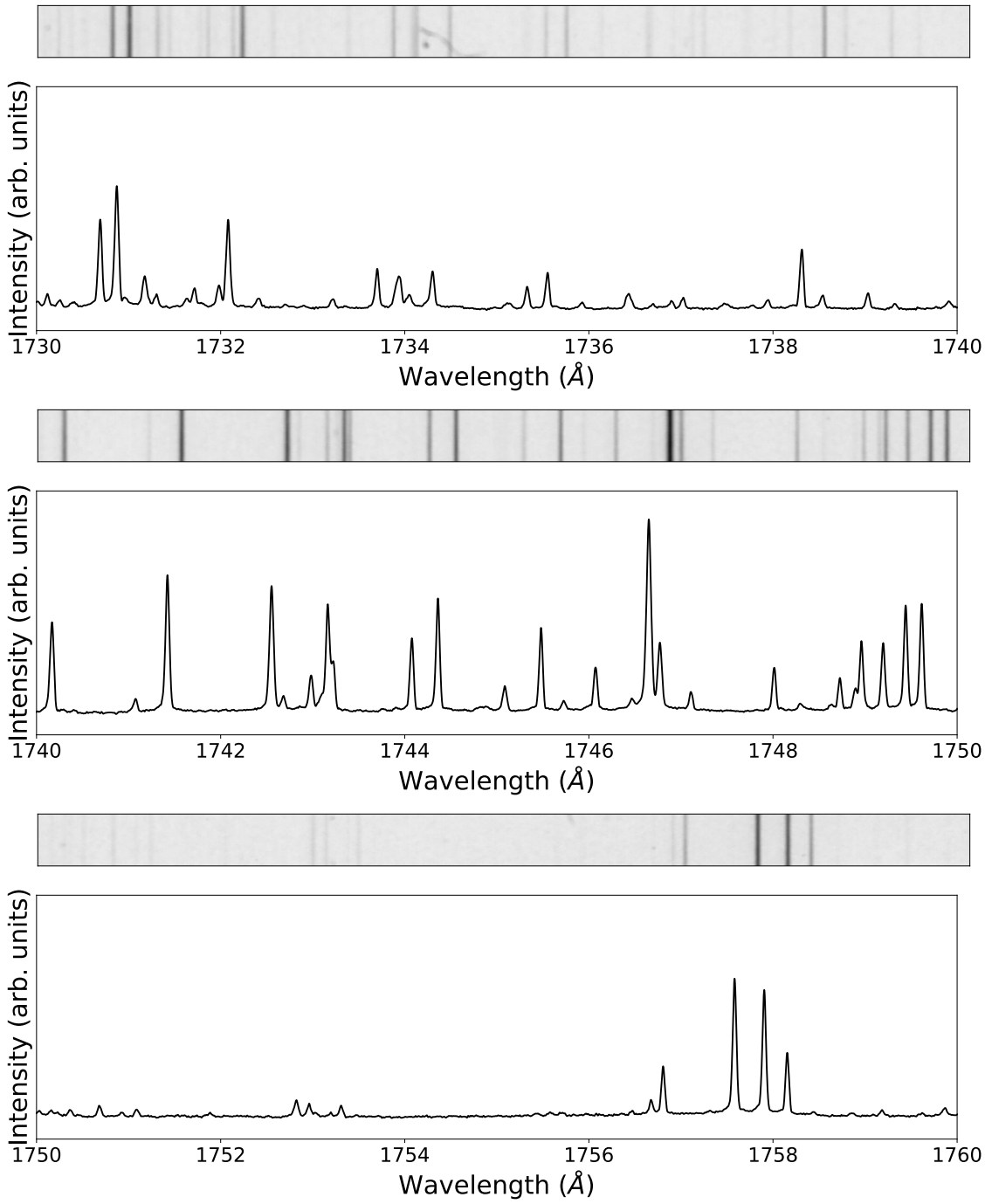


Image x1015_plate2b, Track 5.3, 5-minute exposure (continued)

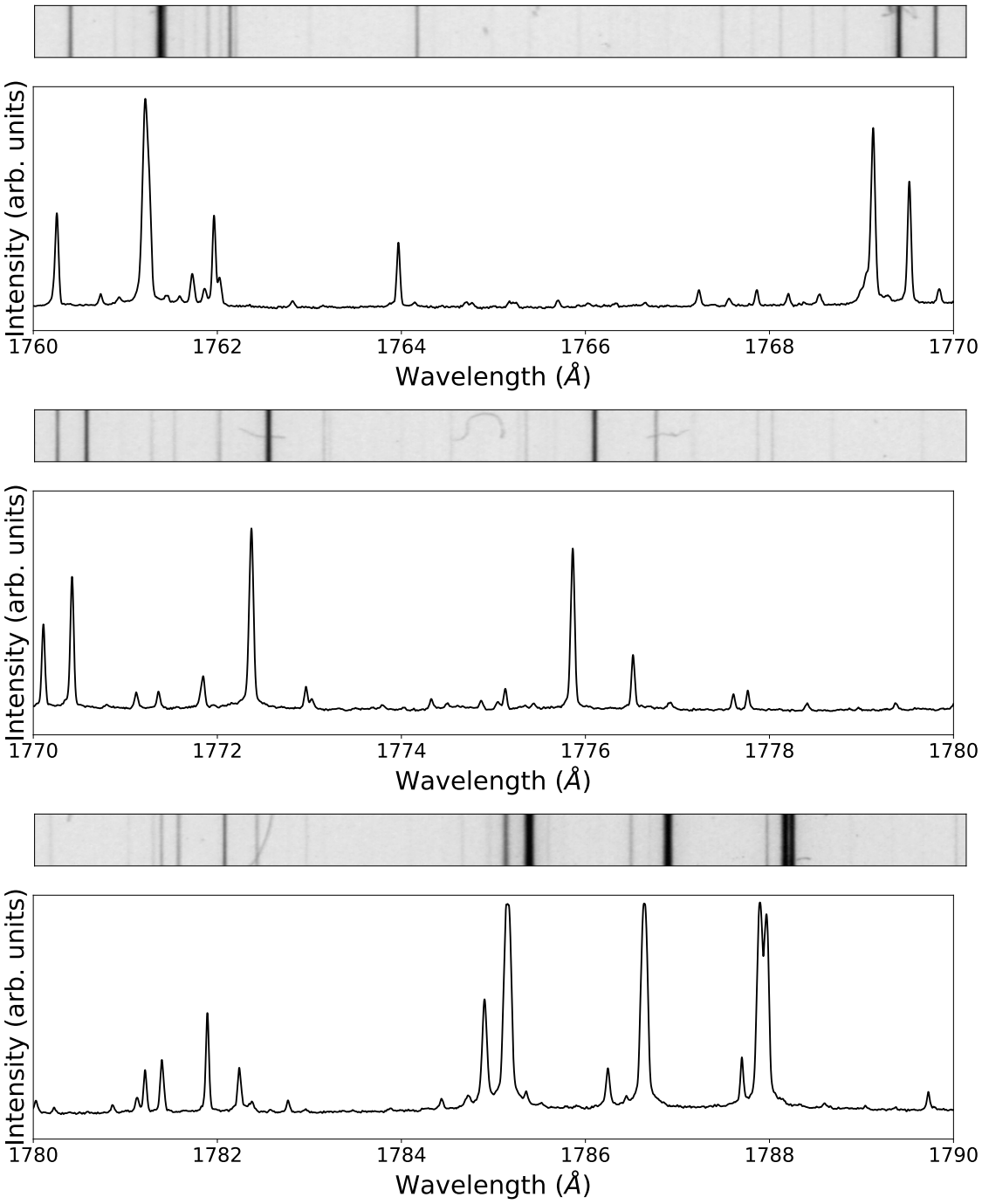
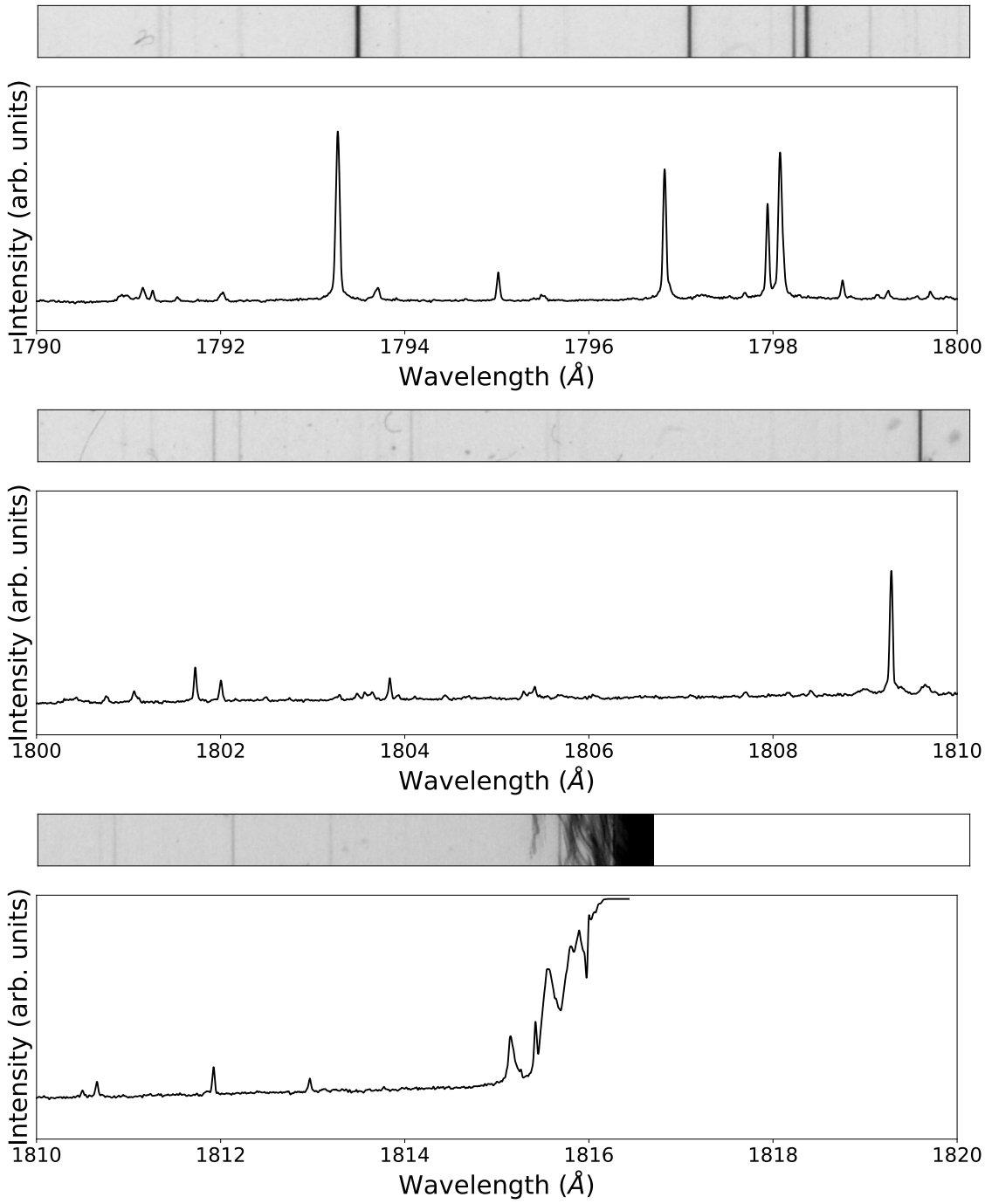


Image x1015_plate2b, Track 5.3, 5-minute exposure (continued)



F.10 Image x1015_plate2b, Track 5.3, 45-minute exposure

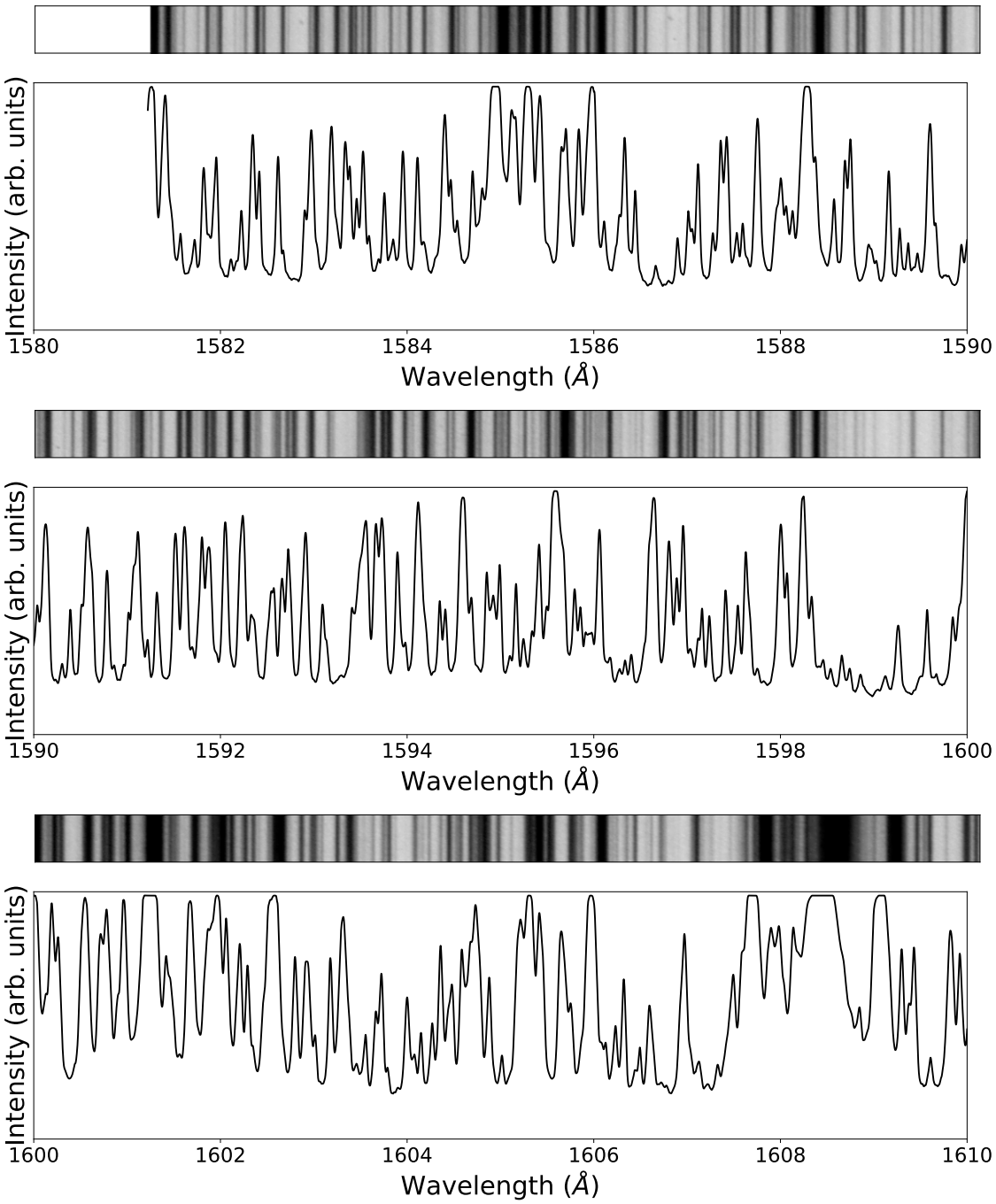


Image x1015_plate2b, Track 5.3, 45-minute exposure (continued)

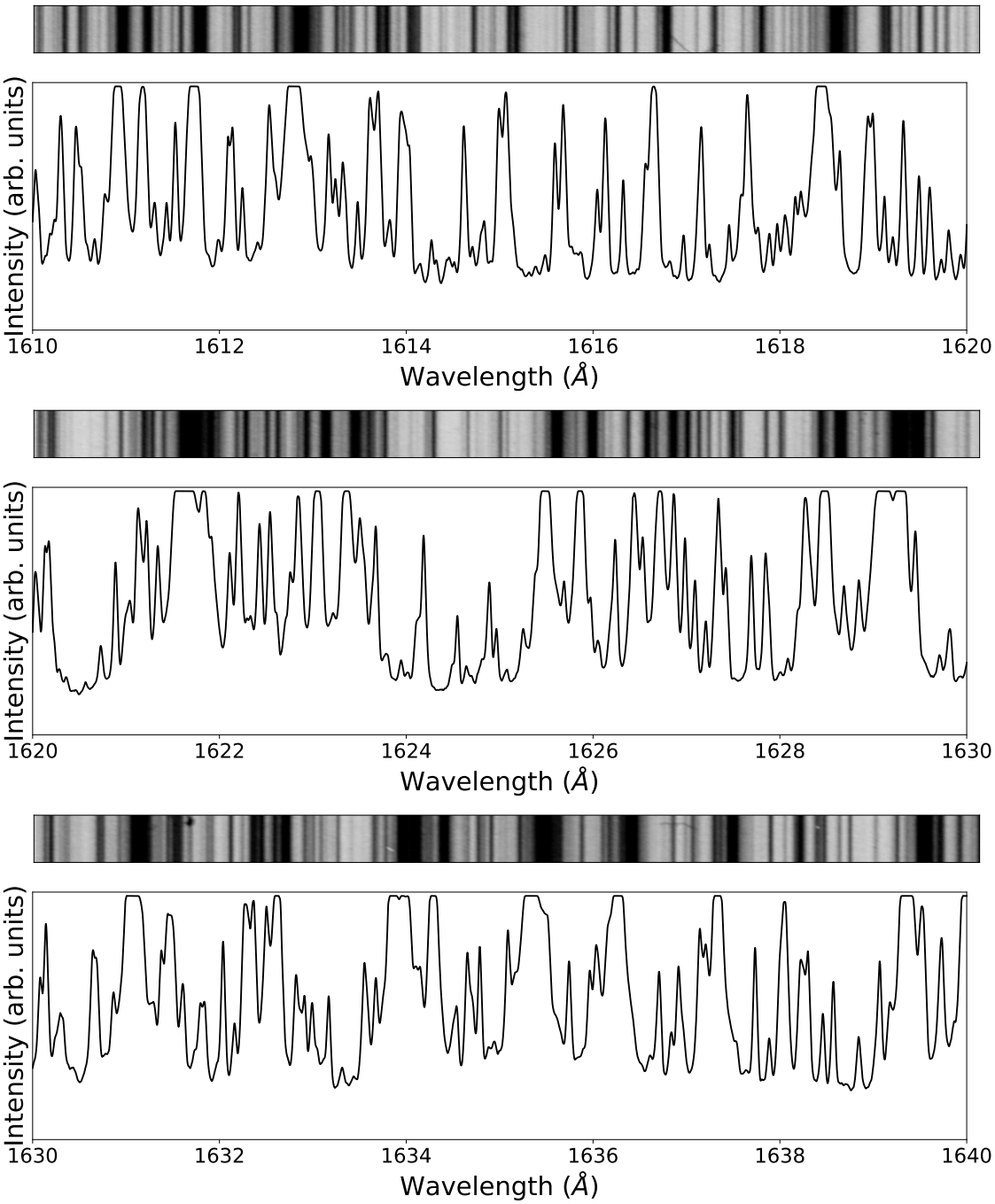


Image x1015_plate2b, Track 5.3, 45-minute exposure (continued)

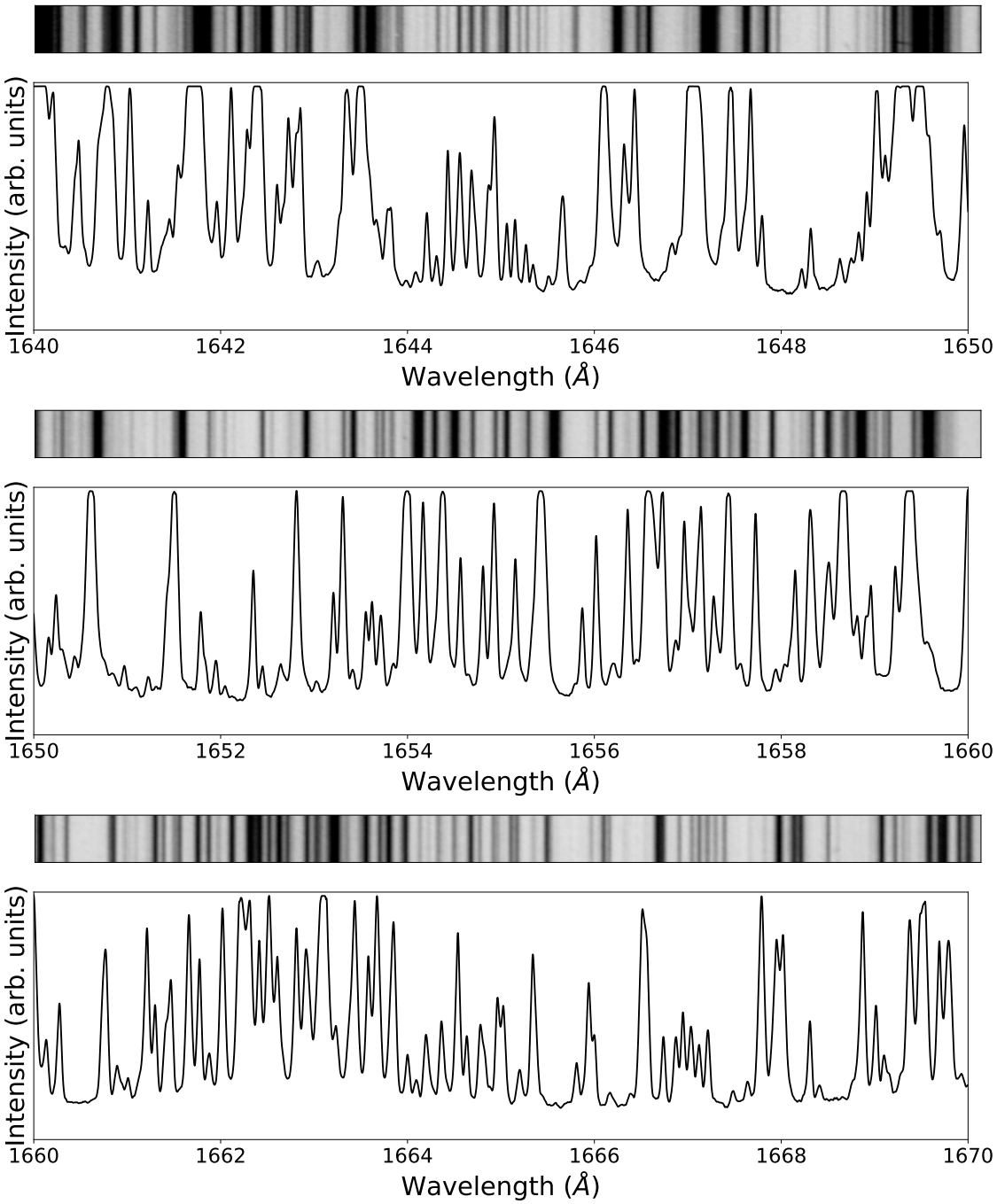


Image x1015_plate2b, Track 5.3, 45-minute exposure (continued)

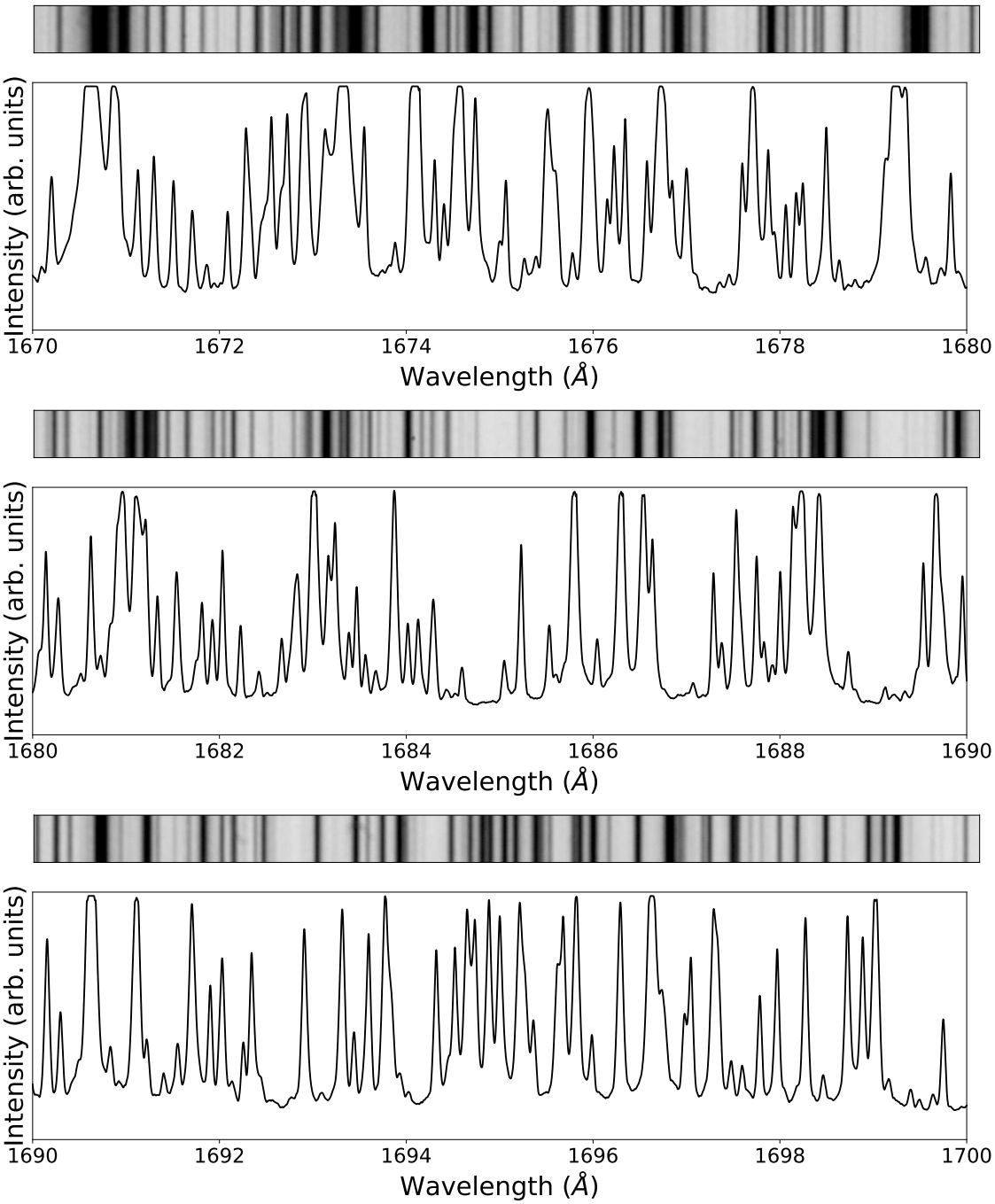


Image x1015_plate2b, Track 5.3, 45-minute exposure (continued)

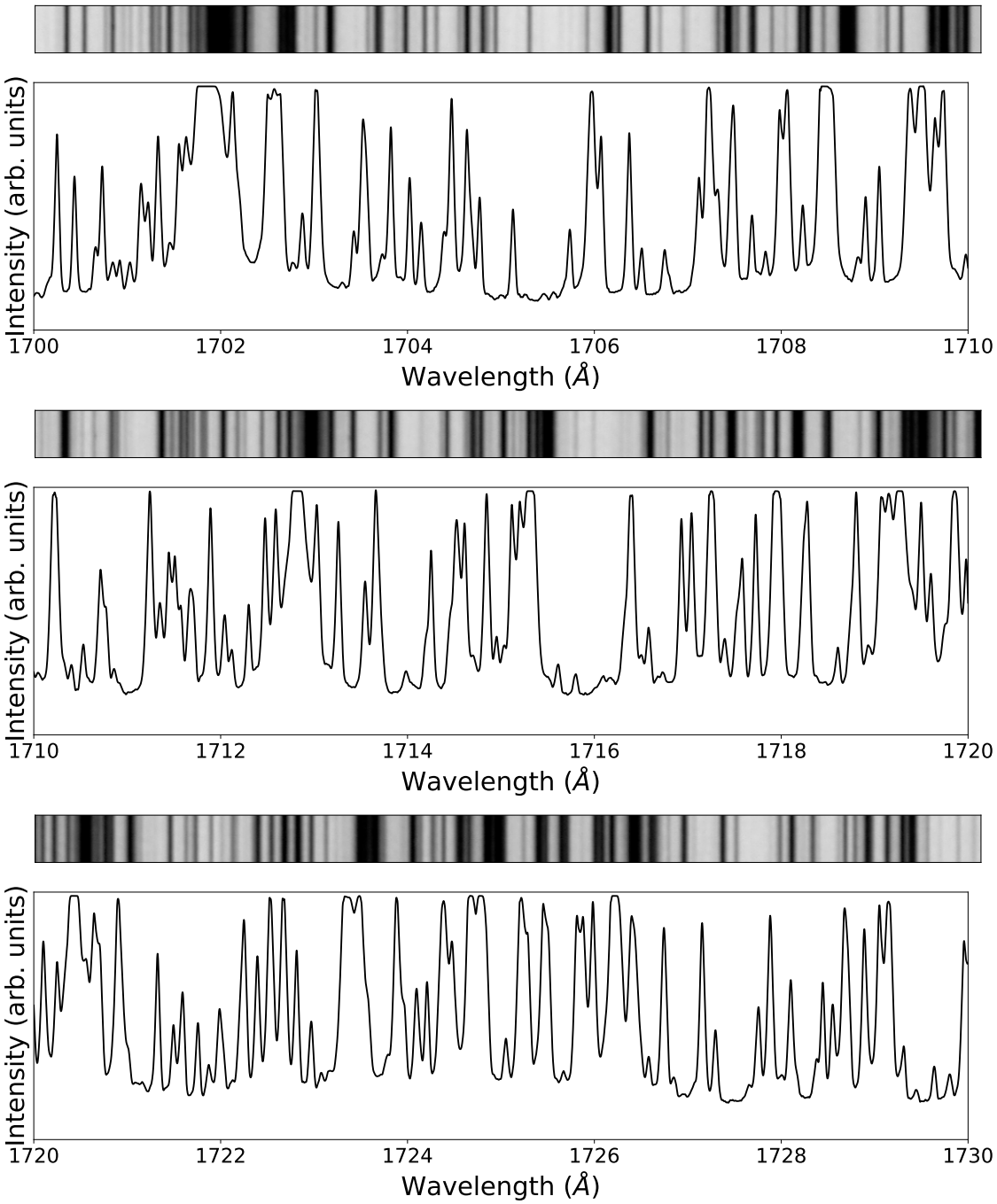


Image x1015_plate2b, Track 5.3, 45-minute exposure (continued)

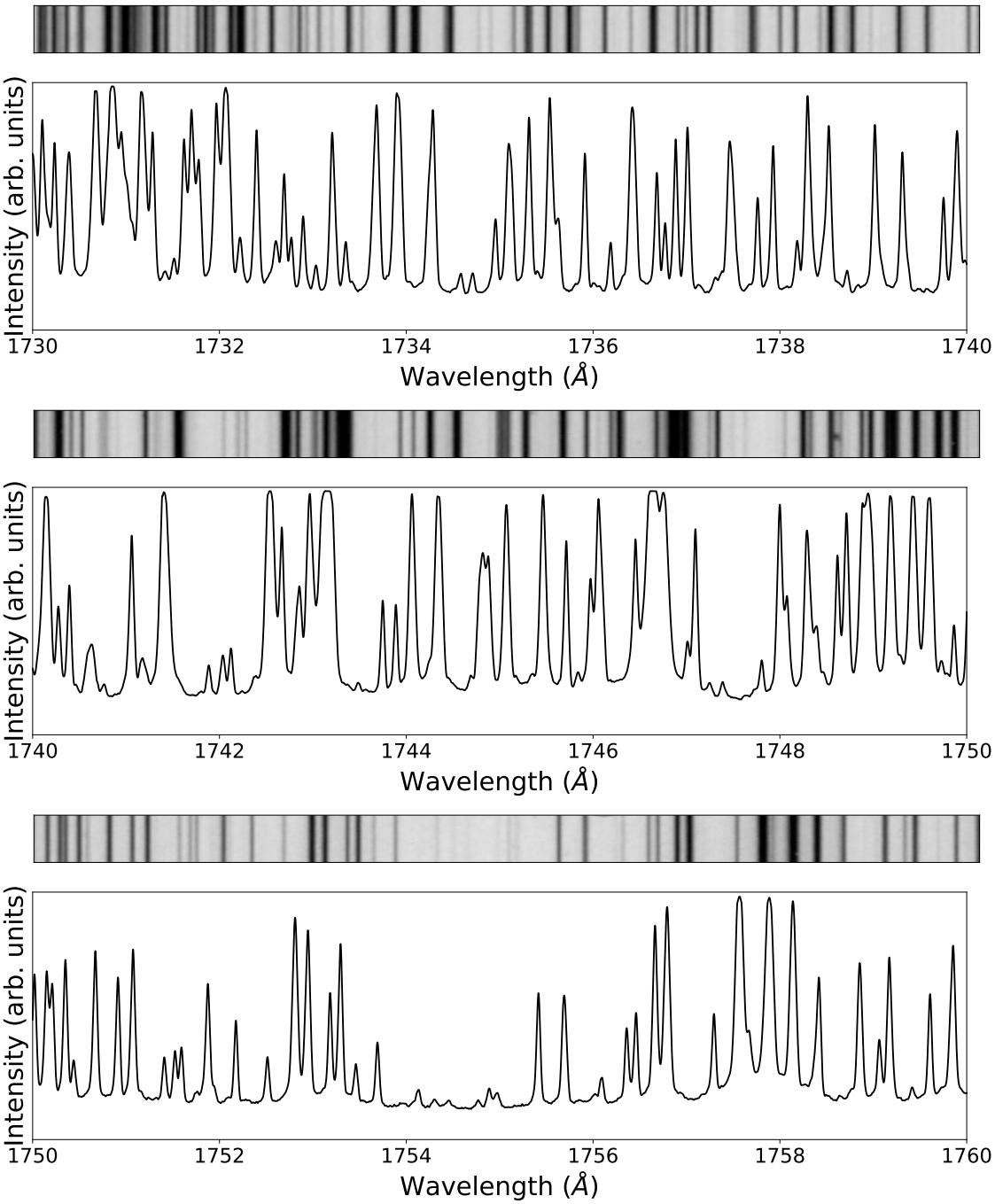


Image x1015_plate2b, Track 5.3, 45-minute exposure (continued)

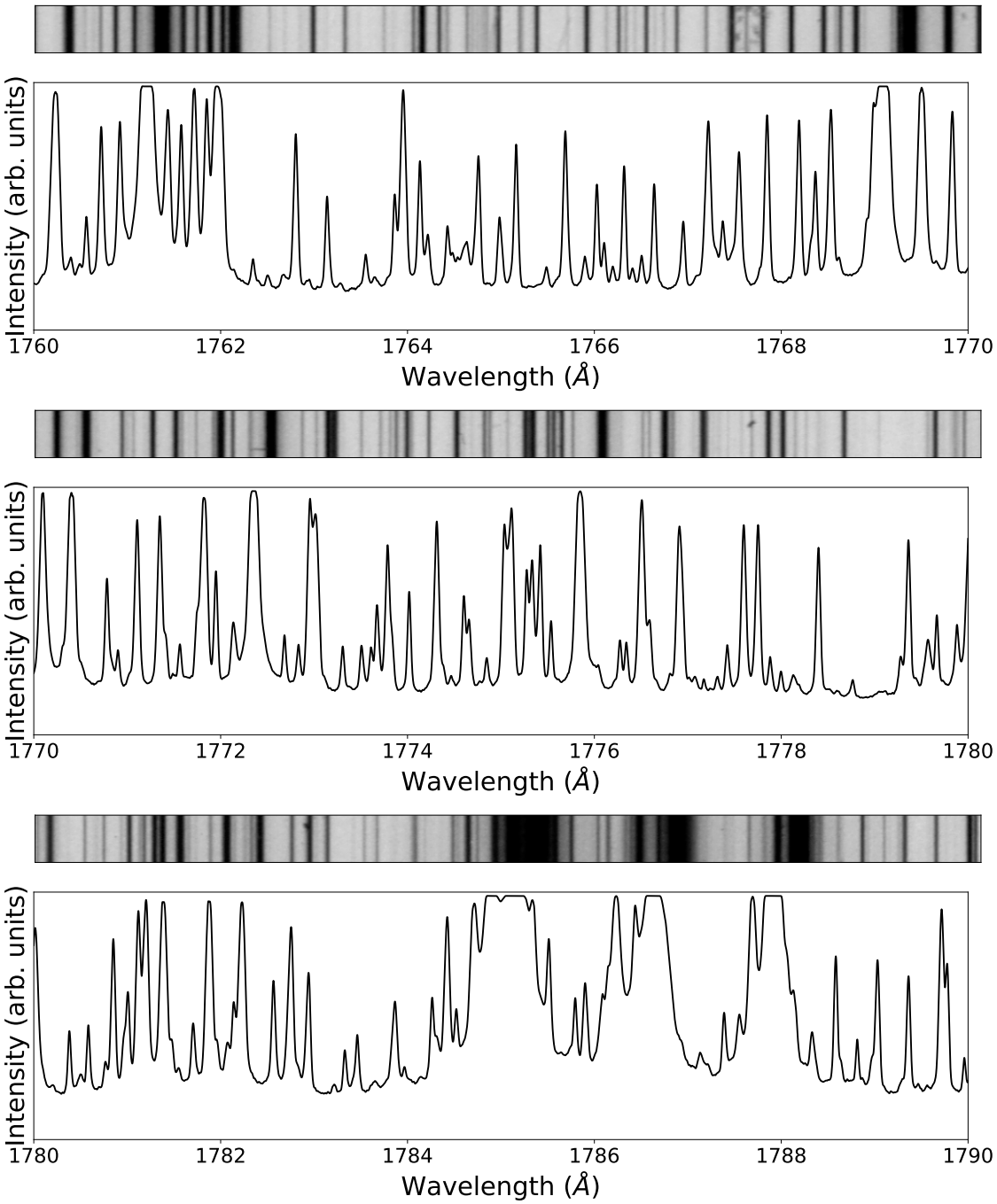


Image x1015_plate2b, Track 5.3, 45-minute exposure (continued)

